



Alshibane, Ihfaf (2018) *Phase transformations of ternary carbides, nitrides and carbonitrides*. PhD thesis.

<https://theses.gla.ac.uk/30702/>

Copyright and moral rights for this work are retained by the author

A copy can be downloaded for personal non-commercial research or study, without prior permission or charge

This work cannot be reproduced or quoted extensively from without first obtaining permission in writing from the author

The content must not be changed in any way or sold commercially in any format or medium without the formal permission of the author

When referring to this work, full bibliographic details including the author, title, awarding institution and date of the thesis must be given

Enlighten: Theses

<https://theses.gla.ac.uk/>
research-enlighten@glasgow.ac.uk



University
of Glasgow

Phase Transformations of Ternary Carbides, Nitrides and Carbonitrides

Ihfaf Alshibane

A thesis submitted to the University for the Degree of
Doctor of Philosophy

Supervisor: Professor Justin Hargreaves

School of Chemistry
College of Science and Engineering
University of Glasgow

May 2018

Dedication

To My Parents and My Family

Abstract

The development of novel efficient catalytic materials to improve the efficiency of industrial processes has been the driving force for many academic and industrial studies. The general approach adopted to enhance the activity of a given catalytic formulation is usually based on enhancing the structural and structural properties (e.g. crystal size and surface area) by adopting new synthesis methods, by supporting the active phase or by modifying the reactivity of the parent materials by adding dopants. However, in a less studied approach, it has been shown that the presence of interstitial species such as carbon or nitrogen can modify the electronic structure of parent metals apparently conferring, in the case of systems such as molybdenum carbide, properties akin to precious metals. This approach allows not just improvement of the catalytic activity in an incremental manner but also the design entirely new catalytic formulations. In this context, the effect of the interstitial elements carbon and nitrogen upon the activity of a range binary and ternary molybdenum based materials for ammonia synthesis and methane cracking has been investigated within this thesis.

The performance of $\text{Co}_3\text{Mo}_3\text{N}$, $\text{Co}_3\text{Mo}_3\text{C}$, and $\text{Co}_6\text{Mo}_6\text{C}$ for ammonia synthesis has been compared. Depending on the chemical composition, significant difference in catalytic activity was apparent. In contrast to $\text{Co}_3\text{Mo}_3\text{N}$, which is active at 400 °C, $\text{Co}_3\text{Mo}_3\text{C}$ was found to be only active at a reaction temperature of 500 °C. Furthermore, *in-situ* NPD revealed that the catalytic activity of ternary cobalt molybdenum systems is associated with the presence of N in the 16c Wyckoff crystallographic site. $\text{Co}_6\text{Mo}_6\text{C}$ was found to be inactive under the conditions tested.

The same comparison between the chemical composition and the catalytic activity has been made in the context of methane cracking. Although all the prepared materials (i.e. $\text{Co}_3\text{Mo}_3\text{N}$, $\text{Co}_6\text{Mo}_6\text{N}$, $\text{Co}_3\text{Mo}_3\text{C}$, and $\text{Co}_6\text{Mo}_6\text{C}$) displayed catalytic activity, differences as a function of chemical composition were observed. Among the evaluated catalysts, the $\text{Co}_6\text{Mo}_6\text{N}$ sample showed the highest activity. However, *in-situ* and post-reaction analysis revealed a significant phase transformation during reaction which explains the differences in terms of catalytic reactivity.

In summary, this thesis details a comparison between the catalytic performance of a range of binary and ternary molybdenum based materials presenting different chemical

compositions. Particular attention has been directed towards the role of, and the interconversion between, lattice C and N species with the intention of elucidating their influence upon catalytic behaviour.

Table of Contents

Title page	
Dedication	2
Abstract	i
Table of Contents	iii
Table of Tables	vi
Table of Figures	viii
Table of equations.....	xvi
Acknowledgement	xvii
Author's Declaration	xviii
Definitions/Abbreviations	xix
Publications	xx
Chapter 1. Thesis summary.....	1
Chapter 2. Experimental techniques	3
2.1 Material synthesis	3
2.1.1 Binary compounds.....	3
2.1.2 Ternary compounds.....	4
2.2 Reactor design	5
2.2.1 Ammonolysis reactor	5
2.2.2 Carburisation and reduction reactor	6
2.2.3 Ammonia synthesis reactor	7
2.2.4 Methane cracking reactor	7
2.3 Catalyst characterisation	8
2.3.1 Gas chromatography (GC-TCD)	8
2.3.2 Thermogravimetric analysis with mass spectrometry (TGA-MS).....	9
2.3.3 Powder neutron diffraction (PND)	9
2.3.4 Powder X-ray diffraction (PXRD)	10
2.3.5 Hot stage powder X-ray diffraction (HSPXRD)	10
2.3.6 Thermal gravimetric analysis (TGA).....	11
2.3.7 Elemental analysis (CHN).....	11
2.3.8 Scanning electron microscopy (SEM) and energy dispersive X-ray spectroscopy (EDXS).....	11
2.3.9 Surface area measurement (BET).....	12
2.3.10 Raman spectroscopy	12
2.3.11 Fourier transform infrared spectroscopy (FTIR).....	12
2.3.12 Transmission electron microscopy (TEM) and high resolution transmission electron microscopy (HRTEM)	13

Chapter 3. Carbide and nitride transformation sequences.....	14
3.1 Introduction.....	14
3.1.1 Metal carbides and nitrides.....	14
3.1.2 Crystal structure and composition	15
3.1.3 Synthesis of binary molybdenum nitrides and carbides	16
3.1.4 Synthesis of ternary cobalt molybdenum nitrides and carbides	19
3.1.5 Activity and reactivity of ternary CoMo nitrides and carbides	20
3.2 Results and discussion.....	23
3.2.1 Molybdenum trioxide (MoO_3).....	23
3.2.2 Gamma molybdenum nitride ($\gamma\text{-Mo}_2\text{N}$)	27
3.2.3 Beta molybdenum carbide ($\beta\text{-Mo}_2\text{C}$)	31
3.2.4 Alpha molybdenum carbide ($\alpha\text{-Mo}_2\text{C}$)	35
3.2.5 Cobalt molybdenum oxide ($\text{CoMoO}_{4.n}\text{H}_2\text{O}$).....	38
3.2.6 Cobalt molybdenum nitride ($\eta\text{-6 Co}_3\text{Mo}_3\text{N}$).....	48
3.2.7 Cobalt molybdenum nitride ($\eta\text{-12 Co}_6\text{Mo}_6\text{N}$).....	58
3.2.8 Cobalt molybdenum carbide ($\eta\text{-6 Co}_3\text{Mo}_3\text{C}$).....	68
3.2.9 Cobalt molybdenum carbide ($\eta\text{-12 Co}_6\text{Mo}_6\text{C}$).....	78
3.2.10 Investigation of the transformation of CoMo nitride to CoMo carbide	90
3.2.11 Investigation of the transformation of CoMo carbide to CoMo nitride ..	100
3.2.12 Pathways of reduction of $\text{Co}_3\text{Mo}_3\text{C}$ with H_2/Ar	116
3.2.13 Pathways of reduction of $\text{Co}_3\text{Mo}_3\text{N}$ with H_2/Ar	117
3.3 Conclusion	121
Chapter 4. Ammonia synthesis	124
4.1 Introduction.....	124
4.1.1 Importance of Ammonia in modern society	124
4.2 Results and discussion.....	130
I. Binary molybdenum nitride and carbides.....	130
4.2.1 Gamma molybdenum nitride ($\gamma\text{-Mo}_2\text{N}$)	130
4.2.2 Beta Molybdenum Carbide ($\beta\text{-Mo}_2\text{C}$).....	133
4.2.3 Alpha Molybdenum Carbide ($\alpha\text{-Mo}_2\text{C}$).....	137
II. Ternary molybdenum nitride and carbides.....	141
4.2.4 Dehydrated Cobalt molybdenum oxide (CoMoO_4)	141
4.2.5 Cobalt molybdenum nitride ($\eta\text{-6 Co}_3\text{Mo}_3\text{N}$).....	143
4.2.6 Cobalt molybdenum carbide ($\eta\text{-6 Co}_3\text{Mo}_3\text{C}$).....	147
4.2.7 Cobalt molybdenum carbide ($\eta\text{-12 Co}_6\text{Mo}_6\text{C}$).....	155
4.3 Conclusion	161
Chapter 5. Cracking of methane	162

5.1	Introduction.....	162
5.1.1	Hydrogen production	162
5.1.2	Carbon production	170
5.2	Results and discussion.....	178
5.2.1	Molybdenum trioxide (MoO_3).....	178
5.2.2	Cobalt molybdenum oxide (CoMoO_4)	185
5.2.3	Cobalt molybdenum nitride (η -6 structured $\text{Co}_3\text{Mo}_3\text{N}$).....	191
5.2.4	Cobalt molybdenum nitride (η -12 structured $\text{Co}_6\text{Mo}_6\text{N}$).....	197
5.2.5	Cobalt molybdenum carbide (η -6 structured $\text{Co}_3\text{Mo}_3\text{C}$).....	203
5.2.6	Cobalt molybdenum carbide (η -12 structured $\text{Co}_6\text{Mo}_6\text{C}$).....	209
5.2.7	Si_3N_4 and VN/ Si_3N_4 materials.....	217
5.3	Conclusion	229
Chapter 6.	Conclusions and further work.....	231
6.1	Conclusion	231
6.2	Further work.....	234
7	References.....	235
8	Appendix	247

Table of Tables

Table 3.1-1: Known carbides and nitrides within Groups IV, V, and VI. ¹⁰	15
Table 3.1-2: Approaches to synthesising binary molybdenum nitrides and carbides.....	17
Table 3.1-3: Temperature-programmed methods of synthesising binary molybdenum nitride and carbides.	18
Table 3.1-4: Temperature-programmed methods of synthesising ternary CoMo carbides and nitrides.	19
Table 3.2-1: PXRD refined crystallographic parameters for CoMoO ₄ .nH ₂ O.....	41
Table 3.2-2: PXRD refined parameters for CoMoO ₄ .nH ₂ O.....	41
Table 3.2-3: Crystallographic parameters of Co ₃ Mo ₃ N from PXRD and PND refined data.	51
Table 3.2-4: Co ₃ Mo ₃ N PXRD refined parameters.....	52
Table 3.2-5: Co ₃ Mo ₃ N PND refined parameters.	52
Table 3.2-6: Bond angles for Co ₃ Mo ₃ N from PXRD and PND refined data.	53
Table 3.2-7: Bond lengths for Co ₃ Mo ₃ N from PXRD and PND refined data.	53
Table 3.2-8: Crystallographic parameters of Co ₆ Mo ₆ N from PXRD and PND refined data.	61
Table 3.2-9: Co ₆ Mo ₆ N PXRD refined parameters.....	62
Table 3.2-10: Co ₆ Mo ₆ N PND refined parameters.	62
Table 3.2-11: Bond lengths for Co ₆ Mo ₆ N from PXRD and PND refined data.	63
Table 3.2-12: Bond angles for Co ₆ Mo ₆ N from PXRD and PND refined data.....	63
Table 3.2-13: Crystallographic parameters of Co ₃ Mo ₃ C from PXRD and PND refined data.	71
Table 3.2-14: Co ₃ Mo ₃ C PXRD refined parameters.	71
Table 3.2-15: Co ₃ Mo ₃ C PND refined parameters.....	71
Table 3.2-16: Selected atomic angles for Co ₃ Mo ₃ C from PXRD and PND refined data.	73
Table 3.2-17: Bond lengths for Co ₃ Mo ₃ C from PXRD and PND refined data.	73
Table 3.2-18: Crystallographic parameters of Co ₆ Mo ₆ C from PXRD and PND refined data.	81
Table 3.2-19: Co ₆ Mo ₆ C PND refined parameters.....	82
Table 3.2-20: Co ₆ Mo ₆ C PXRD refined parameters.	82
Table 3.2-21: Bond lengths for Co ₆ Mo ₆ C from PXRD and PND refined data.	83
Table 3.2-22: Bond angles for Co ₆ Mo ₆ C from PXRD and PND data.	83
Table 3.2-23: Structure parameters of Co ₃ Mo ₃ N after reaction with 60 ml min ⁻¹ of 20 vol. % CH ₄ in H ₂ at 632 °C obtained from neutron diffraction data.	95
Table 3.2-24: Structure parameters of Co ₆ Mo ₆ N after reaction with 60 ml min ⁻¹ of CH ₄ (BOC, 99.98%) at 678 °C obtained from neutron diffraction data.....	100
Table 3.2-25: Structure parameters of Co ₃ Mo ₃ C after 2 h of reaction with 60 ml min ⁻¹ of 75 vol. % H ₂ in N ₂ (BOC, 99.98%) at 500 °C obtained from neutron diffraction data.....	107
Table 3.2-26: Structure parameters of Co ₆ Mo ₆ C after reaction with 60 ml min ⁻¹ of N ₂ (BOC, 99.98%) at 695°C obtained from neutron diffraction data.....	114
Table 3.2-27: Structure parameters of Co ₆ Mo ₆ C after reaction with 60 ml min ⁻¹ of N ₂ (BOC, 99.98%) at 697°C obtained from neutron diffraction data.....	115
Table 3.2-28: Structure parameters of Co ₃ Mo ₃ N after 220 minutes of reaction with 60 ml min ⁻¹ of 75 vol.% H ₂ in Ar (BOC, 99.98%) at 820°C and cooling down to 394°C obtained from neutron diffraction data.....	120
Table 8.2-1: Evolution of the C/N occupancy of the 16c Wyckoff lattice site in Co ₃ Mo ₃ N as a function of reaction at different temperature with 60 ml min ⁻¹ of 20 vol. % CH ₄ in H ₂ .	

Fractional nitrogen and carbon content as determined from the Rietveld refinement against <i>in-situ</i> powder neutron diffraction data.....	248
Table 8.2-2: analysis of phase fractions of $\text{Co}_6\text{Mo}_6\text{N}$ and $\text{Co}_3\text{Mo}_3\text{C}$ present during the reaction.	249
Table 8.2-3: analysis of phase fractions of $\text{Co}_3\text{Mo}_3\text{N}$ and $\text{Co}_6\text{Mo}_6\text{N}$ present during the reaction.	250
Table 8.2-4: analysis of phase fractions of $\text{Co}_6\text{Mo}_6\text{C}$ and $\text{Co}_3\text{Mo}_3\text{N}$ present during the reaction.	251

Table of Figures

Figure 2.2-1: Schematic showing the ammonolysis reactor set-up.....	5
Figure 2.2-2: Schematic showing the carburisation and reduction reactor set-up.....	6
Figure 2.2-3: Schematic showing the ammonia synthesis reactor set-up.....	7
Figure 2.2-4: Schematic showing the methane cracking reactor set-up.....	8
Figure 2.3-1: Images of the <i>In-situ</i> cell used on POLARIS; (A) the cell prior attached to the collimator and (B) the cell and collimator attached to the stick, thermocouple, 90° bank (as inducted by yellow arrow); gas flows from the bottom to the top of the cell.....	9
Figure 2.3-2: Image of the sample holder of the hot stage instrument.....	11
Figure 2.3-3: Images of the transmission FTIR cell.....	13
Figure 3.1-1: Common crystal structures of molybdenum carbide and nitride catalyst. ¹⁹	16
Figure 3.1-2: Gibbs free energy as a function of the decomposition temperature of methane on cobalt and the hydrogenation of cobalt carbide to ethane. ⁴⁴	20
Figure 3.1-3: Temperature-programmed hydrogenation of surface carbon created by methane decomposition on a 3 wt.% silica-supported rhodium catalyst. ⁴³	21
Figure 3.2-1: Indexed PXRD pattern of molybdenum trioxide.....	23
Figure 3.2-2: Mo-O bonds in MoO ₃ catalyst.....	24
Figure 3.2-3: Raman spectrum of molybdenum trioxide.....	25
Figure 3.2-4: SEM images of molybdenum trioxide.....	26
Figure 3.2-5: EDX spectrum of molybdenum trioxide.....	26
Figure 3.2-6: Indexed PXRD pattern of gamma molybdenum nitride, (● trace peak of MoO ₂).	27
Figure 3.2-7: Unit cell of gamma molybdenum nitride.....	28
Figure 3.2-8: Raman spectrum of gamma molybdenum nitride.....	29
Figure 3.2-9: SEM images of gamma molybdenum nitride.....	30
Figure 3.2-10: EDX analysis of gamma molybdenum nitride.....	30
Figure 3.2-11: Indexed PXRD pattern of beta molybdenum carbide.....	31
Figure 3.2-12: Unit cell of β-Mo ₂ C. Mo1 and C1 refer to molybdenum and carbon atoms respectively.....	32
Figure 3.2-13: Raman spectrum of beta molybdenum carbide.....	33
Figure 3.2-14: SEM images of beta molybdenum carbide.....	33
Figure 3.2-15: EDX analysis of beta molybdenum carbide.....	34
Figure 3.2-16: Indexed PXRD pattern of alpha molybdenum carbide.....	35
Figure 3.2-17: Unit cell of alpha molybdenum carbide.....	36
Figure 3.2-18: Raman spectrum of alpha molybdenum carbide.....	37
Figure 3.2-19: SEM images of alpha molybdenum carbide.....	37
Figure 3.2-20: EDX analysis of alpha molybdenum carbide.....	38
Figure 3.2-21: Indexed PXRD pattern of hydrated cobalt molybdenum oxide.....	39
Figure 3.2-22: Indexed PXRD pattern of beta cobalt molybdenum oxide.....	40
Figure 3.2-23: PXRD refinement of CoMoO ₄ .nH ₂ O.....	42
Figure 3.2-24: Unit cell of hydrated cobalt molybdate.....	43
Figure 3.2-25: Unit cell of the anhydrous beta CoMoO ₄ phase.....	43
Figure 3.2-26: PXRD patterns of hydrated cobalt molybdenum oxide calcined under air (A) CoMoO ₄ .nH ₂ O; (B) 200 °C, 1h; (C) 300 °C, 1h; (D) 350 °C, 1h; (E) 400 °C, 1h; (F) 500 °C, 1h.(the peak at 2θ= 29° which is related to CoMoO ₄ .nH ₂ O which completely disappeared at 350 °C as highlighted by the red arrow).	44
Figure 3.2-27: TGA trace of CoMoO ₄ .nH ₂ O performed from room temperature up to 500 °C in air.....	45

Figure 3.2-28: Raman spectrum of dehydrated β -phase cobalt molybdenum oxide.....	46
Figure 3.2-29: SEM images of the hydrate $\text{CoMoO}_4 \cdot n\text{H}_2\text{O}$ phase.....	47
Figure 3.2-30: SEM images of the anhydrous beta CoMoO_4 phase.....	47
Figure 3.2-31: Indexed PXRD pattern of $\text{Co}_3\text{Mo}_3\text{N}$ showing indexed reflections.....	48
Figure 3.2-32: Fitted PXRD data profiles from Rietveld refinement for $\text{Co}_3\text{Mo}_3\text{N}$	49
Figure 3.2-33: Fitted PND data profiles from Rietveld refinement for $\text{Co}_3\text{Mo}_3\text{N}$	50
Figure 3.2-34: The Unit cell of $\text{Co}_3\text{Mo}_3\text{N}$ on the left hand side and Mo-N coordination on the right hand side by using VESTA software. Brown, grey, green and blue spheres represent the Mo, N, Co1 and Co2 respectively.....	54
Figure 3.2-35: Atomic coordination of Co1 (32e), Co2 (16d), Mo (48f) and N1 (16c) sites.....	55
Figure 3.2-36: Raman spectrum of $\text{Co}_3\text{Mo}_3\text{N}$	56
Figure 3.2-37: Typical SEM images of the $\text{Co}_3\text{Mo}_3\text{N}$ phase.	57
Figure 3.2-38: EDX analysis of $\text{Co}_3\text{Mo}_3\text{N}$	57
Figure 3.2-39: Indexed PXRD pattern of the $\text{Co}_6\text{Mo}_6\text{N}$ phase.	58
Figure 3.2-40: Fitted PXRD data profiles from Rietveld refinement for $\text{Co}_6\text{Mo}_6\text{N}$	59
Figure 3.2-41: Fitted PND data profiles from Rietveld refinement for $\text{Co}_6\text{Mo}_6\text{N}$	60
Figure 3.2-42: The Unit cell of $\text{Co}_6\text{Mo}_6\text{N}$ on the left hand side and Mo-N coordination on the right hand side drawn using VESTA software. Brown, grey, green and blue spheres represent the Mo, N, Co1 and Co2 respectively.....	64
Figure 3.2-43: Atomic coordination of Co1 (32e) and Co2 (16d), Mo (48f) and N2 (8a) sites.	65
Figure 3.2-44: Raman spectrum of $\text{Co}_6\text{Mo}_6\text{N}$	66
Figure 3.2-45: Representative SEM images of $\text{Co}_6\text{Mo}_6\text{N}$	67
Figure 3.2-46: EDX analysis of $\text{Co}_6\text{Mo}_6\text{N}$	67
Figure 3.2-47: Indexed PXRD patterns of $\text{Co}_3\text{Mo}_3\text{C}$	68
Figure 3.2-48: Fitted PXRD data profiles from Rietveld refinement for $\text{Co}_3\text{Mo}_3\text{C}$	69
Figure 3.2-49: Fitted PND data profiles from Rietveld refinement for $\text{Co}_3\text{Mo}_3\text{C}$	70
Figure 3.2-50: The Unit cell of $\text{Co}_3\text{Mo}_3\text{C}$ shown on the left hand side and the Mo-C coordination on the right hand side as determined using VESTA software. Brown, dark brown, green and blue spheres represent the Mo, C, Co1 and Co2 respectively.....	74
Figure 3.2-51: Atomic coordination of Co1 (32e) and Co2 (16d), Mo (48f) and C1 (16c) sites.	75
Figure 3.2-52: Raman spectrum of $\text{Co}_3\text{Mo}_3\text{C}$	76
Figure 3.2-53: SEM images of $\text{Co}_3\text{Mo}_3\text{C}$	77
Figure 3.2-54: EDX analysis of $\text{Co}_3\text{Mo}_3\text{C}$	77
Figure 3.2-55: Indexed PXRD pattern of $\text{Co}_6\text{Mo}_6\text{C}$	78
Figure 3.2-56: Fitted PXRD data profiles from Rietveld refinement for $\text{Co}_6\text{Mo}_6\text{C}$	79
Figure 3.2-57: Fitted PND data profiles from Rietveld refinement for $\text{Co}_6\text{Mo}_6\text{C}$	80
Figure 3.2-58: The Unit cell of $\text{Co}_6\text{Mo}_6\text{C}$ on the left hand side and Mo-C coordination on the right hand side drawn using VESTA software. Brown, dark brown, green and blue spheres represent the Mo, C, Co1 and Co2 respectively.	84
Figure 3.2-59: Atomic coordination of Co1 (32e) and Co2 (16d), Mo (48f) and C2 (8a) sites.	85
Figure 3.2-60: Comparison of PXRD patterns for 331C (red), 661C (green), 331N (blue) and 661N (black).	86
Figure 3.2-61: Raman spectrum of $\text{Co}_6\text{Mo}_6\text{C}$	86
Figure 3.2-62: Representative SEM images of $\text{Co}_6\text{Mo}_6\text{C}$	87
Figure 3.2-63: EDX analysis of $\text{Co}_6\text{Mo}_6\text{C}$	88
Figure 3.2-64: The TGA and derivative weight curves for $\text{Co}_3\text{Mo}_3\text{C}$ with 3:1 H_2/Ar up to 1000 $^\circ\text{C}$	89

Figure 3.2-65: The MS fragment ion curves for 15 m/z.	89
Figure 3.2-66: <i>Ex-situ</i> PXRD patterns collected upon reaction of 331N with 12 ml min ⁻¹ of 20 vol. % CH ₄ in H ₂ at various temperatures and applying a temperature ramp rate of 10 °C min ⁻¹ ; A (at room temperature), B (500 °C), C (600 °C), D (700 °C), E (700 °C, 2h), F (700 °C, 3h).	91
Figure 3.2-67: <i>In-situ</i> PND patterns collected at different temperatures for Co ₃ Mo ₃ N heated under 60 ml min ⁻¹ of 20 vol. % CH ₄ in H ₂	92
Figure 3.2-68: <i>In-situ</i> PND patterns collected at different temperature for Co ₃ Mo ₃ N heated under 60 ml min ⁻¹ of 20 vol. % CH ₄ in H ₂ with zoom in on d-spacing range between 1.9 and 2.3 Å.	92
Figure 3.2-69: The evolution of lattice parameters obtained from Rietveld refinements of <i>in-situ</i> PND data collected at different temperatures for Co ₃ Mo ₃ N heated under 60 ml min ⁻¹ of 20 vol. % CH ₄ in H ₂	94
Figure 3.2-70: Evolution of the C/N occupancy of the 16c Wyckoff lattice site in Co ₃ Mo ₃ N as a function of reaction with 60 ml min ⁻¹ of 20 vol. % CH ₄ in H ₂ at different temperatures. (■) Fractional carbon content and (●) fractional nitrogen content as determined from the Rietveld refinement against <i>in-situ</i> powder neutron diffraction data.	94
Figure 3.2-71: Fitted powder neutron diffraction profile from Rietveld refinement against powder neutron diffraction data for Co ₃ Mo ₃ N after reaction with 60 ml min ⁻¹ of 20 vol. % CH ₄ in H ₂ at 632 °C.	95
Figure 3.2-72: PXRD patterns of Co ₆ Mo ₆ N with 60 ml min ⁻¹ CH ₄ gas under various temperature and times on stream at A (at room temperature), B (678 °C), C (800 °C, 3h).	96
Figure 3.2-73: <i>In-situ</i> PND data of Co ₆ Mo ₆ N through heating with 60 ml min ⁻¹ CH ₄	97
Figure 3.2-74: Evolution of lattice parameters obtained from Rietveld refinements of <i>in-situ</i> PND data collected at different temperature for Co ₆ Mo ₆ N heated under 60 ml min ⁻¹ CH ₄	98
Figure 3.2-75: Investigation of phase fractions of Co ₆ Mo ₆ N (◆) and Co ₃ Mo ₃ C (●) present during reaction of Co ₆ Mo ₆ N with 60 ml min ⁻¹ CH ₄ at different temperature as determined from the Rietveld refinement against <i>in-situ</i> powder neutron diffraction data.	98
Figure 3.2-76: Fitted powder neutron diffraction profile from Rietveld refinement against powder neutron diffraction data for: Co ₆ Mo ₆ N after reaction with 60 ml min ⁻¹ of CH ₄ (BOC, 99.98%) at 678 °C.	99
Figure 3.2-77: PXRD patterns of Co ₃ Mo ₃ C after reaction with 3:1 H ₂ /N ₂ at 500 °C stopped at 0, 1, 2, 3 and 4 h on stream; A 331C (at room temperature), B (when reached 500 °C), C (500 °C, 1h), D (500 °C, 2h), E (500 °C, 3h), F (500 °C, 4h).	101
Figure 3.2-78: PXRD patterns of Co ₃ Mo ₃ C after reaction with 60 ml min ⁻¹ N ₂ at various temperatures and times on stream; A (at room temperature), B (500 °C, 5h), C (600 °C, 5h), D (700 °C, 3h).	102
Figure 3.2-79: <i>In-situ</i> PXRD patterns of Co ₃ Mo ₃ C with 60 ml min ⁻¹ N ₂ under various temperatures and times on stream; A (at room temperature), B (500 °C), C (600 °C, 1h), D (600 °C, 2h) and E (600 °C, 3h).	103
Figure 3.2-80: <i>In-situ</i> PND patterns collected at (A) different temperatures and (B) isothermal conditions at 500 °C over different durations for Co ₃ Mo ₃ C heated under 60 ml min ⁻¹ of 75 vol. % H ₂ in N ₂	104
Figure 3.2-81: <i>In-situ</i> PND patterns collected at isothermal conditions at 500 °C for Co ₃ Mo ₃ C heated under 60 ml min ⁻¹ of 75 vol. % H ₂ in N ₂ with an expanded on d-spacing range between 1.9 and 2.3 Å; A (427 °C), B (482 °C), C (500 °C), D (500 °C, 10 min), E (20 min), F (30 min), G (60 min), H (90 min), I (140 min), J (300 min).	105

Figure 3.2-82: Evolution of the lattice parameter taken from Rietveld refinements of <i>in-situ</i> PND data of $\text{Co}_3\text{Mo}_3\text{C}$ reacted with 60 ml min^{-1} 75 vol. % H_2 in N_2 (BOC, 99.98%) as function of temperature and time: (A) temperature programmed reaction and (B) isothermal conditions at $500 \text{ }^\circ\text{C}$	106
Figure 3.2-83: Evolution of the C/N occupancy of the 16c Wyckoff lattice site in $\text{Co}_3\text{Mo}_3\text{C}$ as a function of reaction time with 60 ml min^{-1} of 75 vol. % H_2 in N_2 at $500 \text{ }^\circ\text{C}$. (\blacktriangle) fractional carbon content and (\bullet) fractional nitrogen content as determined from the Rietveld refinement against PND data.	106
Figure 3.2-84: Fitted powder neutron diffraction profile from Rietveld refinement against powder neutron diffraction data for: $\text{Co}_3\text{Mo}_3\text{C}$ after 2 h of reaction with 60 ml min^{-1} of 75 vol. % H_2 in N_2 at $500 \text{ }^\circ\text{C}$	107
Figure 3.2-85: PXRD patterns of $\text{Co}_6\text{Mo}_6\text{C}$ with 60 ml min^{-1} N_2 under various temperature and time on stream; A (room temperature), B ($400 \text{ }^\circ\text{C}$, 3h), C ($500 \text{ }^\circ\text{C}$, 3h), D ($600 \text{ }^\circ\text{C}$, 3h), E ($700 \text{ }^\circ\text{C}$, 4h), F ($800 \text{ }^\circ\text{C}$, 8h).	108
Figure 3.2-86: <i>In-situ</i> PXRD patterns of $\text{Co}_6\text{Mo}_6\text{C}$ with 60 ml min^{-1} N_2 after various temperatures and times on stream; A (at room temperature), B ($600 \text{ }^\circ\text{C}$), C ($700 \text{ }^\circ\text{C}$, 1h), D ($700 \text{ }^\circ\text{C}$, 2h), E ($700 \text{ }^\circ\text{C}$, 3h).	109
Figure 3.2-87: <i>Ex-situ</i> PXRD patterns of $\text{Co}_6\text{Mo}_6\text{C}$ with 60 ml min^{-1} 75 vol. % H_2 in N_2 under various temperature and time on stream; A (at room temperature), B ($400 \text{ }^\circ\text{C}$, 5h), C ($500 \text{ }^\circ\text{C}$, 5h), D ($600 \text{ }^\circ\text{C}$, 1h), E ($700 \text{ }^\circ\text{C}$, 5h).	110
Figure 3.2-88: <i>In-situ</i> PND patterns collected at (A) different temperature and (B) isothermal conditions at $700 \text{ }^\circ\text{C}$ for $\text{Co}_6\text{Mo}_6\text{C}$ heated under 60 ml min^{-1} N_2	111
Figure 3.2-89: Evolution of the lattice parameter taken from Rietveld refinements of <i>in-situ</i> PND data of $\text{Co}_6\text{Mo}_6\text{C}$ reacted with 60 ml min^{-1} N_2 as function of temperature and time: (a) temperature programmed reaction and (b) isothermal conditions at $700 \text{ }^\circ\text{C}$	112
Figure 3.2-90: Investigation of phase fractions of $\text{Co}_6\text{Mo}_6\text{C}$ (\blacksquare) and $\text{Co}_3\text{Mo}_3\text{N}$ (\bullet) present during reaction of $\text{Co}_6\text{Mo}_6\text{C}$ with 60 ml min^{-1} N_2 as a function of temperature as determined from the Rietveld refinement against <i>in-situ</i> powder neutron diffraction data.	112
Figure 3.2-91: Fitted powder neutron diffraction profile from Rietveld refinement against powder neutron diffraction data for: $\text{Co}_6\text{Mo}_6\text{C}$ after reaction with 60 ml min^{-1} of N_2 (BOC, 99.98%) at $695 \text{ }^\circ\text{C}$	113
Figure 3.2-92: Fitted powder neutron diffraction profile from Rietveld refinement against powder neutron diffraction data for: $\text{Co}_6\text{Mo}_6\text{C}$ after reaction with 60 ml min^{-1} of N_2 (BOC, 99.98%) at $697 \text{ }^\circ\text{C}$	114
Figure 3.2-93: <i>Ex-situ</i> PXRD patterns of $\text{Co}_3\text{Mo}_3\text{C}$ with 60 ml min^{-1} 75 vol. % H_2 in Ar under various temperatures and times on stream; A (room temperature), B ($500 \text{ }^\circ\text{C}$), C ($700 \text{ }^\circ\text{C}$, 5h), D ($800 \text{ }^\circ\text{C}$, 4h), E ($850 \text{ }^\circ\text{C}$, 5h), F ($900 \text{ }^\circ\text{C}$, 5h).	116
Figure 3.2-94: <i>In-situ</i> PND patterns collected at (A) different temperature and (B) isothermal conditions at $820 \text{ }^\circ\text{C}$ for $\text{Co}_3\text{Mo}_3\text{N}$ heated under 60 ml min^{-1} of 75 vol. % H_2 in Ar.	117
Figure 3.2-95: Evolution of the lattice parameter taken from Rietveld refinements of <i>in-situ</i> PND data of $\text{Co}_3\text{Mo}_3\text{N}$ reacted with 60 ml min^{-1} 75 vol. % H_2 in Ar as function of temperature and time: (A) temperature programmed reaction and (B) isothermal conditions at $820 \text{ }^\circ\text{C}$ with mixed phases of (\bullet) 331N and (\blacksquare) 661N.	118
Figure 3.2-96: Investigation of phase fractions of $\text{Co}_6\text{Mo}_6\text{N}$ (\blacksquare) and $\text{Co}_3\text{Mo}_3\text{N}$ (\bullet) present during reaction of $\text{Co}_3\text{Mo}_3\text{N}$ with 60 ml min^{-1} 75 vol. % H_2 in Ar at $820 \text{ }^\circ\text{C}$ as determined from the Rietveld refinement against <i>in-situ</i> powder neutron diffraction data.	119
Figure 3.2-97: Fitted powder neutron diffraction profile from Rietveld refinement against powder neutron diffraction data for: $\text{Co}_3\text{Mo}_3\text{N}$ after 220 minutes of reaction with 60 ml	

min ⁻¹ of 75 vol.% H ₂ in Ar (BOC, 99.98%) at 820°C and cooling down to 394°C under same gas.	120
Figure 4.1-1: Trend in human population and the effect of Haber-Bosch process on the world population throughout the 20th Century. ⁸²	125
Figure 4.1-2 Calculated turnover frequencies for ammonia synthesis as a function of the adsorption energy of nitrogen. The synthesis conditions are 400 °C, 50 bar, gas composition H ₂ :N ₂ = 3:1 containing 5% NH ₃ . ¹⁰⁴	128
Figure 4.2-1: Conductivity Profile for γ-Mo ₂ N reacted with 75 vol. % H ₂ in N ₂ at A (400 °C for 4 h and 500 °C for 4 h) and B (500 °C for 4 h and 400 °C for 4 h).	131
Figure 4.2-2: PXRD pattern of the post-reaction of γ-Mo ₂ N: A (400 °C for 4 h and 500 °C for 4 h) and B (500 °C for 4 h and 400 °C for 4 h).	132
Figure 4.2-3: SEM images of the post-reaction of γ-Mo ₂ N: A (400 °C for 4 h and 500 °C for 4 h) and B (500 °C for 4 h and 400 °C for 4 h).	133
Figure 4.2-4: Conductivity Profile for β-Mo ₂ C reacted with 75 vol. % H ₂ in N ₂ at A (400 °C for 4 h and 500 °C for 4 h) and B (500 °C for 4 h and 400 °C for 4 h).	134
Figure 4.2-5: PXRD pattern of the post-reaction of β-Mo ₂ C: A (400 °C for 4 h and 500 °C for 4 h) and B (500 °C for 4 h and 400 °C for 4 h).	135
Figure 4.2-6: SEM images of the post-reaction of β-Mo ₂ C: A (400 °C for 4 h and 500 °C for 4 h) and B (500 °C for 4 h and 400 °C for 4 h).	136
Figure 4.2-7: Conductivity Profile for α-Mo ₂ C reacted with 75 vol. % H ₂ in N ₂ at A (500 °C for 4 h and 400 °C for 4 h) and B (400 °C for 4 h and 500 °C for 4 h).	137
Figure 4.2-8: PXRD patterns of the pre- and post-reaction of α-Mo ₂ C: A (as prepared), B (500 °C for 4 h and 400 °C for 4 h) and C (400 °C for 4 h and 500 °C for 4 h).	138
Figure 4.2-9: SEM images of the post-reaction of α-Mo ₂ C: A (500 °C for 4 h and 400 °C for 4 h) and B (400 °C for 4 h and 500 °C for 4 h).	139
Figure 4.2-10: Extended reaction conductivity profile for CoMoO ₄ under 75 vol. % H ₂ in N ₂ gas at 500 °C for 48 h. The inset corresponds to the expanded induction period.	141
Figure 4.2-11: PXRD patterns of pre- and post-reaction dehydrated CoMoO ₄ for A and B respectively.	142
Figure 4.2-12: Typical SEM images of the post-reaction dehydrated CoMoO ₄	143
Figure 4.2-13: Extended reaction conductivity profile for Co ₃ Mo ₃ N under 75 vol. % H ₂ in N ₂ gas at 500 °C for 48 h. The inset corresponds to the expanded initial portion.	144
Figure 4.2-14: PXRD patterns for the pre and post-reaction Co ₃ Mo ₃ N for A and B respectively.	145
Figure 4.2-15: Typical images of the post-reaction Co ₃ Mo ₃ N.	145
Figure 4.2-16: Comparison reaction profiles for Co ₃ Mo ₃ N under 75 vol. % H ₂ in N ₂ at 400 and 500 °C.	146
Figure 4.2-17: Extended reaction conductivity profile for Co ₃ Mo ₃ C under 75 vol. % H ₂ in N ₂ at 500 °C for 48 h. The insert corresponds to the expanded induction period.	147
Figure 4.2-18: PRDX patterns for pre- and post- reaction Co ₃ Mo ₃ C for A and B respectively.	148
Figure 4.2-19: SEM images of the post-reaction of Co ₃ Mo ₃ C reacted with 75 vol. % H ₂ in N ₂ under 500 °C and 48 h on stream.	149
Figure 4.2-20: HRTEM micrograph (A) of as-prepared Co ₃ Mo ₃ N, ¹¹¹ (B) of as-prepared Co ₃ Mo ₃ C, ¹¹⁰ (C) of pre-reaction Co ₃ Mo ₃ C and (D) of post-reaction of Co ₃ Mo ₃ C reacted with 75 vol. % H ₂ in N ₂ at 500 °C for 48 h.	150
Figure 4.2-21: Reaction profile for Co ₃ Mo ₃ C with 75 vol. % H ₂ in N ₂ under different temperatures and time on stream (400 °C, 4h), (500 °C, 2h), (600 °C, 1h), (700 °C, 1h). .	151

Figure 4.2-22: Extended reaction profile for $\text{Co}_3\text{Mo}_3\text{C}$ with 75 vol. % H_2 in N_2 under different temperatures and time on stream (400 °C, 8h), (500 °C, 4h) after pre-treatment for 2 hours at 700 °C.	152
Figure 4.2-23: Evolution of the $\text{Co}_3\text{Mo}_3\text{C}$ chemical composition after different reaction time with 60 ml min^{-1} of 75 vol. % H_2 in N_2 (BOC, 99.98%) at 500 °C. (▲) fractional carbon content and (●) fractional nitrogen content as determined by elemental analysis. The first data point corresponds to a material which was immediately cooled under the reaction flow upon attaining 500 °C.	154
Figure 4.2-24: SEM images of pre- and post-reaction $\text{Co}_3\text{Mo}_3\text{C}$ reacted with 75 vol. % H_2 in N_2 under 500 °C stopped at 0, 1, 2, 3 and 4 h on stream (labelled as A, B, C, D, E and F respectively).	155
Figure 4.2-25: Reaction conductivity profile for $\text{Co}_6\text{Mo}_6\text{C}$ under 75 vol. % H_2 in N_2 at 500 °C for 48 h.	156
Figure 4.2-26: PRDX patterns for the pre and post-reaction $\text{Co}_6\text{Mo}_6\text{C}$ for A and B respectively.	156
Figure 4.2-27: Typical SEM images of the post-reaction of $\text{Co}_6\text{Mo}_6\text{C}$ reacted with 75 vol. % H_2 in N_2 under 500 °C and 48 h on stream.	157
Figure 4.2-28: The rates of ammonia synthesis of CoMoO_4 , $\text{Co}_3\text{Mo}_3\text{N}$, $\text{Co}_3\text{Mo}_3\text{C}$, $\text{Co}_6\text{Mo}_6\text{C}$ at 500 °C for 48 h.	158
Figure 5.1-1: Schematic representation of various methods of activating methane. ¹¹⁸ ...	163
Figure 5.1-2: Graphical representation of the bulk of literature data on catalysts, preferred temperature range and carbon products related to catalytic methane decomposition reaction. Catalysts: 1—Ni-based, 2—Fe-based, 3—carbon-based, 4—summary of data related to Co, Ni, Fe, Pd, Pt, Cr, Ru, Mo, W catalysts, 5—non-catalytic decomposition. Carbon products: CF—carbon filaments, TC—turbostratic carbon, GC—graphitic carbon, AmC—amorphous carbon. ¹²⁷	165
Figure 5.1-3: Theoretical model of fouling, crystallite encapsulation and pore plugging of a supported metal catalyst due to carbon deposition. ¹⁵⁴	168
Figure 5.1-4: Two theoretical models for crystallite growth due to sintering by (A) atomic migration or (B) crystallite migration. ¹⁵⁴	169
Figure 5.1-5: Schematic representation of an amorphous carbon (A) ¹⁵⁷ and a graphitic carbon (B) ¹⁵⁸ structures.	170
Figure 5.1-6: Schematic representation of the single-wall and multi-wall carbon nanotubes. ¹⁶¹	171
Figure 5.1-7: HRTEM images of the deposited carbon on the Fe/MgO catalysts. ¹⁶²	172
Figure 5.1-8: HRTEM images of the both tip and base growth types of CNTs. ¹⁷²⁻¹⁷³	172
Figure 5.1-9: Schematic representation of the tip and base growth mechanisms of CNTs. ¹⁷⁶	173
Figure 5.1-10: TEM and schematic representations of the (A) platelet, (B) herringbone, and (C) ribbon structure of CNFs. ¹⁷⁹	174
Figure 5.1-11: Schematic representation of the growth mechanisms of CNFs (A) and CNTs (B). ¹¹⁶	175
Figure 5.1-12: HRTEM images of the carbon nano-onion formed from methane cracking over Ni/Al catalyst, (A) metal particle-filled core and (B) hollow core. ¹⁸²	176
Figure 5.1-13: Schematic illustration of the growth processes of the carbon-encapsulated catalytic particles and hollow carbon onions by CVD. ¹⁸³	177
Figure 5.2-1: Hydrogen formation rate as a function of time on stream for CH_4 cracking over the MoO_3 catalyst at 800 °C. The solid line is a guide for the eye.	178

Figure 5.2-2: FTIR analysis of gas phase products from MoO ₃ with CH ₄ /N ₂ (A) background of the gas; (B) 800 °C; (C) 800 °C, 12 min; (D) 800 °C, 25 min; (E) 800 °C, 36 min; (F) 800 °C, 50 min; (G) 800 °C, 70 min; (H) 800 °C, 90 min.	179
Figure 5.2-3: Indexed PXRD pattern of post-reaction MoO ₃ material.	180
Figure 5.2-4: TGA trace and derivative weight of post-reaction MoO ₃ under air up to 1000 °C.	181
Figure 5.2-5: EDX analysis of post-reaction MoO ₃ catalyst.	182
Figure 5.2-6: SEM images of pre and post-reaction MoO ₃ . (A, B pre-reaction at 2000, 4000 magnification), (C, D, E, F, G and H post-reaction at 2000, 4000, 10000, 10000, 25000 and 100000 magnification respectively).	183
Figure 5.2-7: Raman spectrum of post-reaction MoO ₃ material.	184
Figure 5.2-8: Hydrogen formation rate as a function of time on stream for CH ₄ cracking over CoMoO ₄ at 800 °C. The solid line is a guide for the eye.	185
Figure 5.2-9: FTIR analysis of gas phase products from the reacted CoMoO ₄ with CH ₄ /N ₂ (A) background of the gas, (B) 800 °C, (C) 800 °C, 20 min; (D) 800 °C, 50 min; and (E) 800 °C, 60 min.	186
Figure 5.2-10: PXRD pattern of the post-reaction CoMoO ₄ material (1, 2, 3 represent β-Mo ₂ C, α-Co and graphite respectively).	186
Figure 5.2-11: TGA trace and derivative weight profile of the post-reaction CoMoO ₄ under air in the range from room temperature to 1000 °C.	187
Figure 5.2-12: EDX analysis of post-reaction CoMoO ₄	188
Figure 5.2-13: SEM images of pre- and post-reaction CoMoO ₄ . (A, B pre-reaction at 2000, 4000 magnification), (C, D, E, F, G and H post-reaction at 2000, 4000, 25000, 25000, 100000 and 100000 magnification).	189
Figure 5.2-14: Raman spectrum of post-reaction CoMoO ₄	190
Figure 5.2-15: Hydrogen formation rate as a function of time on stream for CH ₄ cracking over the Co ₃ Mo ₃ N material at 800 °C. The solid line is a guide for the eye.	191
Figure 5.2-16: PXRD pattern of the post-reaction Co ₃ Mo ₃ N material [1 Co ₃ Mo ₃ C (03-065-7128), 2 Beta-Mo ₂ C (001-1188), 3 Graphite (003-0401), 4 α-Co (01-089-7093)].	192
Figure 5.2-17: TGA trace and derivative weight of post-reaction Co ₃ Mo ₃ N under air from RT to 1000 °C.	193
Figure 5.2-18: EDX analysis of post-reaction Co ₃ Mo ₃ N.	194
Figure 5.2-19: SEM images of pre (A, B) and post (C, D at low magnification and E, F, G, H at high magnification)-reaction Co ₃ Mo ₃ N.	195
Figure 5.2-20: Raman spectrum of post-reaction Co ₃ Mo ₃ N.	196
Figure 5.2-21: Hydrogen formation rate as a function of time on stream for CH ₄ cracking over Co ₆ Mo ₆ N.	197
Figure 5.2-22: PXRD pattern of the post-reaction Co ₆ Mo ₆ N material [1 Co ₃ Mo ₃ C (03-065-7128), 2 β-Mo ₂ C (001-1188), 3 Graphite (003-0401), 4 α-Co (01-089-7093)].	198
Figure 5.2-23: TGA trace and derivative weight of post-reaction Co ₆ Mo ₆ N under air up to 1000 °C.	199
Figure 5.2-24: EDX analysis of post-reaction Co ₆ Mo ₆ N.	200
Figure 5.2-25: SEM image of pre- and post-reaction Co ₆ Mo ₆ N.	201
Figure 5.2-26: Raman spectrum of post-reaction Co ₆ Mo ₆ N.	202
Figure 5.2-27: Hydrogen formation rate as a function of time on stream for CH ₄ over Co ₃ Mo ₃ C at 800 °C. (● First reaction run and ■ second reaction run) The solid line is a guide for the eye.	203
Figure 5.2-28: PXRD pattern of two attempts (A, B) of post-reaction Co ₃ Mo ₃ C [1 for Co ₃ Mo ₃ C (03-065-7128), 2 for Beta-Mo ₂ C (001-1188), 3 for Graphite (003-0401), 4 for α-Co (01-089-7093)].	204

Figure 5.2-29: TGA trace (A) and derivative weight (B) of post-reaction $\text{Co}_3\text{Mo}_3\text{C}$ under air up to 1000 °C.....	205
Figure 5.2-30: EDX analysis of post-reaction $\text{Co}_3\text{Mo}_3\text{C}$ for first reaction run.	206
Figure 5.2-31: SEM images of pre- and post-reaction $\text{Co}_3\text{Mo}_3\text{C}$	207
Figure 5.2-32: Raman spectrum of post-reaction $\text{Co}_3\text{Mo}_3\text{C}$: (A) first reaction run and (B) second reaction run.	208
Figure 5.2-33: Hydrogen formation rate as a function of time on stream for methane cracking over $\text{Co}_6\text{Mo}_6\text{C}$ at 800 °C. The solid line is a guide for the eye.	209
Figure 5.2-34: PXRD pattern of post-reaction $\text{Co}_6\text{Mo}_6\text{C}$ [1 $\text{Co}_3\text{Mo}_3\text{C}$ (03-065-7128), 2 Beta- Mo_2C (001-1188), 3 Graphite (003-0401) and 4 α -Co (01-089-7093)].	210
Figure 5.2-35: TGA trace and derivative weight of post-reaction $\text{Co}_6\text{Mo}_6\text{C}$ under air up to 1000 °C.	211
Figure 5.2-36: EDX analysis of post-reaction $\text{Co}_6\text{Mo}_6\text{C}$	212
Figure 5.2-37: SEM images of pre- and post-reaction $\text{Co}_6\text{Mo}_6\text{C}$	213
Figure 5.2-38: Raman spectrum of post-reaction $\text{Co}_6\text{Mo}_6\text{C}$	214
Figure 5.2-39: Hydrogen formation rate as a function of time on stream of VN/ Si_3N_4 at 800 °C. Similar values were obtained in a repeat run with the same mass of material; the solid line is a guide for the eye.	218
Figure 5.2-40: Hydrogen formation rate as a function of time on stream of Si_3N_4 at 800 °C. Similar values were obtained in a repeat run with the same mass of material; the solid line is a guide for the eye.	219
Figure 5.2-41: PXRD pattern of (A) pre- and (B) post- reaction Si_3N_4	220
Figure 5.2-42: PXRD pattern of (A) pre- and (B) post- reaction VN/ Si_xN_y	221
Figure 5.2-43: TGA trace and derivative weight of post-reaction VN/ Si_3N_4 under air up to 1000 °C.	221
Figure 5.2-44: TGA trace and derivative weight of post-reaction Si_3N_4 under air up to 1000 °C.	222
Figure 5.2-45: Raman spectrum of post-reaction Si_3N_4	223
Figure 5.2-46: Raman spectrum of post-reaction VN/ Si_3N_4	223
Figure 5.2-47: SEM images of (A) pre- and (B, C, D, E, F) post-reaction Si_3N_4	224
Figure 5.2-48: EDX analysis of pre-reaction Si_3N_4	225
Figure 5.2-49: EDX analysis of post-reaction Si_3N_4	225
Figure 5.2-50: SEM image of (A) pre- and (B, C, D, E and F for 4000, 10000, 10000, 25000 and 10000 magnification respectively) post-reaction VN/ Si_3N_4	227
Figure 5.2-51: EDX analysis of pre-reaction VN/ Si_3N_4	228
Figure 5.2-52: EDX analysis of post-reaction VN/ Si_3N_4	228

Table of equations

$3 \text{ H}_2 (\text{g}) + \text{N}_2 (\text{g}) \leftrightarrow 2 \text{ NH}_3 (\text{g})$	$(\Delta H^\ominus = -92 \text{ kJ mol}^{-1})$	Equation 4-1 ..126
$\text{CH}_4 + \text{H}_2\text{O} \rightarrow \text{CO} + 3\text{H}_2$	$(\Delta H_{298\text{K}}^\ominus = 206 \text{ kJ mol}^{-1})$	Equation 5-1164
$\text{CH}_4 + \text{CO}_2 \rightarrow 2\text{CO} + 2\text{H}_2$	$(\Delta H_{298\text{K}}^\ominus = 247 \text{ kJ mol}^{-1})$	Equation 5-2164
$\text{CH}_4 + \frac{1}{2} \text{ O}_2 \rightarrow \text{CO} + 2\text{H}_2$	$(\Delta H_{298\text{K}}^\ominus = -35 \text{ kJ mol}^{-1})$	Equation 5-3164
$\text{CH}_4 + x (\text{O}_2) + (2- 2x) \text{ H}_2\text{O} \leftrightarrow \text{CO}_2 + (4- 2x) \text{ H}_2$		Equation 5-4164
$\text{CH}_4 \rightarrow \text{C}_{(\text{s})} + 2\text{H}_2$	$(\Delta H_{298\text{K}}^\ominus = 75.6 \text{ kJ mol}^{-1})$	Equation 5-5 .165

Acknowledgement

First of all I am most grateful to Allah, the Great, for giving me the strength to finish this project.

Foremost I offer my sincerest appreciation to my supervisor. I would like to thank my main supervisor Professor Justin Hargreaves who has supported me throughout the duration of the PhD with his patience and knowledge, supervision and guidance. Without his help and encouragement I would not have reached this stage.

I owe a great deal of appreciation and gratitude to Dr. Heather Greer and Prof. Wuzong Zhou Zhou for carrying out TEM at the University of St. Andrews and Dr. Jose L. Rico from Universidad Michoacana de San Nicolas de Hidalgo, Michoacan, Mexico for carrying out SEM with high magnification. I also gratefully acknowledge the help of Prof. Andrew L Hector from University of Southampton for the provision of VN/Si_xN_y samples and his assistance with *in-situ* PND. I would like to thank all Rutherford Appleton Laboratory staff who helped in the collection of PND data.

I am thankful to my many colleagues for providing a stimulating and fun filled environment. My thanks go in particular to the Hargreaves and Jackson groups, for their encouragement during the good and difficult times, which kept me going.

Furthermore, I would like to thank all members of the research and the technical staff in the School of chemistry at University of Glasgow. Special thanks to Dr. Andrew McFarlane and Dr. Said Laassiri for their continued support at various stages of my PhD in the lab, Mrs. Kim Wilson and Mr. M. G. Reddy for CHN elemental analysis, Mr. Jim Gallagher for SEM assistance, Mr. Andrew Monaghan for help with the acquisition of BET and TGA data and Dr. Claire Wilson for her assistance with several matters related to XRD analysis.

Finally and most significantly, I would like to express my greatest appreciation to my family. They have always been my number one supporters and I know that wherever life brings me, I have them. Words will never be enough to express my love for them.

I appreciatively acknowledge the financial support from the Libyan government.

Author's Declaration

I declare that the information presented within this thesis which is submitted for the Degree of Philosophy represents my own work except where due acknowledgement is made to the contribution of others.

Signed: Ihfaf Alshibane

Date: May 2018

Definitions/Abbreviations

Table of Symbols, Abbreviations and nomenclature

Symbol	Definition
BET	Brunauer-Emmett-Teller (surface area)
EDX	Energy Dispersive X-ray Spectroscopy
a.u.	Arbitrary units
HRTEM	High Resolution Electron Microscopy
SEM	Scanning Transmission Electron Microscopy
PXRD	Powder X-ray Diffraction
α - MoO ₃	Orthorhombic molybdenum trioxide
β - Mo ₂ C	Hexagonal molybdenum carbide
α - Mo ₂ C	Face centered cubic molybdenum carbide
γ - Mo ₂ N	Face centered cubic molybdenum nitride
331C or η -6 Co ₃ Mo ₃ C	Face centered cubic Cobalt Molybdenum Carbide
661C or η -12 Co ₆ Mo ₆ C	Face centered cubic cobalt molybdenum carbide reduction phase
331N or η -6 Co ₃ Mo ₃ N	Face centered cubic cobalt molybdenum nitride
661N or η -12 Co ₆ Mo ₆ N	Face centered cubic Cobalt molybdenum nitride reduction phase
Co ₃ Mo ₃ C _x N _y	Face centered cubic cobalt molybdenum carbonitride
GC	Gas Chromatography
TCD	Thermal Conductivity Detection
PND	Powder Neutron Diffraction
PXRD	Powder X-ray Diffraction
TGA	Thermal Gravimetric Analysis
CHN	Carbon, Hydrogen and Nitrogen
FTIR	Fourier-Transform Infrared Spectroscopy
GSAG	Generalized Structure Analysis System
EXPGUI	Graphical User Interface for GSAG
ICSD	Inorganic Crystal Structure Database
JCPDS	Joint Committee on Powder Diffraction Standards
ToF	Time of Flight

Publications

- Alshibane, I.; Hargreaves, J. S. J.; Hector, A. L.; Levason, W.; McFarlane, A., Synthesis and methane cracking activity of a silicon nitride supported vanadium nitride nanoparticle composite. *Dalton Transactions* **2017**, 46 (27), 8782-8787.
- Alshibane, I.; Daisley, A.; Hargreaves, J. S. J.; Hector, A. L.; Laassiri, S.; Rico, J. L.; Smith, R. I., The Role of Composition for Cobalt Molybdenum Carbide in Ammonia Synthesis. *ACS Sustainable Chemistry & Engineering* **2017**, 5 (10), 9214-9222.
- MacDonald, L.; McGlynn, J. C.; Irvine, N.; Alshibane, I.; Bloor, L. G.; Rausch, B.; Hargreaves, J. S. J.; Cronin, L., Using earth abundant materials for the catalytic evolution of hydrogen from electron-coupled proton buffers. *Sustainable Energy & Fuels* **2017**, 1 (8), 1782-1787.
- Alshibane, I.; Laassiri, S.; Rico, J. L.; Hargreaves, J. S. J., Methane Cracking over Cobalt Molybdenum Carbides. *Catalyst Letters* **2018**, 148 (5), DOI 101007/s10562-018-2378-4.

Chapter 1. Thesis summary

From the advent of the industrial chemistry era, developing highly efficient and active materials capable of reactions has been of major interest. In the last decades, heterogeneous catalysis has been dominated by the use of metal and metal oxide based materials. However, to meet the increasingly challenging economic and environmental targets imposed by recent shifts in economic and environmental policies, attention has been directed towards the development of alternative catalyst families displaying better catalytic performance in order to improve the efficiency of chemical processes. In this context, the presence of interstitial species such as carbon or nitrogen has been argued to modify the electronic structure of parent metals conferring, in the case of systems such as molybdenum carbide, to these materials properties akin to precious metals. In this context, the role of the interstitial elements, carbon and/or nitrogen, in the activity of binary and ternary molybdenum based materials, has been explored within this thesis with particular emphasis being focussed upon the evolution of structural and textural properties during the catalytic reaction studies.

In this work particular attention has been directed towards the transformation pathways from nitride to carbide counterparts and vice-versa. The results of *in-situ* neutron diffraction and *in-situ* X-ray diffraction studies, presented in Chapter 3, pinpointed the important role of synthesis conditions on the transformation pathways. For instance, in the presence of hydrogen during the carburisation process of $\text{Co}_3\text{Mo}_3\text{N}$, using methane as source of carbon, the formation of an intermediate carbonitride phase $\text{Co}_3\text{Mo}_3\text{N}_{1-x}\text{C}_x$ without any phase segregation occurs. In contrast, the absence of hydrogen results in the presence of a binary phase intermediate stage ($\text{Co}_3\text{Mo}_3\text{N}$ and $\text{Co}_3\text{Mo}_3\text{C}$) before carburisation is complete. A similar observation was observed during the nitridation of $\text{Co}_3\text{Mo}_3\text{C}$ to $\text{Co}_3\text{Mo}_3\text{N}$. In presence of hydrogen and nitrogen, the nitridation process occurs via the formation of a carbonitride while in the presence of nitrogen only, a biphasic system is observed. The control of reaction temperature, time, atmosphere composition and initial precursors is of crucial importance for the preparation of monophasic carbide and nitride systems.

The Influence of composition of cobalt molybdenum based materials was studied in ammonia synthesis which is an important industrial process for atmospheric nitrogen

fixation. The performance of $\text{Co}_3\text{Mo}_3\text{N}$, $\text{Co}_3\text{Mo}_3\text{C}$, and $\text{Co}_6\text{Mo}_6\text{C}$ has been compared and the results are presented in Chapter 4. Depending upon the chemical composition, large differences in the catalytic behaviour was observed. In contrast to $\text{Co}_3\text{Mo}_3\text{N}$, which is active at 400 °C, a reaction temperature of 500 °C, preceded by an induction period, was necessary for the establishment of steady state activity for $\text{Co}_3\text{Mo}_3\text{C}$. During the induction period, nitridation of the $\text{Co}_3\text{Mo}_3\text{C}$ lattice was evidenced by *in-situ* neutron diffraction studies, and this process continued throughout the period of steady state reaction with the material transforming in composition towards pure $\text{Co}_3\text{Mo}_3\text{N}$. However, $\text{Co}_6\text{Mo}_6\text{C}$ was found to be inactive under the conditions tested. These observations demonstrate that ammonia synthesis activity in ternary cobalt molybdenum systems is associated with the presence of N in the 16c Wyckoff lattice site.

In Chapter 5, the catalytic behaviour of $\text{Co}_3\text{Mo}_3\text{C}$, $\text{Co}_6\text{Mo}_6\text{C}$, $\text{Co}_3\text{Mo}_3\text{N}$ and $\text{Co}_6\text{Mo}_6\text{N}$ for methane cracking has been studied to determine the relationship between the methane cracking activity and chemical composition. All the prepared materials were found to display activity for hydrogen production under the reaction conditions studied. However, the activity of these materials varied depending upon initial composition. Among the evaluated catalysts, the $\text{Co}_6\text{Mo}_6\text{N}$ sample showed the highest activity. Post-reaction analysis and *in-situ* neutron diffraction studies revealed a significant phase transformation, which depends on initial composition, from metal nitrides to $\text{Co}_3\text{Mo}_3\text{C}$, $\alpha\text{-Co}$ and $\beta\text{-Mo}_2\text{C}$ occurring. In the case of $\text{Co}_6\text{Mo}_6\text{C}$ for instance relocation of the carbon in the 0 0 0 (8a) site to $1/8\ 1/8\ 1/8$ (16c) sites resulting in the formation of $\text{Co}_3\text{Mo}_3\text{C}$ was observed. The active phase is believed to be a mixture of $\text{Co}_3\text{Mo}_3\text{C}$, $\beta\text{-Mo}_2\text{C}$ and $\alpha\text{-Co}$.

In the current thesis, comparison was made between the performance in the reactivity of a range of binary and ternary molybdenum based materials presenting different chemical compositions. The topotactic transformation pathways and pseudomorphic nature of the cobalt molybdenum carbide and nitride families, evidenced in this work, offer an elegant route to study the effect of interstitial carbon/nitrogen on the catalytic activity of cobalt molybdenum materials. In most cases, an important effect of chemical composition was observed. Comparison is also made between binary molybdenum carbide and molybdenum nitride systems for completeness.

Chapter 2. Experimental techniques

In this chapter the experimental techniques are divided into three sections; material synthesis, testing and characterisation.

2.1 Material synthesis

Two general classes of materials have been prepared in this work; binary compounds (γ -Mo₂N, β -Mo₂C and α -Mo₂C) and ternary compounds (Co₃Mo₃N, Co₆Mo₆N, Co₃Mo₃C and Co₆Mo₆C).

2.1.1 Binary compounds

Gamma molybdenum nitride¹ (γ -Mo₂N) was prepared by ammonolysis of 500 mg of MoO₃ under NH₃ (BOC, 99.98 %) at a flow rate of 100 ml min⁻¹ at 700 °C for 2 h, using the ammonolysis reactor as represented in Figure 2.2-1. The ramp rate applied was that the temperature was increased from ambient to 350 °C at 5.6 °C min⁻¹, then to 700 °C at 1 °C min⁻¹. The material was subsequently cooled down to ambient temperature in the ammonia flow before to passivation for 1 h, using a gas mixture containing 0.2 vol. % O₂ in Ar and nitrogen to prevent it from being exposed to air.

Beta molybdenum carbide² (β -Mo₂C) was synthesised using the carburisation reactor as depicted in Figure 2.2-2 and 20 vol. % CH₄ in H₂ (BOC, 99.98 %) was performed by temperature programmed reaction (TPR), using a 12 ml min⁻¹ flow rate at ambient pressure. Initially, 500 mg of MoO₃ (B.D.H, 99 %) was loaded into an 8 mm (i.d.) horizontal quartz tube packed with quartz wool on both sides to hold the material in the middle of tube. The sample was heated at 6 °C min⁻¹ from room temperature to 350 °C, and then heated to a final temperature of 800 °C using a ramp rate of 1 °C min⁻¹ and held at 800 °C for 2 hours. The material was cooled to ambient temperature under the same gas mixture.

Alpha molybdenum carbide³ (α -Mo₂C) was prepared by the carburization of 500 mg of γ -Mo₂N under 20 vol. % CH₄ in H₂ (BOC, 99.98 %) at a flow rate of 12 ml min⁻¹ at 700 °C for 2 h with a temperature ramp rate of 6 °C min⁻¹ to reach 350 °C followed by 1 °C min⁻¹ to attain 700 °C. The carburisation reactor as presented in Figure 2.2-2 was used for this procedure. The material was cooled to ambient temperature under the same gas mixture.

2.1.2 Ternary compounds

Dehydrated cobalt molybdenum oxide (CoMoO_4) was prepared as described elsewhere.⁴ In summary, 4.00 g of ammonium heptamolybdate ($(\text{NH}_4)_6\text{Mo}_7\text{O}_{24} \cdot 4\text{H}_2\text{O}$ (99.98 %, Sigma-Aldrich) and 5.59 g of $\text{Co}(\text{NO}_3)_2 \cdot 6\text{H}_2\text{O}$ (>98 %, Sigma-Aldrich) were dissolved in 200 ml of deionized water. The solution was then heated to 85 °C and held at this temperature for 5 h. The resulting purple precipitate was filtered and washed twice with distilled water and once with ethanol. The precipitate was then calcined at 500 °C for 3 h in air.

Cobalt molybdenum nitride (η -6 $\text{Co}_3\text{Mo}_3\text{N}$) was prepared by ammonolysis (using the ammonolysis reactor as presented in Figure 2.2-2) of 1000 mg of CoMoO_4 under NH_3 (BOC, 99.98 %) at a flow rate of 100 ml min^{-1} at 785 °C for 5 h. The temperature ramp rate applied was that the temperature was increased from ambient to 357 °C at 5.6 °C min^{-1} , then after to 447 °C min^{-1} at 0.2 °C min^{-1} before being finally increased to 785 °C at 2.1 °C min^{-1} . The material was subsequently cooled down to ambient temperature in the ammonia flow before to passivation for 1 h, using a gas mixture containing 0.2 vol. % O_2 in Ar further diluted with N_2 .

Cobalt molybdenum nitride (η -12 $\text{Co}_6\text{Mo}_6\text{N}$) was prepared by reducing 300 mg of $\text{Co}_3\text{Mo}_3\text{N}$ under 75 vol. % H_2 in Ar (BOC, 99.98 %) at a flow rate of 60 ml min^{-1} . The reduction was conducted at 700 °C for 7 h with a ramp rate of 10 °C min^{-1} .

The preparation of cobalt molybdenum carbide (η -6 $\text{Co}_3\text{Mo}_3\text{C}$) was undertaken in the carburisation reactor. $\text{Co}_3\text{Mo}_3\text{N}$ was carburised by the decomposition of methane, using a 20 vol. % CH_4 in H_2 (BOC, 99.98%) with a 12 ml min^{-1} flow rate. 400 mg of nitride was loaded into an 8 mm (i.d.) quartz tube packed with quartz wool on both sides. The sample was heated from ambient temperature to 350 °C with a ramp rate at 6 °C min^{-1} and then at 1 °C min^{-1} to a final temperature of 700 °C, after which the obtained product was cooled to room temperature. This cooling process was performed in the reactor under the reaction gas, prior to the materials being exposed to air at ambient temperature by opening the reactor tube from one side and leaving overnight under back diffusion of air, to prevent further rapid bulk oxidation.

Cobalt molybdenum carbide (η -12 $\text{Co}_6\text{Mo}_6\text{C}$) was prepared by reducing 300 mg $\text{Co}_3\text{Mo}_3\text{C}$ under 75 vol. % H_2 in Ar (BOC, 99.98 %) at a flow rate of 60 ml min^{-1} . The reduction was

conducted at 900 °C for 5 h with a temperature ramp rate of 10 °C min⁻¹, and the material was passivated in the same manner as for Co₃Mo₃C.

2.2 Reactor design

The reactors used during this project have mass flow controller controlled gas flows and quartz reactor tubes for containing the samples. They are explained in more detail below.

2.2.1 Ammonolysis reactor

Figure 2.2-1 presents a schematic of the ammonolysis reactor which is used to synthesise gamma molybdenum nitride (γ -Mo₂N) and ternary cobalt molybdenum nitride (η -6 Co₃Mo₃N). A 10 mm (i.d.) vertical sintered quartz reactor was used to place the sample in the centre of a Carbolite furnace. This furnace was programmed to heat the material in various heating stages using a temperature controller.

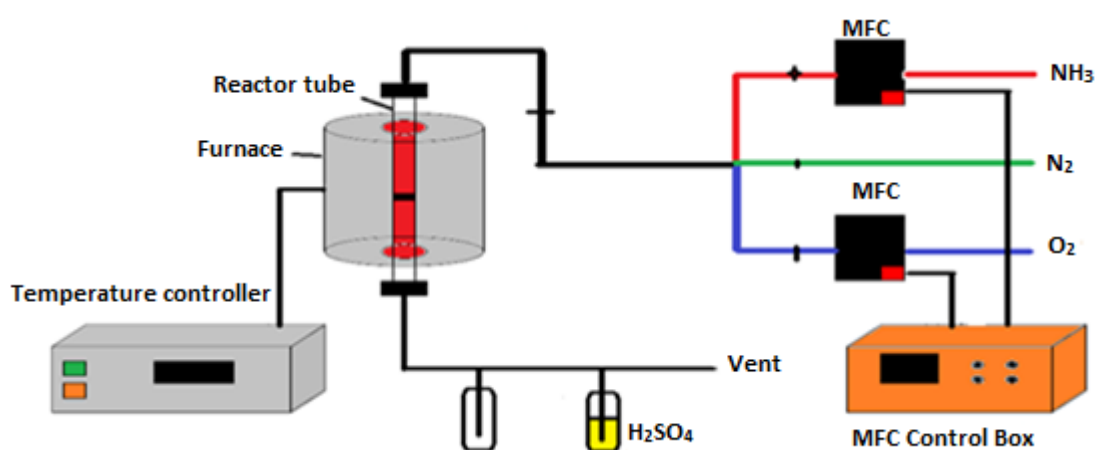


Figure 2.2-1: Schematic showing the ammonolysis reactor set-up.

Ammonia (BOC, grade N3.8, NH₃) was introduced into the reactor through a Brooks 5850 TR mass flow controller at a 100 ml min⁻¹ flow rate. The vented gas was bubbled through an acid solution to scrub out unreacted ammonia. The material was passivated at ambient temperature using a gas mixture containing 0.2 vol. % O₂ in Ar and further diluted with N₂.

2.2.2 Carburisation and reduction reactor

Figure 2.2-2 depicts both the carburisation and reduction reactors. In the case of the carburisation reactor which was used to prepare β -Mo₂C, α -Mo₂C and η -6 Co₃Mo₃C materials, an 8 mm (i.d.) quartz glass reactor was used to mount the sample. The material was held centrally in the quartz reactor tube between two plugs of silica wool positioned in a Carbolite furnace. The materials were treated at 700 °C for α -Mo₂C and η -6 Co₃Mo₃C and 800 °C for β -Mo₂C, using ramp rates of 6 °C min⁻¹ from ambient temperature to 350 °C and then from 6 °C min⁻¹ to the desired final temperature. A gas feed mixture of 20 vol. % CH₄ in H₂ (BOC, 99.98 %) was introduced into the reactor through a mass flow controller at a flow rate of 12 ml min⁻¹.

In the case of the reduction reactor which was used to prepare η -12 Co₆Mo₆N and η -12 Co₆Mo₆C materials, the materials were heated at 700 °C for 7 h for Co₆Mo₆N and 900 °C for 5 h for Co₆Mo₆C, using a ramp rate of 10 °C min⁻¹ for both. A gas feed mixture of 75 vol. % H₂ in Ar (BOC, 99.98 %) with a flow rate of 60 ml min⁻¹ was applied. All materials were cooled to ambient temperature under the flowing reactant gas mixture and then the reactor tube was opened allowing back diffusion of air overnight prior to sample discharge.

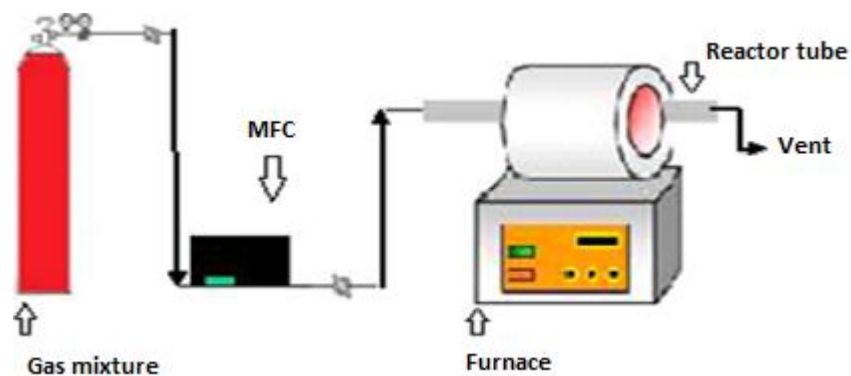


Figure 2.2-2: Schematic showing the carburisation and reduction reactor set-up.

2.2.3 Ammonia synthesis reactor

Reactions were performed using 0.3 g of material under an atmosphere of 75 vol. % H₂ in N₂ (BOC, 99.98%) at ambient pressure employing a total gas feed of 60 ml min⁻¹. An 8 mm (i.d.) quartz reactor was used to mount the sample. The material was held centrally in the quartz reactor tube between two plugs of silica wool positioned in a Carbolite furnace. Ammonia production was determined by measurement of the decrease in the conductivity of 200 ml of a 0.0018 M H₂SO₄ solution through which the reactor effluent stream flowed. An automated HACH HQ14d Portable Conductivity Meter was used. The calibration value applied for calculated ammonia synthesis rate is provided in the Appendix 3.

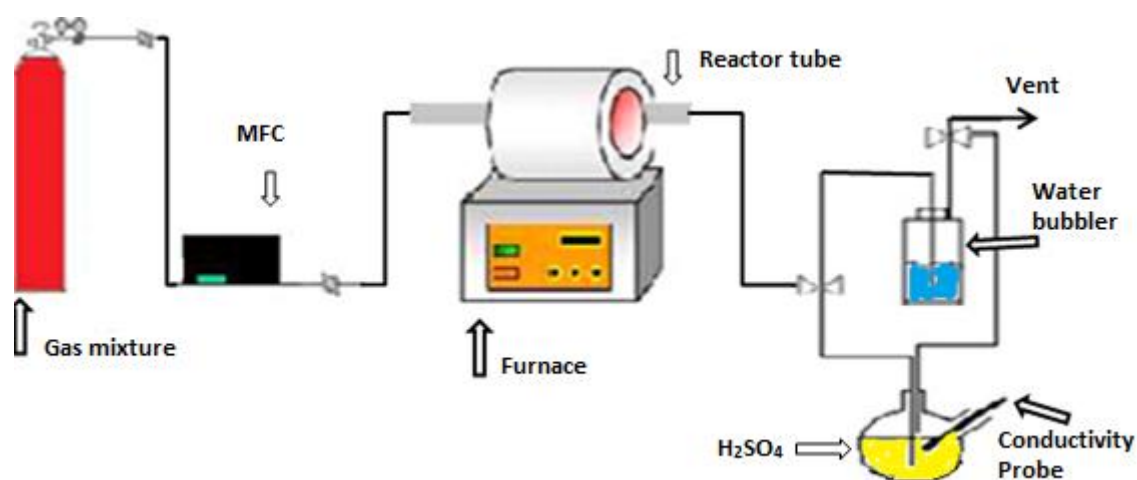


Figure 2.2-3: Schematic showing the ammonia synthesis reactor set-up.

2.2.4 Methane cracking reactor

Figure 2.2-4 depicts the methane cracking reactor. An 8-mm (i.d.) quartz glass reactor was used to mount the catalyst sample. The sample was held centrally in the quartz reactor tube between two plugs of silica wool and the reactor tube was positioned in a Carbolite furnace. Reaction tests were performed at 800 °C, at a 50 °C min⁻¹ ramp rate. A feed gas mixture of 75 vol. % methane in nitrogen (BOC, 99.98%) was introduced into the reactor through a Brooks 5850TR mass flow controller at a 12 ml min⁻¹ flow rate. Nitrogen was used as an internal standard. Product analysis was carried out by on-line gas chromatography (GC). Hydrogen, nitrogen, and methane quantification was performed using thermal conductivity detection (TCD).

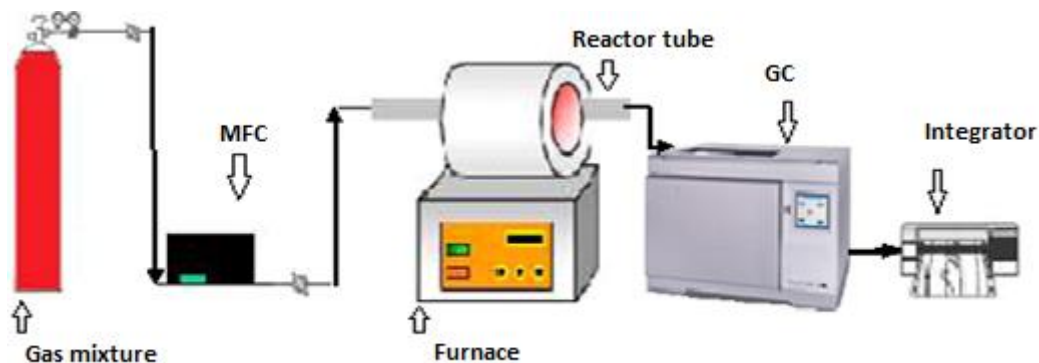


Figure 2.2-4: Schematic showing the methane cracking reactor set-up.

2.3 Catalyst characterisation

Material characterisation is a significant aspect of this study. In this project, a number of different techniques were used to characterize materials and these methods are explained in the following subsections.

2.3.1 Gas chromatography (GC-TCD)

The methane cracking products were analysed using an on-line Hewlett Packard 5890A gas chromatograph (GC). Hydrogen, nitrogen, and methane quantification was performed using a Molecular Sieve 13X filled column of 12 feet in length and thermal conductivity detection (TCD) with argon employed as the carrier gas. The primary product of interest in this project is hydrogen; therefore the calibration of hydrogen was performed using three different known compositions of hydrogen 2%, 5% and 25% to attain the response factor. Gas mixtures of different compositions were passed through the GC and the average of the numerical values of six consistent measurements for each data point was calculated. It was possible to obtain a straight line graph and a linear relationship of the GC peak intensity against concentration. The resultant gradient obtained was used as the response factor. The obtained factor for hydrogen was employed for the subsequent calculation of GC data. The equation applied is provided in the Appendix 4.

2.3.2 Thermogravimetric analysis with mass spectrometry (TGA-MS)

Thermogravimetric analysis was carried out on a TA SDT-Q600 Instrument coupled to an ESS evolution mass spectrometer. 8.73 mg of material was heated from room temperature to 1000 °C in 75 vol. % H₂ in Ar gas mixture using a ramp rate of 10 °C min⁻¹ and mass spectrometry was carried out in multiple ion detection mode (MID mode). The analysis was kindly performed by Mr. Andrew Monaghan.

2.3.3 Powder neutron diffraction (PND)

In-situ controlled atmosphere high temperature time-of-flight (ToF) PND data was collected using the high intensity Polaris diffractometer at the ISIS pulsed spallation source (Rutherford Appleton Laboratory, UK). Powder samples (ca. 1 g) were loaded into 11 mm diameter thin-walled stainless steel cells and held in place between quartz glass frits to permit a flow of reaction gas to circulate through the samples during data collection.

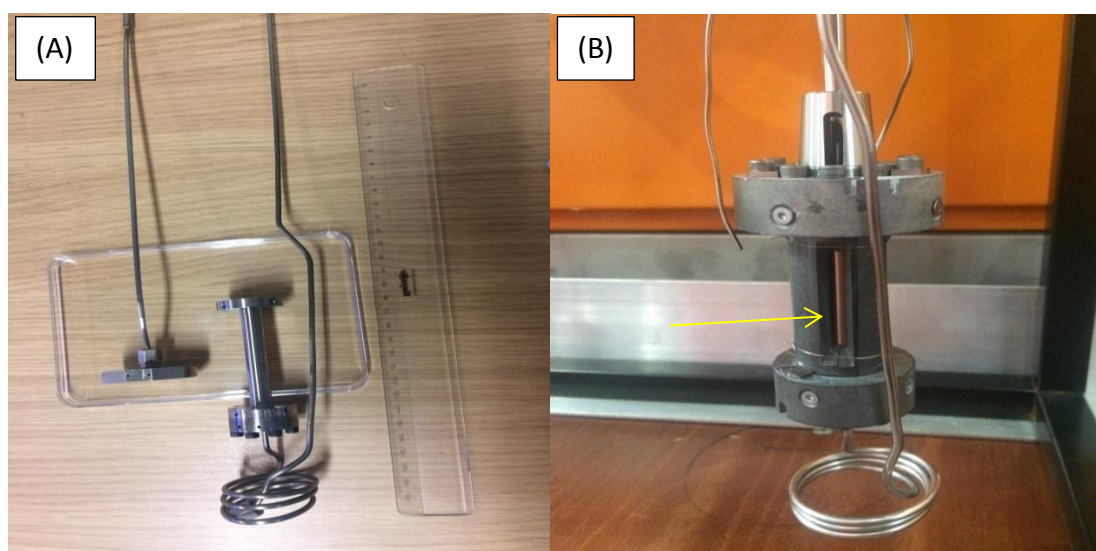


Figure 2.3-1: Images of the *In-situ* cell used on POLARIS; (A) the cell prior attached to the collimator and (B) the cell and collimator attached to the stick, thermocouple, 90° bank (as indicated by yellow arrow); gas flows from the bottom to the top of the cell.

The cell assembly (as shown in Figure 2.3-1) was mounted in a dedicated neutron diffraction furnace capable of heating from room temperature to 900 °C. It was connected to a gas panel fitted with mass flow controllers allowing a mixture of gases to flow through the sample at controlled flow rates during data collection. A collimator manufactured from

neutron-absorbing boron nitride ceramic placed around the cell enabled diffraction patterns to be collected in the Polaris $2\theta \approx 90^\circ$ detector bank which was free of Bragg reflections from the steel walls of the cell. Rietveld refinements against PND data were performed using the General Structure Analysis System (GSAS) through the EXPGUI interface and the powder pattern is calculated according to the equations provided in the Appendix 1.⁵⁻⁶

2.3.4 Powder X-ray diffraction (PXRD)

Powder X-ray diffraction (PXRD) patterns were acquired at room temperature on a Panalytical X'Pert PRO instrument fitted with a reflection/transmission spinning flat plate, using 40 kV and 40 mA with Cu K α radiation ($\lambda = 0.154$ nm). Data were collected over a range of 2θ values, from 5° to 85° , using a step size of 0.0167° and a counting rate of 1 second step⁻¹. The samples were mounted into a round metallic sample holder. Phase identification was undertaken by comparison with JCPDS database files.

2.3.5 Hot stage powder X-ray diffraction (HSPXRD)

Hot stage PXRD analyses was conducted on the Panalytical X'Pert PRO instrument using an Anton-Parr HTK 1200N chamber fitted with a reflection/transmission spinning flat plate, using Cu K α radiation ($\lambda = 0.154$ nm). Only two experiments were undertaken, Co₃Mo₃C and Co₆Mo₆C reacted with N₂, using *in-situ* hot stage PXRD. The powder samples were loaded into the sample pan and then the pan was held in place (as shown by the yellow arrow in Figure 2.3-2) by a flexible ring. The samples were heated *in-situ* from room temperature to 700 °C at a rate of 10 °C min⁻¹ under N₂. The data were investigated over a range of 2θ values from 5 to 85° , using a step size of 0.0167° and a counting rate of 1 second step⁻¹. Scans were taken at room temperature, 500 °C and 600 °C (1h, 2h, 3h) for Co₃Mo₃C and room temperature, 600 °C and 700 °C (1h, 2h, 3h) for Co₆Mo₆C. The system was programmed and held 1 hour for taking a scan at each reaction condition.



Figure 2.3-2: Image of the sample holder of the hot stage instrument.

2.3.6 Thermal gravimetric analysis (TGA)

Thermal gravimetric analysis was carried out on a TA Instruments TGA Q500 series instrument. The sample weights applied were roughly 0.008 g. The sample was heated from room temperature to 1000 °C in 50 ml min⁻¹ of flowing air at a temperature ramp rate of 10 °C min⁻¹.

2.3.7 Elemental analysis (CHN)

Carbon, hydrogen, and nitrogen (CHN) analysis was performed on materials by combustion, using a CE-440 elemental analyser under pure oxygen. Analyses were kindly performed by Mrs. Kim Wilson and Mr. M. G. Reddy.

2.3.8 Scanning electron microscopy (SEM) and energy dispersive X-ray spectroscopy (EDXS)

SEM images of the materials were obtained using a Philips XL30 environmental scanning electron microscope. The samples were coated to prevent sample charging, using a Polarn SC7640 Auto high-resolution sputter coater with a palladium/gold target. Some images were collected with the kind assistance of Mr. Jim Gallagher and some images with higher magnification were collected with the kind assistance of Dr. Jose L. Rico from Universidad

Michoacana de San Nicolas de Hidalgo, Michoacan, Mexico. Furthermore, the Glasgow SEM system was connected with an energy dispersive X-ray spectroscopy (EDXS) device with Oxford Instruments AZtec Software for SEM combined with x-act 10 mm² SDD detector, used for chemical elemental analyses.

2.3.9 Surface area measurement (BET)

BET surface areas were determined from N₂ physisorption isotherms collected at -196 °C upon samples using a Micromeritics Gemini Surface Area Analyser. The samples (0.05 g) were placed in a quartz U-tube after degassing at a 60-sccm flow of N₂ overnight at 110 °C to remove moisture and physisorbed gases. The method of surface area determination applied was that detailed by Brunauer, Emmett, and Teller.⁶

2.3.10 Raman spectroscopy

Raman spectra of pre-reaction and post-reaction materials were recorded at room temperature on a Horiba Jobin Yvon LabRAM HR confocal Raman microscope, using 532 nm laser excitation. Samples were illuminated for 10 seconds using a 50x objective lens and a grating of 600 gr/mm. The spectral region acquired was in the region of 100 ~ 3000 cm⁻¹.

2.3.11 Fourier transform infrared spectroscopy (FTIR)

Fourier-transform infrared spectra were recorded using a FTIR-8400S Shimadzu apparatus. Each spectrum was collected at a spectral resolution of 2 cm⁻¹, applying a scan range of 500 to 3500 cm⁻¹. A background spectrum (as reference) was acquired. A transmission FTIR cell (4 cm internal diameter and 12 cm length) was used carefully to sample the reactor element in a periodic manner for determination of CO and CO₂ by off-line FTIR analyses.

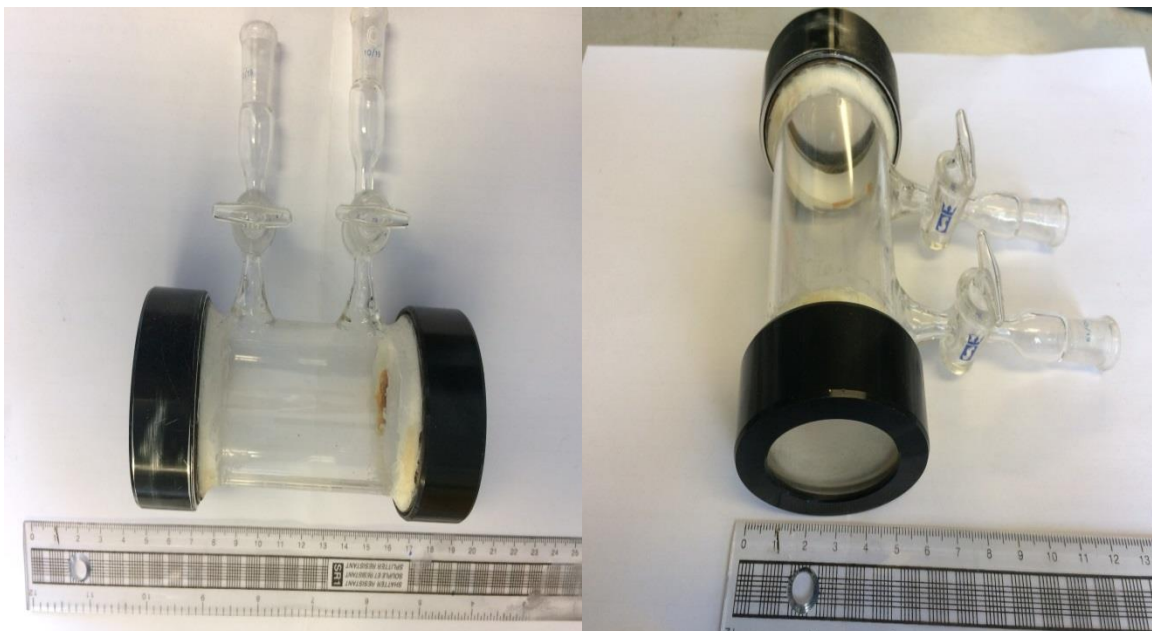


Figure 2.3-3: Images of the transmission FTIR cell.

2.3.12 Transmission electron microscopy (TEM) and high resolution transmission electron microscopy (HRTEM)

TEM and HRTEM were carried out on samples using a Jeol JEM-2011 electron microscope fitted with a LaB6 filament. The TEM samples were prepared by dissolving a small amount of material on acetone solvent and dropping onto a holey carbon grid. The grid was left to dry prior to analysis. Measurements were kindly performed at the University of St. Andrews by Dr. Heather Greer and Prof. Wuzong Zhou.

Chapter 3. Carbide and nitride transformation sequences

3.1 Introduction

Transition metal carbides and nitrides have many properties that make them interesting catalytic materials in technological applications and science.⁷ Interstitial carbides are similar to interstitial nitrides in composition and structure. Carbides can be very hard materials whereas nitrides are not as hard as carbides. The nitrides of Groups IV and V have melting points above 1800 °C, whereas the nitrides of Group VI (molybdenum, tungsten and chromium) have lower melting points of ~1000 °C⁸ and carbides have higher melting points in the range 2000-4000 °C (e.g., tantalum carbide has the highest known melting point at ~3983 °C) and tensile strengths more than 300 GPa in the range of ceramic materials. This has given them applications as cutting tools.⁹ However, they also possess good electrical and thermal conductivity, resistance to corrosion, resistance to poisoning, magnetic properties and chemical stability¹⁰ which has resulted in their application as diffusion barriers, high temperature structural materials, superconductors and magnetic devices. Transition metal carbides have interesting catalytic properties as demonstrated by Boudart and Levy¹¹ in 1973. The discovery of Pt-like catalytic behaviour of tungsten carbide has significantly advanced the progress of their potential catalytic properties as heterogeneous catalysts. These compounds have excellent catalytic activity in ammonia decomposition and synthesis,¹² isomerization,¹³ methanation, hydrogenolysis¹⁴ and hydroprocessing¹⁵. The reason behind the interest in these materials in catalysis rather than noble metals is related to their low cost and availability. Since 1973 in particular, a wide range of studies have been conducted in which authors have frequently drawn comparisons between the performance of nitrides and carbides and the catalytic activity of expensive noble metals.

3.1.1 Metal carbides and nitrides

Metal carbides and nitrides can be categorised into several groups, according to their position in the periodic table as shown in Table 3.1-1. The Group IV to VI transition metal nitrides and carbides are known as interstitial alloys which are formed from the occupation of nitrogen or carbon atoms in the interstitial positions of their parent metals. Nitrides and carbides are closely linked in crystal structure forms and bonding characteristics as well as

in their electronic and magnetic properties. This close relationship is easy to understand owing to similarities in electronic structures but at the same time it is important to consider the differences between nitrogen and carbon which can affect their properties. As summarized by Chen, these materials comprise three different classes of materials; ionic crystals, covalent solids and transition metals. The bonding in these materials can comprise simultaneous contributions from covalent, metallic and ionic interactions. Covalent bonding originates from the interaction of nitrogen or carbon 2s and 2p orbitals with metal d orbitals; metallic bonding is associated to the metal-metal bonds and the ionic contribution is correlated to the charge transfer between metal and nitrogen or carbon atoms.⁹ When synthesising high surface area carbides and nitrides via a temperature-programmed reaction, molybdenum and tungsten were shown to be the most active and stable catalysts for dry methane reforming, methane steam reforming, and the partial oxidation of methane.¹⁶⁻¹⁸ Of these materials, it can be argued molybdenum carbides and nitrides have shown the greatest promise as substitute noble catalysts.

Table 3.1-1: Known carbides and nitrides within Groups IV, V, and VI.¹⁰

Group IV	Group V	Group VI
TiC, TiN, Ti ₂ N	V ₂ C, VC, V ₂ N, VN	Cr ₂₃ C ₆ , Cr ₇ C ₃ , Cr ₃ C ₂ , CrN
ZrC _{1-x} , ZrN	Nb ₂ C, NbC, Nb ₂ N, NbN, Nb ₄ N ₃ ,	β-Mo ₂ C, Mo ₃ C ₂ , α-MoC _{1-x} , β-Mo ₂ N, γ-Mo ₂ N
HfC _{1-x} , HfN	Ta ₂ C, TaC, Ta ₂ N, TaN, Ta ₃ N ₅	W ₂ C, WC _{1-x} , WC, W ₃ C ₂ , WN, β-W ₂ N

3.1.2 Crystal structure and composition

The structure and composition of molybdenum carbides and nitrides has been extensively studied and well documented. Interstitial carbides and nitrides represent simple crystal structures of early transition metals. According to Oyama,¹⁵ there are two fundamental factors that influence the structure of carbides and nitrides: geometric and electronic. In geometric considerations, non-metal atoms are inserted into the interstitial space of the host metal close-packed layering in arrangements that constitute common structures, such as those based upon face-centred cubic (fcc), hexagonally close packed (hcp), and simple

hexagonal structures as illustrated in Figure 3.1-1. These metal substructures can also be described according to their geometric sequence of packed metal layers, such as ABCABC for fcc, ABABAB for hcp, and AAAA for simple hexagonal. Electronic effects relating to the structure of carbides and nitrides can be explained by Engel–Brewer theory, wherein the structure of metal depends on the s-p electron count, which represents the number of s-p valence electrons per atom (e/a). On this basis, the hcp structure is formed when $e/a = 1.7$ – 2.1 , and $e/a = 2.5$ – 3 occurs for the fcc structure.⁷

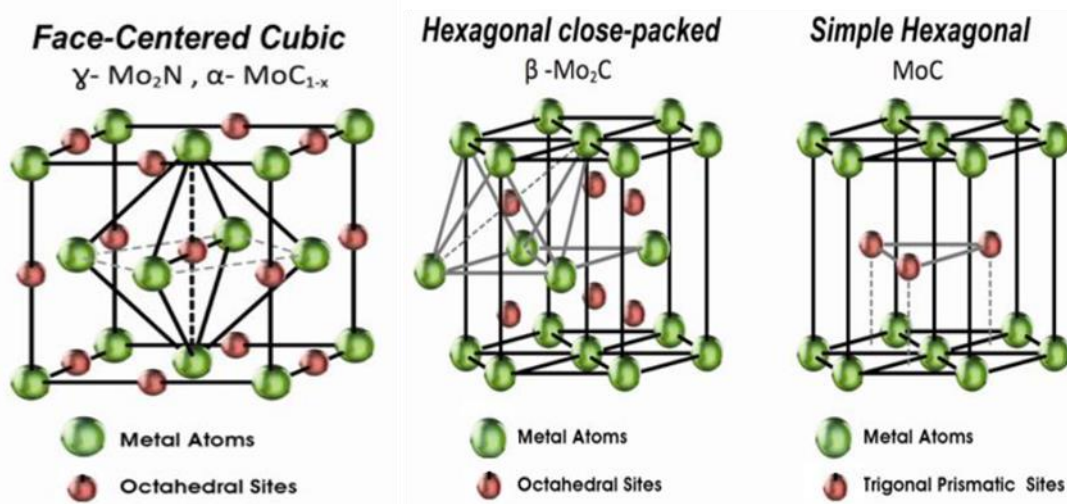


Figure 3.1-1: Common crystal structures of molybdenum carbide and nitride catalyst.¹⁹

Within the current chapter, gamma molybdenum nitride ($\gamma\text{-Mo}_2\text{N}$), beta molybdenum carbide ($\beta\text{-Mo}_2\text{C}$) and alpha molybdenum carbide ($\alpha\text{-Mo}_2\text{C}$) are included within this study although cobalt molybdenum nitride ($\text{Co}_3\text{Mo}_3\text{N}$, $\text{Co}_6\text{Mo}_6\text{N}$) and cobalt molybdenum carbide ($\text{Co}_3\text{Mo}_3\text{C}$, $\text{Co}_6\text{Mo}_6\text{C}$) are the main focus.

3.1.3 Synthesis of binary molybdenum nitrides and carbides

In the literature, molybdenum carbides and nitrides have been prepared by various synthetic methods including sonochemical synthesis from molybdenum hexacarbonyl,²⁰ a solution synthesis method using sucrose as a carbon source²¹ and electrochemical and temperature programmed reactions.²² Table 3.1-2 presents a summary of the reported different approaches to synthesising molybdenum carbides and nitrides.

Table 3.1-2: Approaches to synthesising binary molybdenum nitrides and carbides.

Preparation method	Reaction	Phase
Direct reaction of metal or metal oxide with carbon. ^{7, 19}	Mo + C MoO ₃ + C	Mo ₂ C Mo ₂ C
Reaction of metal or oxide with carburizing or nitriding gas reagent. ¹⁹	Mo + CO MoO ₃ + CO MoO ₃ + N ₂ /H ₂	Mo ₂ C Mo ₂ C β-Mo ₂ N
Reaction of the metal oxide with either a carburizing or Ammonolysis gas using temperature-programmed methods. ^{19, 23}	MoO ₃ + CH ₄ /H ₂ or C ₂ H ₆ /H ₂ MoO ₃ + NH ₃	β-Mo ₂ C, α-MoC _{1-x} γ-Mo ₂ N
Reaction of metal oxide vapour with gasified carbon under vacuum. ¹⁹	MoO ₃ + C	Mo ₂ C
Pyrolysis of organometallic compounds under hydrocarbon. ¹⁹	Cp ₂ + Mo ₂ (CO) ₄ (dimethyl acetylenedicarboxylate)	Mo ₂ C
Reaction of metal chloride or metal carbonyl under hydrocarbon gas in hydrogen. ^{19, 24}	Mo(CO) ₆ + CO, H ₂ MoCl ₅ + CH ₄ + H ₂	Mo ₂ C
Sonochemical decomposition of metal carbonyl. ¹⁹	Mo(CO) ₆	Mo ₂ C
Nitriding the metal or metal hydride. ²³	Mo + N ₂ MoH + N ₂	Mo ₂ N
Reaction of metal chlorides with ammonia or with H ₂ /N ₂ gas. ⁷	MoCl ₄ + NH ₃ MoCl ₄ + N ₂ /H ₂	Mo ₂ N

An important method of synthesising molybdenum carbide and nitride involves the direct carburisation or nitridation of MoO₃ at a high temperature; however, this method can result in low surface area products. Metal carbides and nitrides with higher surface areas were obtained after conducting temperature-programmed reduction (TPR) involving high space velocities and controlled ramp rates to minimise hydrothermal sintering and thermal sintering respectively.²⁵ Since their first application, TPR methods have been used in the preparation of many carbides and nitrides, with different precursors, carburisation and nitridation reagents and heating rates being reported in the literature. The precursors to

carbides include metals, metal oxides and metal nitrides. The carburisation reagents used most often are 20% CH₄/H₂,^{2-3, 22, 26-28} 10% C₂H₆/H₂,^{27, 29} 10% C₂H₂/H₂,²⁹ 5% n-C₄H₁₀/H₂³⁰ and to a lesser extent, C₃H₈/H₂.³¹ The direct TPR and carburisation of MoO₃ under pre-activation control in a hydrogen or hydrocarbon mixture yields two phases of carbide: the thermodynamically stable phase β-Mo₂C and the metastable phase α-MoC_{1-x}. For further information see Table 3.1-3.

Table 3.1-3: Temperature-programmed methods of synthesising binary molybdenum nitride and carbides.

References	Precursor	Temperature	Phase
Volpe, Boudart 1985 ²	MoO ₃ + CH ₄ /H ₂	920 K	β-Mo ₂ C (60 m ² g ⁻¹)
Lee <i>et al.</i> 1987 ²²	MoO ₃ + CH ₄ /H ₂	875 K	β-Mo ₂ C (84 m ² g ⁻¹)
Lee <i>et al.</i> 1988 ³	MoO ₃ + ammonia → γ-Mo ₂ N+ CH ₄ /H ₂ → MoO ₃ + Pt + CH ₄ /H ₂ →	970 K	γ-Mo ₂ N α-MoC _{1-x} (200 m ² g ⁻¹) α-MoC _{1-x}
Xiang <i>et al.</i> 2007 ³²	MoO ₃ or CoMoO ₄ under flow of CH ₄ /H ₂	973 K	K/β-Mo ₂ C (3.5 m ² g ⁻¹), Co/β-Mo ₂ C (9.2 m ² g ⁻¹)
Wang <i>et al.</i> 2006 ³¹	MoO ₃ + C ₃ H ₈ /H ₂	973 K	β-Mo ₂ C bulk and SiO ₂ - supported (166 m ² g ⁻¹)
Xiao <i>et al.</i> 2002 ²⁹	MoO ₃ under flow 10% C ₂ H ₂ /H ₂	550, 630 K	Mo ₂ C-550 (26.6 m ² g ⁻¹), Mo ₂ C-630 (36.2 m ² g ⁻¹)
Bouchy <i>et al.</i> 2000 ³³	MoO ₃ + pure CH ₄	983 K	β-Mo ₂ C
Zhu <i>et al.</i> 2007 ³⁴	MoO ₃ + toluene	923 K	β-Mo ₂ C
Bouchy <i>et al.</i> 2000 ³⁵	MoO ₃ + dihydrogen for 24h replaced by CH ₄	983 K	α-MoC _{1-x}

3.1.4 Synthesis of ternary cobalt molybdenum nitrides and carbides

The preparation of $\text{Co}_3\text{Mo}_3\text{N}$, reduced phase $\text{Co}_6\text{Mo}_6\text{N}$, $\text{Co}_3\text{Mo}_3\text{C}$ and reduced phase $\text{Co}_6\text{Mo}_6\text{C}$ have been described in various studies as shown in Table 3.1-4.

Table 3.1-4: Temperature-programmed methods of synthesising ternary CoMo carbides and nitrides.

References	Method	Precursor	Phase
Kojima <i>et al.</i> 2000 ³⁶	TPR	CoMoO_4 reacted with NH_3	$\text{Co}_3\text{Mo}_3\text{N}$
Mckay <i>et al.</i> 2007 ³⁷	TPR	$\text{Co}_3\text{Mo}_3\text{N}$ reacted with 3:1 H_2/Ar	$\text{Co}_6\text{Mo}_6\text{N}$
Newsam 1988 ³⁸	Two-step reaction	$\text{Co(en)}_3\text{MoO}_4$ reacted with CO/CO_2	$\text{Co}_3\text{Mo}_3\text{C}$ and $\text{Co}_6\text{Mo}_6\text{C}$
Korlann 2002 ³⁹	TPR	$\text{Co}_3\text{Mo}_3\text{N}$ with CH_4/H_2	Bulk and supported $\text{Co}_3\text{Mo}_3\text{C}$
Alconchel <i>et al.</i> 2004 ⁴⁰	TPR	$\text{Co}_3\text{Mo}_3\text{N}$, $\text{Fe}_3\text{Mo}_3\text{N}$ with $\text{CH}_4/\text{H}_2/\text{Ar}$	Bulk and supported $\text{Co}_3\text{Mo}_3\text{C}$, $\text{Fe}_3\text{Mo}_3\text{C}$
Wang <i>et al.</i> 2008 ⁴¹	One-step thermal decomposition	hexamethylenetetramine (HMT) with $\text{Co}(\text{CH}_3\text{COO})_2 \cdot 4\text{H}_2\text{O}$, $(\text{NH}_4)_6\text{Mo}_7\text{O}_{24} \cdot 4\text{H}_2\text{O}$ with a mole ratio of 7:1:37 in 15% $\text{NH}_3 \cdot \text{H}_2\text{O}$, under 1:4 CH_4/H_2	$\text{Co}_3\text{Mo}_3\text{C}$
Wang <i>et al.</i> 2008 ⁴¹	One-step thermal decomposition	HMT with $\text{Co}(\text{NO}_3)_2 \cdot 6\text{H}_2\text{O}$, $(\text{NH}_4)_6\text{Mo}_7\text{O}_{24} \cdot 4\text{H}_2\text{O}$ with a mole ratio of 7:1:23 in 15% $\text{NH}_3 \cdot \text{H}_2\text{O}$, under 1:4 CH_4/H_2	$\text{Co}_6\text{Mo}_6\text{C}$

Kojima *et al.*³⁶ synthesised $\text{Co}_3\text{Mo}_3\text{N}$ and Cs-promoted $\text{Co}_3\text{Mo}_3\text{N}$ from dehydrated cobalt molybdenum oxide reacted with ammonia gas. McKay *et al.*³⁷ prepared the reduced phase $\text{Co}_6\text{Mo}_6\text{N}$ from $\text{Co}_3\text{Mo}_3\text{N}$ by heating under 3:1 $\text{H}_2:\text{Ar}$ for 2 hours at 700 °C. Hunter *et al.*⁴ prepared $\text{Co}_3\text{Mo}_3\text{N}$ and $\text{Co}_6\text{Mo}_6\text{N}$ and investigated its structure in detail using PND. Newsam *et al.*³⁸, prepared $\text{Co}_3\text{Mo}_3\text{C}$ and $\text{Co}_6\text{Mo}_6\text{C}$ using two-stage reaction methods, with $\text{Co(en)}_3\text{MoO}_4$ as a precursor with CO/CO_2 gas in first step. Korlann *et al.*³⁹ and Alconchel *et al.*⁴⁰ used temperature-programmed reduction to synthesise $\text{Co}_3\text{Mo}_3\text{C}$ and alumina-supported $\text{Co}_3\text{Mo}_3\text{C}$ from the nitride precursor $\text{Co}_3\text{Mo}_3\text{N}$ heated with CH_4/H_2 gas. Wang *et al.*²⁵, successfully prepared $\text{Co}_3\text{Mo}_3\text{C}$ and $\text{Co}_6\text{Mo}_6\text{C}$ through a simple one-step thermal

decomposition using a hexamethylenetetramine-based method without temperature-programmed carburisation.

3.1.5 Activity and reactivity of ternary CoMo nitrides and carbides

The unusual properties and their structures make both carbide and nitride materials interesting. Their activity in processes such as homologation of methane to produce higher hydrocarbons will be discussed in this chapter whereas application to ammonia synthesis and methane cracking will be discussed in more detail in subsequent chapters.

In terms of direct routes, the non-oxidative, low-temperature, homologation of methane has been proposed as an alternative to the oxidative coupling of methane (OCM) for the production of higher hydrocarbons to avoid deep oxidation to CO and CO₂. van Santen's and Amariglio's research groups independently reported a two-step process.⁴² van Santen and colleagues operated the process at two different temperatures to circumvent thermodynamic limitations (see Figure 3.1-2). At 450 °C, methane dissociative adsorption was carried out on silica-supported transition metal catalysts (Ru, Rh, and Co), followed by a hydrogenation step to produce higher hydrocarbons at a lower temperature (100 °C) and atmospheric pressure.⁴³

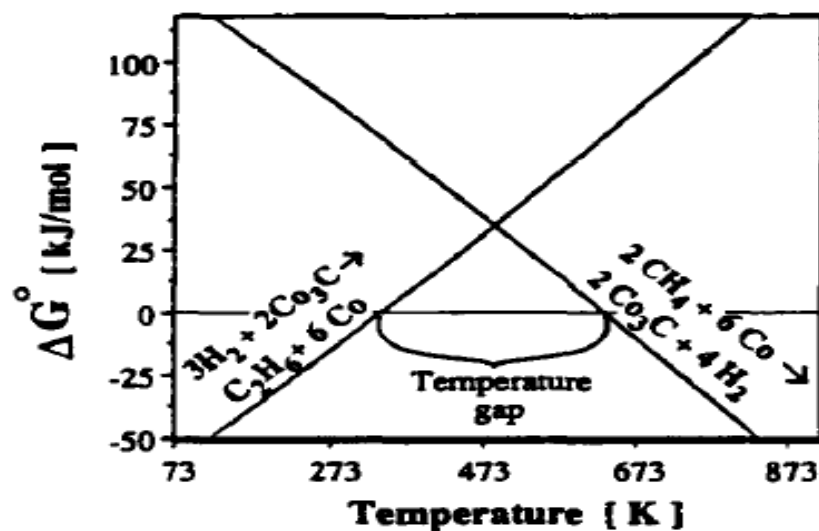


Figure 3.1-2: Gibbs free energy as a function of the decomposition temperature of methane on cobalt and the hydrogenation of cobalt carbide to ethane.⁴⁴

The Amariglio group conducted the two-step process under isothermal conditions on Pt, Ru, and Co. They suggested that C–C bonding could take place between the H-deficient CH_x formed during the first step of methane chemisorption, while H_2 saturated the alkane precursors in the second step and separated them from the surface.⁴²

As shown in Figure 3.1-3, Koerts and colleagues identified three different types of surface carbon species, denoted C_α , C_β and C_γ according to their reactivity with H_2 gas during temperature programmed surface reaction (TPSR). The C_α species is a highly active carbidic phase, which reacts rapidly with hydrogen and which appears to be the major form of carbon in the formation of higher hydrocarbons. C_β (amorphous carbon) is a less reactive species hydrogenated to yield methane between 100 °C and 400 °C. Finally, C_γ (graphitic carbon) species is the least reactive, and hydrogenatable only between 400 °C and 600 °C.⁴⁵ It was demonstrated that homologation of olefins (C_2H_4 , C_3H_6 , C_2H_2 , etc.) with methane could occur over Ru/ SiO_2 and Co/ SiO_2 catalysts.⁴³

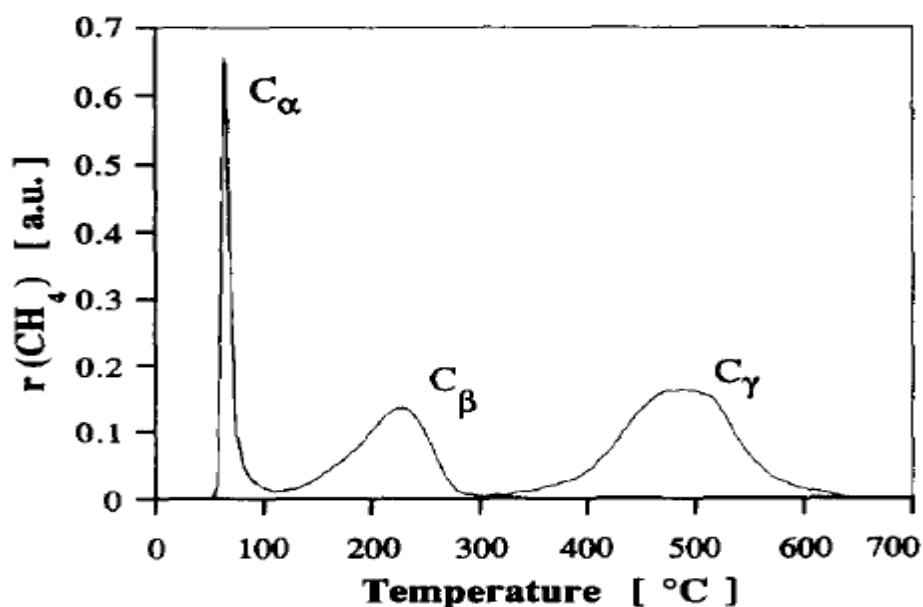


Figure 3.1-3: Temperature-programmed hydrogenation of surface carbon created by methane decomposition on a 3 wt.% silica-supported rhodium catalyst.⁴³

As mentioned previously, non-oxidative conversion of methane to higher hydrocarbons through isothermal condition, two-step reactions on Pt/ SiO_2 (EUROPT-1) and Ru/ SiO_2 catalysts was reported by Amariglio *et al.*⁴⁶ The selectivity to heavier alkanes could be

increased by lowering of the hydrogenation temperature on both catalysts, when chemisorption of methane was set at a fixed temperature (usually below 320 °C).

The two-step process can also be carried out over a number of bimetallic catalysts and oxide or zeolite-supported transition metals.⁴² Guzzi et al demonstrated that there was a correlation between the hydrogen content of the surface CH_x species and the chain length of the hydrocarbons produced in the hydrogenation step. The chemisorbed CH_x species had the highest concentration, and all of the CH_x species were hydrogenated in the second step, giving a selectivity of C_{2+} close to 84 % on Co-Pt/ NaY and 92.6 % on Co-Pt/ Al_2O_3 .⁴⁷ Bhasin and co-workers investigated Ru/ SiO_2 and Cu-Ru/ SiO_2 catalysts via non-oxidative conversion of methane into higher hydrocarbons at temperatures between 127 °C and 527 °C. The results showed that with a Cu-Ru/ SiO_2 catalyst, about 95 % of the carbon deposit could be hydrogenated at 95 °C to enhance the net ethane yield.⁴⁸ Solymosi and Cserenyi⁴⁹ explained that the improved formation of C_2H_6 and higher hydrocarbons could be observed in the two-step process over a Cu-promoted Rh/ SiO_2 catalyst. Wang and colleagues reported that Mo/ H-ZSM-5 catalysts exhibited excellent catalytic activity and selectivity in the formation of aromatics (mainly C_6H_6) for the dehydrogenation and aromatisation of methane at 700 °C under non-oxidising conditions in a single-stage continuous reaction.⁵⁰ This reaction has received great attention, as it is a potential method of adding value to methane, a relatively cheap and abundant raw material, yielding aromatic hydrocarbons.

Recently, based upon the Mars-van Krevelen mechanism most commonly observed in oxidation reactions catalyzed by oxide catalysts, McKay *et al.* have revealed the ability of lattice nitrogen in ternary molybdenum nitrides to act as reservoir of activated nitrogen. The reduced phase $\text{Co}_6\text{Mo}_6\text{N}$ was obtained from $\text{Co}_3\text{Mo}_3\text{N}$ reacted with 3:1 H_2/Ar gas to produce N_2 and NH_3 gases. Following the regeneration step of $\text{Co}_3\text{Mo}_3\text{N}$ from $\text{Co}_6\text{Mo}_6\text{N}$ the use of 3:1 H_2/N_2 gas mixture or solely N_2 gas was found to complete the cycle. Based upon the analogous behaviour of carbides and nitrides, it is of interest to determine whether a similar two stage process can be conducted with $\text{Co}_3\text{Mo}_3\text{C}$ to indirectly yield higher hydrocarbons from CH_4 and this forms an aspect of this chapter.

3.2 Results and discussion

In this chapter, the results and discussion will focus on the synthesis and characterization of a series of binary and ternary molybdenum-containing nitrides and carbides, as well as investigation of their intermediate phases when they are transformed from nitride to carbide and vice versa.

3.2.1 Molybdenum trioxide (MoO_3)

Commercial molybdenum trioxide powder is chemical compound with the formula MoO_3 . This compound was used to prepare binary molybdenum nitride ($\gamma\text{-Mo}_2\text{N}$) and carbide ($\beta\text{-Mo}_2\text{C}$) using the temperature programmed method. Its structure and characterisation is explained below in more detail.

3.2.1.1 Powder X-ray Diffraction (PXRD)

Crystalline molybdenum trioxide usually has three forms: the well-known thermodynamically stable orthorhombic phase ($\alpha\text{-MoO}_3$) as well as two metastable phases (monoclinic $\beta\text{-MoO}_3$ and hexagonal $h\text{-MoO}_3$).⁵¹ The PXRD pattern of the commercial $\alpha\text{-MoO}_3$ used in this study is shown in Figure 3.2-1. The strong diffraction peaks can be indexed to the orthorhombic phase of $\alpha\text{-MoO}_3$ by reference to JCPDS 035-0609, $a = 3.963 \text{ \AA}$, $b = 13.856 \text{ \AA}$, $c = 3.697 \text{ \AA}$, $\alpha = \beta = \gamma = 90^\circ$, space group $Pbnm$.

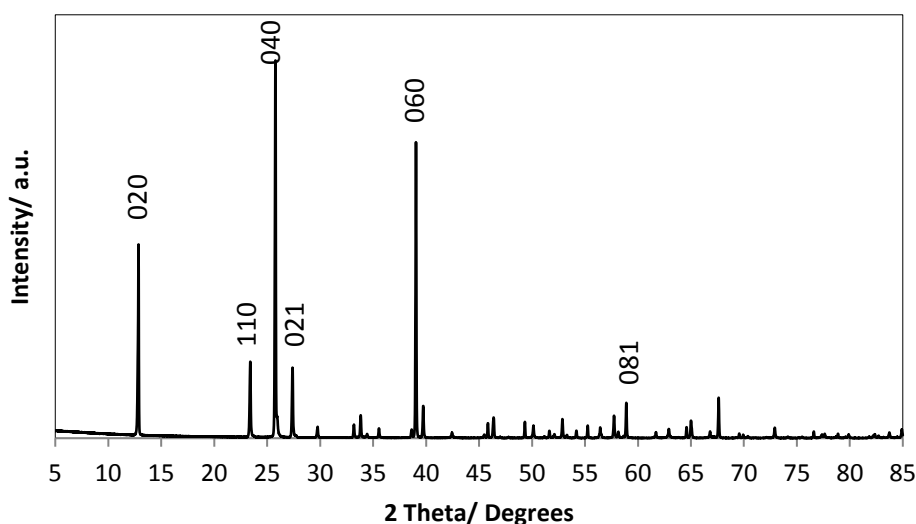


Figure 3.2-1: Indexed PXRD pattern of molybdenum trioxide.

The intense diffraction peaks at $2\theta = 12.9, 25.9$ and 39.1° are indexed as the (020), (040) and (060) hkl crystal planes of the α - MoO_3 phase respectively which is consistent with previous publications.⁵¹

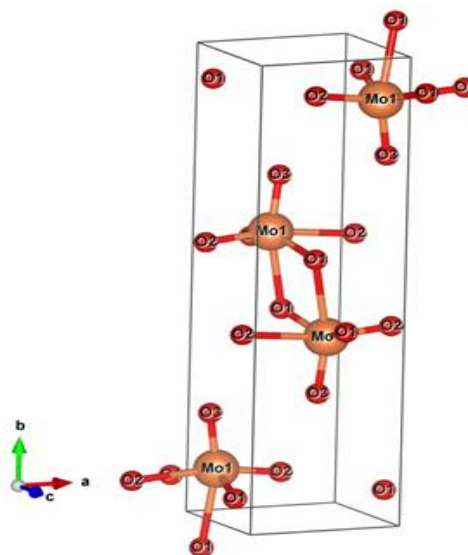


Figure 3.2-2: Mo-O bonds in MoO_3 catalyst.

Alpha molybdenum trioxide has an orthorhombic crystal structure comprising of MoO_6 octahedral units in which each molybdenum species is coordinated by six oxygen species. In this study we used VESTA software to draw ball and stick representations and to derive interatomic distances, bond angles information for all structures using previously published CIF files. MoO_3 was published by Kihlberg⁵² in 1963 with code number 35076 in the Inorganic Crystal Structure Database Web. The Mo-O coordination of distorted octahedra and three inequivalent oxygen atoms namely O1, O2, and O3 respectively shown in Figure 3.2-2. The length of the shortest bond is 1.67 Å. This corresponds to the Mo-O3 bond. In the a axis direction, there are two Mo-O2 bonds with the distances of 2.25 Å and 1.73 Å, respectively. There are three bonding interactions between O1 and Mo; two equal bonding interactions are along the c axis with the distance of 1.95 Å and the third bonding interaction is in the b axis direction with the distance of 2.33 Å.

3.2.1.2 Raman spectroscopy

Raman spectroscopy is a technique which can be used to determine the structure of different molybdenum oxide crystal types, as each of them possess different atomic arrangements and display different Raman vibration bands. A Kimmon IK series He-Cd 532.17 nm laser was employed as the excitation source. For the MoO₃ material, the spectral range scanned was in the range up to 2000 cm⁻¹ because there are no expected peaks beyond 2000 cm⁻¹.

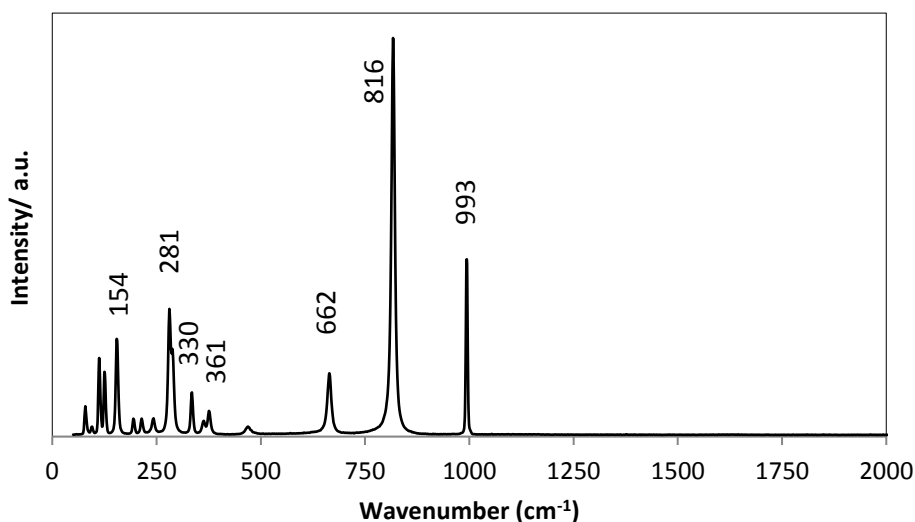


Figure 3.2-3: Raman spectrum of molybdenum trioxide.

The Raman spectrum of MoO₃ is shown in Figure 3.2-3. The material displays the expected Raman scattering bands of α -MoO₃. The absorption bands at 993, 816, 662, 361, 330, 281 and 154 cm⁻¹ correspond to the asymmetric stretching, vibration and wagging modes of α -MoO₃ respectively. All Raman peaks observed are in good agreement with those which have been described in the literature.⁵³ According to Kihlborg's⁵² results the stretching vibrations of Mo=O bonds at a- and b-axes are the most intense signals of the Raman spectrum observed at 995 and 823 cm⁻¹; the orthorhombic MoO₃ structure consisting of two layers of chains of MoO₄ tetrahedra existing along the c-axis. According on Rao's publication, the orthorhombic MoO₃ structure consists of two layers of MoO₆ octahedra associated by covalent forces in the (100) and (001) directions but by van der Waals forces in the (010) direction.⁵⁴

3.2.1.3 EDX and SEM analyses

The morphology of alpha molybdenum trioxide was examined using scanning electron microscopy (SEM). In this characterization, the sample was put directly on the microscope holder without coating. In general, SEM analysis of molybdenum trioxide was taken at a scale bar range interval from 100 nm to 30 μm at magnification varying from 800 to 10000.

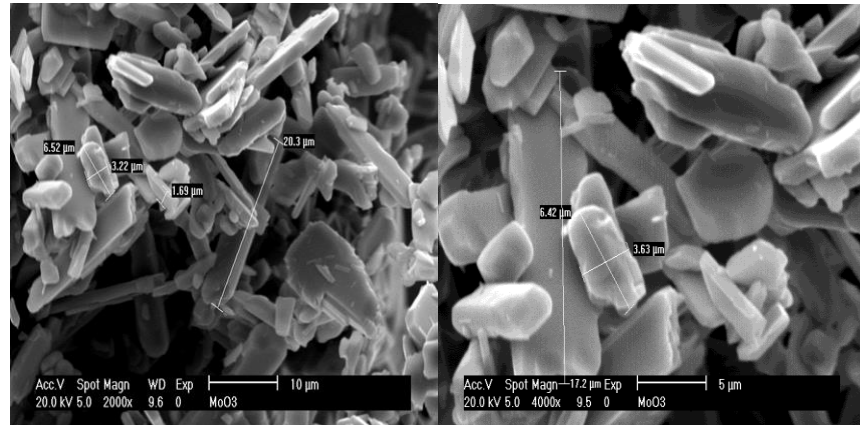


Figure 3.2-4: SEM images of molybdenum trioxide.

Figure 3.2-4 presents typical SEM images at 2000 and 4000 magnification of the $\alpha\text{-MoO}_3$. The MoO_3 is composed of uniform hexagonal sheets with width of 1000- 3000 nm, smaller thickness and length up to several tens of micrometres. A nanoparticle morphology was reported in earlier research.⁵⁵ An EDX spectrum of MoO_3 is shown in Figure 3.2-5. The EDX spectrum of MoO_3 showed it to be composed of elemental molybdenum (39.5 wt. %) and oxygen (60.5 wt. %) with an atomic ratio of 1:3 Mo:O which suggests this material to be pure MoO_3 .

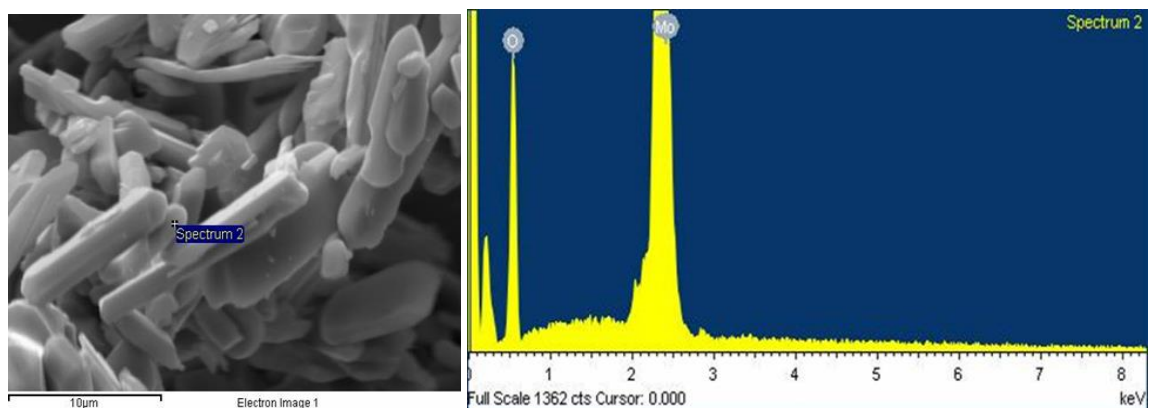


Figure 3.2-5: EDX spectrum of molybdenum trioxide.

3.2.2 Gamma molybdenum nitride (γ -Mo₂N)

Previously, gamma molybdenum nitride (γ -Mo₂N) with high surface area was prepared by Volpe *et al.* from molybdenum trioxide using a temperature programmed reduction (TPR) method.¹ Its structure was investigated by Bull *et al.*⁵⁶ using PND and PXR. In the current study, γ -Mo₂N was synthesised and characterized by using PXR, BET, Raman spectroscopy, SEM, EDX and CHN analysis as discussed in more detail below.

3.2.2.1 PXR analysis

The preparation of gamma molybdenum nitride was performed by the direct ammonolysis of MoO₃ (Sigma Aldrich, 99.5%) using a flow rate of 86 ml min⁻¹ NH₃ (BOC, 99.98%) at 700 °C for 2 hr as described in Chapter 2. The γ -Mo₂N phase was determined by using PXR. The PXR data were collected with a step size of 0.0167° (2 θ) over the range 20 ≤ 2 θ /° ≤ 85 and scan speed 0.002 degree per second for 12 hours to obtain a high quality pattern.

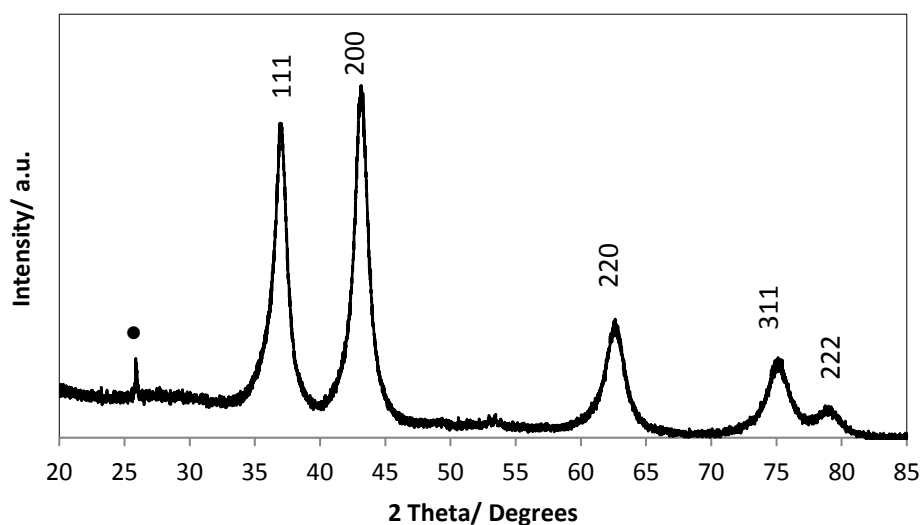


Figure 3.2-6: Indexed PXR pattern of gamma molybdenum nitride, (● trace peak of MoO₂).

The PXR pattern in Figure 3.2-6 confirmed the formation of gamma molybdenum nitride. The strong diffraction peaks at 2 θ = 37.4, 43.4, 63.2, 75.7 and 79.8° are indexed as the (111), (200), (220), (311) and (222) hkl crystal planes of the γ -Mo₂N phase respectively which is consistent with reference JCPDS 003-0907 pdf file and previous publications.¹ The nitrogen content of the material obtained from CHN analysis was 10.5 wt. % which

corresponds to a Mo:N atomic ratio of 2:1.4. This result indicates that the nitrogen content was significantly higher than expected in Mo₂N for which the stoichiometric N content would be 6.8 wt. %. This excess N might be, at least partly, as a result of surface bound NH_x residues.

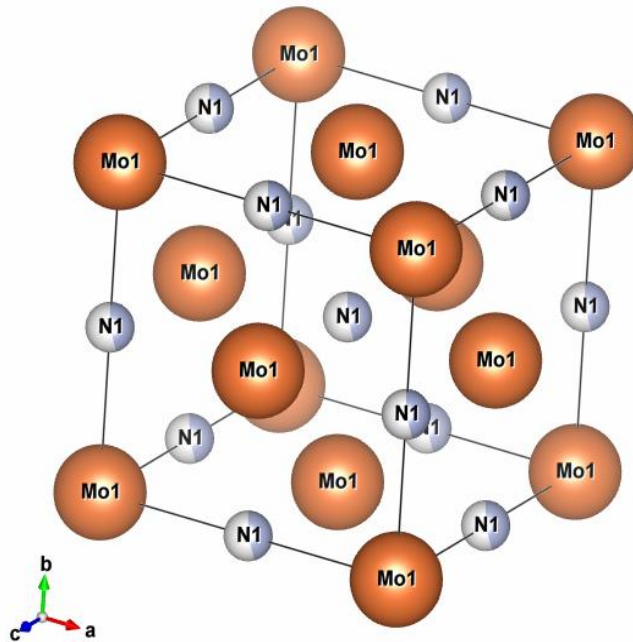


Figure 3.2-7: Unit cell of gamma molybdenum nitride.

The structure of gamma Mo₂N (VESTA using previous published CIF files by Bull *et al.* in 2006⁵⁶ with code number 172801 in the Inorganic Crystal Structure Database Web) is shown in Figure 3.2-7. The structure of gamma Mo₂N can be defined as a face centred cubic arrangement of molybdenum with nitrogen occupying one-half of the octahedral interstitial positions of the host metal. The space group is *Fm-3m*, $a = b = c = 4.161 \text{ \AA}$, $\beta = \gamma = \alpha = 90^\circ$ and the unit cell volume = 72.06 \AA^3 .

3.2.2.2 Raman spectroscopy

Raman spectroscopy was conducted at room temperature and in air on the molybdenum nitride sample. A Kimmon IK series He-Cd 532.17 nm laser was employed as the excitation source for the laser. For the γ -Mo₂N material, the spectral range scanned was in the range up to 2000 cm⁻¹ because peaks beyond 2000 cm⁻¹ are not expected.

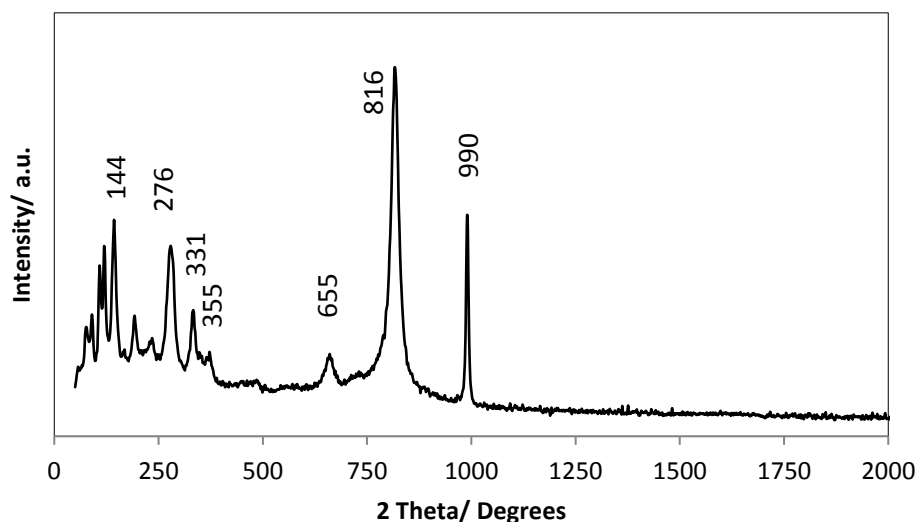


Figure 3.2-8: Raman spectrum of gamma molybdenum nitride.

The Raman spectrum of the γ -Mo₂N sample is shown in Fig. 3.2-8 and corresponds to that expected for MoO₃. The absorption bands at 990, 816, 655; 355, 331, 276 and 144 cm⁻¹ correspond to the asymmetric stretching, vibration and wagging modes of α -MoO₃. This result suggested that there is an oxide layer on the surface of nitride material which may be a result of the expected surface passivation layer given that γ -Mo₂N is air sensitive. All Raman peaks observed are in good agreement with that which has been described by Suszko *et al.*⁵⁷

3.2.2.3 EDX and SEM analyses

The morphology of gamma molybdenum nitride powder was characterized by scanning electron microscopy. For this characterization, the samples were observed directly without coating. From Figure 3.2-9 the gamma molybdenum nitride morphology appears to comprise smooth platelets and the morphology of the parent oxide particles is retained. It is well known that the transformation of MoO₃ platelets to γ -Mo₂N when using the temperature programmed ammonolysis is topotactic due to the (100) planes of Mo₂N

being analogous to (010) planes of MoO_3 ¹ and also Hargreaves and co-workers⁵⁸ mentioned that this type of ammonolysis system is known to yield $\gamma\text{-Mo}_2\text{N}$ with pseudomorphic morphology in relation to the MoO_3 precursor. The BET surface area results increased to a $63\text{ m}^2\text{g}^{-1}$, pore volume $0.09\text{ cm}^3\text{g}^{-1}$, pore diameter 6.0 nm compared with fresh MoO_3 which was a $10\text{ m}^2\text{g}^{-1}$ with a pore volume $0.003\text{ cm}^3\text{g}^{-1}$ and pore diameter 1.4 nm . The increased value of BET surface area for $\gamma\text{-Mo}_2\text{N}$ is consistent with the previously published observations of Mckay *et al.*⁵⁹ ($85\text{ m}^2\text{g}^{-1}$).

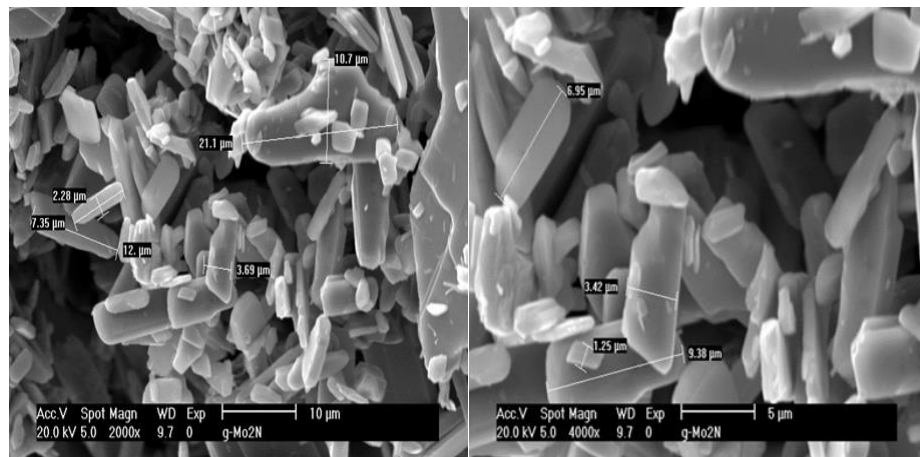


Figure 3.2-9: SEM images of gamma molybdenum nitride.

An EDX spectrum of $\gamma\text{-Mo}_2\text{N}$ is shown in Figure 3.2-10. The spectrum showed that the sample was composed of elemental molybdenum and nitrogen with 7.6 wt. % N, 92.4 wt. % Mo. These values are close to the expected stoichiometric value of 93.2 wt. % Mo and 6.8 wt. % N in Mo_2N which suggests that this material is pure Mo_2N .

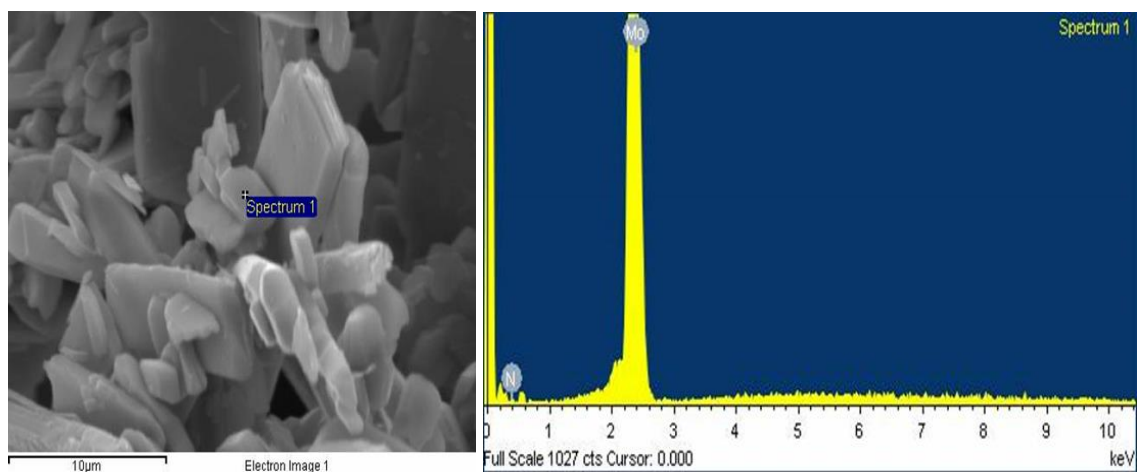


Figure 3.2-10: EDX analysis of gamma molybdenum nitride.

3.2.3 Beta molybdenum carbide (β -Mo₂C)

Beta molybdenum carbide was prepared by Boudart⁶⁰ in 1979 from molybdenum hexacarbonyl Mo(CO)₆. Prior to this Lander⁶¹ first prepared molybdenum carbide by decomposition of the carbonyl at low temperature. In 1985 Boudart² applied the temperature programmed reaction of a methane/ hydrogen gas mixture with molybdenum trioxide to prepare molybdenum carbide as used in the current study. The obtained phase was characterised by X-ray diffraction, BET, SEM, CHN analysis as described below in more detail.

3.2.3.1 PXRD analysis

Previously, the structure of beta molybdenum carbide (β -Mo₂C) was reported by Volpe and Boudart² who, as stated above, prepared the transition metal carbide from molybdenum trioxide using a temperature programmed reduction (TPR) method under a mixture of methane and hydrogen. In this project, the preparation of beta molybdenum carbide from molybdenum trioxide was performed by the direct carburisation of MoO₃ using a flow of 12 ml min⁻¹ of 20 vol. % CH₄ in H₂ gas at 800 °C for 2 h.

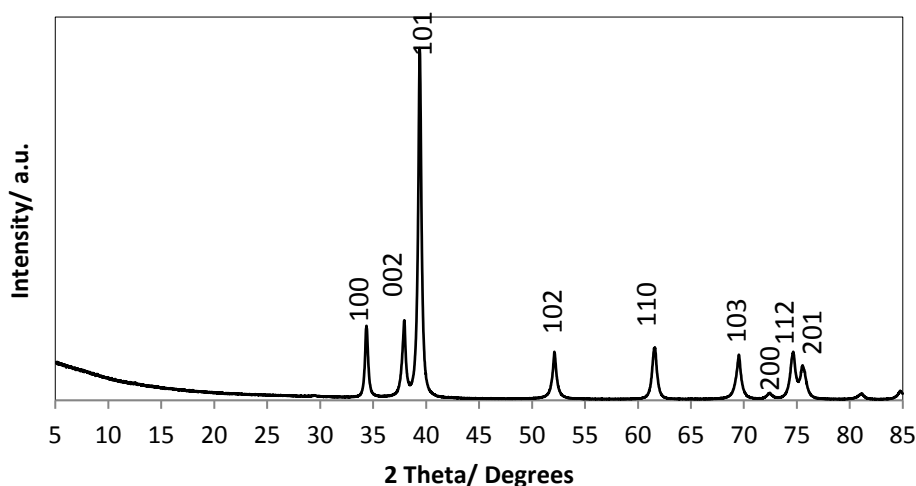


Figure 3.2-11: Indexed PXRD pattern of beta molybdenum carbide.

The PXRD pattern in Figure 3.2-11 confirmed the formation of beta molybdenum carbide. The diffraction peaks at $2\theta = 34.4, 37.9, 39.4, 52.1, 61.5, 69.5, 72.3, 74.6$ and 75.5° are indexed as the (100), (002), (101), (102), (110), (103), (200), (112) and (201) hkl crystal planes of the β -Mo₂C phase respectively, indicating a high degree of phase purity. The

diffraction pattern of this hcp phase is consistent with reference to the JCPDS 001-1188 PDF file and previous publications.^{3, 30, 62} The carbon content of the material obtained from CHN analysis was 5.8 wt. % which corresponds to the expected Mo:C molecular ratio of 2:1.

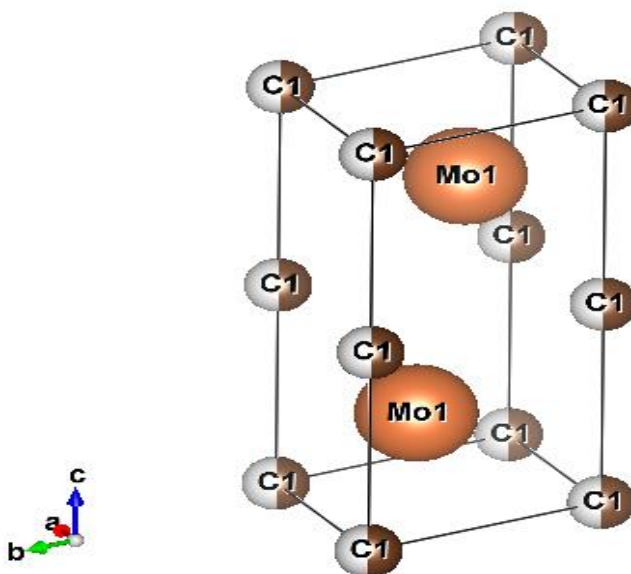


Figure 3.2-12: Unit cell of β -Mo₂C. Mo1 and C1 refer to molybdenum and carbon atoms respectively.

The structure of beta Mo₂C (VESTA using previous published CIF files by Fries *et al.* in 1960⁶³ with code number 43669 in the Inorganic Crystal Structure Database Web) is shown in Figure 3.2-12. The structure of beta Mo₂C can be defined as a hexagonal close packed array with literature unit cell information: space group $P 63/m m c (194)$, $a = b = 3.003$ and $c = 4.729 \text{ \AA}$, $\beta = \gamma = 90$ and $\alpha = 120^\circ$ and unit cell volume = 36.93 \AA^3 .

3.2.3.2 Raman spectroscopy

Raman spectroscopy was conducted at room temperature in air on the molybdenum carbide sample. A Kimmon IK series He-Cd 532.17 nm laser was employed as the excitation source for the laser. For the β -Mo₂C material, the spectral range scanned was in the range up to 2000 cm^{-1} . The Raman spectrum of β - Mo₂C is shown in Figure 3.2-13 and, as for the nitride discussed previously, the material presents the typical Raman scattering bands of MoO₃. The absorption bands at 990, 816, 656; 352, 334, 277; and 144 cm^{-1} correspond to the asymmetric stretching, vibration and wagging modes of α -MoO₃. Two weaker characteristic peaks for the disorder (D) and graphite (G) bands of carbon are detected at 1310 and 1548 cm^{-1} respectively which may be related to preparative method at high

temperature. All Raman peaks observed are in good agreement with those which have been described in literature for α -MoO₃.²⁹

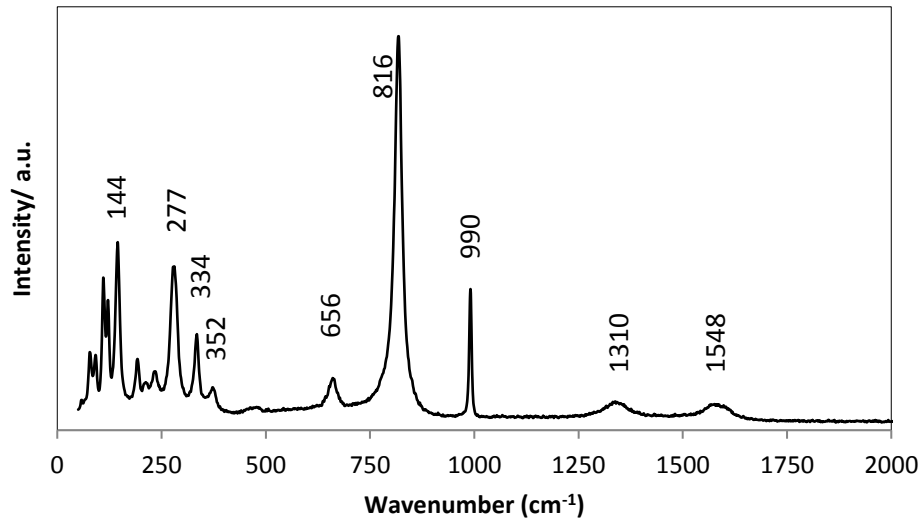


Figure 3.2-13: Raman spectrum of beta molybdenum carbide.

3.2.3.3 EDX and SEM analyses

The morphology of the molybdenum carbide material was characterized by scanning electron microscopy. For this characterization, the samples were placed directly onto the microscope holder without coating.

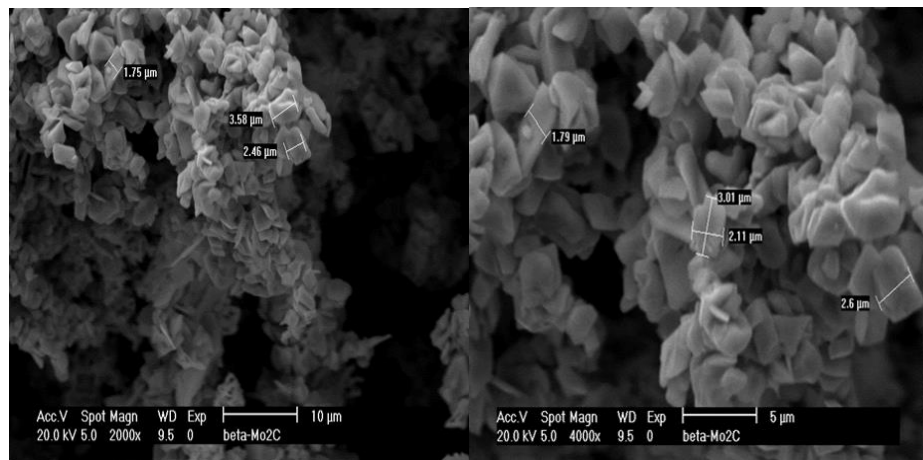


Figure 3.2-14: SEM images of beta molybdenum carbide.

After the molybdenum trioxide was carburised at 800 °C for 2 h, the morphology (as shown in Figure 3.2-14) undergoes a significant change. From both the 2000 and 4000 magnification images, it appears the particles aggregate producing cubes of various sizes. BET surface area results show that beta molybdenum carbide was not significantly changed in its surface area which was $13 \text{ m}^2\text{g}^{-1}$ with pore volume $0.005 \text{ cm}^3\text{g}^{-1}$ and pore diameter 1.5 nm as compared to that of fresh MoO_3 which was $10 \text{ m}^2\text{g}^{-1}$ with pore volume $0.003 \text{ cm}^3\text{g}^{-1}$ and pore diameter 1.4 nm. Direct carburisation of the oxide precursor does not result in pseudomorphism as was the case for ammonolysis to prepare the nitride.³ An EDX spectrum of beta molybdenum carbide is shown in Figure 3.2-15 The EDX spectrum of $\beta\text{-Mo}_2\text{C}$ showed that it was composed solely of elemental molybdenum and carbon with an atomic ratio of 1:3 respectively which suggests that the carbon content was quite high which could be due to the carbon based discs used as the sample holders during the SEM/EDX measurements as well as additional carbon formed in the process as evidenced in the Raman spectrum. The stoichiometric content of carbon corresponding to the pure Mo_2C phase is expected to be 5.8 wt. %.

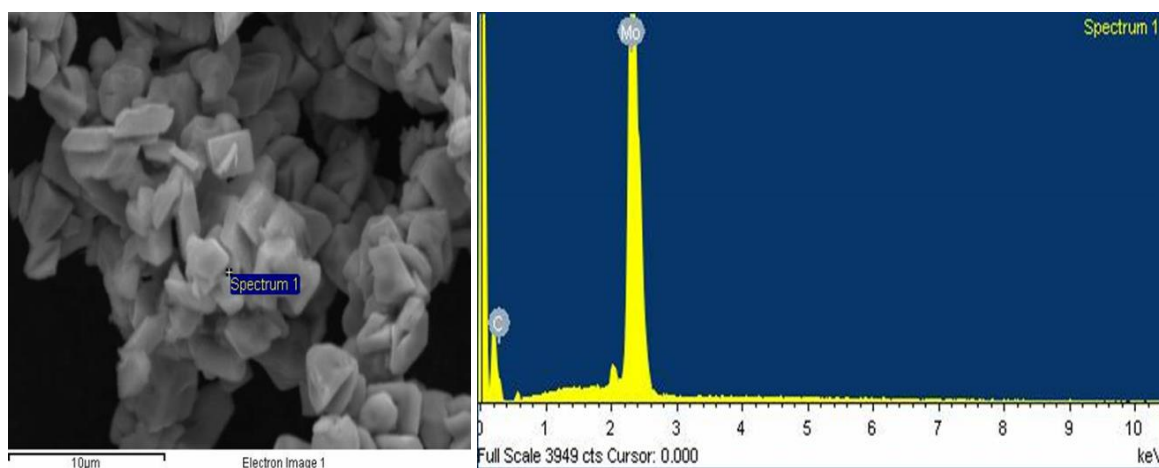


Figure 3.2-15: EDX analysis of beta molybdenum carbide.

3.2.4 Alpha molybdenum carbide (α -Mo₂C)

Previously, alpha molybdenum carbide (α -Mo₂C) with high surface area was prepared by Volpe *et al.* from a gamma molybdenum nitride precursor using a temperature programmed reduction (TPR) method.¹ Its structure was investigated by Lee *et al.*³ using PXRD. In this study, α -Mo₂C was synthesised and characterised by using PXRD, BET, Raman spectroscopy, SEM, EDX and CHN analysis as discussed in more detail below.

3.2.4.1 PXRD analysis

The formation of metastable cubic molybdenum carbide with a specific surface area of ca. 200 m²g⁻¹ using (TPR) has been previously described by Lee *et al.* The interstitial nitrogen atoms in γ -Mo₂N can be replaced by carbon to produce α -Mo₂C with high surface area. Characterization was undertaken using PXRD, SEM, BET and CHN analysis. The PXRD pattern in Figure 3.2-16 confirmed the formation of alpha molybdenum carbide. The diffraction peaks at $2\theta = 36.9, 42.8, 62.2, 74.5$ and 78.2° are indexed as the (111), (200), (220), (311) and (222) hkl crystal planes of the α -Mo₂C phase respectively which is consistent with reference to the JCPDS 015-0457 PDF file and other previous publications.^{2-3, 64} The carbon content of the material obtained from CHN analysis was 5.8 wt. % which corresponds to a Mo:C ratio of 2:1.

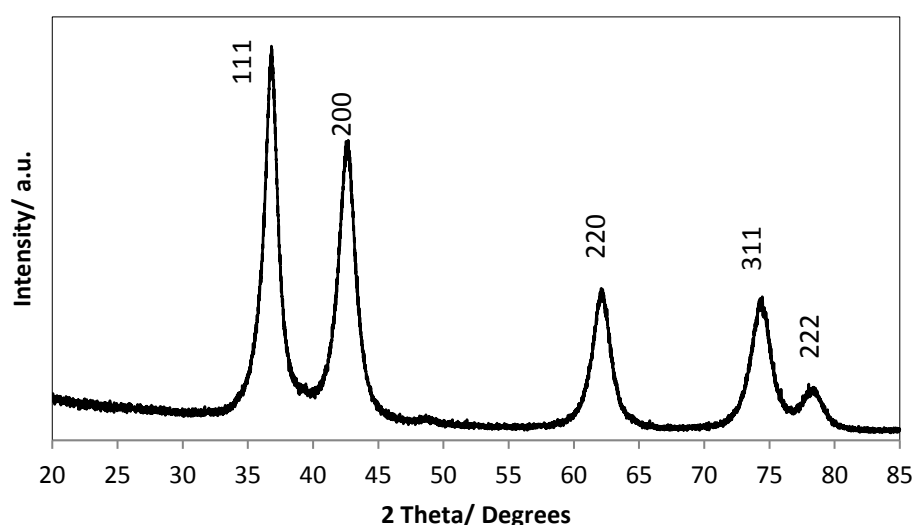


Figure 3.2-16: Indexed PXRD pattern of alpha molybdenum carbide.

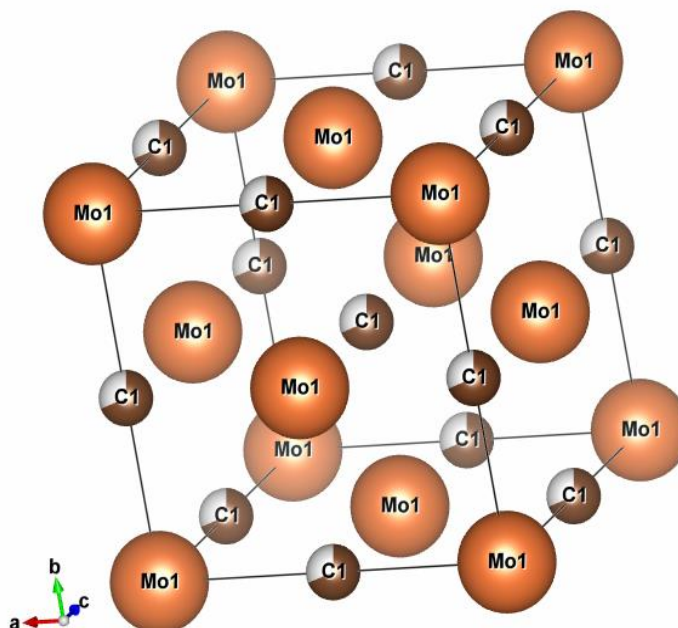


Figure 3.2-17: Unit cell of alpha molybdenum carbide.

The structure of alpha Mo_2C (VESTA using previous published CIF files by Sathish *et al.* in 2012⁶⁵ with code number 236296 in the Inorganic Crystal Structure Database Web) is shown in Figure 3.2-17. The structure of alpha Mo_2C can be defined as a face centred cubic array of molybdenum atoms with carbon atoms occupying one-half of the octahedral interstitial positions of the host metal with the literature reported unit cell information: space group $Fm-3m$, $a = b = c = 4.26 \text{ \AA}$, $\beta = \gamma = \alpha = 90^\circ$, unit cell volume = 77.66 \AA^3 .

3.2.4.2 Raman spectroscopy

Raman spectroscopy was conducted at room temperature in air on the molybdenum carbide sample. A Kimmon IK series He-Cd 532.17 nm laser was employed as the excitation source for the laser. For the α - Mo_2C material, the spectral range scanned was in the range up to 2000 cm^{-1} .

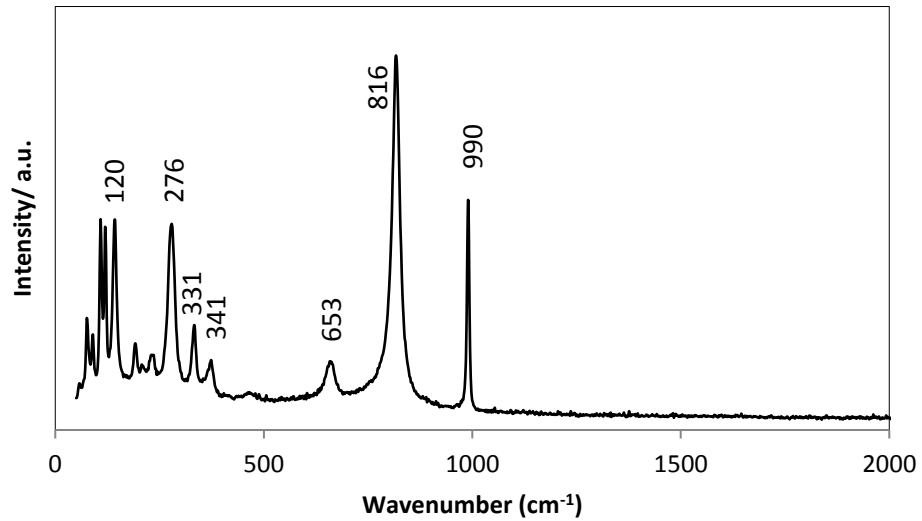


Figure 3.2-18: Raman spectrum of alpha molybdenum carbide.

The Raman spectrum of α -Mo₂C is shown in Figure 3.2-18 and, as for the previous two samples (γ -Mo₂N and β -Mo₂C), the material demonstrates the typical Raman scattering bands of alpha-MoO₃. The Raman spectrum of alpha molybdenum carbide could not be found in literature.

3.2.4.3 EDX and SEM analyses

The morphology of alpha molybdenum carbide powder was characterized by scanning electron microscopy. Figure 3.2-19 shows typical SEM images obtained at 2000 and 4000 times magnification.

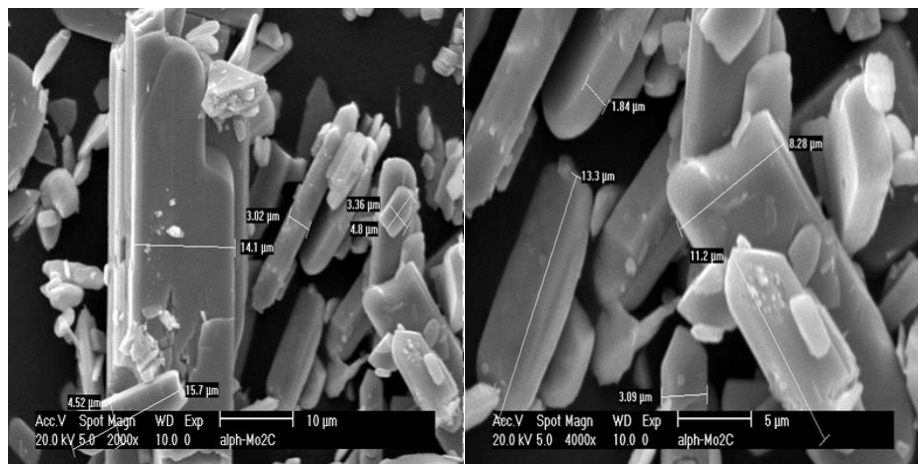


Figure 3.2-19: SEM images of alpha molybdenum carbide.

Alpha-Mo₂C has a similar morphology to γ -Mo₂N, comprising smooth platelets. The morphology of the parent oxide is retained in gamma molybdenum nitride and alpha molybdenum carbide. Lee *et al.*³ reported that the reactions involved in ammonolysis of α -MoO₃ to produce γ -Mo₂N and subsequent carburisation to produce α -Mo₂C processes are topotactic and are pseudomorphic with respect to the parent platelets of MoO₃. The BET surface area decreased to 52 m²g⁻¹ (0.07 cm³g⁻¹, 5.5 nm) for α -Mo₂C compared with γ -Mo₂N (63 m²g⁻¹). EDX spectra of alpha molybdenum carbide are shown in Fig. 3.2-20. The EDX spectrum of α -Mo₂C showed that it was composed of only elemental molybdenum and carbon with an atomic ratio of 1:3 respectively which suggests that the carbon wt. % was very high which could be due to the issue with the sample holders discussed previously. The corresponding stoichiometric values would be 94.2 wt. % Mo and 5.8 wt. % C for Mo₂C. It should also be remembered that the stoichiometry of this molybdenum carbide phase is variable (i.e. the phase is α -MoC_{1-x}).

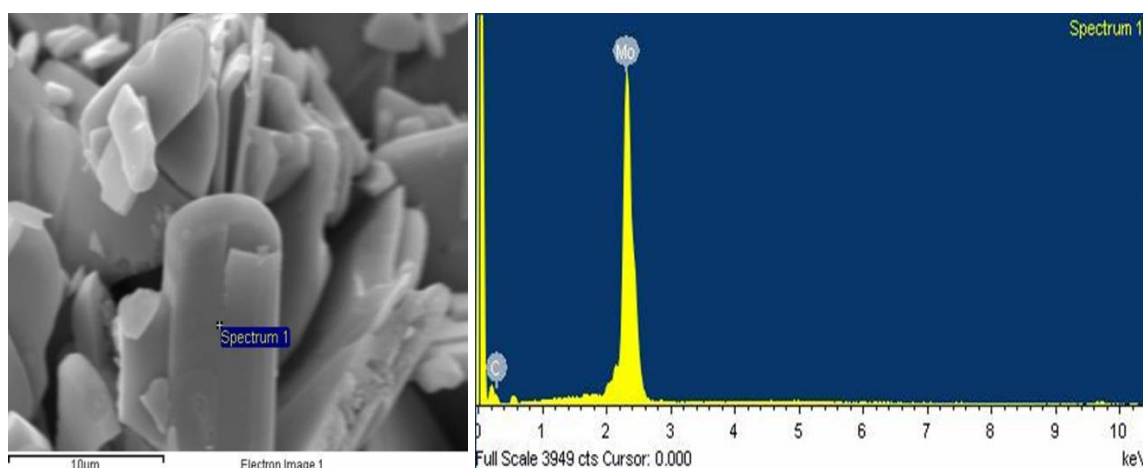


Figure 3.2-20: EDX analysis of alpha molybdenum carbide.

3.2.5 Cobalt molybdenum oxide (CoMoO₄.nH₂O).

Four polymorphs of cobalt molybdate have been previously reported; the low temperature α -phase⁶⁶ with (space group $C2/m$, $a = 9.67 \text{ \AA}$, $b = 8.85 \text{ \AA}$, $c = 7.76 \text{ \AA}$, $\beta = 113.49^\circ$), the high pressure hp-phase⁶⁷ with (space group $P2/c$, $a = 4.65 \text{ \AA}$, $b = 5.68 \text{ \AA}$, $c = 4.91 \text{ \AA}$, $\beta = 90.52^\circ$), the high temperature β -phase⁶⁸ with space group $C2/m$, $a = 10.21 \text{ \AA}$, $b = 9.31 \text{ \AA}$, $c = 7.01 \text{ \AA}$, $\beta = 106.40^\circ$) and the hydrate⁶⁹ a violet phase with space group $P-1$, $a = 6.84 \text{ \AA}$, $b = 6.93 \text{ \AA}$, $c = 9.33 \text{ \AA}$, $\beta = 84.18^\circ$). In this project, a series of hydrated and subsequently dehydrated CoMoO₄ phases was synthesised following the approach described in detail in the literature.⁷⁰⁻⁷¹

3.2.5.1 PXRD analysis

Hydrated compounds $\text{CoMoO}_4 \cdot n\text{H}_2\text{O}$ were synthesised by a hydrothermal method which is greatly reproducible with the same dark purple phase product being repeatedly formed. Cobalt nitrate and ammonium heptamolybdate were dissolved in 200 ml of distilled water and heated with mixing at 80 °C. The obtained precipitate was filtered, washed twice with distilled water and once with ethanol. The product was placed in an oven overnight at 100 °C to dry and then the resulting material was calcined at 500 °C for 3h in static air to obtain the dehydrated cobalt molybdate phase. Single phase products of the hydrated and dehydrated phases were obtained and confirmed by powder X-ray diffraction as shown in Figure 3.2-21 and Figure 3.2-22 respectively.

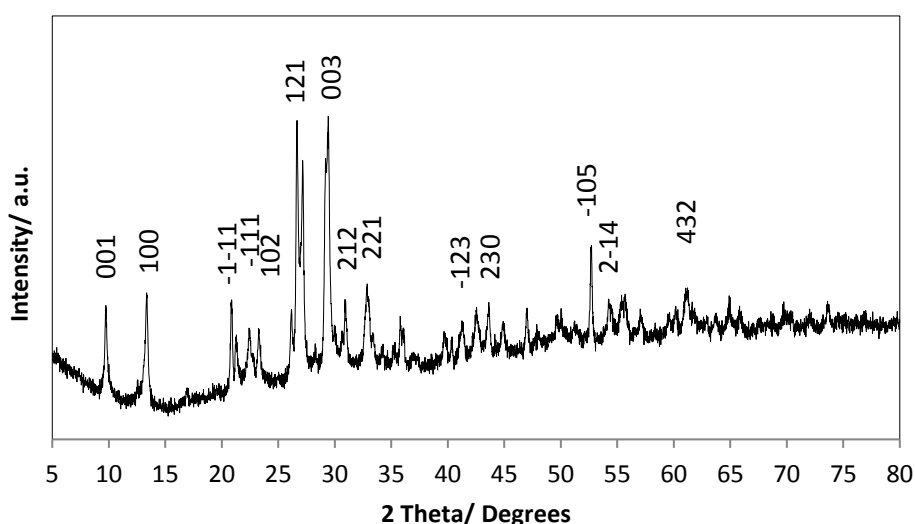


Figure 3.2-21: Indexed PXRD pattern of hydrated cobalt molybdenum oxide.

Figure 3.2-21 displays the powder X-ray diffraction pattern for the $\text{CoMoO}_4 \cdot n\text{H}_2\text{O}$ material. The XRD results are similar to those presented in JCPDS file number 01-074-8729 reported for $\text{CoMoO}_4 \cdot 0.75\text{H}_2\text{O}$ with space group $P-1$ (number 2), $a = 6.84 \text{ \AA}$, $b = 6.93 \text{ \AA}$, $c = 9.33 \text{ \AA}$, $\beta = 84.18^\circ$, $\alpha = 76.61^\circ$, $\gamma = 74.51^\circ$). The diffraction peaks at $2\theta = 9.7, 13.4, 20.9, 22.5, 23.3, 26.6, 29.5, 30.7, 31.0, 32.7, 41.4, 42.5, 43.6, 52.8, 54.2, 55.7$ and 60.9° are indexed and labelled as the (001), (100), (-111), (102), (-1-11), (121), (003), (113), (212), (221), (-123), (-2-22), (230), (-105), (2-14), (412) and (432) hkl crystal planes of the hydrate phase respectively.

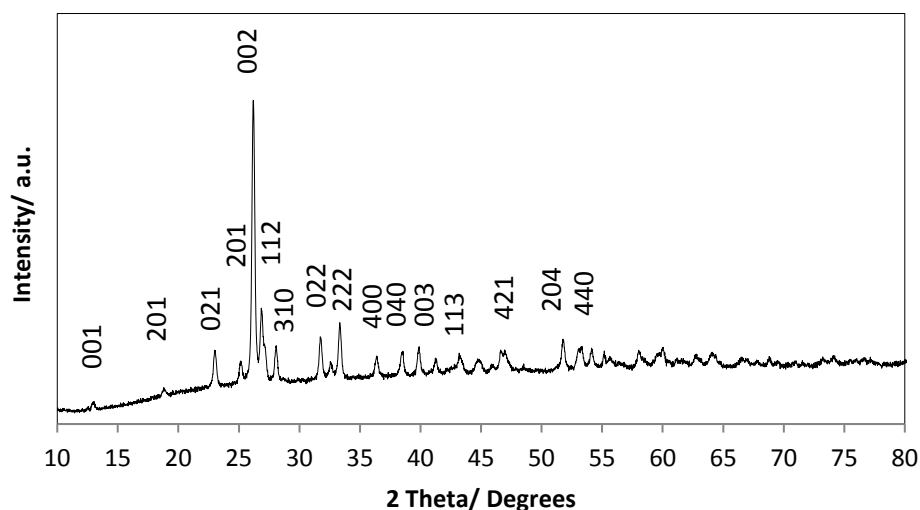


Figure 3.2-22: Indexed PXRD pattern of beta cobalt molybdenum oxide.

Figure 3.2-22 presents the powder X-ray diffraction pattern for the anhydrous β -CoMoO₄ material. This pattern agrees very well with the corresponding JCPDS file number 021-0868 reported for the beta-phase anhydrous cobalt molybdate with (space group $C2/m$, space group number 12, $a = 10.21$, $b = 9.31$, $c = 7.01$ Å, $\beta = 106.4$, $\gamma = \alpha = 90^\circ$). The reflections at $2\theta = 12.8, 18.7, 22.9, 25.1, 26.2, 26.8, 28, 31.7, 33.3, 36.3, 38.4, 39.7, 43.1, 46.5, 51.7$ and 57.9° are indexed and labelled as the (001), (201), (021), (201), (002), (112), (310), (022), (222), (400), (040), (003), (113), (421), (204) and (440) hkl crystal planes of the beta phase respectively.

In order to confirm that the structure was hydrated cobalt molybdenum oxide, Rietveld refinement was performed against PXRD data using the General Structure Analysis System (GSAS) through the EXPGUI interface.⁵⁻⁶ The position in the unit cell of the atoms, the space group and the unit cell parameters of hydrated CoMoO₄ were refined over a 2 theta range of 5 to 80°. The background was modelled by a type 7 function and 23 term Chebyshev polynomial function model in GSAS. The refinement parameters and Rietveld refinement fits are shown in Table 3.2-1, Table 3.2-2 and Figure 3.2-23 respectively.

Table 3.2-1: PXRD refined crystallographic parameters for CoMoO₄.nH₂O.

Parameter	Value
Chemical formula	CoMoO ₄ . 0.75 H ₂ O
Colour of material	Dark violet
Crystal system	Triclinic
Space group	P-1
Space group number	2
Cell parameter, a/ Å	6.8296(3)
Cell parameter, b/ Å	6.9357(5)
Cell parameter, c/ Å	9.3379(1)
Alpha/ Degrees	76.62
Beta/ Degrees	84.19
Gamma/ Degrees	74.72
Unit cell volume/ Å ³	414.71(9)
Calculated weight / gmol ⁻¹	939.472
Calculated density / gcm ⁻³	3.762
Number of observations	4487
Number of variables	78
R _p	0.173
R _{wp}	0.231
χ ²	3.156

Table 3.2-2: PXRD refined parameters for CoMoO₄.nH₂O.

Atoms	Ox state/ sites	X	Y	Z	Occupancy	100*U _{iso}
Co1	+2 (2i)	0.1751(27)	0.6542(30)	0.7007(20)	1.0000	0.500
Co2	+2 (2i)	0.2015(31)	0.8294(28)	0.9832(20)	1.0000	0.500
Mo1	+6 (2i)	-0.0078(17)	0.1962(17)	0.6687(13)	1.0000	0.500
Mo2	+6 (2i)	0.2404(17)	0.2853(17)	0.0543(13)	1.0000	0.500
O1	-2 (2i)	0.160(9)	0.077(9)	0.781(5)	1.0000	0.500
O2	-2 (2i)	0.208(8)	0.426(9)	0.660(7)	1.0000	0.500
O3	-2 (2i)	0.010(10)	0.266(10)	0.400(7)	1.0000	0.500
O4	-2 (2i)	-0.312(8)	0.321(10)	0.637(6)	1.0000	0.500
O5	-2 (2i)	0.231(7)	0.519(9)	1.019(6)	1.0000	0.500
O6	-2 (2i)	0.297(8)	-0.050(9)	1.000(7)	1.0000	0.500
O7	-2 (2i)	0.365(10)	0.293(10)	0.291(7)	1.0000	0.500
O8	-2 (2i)	0.445(9)	0.262(9)	0.051(6)	1.0000	0.500
O9	-2 (2i)	0.554(9)	0.673(10)	0.663(7)	1.0000	0.500
O10	-2 (2i)	-0.628(8)	0.099(8)	0.586(6)	1.0000	0.500

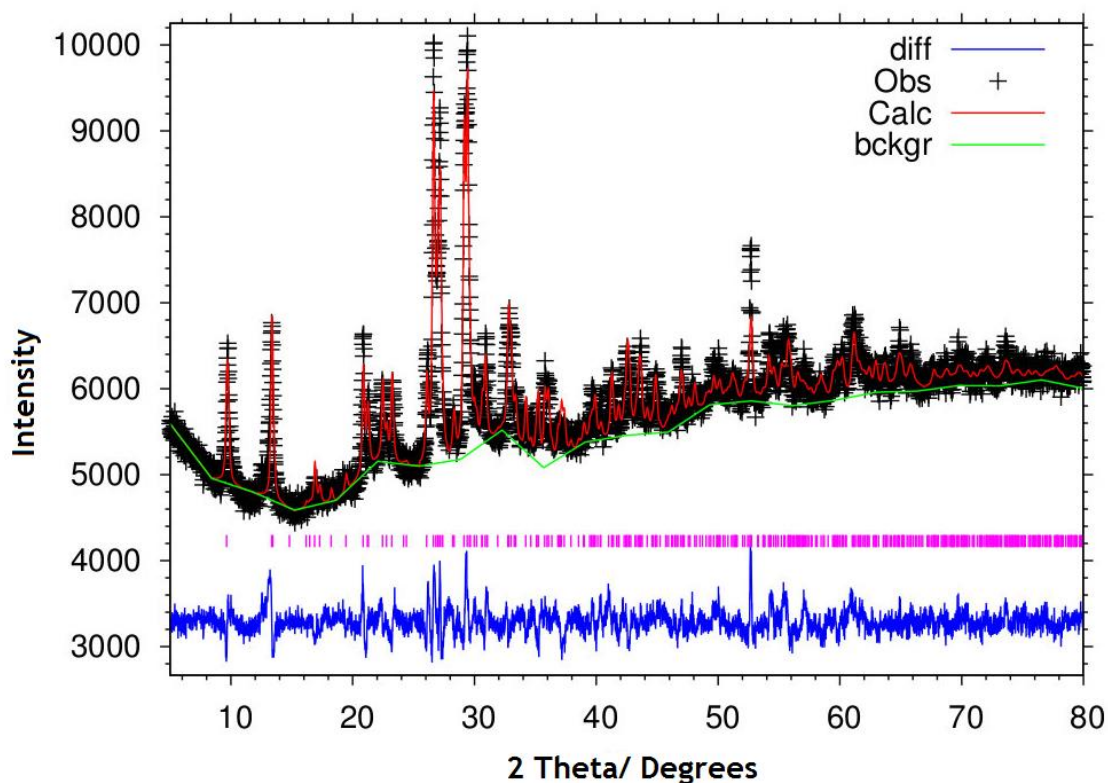


Figure 3.2-23: PXRD refinement of $\text{CoMoO}_4 \cdot n\text{H}_2\text{O}$.

A Crystallographic Information File, which was obtained from ICSD website with code 153169 from Eda *et al.*⁶⁹ for $\text{CoMoO}_4 \cdot 0.75\text{H}_2\text{O}$, was used to refine the obtained XRD data; it gave the best fit for $\text{CoMoO}_4 \cdot n\text{H}_2\text{O}$ compared with other CIF published files. However, the refinement does not produce a very good fit to the data which could be related to different amounts of water present in this material.

The structure of the material has been well studied and it is apparent that cobalt is octahedrally coordinated to oxygen (CoO_6) and molybdenum is tetrahedrally coordinated to oxygen (MoO_4) in both the dehydrated and hydrated phases. Figure 3.2-24 displays the unit cell for the hydrate $\text{CoMoO}_4 \cdot 0.75\text{H}_2\text{O}$ drawn using Vesta software using CIF file code 153169; whereas Figure 3.2-25 presents the unit cell for beta CoMoO_4 using CIF file with code number 23808 as proposed by Smith *et al.* from the ICSD website.⁷²

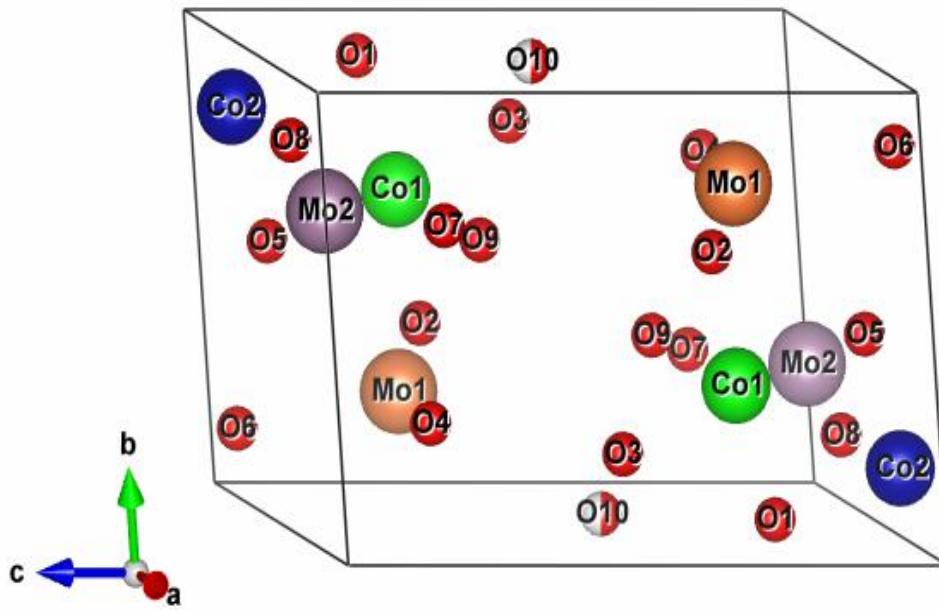


Figure 3.2-24: Unit cell of hydrated cobalt molybdate.

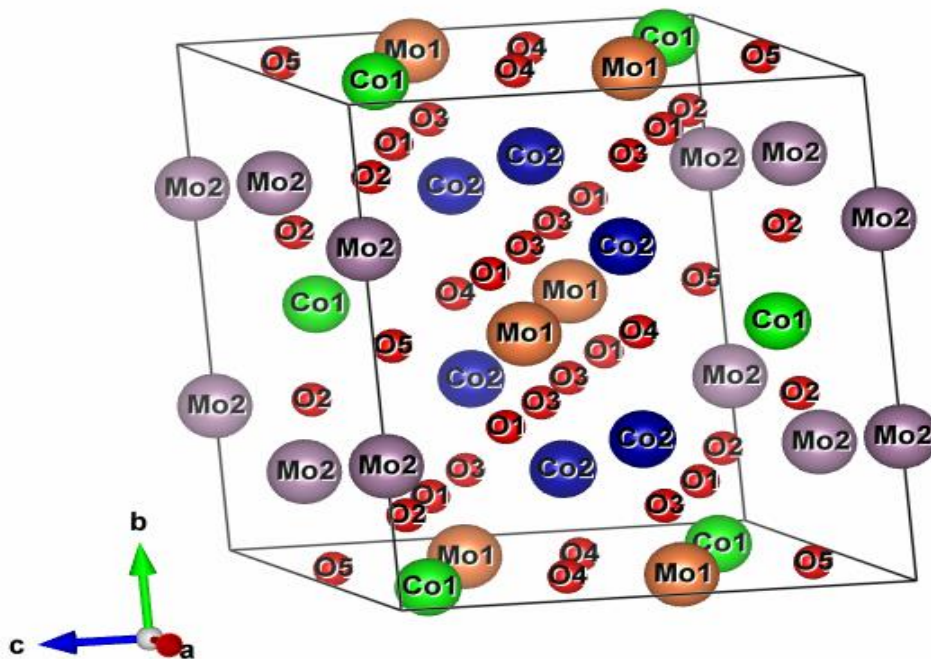


Figure 3.2-25: Unit cell of the anhydrous beta CoMoO_4 phase.

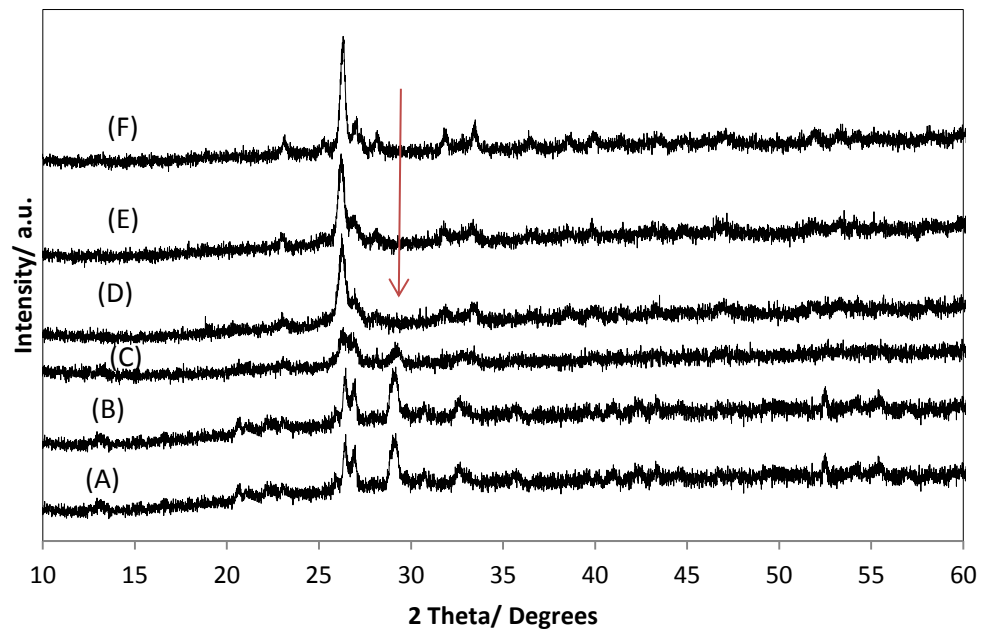


Figure 3.2-26: PXRD patterns of hydrated cobalt molybdenum oxide calcined under air (A) $\text{CoMoO}_4 \cdot n\text{H}_2\text{O}$; (B) 200°C , 1h; (C) 300°C , 1h; (D) 350°C , 1h; (E) 400°C , 1h; (F) 500°C , 1h. (the peak at $2\theta = 29^\circ$ which is related to $\text{CoMoO}_4 \cdot n\text{H}_2\text{O}$ which completely disappeared at 350°C as highlighted by the red arrow).

Ex-situ experiments were performed to investigate the effect of calcination in air from 200 to 500°C for 1 hr, in order to investigate any possible intermediate phases formed when the hydrated phase undergoes transformation to the anhydrous beta phase. The PXRD patterns presented in Figure 3.2-26 indicated that no change in the diffraction pattern was observed at 200°C and the hydrated molybdenum oxide phase transformed to the dehydrated phase between 300 to 350°C . There was no significant change observed beyond 350°C and beyond this point the dark violet hydrated phase converted to the pale violet dehydrated phase. This result agrees well with the TGA result presented below and the work of Rodriguez and co-workers.⁷³

3.2.5.2 TGA analysis

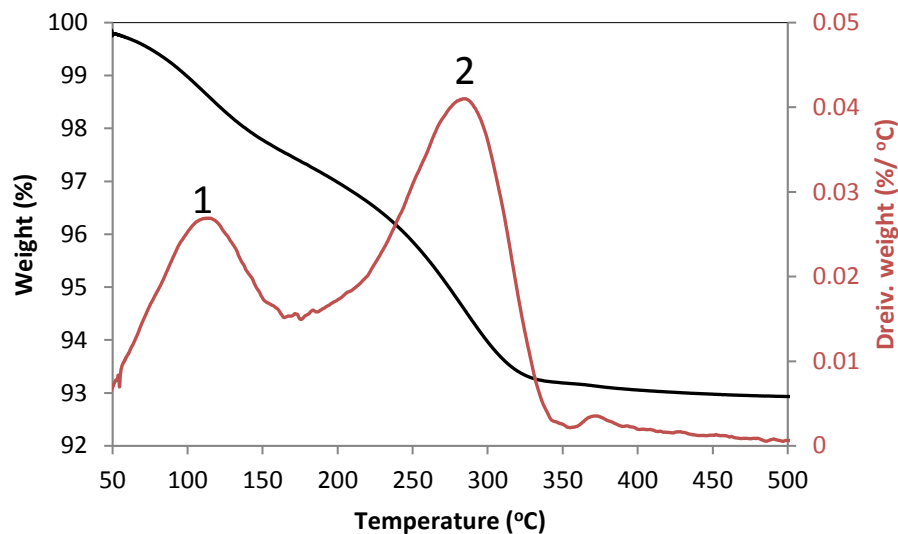


Figure 3.2-27: TGA trace of CoMoO₄.nH₂O performed from room temperature up to 500 °C in air.

TGA for the hydrated cobalt molybdenum oxide was performed from room temperature to 500 °C in air. Upon heating CoMoO₄.nH₂O to high temperature, water loss in two stages was evidenced as can be seen in Figure 3.2-27. The first stage occurs between 50 and 150 °C which is associated with the weight loss corresponding adsorbed water on the surface of the hydrated material. The second peak appears in the range 200 to 350 °C and is assigned to the loss of water molecules from the crystal structure. At the end of the second stage a total loss of around 7 % mass in total of the material, equivalent to that of 0.85 moles of water per formula unit of CoMoO₄, which is more than the expected amount of 0.75 moles.

3.2.5.3 Raman spectroscopy

The Raman spectrum of the anhydrous beta- CoMoO_4 material was recorded in air at room temperature using a Horiba Jobin Yvon LabRam HR confocal Raman microscope with 532.17 nm laser excitation. The scanning range was up to 2000 cm^{-1} .

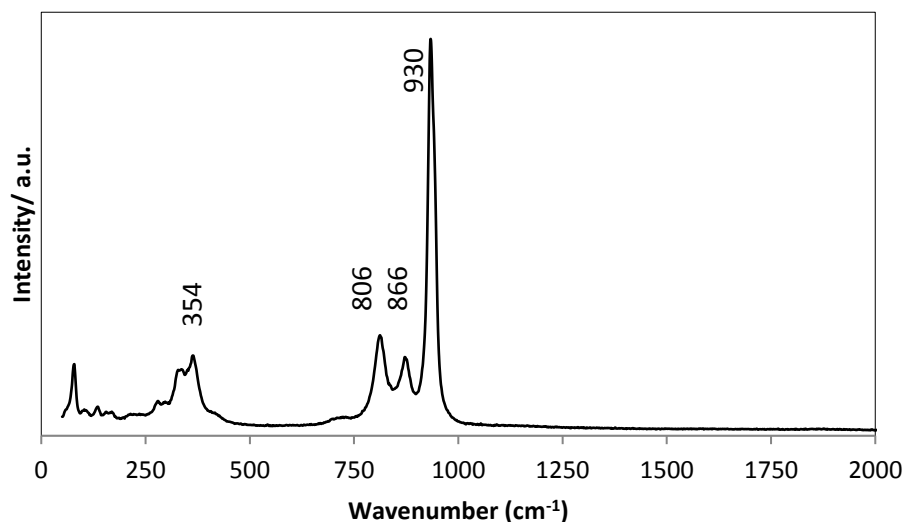


Figure 3.2-28: Raman spectrum of dehydrated β -phase cobalt molybdenum oxide.

The Raman spectrum for the dehydrated β -phase CoMoO_4 material (as prepared material) is presented in Figure 3.2-28. The positions of the Raman bands at 354, 806, 866, 930 and 941 cm^{-1} were attributed to the CoMoO_4 Raman bands at 350, 880 and 930 cm^{-1} assigned to Mo-O-Co stretching vibrations in cobalt molybdate species.⁷⁴ Moreover, the stronger band at 941 cm^{-1} is due to the A1 mode of Mo=O in the MoO_4 tetrahedral unit,³⁰ whereas the band at 806 cm^{-1} occurs also in MoO_3 as a strong band.

3.2.5.4 SEM images

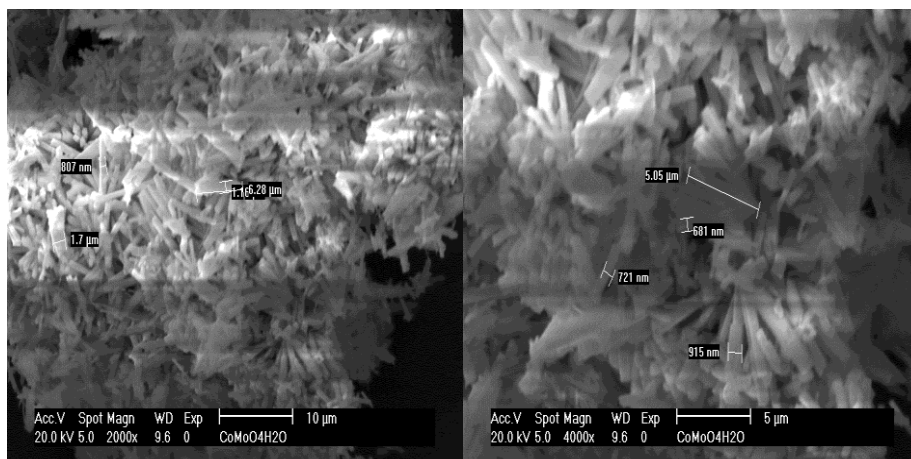


Figure 3.2-29: SEM images of the hydrate $\text{CoMoO}_4 \cdot n\text{H}_2\text{O}$ phase.

Figure 3.2-29 shows the scanning electron microscopy images of hydrated $\text{CoMoO}_4 \cdot n\text{H}_2\text{O}$ nanorods of various lengths (in the range ca. 5 μm) and diameter of ca. 600 nm. Previously, several groups have reported that the hydrated $\text{CoMoO}_4 \cdot n\text{H}_2\text{O}$ material has nanorod morphology.⁷⁵ Figure 3.2-30 presents the SEM images for the beta- CoMoO_4 phase in which rods of various lengths between 1 and 10 μm and diameter ca. 600 nm are evident, in agreement with the observations of Rico *et al.*⁷¹

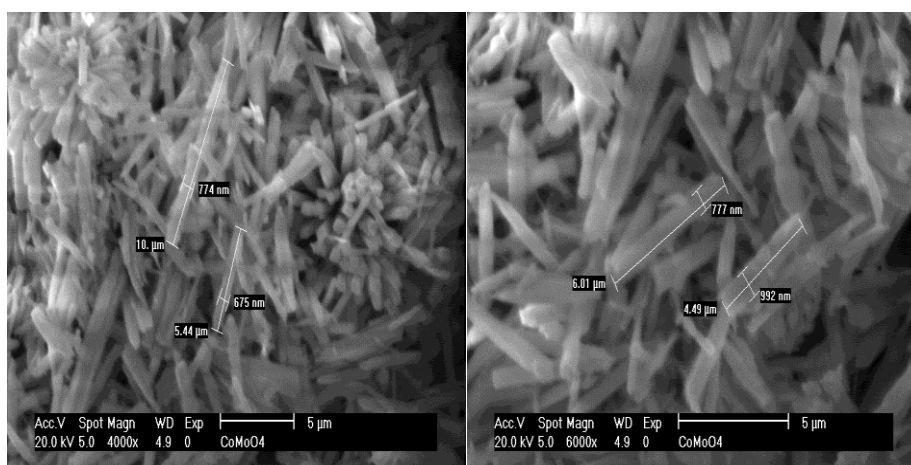


Figure 3.2-30: SEM images of the anhydrous beta CoMoO_4 phase.

3.2.6 Cobalt molybdenum nitride (η -6 $\text{Co}_3\text{Mo}_3\text{N}$)

Cobalt molybdenum nitride is characterised by a face centred cubic arrangement of the Co and Mo species with the lattice nitrogen occupying octahedral interstitial positions located at 16c Wyckoff sites.^{4, 76-77} $\text{Co}_3\text{Mo}_3\text{N}$ has received much attention as a result of its excellent catalytic properties in ammonia synthesis.⁷⁸ This nitride is usually prepared via temperature programmed nitridation of the bimetallic oxide precursor which is obtained from the reaction of cobalt nitrate with ammonium heptamolybdate.⁷⁹ The preparation of this material drew upon prior literature that reported the formation of a pure ternary molybdenum nitride phase.⁷⁰ The goal of the work detailed in the current chapter was to prepare and investigate the intermediate phases for nitride and carbide materials when ternary molybdenum nitrides are converted to ternary molybdenum carbides and vice versa using nitrogen or carbon sources such as N_2/H_2 , N_2 , CH_4/H_2 , CH_4 and H_2/Ar .

3.2.6.1 PXRD and PND analysis

The formation of the η -6 $\text{Co}_3\text{Mo}_3\text{N}$ (abbreviated as 331N) phase was confirmed using PXRD. The obtained material was scanned at a step size of 0.0167° over the range $10 \leq 2\theta/^\circ \leq 90$ and scan speed 0.002 degree per second run over 12 hours to obtain accurate peaks for use in refinement. The pattern was matched using the JCPDS reference standard for η -6 $\text{Co}_3\text{Mo}_3\text{N}$ (01-89-7953).

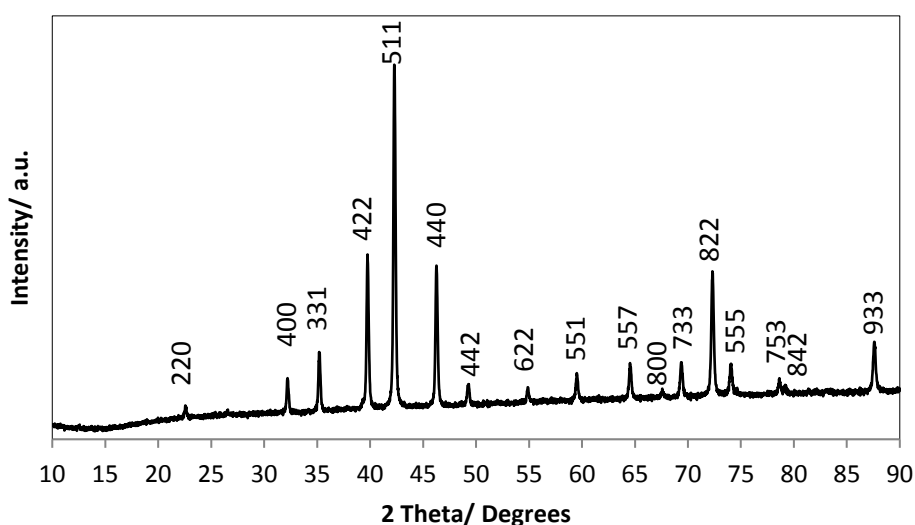


Figure 3.2-31: Indexed PXRD pattern of $\text{Co}_3\text{Mo}_3\text{N}$ showing indexed reflections.

The indexed PXRD pattern for η -6 $\text{Co}_3\text{Mo}_3\text{N}$ is presented in Figure 3.2-31. The 17 reflections in the 2θ range at 20 - 90° ($22.4, 32.2, 35.2, 39.7, 42.3, 46.2, 49.2, 54.7, 59.5, 64.5, 67.9, 69.3, 72.3, 73.9, 79.0, 79.6$ and 88.1°) are representative of the ternary cobalt molybdenum nitride; and the associated hkl crystal planes are identified in the figure. In addition, this result confirms that this obtained material was free from reflections relating to Mo_2N , Co, Mo or oxide formation. Based on the CHN elemental analysis results, the nitrogen content of the material was found to be 3.1 wt. % which is similar to the calculated stoichiometric value for $\text{Co}_3\text{Mo}_3\text{N}$ (which is 2.9 wt. %).

Rietveld analysis was performed to fit a published structural model of $\text{Co}_3\text{Mo}_3\text{N}$ to the experimental PXRD data. The structure of the $\text{Co}_3\text{Mo}_3\text{N}$ was refined by the Rietveld method against PXRD data using GSAS and EXPGUI software packages. The initial model used was the cubic $\text{Fe}_3\text{W}_3\text{C}$ structure type which was proposed by Jackson⁸⁰ *et al.* and taken from the ICSD database website with code 88267, in which the molybdenum atoms are placed at 48f Wyckoff positions and the cobalt species occupy in two non-equivalent the 16d, 32e sites, while the nitrogen species are located at 16c sites.

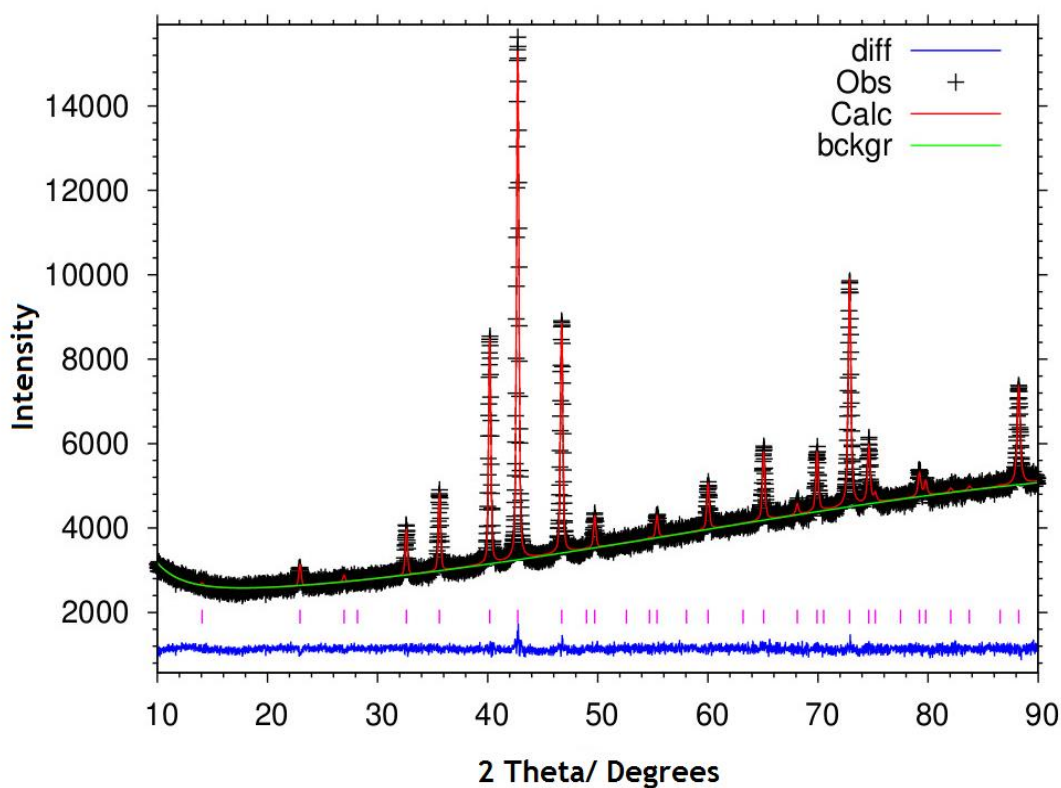


Figure 3.2-32: Fitted PXRD data profiles from Rietveld refinement for $\text{Co}_3\text{Mo}_3\text{N}$.

The background was modelled using a power series in $Q^{2n/n!}$ and $n!/Q^{2n}$ function (function type 6 and 6 terms within GSAS). Cell parameters, scale factor and zero point were also refined in the initial cycles. The isotropic thermal factors (U_{iso}) of the cobalt, molybdenum and nitrogen were refined in final cycle. The nitrogen site occupancy factor was refined which further improved the goodness of fit parameters. The results of $\text{Co}_3\text{Mo}_3\text{N}$ refinement obtained from PXRd data are presented in Figure 3.2-32 and Table 3.2-3.

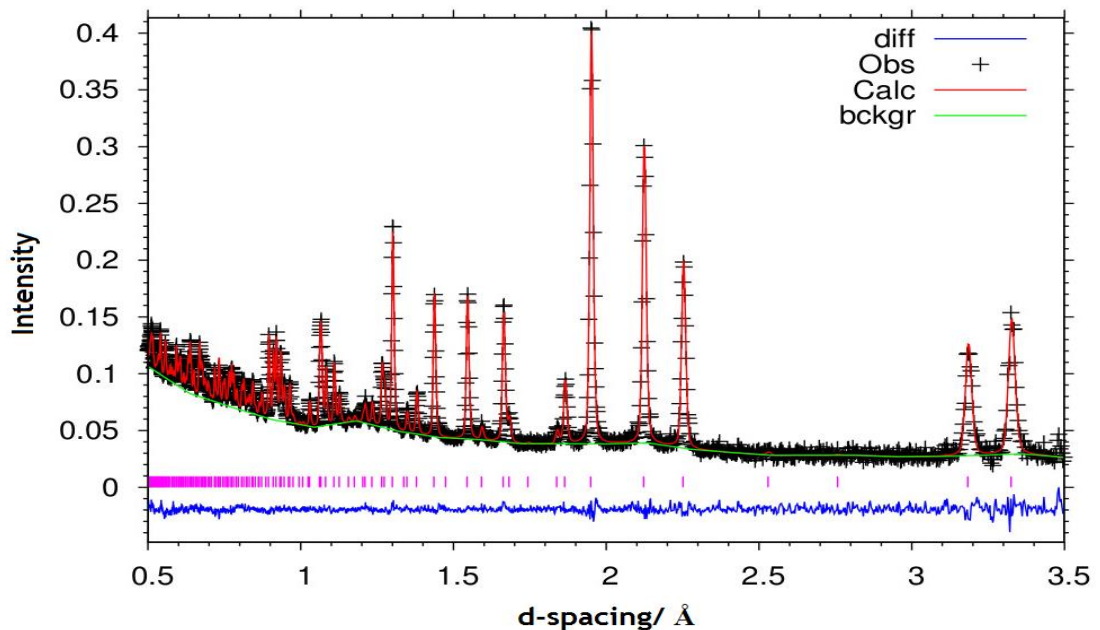


Figure 3.2-33: Fitted PND data profiles from Rietveld refinement for $\text{Co}_3\text{Mo}_3\text{N}$.

PND was used in the current studies to establish how much carbon or nitrogen was present within the bulk carbide or nitride structure as PXRd is unable to distinguish them. The reason for this is based on the fact that the difference between carbon and nitrogen atoms is only one electron which makes their distinction impossible when using X-ray diffraction which is sensitive to electron density, whereas, neutrons are diffracted by nuclei.

At room temperature, time-of-flight (ToF) PND data were collected using the high intensity Polaris diffractometer at the ISIS pulsed spallation source (Rutherford Appleton Laboratory, UK). Powder samples (ca. 1 g) were loaded into 11 mm diameter thin-walled stainless steel cells. A collimator manufactured from a neutron-absorbing boron nitride ceramic placed

around the cell enabled diffraction patterns to be collected in the Polaris $2\theta \approx 90^\circ$ detector bank which were free of Bragg reflections from the steel walls of the cell. Rietveld refinements against PND data were performed using the General Structure Analysis System (GSAS) through the EXPGUI interface.

The background was modelled using a linear interpolation function (function type 7 and 23 terms within GSAS). Cell parameters, the scale factor and zero point were also refined in initial cycles. The isotropic thermal factors (U_{iso}) of the cobalt, molybdenum and nitrogen were refined in the final cycle. The nitrogen site occupancy factor was refined which further improved the goodness of fit parameters. The results of $\text{Co}_3\text{Mo}_3\text{N}$ refinement obtained from PND data are presented in Figure 3.2-33 and Table 3.2-3.

Table 3.2-3: Crystallographic parameters of $\text{Co}_3\text{Mo}_3\text{N}$ from PXRD and PND refined data.

Parameter	PXRD value	PND value
Formula	$\text{Co}_3\text{Mo}_3\text{N}$	$\text{Co}_3\text{Mo}_3\text{N}$
Crystal system	Cubic	Cubic
Space group	$Fd\bar{3}m$	$Fd\bar{3}m$
Space group number	227	227
Cell parameter a/ Å	11.0260(9)	11.0272(8)
Cell parameter b/ Å	11.0260(9)	11.0272(8)
Cell parameter c/ Å	11.0260(9)	11.0272(8)
Alpha/ Degrees	90	90
Beta/ Degrees	90	90
Gamma/ Degrees	90	90
Unit-cell volume/ Å ³	1340.49(6)	1340.92(9)
Calculated formula weight/ gmol ⁻¹	7690.938	7750.530
Calculated density/ gcm ⁻³	9.527	9.598
Number of observations	4787	1945
Number of variables	19	37
R_p	0.0139	0.0394
R_{wp}	0.0176	0.0277
χ^2	1.196	1.031

Rietveld refinement of the X-ray data within the $Fd\bar{3}m$ space group of the η -6 cobalt molybdenum nitride produced an acceptable fit with $R_{wp} = 1.76\%$ and $R_p = 1.39\%$ (Table 3.2-3 and Figure 3.2-32). The ToF neutron diffraction data were also successfully refined

within the same space group, giving $R_{wp} = 2.77\%$ and $R_p = 3.94\%$ (Table 3.2-3, Figure 3.2-33). The lattice parameters determined from X-ray and neutron results were in excellent agreement with each other: $a = 11.0260(9)$ and $a = 11.0272(8)$ Å, respectively. The correspondence between the X-ray and neutron data, and the successful Rietveld refinement of the powder data through the structural model confirms that all N atoms occupy the 16c (0, 0, 0) site within the structure. When using a model in which the nitrogen atoms occupied the 8a (1/8, 1/8, 1/8) site, no reasonable fit to the data was obtained therefore confirming the occupation of the 16c site. The composition of the material has been identified from the structural refinements against PXRD data in Table 3.2-4 and PND data in Table 3.2-5 which are $\text{Co}_3\text{Mo}_3\text{N}_{1.15}$ and $\text{Co}_3\text{Mo}_3\text{N}_{1.02}$ respectively and which is close to that determined by stoichiometric in previous studies $\text{Co}_3\text{Mo}_3\text{N}$.

Table 3.2-4: $\text{Co}_3\text{Mo}_3\text{N}$ PXRD refined parameters.

Atoms/site	X	Y	Z	Occupancy	$100 \cdot U_{\text{iso}} (\text{Å}^2)$
Co1 (32e)	0.292275(0)	0.2922750(0)	0.2922750(0)	1.00	1.78
Co2 (16d)	0.500000(0)	0.500000(0)	0.5000000(0)	1.00	1.52
Mo (48f)	0.324245(0)	0.125000(0)	0.1250000(0)	1.00	2.07
N (16c)	0.000000(0)	0.000000(0)	0.0000000(0)	1.15	4.30

Table 3.2-5: $\text{Co}_3\text{Mo}_3\text{N}$ PND refined parameters.

Atoms/site	X	Y	Z	Occupancy	$100 \cdot U_{\text{iso}} (\text{Å}^2)$
Co1 (32e)	0.290817(0)	0.290817(0)	0.290817(0)	1.00	0.068
Co2 (16d)	0.500000(0)	0.500000(0)	0.500000(0)	1.00	0.123
Mo (48f)	0.32435(9)	0.125000(0)	0.125000(0)	1.00	0.286
N (16c)	0.000000(0)	0.000000(0)	0.000000(0)	1.02	0.391

The structure of $\text{Co}_3\text{Mo}_3\text{N}$ consists of a distorted fcc arrangement of cobalt and molybdenum, with nitrogen occupying distorted octahedral interstitial sites. The cobalt, molybdenum and nitrogen atomic distances and bond angles in $\text{Co}_3\text{Mo}_3\text{N}$ were obtained from Rietveld refinement against PXRD and PND data as illustrated in Tables 3.2-6 and 3.2-7 respectively. PXRD and PND refined data are similar. The distances from the molybdenum atom to the remaining metallic atoms in this range between ca. 2.61(2) to 3.10(6) Å, the distances from cobalt in 32e Wyckoff site to the 16d site species in this range between ca.

2.38(3) to 2.57(9) Å and the distances from molybdenum to nitrogen in the 16c site are ca. 2.11(4) Å. These values are consistent with those published previously.⁴

Table 3.2-6: Bond angles for Co₃Mo₃N from PXRD and PND refined data.

Bond angle (°)	PND value	PXRD value
N-Mo-N*1	134.38(5)	134.436(1)
Mo-N-Mo*6	94.622(32)	94.581(1)
Mo-N-Mo*6	85.378(32)	85.419(1)
Mo-N-Mo*3	180.000(0)	180.000(0)
Mo-Co1-Mo*3	73.035(32)	72.342(1)
Co1-Mo-N*4	86.853(11)	87.027(1)
Co1-Mo-Co1*1	163.72(4)	164.607(0)
Co1-Co2-Co1*6	113.454(0)	114.465(0)
Co1-Co2-Co1*3	180.000(0)	180.000(0)
Co1-Co2-Co1*6	66.546(0)	65.535(0)
Co2-Co1-Mo*3	66.434(21)	66.247(0)
Co2-Co1-Mo*6	124.731(3)	124.232(1)
Co2-Co1-Co2*3	109.102(0)	109.733(0)

Table 3.2-7: Bond lengths for Co₃Mo₃N from PXRD and PND refined data.

Bond length (Å)	PND value	PXRD value
N-Mo*6	2.1148(4)	2.11409(3)
Mo-Mo*6	2.8677(4)	2.86789(5)
Mo-Mo*6	3.1089(13)	3.10688(6)
Co1-Mo*3	2.61222(15)	2.63207(3)
Co1-Mo*3	2.7242(8)	2.72824(4)
Co1-Co1*3	2.62566(9)	2.57990(3)
Co1-Co2*3	2.39294(7)	2.38337(4)
Co2-Mo*6	2.7480(7)	2.74857(4)
Co2-Co1*6	2.39294(7)	2.38337(4)

The structure of η -6 $\text{Co}_3\text{Mo}_3\text{N}$ phase has been previously studied and it is obvious that cobalt (Co1, Co2), molybdenum and nitrogen occupy Wyckoff locations (32e, 16d), 48f and 16c respectively. Figure 3.2-34 displays the unit cell for η -6 $\text{Co}_3\text{Mo}_3\text{N}$ including all elements in the figure on the left hand side (which was drawn by Vesta software using Jackson's CIF file code 88267 from the ICSD database website); whereas only the Mo and N sub-lattice is shown on the right hand side figure.

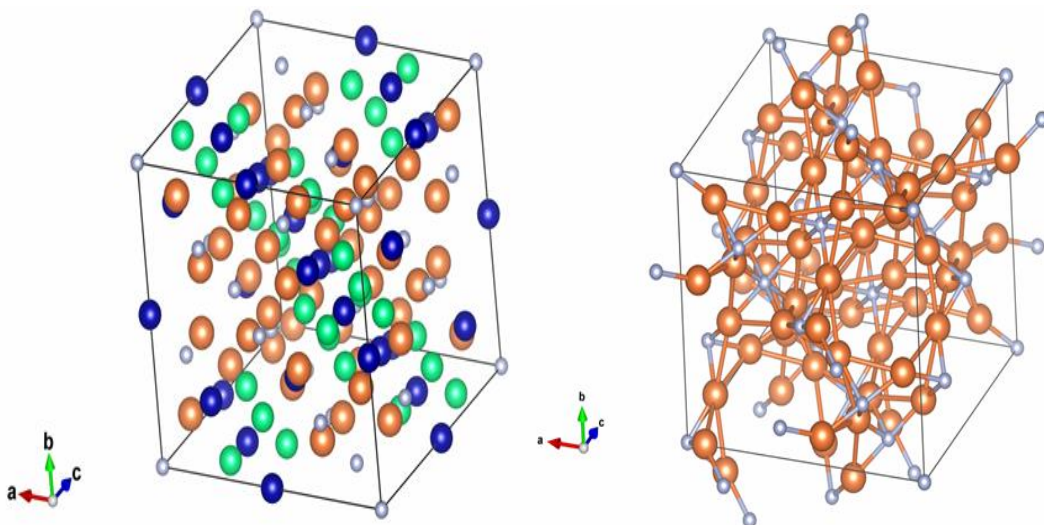


Figure 3.2-34: The Unit cell of $\text{Co}_3\text{Mo}_3\text{N}$ on the left hand side and Mo-N coordination on the right hand side by using VESTA software. Brown, grey, green and blue spheres represent the Mo, N, Co1 and Co2 respectively.

In the structure of $\text{Co}_3\text{Mo}_3\text{N}$, cobalt occupies two non-equivalent sites in which each site is surrounded by six molybdenum and six cobalt atoms resulting in the formation of $\text{Co}[\text{Mo}_6\text{Co}_6]$ units. In the case of molybdenum, the species is surrounded by four molybdenum, six cobalt species and two nitrogen species forming $\text{Mo}[\text{Mo}_4\text{Co}_6\text{N}_2]$ units while nitrogen is surrounded by six molybdenum species and coordinated exclusively to molybdenum in 16c Wyckoff sites, resulting in the formation of $[\text{NMo}_6]$ units as illustrated in Figure 3.2-35.

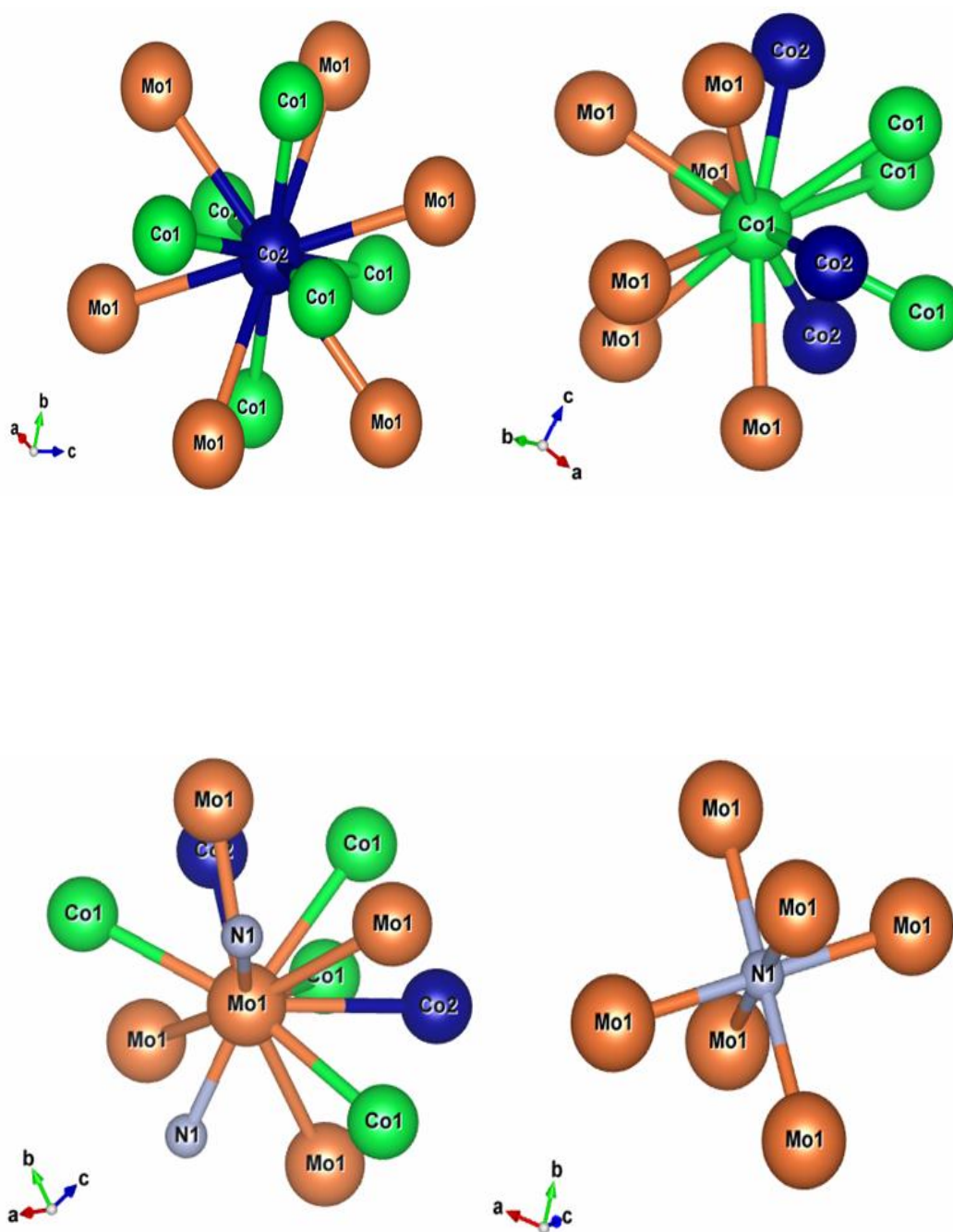


Figure 3.2-35: Atomic coordination of Co1 (32e), Co2 (16d), Mo (48f) and N1 (16c) sites.

3.2.6.2 Raman spectroscopy

The Raman spectrum of $\text{Co}_3\text{Mo}_3\text{N}$ was recorded at room temperature on a Horiba Jobin Yvon LabRam HR confocal Raman microscope in air, using 532.17 nm laser excitation.

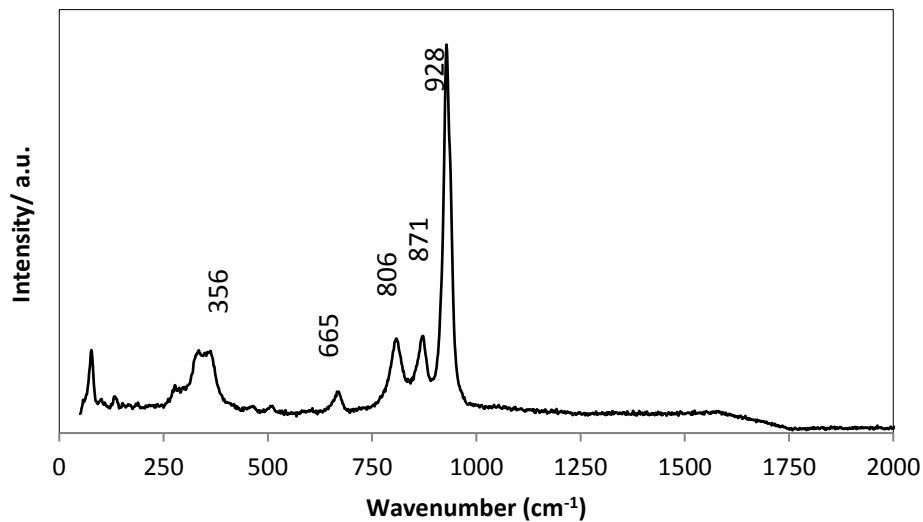


Figure 3.2-36: Raman spectrum of $\text{Co}_3\text{Mo}_3\text{N}$.

The Raman spectrum is presented in Figure 3.2-36. The positions of the Raman bands at 356, 806, 871, 928 cm^{-1} can be attributed to the published CoMoO_4 Raman bands at 350, 880 and 930 assigned to Mo-O-Co stretching vibrations in cobalt molybdate species.⁷⁴ This observation is consistent with the formation of a surface oxide passivation layer.

3.2.6.3 EDX and SEM analyses

Figure 3.2-37 shows the SEM images of $\text{Co}_3\text{Mo}_3\text{N}$. It can be seen that the morphology of η -6 $\text{Co}_3\text{Mo}_3\text{N}$ material appears to consist of aggregates of needles and it still retains its precursor shape and size of the crystallites. The BET surface area recorded for η - $\text{Co}_3\text{Mo}_3\text{N}$ was $18 \text{ m}^2\text{g}^{-1}$ which is higher than that of oxide precursor ($7 \text{ m}^2\text{g}^{-1}$).

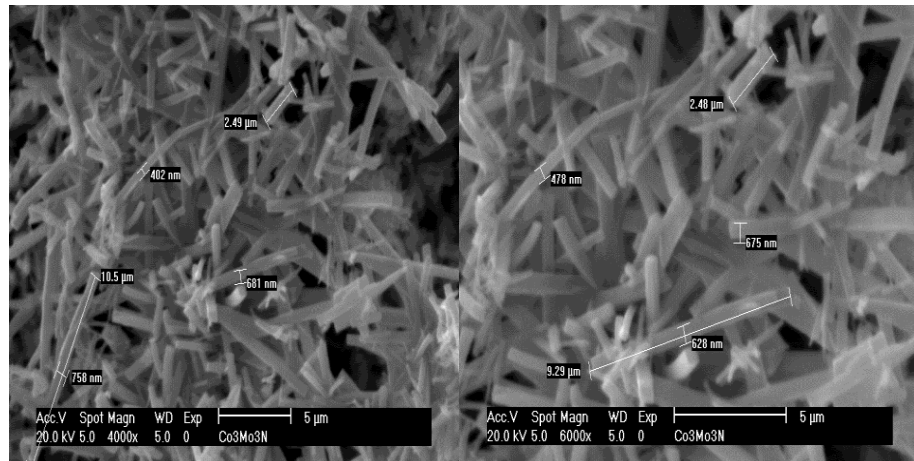


Figure 3.2-37: Typical SEM images of the $\text{Co}_3\text{Mo}_3\text{N}$ phase.

EDX data were collected for several crystallites for η -6 $\text{Co}_3\text{Mo}_3\text{N}$ and showed similar results. All EDX spectra evidenced the presence of molybdenum, cobalt and nitrogen as illustrated in Figure 3.2-38. However, detection and quantification of the N content is challenging. The obtained elemental values (4.1 wt. % N, 50.1 wt. % Co and 45.8 wt. % Mo) can be compared to the 36.9 wt. % Co, 60.2 wt. % Mo and 2.9 wt. % N values expected for $\text{Co}_3\text{Mo}_3\text{N}$.

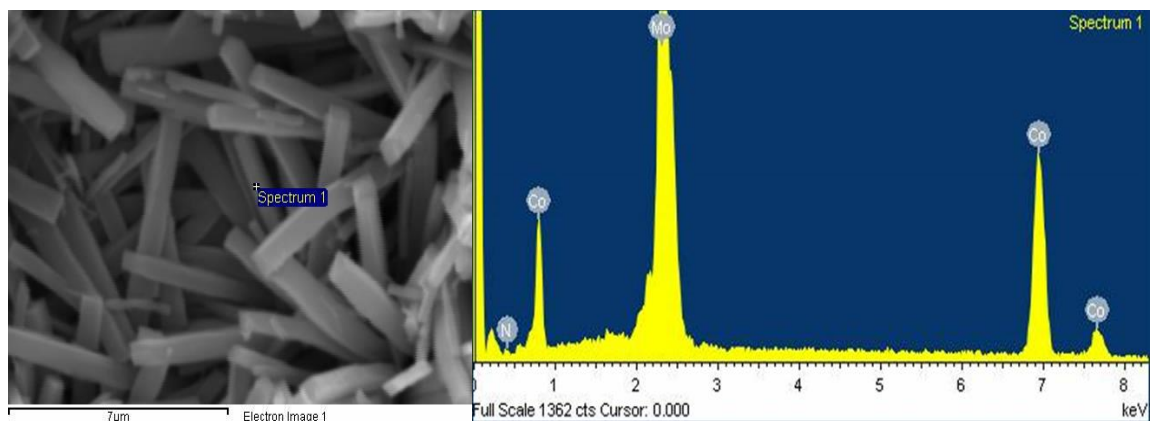


Figure 3.2-38: EDX analysis of $\text{Co}_3\text{Mo}_3\text{N}$.

3.2.7 Cobalt molybdenum nitride (η -12 Co₆Mo₆N)

As mentioned in the experimental chapter, η -12 Co₆Mo₆N was synthesized by reduction of η -6 C₃Mo₃N under a 75 vol. % H₂ in Ar gas mixture at 700 °C for 5 h and it was characterised by PXRD, PND and CHN elemental analysis. The synthesis of the η -12 Co₆Mo₆N phase has been reported previously in the literature.^{4, 37, 81}

3.2.7.1 PXRD and PND analysis

The formation of the η -12 Co₆Mo₆N (abbreviated as 661N) phase was confirmed using PXRD. The PXRD data were collected with a step size of 0.0167° (2 θ) over the range 10 ≤ 2 θ /° ≤ 90 and scan speed 0.002 degree per second for 12 hours to get accurate reflection positions to use for refinement. The patterns were identified using the related JCPDS reference standard for η -12 Co₆Mo₆C (03-065-8115).

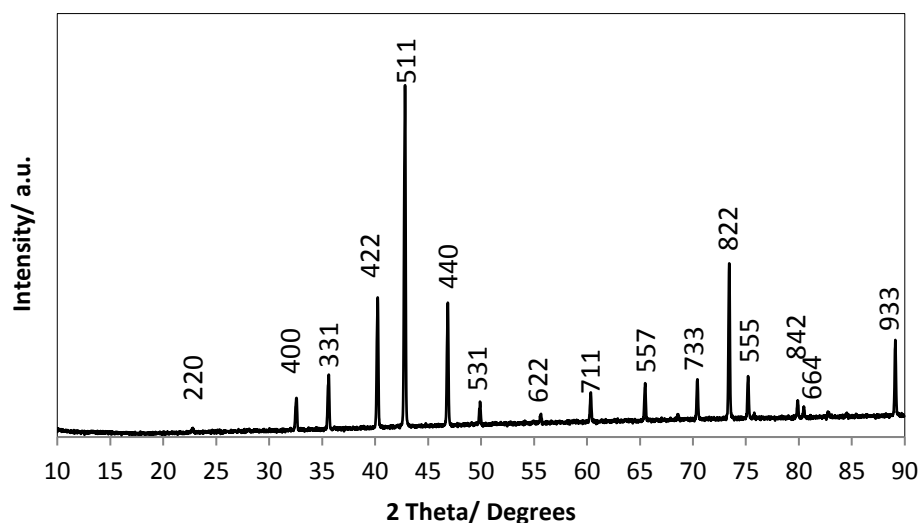


Figure 3.2-39: Indexed PXRD pattern of the Co₆Mo₆N phase.

The PXRD pattern in Figure 3.2-39 presents reflections at 2 theta = 21.9, 32.5, 35.6, 40.3, 42.9, 46.9, 49.9, 54.9, 60.4, 65.5, 70.4, 73.5, 75.2, 79.2, 81.4 and 87.6° which can be assigned to eta-12 cobalt molybdenum nitride; the associated hkl crystal planes are identified and labelled in the figure. According to the CHN elemental analysis results, the nitrogen content of the material was found to be 1.5 wt. % which is consistent with the calculated stoichiometric value for Co₆Mo₆N (1.4 wt. %).

The structure of the $\text{Co}_6\text{Mo}_6\text{N}$ phase was refined applying the Rietveld method against PXRD data using GSAS and EXPGUI software packages. The initial model used was the cubic $\text{Mo}_6\text{Ni}_6\text{C}$ structure type which was proposed by Newsam *et al.* (1988) and taken from the ICSD database website with code 68120, which the molybdenum species are located at 48f positions, the cobalt species occupy two non-equivalent the 16d, 32e Wyckoff positions, whereas the carbon species located at the 8a Wyckoff position were replaced by nitrogen atoms. The background was modelled using a shifted Chebyshev polynomial function (function type 7 and 23 terms within GSAS). The cell parameters, the scale factor and the zero point were also refined in initial cycles. The isotropic thermal factors (U_{iso}) of the cobalt, molybdenum and nitrogen were refined in final cycle. The nitrogen site occupancy factor was refined which quite improved the goodness of fit parameters. The results of $\text{Co}_6\text{Mo}_6\text{N}$ refinement results obtained from the PXRD data are presented in Figure 3.2-40 and Table 3.2-8.

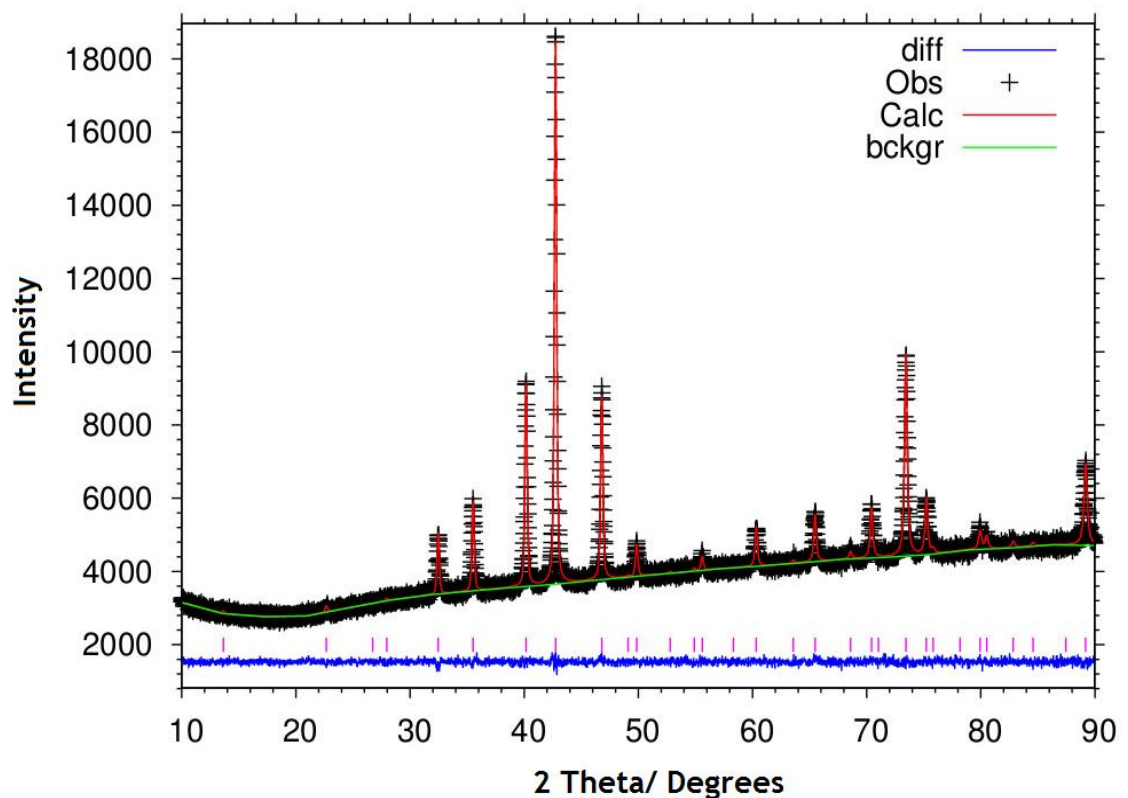


Figure 3.2-40: Fitted PXRD data profiles from Rietveld refinement for $\text{Co}_6\text{Mo}_6\text{N}$.

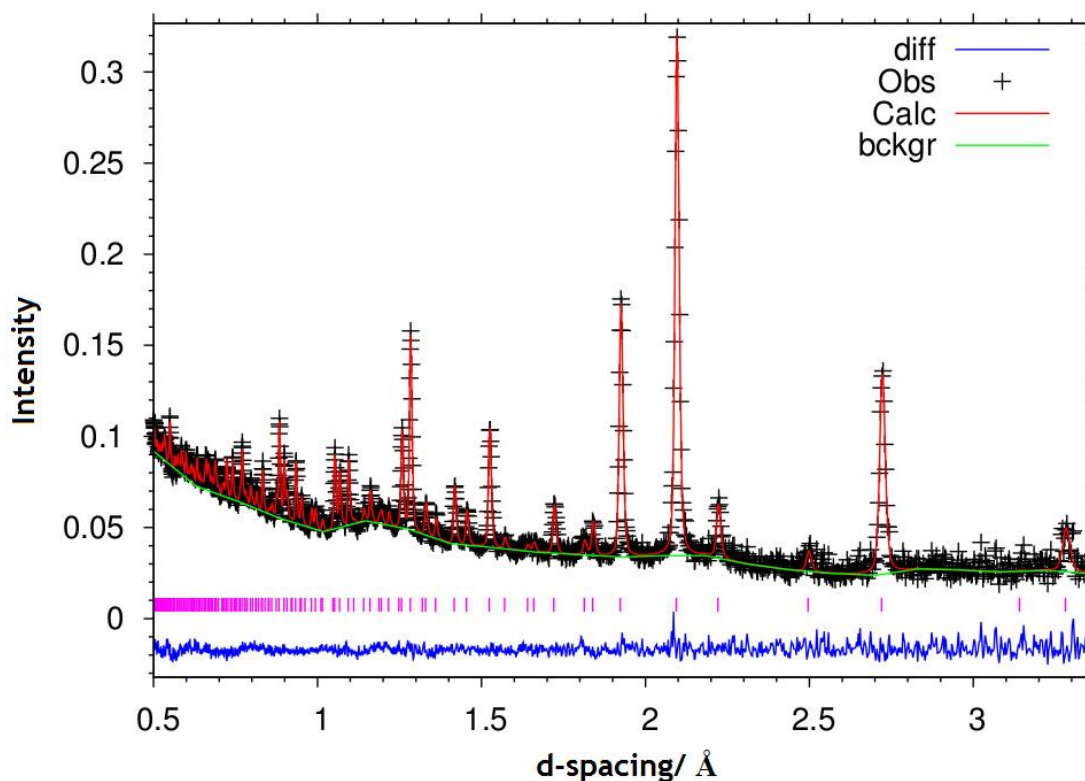


Figure 3.2-41: Fitted PND data profiles from Rietveld refinement for $\text{Co}_6\text{Mo}_6\text{N}$.

At room temperature, time-of-flight (ToF) PND data were collected using the high intensity Polaris diffractometer at the ISIS pulsed spallation source (Rutherford Appleton Laboratory, UK). Powder samples (ca. 1 g) were loaded into 11 mm diameter thin-walled stainless steel cells. A collimator manufactured from neutron-absorbing boron nitride ceramic placed around the cell enabled diffraction patterns to be collected in the Polaris $2\theta \approx 90^\circ$ detector bank which were free of Bragg reflections from the steel walls of the cell. Rietveld refinements against PND data were performed using the General Structure Analysis System (GSAS) through the EXPGUI interface.

The background was modelled using a shifted Chebyshev polynomial function (function type 7 and 23 terms within GSAS). Cell parameters, the scale factor and the zero point were also refined in initial cycles. The isotropic thermal factors (U_{iso}) of the molybdenum and nitrogen were refined whereas cobalt species were constrained in the final cycle. The nitrogen site occupancy factor was refined which further improved the goodness of fit parameters. The results of $\text{Co}_6\text{Mo}_6\text{N}$ refinement obtained from PND data are presented in Figure 3.2-41 and Table 3.2-8.

Table 3.2-8: Crystallographic parameters of Co₆Mo₆N from PXRD and PND refined data.

Parameter	PXRD value	PND value
Formula	Co ₆ Mo ₆ N	Co ₆ Mo ₆ N
Crystal system	Cubic	Cubic
Space group	$Fd\bar{3}m$	$Fd\bar{3}m$
Space group number	227	227
Cell parameter a/ Å	10.8733(8)	10.8809(8)
Cell parameter b/ Å	10.8733(8)	10.8809(8)
Cell parameter c/ Å	10.8733(8)	10.8809(8)
Alpha/ Degrees	90	90
Beta/ Degrees	90	90
Gamma/ Degrees	90	90
Unit-cell volume/ Å ³	1285.56(6)	1288.26(1)
Calculated formula weight/ gmol ⁻¹	7564.208	7548.691
Calculated density/ gcm ⁻³	9.771	9.730
Number of observations	4787	1901
Number of variables	34	34
R _p	0.0133	0.0489
R _{wp}	0.0169	0.0332
χ ²	1.147	1.022

Rietveld refinement of the X-ray data within the $Fd\bar{3}m$ space group of the η-12 cobalt molybdenum nitride produced a successful fit with $R_{wp} = 1.69\%$ and $R_p = 1.33\%$ (Table 3.2-8 and Figure 3.2-40). The ToF neutron diffraction data were also successfully refined within the same space group, giving $R_{wp} = 3.32\%$ and $R_p = 4.89\%$ (Table 3.2-8, Figure 3.2-41). The lattice parameters determined from X-ray and neutron results were in excellent agreement with each other: $a = 10.8733(8)$ and $a = 10.8809(8)$ Å, respectively. The correspondence between the X-ray and neutron data, and the successful Rietveld refinement of the powder data through the structural model confirms that all N species occupy the 8a (1/8, 1/8, 1/8) site within the structure. When using a model in which nitrogen occupied the 16c (0, 0, 0) site, no reasonable fit to the data was obtained, further confirming the occupation of the 8a site. The composition of the material has been identified from the structural refinements against PXRD data in Table 3.2-9 and PND data in Table 3.2-10 which are Co₆Mo₆N_{1.36} and Co₃Mo₃N_{1.02} respectively and which is close to that determined in previous studies.

Table 3.2-9: Co₆Mo₆N PXRd refined parameters.

Atoms/site	X	Y	Z	Occupancy	100*U _{iso} (Å ²)
Co1 (32e)	0.292400(0)	0.292400(0)	0.292400(0)	1.00	1.327
Co2 (16d)	0.500000(0)	0.500000(0)	0.500000(0)	1.00	1.327
Mo (48f)	0.320984(0)	0.125000(0)	0.125000(0)	1.00	1.114
N (8a)	0.125000(0)	0.125000(0)	0.125000(0)	1.36	4.150

Table 3.2-10: Co₆Mo₆N PND refined parameters.

Atoms/site	X	Y	Z	Occupancy	100*U _{iso} (Å ²)
Co1 (32e)	0.292400(0)	0.292400(0)	0.292400(0)	1.00	0.319
Co2 (16d)	0.500000(0)	0.500000(0)	0.500000(0)	1.00	0.319
Mo (48f)	0.32168(14)	0.125000(0)	0.125000(0)	1.00	0.271
N (8a)	0.125000(0)	0.125000(0)	0.125000(0)	1.02	0.692

The structure of Co₆Mo₆N consists of a distorted fcc arrangement of the cobalt and molybdenum, with nitrogen occupying distorted octahedral interstitial sites. The cobalt, molybdenum and nitrogen distances and bond angles in Co₆Mo₆N were obtained from Rietveld refinement against PXRd and PND data as illustrated in Table 3.2-11 and Table 3.2-12 respectively. PXRd and PND refined data are very similar. The distances from the molybdenum species to the remaining metallic species is in the range between ca. 2.59(2) to 2.84(1) Å, the distances from cobalt in 32e Wyckoff site to the 16d site species is in the range between ca. 2.54(7) to 2.34(9) Å and the distances from molybdenum to nitrogen in the 16c site are ca. 2.14 Å from PND and 2.13 Å from PXRd refined data. These values are consistent with those previously reported.⁴

The structural comparison of Co₃Mo₃N and reduced phase Co₆Mo₆N (wherein nitrogen occupies the 8a Wyckoff site as opposed to the 16c site) is discussed here. It is remarkable to observe that regarding the metal–metal distances, the molybdenum to cobalt and molybdenum to molybdenum atomic distances present similar features in both Co₃Mo₃N and Co₆Mo₆N being slightly longer in 331N. Concerning the cobalt 32e site and 16d site atomic distances, they exist as similar distances in both the Co₃Mo₃N and Co₆Mo₆N, being slightly smaller in 661N. Finally, for the Mo-N atomic distances, the Mo-N distance in 661N

is slightly longer than the Mo-N distance in 331N which relates to migration of nitrogen species from the 16c position to the 8a position.

Table 3.2-11: Bond lengths for Co₆Mo₆N from PXRD and PND refined data.

Bond length (Å)	PND value	PXRD value
N-Mo*6	2.1401(15)	2.13101(1)
Mo-Mo*3	3.0265(21)	3.01370(2)
Mo-Mo*3	2.8413(6)	2.84242(1)
Co1-Mo*3	2.59558(21)	2.59285(1)
Co1-Mo*3	2.7173(13)	2.72205(1)
Co1-Co1*3	2.54210(14)	2.54033(1)
Co1-Co2*3	2.35123(13)	2.34959(1)
Co2-Mo*6	2.7322(11)	2.73562(1)
Co2-Co1*6	2.35123(13)	2.34959(1)

Table 3.2-12: Bond angles for Co₆Mo₆N from PXRD and PND refined data.

Bond angle (°)	PND value	PXRD value
N-Mo-N	135.86(8)	136.245(0)
Mo-N-Mo*12	90.000(0)	90.000(0)
Mo-N-Mo*3	180.000(0)	180.000(0)
Co2-Co1-Co2*3	109.787(0)	109.787(0)
Co2-Co1-Mo*6	124.096(6)	124.070(0)
Co2-Co1-Mo*3	66.839(32)	67.005(0)
Mo-Co1-Mo*3	71.33(5)	71.064(0)
Co1-Co2-Co1*6	65.448(0)	65.448(0)
Co1-Co2-Co1*3	180.000(0)	180.000(0)
Co1-Co2-Co1*6	114.552(0)	114.552(0)
Co1-Mo-Co1	165.90(6)	166.231(1)
Co1-Mo-N	82.950(32)	83.115(0)

The structure of η -12 $\text{Co}_6\text{Mo}_6\text{N}$ has been previously studied and it is apparent that cobalt (Co1, Co2), molybdenum and nitrogen occupy Wyckoff locations (32e, 16d), 48f and 8a respectively. Figure 3.2-42 presents the unit cell for η -12 $\text{Co}_6\text{Mo}_6\text{N}$ including all elements in the figure on the left hand side (which was drawn using Vesta software when using the obtained refined cif file by using PND refined data through Newsam's CIF file code 68120 from the ICSD database website); whereas only the Mo and N sub-lattice is shown on the right hand side figure.

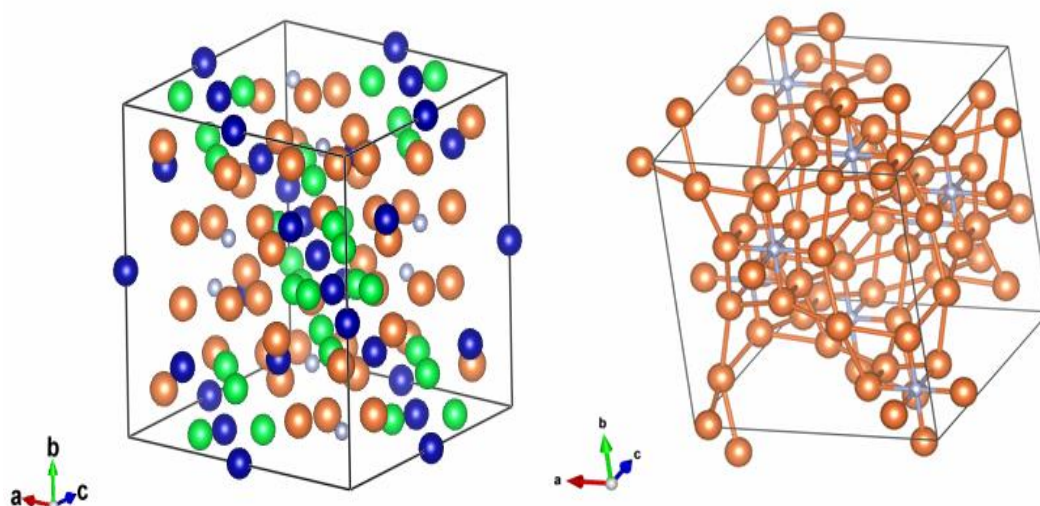


Figure 3.2-42: The Unit cell of $\text{Co}_6\text{Mo}_6\text{N}$ on the left hand side and Mo-N coordination on the right hand side drawn using VESTA software. Brown, grey, green and blue spheres represent the Mo, N, Co1 and Co2 respectively.

In the structure of $\text{Co}_6\text{Mo}_6\text{N}$, cobalt occupies two inequivalent sites in which each site is surrounded by six molybdenum and six cobalt species resulting in the formation of $\text{Co}[\text{Mo}_6\text{Co}_6]$ units. In the case of molybdenum, the molybdenum is surrounded by four molybdenum, six cobalt and one nitrogen forming $\text{Mo}[\text{Mo}_4\text{Co}_6\text{N}_1]$ units while nitrogen in 8a Wyckoff sites is surrounded by six molybdenum and coordinated exclusively to the molybdenum, resulting in the formation of $[\text{NMo}_6]$ units as illustrated in Figure 3.2-43.

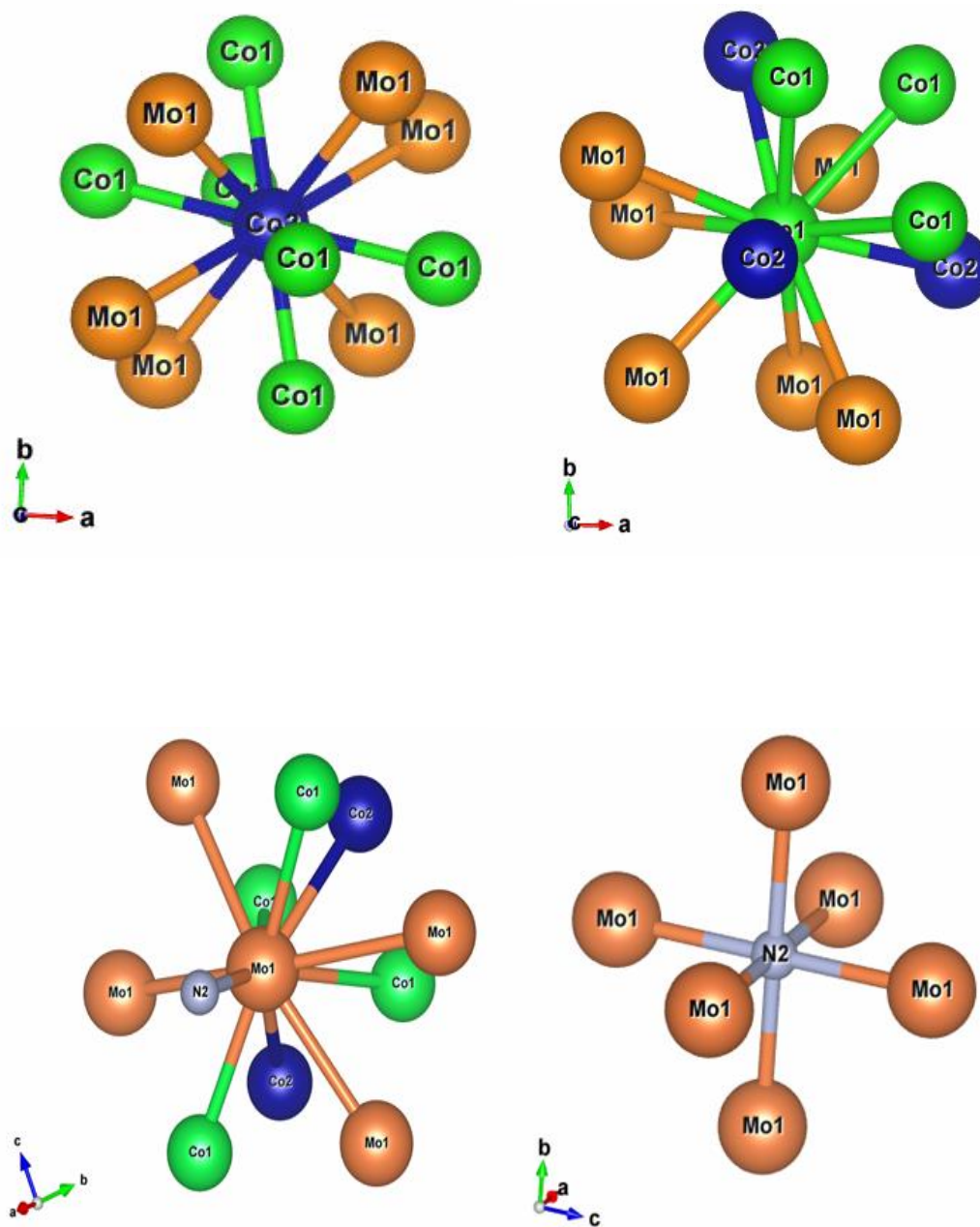


Figure 3.2-43: Atomic coordination of Co1 (32e) and Co2 (16d), Mo (48f) and N2 (8a) sites.

3.2.7.2 Raman spectroscopy

Raman spectroscopy was employed to perform further characterization. Figure 3.2-44 shows the Raman spectrum of the η -12 $\text{Co}_6\text{Mo}_6\text{N}$. Like the η -6 $\text{Co}_3\text{Mo}_3\text{N}$ sample, the Raman spectrum is very similar to that for CoMoO_4 (see Figure 3.2-27). The probable explanation relates to the presence of an oxide phase on the surface of sample due to the passivation of the material upon exposure to air.

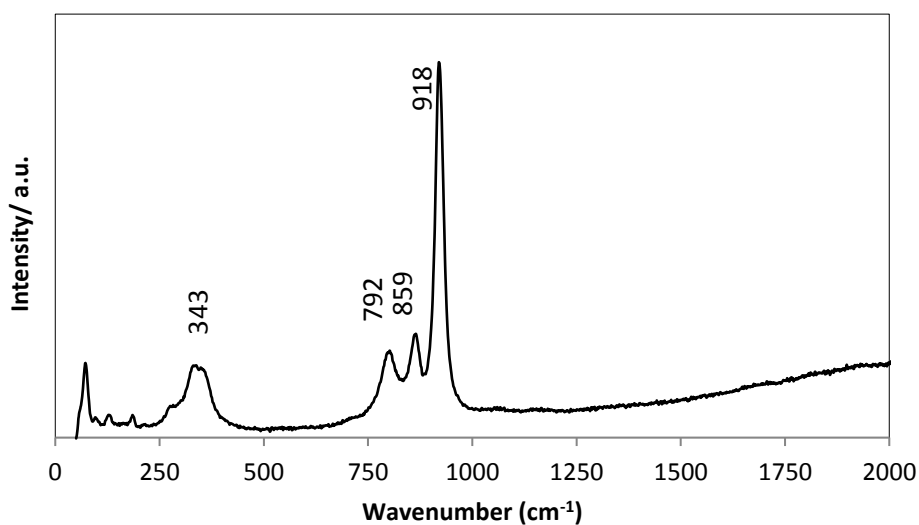


Figure 3.2-44: Raman spectrum of $\text{Co}_6\text{Mo}_6\text{N}$.

The positions of the Raman bands at 343, 792, 859 and 918 cm^{-1} can be inter-related to CoMoO_4 Raman bands at 350, 880 and 930 and assigned to Mo-O-Co stretching vibrations in cobalt molybdate.⁷⁴ This suggests that the main phase on the surface of $\text{Co}_6\text{Mo}_6\text{N}$ is beta- CoMoO_4 .

3.2.7.3 EDX analysis and SEM images

Figure 3.2-45 shows typical SEM images of the $\text{Co}_6\text{Mo}_6\text{N}$ material. It can be seen that the morphology appears to consist of aggregates of needles and it still retains the precursor shape and size of the crystallites. The BET surface area determined for η -12 $\text{Co}_6\text{Mo}_6\text{N}$ is $4 \text{ m}^2\text{g}^{-1}$ which is close to that of oxide precursor ($7 \text{ m}^2\text{g}^{-1}$).

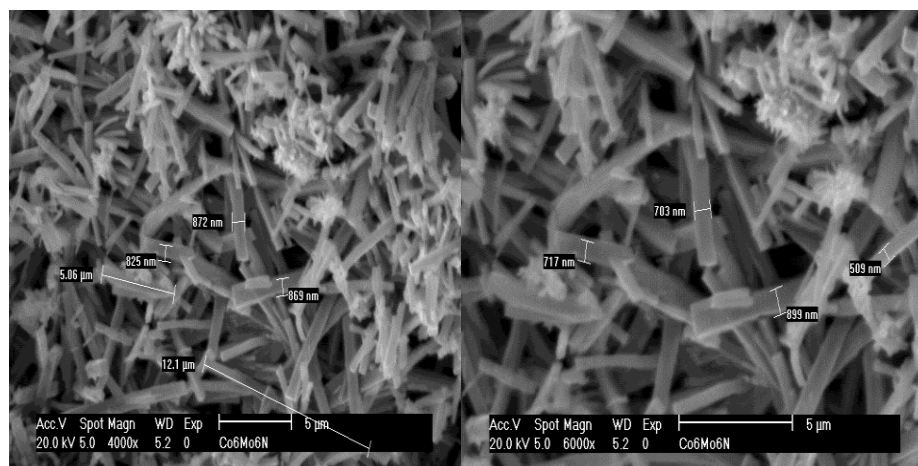


Figure 3.2-45: Representative SEM images of $\text{Co}_6\text{Mo}_6\text{N}$.

EDX data were collected for several crystallites of η -12 $\text{Co}_6\text{Mo}_6\text{N}$ and showed similar results. EDX spectra evidenced the presence of molybdenum, cobalt and nitrogen as illustrated in Figure 3.2-46. These values (55.7 wt. % Co, 34.5 wt. % Mo, 9.8 wt. % N) were found to differ from the calculated values of 37.5 wt. % Co, 61.0 wt. % Mo and 1.5 wt. % N in $\text{Co}_6\text{Mo}_6\text{N}$.

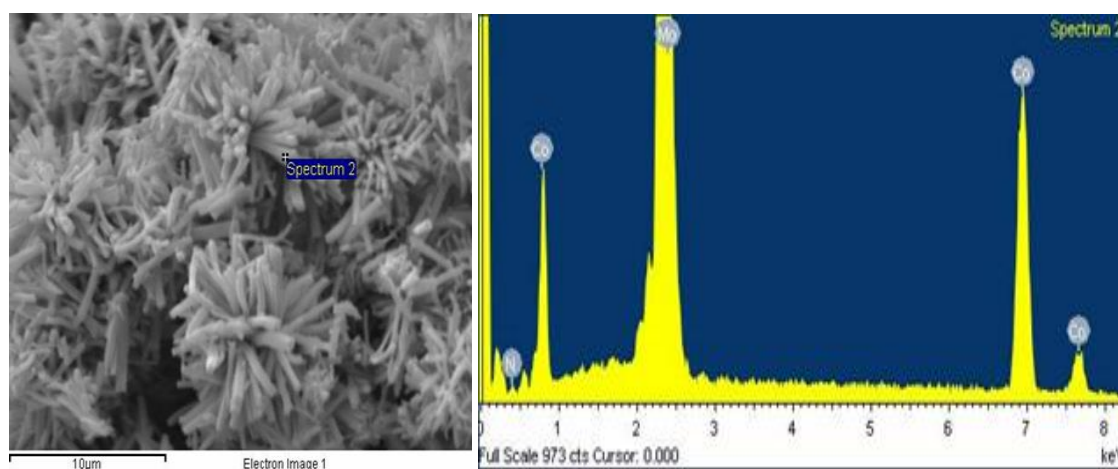


Figure 3.2-46: EDX analysis of $\text{Co}_6\text{Mo}_6\text{N}$.

3.2.8 Cobalt molybdenum carbide (η -6 $\text{Co}_3\text{Mo}_3\text{C}$)

A detailed investigation concerning the formation of cobalt molybdenum carbide was reported by Newsam³⁸ and the preparation of the eta-6 cobalt molybdenum carbide phase from the analogous nitride through the temperature programmed reaction in a 20% CH_4/H_2 mixture at 675 °C was first performed by Korlann.³⁹ In this project, η -6 $\text{Co}_3\text{Mo}_3\text{C}$ was successfully synthesized and investigated by PXRD, PND and CHN elemental analysis.

3.2.8.1 PXRD and PND analysis

The η -6 $\text{Co}_3\text{Mo}_3\text{C}$ (abbreviated as 331C) phase was confirmed by using PXRD. The PXRD data were collected with a scanning step size of 0.0167° (2θ) over the range $10 \leq 2\theta/^\circ \leq 90$ and step size 0.002 run over 12 hours to obtain accurate peaks for use in refinement. The pattern was matched using the related JCPDS reference standard for η -6 $\text{Co}_3\text{Mo}_3\text{C}$ (03-065-7128).

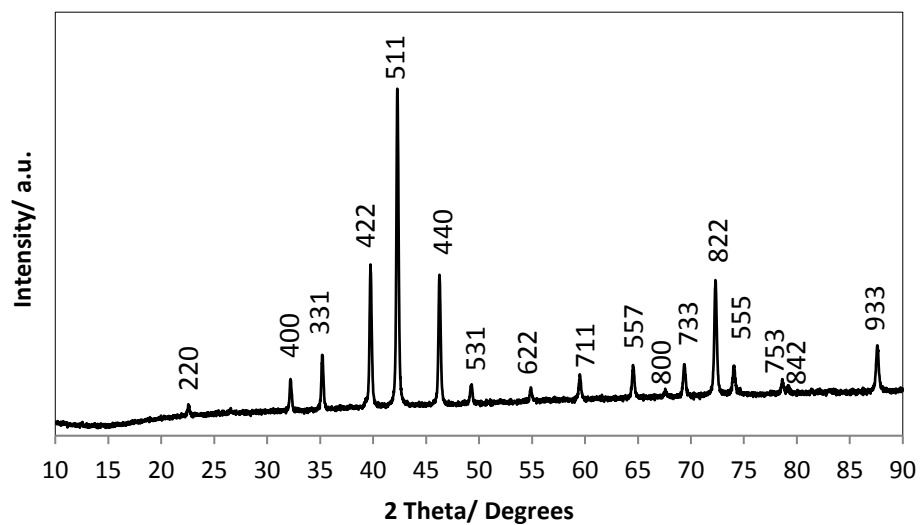


Figure 3.2-47: Indexed PXRD patterns of $\text{Co}_3\text{Mo}_3\text{C}$.

The PXRD pattern for the η -6 $\text{Co}_3\text{Mo}_3\text{C}$ material is presented in Figure 3.2-47. The 17 reflections in the 2θ range at 20 - 90° (22.6 , 32.2 , 35.2 , 39.7 , 42.26 , 46.2 , 49.1 , 54.8 , 59.5 , 64.5 , 66.8 , 69.3 , 72.27 , 73.9 , 78.1 , 78.6 and 87.5°) correspond to the ternary molybdenum carbide; the associated hkl crystal planes are identified in the figure. In addition, this result confirms that this obtained material was free from additional reflections corresponding to

Mo₂C, Co, Mo or oxides. According to the CHN elemental analysis results, the carbon content of the material was found to be 2.8 wt. % which is similar to the calculated stoichiometric value for Co₃Mo₃C (2.6 wt. %).

Rietveld analysis was performed to fit a published structural model of Co₃Mo₃C to experimental PXRD data. The structure of the Co₃Mo₃C was refined applying the Rietveld method against PXRD data using GSAS and EXPGUI software packages. The initial model used was the cubic Fe₃W₃C structure type which was proposed by Alconchel *et al.* (2004) and taken from the ICSD database website with code 190003, in which the molybdenum species are placed at 48f Wyckoff sites, the cobalt species occupy the two non-equivalent 16d, 32e sites and carbon species are located at 16c sites. The background was modelled using a shifted Chebyshev polynomial function (function type 7 and 23 terms within GSAS). Cell parameters, scale factor and zero point were also refined in initial cycles. The isotropic thermal factors (U_{iso}) of the molybdenum and carbon were refined in final cycle whereas cobalt was constrained. The carbon site occupancy factor was refined which further improved the goodness of fit parameters. The results of Co₃Mo₃C refinement obtained from PXRD data are presented in Figure 3.2-48 and Table 3.2-13.

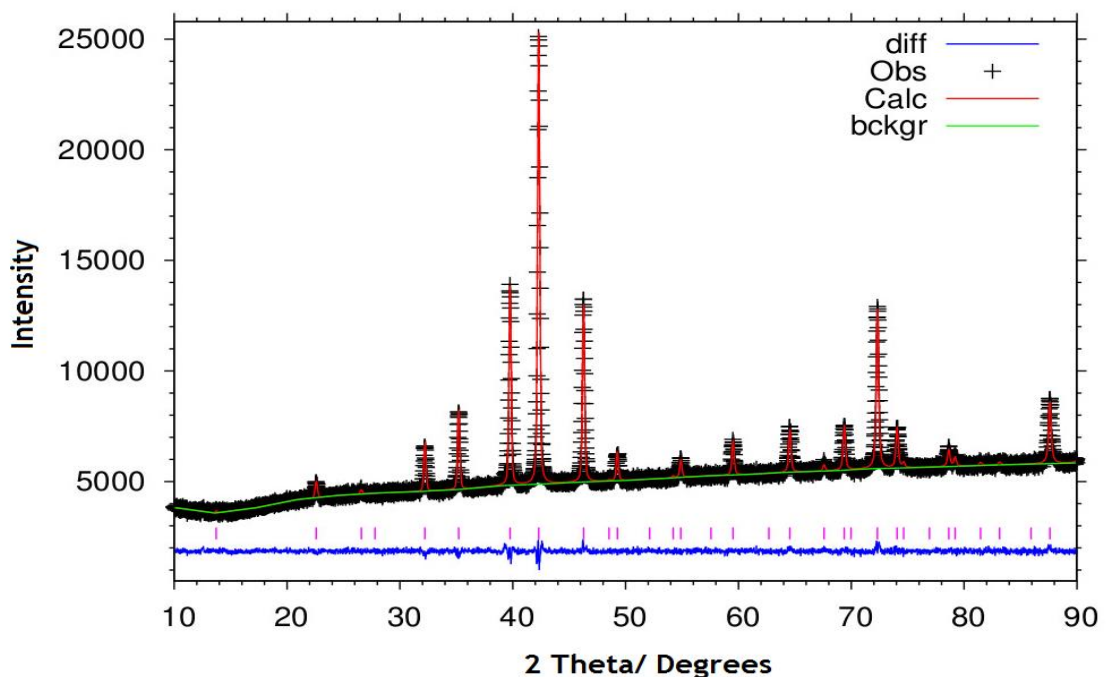


Figure 3.2-48: Fitted PXRD data profiles from Rietveld refinement for Co₃Mo₃C.

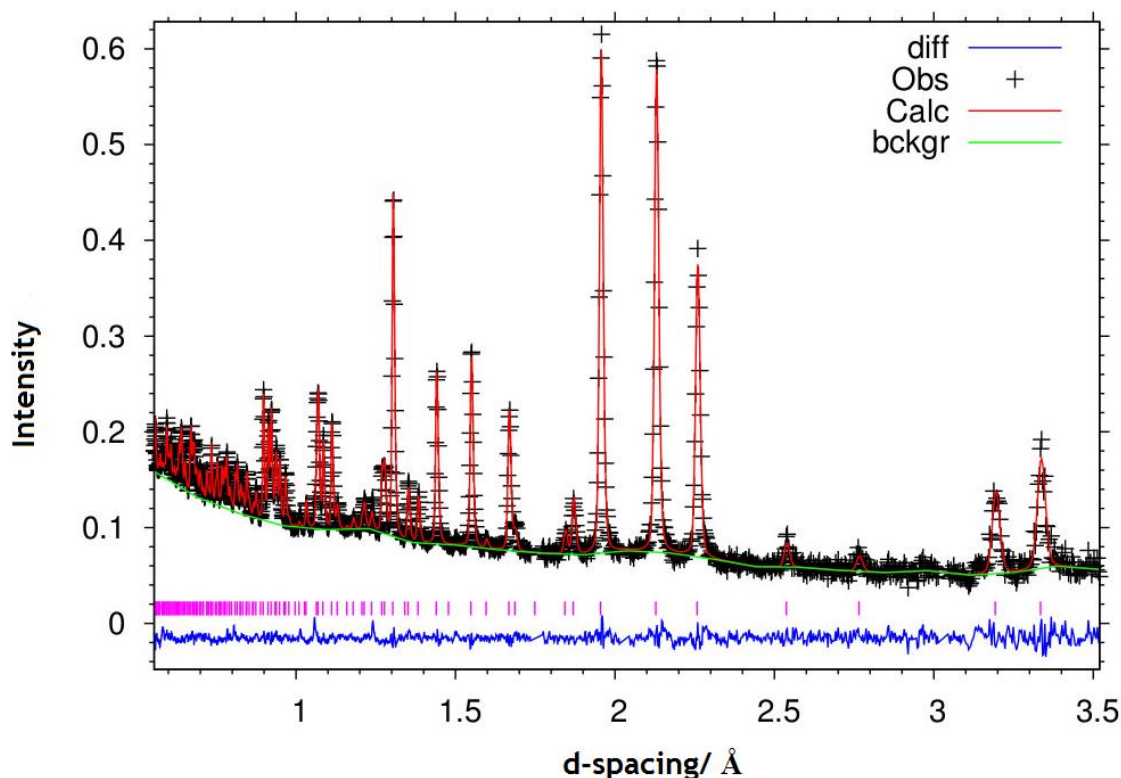


Figure 3.2-49: Fitted PND data profiles from Rietveld refinement for $\text{Co}_3\text{Mo}_3\text{C}$.

At room temperature, time-of-flight (ToF) PND data were collected using the high intensity Polaris diffractometer at the ISIS pulsed spallation source (Rutherford Appleton Laboratory, UK). Powder samples (ca. 1 g) were loaded into 11 mm diameter thin-walled stainless steel cells. A collimator manufactured from neutron-absorbing boron nitride ceramic placed around the cell enabled diffraction patterns to be collected in the Polaris $2\theta \approx 90^\circ$ detector bank which were free of Bragg reflections from the steel walls of the cell. Rietveld refinements against PND data were performed using the General Structure Analysis System (GSAS) through the EXPGUI interface.

The background was modelled using a linear interpolation function (function type 7 and 23 terms within GSAS). Cell parameters, scale factor and zero point were also refined in initial cycles. The isotropic thermal factors (U_{iso}) of the cobalt, molybdenum and nitrogen were refined in final cycle. The nitrogen site occupancy factor was refined which further improved the goodness of fit parameters. The results of $\text{Co}_3\text{Mo}_3\text{C}$ refinement obtained from PND data are presented in Figure 3.2-49 and Table 3.2-13.

Table 3.2-13: Crystallographic parameters of Co₃Mo₃C from PXRD and PND refined data.

Parameter	PXRD value	PND value
Formula	Co ₃ Mo ₃ C	Co ₃ Mo ₃ C
Crystal system	Cubic	Cubic
Space group	$Fd\bar{3}m$	$Fd\bar{3}m$
Space group number	227	227
Cell parameter a/ Å	11.0591(4)	11.0591(6)
Cell parameter b/ Å	11.0591(4)	11.0591(6)
Cell parameter c/ Å	11.0591(4)	11.0591(6)
Alpha/ Degrees	90	90
Beta/ Degrees	90	90
Gamma/ Degrees	90	90
Unit-cell volume/ Å ³	1352.58(5)	1352.59(4)
Calculated formula weight/ gmol ⁻¹	7677.688	7634.640
Calculated density/ gcm ⁻³	9.426	9.373
Number of observations	4787	1805
Number of variables	34	35
R _p	0.0123	0.0385
R _{wp}	0.0156	0.0286
χ ²	1.280	1.550

Table 3.2-14: Co₃Mo₃C PXRD refined parameters.

Atoms/site	X	Y	Z	Occupancy	100*U _{iso} (Å ²)
Co1 (32e)	0.293695(0)	0.293695(0)	0.293695(0)	1.00	0.568
Co2 (16d)	0.500000(0)	0.500000(0)	0.500000(0)	1.00	0.568
Mo (48f)	0.323507(0)	0.125000(0)	0.125000(0)	1.00	0.537
C (16c)	0.000000(0)	0.000000(0)	0.000000(0)	1.27	0.976

Table 3.2-15: Co₃Mo₃C PND refined parameters.

Atoms/site	X	Y	Z	Occupancy	100*U _{iso} (Å ²)
Co1 (32e)	0.293063(0)	0.293063(0)	0.293063(0)	1.00	0.256
Co2 (16d)	0.500000(0)	0.500000(0)	0.500000(0)	1.00	0.350
Mo (48f)	0.32357(9)	0.125000(0)	0.125000(0)	1.00	0.383
C (16c)	0.000000(0)	0.000000(0)	0.000000(0)	1.04	0.641

The structure of $\text{Co}_3\text{Mo}_3\text{C}$ comprises a distorted fcc arrangement of the cobalt and molybdenum, with carbon occupying distorted octahedral interstitial positions. The cobalt, molybdenum and carbon atomic distances and bond angles in $\text{Co}_3\text{Mo}_3\text{C}$ were obtained from Rietveld refinement against PXRD and PND data as illustrated in Table 3.2-16 and Table 3.2-17 respectively. PXRD and PND refined data are analogous. The distances from the molybdenum to the remaining metallic species range between ca. 2.65(0) and 3.10(5) Å, the distances from cobalt in 32e Wyckoff site to 16d site atom in this range between ca. 2.54(3) to 2.38(5) Å and the distance from molybdenum to carbon in the 16c site is ca. 2.11(7) Å. These values are in good agreement with those previously reported.³⁸

The structure of $\text{Co}_3\text{Mo}_3\text{C}$ is very similar to the isostructural $\text{Co}_3\text{Mo}_3\text{N}$ analogue. The metal-metal distances, the molybdenum to cobalt and molybdenum to molybdenum atomic distances present analogous features in both the $\text{Co}_3\text{Mo}_3\text{C}$ and $\text{Co}_3\text{Mo}_3\text{N}$, being slightly longer in the carbide. Concerning the cobalt 32e site and 16d site distances, the Co1(32e)-Co1(32e) distance is slightly smaller in the carbides, whereas the Co1(32e)-Co2(16d) is slightly longer. Finally, comparing the Mo-C and Mo-N distances, the Mo-C distance in 331C is slightly longer than Mo-N in 331N.

Table 3.2-16: Selected atomic angles for Co₃Mo₃C from PXRD and PND refined data.

Bond angle (°)	PND value	XRD value
C-Mo-C*1	134.81(5)	134.843(0)
Mo-C-Mo*6	94.365(1)	94.306(1)
Mo-C-Mo*6	85.635(1)	85.694(1)
Mo-C-Mo*3	180.000(0)	180.000(0)
Mo-Co1-Mo*3	71.785(0)	71.654(0)
Co1-Mo-C*4	87.039(1)	87.226(0)
Co1-Mo-Co1*1	165.31(0)	165.49(0)
Co1-Co2-Co1*6	115.016(0)	115.460(0)
Co1-Co2-Co1*3	180.000(0)	180.000(0)
Co1-Co2-Co1*6	64.984(0)	64.540(0)
Co2-Co1-Mo*3	66.267(0)	66.344(2)
Co2-Co1-Mo*6	123.944(2)	123.924(1)
Co2-Co1-Co2*3	110.070(0)	110.338(0)

Table 3.2-17: Bond lengths for Co₃Mo₃C from PXRD and PND refined data.

Bond length (Å)	PND value	PXRD value
C-Mo*6	2.1176(4)	2.11728(2)
Mo-Mo*4	2.8794(4)	2.87969(3)
Mo-Mo*4	3.1057(14)	3.10465(5)
Co1-Mo*3	2.65008(14)	2.65891(3)
Co1-Mo*3	2.7449(9)	2.74712(4)
Co1-Co1*3	2.56299(10)	2.54322(4)
Co1-Co2*3	2.38560(9)	2.38171(3)
Co2-Mo*6	2.7621(7)	2.76257(3)
Co2-Co1*6	2.38560(9)	2.38171(3)

The structure of η -6 $\text{Co}_3\text{Mo}_3\text{C}$ has been previously studied and it was found that cobalt (Co1, Co2), molybdenum and carbon occupy Wyckoff locations (32e, 16d), 48f and 16c respectively. Figure 3.2-50 presents the unit cell for η -6 $\text{Co}_3\text{Mo}_3\text{C}$ including all elements in the figure on the left hand side (which was drawn by Vesta software when using the Alconchel's CIF file code 190003 from the ICSD database website); whereas only the Mo and C sub-lattices are shown in the right hand side figure.

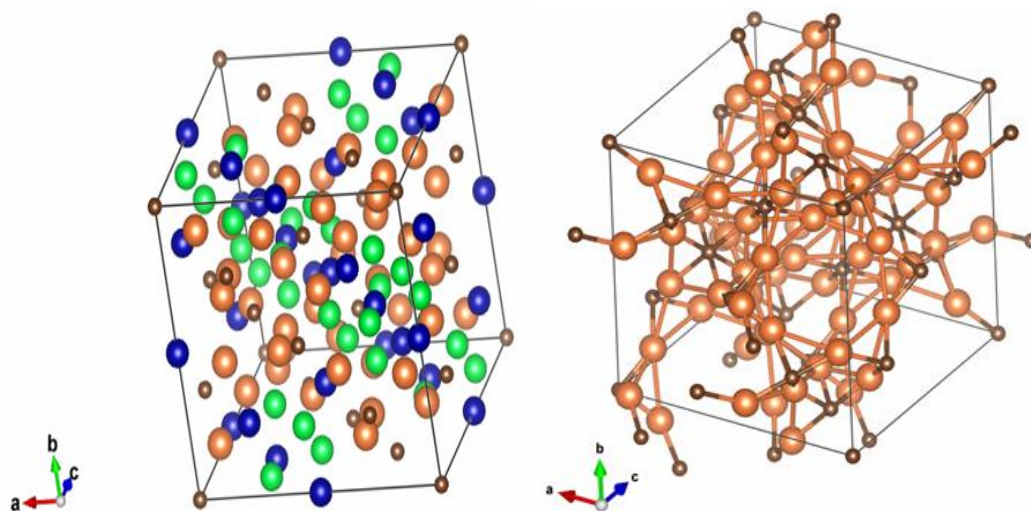


Figure 3.2-50: The Unit cell of $\text{Co}_3\text{Mo}_3\text{C}$ shown on the left hand side and the Mo-C coordination on the right hand side as determined using VESTA software. Brown, dark brown, green and blue spheres represent the Mo, C, Co1 and Co2 respectively.

In the structure of $\text{Co}_3\text{Mo}_3\text{C}$, cobalt occupies two non-equivalent sites in which each site is surrounded by six molybdenum and six cobalt species resulting in the formation of $\text{Co}[\text{Mo}_6\text{Co}_6]$ units. In the case of molybdenum, it is surrounded by four molybdenum, six cobalt and two carbon species forming $\text{Mo}[\text{Mo}_4\text{Co}_6\text{C}_2]$ units while carbon is surrounded by six molybdenum and coordinated exclusively to the molybdenum in 16c Wyckoff sites, resulting in the formation of $[\text{CMo}_6]$ units as illustrated in Figure 3.2-51.

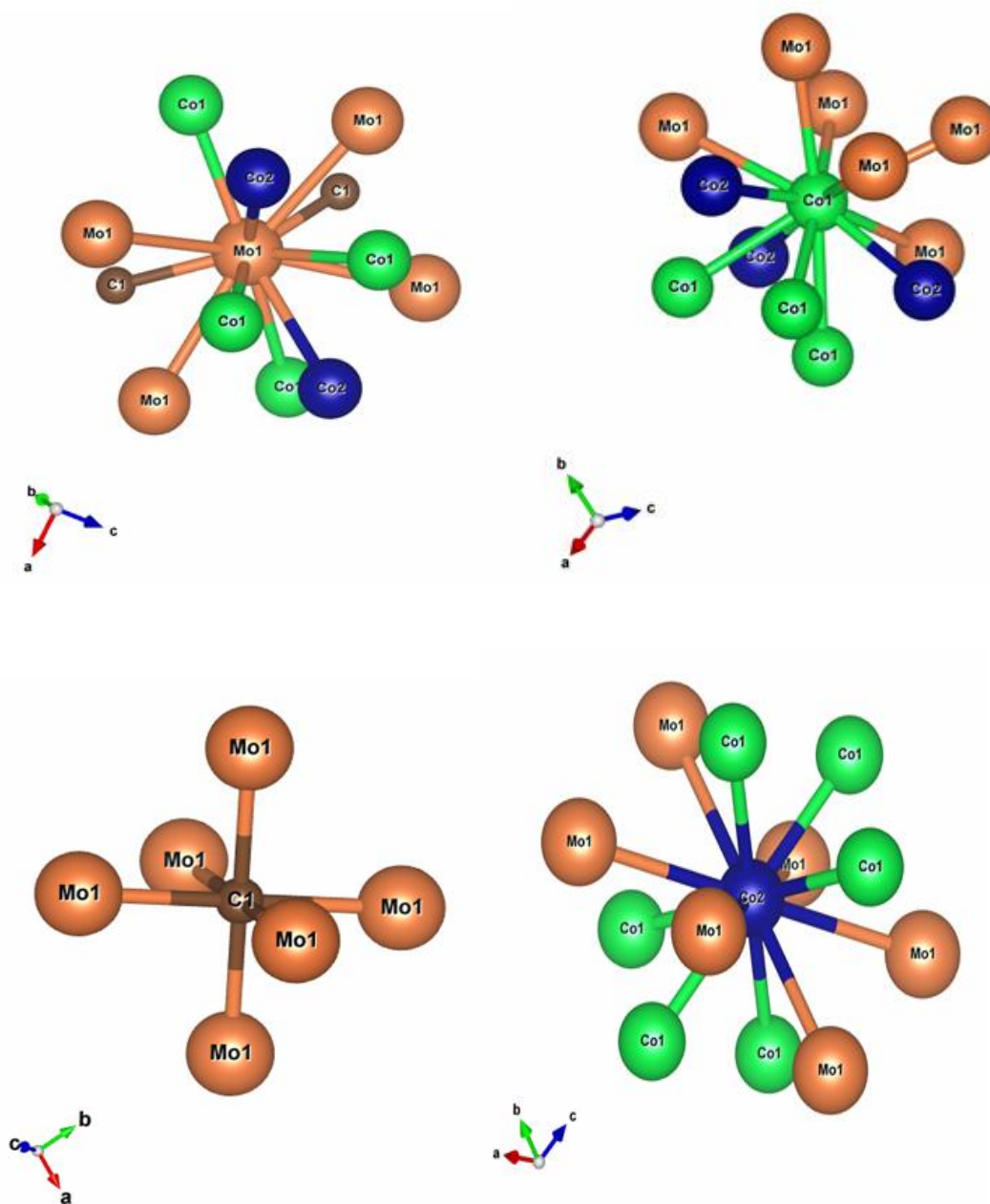


Figure 3.2-51: Atomic coordination of Co1 (32e) and Co2 (16d), Mo (48f) and C1 (16c) sites.

3.2.8.2 Raman spectroscopy

Raman spectroscopy was employed to perform further characterization. Figure 3.2-52 shows the Raman spectrum of the η -6 $\text{Co}_3\text{Mo}_3\text{C}$ material. Like the η -6 $\text{Co}_3\text{Mo}_3\text{N}$ sample, the Raman spectrum is very similar to that for CoMoO_4 (see Figure 3.2-27) which, again, most probably relates to a passivating oxide phase on the surface of sample. The positions of the Raman bands at 330, 807, 863 and 922 cm^{-1} can be attributed to CoMoO_4 .

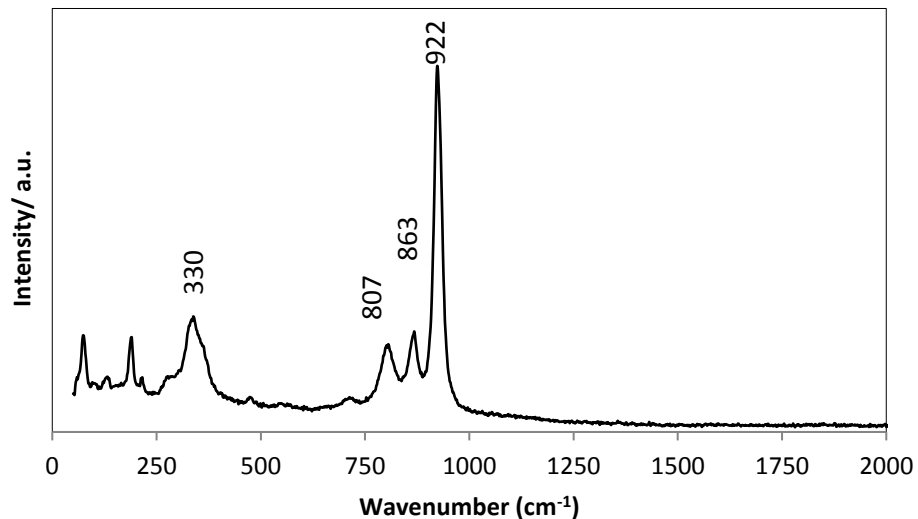


Figure 3.2-52: Raman spectrum of $\text{Co}_3\text{Mo}_3\text{C}$.

3.2.8.3 SEM and EDX analyses

The $\text{Co}_3\text{Mo}_3\text{C}$ material was analysed by Scanning Electron Microscopy (SEM) coupled with Energy-dispersive X-ray Spectroscopy (EDX). Figure 3.2-53 presents representative SEM micrographs. It can be seen that the morphology of the η -6 $\text{Co}_3\text{Mo}_3\text{C}$ material comprises aggregates of needles and it still retains the precursor shape and size. Korlann *et al.*³⁹ reported that the production of 331C from 331N can be considered as topotactic in the sense that the position of the metal atoms remains unchanged, while the nitrogen and carbon species exchange. Alconchel *et al.*⁴⁰ reported that the inter conversion of 331N to 331C is topotactic and pseudomorphic in the sense that both the structure and the morphology are retained. The topotactic production of carbide from nitride has also been previously described for the preparation of bimetallic carbides $\text{W}_9\text{Nb}_8\text{C}_x$, $\text{Mo}_3\text{Nb}_2\text{C}_x$ and

$\text{Mo}_2\text{Ta}_2\text{C}_x$.²⁷ The BET surface area recorded for the $\eta\text{-Co}_3\text{Mo}_3\text{C}$ is $13\text{ m}^2\text{g}^{-1}$ which is a little lower than the $18\text{ m}^2\text{g}^{-1}$ for the $\text{Co}_3\text{Mo}_3\text{N}$ precursor.

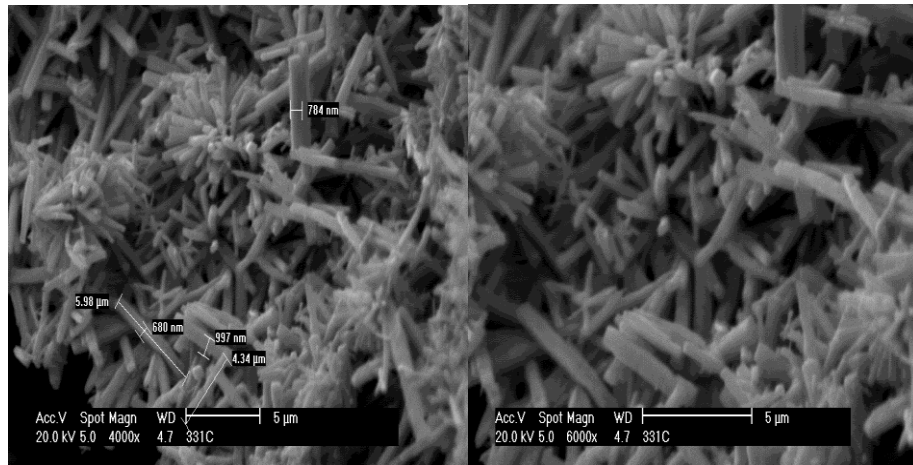


Figure 3.2-53: SEM images of $\text{Co}_3\text{Mo}_3\text{C}$.

EDX data were collected for $\eta\text{-6 Co}_3\text{Mo}_3\text{C}$ and showed comparable results. EDX spectra showed that molybdenum, cobalt and carbon are present as illustrated in Figure 3.2-54. However, the accurate % of carbon was difficult to determine this material due to the fact that carbon based discs were used as sample holders for the SEM/EDX measurements. These values (29.2 wt. % Co, 41.1 wt. % Mo, 29.7 wt. % C) were found to differ from the 37.2 wt. % Co, 60.2 wt. % Mo and 2.6 wt. % C values expected for $\text{Co}_3\text{Mo}_3\text{C}$.

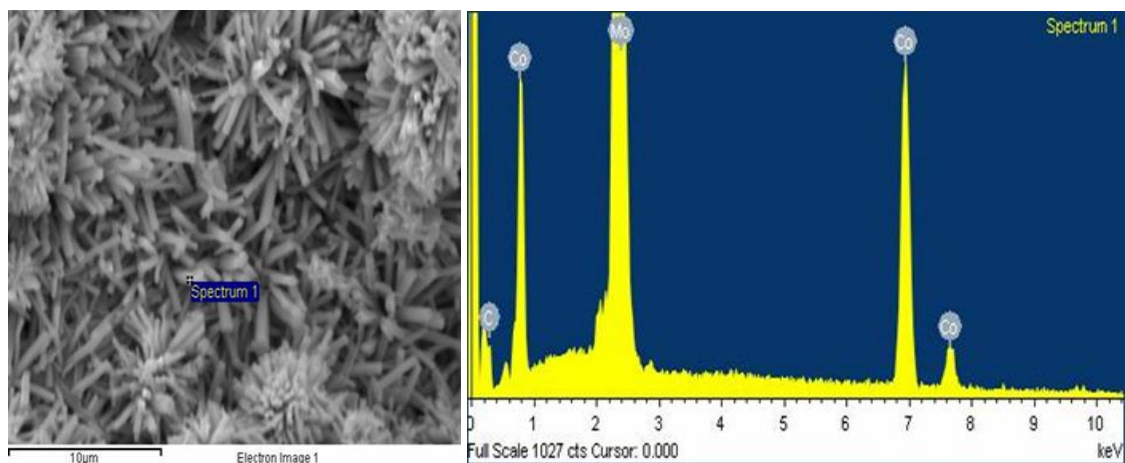


Figure 3.2-54: EDX analysis of $\text{Co}_3\text{Mo}_3\text{C}$.

3.2.9 Cobalt molybdenum carbide (η -12 $\text{Co}_6\text{Mo}_6\text{C}$)

As mentioned in the experimental chapter, the η -12 $\text{Co}_6\text{Mo}_6\text{C}$ was synthesized by reduction of η -6 $\text{C}_3\text{Mo}_3\text{C}$ under a 75 vol. % H_2 in Ar at 900 °C for 5 h. It was characterised by PXRD, PND and CHN elemental analysis. The formation of the η -12 $\text{Co}_6\text{Mo}_6\text{C}$ phase has also been documented in the literature.³⁸

3.2.9.1 PXRD and PND analysis

The formation of the η -12 $\text{Co}_6\text{Mo}_6\text{C}$ (abbreviated as 661C) phase was confirmed using PXRD. The patterns were identified by reference to the JCPDS reference standard for η -12 $\text{Co}_6\text{Mo}_6\text{C}$ (03-065-8115).

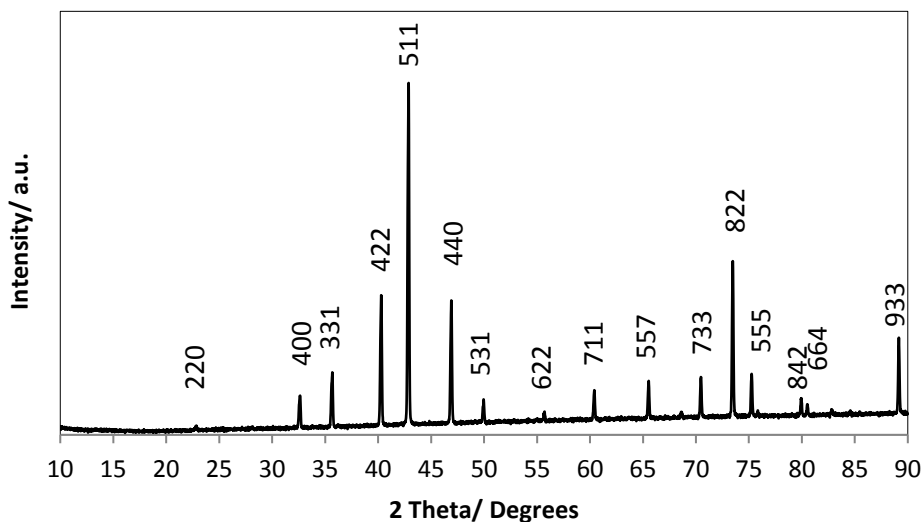


Figure 3.2-55: Indexed PXRD pattern of $\text{Co}_6\text{Mo}_6\text{C}$.

The PXRD pattern in Figure 3.2-55 exhibits reflections at 2 theta = 21.9, 32.5, 35.6, 40.3, 42.9, 46.9, 49.9, 54.9, 60.4, 65.5, 70.4, 73.5 and 75.2° which can be assigned to η -12 $\text{Co}_6\text{Mo}_6\text{C}$; the associated hkl crystal planes are identified and labelled in the figure. According to the CHN elemental analysis, the carbon content of the material was found to be 1.3 wt. % which is consistent with the calculated stoichiometric value for $\text{Co}_6\text{Mo}_6\text{C}$ (1.3 wt. %).

The structure of the $\text{Co}_6\text{Mo}_6\text{C}$ was refined by the Rietveld method against PXRD data using GSAS and EXPGUI software packages. The initial model used was the cubic $\text{Co}_6\text{Mo}_6\text{C}$ structure type proposed by Newsam *et al.* (1988) and taken from the ICSD database website with code 68120, in which the molybdenum species are located at 48f sites, the cobalt atoms occupy non-equivalent the 16d, 32e Wyckoff positions, whereas carbon atoms located at the 8a Wyckoff site. The background was modelled using a shifted Chebyshev polynomial function (function type 7 and 23 terms within GSAS). Cell parameters, the scale factor and the zero point were also refined in initial cycles. The isotropic thermal factors (U_{iso}) of the cobalt, molybdenum and carbon were refined in the final cycle. The carbon site occupancy factor was refined which improved the goodness of fit parameters. The results of $\text{Co}_6\text{Mo}_6\text{C}$ refinement obtained from PXRD data are presented in Figure 3.2-56 and Table 3.2-18.

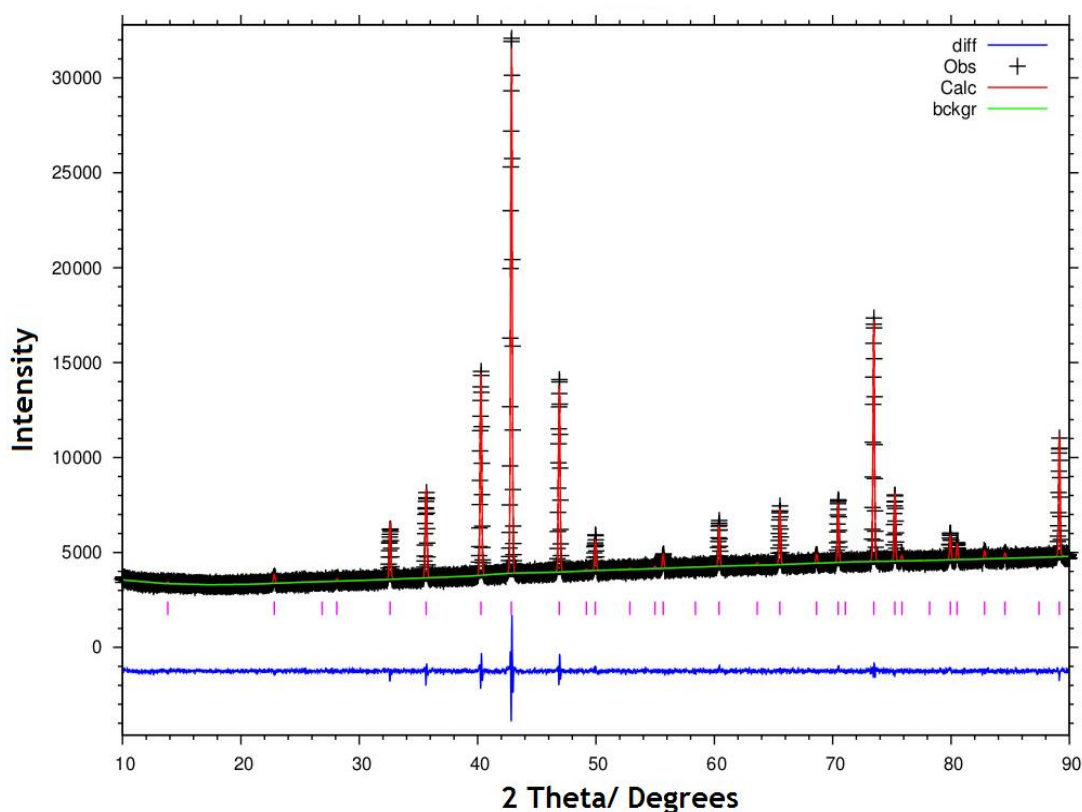


Figure 3.2-56: Fitted PXRD data profiles from Rietveld refinement for $\text{Co}_6\text{Mo}_6\text{C}$.

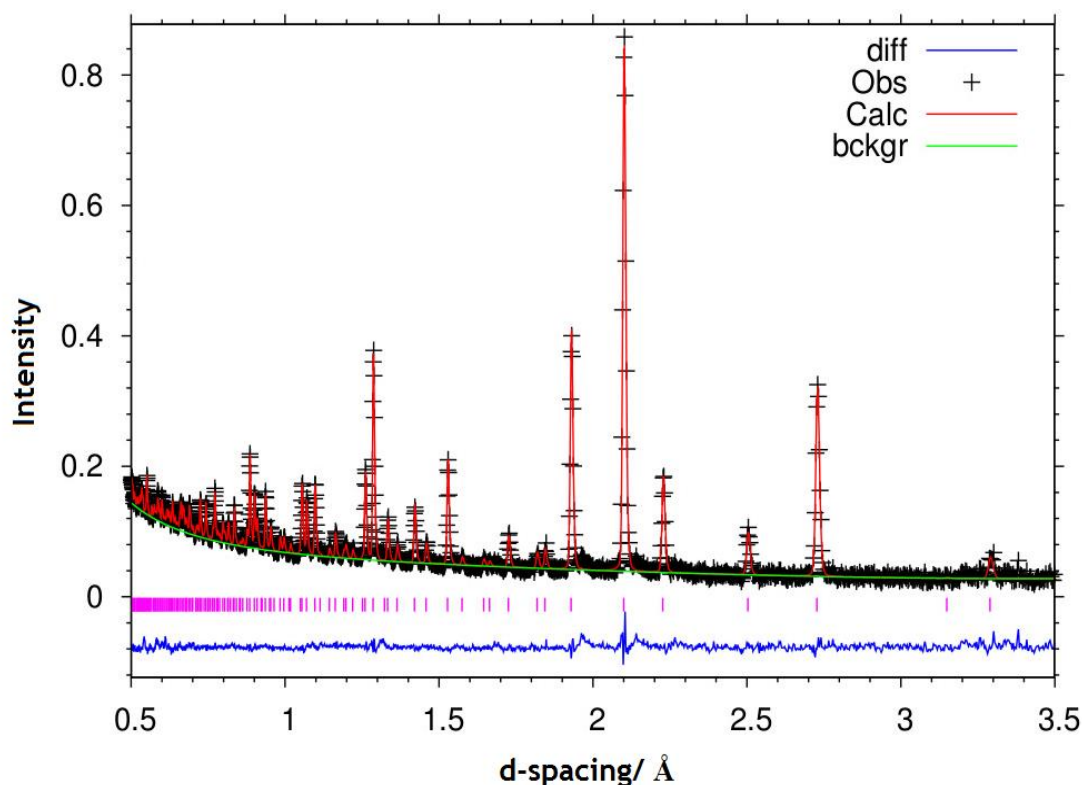


Figure 3.2-57: Fitted PND data profiles from Rietveld refinement for $\text{Co}_6\text{Mo}_6\text{C}$.

At room temperature, time-of-flight (ToF) PND data were collected using the high intensity Polaris diffractometer at the ISIS pulsed spallation source (Rutherford Appleton Laboratory, UK). Powder samples (ca. 1 g) were loaded into 11 mm diameter thin-walled stainless steel cells. A collimator manufactured from neutron-absorbing boron nitride ceramic placed around the cell enabled diffraction patterns to be collected in the Polaris $2\theta \approx 90^\circ$ detector bank which were free of Bragg reflections from the steel walls of the cell. Rietveld refinements against PND data were performed using the General Structure Analysis System (GSAS) through the EXPGUI interface.

The background was modelled using a power series in $Q^{2n/n!}$ and $n!/Q^{2n}$ function (function type 6 and 5 terms within GSAS). Cell parameters, the scale factor and the zero point were also refined in initial cycles. The isotropic thermal factors (U_{iso}) of the cobalt, molybdenum and carbon were refined in the final cycle. The carbon site occupancy factor was refined which further improved the goodness of fit parameters. The results of the $\text{Co}_6\text{Mo}_6\text{C}$ refinement obtained from PND data are presented in Figure 3.2-57 and Table 3.2-18.

Table 3.2-18: Crystallographic parameters of Co₆Mo₆C from PXRD and PND refined data.

Parameter	PXRD value	PND value
Formula	Co ₆ Mo ₆ C	Co ₆ Mo ₆ C
Crystal system	Cubic	Cubic
Space group	$Fd\bar{3}m$	$Fd\bar{3}m$
Space group number	227	227
Cell parameter a/ Å	10.8962(7)	10.9099(8)
Cell parameter B/ Å	10.8962(7)	10.9099(8)
Cell parameter C/ Å	10.8962(7)	10.9099(8)
Alpha/ Degrees	90	90
Beta/ Degrees	90	90
Gamma/ Degrees	90	90
Unit-cell volume/ Å ³	1293.70(2)	1298.56(4)
Calculated formula weight/ gmol ⁻¹	7245.69	7494.14
Calculated density/ gcm ⁻³	9.300	9.584
Number of observations	4787	1945
Number of variables	38	24
R _p	0.0153	0.0531
R _{wp}	0.0207	0.0438
χ ²	1.825	2.086

Rietveld refinement of the X-ray data within the $Fd\bar{3}m$ space group of the η-12 cobalt molybdenum carbide produced a successful fit with $R_{wp} = 2.07\%$ and $R_p = 1.53\%$ (Table 3.2-18 and Figure 3.2-56). The TOF neutron diffraction data were also successfully refined within the same space group, giving $R_{wp} = 4.38\%$ and $R_p = 5.31\%$ (Table 3.2-18, Figure 3.2-57). The lattice parameters determined from X-ray and neutron results were in excellent agreement: $a = 10.8962(7)$ Å and $a = 10.9099(8)$ Å, respectively. The concordance between the X-ray and neutron data, and the successful Rietveld refinement of the powder data through the structural model confirms that all C species occupy the 8a (1/8, 1/8, 1/8) site within the structure. When using a model in which the carbon atoms occupy the 16c (0, 0, 0) site, no reasonable fit to the data was obtained and therefore confirms the occupation of the 8a site. This is contrary to the case for Co₃Mo₃C the composition of the material has been identified from the structural refinements against PXRD data in Table 3.2-20 and PND

data in Table 3.2-19 which are $\text{Co}_6\text{Mo}_6\text{C}_{1.05}$ and $\text{Co}_6\text{Mo}_6\text{C}_{1.03}$ respectively and which are close to that determined in previous studies of $\text{Co}_6\text{Mo}_6\text{C}$.³⁸

Table 3.2-19: $\text{Co}_6\text{Mo}_6\text{C}$ PND refined parameters.

Atoms/site	X	Y	Z	Occupancy	$100*U_{\text{iso}}(\text{\AA}^2)$
Co1 (32e)	0.293090(0)	0.293090(0)	0.293090(0)	1.00	0.203
Co2 (16d)	0.500000(0)	0.500000(0)	0.500000(0)	1.00	0.409
Mo (48f)	0.3215(7)	0.125000(0)	0.125000(0)	1.00	0.178
C (8a)	0.125000(0)	0.125000(0)	0.125000(0)	1.038	0.459

Table 3.2-20: $\text{Co}_6\text{Mo}_6\text{C}$ PXRD refined parameters.

Atoms/site	X	Y	Z	Occupancy	$100*U_{\text{iso}}(\text{\AA}^2)$
Co1 (32e)	0.292600(0)	0.292600(0)	0.292600(0)	1.00	0.044
Co2 (16d)	0.500000(0)	0.500000(0)	0.500000(0)	1.00	0.260
Mo (48f)	0.3221(1)	0.125000(0)	0.125000(0)	1.00	0.044
C (8a)	0.1250	0.125000(0)	0.125000(0)	1.053	0.305

The structure of $\text{Co}_6\text{Mo}_6\text{C}$ consists of a distorted fcc arrangement of cobalt and molybdenum, with atomic carbon occupying distorted octahedral interstitial positions. The cobalt, molybdenum and carbon distances and bond angles in $\text{Co}_6\text{Mo}_6\text{C}$ were obtained from Rietveld refinement against PXRD and PND data as illustrated in Table 3.2-21 and Table 3.2-22 respectively. PXRD and PND refined data are almost equivalent. The distances from the molybdenum species to the remaining metallic species in this range between ca. 2.60(2) to 3.03(3) Å, the distances from cobalt in 32e Wyckoff site to the 16d site species ranges between ca. 2.52(7) to 2.35(3) Å and the distances from molybdenum to carbon in 16c site is ca. 2.14 Å. These values are consistent with those previously reported.³⁸

The structural comparison of $\text{Co}_3\text{Mo}_3\text{C}$ and reduced phase $\text{Co}_6\text{Mo}_6\text{C}$ (when carbon species occupy the 8a Wyckoff site as opposed to the 16c site) is discussed. It is interesting to note that regarding the metal–metal distances, the molybdenum to cobalt and molybdenum to molybdenum distances are slightly longer in the 331C. Concerning the cobalt 32e site and 16d site distances, they are similar in both $\text{Co}_3\text{Mo}_3\text{C}$ and $\text{Co}_6\text{Mo}_6\text{C}$ although they are slightly smaller in 661C. Finally, the Mo–C distances, the Mo–C distance in 661C is slightly longer than Mo–C distance in 331C.

Table 3.2-21: Bond lengths for Co₆Mo₆C from PXRD and PND refined data.

Bond length (Å)	PXRD value	PND value
C-Mo*6	2.1442(7)	2.1467(11)
Mo-Mo*3	3.0338(9)	3.0359(15)
Mo-Mo*3	2.8446(1)	2.8485(5)
Co1-Mo*3	2.6022(24)	2.6122(51)
Co1-Mo*3	2.7202(5)	2.7253(10)
Co1-Co1*3	2.5399(18)	2.5275(79)
Co1-Co2*3	2.3535(14)	2.3532(48)
Co2-Mo*6	2.7347(2)	2.7387(8)
Co2-Co1*6	2.3539(4)	2.3532(48)

Table 3.2-22: Bond angles for Co₆Mo₆C from PXRD and PND data.

Bond angle (°)	PXRD value	PND value
C-Mo-C	136.15(0)	135.91(1)
Mo-C-Mo*12	90.000(0)	90.000(0)
Mo-C-Mo*3	180.000(0)	180.000(0)
Co2-Co1-Co2*3	109.873(2)	110.082(0)
Co2-Co1-Mo*6	124.031(1)	123.856(4)
Co2-Co1-Mo*3	66.771(13)	66.710(24)
Mo-Co1-Mo*3	71.29(2)	71.05(4)
Co1-Co2-Co1*6	65.307(1)	64.965(0)
Co1-Co2-Co1*3	180.000(0)	180.000(0)
Co1-Co2-Co1*6	114.693(1)	115.035(0)
Co1-Mo-Co1*1	165.94(2)	166.24(5)
Co1-Mo-C*2	82.969(16)	83.121(24)

The structure of η -12 $\text{Co}_6\text{Mo}_6\text{C}$ has been previously studied and it is apparent that cobalt (Co1, Co2), molybdenum and carbon occupy Wyckoff locations (32e, 16d), 48f and 8a respectively. Figure 3.2-58 displays the unit cell for η -12 $\text{Co}_6\text{Mo}_6\text{C}$ including all elements in the figure on the left hand side (which was drawn using Vesta software using Newsam's CIF file code 68120 from the ICSD database website); whereas only the Mo and C sub-lattice is shown on the right hand side figure.

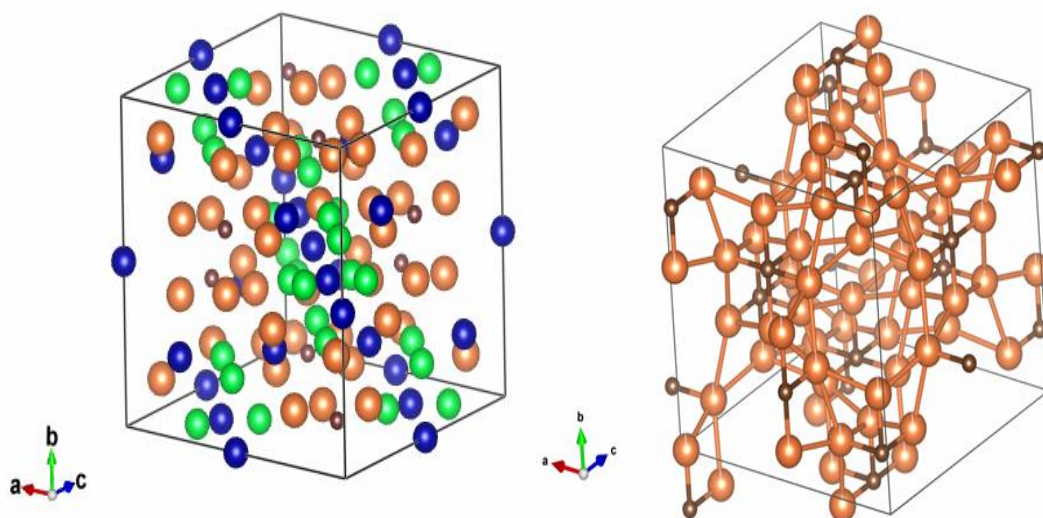


Figure 3.2-58: The Unit cell of $\text{Co}_6\text{Mo}_6\text{C}$ on the left hand side and Mo-C coordination on the right hand side drawn using VESTA software. Brown, dark brown, green and blue spheres represent the Mo, C, Co1 and Co2 respectively.

In the structure of $\text{Co}_6\text{Mo}_6\text{C}$, cobalt occupies two non-equivalent sites in which each site is surrounded by six molybdenum and six cobalt species resulting in the formation of Co $[\text{Mo}_6\text{Co}_6]$ units. In the case of molybdenum, the species is surrounded by four molybdenum and one carbon forming Mo $[\text{Mo}_4\text{Co}_6\text{C}_1]$ units while the carbon species is surrounded by six molybdenum and coordinated exclusively to the molybdenum in 8a Wyckoff sites, resulting in the formation of $[\text{CMo}_6]$ units as illustrated in Figure 3.2-59.

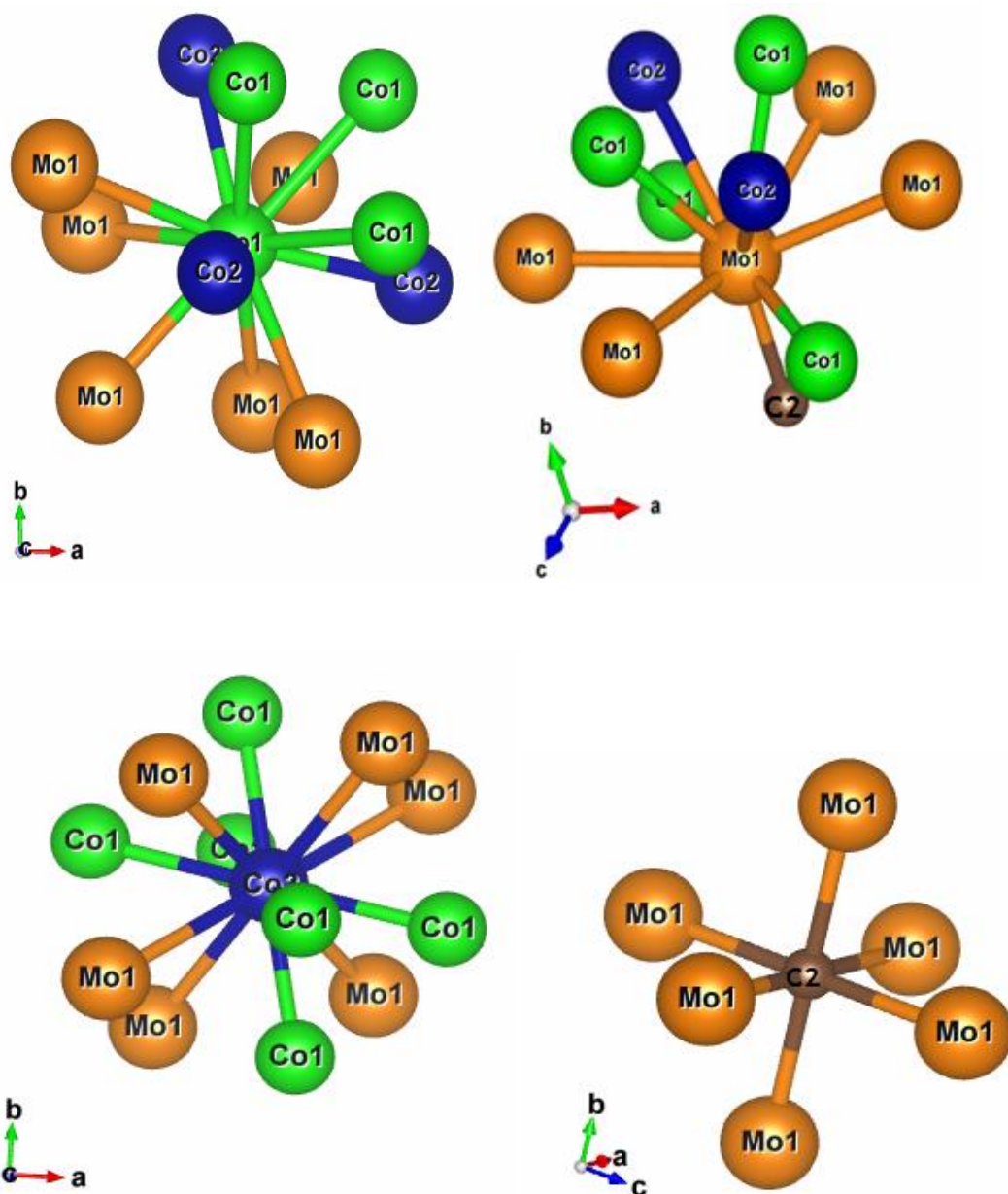


Figure 3.2-59: Atomic coordination of Co1 (32e) and Co2 (16d), Mo (48f) and C2 (8a) sites.

A comparison of η -6 $\text{Co}_3\text{Mo}_3\text{N}$, η -6 $\text{Co}_3\text{Mo}_3\text{C}$, η -12 $\text{Co}_6\text{Mo}_6\text{N}$ and η -12 $\text{Co}_6\text{Mo}_6\text{C}$ PXRD patterns indicate upon reduction of η -6 $\text{Co}_3\text{Mo}_3\text{N}$ and η -6 $\text{Co}_3\text{Mo}_3\text{C}$ to the η -12 $\text{Co}_6\text{Mo}_6\text{N}$ and η -12 $\text{Co}_6\text{Mo}_6\text{C}$ phases respectively, all the peaks are slightly shifted to the right with respect to η -6 $\text{Co}_3\text{Mo}_3\text{C}$. When looking closely in the range between 71 – 74° as seen in Figure 3.2-60; the difference between 661N and 661C is mainly in intensity and for 331C and 331N they are clearly shifted. In addition to this change, microanalysis showed that there was a

reduction in the carbon and nitrogen content of the materials to 1.3 wt. % C for 661C and 1.5 wt. % N for 661N which is close to half 2.8 wt. % of the carbon present prior to reduction of 331C and 3.1 wt. % of the nitrogen present prior to reduction of 331N. This provides a nominal stoichiometry of $\text{Co}_3\text{Mo}_3\text{N}$, $\text{Co}_3\text{Mo}_3\text{N}$, $\text{Co}_6\text{Mo}_6\text{N}$ and $\text{Co}_6\text{Mo}_6\text{C}$ which is in good agreement with the results reported previously by Newsam³⁸, Korlann³⁹ and Hunter⁴.

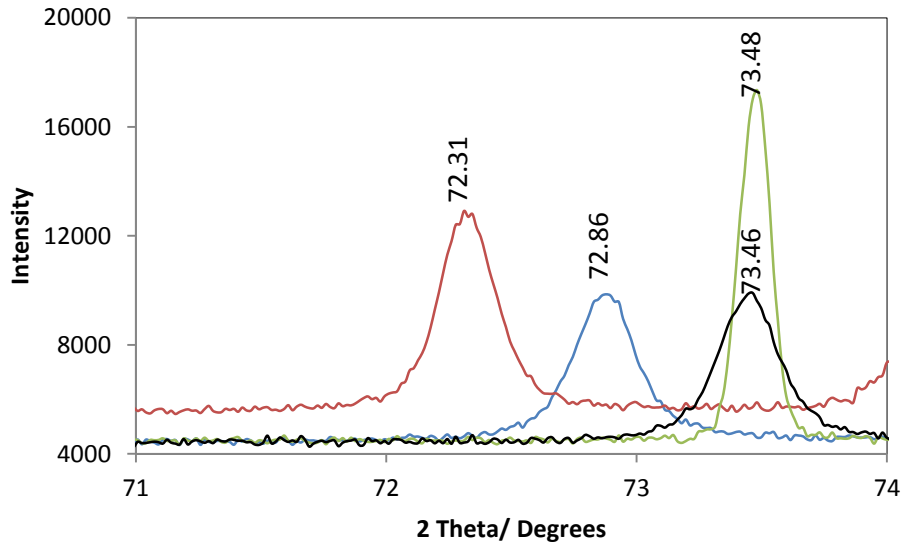


Figure 3.2-60: Comparison of PXRD patterns for 331C (red), 661C (green), 331N (blue) and 661N (black).

3.2.9.2 Raman spectroscopy

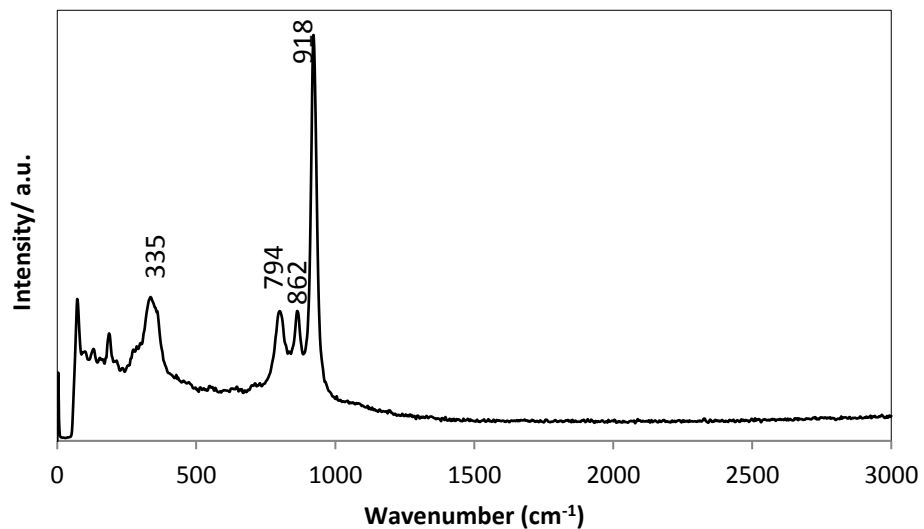


Figure 3.2-61: Raman spectrum of $\text{Co}_6\text{Mo}_6\text{C}$.

Raman spectroscopy was employed to perform further characterization. Figure 3.2-61 shows the Raman spectrum of the η -12 $\text{Co}_6\text{Mo}_6\text{C}$. As for $\text{Co}_3\text{Mo}_3\text{C}$, the Raman spectrum is very similar to that for CoMoO_4 (see Figure 3.2-27) which, again, suggests the presence of a surface oxide phase on the sample.

3.2.9.3 SEM and EDX analyses

The $\text{Co}_6\text{Mo}_6\text{C}$ was analysed by Scanning Electron Microscopy (SEM) coupled with Energy-dispersive X-ray Spectroscopy (EDX) to investigate particle size, morphology and elemental composition. Figure 3.2-62 shows representative SEM micrographs for the η -12 $\text{Co}_6\text{Mo}_6\text{C}$ material. The SEM images for $\text{Co}_6\text{Mo}_6\text{C}$ show a broadly similar morphology to that of the $\text{Co}_3\text{Mo}_3\text{C}$ material. It can be seen that the morphology of η -12 $\text{Co}_6\text{Mo}_6\text{C}$ material appears to consist of aggregates of needles and that it still retains its precursor morphology. The BET surface area recorded for η - $\text{Co}_3\text{Mo}_3\text{C}$ was $3 \text{ m}^2\text{g}^{-1}$ which is lower than that of 331C precursor ($13 \text{ m}^2\text{g}^{-1}$) and may be a consequence of the calcination of the material at the high temperature of 900°C .

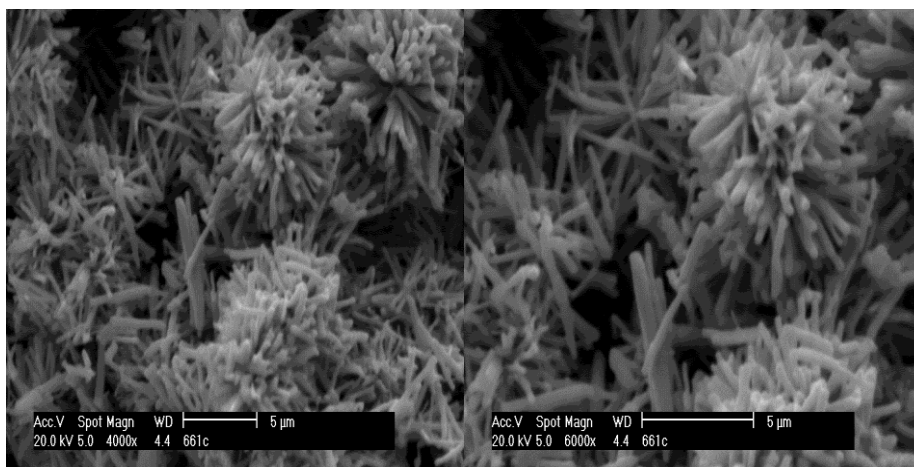


Figure 3.2-62: Representative SEM images of $\text{Co}_6\text{Mo}_6\text{C}$.

EDX data were collected for η -12 $\text{Co}_6\text{Mo}_6\text{C}$. EDX spectra showed that molybdenum, cobalt and carbon are detected as illustrated in Figure 3.2-63. However, the accurate % of carbon was difficult to determine for this material due to the carbon based disc used as the sample holder. The obtained values (33.2 wt. % Co, 42.1 wt. % Mo, 24.7 wt. % C) were found to be different from 37.5 wt. % Co, 61.2 wt. % Mo and 1.3 wt. % C values expected for $\text{Co}_6\text{Mo}_6\text{C}$.

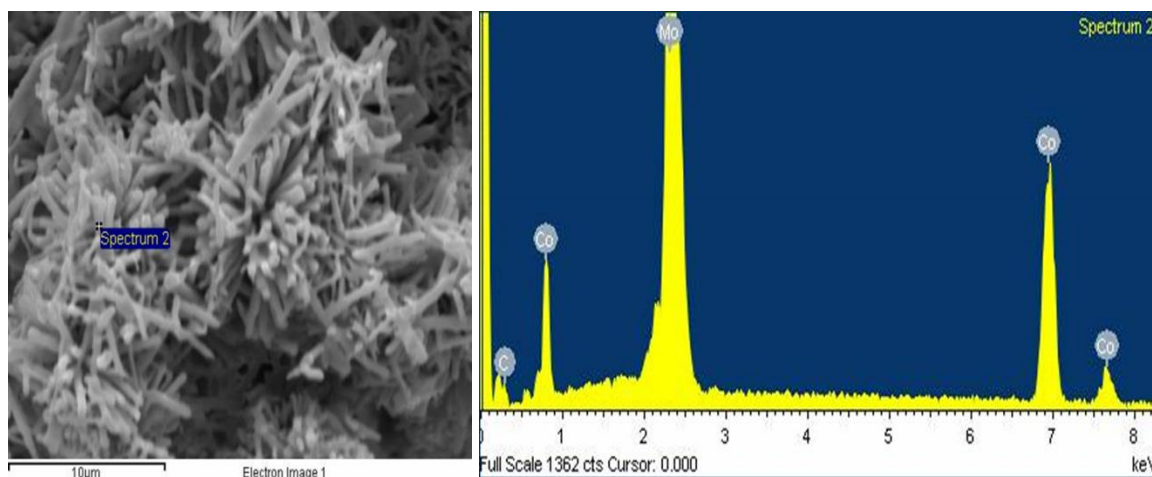


Figure 3.2-63: EDX analysis of $\text{Co}_6\text{Mo}_6\text{C}$.

3.2.9.4 TGA-MS analysis for identified co-products from the homologation of methane step

The two stage homologation of methane was investigated using CH_4/H_2 reduction of $\text{Co}_3\text{Mo}_3\text{N}$ to $\text{Co}_3\text{Mo}_3\text{C}$ and subsequent reduction to $\text{Co}_6\text{Mo}_6\text{C}$. Mass spectrometry was applied to determine the product of reduction of $\text{Co}_3\text{Mo}_3\text{C}$ to yield $\text{Co}_6\text{Mo}_6\text{C}$. Figure 3.2-64 shows the TGA data with the derivative weight loss curves for η -6 $\text{Co}_3\text{Mo}_3\text{C}$ heated under 3:1 H_2/Ar gas mixture at ramp rate of 10 °C/ min from room temperature to 1000 °C. The TGA curve in Figures 3.2-64 exhibits several weight loss steps. The first weight loss step most likely relates to the loss of water from the material around 100 °C. The second weight loss step requires further investigation but could correspond to the removal of the passivation layer. The third weight loss step is attributed to the reaction of carbon to form methane at 616 °C. The MS fragment ion curve for CH_4 (15 m/z) in Figure 3.2-65 displays a large peak that corresponds closely to the individual TGA step at 650 °C. It is not clear what the weight loss beyond 700 °C corresponds to. The possible formation of higher hydrocarbons (28, 29, 30, 32, 43, 44, 46, 55, 56, 71 and 72 m/z) was investigated and excluded.

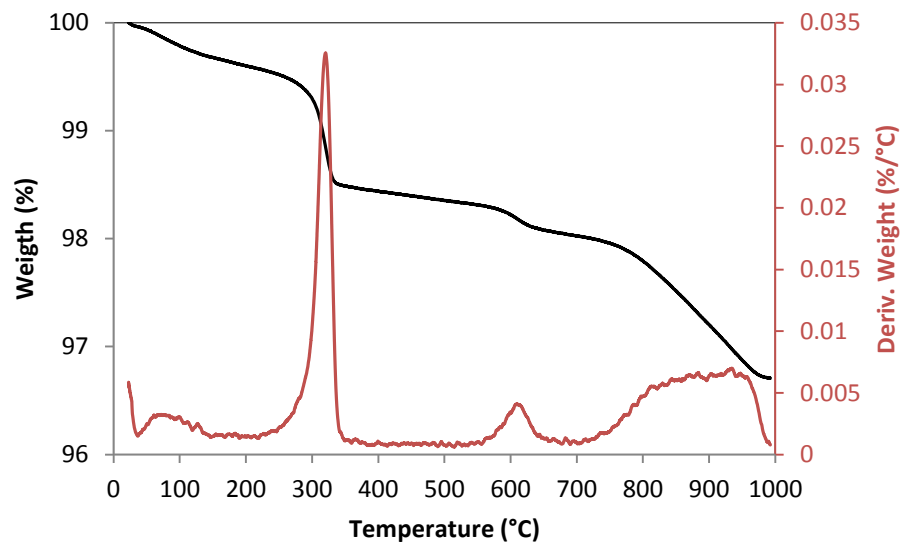


Figure 3.2-64: The TGA and derivative weight curves for $\text{Co}_3\text{Mo}_3\text{C}$ with 3:1 H_2/Ar up to 1000 °C.

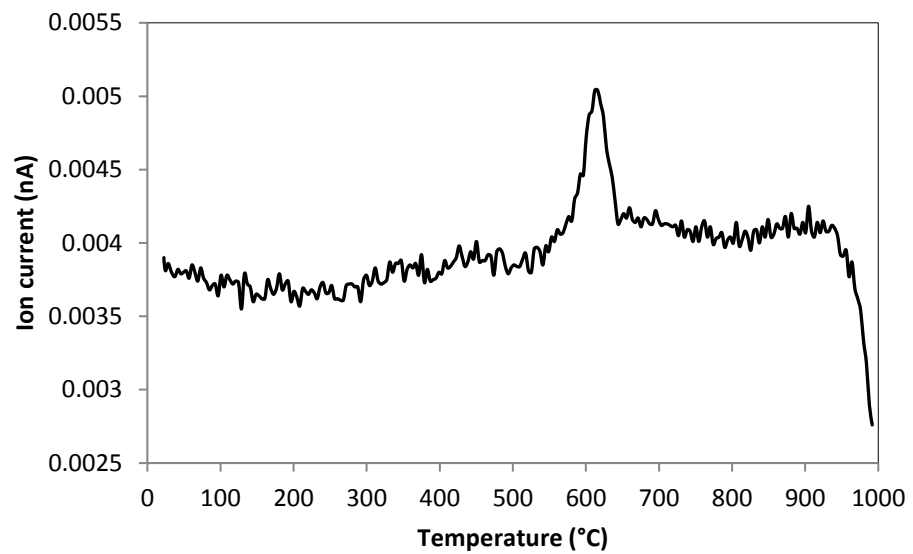


Figure 3.2-65: The MS fragment ion curves for 15 m/z.

3.2.10 Investigation of the transformation of CoMo nitride to CoMo carbide

The lattice nitrogen mobility and reactivity of $\text{Co}_3\text{Mo}_3\text{N}$ towards hydrogen to produce ammonia has been reported by Hargreaves *et al.*^{4, 37, 58} Results of nitrogen isotopic exchange and the ability of $\text{Co}_3\text{Mo}_3\text{N}$ to produce ammonia under reducing conditions have suggested the possible occurrence of a Mars-van Krevelen mechanism where the nitride acts as source of reactive nitrogen. Interestingly, cobalt molybdenum has been reported to form a range of carbide products (e.g. $\text{Co}_3\text{Mo}_3\text{C}$ and $\text{Co}_6\text{Mo}_6\text{C}$) that are structural isomorphs to their nitride counterparts. From an environmental and catalytic point of view, the ability of CoMo nitrides to form interstitial carbide materials upon reaction with CH_4 ³⁹ or CO_2/CO ³⁸ is of interest.

In the current study, the reaction of nitride materials namely $\text{Co}_3\text{Mo}_3\text{N}$ and $\text{Co}_6\text{Mo}_6\text{N}$ with CH_4 in the presence and in absence of hydrogen to form cobalt molybdenum carbide materials has been probed. The structural changes occurring during the carburization stage were studied using a combination of *in-situ* powder neutron diffraction and powder X-ray diffraction techniques. Furthermore, the restoration of the nitride structure by reaction of the resultant carbides with N_2 both in the presence and in the absence of H_2 was investigated.

3.2.10.1 Pathways of carburisation of $\text{Co}_3\text{Mo}_3\text{N}$ with CH_4

The structural evolution of $\text{Co}_3\text{Mo}_3\text{N}$ upon reaction with CH_4 in presence of hydrogen was investigated using a variety of *in-situ* and *ex-situ* diffraction techniques.

a) Structural features of $\text{Co}_3\text{Mo}_3\text{N}$ upon reaction with CH_4

Figure 3.2-66 presents *ex-situ* PXRD patterns collected upon reaction of $\text{Co}_3\text{Mo}_3\text{N}$ with 12 ml min^{-1} of 20 vol. % CH_4 in H_2 at different reaction temperatures. All the diffraction patterns showed only features assignable to the η -6 $\text{Co}_3\text{Mo}_3\text{C}$ structure without any additional phases being apparent during reaction. However, a gradual shift toward lower 2θ was observed for all reflections, indicating that the $\text{Co}_3\text{Mo}_3\text{N}$ retained the same structural features during the carburization process but with different cell parameters, which may be attributed to nitrogen substitution by carbon.

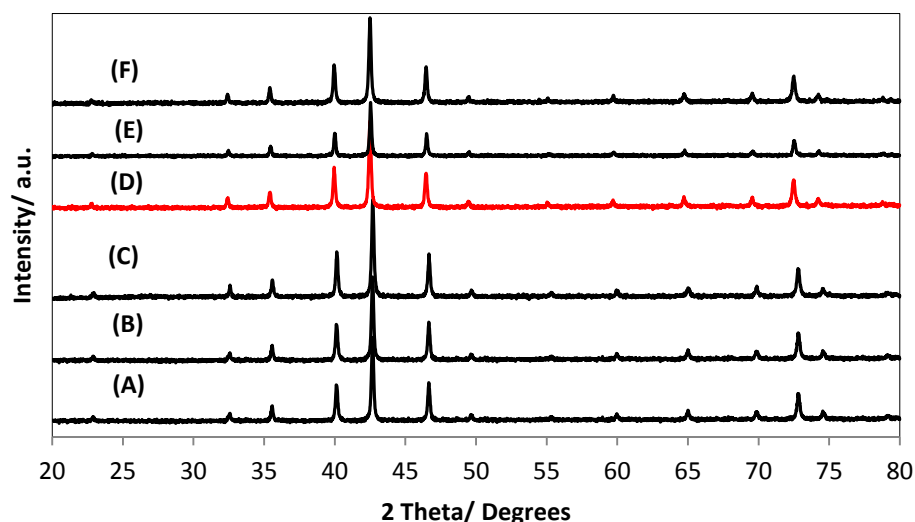


Figure 3.2-66: *Ex-situ* PXRD patterns collected upon reaction of 331N with 12 ml min^{-1} of 20 vol. % CH_4 in H_2 at various temperatures and applying a temperature ramp rate of $10 \text{ }^\circ\text{C min}^{-1}$; A (at room temperature), B ($500 \text{ }^\circ\text{C}$), C ($600 \text{ }^\circ\text{C}$), D ($700 \text{ }^\circ\text{C}$), E ($700 \text{ }^\circ\text{C}$, 2h), F ($700 \text{ }^\circ\text{C}$, 3h).

b) *In-situ* PND study of $\text{Co}_3\text{Mo}_3\text{N}$ phase-structural transformations

In-situ neutron diffraction patterns collected at different temperature for $\text{Co}_3\text{Mo}_3\text{N}$ material upon reaction with 60 ml min^{-1} of 20 vol. % CH_4 in H_2 are presented in Figure 3.2-67. The patterns were fitted applying the Rietveld method using the η -6 nitride $\text{Co}_3\text{Mo}_3\text{N}$ structure as the starting model and η -6 carbide $\text{Co}_3\text{Mo}_3\text{C}$ as the end model. Structure refinements were started by fitting the background to linear interpolation function (background function 7 in GSAS with number of terms 10), lattice parameters, scale factor, peak shapes, atomic parameters and subsequently absorption/reflectivity correction (absorption function 1). The nitrogen and carbon occupancy of 16c sites was allowed to freely vary for the final refinement. During the reaction, no change in the structural features was observed and all diffraction peaks were correlated to the η -6 carbide structure. However, a gradual shift to higher d-spacing was observed in all neutron diffraction peaks indicating a change in the lattice parameter of $\text{Co}_3\text{Mo}_3\text{N}$ during the carburisation process (Figure 3.2-68).

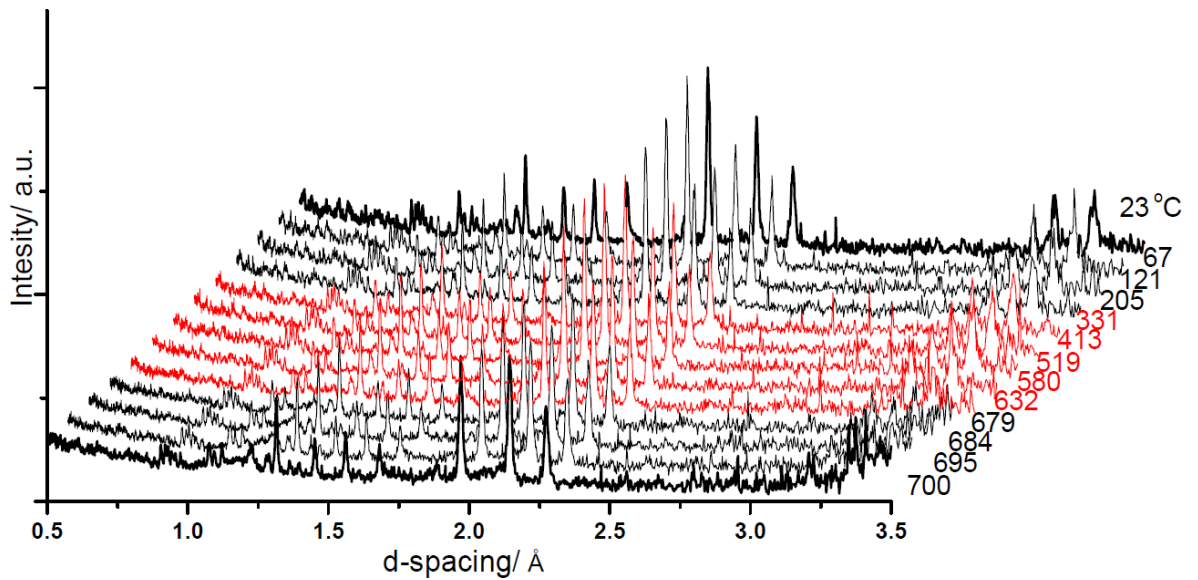


Figure 3.2-67: *In-situ* PND patterns collected at different temperatures for $\text{Co}_3\text{Mo}_3\text{N}$ heated under 60 ml min^{-1} of 20 vol. % CH_4 in H_2 .

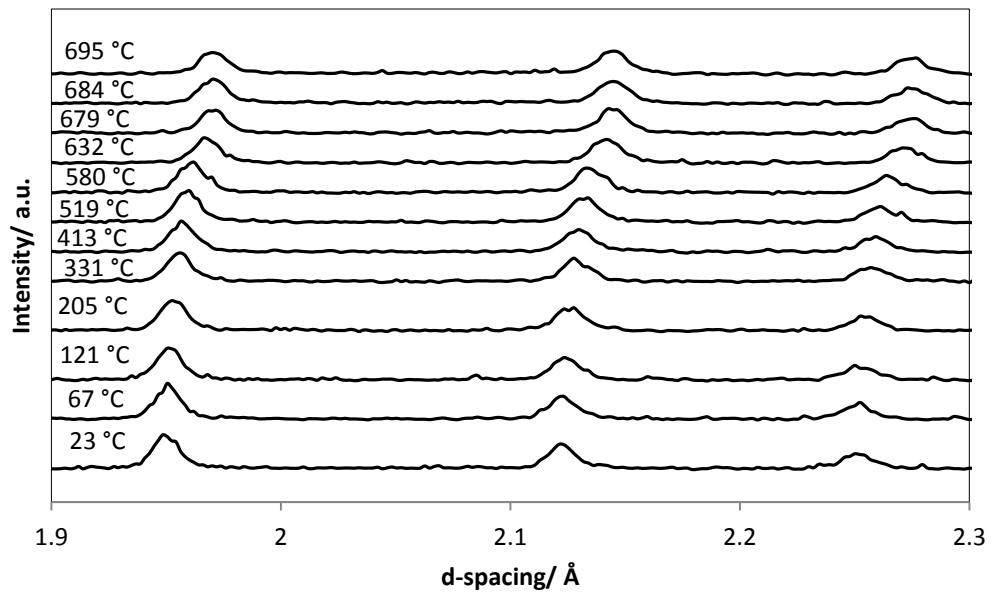


Figure 3.2-68: *In-situ* PND patterns collected at different temperature for $\text{Co}_3\text{Mo}_3\text{N}$ heated under 60 ml min^{-1} of 20 vol. % CH_4 in H_2 with zoom in on d-spacing range between 1.9 and 2.3 Å.

The lattice parameters, determined during the different reaction stages and calculated from Rietveld refinements, are presented in Figure 3.2-69. With increasing temperature to 500 °C, a linear change of lattice parameter was observed. This can be attributed to thermal expansion of the lattice. However, a change in the slope was detected at temperatures ranging above 500 °C, which could be related to the structural transformation of $\text{Co}_3\text{Mo}_3\text{N}$ upon nitrogen substitution by carbon. In addition to lattice parameter determination, the large differences in neutron scattering lengths of carbon (6.646 fm) and nitrogen (9.36 fm) allowed the assessment of the C/N substitution during reaction. The evolution of the C/N occupancy at the 16c Wyckoff lattice site as a function of reaction temperature is presented in Figure 3.2-70 where a gradual substitution of nitrogen by carbon is evidenced. At temperatures lower than 400 °C, no carbon inclusion in the $\text{Co}_3\text{Mo}_3\text{N}$ structure was observed. In contrast, a gradual substitution of nitrogen with carbon is observed at temperatures higher than 400 °C, which accelerated at 600 °C. The refinement of the C/N mixing in the 16c Wyckoff lattice indicates that at 413, 519, 580, 632, 679 °C the C/N sublattice comprised 97.5, 88.3, 79.4, 15.2, 3.2 % C and 2.5, 11.7, 20.6, 84.8, 96.8 % N respectively. Complete conversion to the $\text{Co}_3\text{Mo}_3\text{C}$ was observed when the temperature of the reaction reached 700 °C. $\text{Co}_3\text{Mo}_3\text{C}$ is typically formed upon 2h of $\text{Co}_3\text{Mo}_3\text{N}$ reaction with CH_4/H_2 gas, as evidenced in section 3.2.8, Figure 3.2-49 and Table 3.2-13, page 70. *In-situ* PND confirmed that the carburisation of the $\text{Co}_3\text{Mo}_3\text{N}$ proceeded upon nitrogen substitution by carbon and the formation of carbonitride as a transitional intermediate phase at temperatures ranging between 400 and 600 °C without any phase segregation being observed. An example of $\text{Co}_3\text{Mo}_3\text{C}_x\text{N}_y$ formed at 632 °C is presented in Figure 3.2-71 and Table 3.2-23. The lattice parameter derived from Rietveld refinement was found to be $a = 11.1312(2) \text{ \AA}$, falling between the lattice parameter observed for $\text{Co}_3\text{Mo}_3\text{N}$ ($a = 11.027 \text{ \AA}$ at 23 °C) and $\text{Co}_3\text{Mo}_3\text{C}$ ($a = 11.145$ at 700 °C) as presented in Appendix 2 Table 8.2-1. The refinement of carbon and nitrogen occupancy of the 16c Wyckoff site converged to an estimated chemical composition of $\text{Co}_3\text{Mo}_3\text{C}_{0.85}\text{N}_{0.15}$. For more quantitative analysis data see Appendix 2 Table 8.2-1.

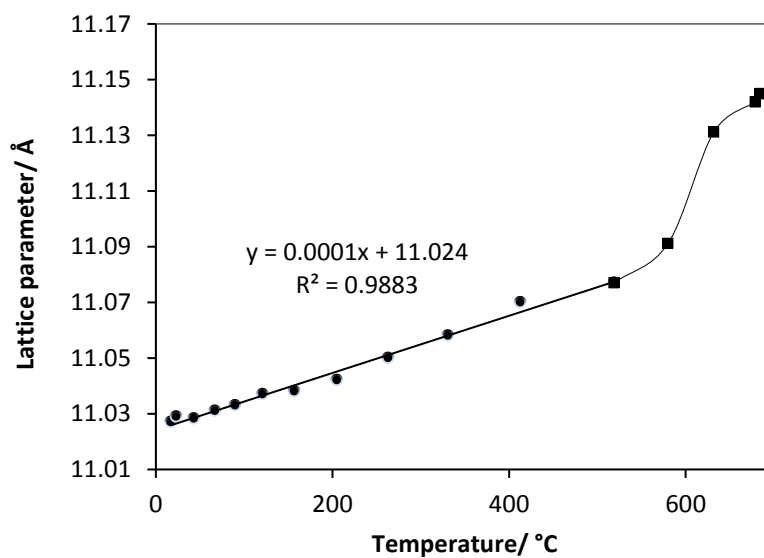


Figure 3.2-69: The evolution of lattice parameters obtained from Rietveld refinements of *in-situ* PND data collected at different temperatures for $\text{Co}_3\text{Mo}_3\text{N}$ heated under 60 ml min^{-1} of 20 vol. % CH_4 in H_2 .

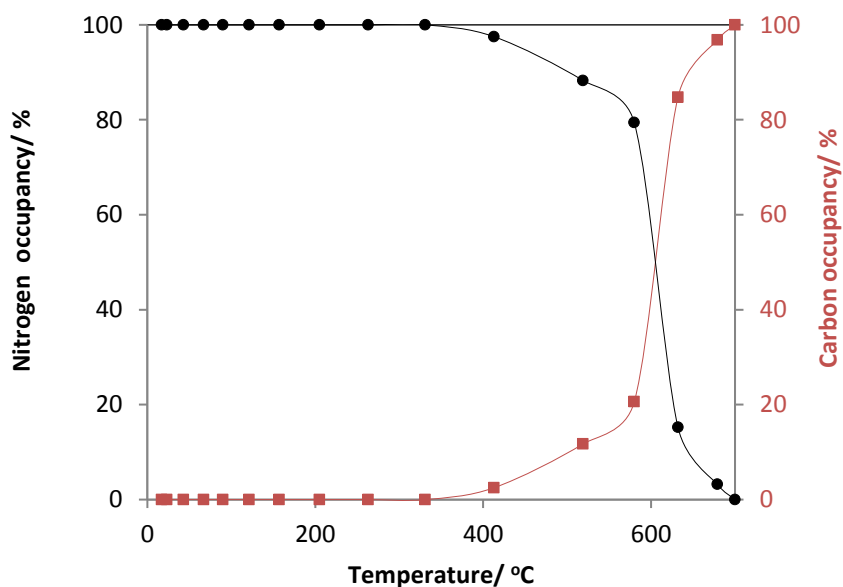


Figure 3.2-70: Evolution of the C/N occupancy of the 16c Wyckoff lattice site in $\text{Co}_3\text{Mo}_3\text{N}$ as a function of reaction with 60 ml min^{-1} of 20 vol. % CH_4 in H_2 at different temperatures. (■) Fractional carbon content and (●) fractional nitrogen content as determined from the Rietveld refinement against *in-situ* powder neutron diffraction data.

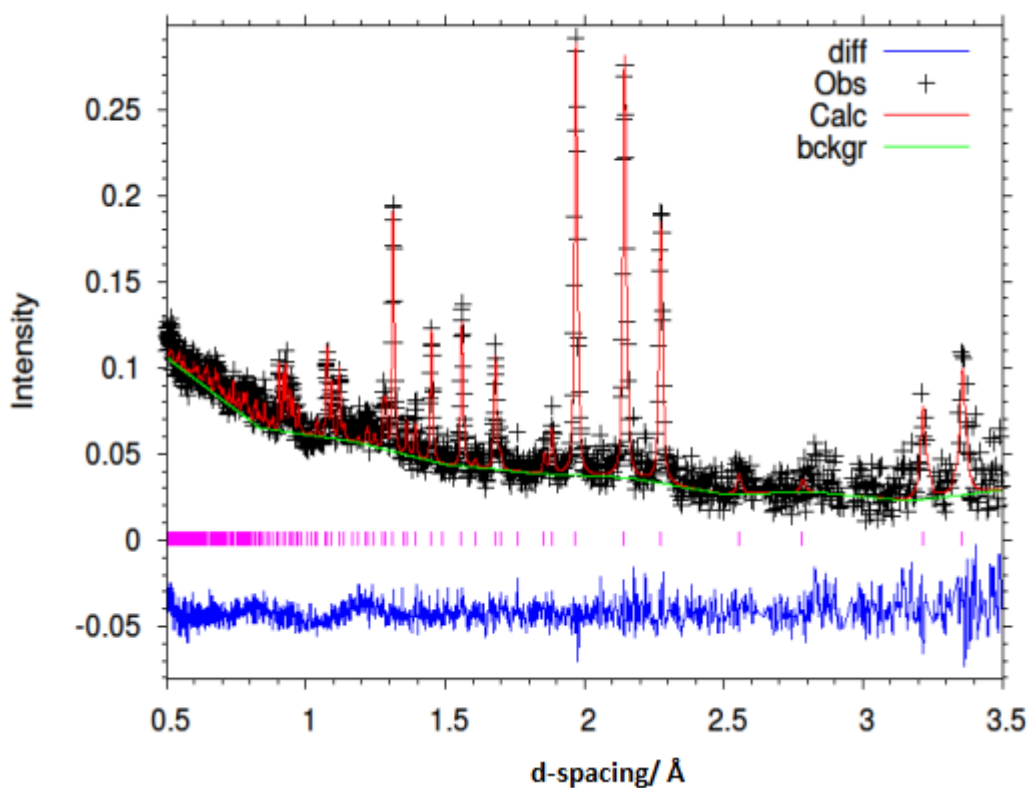


Figure 3.2-71: Fitted powder neutron diffraction profile from Rietveld refinement against powder neutron diffraction data for $\text{Co}_3\text{Mo}_3\text{N}$ after reaction with 60 ml min^{-1} of 20 vol. % CH_4 in H_2 at $632 \text{ }^\circ\text{C}$.

Table 3.2-23: Structure parameters of $\text{Co}_3\text{Mo}_3\text{N}$ after reaction with 60 ml min^{-1} of 20 vol. % CH_4 in H_2 at $632 \text{ }^\circ\text{C}$ obtained from neutron diffraction data.

Atom	Site	Occupancies	x	y	z	$100 \cdot U_{\text{iso}}(\text{\AA}^2)$
Co1	32e	1.000	0.29266(0)	0.29266(0)	0.29266(0)	0.46(0)
Co2	16d	1.000	0.50000(0)	0.50000(0)	0.50000(0)	0.84(0)
Mo1	48f	1.000	0.32358(0)	0.12500(0)	0.12500(0)	1.28(1)
C1	16c	0.848(6)	0.00000(0)	0.00000(0)	0.00000(0)	1.355(5)
N1	16c	0.152(4)	0.00000(0)	0.00000(0)	0.00000(0)	1.355(5)

^a Space group $Fd\bar{3}mZ(227)$; $a = 11.1312(2) \text{ \AA}$, $V = 1379.20(3) \text{ \AA}^3$, $R_{\text{wp}} = 0.0706$, $R_p = 0.1032$, $\chi_{\text{red}}^2 = 0.8720$

3.2.10.2 Pathways of carburisation of $\text{Co}_6\text{Mo}_6\text{N}$ upon reaction with CH_4

The structural evolution of $\text{Co}_6\text{Mo}_6\text{N}$ upon reaction with CH_4 was investigated using a variety of *in-situ* PND and *ex-situ* PXRD techniques.

a) Structural features of $\text{Co}_6\text{Mo}_6\text{N}$ upon reaction with CH_4

Some initial insight into the carburisation process of $\text{Co}_6\text{Mo}_6\text{N}$ can be obtained by XRD. PXRD patterns collected upon $\text{Co}_6\text{Mo}_6\text{N}$ reaction with 60 ml min^{-1} CH_4 at various temperatures are shown in Figure 3.2-72. The PXRD pattern of $\text{Co}_6\text{Mo}_6\text{N}$ collected at room temperature confirmed the preparation of a well-crystallized and pure nitride phase. At 678°C , the PXRD showed that the material is no longer monophasic and $\text{Co}_3\text{Mo}_3\text{C}$ was detected as the major phase along with the $\text{Co}_6\text{Mo}_6\text{N}$ and graphite as minor phases. Reaction at higher temperature (800°C) resulted in the complete conversion of $\text{Co}_6\text{Mo}_6\text{N}$ to $\text{Co}_3\text{Mo}_3\text{C}$ and to the formation of graphite. The initial XRD results seem to indicate that the mechanism of carburisation of $\text{Co}_6\text{Mo}_6\text{N}$ proceeds differently to that which was observed in the case of $\text{Co}_3\text{Mo}_3\text{N}$ and that at two distinct phases are present in the intermediate carburisation stages, although such comparisons must be treated with caution since CH_4/H_2 was used as carburising gas in one case and CH_4 alone in the other.

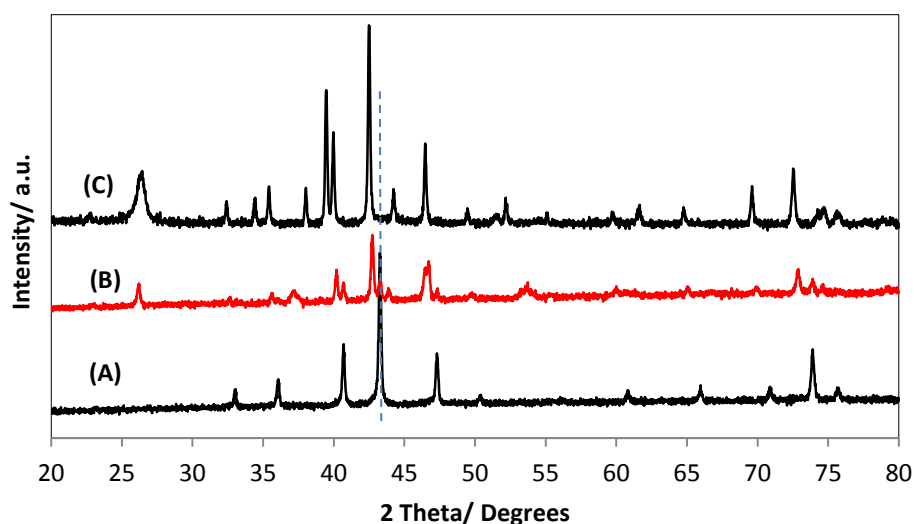


Figure 3.2-72: PXRD patterns of $\text{Co}_6\text{Mo}_6\text{N}$ with 60 ml min^{-1} CH_4 gas under various temperature and times on stream at A (at room temperature), B (678°C), C (800°C , 3h).

b) *In-situ* PND study of Co₆Mo₆N phase-structural transformations

The structural transformation of the Co₆Mo₆N upon reaction with methane was studied using *in-situ* neutron diffraction. Neutron diffraction patterns collected during the reaction of Co₆Mo₆N with 60 ml min⁻¹ CH₄ are presented in Figure 3.2-73.

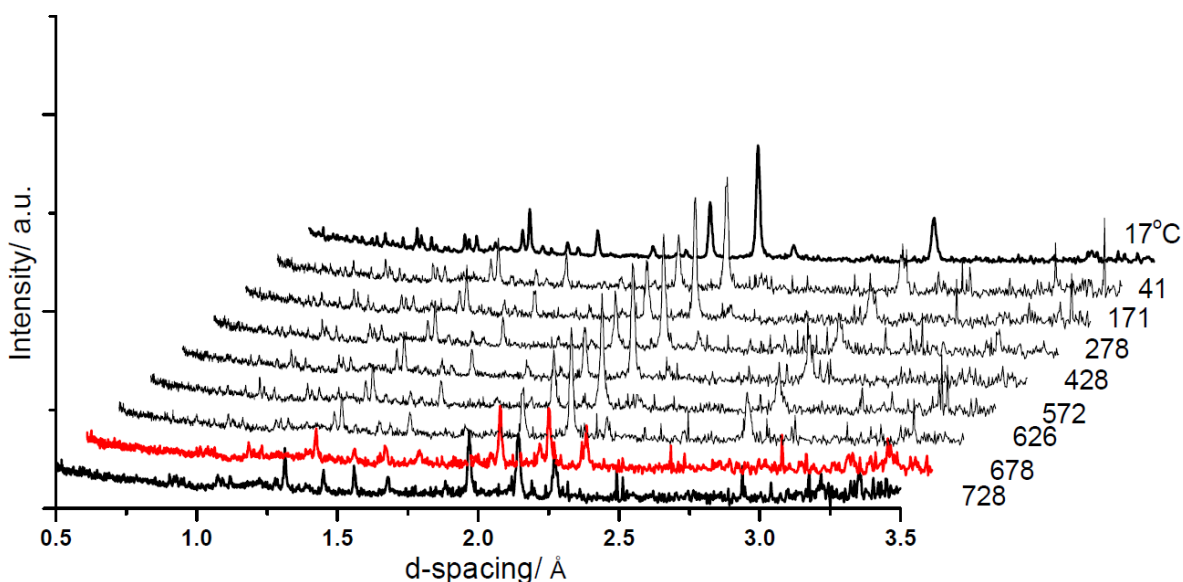


Figure 3.2-73: *In-situ* PND data of Co₆Mo₆N through heating with 60 ml min⁻¹ CH₄.

The results from room temperature PND supported the preparation of a pure Co₆Mo₆N phase ($a = 10.8809(8)$ Å, Table 3.2-8, page 60). Rietveld refinement against PND data were performed using the iso-type structure of Co₆Mo₆C³⁸ with nitrogen replacing carbon in 8a site to model the nitride phase as the starting model. The formation of carbide phases upon reaction with methane was verified using Co₃Mo₃C⁴⁰ as the second phase during Rietveld refinement. The formation of carbonitride phases was verified by refining mixed occupancy of the 16c site and/or 8a site by carbon and nitrogen. From 32 °C up to 678 °C, no apparent change in PND diffraction profiles was detected and all diffraction peaks observed were related to Co₆Mo₆N with the exception of few minor peaks related to the *in-situ* reaction cell. The lattice parameters derived from Rietveld refinements of *in-situ* PND is presented in Figure 3.2-74. A linear change of lattice parameter was observed which can be attributed to thermal expansion of the lattice.

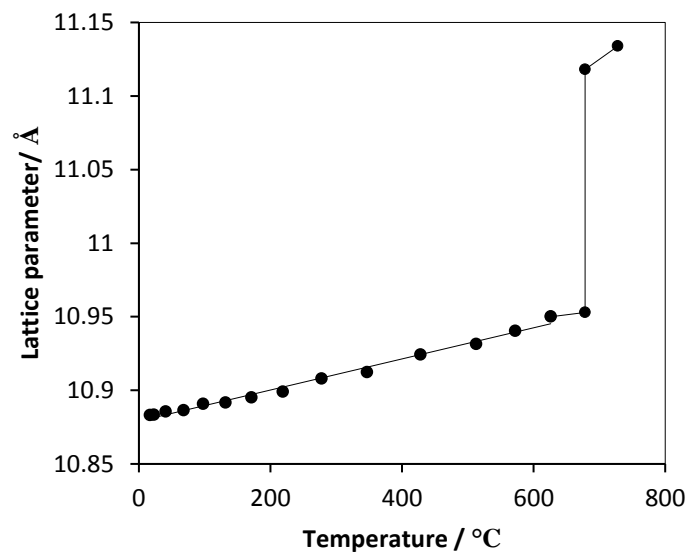


Figure 3.2-74: Evolution of lattice parameters obtained from Rietveld refinements of *in-situ* PND data collected at different temperature for Co₆Mo₆N heated under 60 ml min⁻¹ CH₄.

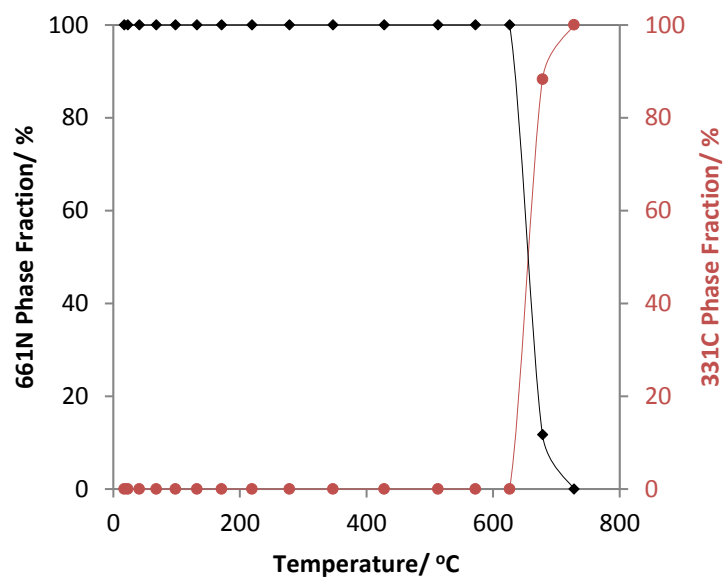


Figure 3.2-75: Investigation of phase fractions of Co₆Mo₆N (◆) and Co₃Mo₃C (●) present during reaction of Co₆Mo₆N with 60 ml min⁻¹ CH₄ at different temperature as determined from the Rietveld refinement against *in-situ* powder neutron diffraction data.

Most importantly, the refinement of the powder neutron diffraction profile against PND data at 678 °C, highlighted in red, has shown that the material is not monophasic any longer and revealed co-existence of $\text{Co}_6\text{Mo}_6\text{N}$ alongside the $\text{Co}_3\text{Mo}_3\text{C}$ phase. The phase fraction derived for the refinement PND profile was estimated to 20.9 wt. % and 79.1 wt. % for $\text{Co}_6\text{Mo}_6\text{N}$ and $\text{Co}_3\text{Mo}_3\text{C}$ respectively. When the temperature reached 728 °C, the material was completely converted to $\text{Co}_3\text{Mo}_3\text{C}$. The gradual formation of $\text{Co}_3\text{Mo}_3\text{C}$ and the concomitant loss of the $\text{Co}_6\text{Mo}_6\text{N}$ during the reaction is presented Figure 3.2-75. It can be clearly seen that the carburisation process was rapid and occurred in a narrow temperature window. The structural features of $\text{Co}_6\text{Mo}_6\text{N}$ and $\text{Co}_3\text{Mo}_3\text{C}$ obtained from the refinement of PND profile are presented in Figure 3.2-76 and Table 3.2-24. The lattice parameter derived from Rietveld refinement was found to be $a = 11.1188(4)$ Å for $\text{Co}_3\text{Mo}_3\text{C}$ and $a = 10.9525(9)$ Å for $\text{Co}_6\text{Mo}_6\text{N}$. The refinement of carbon, nitrogen occupancy of the 16c and in the 331C phase and the 8a site in the 661N respectively (Table 3.2-24) resulted in an estimated chemical composition of $\text{Co}_3\text{Mo}_3\text{C}_{1.03}$ and $\text{Co}_6\text{Mo}_6\text{N}_{0.96}$. For more quantitative analysis data see Appendix 2 Table 8.2-2.

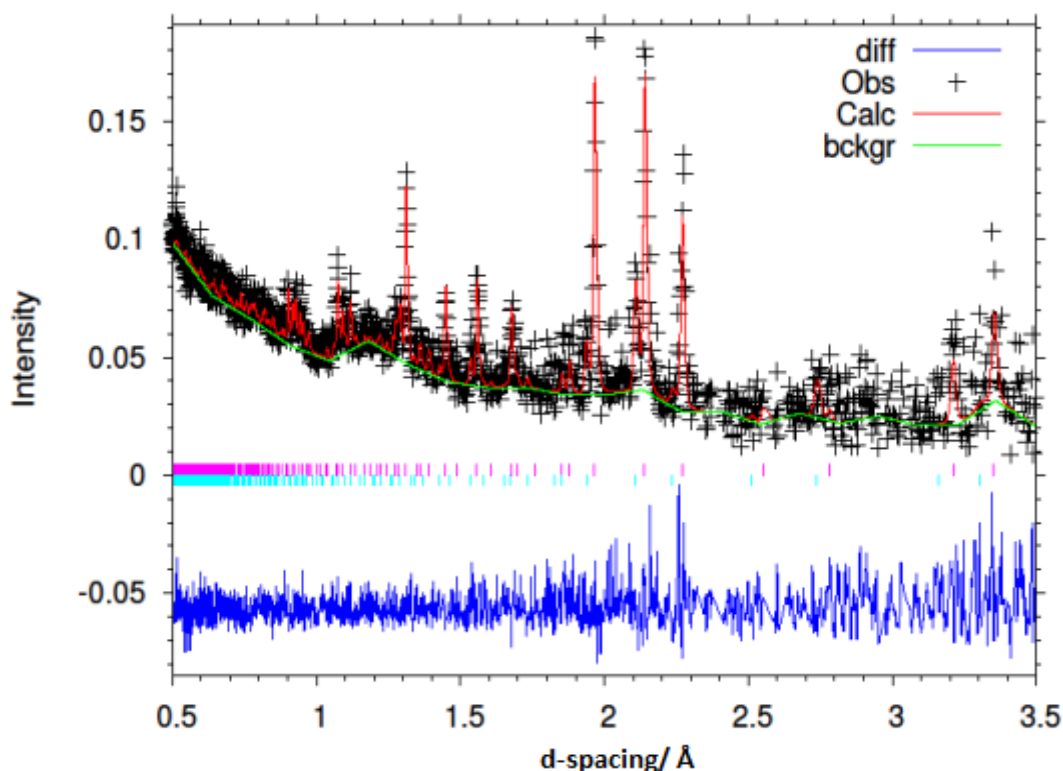


Figure 3.2-76: Fitted powder neutron diffraction profile from Rietveld refinement against powder neutron diffraction data for: $\text{Co}_6\text{Mo}_6\text{N}$ after reaction with 60 ml min^{-1} of CH_4 (BOC, 99.98%) at 678 °C.

Table 3.2-24: Structure parameters of Co₆Mo₆N after reaction with 60 ml min⁻¹ of CH₄ (BOC, 99.98%) at 678 °C obtained from neutron diffraction data.

Atom 331C	site	occupancies	x	y	z	100*U _{iso} (Å ²)
Co1	32e	1.000	0.29266(0)	0.29266(0)	0.29266(0)	1.20(4)
Co2	16d	1.000	0.50000(0)	0.50000(0)	0.50000(0)	1.47(0)
Mo1	48f	1.000	0.32358(0)	0.12500(0)	0.12500(0)	1.29(4)
C1	16c	1.032(7)	0.00000(0)	0.00000(0)	0.00000(0)	1.37(9)

^a Space group $Fd\bar{3}mZ$ (227); $a = 11.1188(4)$ Å, $V = 1374.60(8)$ Å³, $R_{wp} = 0.0766$, $R_p = 0.1252$, $\chi_{red}^2 = 0.7573$

Atom 661N	site	occupancies	x	y	z	100*U _{iso} (Å ²)
Co1	32e	1.000	0.29200(0)	0.29200(0)	0.29200(0)	5.66(8)
Co2	16d	1.000	0.50000(0)	0.50000(0)	0.50000(0)	5.66(8)
Mo1	48f	1.000	0.32100(0)	0.12500(0)	0.12500(0)	2.77(8)
N1	16c	0.000	0.00000(0)	0.00000(0)	0.00000(0)	0.32(9)
N2	8a	0.967(3)	0.12500(0)	0.12500(0)	0.12500(0)	5.64(1)

^a Space group $Fd\bar{3}mZ$ (227); $a = 10.9525(9)$ Å, $V = 1313.86(7)$ Å³, $R_{wp} = 0.1591$, $R_p = 0.1942$, $\chi_{red}^2 = 0.7573$

Again, within the limitations previously stated, the process of the carburisation was inherently different from the carburisation process of Co₃Mo₃N, as in this case no intermediate carbonitride phase was observed. The carburisation process apparently proceeded via the decline of Co₆Mo₆N and the formation of Co₃Mo₃C.

3.2.11 Investigation of the transformation of CoMo carbide to CoMo nitride

In this section, the ability of CoMo nitride to activate CH₄ and form a range of carbide and carbonitride materials that depend upon the nature of the precursors and the carburisation conditions demonstrating the mobility of nitrogen mobility within these structures has been studied. In the following section, the regeneration of the nitride structure using N₂ as well as a mixture of N₂/H₂ is reported.

3.2.11.1 Pathways of nitridation of Co₃Mo₃C structure with H₂/N₂ or N₂

The structural evolution of Co₃Mo₃C upon reaction with H₂/N₂ and N₂ was investigated using a variety of *in-situ* and *ex-situ* diffraction techniques.

a) Evolution of $\text{Co}_3\text{Mo}_3\text{C}$ structure upon reaction with N_2/H_2 or N_2

Initial investigation of the nitridation process of $\text{Co}_3\text{Mo}_3\text{C}$ was conducted by XRD. Figure 3.2-77 presents PXRD patterns collected upon reaction of $\text{Co}_3\text{Mo}_3\text{C}$ with 60 ml min^{-1} of 75 vol. % H_2 in N_2 at $500 \text{ }^\circ\text{C}$ and different reaction times. All the diffraction patterns showed only features attributable to the η -6 $\text{Co}_3\text{Mo}_3\text{C}$ structure without any extra-phases being present. However, a gradual shift to higher 2θ was observed for all reflections, indicating that the $\text{Co}_3\text{Mo}_3\text{C}$ retained the same structural features during the nitridation process but with different cell parameters, which may be related to carbon substitution by nitrogen. CHN elemental analysis was applied to determine the C and N content of the materials. The results are presented in Figure 3.2-77 A (at room temperature), B (stopped when the temperature reached $500 \text{ }^\circ\text{C}$), C (stopped after 1 hour), D (2 hours), E (3 hours), F (4 hours) were (2.8 wt.% C), (2.8 wt.% C, 0.4 wt.% N), (1.9 wt.% C, 1.2 wt.% N), (1.8 wt.% C, 1.7 wt.% N), (1.4 wt.% C, 1.4 wt.% N) and (1.2 wt.% C, 2.1 wt.% N) respectively. This result confirmed that the material was converted to nitride through carbonitride as intermediate single phase.

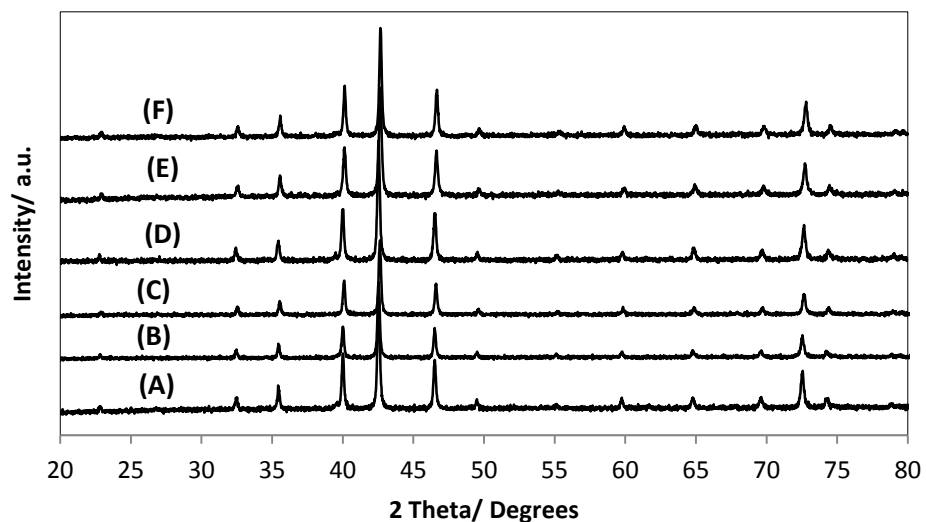


Figure 3.2-77: PXRD patterns of $\text{Co}_3\text{Mo}_3\text{C}$ after reaction with 3:1 H_2/N_2 at $500 \text{ }^\circ\text{C}$ stopped at 0, 1, 2, 3 and 4 h on stream; A 331C (at room temperature), B (when reached $500 \text{ }^\circ\text{C}$), C ($500 \text{ }^\circ\text{C}$, 1h), D ($500 \text{ }^\circ\text{C}$, 2h), E ($500 \text{ }^\circ\text{C}$, 3h), F ($500 \text{ }^\circ\text{C}$, 4h).

In order to investigate the intermediate phase and the possible conversion with only N_2 in the absence of H_2 , PXRD patterns were collected upon Co_3Mo_3C reaction with 60 ml min^{-1} N_2 as shown in Figure 3.2-78.

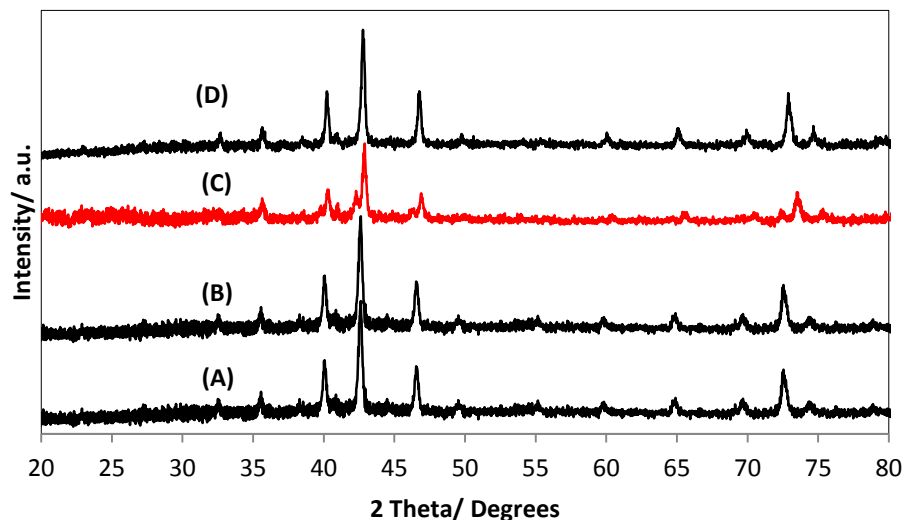


Figure 3.2-78: PXRD patterns of Co_3Mo_3C after reaction with 60 ml min^{-1} N_2 at various temperatures and times on stream; A (at room temperature), B ($500\text{ }^\circ\text{C}$, 5h), C ($600\text{ }^\circ\text{C}$, 5h), D ($700\text{ }^\circ\text{C}$, 3h).

The PXRD pattern of Co_3Mo_3C collected at room temperature confirmed the preparation of a well-crystallized and pure carbide phase. At $600\text{ }^\circ\text{C}$ (in Figure 3.2-78 C), the PXRD showed that the material is no longer monophasic and Co_3Mo_3C was detected as a minor phase along with $Co_6Mo_6N_x$ and graphite as major phases. Reaction at higher temperature ($700\text{ }^\circ\text{C}$ in Figure 3.2-78 E) resulted in the complete conversion of Co_3Mo_3C to Co_3Mo_3N . The removal of carbon from the lattice and its exchange for nitrogen was identified by using CHN microanalysis which confirmed that the starting composition of Co_3Mo_3C corresponded to 2.8 wt. % C and the final composition of $Co_3Mo_3N_x$ corresponded to 2.7 wt. % N. The initial XRD results seem to indicate that the mechanism of nitridation of Co_3Mo_3C proceeds differently to that observed in the case of presence of hydrogen in that two segregated phases are present in the intermediate nitridation stages and the change occurred at higher temperature. Also, the same result was confirmed using an *in-situ* PXRD experiment as presented in Figure 3.2-79.

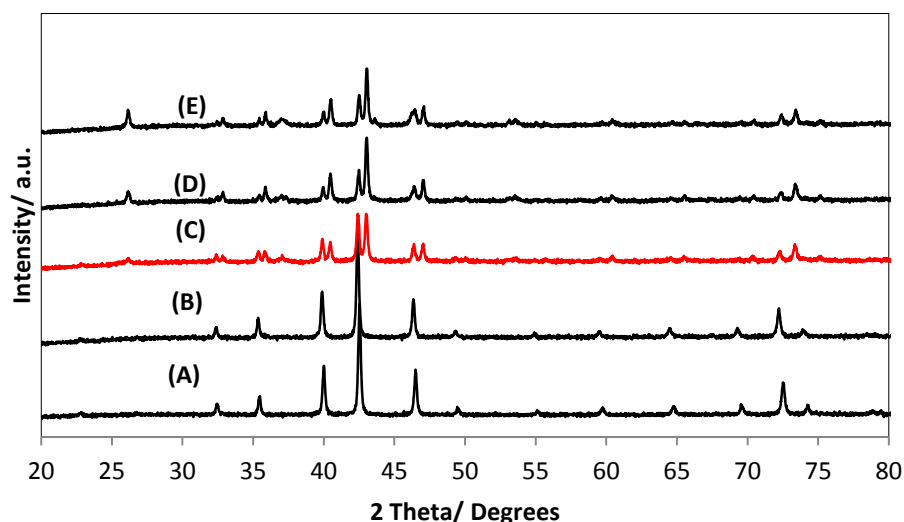


Figure 3.2-79: *In-situ* PXRD patterns of $\text{Co}_3\text{Mo}_3\text{C}$ with $60 \text{ ml min}^{-1} \text{ N}_2$ under various temperatures and times on stream; A (at room temperature), B ($500 \text{ }^\circ\text{C}$), C ($600 \text{ }^\circ\text{C}$, 1h), D ($600 \text{ }^\circ\text{C}$, 2h) and E ($600 \text{ }^\circ\text{C}$, 3h).

b) *In-situ* PND for nitride formation using $\text{Co}_3\text{Mo}_3\text{C}$

In-situ neutron diffraction patterns collected upon reaction of $\text{Co}_3\text{Mo}_3\text{C}$ at different temperatures and reaction times for $\text{Co}_3\text{Mo}_3\text{C}$ reacting with 60 ml min^{-1} of 75 vol. % H_2 in N_2 are presented in Figure 3.2-80. The crystal structure of $\text{Co}_3\text{Mo}_3\text{C}$ along with the lattice parameters derived from Rietveld refinement against PND data collected at room temperature were presented in section 3.2.8.1, Figure 3.2-49, Table 3.2-13. During the regeneration reaction, the phase composition and concentration of each phase were analysed by the Rietveld method using $\text{Co}_3\text{Mo}_3\text{C}^{40}$ as the starting model and the formation of carbonitride phases was assessed by refining the C/N mixed occupancy of 16c Wyckoff site. The presence of $\text{Co}_6\text{Mo}_6\text{N}$ and $\text{Co}_3\text{Mo}_3\text{N}$ was also assessed. The *in-situ* PND patterns were all similar in the range of temperature studied indicating that the material retained its initial structure (space group $Fd\bar{3}m$) upon reaction with 3:1 $\text{H}_2:\text{N}_2$. However a gradual shift to lower d-spacing was observed during the temperature programmed section of the reaction while a shift to higher d-spacing was observed during isothermal conditions at $500 \text{ }^\circ\text{C}$, as evidenced in Figure 3.2-81, indicating a change in the lattice parameter.

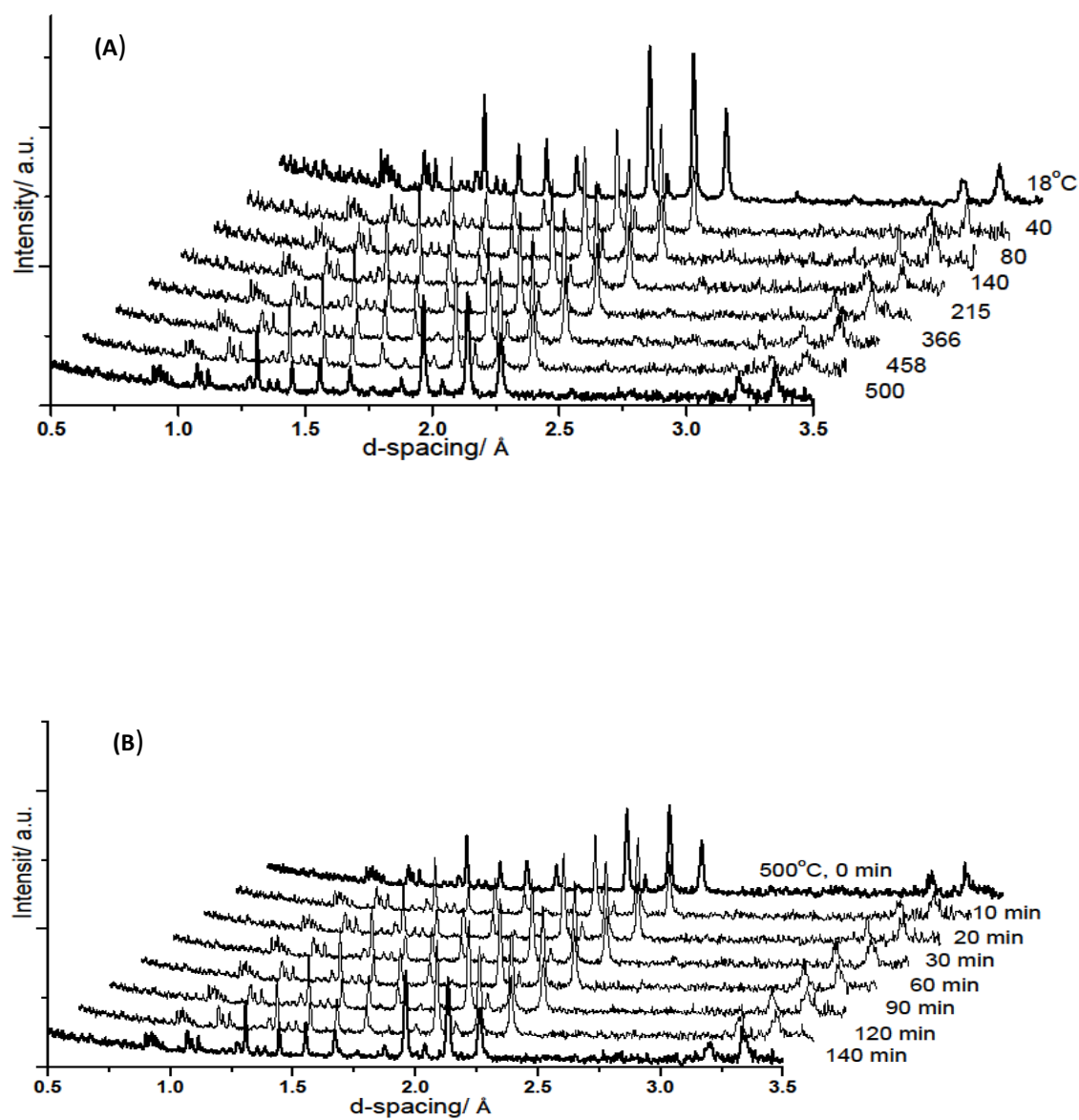


Figure 3.2-80: *In-situ* PND patterns collected at (A) different temperatures and (B) isothermal conditions at 500 °C over different durations for $\text{Co}_3\text{Mo}_3\text{C}$ heated under 60 ml min^{-1} of 75 vol. % H_2 in N_2 .

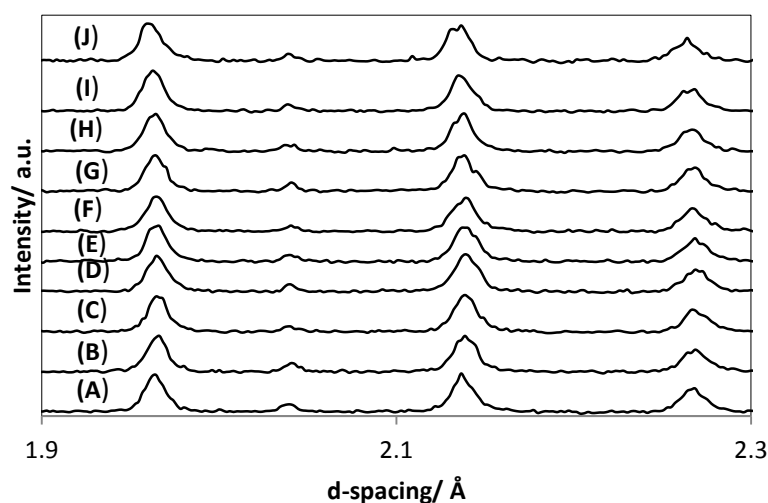


Figure 3.2-81: *In-situ* PND patterns collected at isothermal conditions at 500 °C for $\text{Co}_3\text{Mo}_3\text{C}$ heated under 60 ml min^{-1} of 75 vol. % H_2 in N_2 with an expanded on d-spacing range between 1.9 and 2.3 Å; A (427 °C), B (482 °C), C (500 °C), D (500 °C, 10 min), E (20 min), F (30 min), G (60 min), H (90 min), I (140 min), J (300 min).

The evolution of the lattice parameter during the different segments of reaction is presented in Figure 3.2-82. When increasing the temperature to 500 °C, a linear change of lattice parameter as a function of temperature was generally observed. This can be attributed to thermal expansion of the lattice. However, a change in the slope was detected at temperatures ranging between 400 and 500 °C, which could relate to structural transformation. At 500 °C, no variation of the lattice parameters was observed within the first 10 minutes of reaction. Thereafter, a gradual contraction of the lattice with reaction time was detected which can be correlated to carbon substitution by nitrogen. The evolution of the C/N occupancy at the 16c Wyckoff lattice site as a function of reaction time at 500 °C is presented in Figure 3.2-83. Gradual substitution of carbon with nitrogen under reaction conditions is evidenced. The refinement of C/N occupancy indicate that at 500 °C the material was composed both of 85.6, 76.7, 74.9, 67.3, 61.8, 59.3, 55.9, 53.8 % of C and 14.4, 23.3, 25.1, 32.7, 38.2, 40.7, 44.1, 46.2 % of N at reaction times 0, 10, 30, 40, 65, 95, 110, 125 minutes respectively. The transformation therefore seems to occur via a single intermediate carbonitride phase.

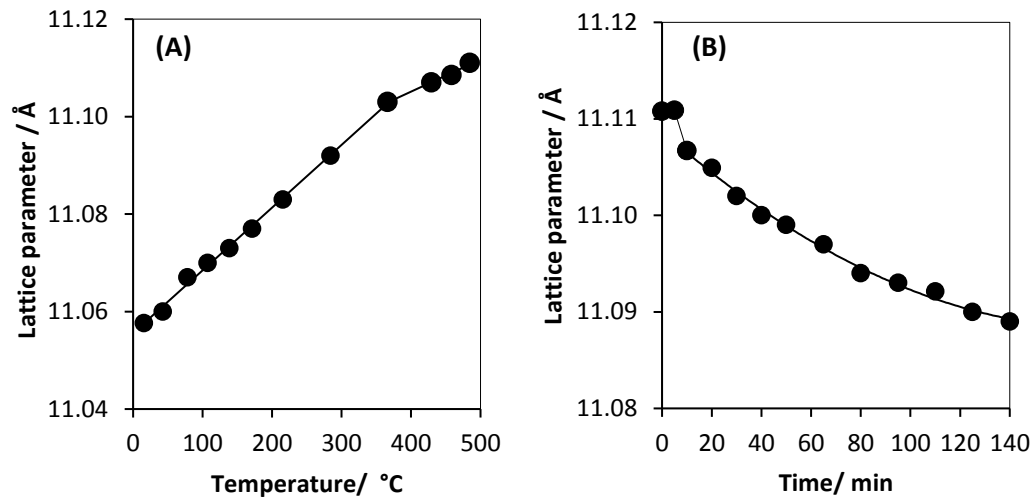


Figure 3.2-82: Evolution of the lattice parameter taken from Rietveld refinements of *in-situ* PND data of $\text{Co}_3\text{Mo}_3\text{C}$ reacted with 60 ml min^{-1} 75 vol. % H_2 in N_2 (BOC, 99.98%) as function of temperature and time: (A) temperature programmed reaction and (B) isothermal conditions at 500 °C.

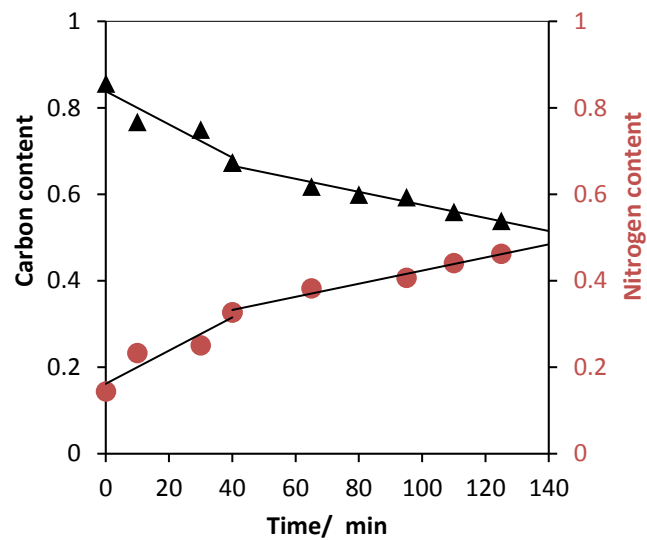


Figure 3.2-83: Evolution of the C/N occupancy of the 16c Wyckoff lattice site in $\text{Co}_3\text{Mo}_3\text{C}$ as a function of reaction time with 60 ml min^{-1} of 75 vol. % H_2 in N_2 at 500 °C. (▲) fractional carbon content and (●) fractional nitrogen content as determined from the Rietveld refinement against PND data.

The results of the Rietveld refinement against PND data collected at isothermal conditions showed the formation of intermediate carbonitride phases before complete conversion to $\text{Co}_3\text{Mo}_3\text{N}$ structure upon higher time of reaction. Representative $\text{Co}_3\text{Mo}_3\text{C}_x\text{N}_{1-x}$ refinement data obtained from PND data at 500 °C and 2h of reaction are presented in Figure 3.2-84 and Table 3.2-25. The lattice parameter derived from Rietveld refinement was found to be $a = 11.0370(3)$ Å. The refinement of carbon, nitrogen occupancy of the 16c Wyckoff site in $\text{Co}_3\text{Mo}_3\text{C}_x\text{N}_{1-x}$ phase (Table 3.2-25) resulted in an estimated chemical composition of $\text{Co}_3\text{Mo}_3\text{C}_{0.33}\text{N}_{0.66}$.

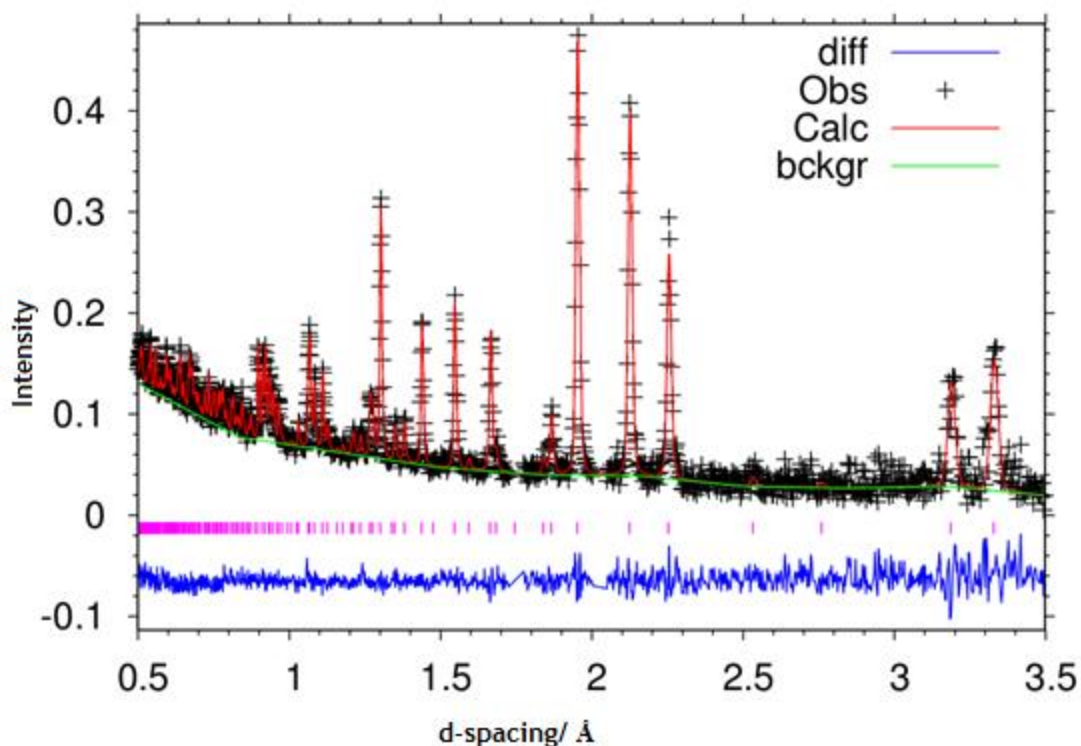


Figure 3.2-84: Fitted powder neutron diffraction profile from Rietveld refinement against powder neutron diffraction data for: $\text{Co}_3\text{Mo}_3\text{C}$ after 2 h of reaction with 60 ml min^{-1} of 75 vol. % H_2 in N_2 at 500 °C.

Table 3.2-25: Structure parameters of $\text{Co}_3\text{Mo}_3\text{C}$ after 2 h of reaction with 60 ml min^{-1} of 75 vol. % H_2 in N_2 (BOC, 99.98%) at 500 °C obtained from neutron diffraction data.

atom	site	occupancies	x	y	z	$100 \cdot U_{\text{iso}} (\text{Å}^2)$
Co1	32e	1.000	0.2936(3)	0.2936(3)	0.2936(3)	0.11(9)
Co2	16d	1.000	0.50000(0)	0.50000(0)	0.50000(0)	0.19(1)
Mo1	48f	1.000	0.3237(4)	0.12500(0)	0.12500(0)	0.19(3)
N1	16c	0.66(4)	0.00000(0)	0.00000(0)	0.00000(0)	0.65(3)
C1	16c	0.33(5)	0.00000(0)	0.00000(0)	0.00000(0)	0.65(3)

^a Space group $Fd\bar{3}mZ(227)$; $a = 11.0370(3)$ Å, $V = 1344.5(2)$ Å³, $R_{\text{wp}} = 0.0624$, $R_p = 0.1001$, $\chi_{\text{red}}^2 = 0.9175$

3.2.11.2 Pathways of nitridation of $\text{Co}_6\text{Mo}_6\text{C}$ with H_2/N_2 or N_2

With the intention of considering the intermediate phase and occupation of the 16c Wyckoff site in $\text{Co}_6\text{Mo}_6\text{C}$ by reaction with H_2/N_2 or N_2 , the structural evolution of $\text{Co}_6\text{Mo}_6\text{C}$ upon reaction with H_2/N_2 or N_2 was investigated using a variety of *in-situ* PND and *ex-situ* PXRD measurements.

a) Evolution of $\text{Co}_6\text{Mo}_6\text{C}$ structure upon reaction with N_2 or N_2/H_2

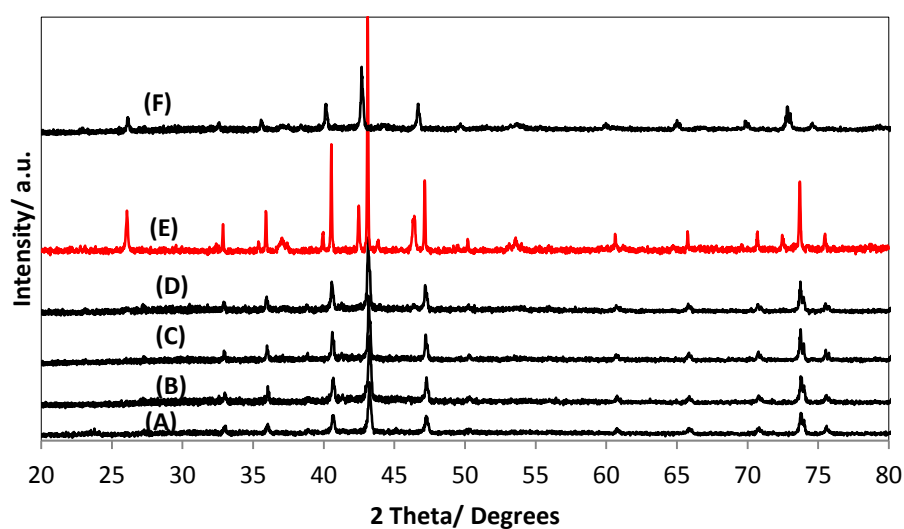


Figure 3.2-85: PXRD patterns of $\text{Co}_6\text{Mo}_6\text{C}$ with $60 \text{ ml min}^{-1} \text{ N}_2$ under various temperature and time on stream; A (room temperature), B ($400 \text{ }^\circ\text{C}$, 3h), C ($500 \text{ }^\circ\text{C}$, 3h), D ($600 \text{ }^\circ\text{C}$, 3h), E ($700 \text{ }^\circ\text{C}$, 4h), F ($800 \text{ }^\circ\text{C}$, 8h).

Some initial understanding of the nitridation process of $\text{Co}_6\text{Mo}_6\text{C}$ can be achieved by XRD. PXRD patterns collected upon reaction of $\text{Co}_6\text{Mo}_6\text{C}$ with $60 \text{ ml min}^{-1} \text{ N}_2$ at various temperatures are shown in Figure 3.2-85. The PXRD pattern of the $\text{Co}_6\text{Mo}_6\text{C}$ precursor collected at room temperature confirmed the preparation of a well-crystallized and pure carbide phase. At $700 \text{ }^\circ\text{C}$ (in Figure 3.2-85 E), the PXRD showed that the material is no longer monophasic and $\text{Co}_3\text{Mo}_3\text{N}$ was detected as a minor phase along with $\text{Co}_6\text{Mo}_6\text{C}$ and graphite as major phases. Reaction at higher temperature ($800 \text{ }^\circ\text{C}$ in Figure 3.2-85 F) resulted in the complete conversion of $\text{Co}_6\text{Mo}_6\text{C}$ to $\text{Co}_3\text{Mo}_3\text{N}$. Loss of carbon and increase in nitrogen content was identified by using CHN microanalysis which confirmed that the starting

formula of $\text{Co}_6\text{Mo}_6\text{C}$ was 1.3 wt. % of C and resultant end formula of $\text{Co}_3\text{Mo}_3\text{N}_x$ was 2.4 wt. % N. The initial XRD results seem to indicate that the mechanism of nitridation of $\text{Co}_6\text{Mo}_6\text{C}$ proceeds differently to what was observed in the case of $\text{Co}_3\text{Mo}_3\text{C}$ and that at two distinct phases are present in the intermediate nitridation stages. This result was also confirmed by using *in-situ* PXR D of $\text{Co}_6\text{Mo}_6\text{C}$ heated with $60 \text{ ml min}^{-1} \text{ N}_2$ at various temperatures as presented in Figure 3.2-86.

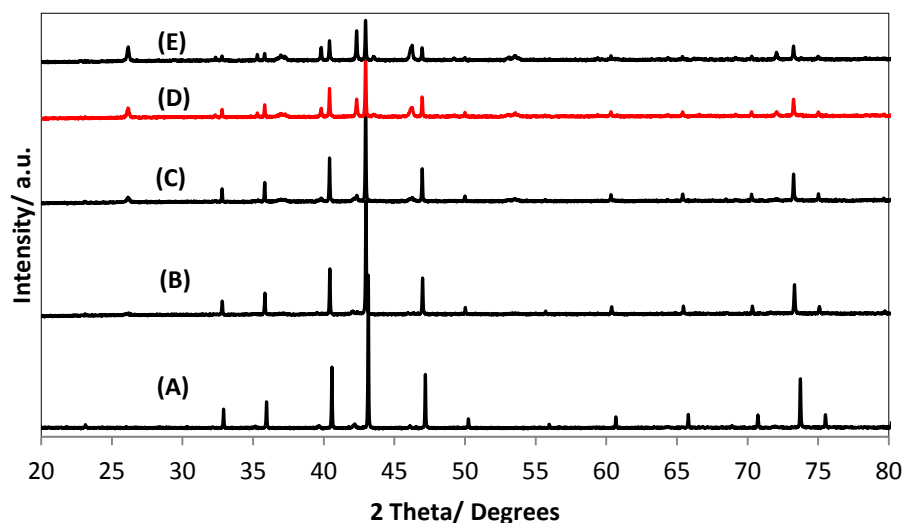


Figure 3.2-86: *In-situ* PXR D patterns of $\text{Co}_6\text{Mo}_6\text{C}$ with $60 \text{ ml min}^{-1} \text{ N}_2$ after various temperatures and times on stream; A (at room temperature), B ($600 \text{ }^\circ\text{C}$), C ($700 \text{ }^\circ\text{C}$, 1h), D ($700 \text{ }^\circ\text{C}$, 2h), E ($700 \text{ }^\circ\text{C}$, 3h).

With the aim of examining the intermediate phase and occupation of the 16c Wyckoff site in $\text{Co}_6\text{Mo}_6\text{C}$ upon reaction with H_2/N_2 instead of only N_2 ; PXR D patterns of $\text{Co}_6\text{Mo}_6\text{C}$ reacted with $60 \text{ ml min}^{-1} 75 \text{ vol. } \% \text{ H}_2$ in N_2 gas at various temperatures are presented in Figure 3.2-87. The PXR D pattern of $\text{Co}_6\text{Mo}_6\text{C}$ collected at room temperature confirmed the preparation of a pure carbide phase. At $500 \text{ }^\circ\text{C}$ (in Figure 3.2-87 C), the PXR D showed that the material is no longer monophasic and $\text{Co}_3\text{Mo}_3\text{N}$ was detected as the minor phase along with $\text{Co}_6\text{Mo}_6\text{C}$ as major phase. Reaction at higher temperature ($600 \text{ }^\circ\text{C}$ in Figure 3.2-85 D) resulted in the complete conversion of $\text{Co}_6\text{Mo}_6\text{C}$ to $\text{Co}_3\text{Mo}_3\text{N}$. As opposed to the case when using only N_2 , the XRD results seem to indicate that the intermediate stage of nitridation of $\text{Co}_6\text{Mo}_6\text{C}$ comprises distinct $\text{Co}_6\text{Mo}_6\text{C}$ and $\text{Co}_3\text{Mo}_3\text{N}$ phases at lower temperature.

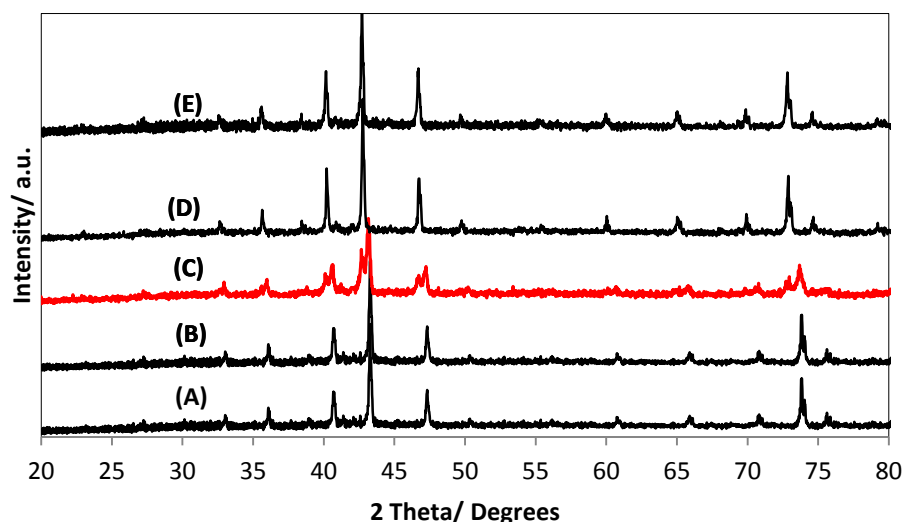


Figure 3.2-87: *Ex-situ* PXRD patterns of $\text{Co}_6\text{Mo}_6\text{C}$ with 60 ml min^{-1} 75 vol. % H_2 in N_2 under various temperature and time on stream; A (at room temperature), B ($400 \text{ }^\circ\text{C}$, 5h), C ($500 \text{ }^\circ\text{C}$, 5h), D ($600 \text{ }^\circ\text{C}$, 1h), E ($700 \text{ }^\circ\text{C}$, 5h).

b) *In-situ* PND for nitride formation using $\text{Co}_6\text{Mo}_6\text{C}$

In-situ neutron diffraction patterns collected at different temperatures for the $\text{Co}_6\text{Mo}_6\text{C}$ material reacted with 60 ml min^{-1} N_2 gas are presented in Figure 3.2-88. The diffraction patterns demonstrated that there was a change in the structure. The results from room temperature PND confirmed the initial preparation of a pure $\text{Co}_6\text{Mo}_6\text{C}$ phase ($a = 10.9099(8) \text{ \AA}$, Table 3.2-18 in section 3.2.9.1). Rietveld refinement against PND data were performed using the structure of $\text{Co}_6\text{Mo}_6\text{C}^{38}$ with carbon in the 8a site. The formation of nitride phases upon reaction with nitrogen was verified using $\text{Co}_3\text{Mo}_3\text{N}$ as a second phase during Rietveld refinement. The formation of carbonitride phases was verified by refining mixed occupancy of the 16c site and/or 8a site by carbon and nitrogen. From $17 \text{ }^\circ\text{C}$ to $681 \text{ }^\circ\text{C}$, no apparent change in PND diffraction profiles was detected and all diffraction peaks observed were related to the $\text{Co}_6\text{Mo}_6\text{C}$ with the exception of few minor peaks related to the *in-situ* reaction cell. The examination of the lattice parameters derived from Rietveld refinements of *in-situ* PND is presented in Figure 3.2-89. A linear change of lattice parameter was observed which could be attributed to thermal expansion of the lattice.

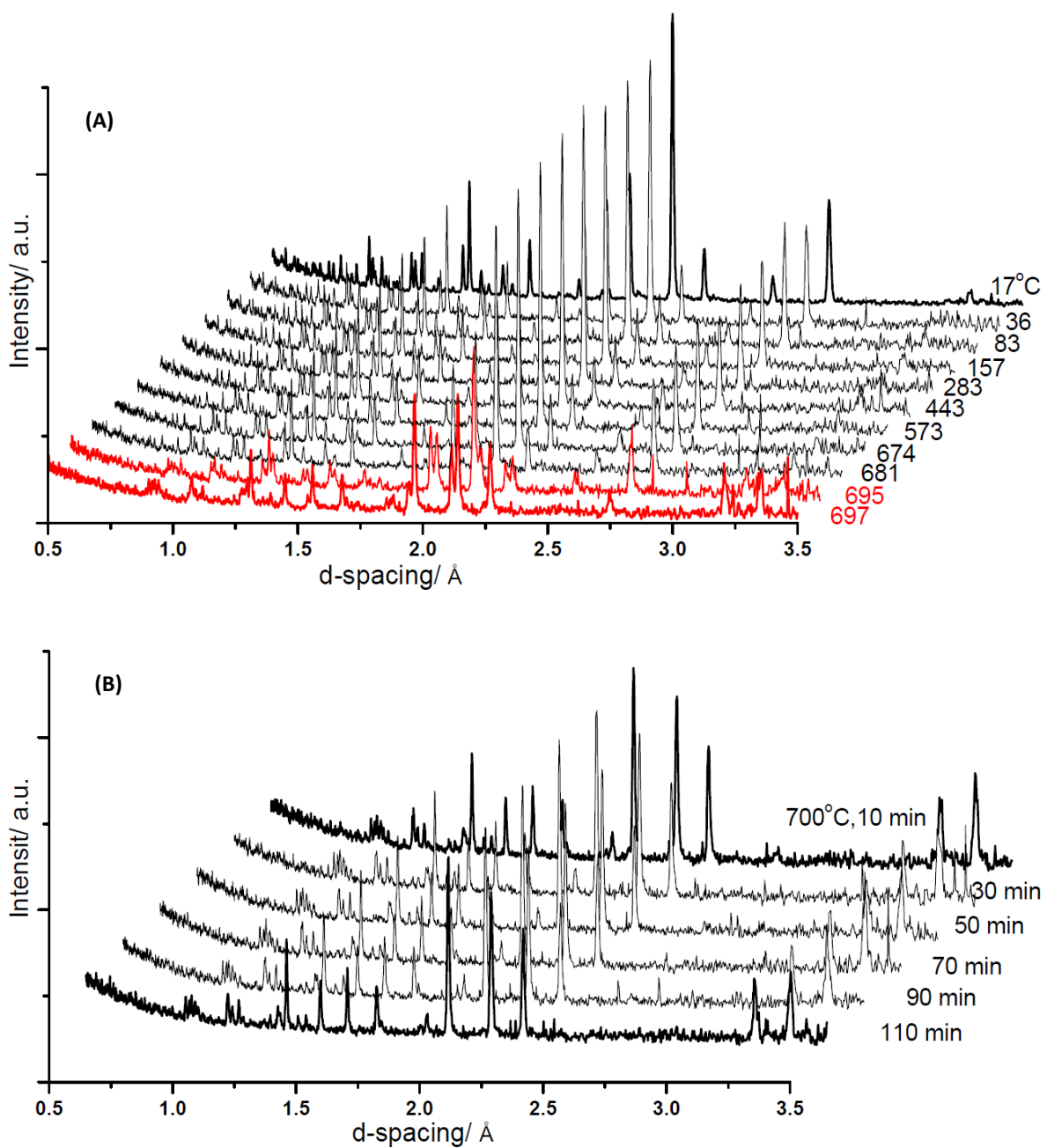


Figure 3.2-88: *In-situ* PND patterns collected at (A) different temperature and (B) isothermal conditions at 700°C for $\text{Co}_6\text{Mo}_6\text{C}$ heated under $60\text{ ml min}^{-1}\text{ N}_2$.

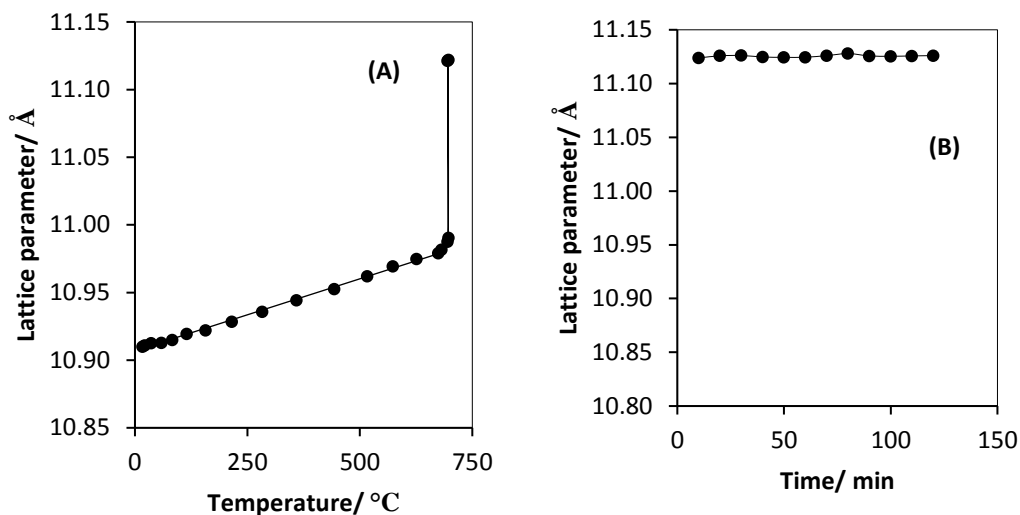


Figure 3.2-89: Evolution of the lattice parameter taken from Rietveld refinements of *in-situ* PND data of $\text{Co}_6\text{Mo}_6\text{C}$ reacted with $60 \text{ ml min}^{-1} \text{ N}_2$ as function of temperature and time: (a) temperature programmed reaction and (b) isothermal conditions at $700 \text{ }^\circ\text{C}$.

The investigation of the fractional carbon and nitrogen occupancy of the 16c and 8a Wyckoff lattice sites in $\text{Co}_3\text{Mo}_3\text{N}$ and $\text{Co}_6\text{Mo}_6\text{C}$ respectively as a function of temperature as obtained from the Rietveld refinement against *In-situ* PND data is presented in Figure 3.2-90. The refinement obtained data indicate that at 695 and 697 °C the materials were comprised of 58.2 and 26.2 % of the 661C phase with C occupancy of the 8a Wyckoff lattice site and 41.8 and 73.8 % of 331N fractional phase with N occupancy of the 16c Wyckoff lattice site respectively. When the temperature reached $700 \text{ }^\circ\text{C}$, the material was completely converted to $\text{Co}_3\text{Mo}_3\text{N}$. For more quantitative analysis data see Appendix 2 Table 8.2-4.

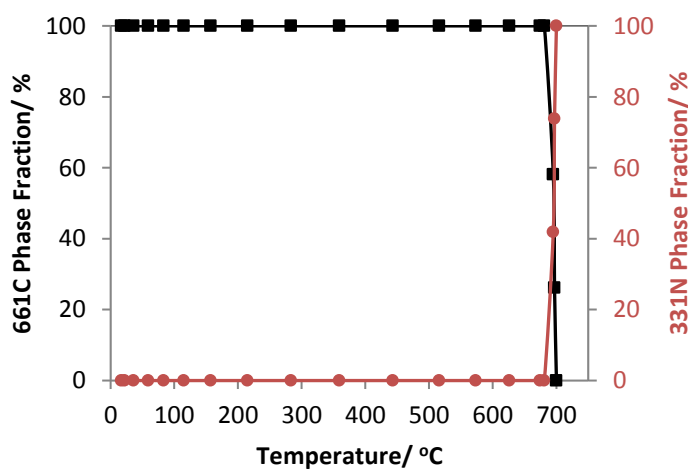


Figure 3.2-90: Investigation of phase fractions of $\text{Co}_6\text{Mo}_6\text{C}$ (■) and $\text{Co}_3\text{Mo}_3\text{N}$ (●) present during reaction of $\text{Co}_6\text{Mo}_6\text{C}$ with $60 \text{ ml min}^{-1} \text{ N}_2$ as a function of temperature as determined from the Rietveld refinement against *in-situ* powder neutron diffraction data.

Most importantly, the refinement of powder neutron diffraction profiles against PND data at 695 and 697 °C, highlighted in red, has shown that the material is not monophasic any longer and revealed co-existence of $\text{Co}_6\text{Mo}_6\text{C}$ alongside the $\text{Co}_3\text{Mo}_3\text{N}$ phase. When the temperature reached 700 °C, the material was completely converted to $\text{Co}_3\text{Mo}_3\text{N}$. The evolution of the formation of $\text{Co}_3\text{Mo}_3\text{N}$ and the decay of the $\text{Co}_6\text{Mo}_6\text{C}$ during the reaction is presented in Figure 3.2-90. It can be clearly seen that the carburisation process was rapid and occurred in a narrow temperature window. The structural features of $\text{Co}_6\text{Mo}_6\text{C}$ and $\text{Co}_3\text{Mo}_3\text{N}$ obtained from the refinement of PND profiles are presented in Figure 3.2-91, Table 3.2-26 at 695 °C and Figure 3.2-92, Table 3.2-27 at 697 °C. The lattice parameter derived from Rietveld refinement was found to be $a = 11.1211(4)$ Å for $\text{Co}_3\text{Mo}_3\text{N}$ and $a = 10.987(4)$ Å for $\text{Co}_6\text{Mo}_6\text{C}$ at 695 °C, and $a = 11.1218(1)$ Å for $\text{Co}_3\text{Mo}_3\text{N}$ and $a = 10.9903(2)$ Å for $\text{Co}_6\text{Mo}_6\text{C}$ at 697 °C. The refinement of carbon, and nitrogen occupancy of the 16c (331N phase), and 8a (661C) Wyckoff sites respectively (Table 3.2-26 and 3.2-27) resulted in an estimated chemical composition of, $\text{Co}_3\text{Mo}_3\text{N}_{0.96}$, $\text{Co}_6\text{Mo}_6\text{C}_{1.03}$ at 695 °C and $\text{Co}_3\text{Mo}_3\text{N}_{0.8}$, $\text{Co}_6\text{Mo}_6\text{C}_{1.17}$ at 697 °C.

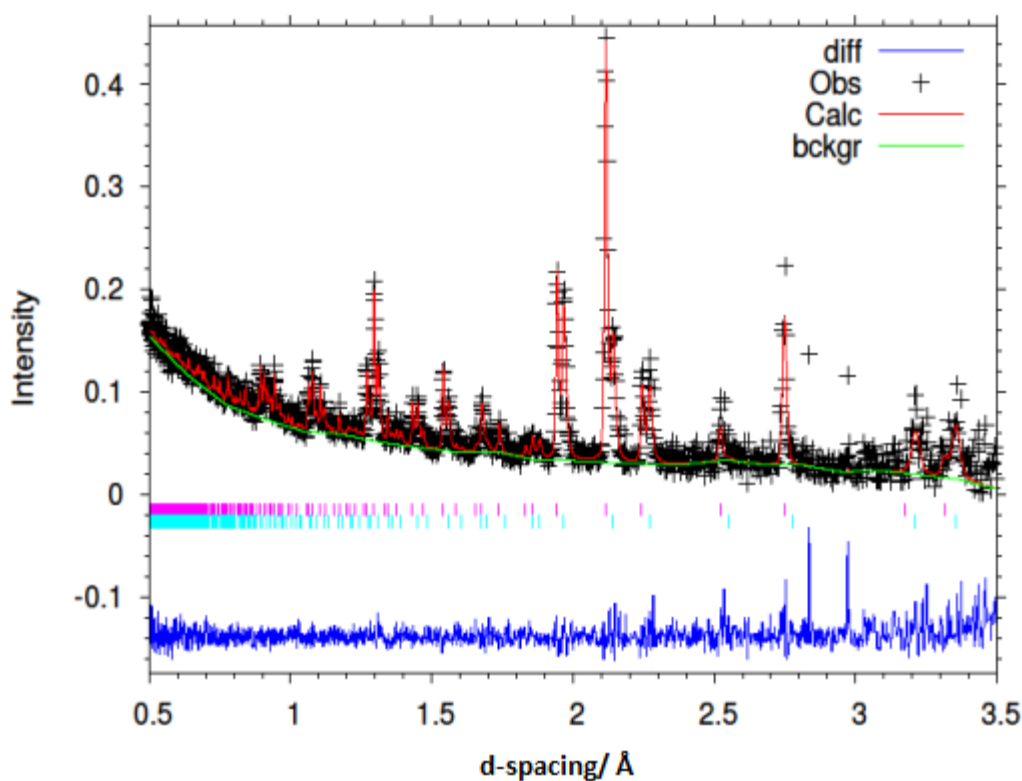


Figure 3.2-91: Fitted powder neutron diffraction profile from Rietveld refinement against powder neutron diffraction data for: $\text{Co}_6\text{Mo}_6\text{C}$ after reaction with 60 ml min^{-1} of N_2 (BOC, 99.98%) at 695°C.

Table 3.2-26: Structure parameters of $\text{Co}_6\text{Mo}_6\text{C}$ after reaction with 60 ml min^{-1} of N_2 (BOC, 99.98%) at 695°C obtained from neutron diffraction data.

Atom 661C	site	occupancies	x	y	z	$100 \cdot U_{\text{iso}}(\text{\AA}^2)$
Co1	32e	1.000	0.29200(0)	0.29200(0)	0.29200(0)	1.77(2)
Co2	16d	1.000	0.50000(0)	0.50000(0)	0.50000(0)	1.94(3)
Mo1	48f	1.000	0.32100(0)	0.12500(0)	0.12500(0)	1.22(6)
C1	16c	0.000	0.00000(0)	0.00000(0)	0.00000(0)	0.32(9)
C2	8a	1.025(9)	0.12500(0)	0.12500(0)	0.12500(0)	0.77(4)

^a Space group $Fd\bar{3}mZ(227)$; $a = 10.987(4) \text{\AA}$, $V = 1326.43(6) \text{\AA}^3$, $R_{\text{wp}} = 0.0712$, $R_p = 0.1149$, $\chi_{\text{red}}^2 = 0.7578$

Atom 331N	site	occupancies	x	y	z	$100 \cdot U_{\text{iso}}(\text{\AA}^2)$
Co1	32e	1.000	0.29220(0)	0.29220(0)	0.29220(0)	0.07(7)
Co2	16d	1.000	0.50000(0)	0.50000(0)	0.50000(0)	0.07(7)
Mo1	48f	1.000	0.32390(0)	0.12500(0)	0.12500(0)	1.06(4)
N1	16c	0.975(1)	0.00000(0)	0.00000(0)	0.00000(0)	2.40(3)

^a Space group $Fd\bar{3}mZ(227)$; $a = 11.1211(4) \text{\AA}$, $V = 1375.46(3) \text{\AA}^3$, $R_{\text{wp}} = 0.1891$, $R_p = 0.1665$, $\chi_{\text{red}}^2 = 0.7578$

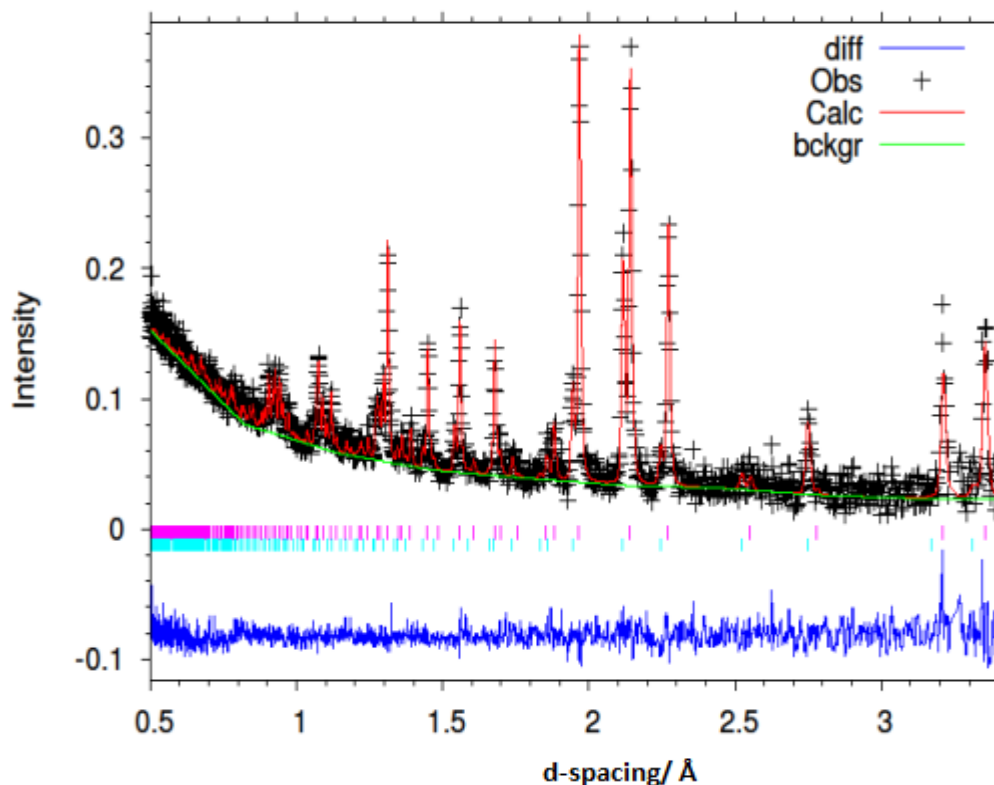


Figure 3.2-92: Fitted powder neutron diffraction profile from Rietveld refinement against powder neutron diffraction data for: $\text{Co}_6\text{Mo}_6\text{C}$ after reaction with 60 ml min^{-1} of N_2 (BOC, 99.98%) at 697°C .

Table 3.2-27: Structure parameters of $\text{Co}_6\text{Mo}_6\text{C}$ after reaction with 60 ml min^{-1} of N_2 (BOC, 99.98%) at 697°C obtained from neutron diffraction data.

Atom 331N	site	occupancies	x	y	z	$100 \cdot U_{\text{iso}}(\text{\AA}^2)$
Co1	32e	1.000	0.29220(0)	0.29220(0)	0.29220(0)	1.52(0)
Co2	16d	1.000	0.50000(0)	0.50000(0)	0.50000(0)	1.32(2)
Mo1	48f	1.000	0.32390(0)	0.12500(0)	0.12500(0)	1.49(4)
N1	16c	0.829(4)	0.00000(0)	0.00000(0)	0.00000(0)	1.27(0)

^a Space group $Fd\bar{3}mZ$ (227); $a = 11.1218(1) \text{ \AA}$, $V = 1375.71(0) \text{ \AA}^3$, $R_{\text{wp}} = 0.0616$, $R_p = 0.0962$, $\chi_{\text{red}}^2 = 0.7609$

Atom 661C	site	occupancies	x	y	z	$100 \cdot U_{\text{iso}}(\text{\AA}^2)$
Co1	32e	1.000	0.29200(0)	0.29200(0)	0.29200(0)	2.01(1)
Co2	16d	1.000	0.50000(0)	0.50000(0)	0.50000(0)	1.80(0)
Mo1	48f	1.000	0.32100(0)	0.12500(0)	0.12500(0)	1.80(0)
C1	16c	0.000	0.00000(0)	0.00000(0)	0.00000(0)	0.32(9)
C2	8a	1.170(6)	0.12500(0)	0.12500(0)	0.12500(0)	1.63(0)

^a Space group $Fd\bar{3}mZ$ (227); $a = 10.9903(2) \text{ \AA}$, $V = 1327.49(0) \text{ \AA}^3$, $R_{\text{wp}} = 0.0616$, $R_p = 0.0962$, $\chi_{\text{red}}^2 = 0.7609$

The process of the nitridation of $\text{Co}_6\text{Mo}_6\text{C}$ was different from the nitridation of $\text{Co}_3\text{Mo}_3\text{C}$, as in this case no carbonitride intermediate phase was observed. The nitridation process proceeded via the decline of $\text{Co}_6\text{Mo}_6\text{C}$ and the concomitant formation of $\text{Co}_3\text{Mo}_3\text{N}$.

3.2.12 Pathways of reduction of $\text{Co}_3\text{Mo}_3\text{C}$ with H_2/Ar

With the aim of investigating the intermediate phases and reduction phase in which carbon atoms transferred from the 16c to 8a Wyckoff site, *ex-situ* PXRD of $\text{Co}_3\text{Mo}_3\text{C}$ heated with 60 ml min^{-1} 75 vol. % H_2 in Ar gas at various temperatures was undertaken as shown in Figure 3.2-93.

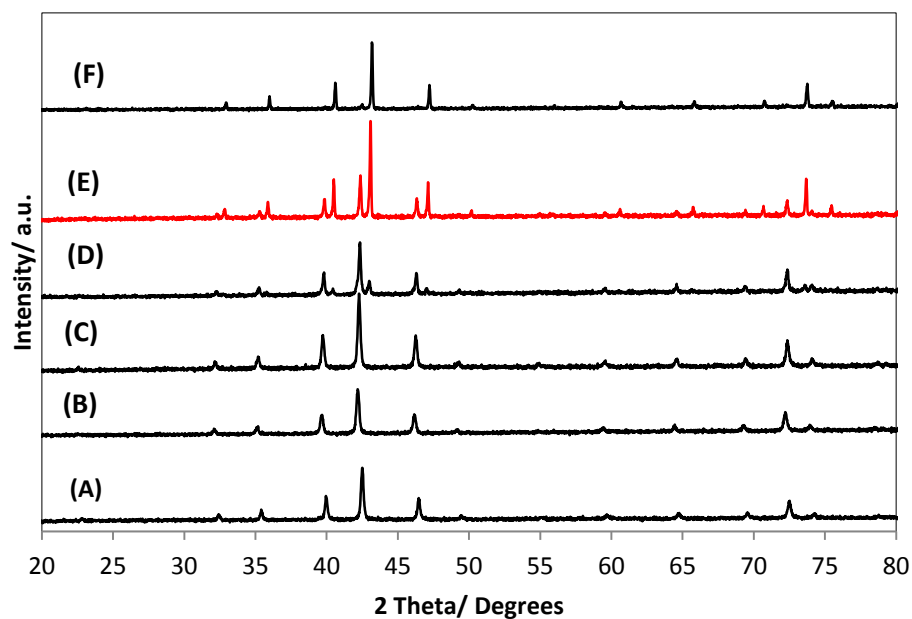


Figure 3.2-93: *Ex-situ* PXRD patterns of $\text{Co}_3\text{Mo}_3\text{C}$ with 60 ml min^{-1} 75 vol. % H_2 in Ar under various temperatures and times on stream; A (room temperature), B (500 °C), C (700 °C, 5h), D (800 °C, 4h), E (850 °C, 5h), F (900 °C, 5h).

The PXRD patterns show that all patterns of $\text{Co}_3\text{Mo}_3\text{C}$ are slightly shifted to the right as a function of reaction temperature to form directly η -12 $\text{Co}_6\text{Mo}_6\text{C}$ without any intermediate phase. The shift was clear within Figure 3.2-93 D when temperature reached 800 °C; the 661C related pattern was starting to appear. When the temperature was increased to 850 °C as in Figure 3.2-93 E, the patterns of 661 were further increased with respect to those of 331C. When the temperature was increased to 900 for 5 hours, the transformation to the 661C phase was completed. Removal of carbon from the lattice was substantiated using CHN microanalysis which confirmed that the starting phase of $\text{Co}_3\text{Mo}_3\text{C}$ was 2.8 wt. % C and final phase of $\text{Co}_6\text{Mo}_6\text{C}$ contained 1.3 wt. % C.

3.2.13 Pathways of reduction of $\text{Co}_3\text{Mo}_3\text{N}$ with H_2/Ar

In-situ neutron diffraction patterns collected at different temperatures for $\text{Co}_3\text{Mo}_3\text{N}$ material (as post-reaction material which was obtained from reacting $\text{Co}_3\text{Mo}_3\text{C}$ with H_2/N_2 at 500°C during *in-situ* PND) reacted with 60 ml min^{-1} of 75 vol. % H_2 in Ar gas presented in Figure 3.2-94. The diffraction patterns demonstrated that there was a change in structure. The patterns also display minor impurity peaks present within the material when increasing temperature, although these could not be easily assigned such as that with a d-spacing at 2.05 \AA . A possible source of impurity peaks came from the vanadium sample can; which was excluded from the refinements.

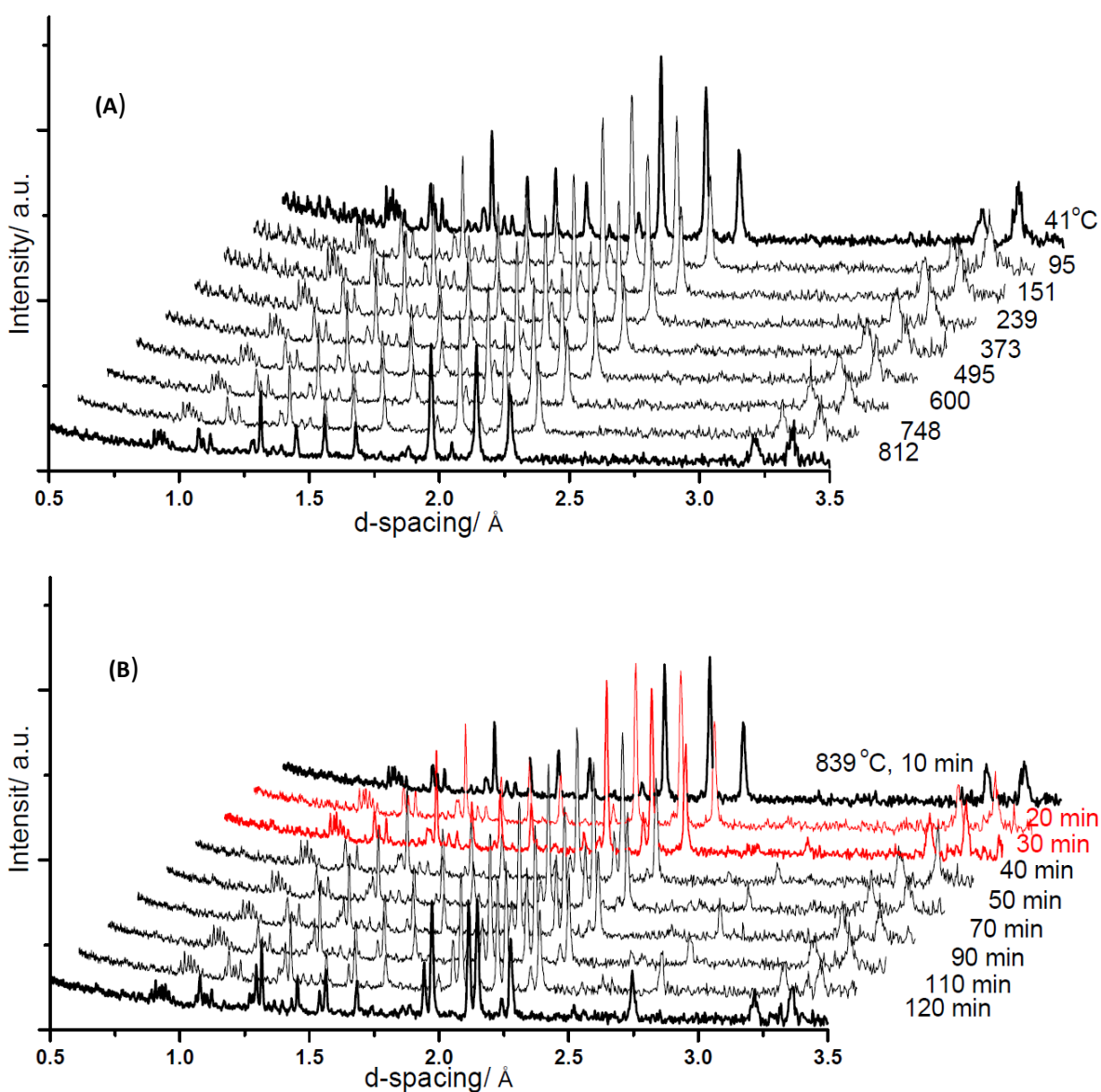


Figure 3.2-94: *In-situ* PND patterns collected at (A) different temperature and (B) isothermal conditions at 820°C for $\text{Co}_3\text{Mo}_3\text{N}$ heated under 60 ml min^{-1} of 75 vol. % H_2 in Ar.

The lattice parameters taken from Rietveld refinements of *in-situ* PND data collected at different temperatures and dwell times for $\text{Co}_3\text{Mo}_3\text{N}$ heated from room temperature to 820 °C under 60 ml min^{-1} of 75 vol. % H_2 in Ar gas is presented in Figure 3.2-95. With increasing temperature to 820 °C, a linear change of lattice parameter as a function of temperature was observed as presented in Figure 3.2-95 A. This can be attributed to thermal expansion of the lattice. However, a change in the slope was detected at temperatures beyond 820 °C as illustrated in Figure 3.2-95 B, which could relate to the structural transformation from 331N to 661N forming mixed phases of 331N and 661N. The reaction was left for 4 hours on stream before being cooled to room temperature under the same gas, within this period, the lattice parameters corresponded to 331N (around 11.15 Å) and 661N (around 10.98 Å).

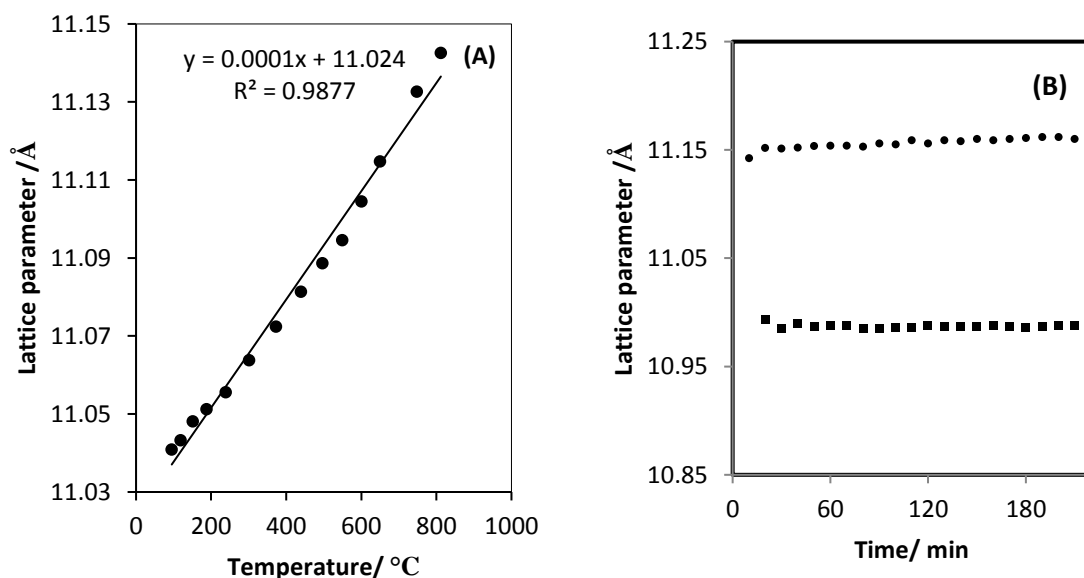


Figure 3.2-95: Evolution of the lattice parameter taken from Rietveld refinements of *in-situ* PND data of $\text{Co}_3\text{Mo}_3\text{N}$ reacted with 60 ml min^{-1} 75 vol. % H_2 in Ar as function of temperature and time: (A) temperature programmed reaction and (B) isothermal conditions at 820 °C with mixed phases of (●) 331N and (■) 661N.

The investigation of the fractional nitrogen occupancy of the 16c and 8a Wyckoff lattice sites in $\text{Co}_3\text{Mo}_3\text{N}$ and $\text{Co}_6\text{Mo}_6\text{N}$ respectively as a function of time on stream at 820 °C as obtained from the Rietveld refinement against *In-situ* PND data are presented in Figure 3.2-96. The refinement obtained data indicate that at, for example, 50, 120, 160 minutes and an iso-temperature 820 °C the material was composed of 81.3, 64.8, and 59.7 % of 331N fraction with N occupancy of the 16c Wyckoff lattice site and 18.7, 35.2 and 40.3 % of 661N with N occupancy of the 8a Wyckoff lattice site. For more quantitative analysis see Appendix 2 Table 8.2-3.

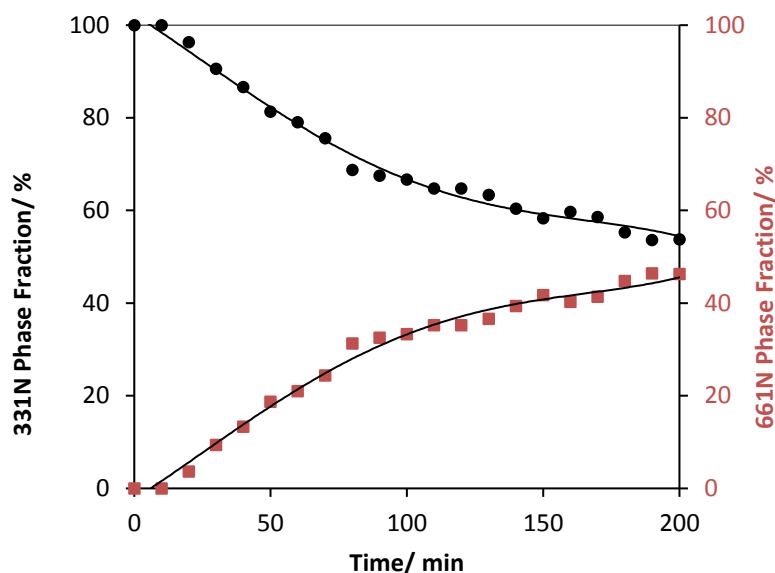


Figure 3.2-96: Investigation of phase fractions of $\text{Co}_6\text{Mo}_6\text{N}$ (■) and $\text{Co}_3\text{Mo}_3\text{N}$ (●) present during reaction of $\text{Co}_3\text{Mo}_3\text{N}$ with 60 ml min^{-1} 75 vol. % H_2 in Ar at $820 \text{ }^\circ\text{C}$ as determined from the Rietveld refinement against *in-situ* powder neutron diffraction data.

When the refinement had converged the thermal parameters were varied isotopically except for the cobalt species in both nitride phases which were constrained. The $\text{Co}_6\text{Mo}_6\text{N}$ phase was investigated and the same process was performed. The nitrogen occupancy of 8a and 16c sites were allowed to freely vary for the final refinement. The results of the $\text{Co}_3\text{Mo}_3\text{N}$ and $\text{Co}_6\text{Mo}_6\text{N}$ refinement obtained from PND data were discussed earlier in Sections 3.2.6.1 and 3.2.7.1 respectively. Selected results of mixed phases of $\text{Co}_3\text{Mo}_3\text{N}$ and $\text{Co}_6\text{Mo}_6\text{N}$ refinement gained from PND data are presented in Figure 3.2-97 and Table 3.2-26.

Once all of the parameters were refined, a good fit to the selected model when the reaction reached $820 \text{ }^\circ\text{C}$ and cooling down to $394 \text{ }^\circ\text{C}$ corresponding to a mixture of both $\text{Co}_6\text{Mo}_6\text{N}$ and $\text{Co}_3\text{Mo}_3\text{N}$ phases was obtained. The results are shown in Figure 3.2-97 and Table 3.2-28. The lattice parameter derived from Rietveld refinement was found to be $a = 11.1179(8) \text{ \AA}$ for $\text{Co}_3\text{Mo}_3\text{N}$ and $a = 10.9438(5) \text{ \AA}$ for $\text{Co}_6\text{Mo}_6\text{N}$. The refinement of nitrogen occupancy of the 16c in 331N phase, 8a in 661N Wyckoff sites respectively (Table 3.2-28) resulted in an estimated chemical composition of $\text{Co}_3\text{Mo}_3\text{N}_{0.89}$ and $\text{Co}_6\text{Mo}_6\text{N}_{1.10}$.

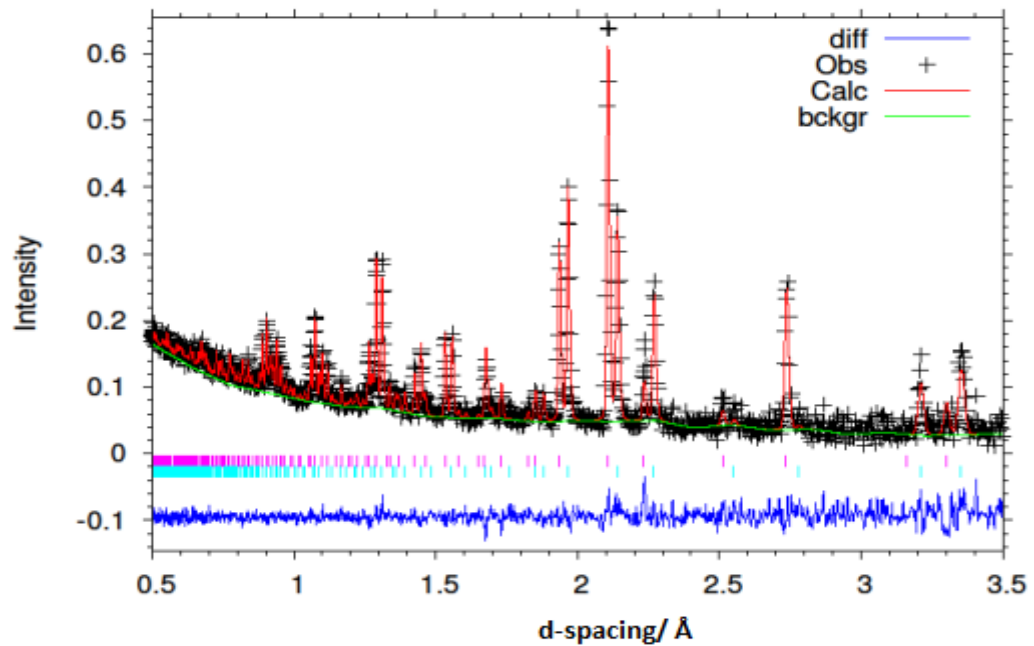


Figure 3.2-97: Fitted powder neutron diffraction profile from Rietveld refinement against powder neutron diffraction data for: $\text{Co}_3\text{Mo}_3\text{N}$ after 220 minutes of reaction with 60 ml min^{-1} of 75 vol.% H_2 in Ar (BOC, 99.98%) at 820°C and cooling down to 394°C under same gas.

Table 3.2-28: Structure parameters of $\text{Co}_3\text{Mo}_3\text{N}$ after 220 minutes of reaction with 60 ml min^{-1} of 75 vol.% H_2 in Ar (BOC, 99.98%) at 820°C and cooling down to 394°C obtained from neutron diffraction data.

Atom	site	occupancies	x	y	z	$100 \cdot U_{\text{iso}}(\text{\AA}^2)$
661N						
Co1	32e	1.000	0.29200(0)	0.29200(0)	0.29200(0)	1.07(3)
Co2	16d	1.000	0.50000(0)	0.50000(0)	0.50000(0)	1.07(3)
Mo1	48f	1.000	0.32100(0)	0.12500(0)	0.12500(0)	0.66(7)
N1	16c	0.000	0.00000(0)	0.00000(0)	0.00000(0)	0.32(9)
N2	8a	1.10(5)	0.12500(0)	0.12500(0)	0.12500(0)	3.02(1)

^a Space group $Fd\bar{3}mZ(227)$; $a = 10.9438(5) \text{ \AA}$, $V = 1310.72(1) \text{ \AA}^3$, $R_{\text{wp}} = 0.0556$, $R_p = 0.0921$, $\chi_{\text{red}}^2 = 0.9041$

Atom	site	occupancies	x	y	z	$100 \cdot U_{\text{iso}}(\text{\AA}^2)$
331N						
Co1	32e	1.000	0.29266(0)	0.29266(0)	0.29266(0)	0.35(1)
Co2	16d	1.000	0.50000(0)	0.50000(0)	0.50000(0)	0.35(1)
Mo1	48f	1.000	0.32358(0)	0.12500(0)	0.12500(0)	0.90(2)
N1	16c	0.89(5)	0.00000(0)	0.00000(0)	0.00000(0)	1.89(6)

^a Space group $Fd\bar{3}mZ(227)$; $a = 11.1179(8) \text{ \AA}$, $V = 1374.27(8) \text{ \AA}^3$, $R_{\text{wp}} = 0.0811$, $R_p = 0.1107$, $\chi_{\text{red}}^2 = 0.9063$

The process of the reduction of $\text{Co}_3\text{Mo}_3\text{C}$ was investigated and as result in this case no intermediate phase was observed. The reduction process proceeded via the decline of

Co₃Mo₃C and the formation of Co₆Mo₆C when using 3:1 H₂:Ar. The co-product from this process, based on TGA-MS result in section 3.2.9.4, to our knowledge was only methane. On the other hand, a similar pathway of the reduction of Co₃Mo₃N was observed, elsewhere such a reduction process has been shown to produce N₂ and NH₃.³⁷

3.3 Conclusion

In this chapter, the analysis of the structure and synthesis of binary molybdenum nitride (γ -Mo₂N), molybdenum carbides (β -Mo₂C, α -Mo₂C) and ternary cobalt molybdenum nitrides (η -6 Co₃Mo₃N, η -12 Co₆Mo₆N) and ternary cobalt molybdenum carbides (η -6 Co₃Mo₃C, η -12 Co₆Mo₆C) were successfully undertaken using a variety of characterisation techniques. The systems investigated are outlined in the following bullet points:

- Pure binary gamma molybdenum nitride (γ -Mo₂N) has been synthesised and confirmed by PXRD, ESM, EDX, BET and CHN elemental analysis.
- Pure binary beta and alpha molybdenum carbide (β -Mo₂C and α -Mo₂C) have been synthesised and confirmed by PXRD, ESM, EDX, BET and CHN elemental analysis.
- Two pure ternary molybdenum nitrides (η -6 Co₃Mo₃N and η -12 Co₆Mo₆N) have been synthesised and confirmed by PXRD, PND, ESM, EDX, BET and CHN elemental analysis.
- Two pure ternary molybdenum carbides (η -6 Co₃Mo₃C and η -12 Co₆Mo₆C) have been synthesised and confirmed by PXRD, PND, ESM, EDX, BET and CHN elemental analysis.

In this work, the synthesis conditions (e.g. reaction atmosphere, reaction time and temperature) of binary molybdenum nitride, binary molybdenum carbides and ternary cobalt molybdenum nitrides, carbides were identified resulting in the preparation of highly pure phases.

All the above materials were previously synthesised and extensively studied except for η -12 Co₆Mo₆C which was quite difficult to optimize in relation to the temperature required

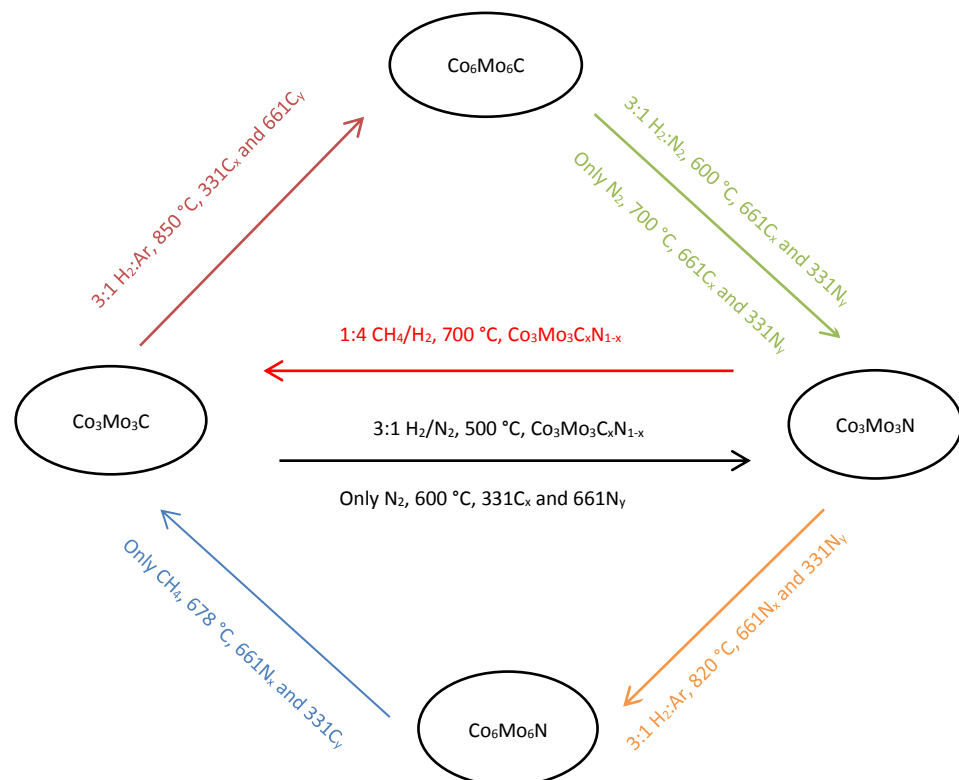
for complete reduction. Moreover, all these materials have been used in ammonia synthesis and methane cracking as detailed in Chapters 4 and 5.

Furthermore, the ability of $\text{Co}_3\text{Mo}_3\text{N}$ or $\text{Co}_3\text{Mo}_3\text{C}$ to uptake and release carbon and/or nitrogen was studied. *In-situ* neutron diffraction studies revealed that in both cases, nitridation of the $\text{Co}_3\text{Mo}_3\text{C}$ or carburisation of $\text{Co}_3\text{Mo}_3\text{N}$ in presence of hydrogen proceeded via the formation of an intermediate carbonitride phase ($\text{Co}_3\text{Mo}_3\text{C}_x\text{N}_{1-x}$) with carbon and nitrogen both occupying the 16c Wyckoff site. However, the results of carburisation of $\text{Co}_6\text{Mo}_6\text{N}$ and the nitridation of $\text{Co}_6\text{Mo}_6\text{C}$ followed a different reaction path. Major findings are summarized below:

- The η -6 $\text{Co}_3\text{Mo}_3\text{N}$ phase was converted to η -6 $\text{Co}_3\text{Mo}_3\text{C}$ using 1:4 $\text{CH}_4:\text{H}_2$ through the formation of intermediate $\text{Co}_3\text{Mo}_3\text{C}_x\text{N}_{1-x}$ (with various % of C and N) phases in the temperature range between 600 to 700 °C. The process was confirmed by *in-situ* PND, *ex-situ* PXRD and CHN elemental analysis. The atomic site occupancies were determined by Rietveld refinement of ToF neutron diffraction data. The results showed that nitrogen and carbon atoms simultaneously occupy 16c sites within the intermediate carbonitride structures.
- The η -12 $\text{Co}_6\text{Mo}_6\text{N}$ phase was converted to η -6 $\text{Co}_3\text{Mo}_3\text{C}$ when reacted with methane. The reaction proceeded via the formation of $\text{Co}_3\text{Mo}_3\text{C}$ phase and the destruction of the $\text{Co}_6\text{Mo}_6\text{N}$ phase. The presence of the two segregated phases was only observable in a narrow temperature window around 678 °C.
- The η -6 $\text{Co}_3\text{Mo}_3\text{C}$ phase was converted to η -6 $\text{Co}_3\text{Mo}_3\text{N}$ upon reaction with 1:3 N_2/H_2 gas mixtures. As also observed in the case of carburisation of the η -6 $\text{Co}_3\text{Mo}_3\text{N}$ phase, the reaction proceeded through the formation of $\text{Co}_3\text{Mo}_3\text{C}_x\text{N}_{1-x}$ at 500 °C intermediate phases and no additional phases were observed.
- When reacted with N_2 , η -6 $\text{Co}_3\text{Mo}_3\text{C}$ was converted to η -6 $\text{Co}_3\text{Mo}_3\text{N}$. However, two segregated ($\text{Co}_3\text{Mo}_3\text{C}$, $\text{Co}_6\text{Mo}_6\text{N}$) phases were observed at 600 °C and this result was confirmed by *ex* and *in-situ* PXRD and CHN elemental analysis.

- In the reduction step, the η -6 $\text{Co}_3\text{Mo}_3\text{C}$ phase was converted to η -12 $\text{Co}_6\text{Mo}_6\text{C}$ through two segregated ($\text{Co}_3\text{Mo}_3\text{C}$, $\text{Co}_6\text{Mo}_6\text{C}$) phases at 800 °C when using 3:1 H_2/Ar . When reacting η -6 $\text{Co}_3\text{Mo}_3\text{N}$ with 3:1 H_2/Ar , the material reduced to η -12 $\text{Co}_6\text{Mo}_6\text{N}$ through two segregated ($\text{Co}_3\text{Mo}_3\text{N}_x$, $\text{Co}_6\text{Mo}_6\text{N}_x$) phases at 820 °C.
- The η -12 $\text{Co}_6\text{Mo}_6\text{C}$ phase was converted to η -12 $\text{Co}_3\text{Mo}_3\text{N}$ through two segregated ($\text{Co}_6\text{Mo}_6\text{C}_x$, $\text{Co}_3\text{Mo}_3\text{N}_x$) phases at 700 °C when using only N_2 ; whereas when using 3:1 H_2/N_2 a similar result was observed at 500 °C.
- In terms of the homologation of methane to produce C_{2+} products, η -6 $\text{Co}_3\text{Mo}_3\text{C}$ was reduced to synthesize η -12 $\text{Co}_6\text{Mo}_6\text{C}$ using a 3:1 H_2/Ar gas mixture at 900 °C for 5 hours and the products were detected by TGA-MS. According to the mass spectroscopy results, methane as opposed to higher hydrocarbons, is the sole product of reduction which indicates a limitation of this system for application in methane homologation.

The phase transformation pathways for the ternary systems investigated within this chapter is summarized as:



Chapter 4. Ammonia synthesis

4.1 Introduction

4.1.1 Importance of ammonia in modern society

Nitrogen containing products are important in many industrial applications but also in many biological processes. In fact, proteins which are the main building blocks of muscles, skin and hair etc., are made up of varying combinations of nitrogen containing amino acids.⁸² Nitrogen is one of the most abundant elements in nature with ~ 78 % of our atmosphere being constituted of diatomic nitrogen providing an almost limitless source of nitrogen. However, due to the strong nitrogen-nitrogen triple bond, diatomic nitrogen is relatively inert and needs to undergo many complex and slow biological transformations to produce reactive nitrogen. In this context, the Haber - Bosch process, which is the current large-scale industrial process for nitrogen fixation, is considered one of the most significant achievements.⁸³ The process provides a direct and rapid route for the fixation of diatomic nitrogen into the more reactive nitrogen building block ammonia.

The advent of the Haber - Bosch (H-B) process is usually linked to the net increase in the global population which occurred during the 20th Century. Although the increase in the global population is attributed to many factors, there is a consensus that the actual raise of the population could not be sustained without the artificial production of reactive nitrogen (ammonia). The production of ammonia from the H-B process enabled the production of fertilizers at an industrial scale and thus supported intensive agriculture and farming.⁸⁴⁻⁸⁵ Figure 4.1-1 illustrates the effect of the development of the H-B process upon the development of the global population. Nowadays, about 6000 million tons of artificial fertilizer is made every year by Haber-Bosch process sustaining ~48 % of the population of the world. Meanwhile, the Haber-Bosch process as currently operated uses about 1 % of the total world energy supply.⁸⁶ Therefore, if the population continues to grow as expected, then by 2050, about 270 million tons of coal or equivalent energy will be needed to produce enough fertilizer to prevent mass starvation.⁸⁷ Thus, there is a need to improve the present technology to develop a low energy demand process, which can be operated on a more localised scale using hydrogen generated from renewable electricity.

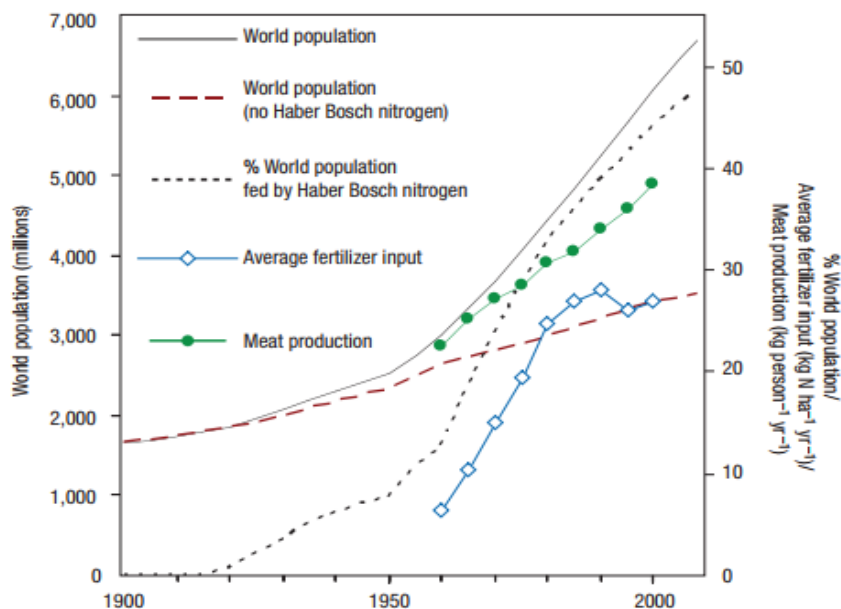


Figure 4.1-1: Trend in human population and the effect of Haber-Bosch process on the world population throughout the 20th Century. ⁸²

Industrial production of Ammonia: Haber –Bosch process

The development of the H-B process provided a direct and affordable route for reactive nitrogen building block production in the form of ammonia. The majority of ammonia produced industrially is consumed for the preparation of fertilizers. However, an important part is utilized for the preparation of nitrogen containing products of industrial importance including urea (NH_2CONH_2), nitric acid (HNO_3), hydrogen cyanide (HCN), cleaning fluids, refrigerants, polymers and explosives etc. The global ammonia production is dominated by the H-B process and it has been constantly growing, at rate of 1-2 % per annum, since the first H-B ammonia synthesis plants, peaking at 140 million tonnes produced in 2012 which consumed about 2 % of the world's energy. ⁸⁸⁻⁸⁹

The production of ammonia in H-B plants is conducted by combining diatomic nitrogen with dihydrogen, as depicted in Eq. 4.1, ⁵⁸ over a promoted iron catalyst. The reaction is generally conducted at temperature ranging between 400 and 500°C and at very high pressure, e.g. 200 bar, using an iron based catalyst and very pure nitrogen and hydrogen. In the first attempts to develop industrial scale ammonia production, scientists had to face many challenges related to the thermodynamic limitations of ammonia synthesis and the poor reaction kinetics at low temperature.



The basis of the H-B process was established by Fritz Haber in the early 1900's.^{83, 90-91} In the earliest work for the development of a viable ammonia synthesis catalyst, uranium and osmium based catalysts were found to be the first promising candidates. However, the use of these materials at an industrial level would be very strongly limited due to their high cost and low abundance. The first viable catalyst for industrial ammonia synthesis was developed by Alwin Mittasch after numerous trial-and-error experiments resulting in the development of the "promoted iron" based catalyst. While non-promoted iron proved to be initially a poor catalyst, the addition of promoters such as potassium and alumina increased the reaction rate by over two orders of magnitude. The presence of potassium is believed to facilitate the desorption of ammonia from the surface of the catalyst and to enhance the nitrogen dissociation process by weakening the dinitrogen bond via an electron-donor effect. In this catalytic formulation, alumina is added the development of "promoted iron" catalyst is considered as the genuine start of the industrial ammonia production era.⁹²

Alternative materials for ammonia generation

The actual production of ammonia is currently dominated by the H-B process. In spite of its industrial efficiency, as mentioned previously, the process is estimated to account for >1 % of global energy demand when the production of the reactants is taken in account. Furthermore, the process is estimated to contribute ca. 3 % of global greenhouse gas emissions.⁹³ Thus, effort was directed towards the development of new catalytic materials that could operate at lower temperatures and pressures in order to reduce the energy consumption, production cost of the process and lower industrial ammonia carbon footprint. Over the years, iron based catalysts for ammonia generation have been subject to many studies to improve catalytic activity and life expectancy. However, no significant improvement was obtained and the industrial catalyst is practically the same as that of the original formulation.

Non-ferrous based catalysts

Since no appreciable improvement was obtained since the development of the iron based catalyst, scientists started to investigate other non-ferrous alternative based catalysts. Among these catalysts, Ru was reported for its high activity for ammonia generation. The earliest studies can be dated to Mittasch's work in the early 1900's in which 20000 mixtures for their catalytic activity were screened.⁹⁴⁻⁹⁵ The work of Aika and Ozaki rekindled the interest for ruthenium based materials and eventually an doubly promoted ruthenium catalyst supported on graphitised carbon was developed as a novel ammonia catalyst.⁹⁶ The potential of alkali as a promoter on Ru based catalysts was demonstrated by Ozaki *et al.*⁹⁷ The study emphasises that the use of both Cs⁺ and Ba²⁺ greatly enhances Ru ammonia synthesis activity. In 1980, the M. W. Kellogg and British Petroleum companies cooperated to develop a novel ammonia synthesis process (KAAP), in which BP was to create a new Ru-based catalyst with a high surface graphite support and high activity at low temperatures and low pressures.⁹⁸ After 14 years, an doubly promoted Ru catalyst was first implemented in the KAAP process in 1994. The high activity of the Ru/Cs/Ba/HSAG catalyst which is ~20 times more active than conventional iron catalyst allowed the KAAP process to operate lower pressure, lower temperature and at higher ammonia concentration than the H-B process leading to an appreciable reduction of the operational cost.⁹⁹ The main part of the KAAP process is the converter which reaches 21.7 % of ammonia concentration at the outlet. The methanation of the carbon material with time might be avoided when the reaction is performed at relatively low temperature in the KAAP system.⁹⁸ It is still of interest to further develop highly active materials for ammonia generation.

In same line of work to develop non-ferrous-based catalyst, unsupported CoRe related materials were found to be promising. In recent work which done by Hargreaves group, CoRe₄ was reported to be a very active material for ammonia synthesis at ambient pressure especially when prepared without an ammonolysis step. *In-situ* XAS analysis suggests the cobalt rhenium active phase is bimetallic in nature and that both Co and Re need to be reduced prior to being active. Furthermore, CoRe₄ has been shown to maintain high activity on repeated reaction and after exposure to air and ambient moisture, which is of potential industrial relevance. However, no study on the behaviour of this material in high-pressure ammonia synthesis is available currently.¹⁰⁰

Metal nitride based materials

Mittasch was among the first to study nitride materials as an indirect route to activate nitrogen from air. In his earliest work, Mittasch determined the ability of some metals to form nitrides under ammonia synthesis conditions but the studied materials didn't show particularly promising activity. Over the years, the use of nitrides as catalytic materials for ammonia synthesis was then explored by a number of researchers. Vanadium oxynitride¹⁰¹ and uranium nitride have been among the first materials studied as source of activated nitrogen than can be rapidly hydrogenated to produce ammonia.¹⁰² Molybdenum nitride has been also reported to be an active catalyst for ammonia generation. The activity of γ -Mo₂N, β -Mo₂C and α -Mo₂C for ammonia synthesis was investigated by Kojima and Aika, and the results show that the β -Mo₂C is more active than α -Mo₂C and γ -Mo₂N at 400 °C; the activity of the β -Mo₂C being comparable with that of promoted iron.¹⁰³

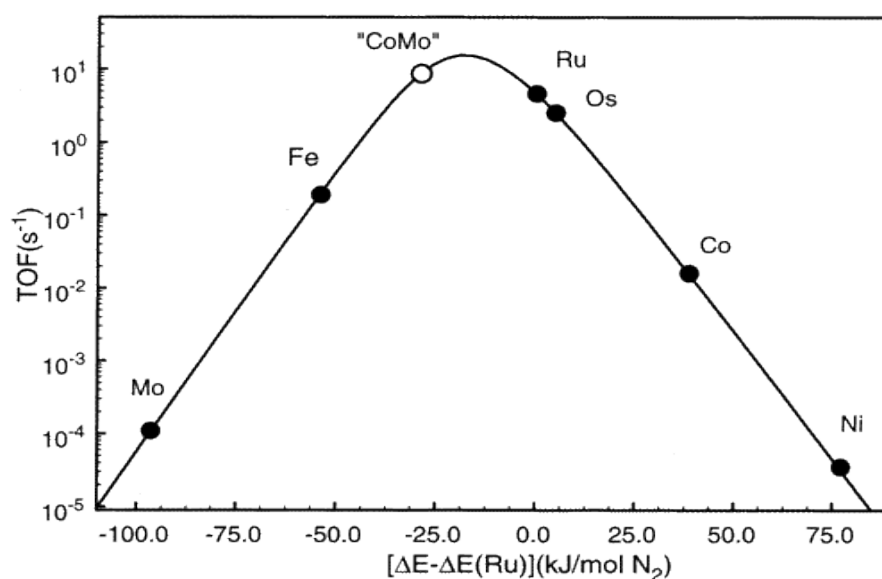


Figure 4.1-2 Calculated turnover frequencies for ammonia synthesis as a function of the adsorption energy of nitrogen. The synthesis conditions are 400 °C, 50 bar, gas composition H₂:N₂ = 3:1 containing 5% NH₃.¹⁰⁴

Within the nitrides subsequently studied for ammonia synthesis, Co₃Mo₃N is of particular interest due to its high catalytic activity, especially when promoted with Cs⁺.³⁶ It is interesting to note that the development of this material was based on a simple assumption. According to Nørskov *et al.*,¹⁰⁴ a material presenting an optimal nitrogen binding energy can be obtained by mixing an element presenting a low N₂ binding energy (Co in this case) with a second element presenting a high N₂ binding energy (Mo in this

case) with N_2 binding being a descriptor of ammonia synthesis performance. The combination of Co and Mo in Co_3Mo_3N was proposed to result in the creation of the (111) surface presenting optimal properties for ammonia generation (Figure 4.1-2). The role of nitrogen in the Co_3Mo_3N was limited by the authors to the creation of the correct crystallographic ordering without the lattice N being involved in the reaction. Experimental observations tend to confirm the ability of Co_3Mo_3N to act as source of reactive nitrogen. The work of Hargreaves *et al.*³⁷ demonstrated the ability of Co_3Mo_3N to directly produce ammonia under reducing conditions. The reaction was associated with the reduction of nitrogen content in the Co_3Mo_3N to Co_6Mo_6N and the relocation of nitrogen from the 16c Wyckoff to the 8a site.⁴ Furthermore, isotopic exchange experimentation showed that a large fraction of lattice nitrogen is exchangeable under conditions relevant to ammonia synthesis.¹⁰⁵ Further evidence suggesting an important role of lattice nitrogen in ammonia synthesis was recently provided by computational studies. In a recent work, Catlow *et al.* showed the occurrence of high concentration of surface vacancy sites in the (111) surface that are capable of activating nitrogen N_2 under conditions that are of relevance for ammonia generation. The study found that the occurrence of nitrogen vacancies exposes Co_8 clusters and Mo_3 clusters that could adsorb and activate N_2 .¹⁰⁶⁻¹⁰⁷

Thus, experimental observations and theoretical investigations tend to confirm the lability and reactivity of lattice nitrogen suggesting its possible role in the mechanism of ammonia synthesis reaction in Co_3Mo_3N related materials. In such a mechanism, ammonia is generated directly via the hydrogenation of the lattice nitrogen, resulting in the creation of nitrogen vacancies (Co_8 clusters and Mo_3 clusters) which are, subsequently, replenished from gas phase N_2 .

In this chapter, the catalytic performance of cobalt molybdenum carbide material, Co_3Mo_3C and Co_6Mo_6C , in ammonia synthesis will be investigated. The particular interest in these systems arises from their related structures to the Co_3Mo_3N and Co_6Mo_6N . In spite of evidence of a Mars–van Krevelen pathway for ammonia synthesis, the efficacy of Co_3Mo_3N for ammonia synthesis is still often attributed to the combination of the Co and Mo components having a close to optimal binding energy for N_2 . It is of interest consequently, to prove the extent in which the carbide materials exhibit related behaviour to their nitrides counterparts. Accordingly, the requirement of lattice nitrogen, in the CoMo reactivity will be assessed in this study.

4.2 Results and discussion

Ammonia synthesis over ternary nitride (η -6 $\text{Co}_3\text{Mo}_3\text{N}$) and carbides (η -6 $\text{Co}_3\text{Mo}_3\text{C}$, η -12 $\text{Co}_6\text{Mo}_6\text{C}$) were conducted and compared with binary nitride (γ - Mo_2N) and carbides (β - Mo_2C , α - Mo_2C) under the same conditions.

I. Binary molybdenum nitride and carbides

This section presents information related to ammonia synthesis using binary γ - Mo_2N , β - Mo_2C and α - Mo_2C materials. The activity of these materials for ammonia synthesis has been investigated previously at 400 °C and 0.1 MPa. Kojima and Aika have stated that β - Mo_2C is more active than γ - Mo_2N and α - Mo_2C materials for ammonia synthesis.¹⁰³

4.2.1 Gamma molybdenum nitride (γ - Mo_2N)

Gamma molybdenum nitride was extensively investigated and has been identified as an active ammonia synthesis material. Most of these studies were carried out with experiments at 400 °C and 0.1 MPa, closely following conditions employed by Aika and Kojima.¹⁰³ The ammonia synthesis rate of γ - Mo_2N was reported to be $43 \mu\text{molNH}_3 \text{ h}^{-1}\text{g}^{-1}$. However, this material was tested to compare to binary carbides at different temperatures. Within the current study, the material was reacted under 75 vol. % H_2 in N_2 at different temperatures and times on stream. The vent gas was bubbled through a solution of 0.00108 M H_2SO_4 and conductivity monitored. The post-reaction sample was investigated by PXRD, SEM and CHN analysis as discussed in more detail below.

4.2.1.1 Conductivity

Figure 4.2-1A presents a plot of conductivity versus temperature and time on stream for γ - Mo_2N reacted with 75 vol. % H_2 in N_2 at 400 °C for 4 hours then changed to 500 °C for 4 hours under the same gas or in the opposite way in Figure 4.2-1B. The reaction profile in both figures shows that over the initial hour there is a high rate of reaction which could be correlated to the hydrogenation of residual NH_x species upon the surface of the material. After the initial hour a rate of $123 \mu\text{molNH}_3 \text{ h}^{-1}\text{g}^{-1}$ at 400 °C, $188 \mu\text{molNH}_3 \text{ h}^{-1}\text{g}^{-1}$ at 500 °C for A and $202 \mu\text{molNH}_3 \text{ h}^{-1}\text{g}^{-1}$ at 500 °C, $48 \mu\text{molNH}_3 \text{ h}^{-1}\text{g}^{-1}$ at 400 °C for B could be determined from the gradients to the profiles shown below.

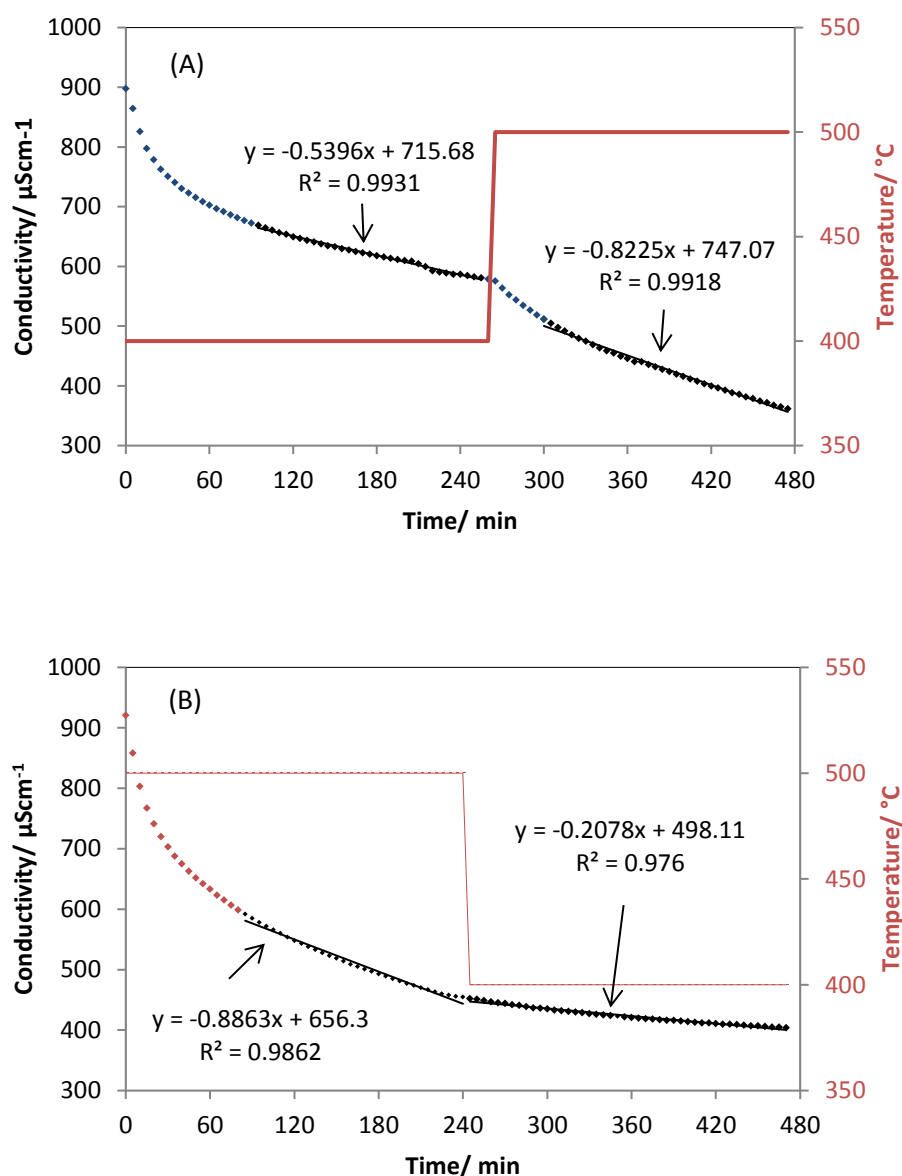


Figure 4.2-1: Conductivity Profile for γ - Mo_2N reacted with 75 vol. % H_2 in N_2 at A (400 °C for 4 h and 500 °C for 4 h) and B (500 °C for 4 h and 400 °C for 4 h).

4.2.1.2 PXRD analysis

From studying the PXRD patterns for the pre- and post-reaction γ -Mo₂N it can be seen that the formation of ammonia does not apparently affect the bulk structure of the material. The PXRD patterns for post-reaction γ -Mo₂N shown in Figure 4.2-2A (400 °C for 4 h and 500 °C for 4 h) and Figure 4.2-2B (500 °C for 4 h and 400 °C for 4 h) coincide, presenting five main peaks at $2\theta = 37.4, 43.4, 63.3, 75.7$ and 79.8° that can be matched to the (111), (200), (220), (311) and (222) hkl crystal planes of cubic γ -Mo₂N (JCPDS 003-0907). The nitrogen content of the post-reaction samples were decreased from 10.1 wt. % as prepared to 6.2 wt. % N for A and 6.0 wt. % N for B. The expected stoichiometric N content of Mo₂N is 6.8 wt. %.

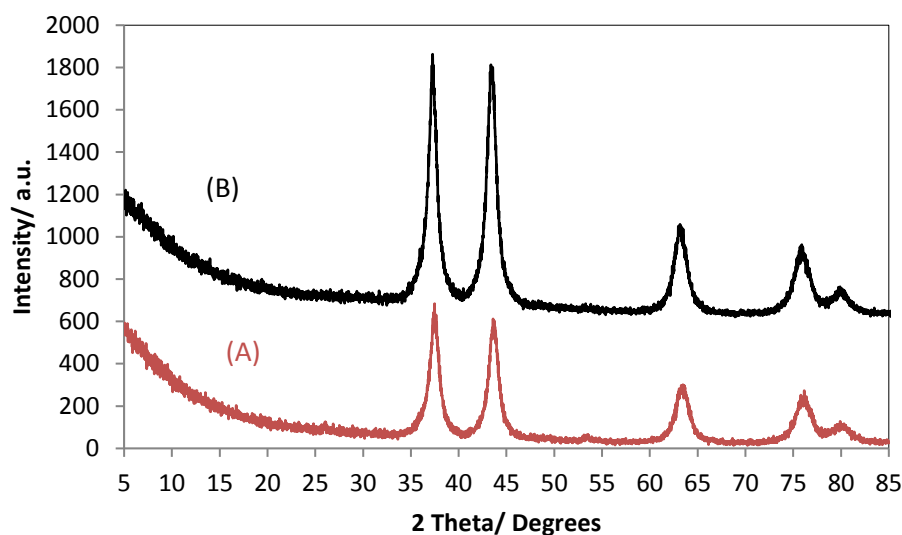


Figure 4.2-2: PXRD pattern of the post-reaction of γ -Mo₂N: A (400 °C for 4 h and 500 °C for 4 h) and B (500 °C for 4 h and 400 °C for 4 h).

4.2.1.3 SEM Images

In order to consider the morphology and structural evolution of the material during the ammonia synthesis reaction of γ -Mo₂N, SEM analysis was conducted. The representative SEM images of the post-reaction γ -Mo₂N, are presented in Figure 4.2-3A (400 °C for 4 h and 500 °C for 4 h) and Figure 4.2-3B (500 °C for 4 h and 400 °C for 4 h). The materials exhibit a platelet morphology, as described in earlier research.⁵⁵ The SEM morphology of both samples is similar to that of pre-reaction material in section 3.2.1.3, and predominantly comprises large (ca. 5.42 x 3.16 μm) platelet crystals with secondary, smaller (ca. 1.38 x

1.84 μm) rod-like formations. This suggests retention of the platelet morphology characteristic of their precursor structures.

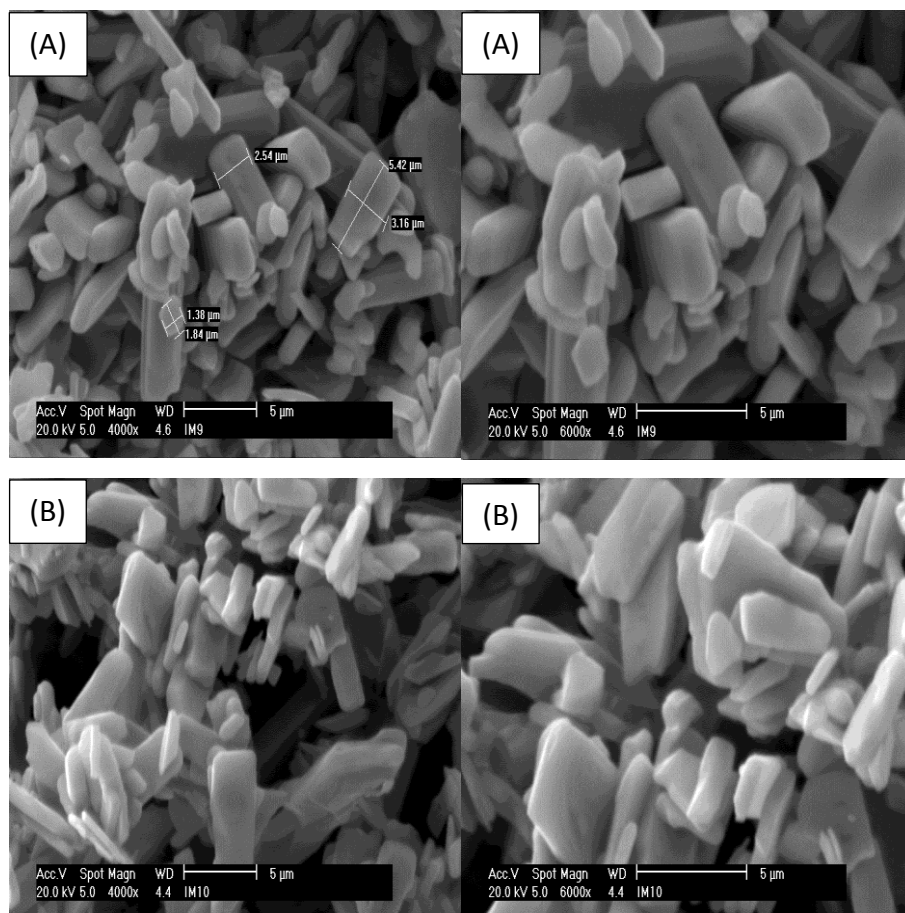


Figure 4.2-3: SEM images of the post-reaction of $\gamma\text{-Mo}_2\text{N}$: A (400 °C for 4 h and 500 °C for 4 h) and B (500 °C for 4 h and 400 °C for 4 h).

4.2.2 Beta Molybdenum Carbide ($\beta\text{-Mo}_2\text{C}$)

With the purpose of examination of the ability of beta molybdenum carbide to produce ammonia, the material was reacted under 75 vol. % H_2 in N_2 at different temperatures and times on stream. The vent gas was bubbled through a solution of 0.00108 M H_2SO_4 and conductivity monitored. The post-reaction sample was investigated by PXRD, SEM and CHN analysis as discussed in more details below. Oyama¹⁵ and Kojima¹⁰³ have reported that $\beta\text{-Mo}_2\text{C}$ is more active than $\gamma\text{-Mo}_2\text{N}$ for ammonia synthesis at 400 °C.

4.2.2.1 Conductivity

Figure 4.2-4A presents a plot of conductivity versus temperature and time on stream for β - Mo_2C reacted with 75 vol. % H_2 in N_2 at 400 °C for 4 hours then increased temperature to 500 °C for 4 hours under the same gas or with the temperature profile applied in the opposite direction as shown in Figure 4.2-1B.

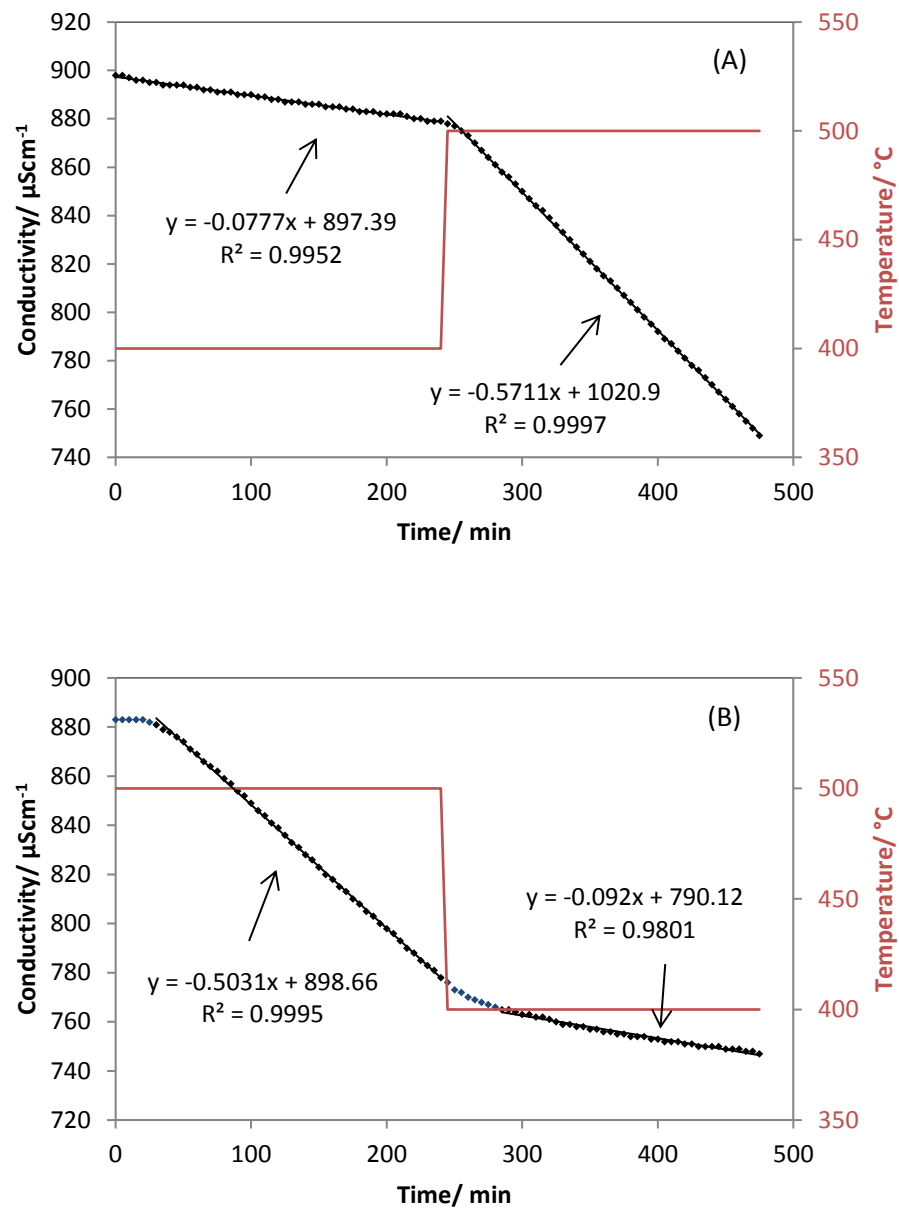


Figure 4.2-4: Conductivity Profile for β - Mo_2C reacted with 75 vol. % H_2 in N_2 at A (400 °C for 4 h and 500 °C for 4 h) and B (500 °C for 4 h and 400 °C for 4 h).

The reaction profile in Figure 4.2-4A shows that over the initial 4 hours when temperature was 400 °C there is a low steady state rate of reaction ($18 \mu\text{molNH}_3 \text{ h}^{-1}\text{g}^{-1}$), while after increasing temperature to 500 °C a high steady state rate of reaction ($131 \mu\text{molNH}_3 \text{ h}^{-1}\text{g}^{-1}$) was observed. The reaction profile in Figure 4.2-4B shows that the decrease was observed after an induction period of approximately 30 minutes with rate of $115 \mu\text{molNH}_3 \text{ h}^{-1}\text{g}^{-1}$ and then the changed temperature to 400 °C after 4 hours on stream resulted in a decrease of the ammonia production rate to $21 \mu\text{molNH}_3 \text{ h}^{-1}\text{g}^{-1}$.

4.2.2.2 PXRD analysis

From studying the PXRD patterns for the pre- and post-reaction $\beta\text{-Mo}_2\text{C}$ it can be seen that the formation of ammonia does not apparently affect the bulk structure of the material. The PXRD patterns for post-reaction $\beta\text{-Mo}_2\text{C}$ shown in Figure 4.2-5 A (400 °C for 4 h and 500 °C for 4 h) and Figure 4.2-5 B (500 °C for 4 h and 400 °C for 4 h) coincide, presenting eight intense peaks at $2\theta = 34.4, 37.9, 39.4, 52.1, 61.5, 69.5, 72.3,$ and 74.59° that can be matched to the (100), (002), (101), (102), (110), (103), (200) and (112) hkl crystal planes of $\beta\text{-Mo}_2\text{C}$ (JCPDS 001-1188) respectively. The carbon content obtained from CHN analysis of the post-reaction samples were 7.0 wt. % C for A and 7.1 wt. % for B, these results were decreased from the pre-reaction samples 7.5 wt. % for A and 7.6 wt. % for B. The expected stoichiometric C content of Mo_2C is 5.8 wt. %.

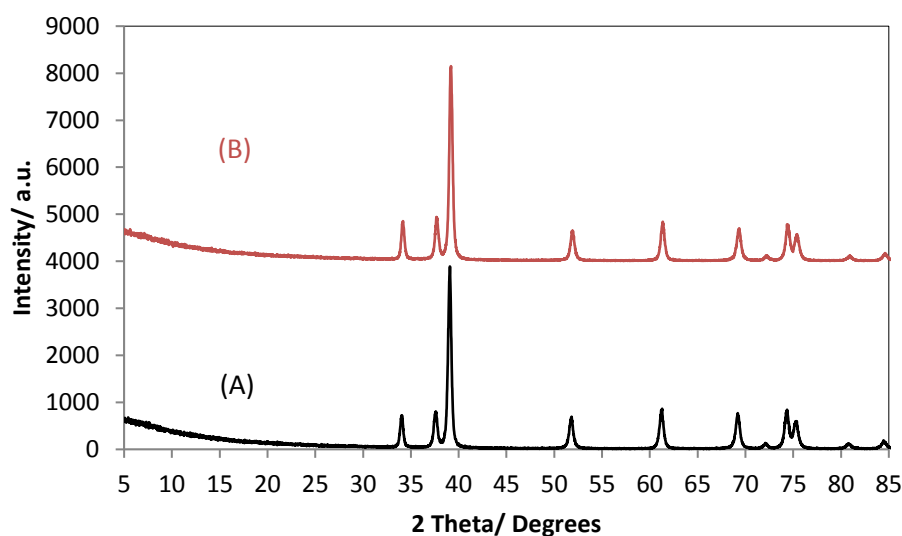


Figure 4.2-5: PXRD pattern of the post-reaction of $\beta\text{-Mo}_2\text{C}$: A (400 °C for 4 h and 500 °C for 4 h) and B (500 °C for 4 h and 400 °C for 4 h).

4.2.2.3 SEM Images

Figure 4.2-6 presents typical SEM images at 4000 and 6000 magnification of the post-reaction β -Mo₂C: A (400 °C for 4 h and 500 °C for 4 h) and B (500 °C for 4 h and 400 °C for 4 h). It can be seen that the post-reaction sample consists of aggregates of cubes and it still retains the pre-reaction morphology.

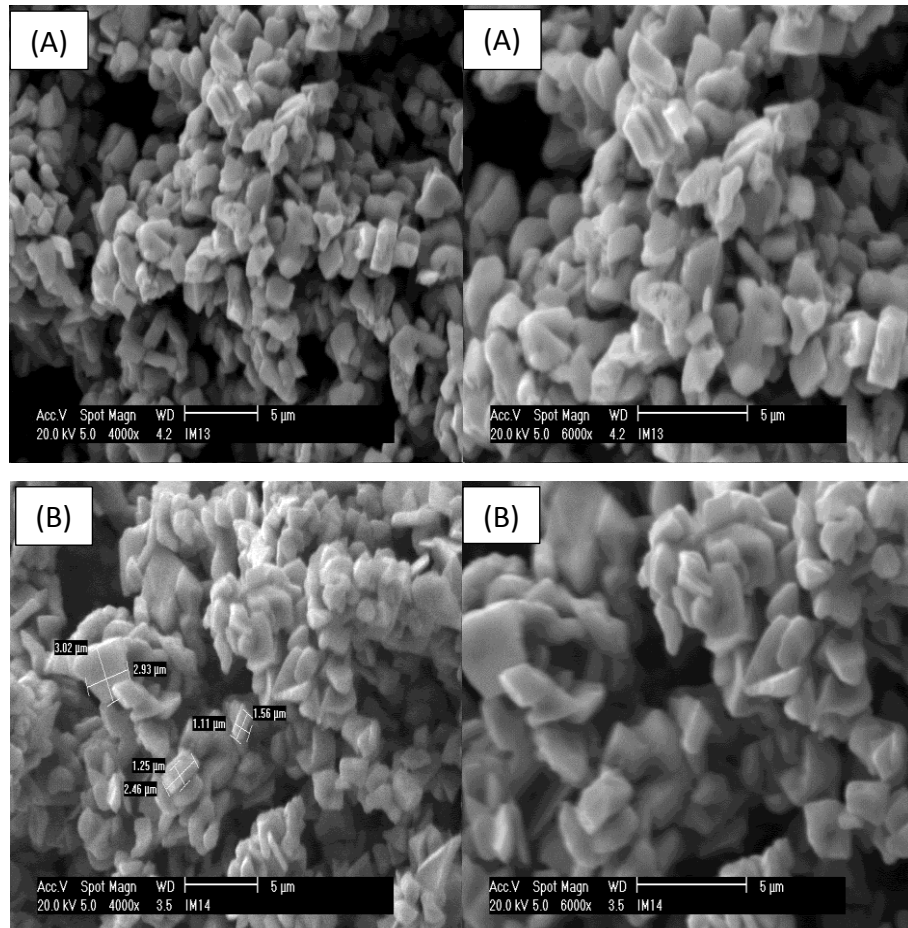


Figure 4.2-6: SEM images of the post-reaction of β -Mo₂C: A (400 °C for 4 h and 500 °C for 4 h) and B (500 °C for 4 h and 400 °C for 4 h).

4.2.3 Alpha Molybdenum Carbide (α -Mo₂C)

With the intention of consideration of the ability of alpha molybdenum carbide to produce ammonia, the material was reacted under 75 vol. % H₂ in N₂ at different temperatures and time on stream.

4.2.3.1 Conductivity

Figure 4.2-7A presents a plot of conductivity versus temperature and time on stream for α -Mo₂C reacted with 75 vol. % H₂ in N₂ at 500 °C for 4 hours followed by decreased temperature to (400 °C for 4 hours) with the opposite temperature profile as shown in Figure 4.2-1B.

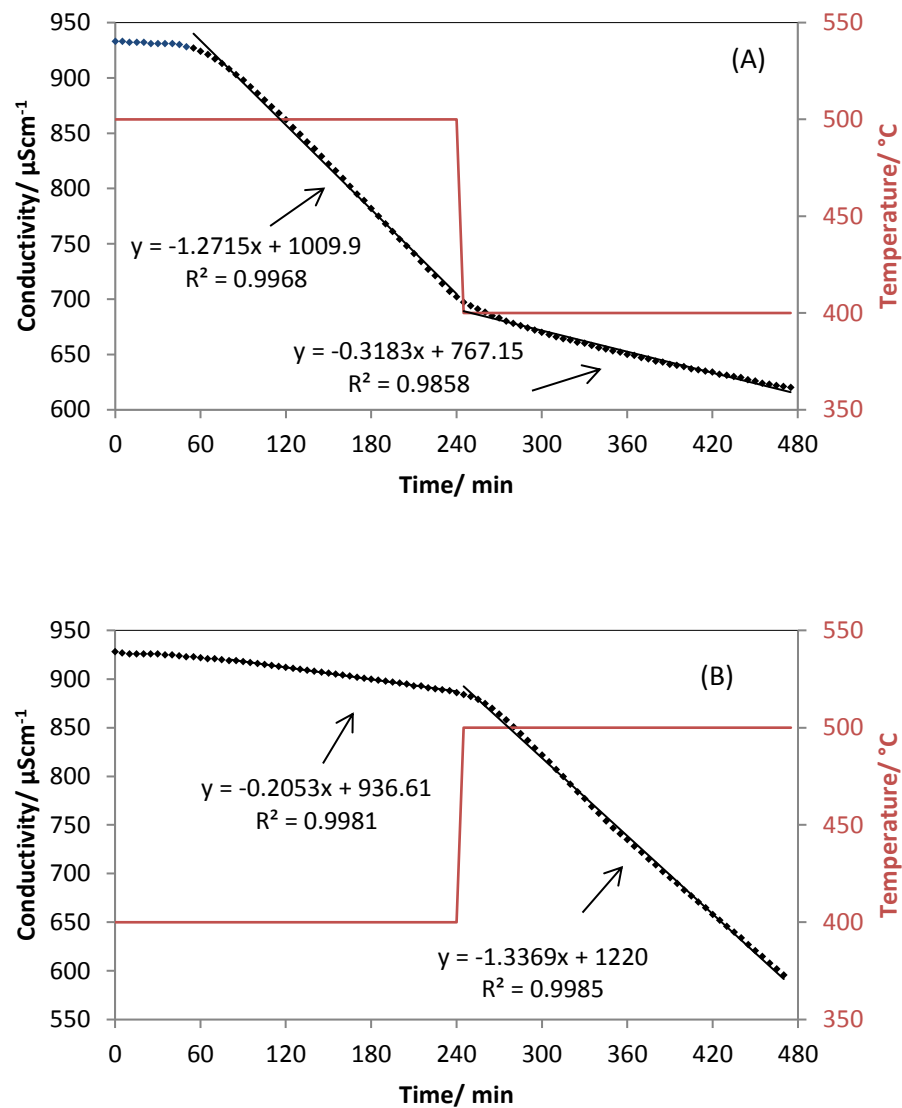


Figure 4.2-7: Conductivity Profile for α -Mo₂C reacted with 75 vol. % H₂ in N₂ at A (500 °C for 4 h and 400 °C for 4 h) and B (400 °C for 4 h and 500 °C for 4 h).

The reaction profile in Figure 4.2-7A shows that the decrease was observed after an induction period of approximately 40 minutes with a rate of $291 \mu\text{molNH}_3 \text{ h}^{-1}\text{g}^{-1}$ and then $73 \mu\text{molNH}_3 \text{ h}^{-1}\text{g}^{-1}$. The reaction profile in Figures 4.2-7B shows that over the initial 4 hours when temperature was 400°C there is a small steady state rate of reaction ($47 \mu\text{molNH}_3 \text{ h}^{-1}\text{g}^{-1}$), while at 500°C a high steady state rate of reaction of $306 \mu\text{molNH}_3 \text{ h}^{-1}\text{g}^{-1}$ was observed.

4.2.3.2 PXRD analysis

From studying the PXRD patterns for the pre- and post-reaction $\alpha\text{-Mo}_2\text{C}$ it can be seen that the formation of ammonia does apparently affect the bulk structure of the material. The PXRD patterns for pre- and post-reaction $\alpha\text{-Mo}_2\text{C}$ shown in Figure 4.2-8 A (as prepared), Figure 4.2-8 B (500°C for 4 h and 400°C for 4 h) and Figure 4.2-8 C (400°C for 4 h and 500°C for 4 h) coincide, presenting five main peaks that can be matched to the (111), (200), (220), (311) and (222) hkl crystal planes of cubic $\alpha\text{-Mo}_2\text{C}$ (JCPDS 015-0457) with a small shift to higher 2θ after reaction which suggests that the material may have been transformed from carbide phase to carbonitride. The carbon and nitrogen content of the post-reaction samples were 4.1 wt. % C and 1.8 wt. % N for A, and 3.0 wt. % C, and 2.8 wt. % N for B which corresponds to carbonitride material, with the stoichiometric C content of Mo_2C being 5.8 wt. %.

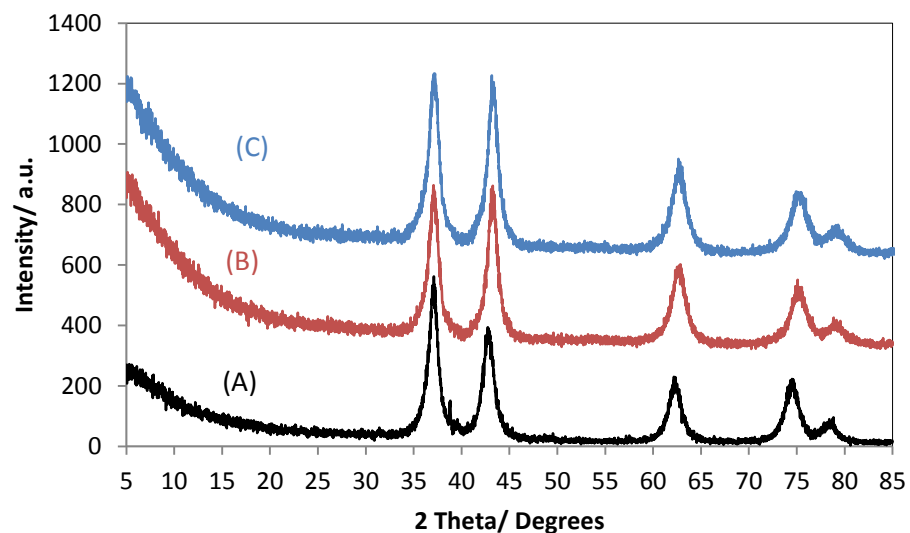


Figure 4.2-8: PXRD patterns of the pre- and post-reaction of $\alpha\text{-Mo}_2\text{C}$: A (as prepared), B (500°C for 4 h and 400°C for 4 h) and C (400°C for 4 h and 500°C for 4 h).

4.2.3.3 SEM images

Figure 4.2-9 presents typical SEM images at 4000 and 6000 magnification of the post-reaction α -Mo₂C: A (500 °C for 4 h and 400 °C for 4 h) and B (400 °C for 4 h and 500 °C for 4 h). It can be seen that the post-reaction sample consists of aggregates of plates. The material retains its morphology upon reaction.

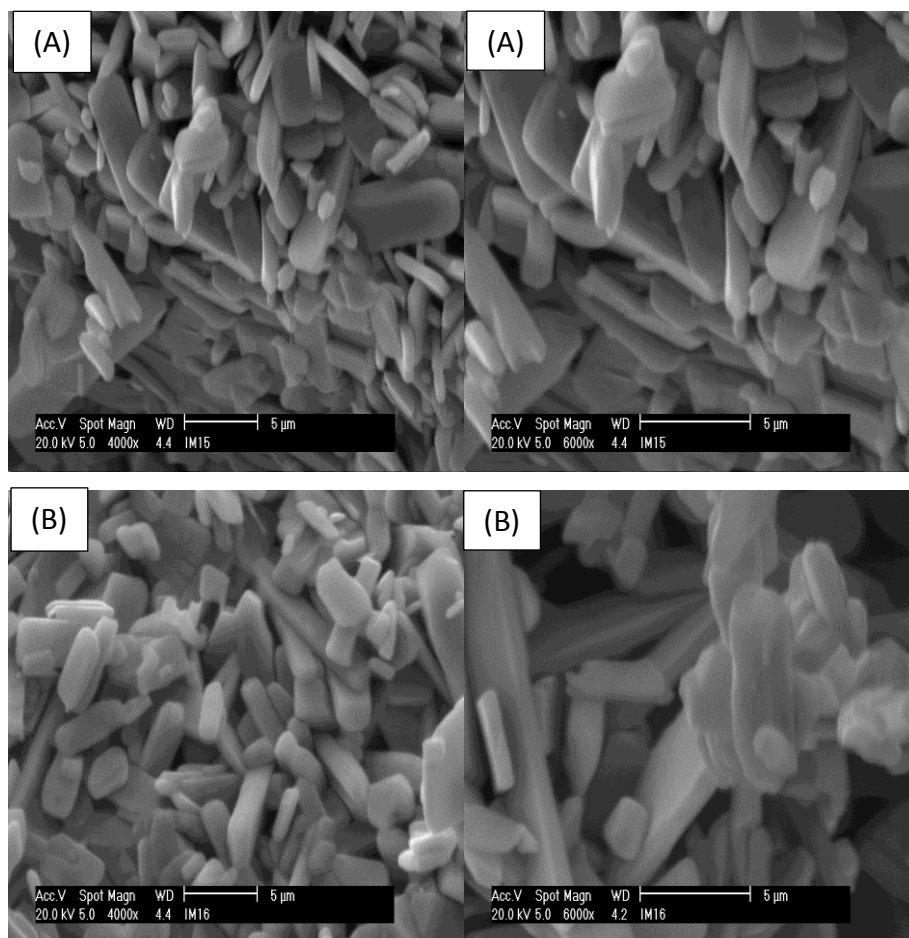


Figure 4.2-9: SEM images of the post-reaction of α -Mo₂C: A (500 °C for 4 h and 400 °C for 4 h) and B (400 °C for 4 h and 500 °C for 4 h).

Comparison between γ -Mo₂N, β -Mo₂C, α -Mo₂C for ammonia synthesis

The role of the lattice nitrogen and carbon in the catalytic activity was studied by comparing the results of β -Mo₂C and α -Mo₂C for ammonia synthesis to the activity of the γ -Mo₂N system. The α -Mo₂C system was found to be highly active for ammonia synthesis at 500 °C and ambient pressure exhibiting a rate of ca. $299 \pm 8 \mu\text{molNH}_3 \text{ g}^{-1} \text{ h}^{-1}$ which is very high and is worthy of further study. Under the same reaction conditions, the β -Mo₂C ($123 \pm 8 \mu\text{molNH}_3 \text{ g}^{-1} \text{ h}^{-1}$) system displayed a lower activity than γ -Mo₂N ($195 \pm 7 \mu\text{molNH}_3 \text{ g}^{-1} \text{ h}^{-1}$). However, this was only exhibited after an induction time of ca. 40 minutes for α -Mo₂C and 30 minutes for β -Mo₂C, during which the materials demonstrated very poor activity. Nonetheless beyond the induction time, the materials exhibited a steady state performance during 4 h of reaction with no sign of deactivation before the temperature was changed to 400 °C. PXRD patterns of post-reaction β -Mo₂C and γ -Mo₂N were very similar to the pre-reaction samples; whereas the reflections in α -Mo₂C had shifted toward the higher 2θ . From elemental analyses, the nitrogen content in post-reaction γ -Mo₂N was decreased compared to pre-reaction material (from 10.1 to 6.2 wt. % N) and no presence of nitrogen was found in post-reaction β -Mo₂C, which suggests that these phases are stable under ammonia synthesis at 500 °C although α -Mo₂C was transformed into a carbonitride under the same conditions. In this context it is noteworthy that α -Mo₂C can have a variable stoichiometry and is often described as MoC_{1-x} in this context. This may facilitate incorporation of lattice N under reaction conditions. The SEM studies indicate that the morphologies of post-reaction β -Mo₂C, α -Mo₂C and γ -Mo₂N are similar when compared to the pre-reaction β -Mo₂C, α -Mo₂C and γ -Mo₂N materials. On this basis, there is strong evidence that the influence of difference in morphology and the nitrogen or carbon presence within the structure can lead to a difference in performance; it is the difference in composition between Mo₂N and Mo₂C that emphasises this. Indeed it is the case that the lag period associated with the development of activity, in the case of the carbides, corresponds to the further replacement of lattice C with N. This would be consistent with the operation of a Mars-van Krevelen mechanism in which the presence of lattice nitrogen has to be present for ammonia synthesis to occur once a critical population of lattice N is established.

II. Ternary molybdenum nitride and carbides

Ammonia synthesis using ternary oxide, nitride and carbides was conducted according to the procedure documented in the catalyst testing section in Chapter 2.

4.2.4 Dehydrated Cobalt molybdenum oxide (CoMoO₄)

Dehydrated cobalt molybdenum oxide was investigated for ammonia synthesis at 500 °C under 75 vol. % H₂ in N₂ for 48 hours. The post-reaction material was characterized using PXRD, SEM and CHN analysis as discussed in more detail below.

4.2.4.1 Conductivity

Experiments were undertaken in order to clarify the relation between structures of CoMo oxide, nitride and carbides in relation to catalytic activity and to determine whether the activity for ammonia production required the presence of lattice nitrogen within the material. Figure 4.2-10 presents a plot of conductivity versus time for dehydrated CoMoO₄ at 500 °C under 75 vol. % H₂ in N₂ run for 48 hours. The reaction profile in this figure shows that the decrease was observed after an induction period approximately 100 minutes, during which the material demonstrated very poor activity, and beyond which the material exhibited steady state performance during 48 h of reaction with a rate of $219 \pm 73 \mu\text{molNH}_3 \text{ h}^{-1}\text{g}^{-1}$ and with no sign of deactivation.

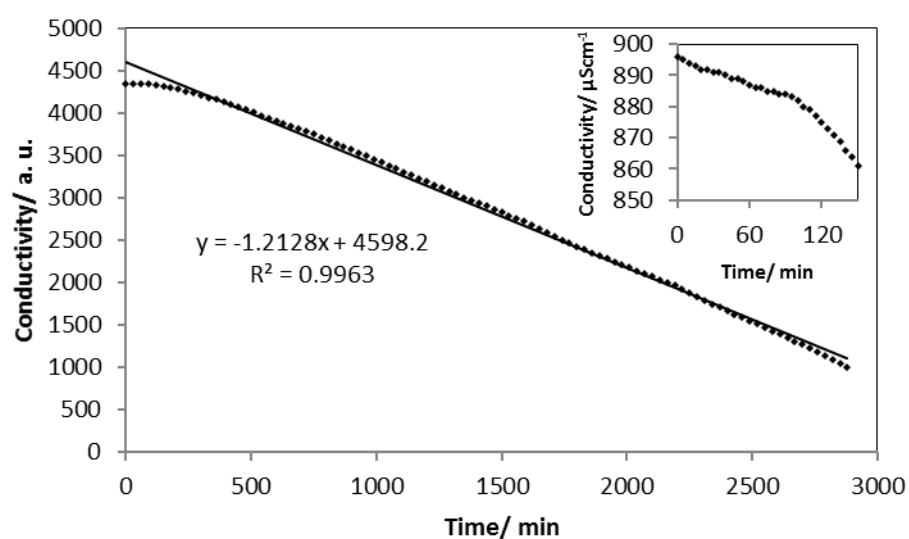


Figure 4.2-10: Extended reaction conductivity profile for CoMoO₄ under 75 vol. % H₂ in N₂ gas at 500 °C for 48 h. The inset corresponds to the expanded induction period.

The vent gas was bubbled through a solution of 0.00108 M H_2SO_4 and this solution had to be changed many times since it had been completely consumed by the ammonia produced from the reaction and the conductivity measurements continued. The standard error calculation applied is provided in the Appendix 4.

4.2.4.2 PXRD analysis

To investigate any changes in phase, PXRD was performed and the results are presented in Figure 4.2-11 for pre- and post-reaction materials denoted as A and B respectively. The PXRD patterns shown in Figure 4.2-11B; present a poorly crystalline phase of post-reaction material. The diffraction peaks at $2\theta = 36.8, 42.9$ and 62.1° could be related to CoO (JCPDS card No. 01-072-1474), $2\theta = 18.3, 36.8$ and 56.6° could be related to MoO_2 (JCPDS card No. 01-078-1072) and $2\theta = 35.3, 42.9^\circ$ could be related to $\text{Co}_3\text{Mo}_3\text{N}$ (JCPDS card No. 01-089-7953). Based on CHN analysis, the nitrogen content of the post-reaction sample was found to be 1.0 wt. % with 0.4 wt. % hydrogen content. This result potentially indicated that the substitution of lattice oxygen by nitrogen is initiated during the induction time, although further investigation to eliminate alternative possibilities is required.

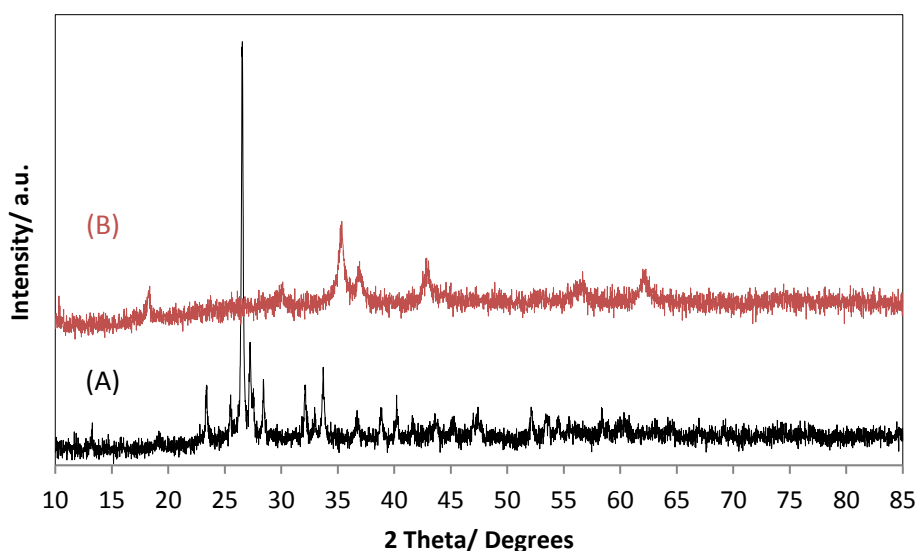


Figure 4.2-11: PXRD patterns of pre- and post-reaction dehydrated CoMoO_4 for A and B respectively.

4.2.4.3 SEM analyses

Figure 4.2-12 presents typical SEM images at 5000 and 6000 magnification of the post-reaction dehydrated CoMoO_4 . It can be seen that the post-reaction sample consists of aggregates of needles which retain the precursor shape and size.

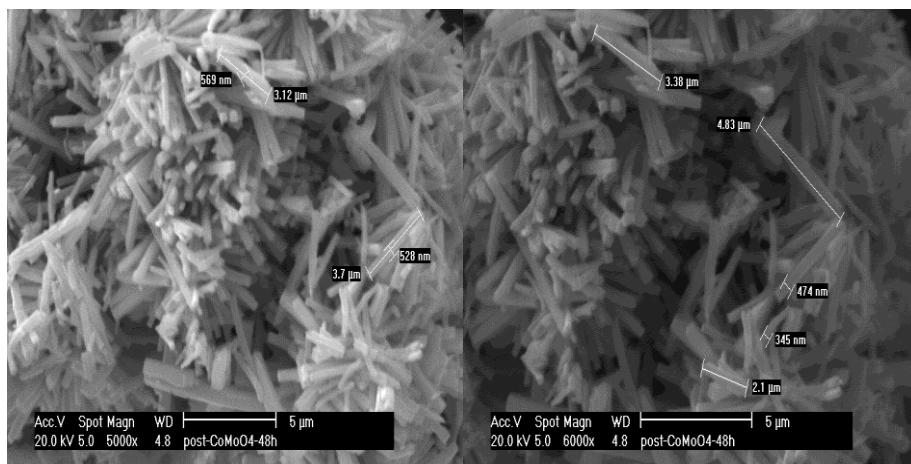


Figure 4.2-12: Typical SEM images of the post-reaction dehydrated CoMoO_4 .

4.2.5 Cobalt molybdenum nitride (η -6 $\text{Co}_3\text{Mo}_3\text{N}$)

$\text{Co}_3\text{Mo}_3\text{N}$ has been extensively investigated in terms of lattice nitrogen reactivity and high ammonia synthesis activity. Most of these studies were carried out with experiments at 400 °C and 0.1 MPa, closely following conditions employed by Aika and Kojima.¹⁰⁸ The higher ammonia synthesis rates ($\mu\text{molNH}_3 \text{ g}^{-1}\text{h}^{-1}$) reported in the literature are 986 for $\text{Co}_3\text{Mo}_3\text{N-Cs}_2$, 869 for $\text{Co}_3\text{Mo}_3\text{N-K}_5$, 652 for $\text{Co}_3\text{Mo}_3\text{N}$, 492 for CoR_4 ,¹⁰⁹ 330 for $\text{Fe-K}_2\text{O-Al}_2\text{O}_3$, 275 for Ni-Mo-N , and 143 for Fe-Mo-N .^{58, 108} The ammonia synthesis rates for all catalysts must be compared to the equilibrium restriction, where if the thermodynamic equilibrium was achieved under the same reaction conditions (400 °C, 0.1 MPa), it would correspond to a 0.4 % product yield and a limiting mass normalised rate of 2140 $\mu\text{molNH}_3 \text{ g}^{-1}\text{h}^{-1}$ as tested within this thesis.¹⁰⁰

4.2.5.1 Conductivity

The conductivity as function of time plots for the reaction of $\text{Co}_3\text{Mo}_3\text{N}$ under 75 vol. % H_2 in N_2 at 500 °C and ambient pressure for 48 hours is shown in Figure 4.2-13. The reaction profile shows an immediate linear decrease in conductivity over time and there was not a sign of an induction period as was observed in the case of dehydrated CoMoO_4 . Although this material has oxide passivating layer on the surface from the passivation step, it is active from the beginning of the reaction. It is also clear that this material already contains nitrogen. The rate observed was $489 \pm 17 \mu\text{mol NH}_3 \text{ g}^{-1}\text{h}^{-1}$.

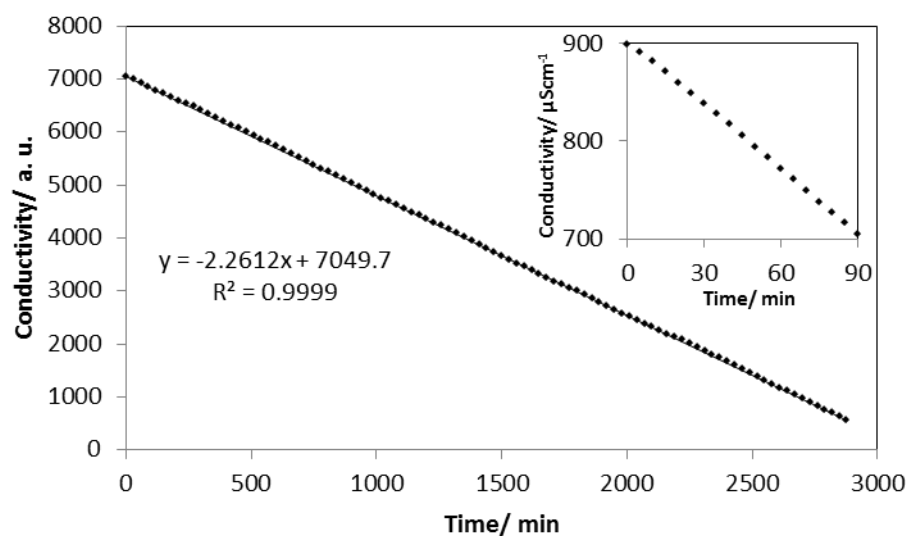


Figure 4.2-13: Extended reaction conductivity profile for $\text{Co}_3\text{Mo}_3\text{N}$ under 75 vol. % H_2 in N_2 gas at 500 °C for 48 h. The inset corresponds to the expanded initial portion.

4.2.5.2 PXRD analysis

The post-reaction PXRD patterns of the pre- and post-reaction $\text{Co}_3\text{Mo}_3\text{N}$ samples for A and B respectively studied under the conditions described in Chapter 2 are presented in Figure 4.2-14. The diffraction patterns of the pre-reaction $\text{Co}_3\text{Mo}_3\text{N}$ sample in Figure 4.2-14A show the same characteristic reflections. Also, the post-reaction microanalysis shows there is no change in the nitrogen content upon the reaction time which is 2.8 wt. %.

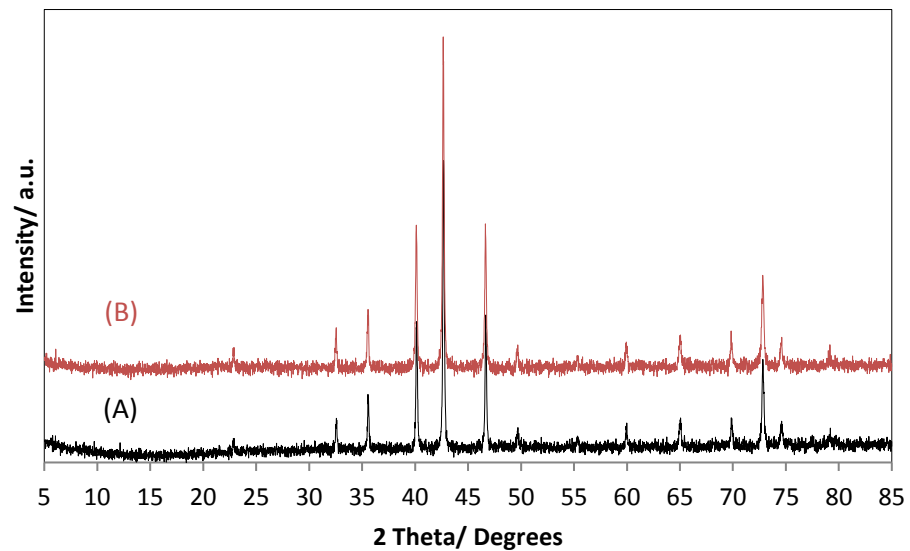


Figure 4.2-14: PXRD patterns for the pre and post-reaction $\text{Co}_3\text{Mo}_3\text{N}$ for A and B respectively.

4.2.5.3 SEM analyses

Figure 4.2-15 presents typical SEM images at 5000 and 6000 magnification of the post-reaction $\text{Co}_3\text{Mo}_3\text{N}$. It can be seen that the post-reaction sample consists of aggregates of needles and it still retains the precursor crystallite shape and size.

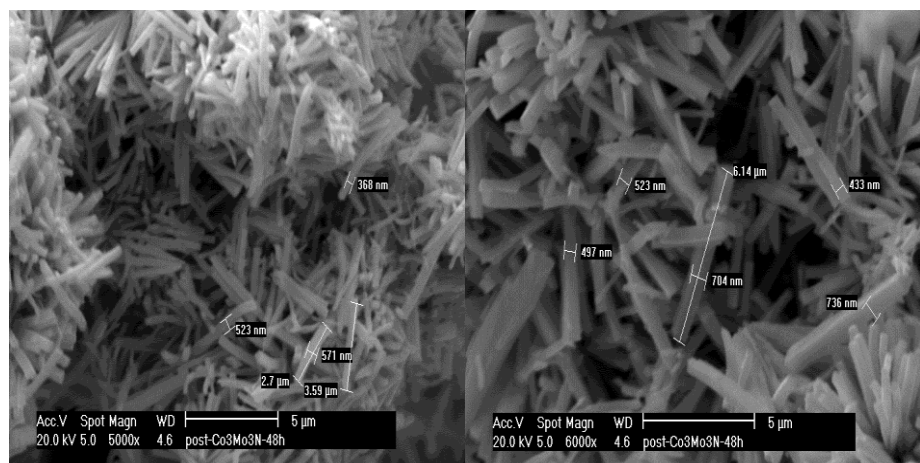


Figure 4.2-15: Typical images of the post-reaction $\text{Co}_3\text{Mo}_3\text{N}$.

4.2.5.4 Effect of reaction temperature

The ammonia synthesis reaction is exothermic and temperature dependent. Consequently, it is important to assess the activity of $\text{Co}_3\text{Mo}_3\text{N}$ at 400 °C for consistency with the literature and 500 °C to compare to cobalt molybdenum oxide and carbide as detailed below. Using $\text{Co}_3\text{Mo}_3\text{N}$ and a 75 vol. % H_2 in N_2 gas feed different temperatures were examined and the results are presented in Figure 4.2-16. Comparison between 400 and 500 °C, shows that there is an increase in the ammonia synthesis rate with increasing reaction temperature. At 500 °C there was a sharp decay in conductivity, which was observed within 4 hours without any deactivation.

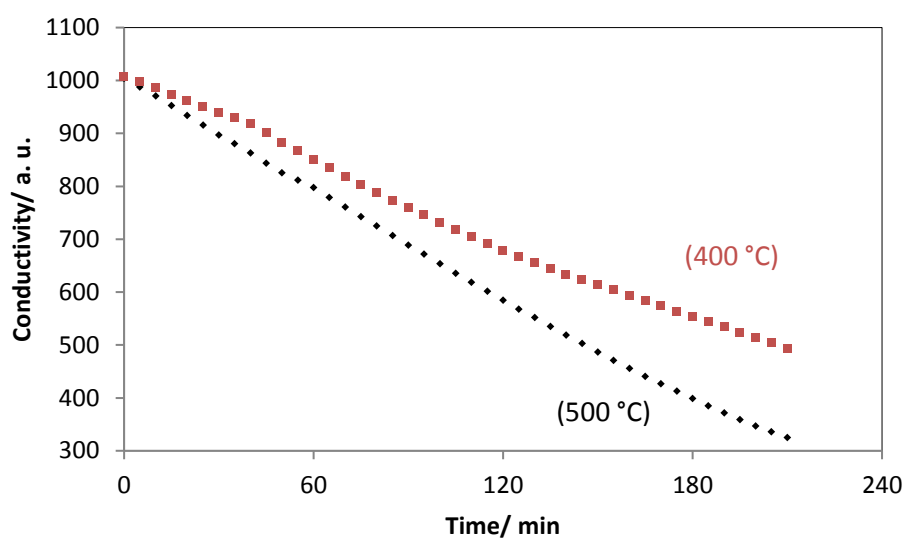


Figure 4.2-16: Comparison reaction profiles for $\text{Co}_3\text{Mo}_3\text{N}$ under 75 vol. % H_2 in N_2 at 400 and 500 °C.

4.2.6 Cobalt molybdenum carbide (η -6 $\text{Co}_3\text{Mo}_3\text{C}$)

$\text{Co}_3\text{Mo}_3\text{C}$ was investigated for ammonia synthesis at 500 °C under 75 vol. % H_2 in N_2 for 48 hours and the post-reaction material was characterized using PND, PXRD, SEM and CHN analysis as discussed in more detail below.

4.2.6.1 Conductivity

The conductivity versus time on stream plots for the reaction of $\text{Co}_3\text{Mo}_3\text{C}$ under 75 vol. % H_2 in N_2 at 500 °C and ambient pressure for 48 hours is shown in Figure 4.2-17. It is evident that 500 °C gives an induction period of approximately 40 minutes prior to the catalyst developing ammonia synthesis activity. This is in contrast to $\text{Co}_3\text{Mo}_3\text{N}$ which is an active material characterised by an immediate linear decrease in conductivity over time. In the case of $\text{Co}_3\text{Mo}_3\text{C}$, it is of interest to note that beyond the induction period, during which the material is apparently inactive, the reaction has reached steady state performance close to that of the $\text{Co}_3\text{Mo}_3\text{N}$ ammonia synthesis rate. This material also exhibits behaviour analogous to that of the CoMoO_4 under the same conditions. The ammonia synthesis rate of $\text{Co}_3\text{Mo}_3\text{C}$ was $461 \pm 17 \mu\text{molHN}_3 \text{ g}^{-1}\text{h}^{-1}$.

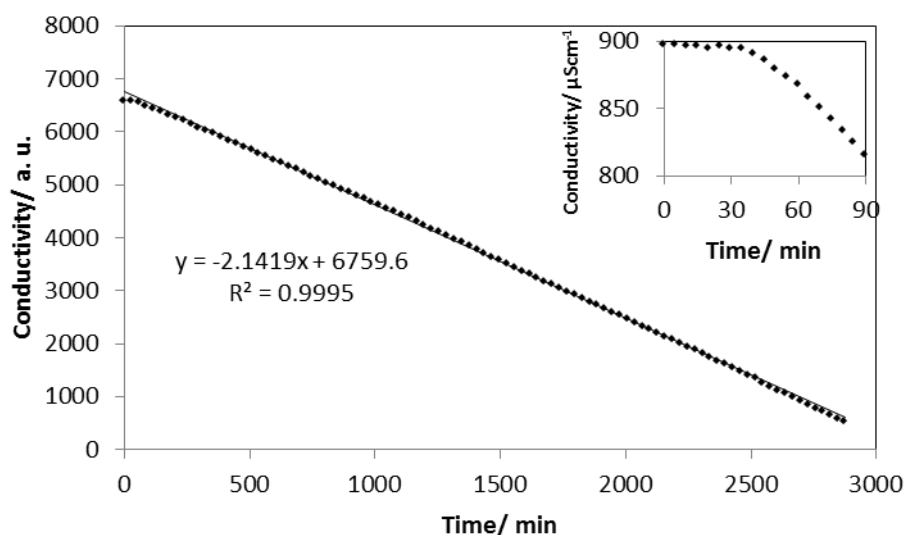


Figure 4.2-17: Extended reaction conductivity profile for $\text{Co}_3\text{Mo}_3\text{C}$ under 75 vol. % H_2 in N_2 at 500 °C for 48 h. The insert corresponds to the expanded induction period.

4.2.6.2 PXRD analysis

The pre- and post-reaction X-ray diffraction patterns of the $\text{Co}_3\text{Mo}_3\text{C}$ samples are presented in Figure 4.2-18A and B respectively. From the Figure 4.2-18 all XRD reflections of $\text{Co}_3\text{Mo}_3\text{C}$ are shifted to slightly higher 2θ angles upon reaction. This shift confirms the conversion of $\text{Co}_3\text{Mo}_3\text{C}$ to a material of composition close to $\text{Co}_3\text{Mo}_3\text{C}_x\text{N}_{1-x}$ which was previously reported by Xiao *et al.*¹¹⁰ The post-reaction carbon and nitrogen contents of the $\text{Co}_3\text{Mo}_3\text{C}$ material can be used to precisely determine if this material is in fact a carbonitride, which has been previously reported by Bussell *et al.*³⁹ as intermediate during analogous process to the carburisation of $\text{Co}_3\text{Mo}_3\text{N}$ using 20 vol. % CH_4 in H_2 . The chemical composition of post-reaction material is $\text{Co}_3\text{Mo}_3\text{C}_{0.13}\text{N}_{0.87}$ based on carbon (0.3 wt. %) and nitrogen (2.5 wt. %) elemental analysis results. The post-reaction carbon/ nitrogen content of the $\text{Co}_3\text{Mo}_3\text{C}_{0.13}\text{N}_{0.87}$ carbonitride material confirms the incomplete removal of carbon from the ternary carbide to the equivalent nitride.

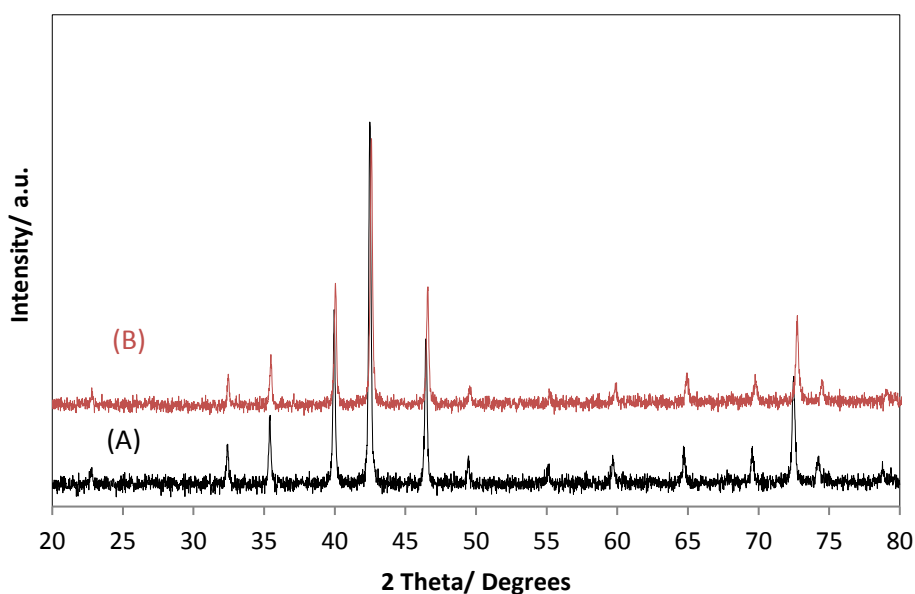


Figure 4.2-18: PXRD patterns for pre- and post- reaction $\text{Co}_3\text{Mo}_3\text{C}$ for A and B respectively.

4.2.6.3 SEM and TEM analyses

SEM analyses were performed to further study the microstructures of the materials. The typical SEM images at 4000 and 6000 magnification of the post-reaction $\text{Co}_3\text{Mo}_3\text{C}$ material are depicted in Figure 4.2-19. It can be seen that post-reaction $\text{Co}_3\text{Mo}_3\text{C}$ consists of aggregates of needles and that it still retains the precursor crystallite shape and size.

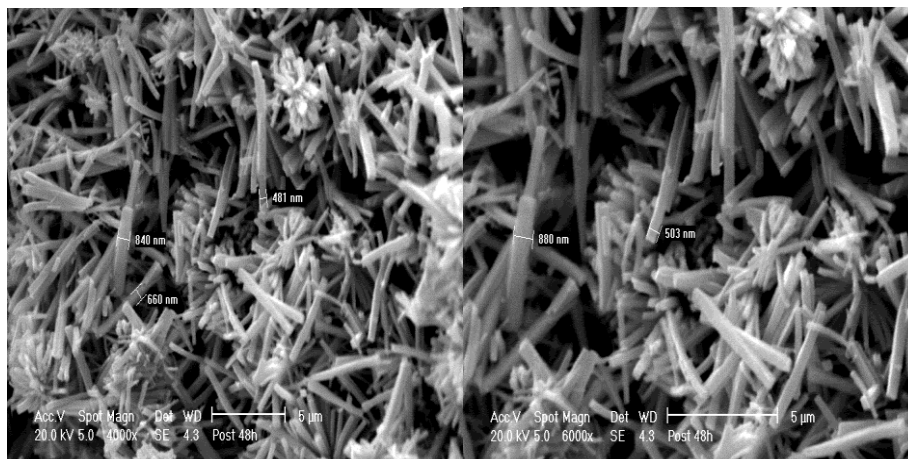


Figure 4.2-19: SEM images of the post-reaction of $\text{Co}_3\text{Mo}_3\text{C}$ reacted with 75 vol. % H_2 in N_2 under 500 °C and 48 h on stream.

As explained in the introduction, it is still uncertain whether the production of ammonia is due to a Mars van Krevelen mechanism in which lattice nitrogen may be active or whether performance can be attributed to the combination of the Co and Mo components having a close to optimal binding energy for N_2 . It is of interest therefore to prove to the extent in which the carbide materials exhibit related behaviour to their nitride counterparts. To this end, the reaction of lattice N in $\text{Co}_3\text{Mo}_3\text{N}$ with hydrogen has been previously investigated, where it was found that some NH_3 could be produced in the absence of gas-phase N_2 .^{59, 70} Recent computational modelling has indicated the occurrence of significant concentrations of surface N vacancies at the (111) surface of $\text{Co}_3\text{Mo}_3\text{N}$ under conditions of relevance to the ammonia synthesis reaction.¹⁰⁶ The current aim was to determine whether it is possible to use HRTEM to investigate and compare the (111) surface plane which expresses both Co and Mo in $\text{Co}_3\text{Mo}_3\text{N}$ and equivalent materials.

TEM was performed at the University of St. Andrews by Prof. Wuzong Zhou and Dr. Heather Greer, to estimate the particle size and d-spacing values of the pre- and post-reaction $\text{Co}_3\text{Mo}_3\text{C}$ material, HRTEM was carried out. Figure 4.2-20 shows the HRTEM micrographs of several nanoparticles on the surface of pre- and post-reaction $\text{Co}_3\text{Mo}_3\text{C}$. The highlighted neighbouring interlayer distance in Figure 4.2-20C for pre-reaction $\text{Co}_3\text{Mo}_3\text{C}$ and Figure 4.2-20 D for post-reaction $\text{Co}_3\text{Mo}_3\text{C}$ is less than 0.5 nm. Compared to previous studies for $\text{Co}_3\text{Mo}_3\text{N}^{111}$ and for $\text{Co}_3\text{Mo}_3\text{C}^{110}$, d-spacing values of 0.64, 0.39 nm and 0.25 nm respectively corresponding to the (111), (220) and (422) crystallographic planes are presented in Figure 4.2-20 A and B. The materials present passivation layers which make definitive identification of surface termination planes problematic, and so this approach could not be taken further.

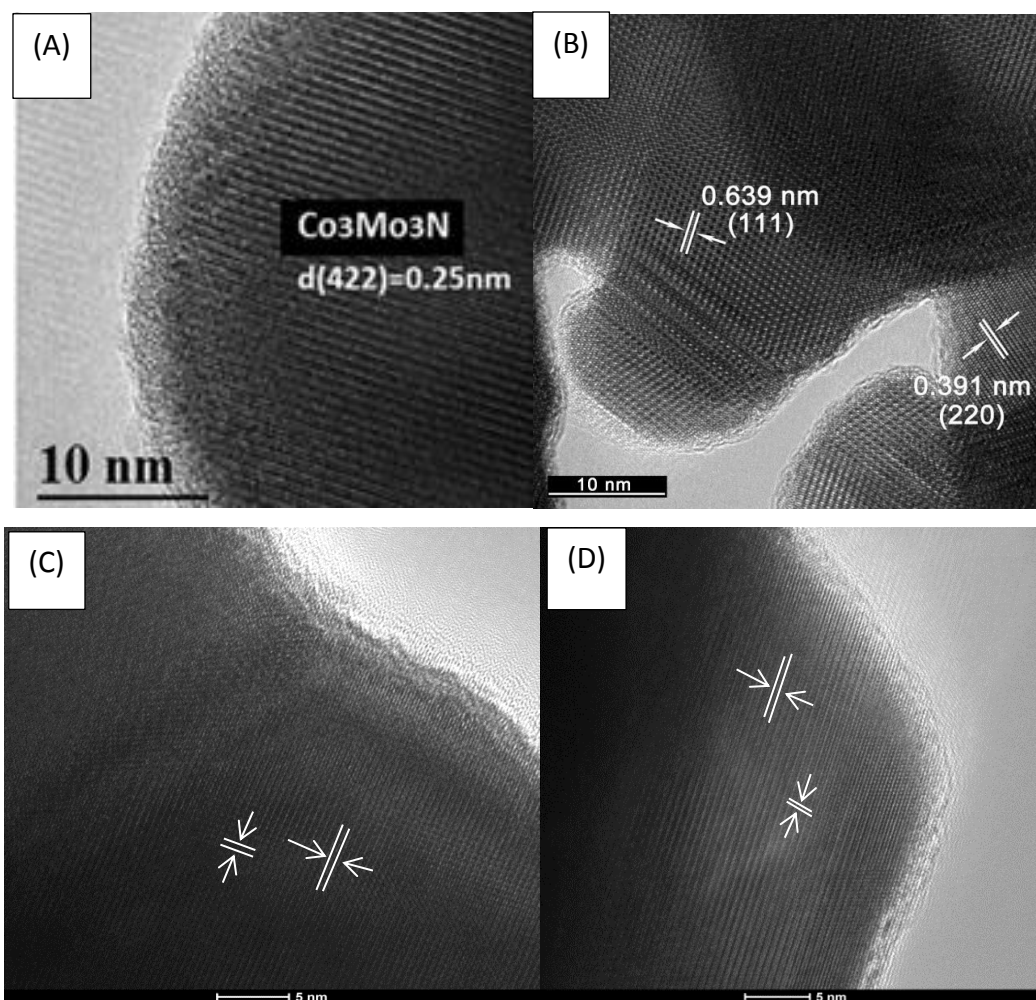


Figure 4.2-20: HRTEM micrograph (A) of as-prepared $\text{Co}_3\text{Mo}_3\text{N}^{111}$ (B) of as-prepared $\text{Co}_3\text{Mo}_3\text{C}^{110}$ (C) of pre-reaction $\text{Co}_3\text{Mo}_3\text{C}$ and (D) of post-reaction of $\text{Co}_3\text{Mo}_3\text{C}$ reacted with 75 vol. % H_2 in N_2 at 500 °C for 48 h.

4.2.6.4 Investigation of $\text{Co}_3\text{Mo}_3\text{C}$ materials for ammonia synthesis at different temperatures and times on stream

As mentioned before the ammonia synthesis reaction is exothermic and temperature dependent. Therefore, it is crucial to consider the activity of $\text{Co}_3\text{Mo}_3\text{C}$ under different temperature regimes. Using $\text{Co}_3\text{Mo}_3\text{C}$ and a 75 vol. % H_2 in N_2 gas feed different temperatures were studied and the results are presented in Figure 4.2-21. This material is essentially inactive for ammonia synthesis at 400 °C over 4 hours while at 500 °C within 2 hours the material is significantly more active ($403 \mu\text{molNH}_3 \text{ g}^{-1}\text{h}^{-1}$). At 600 °C within 1 hour a less sharp decay in conductivity was observed ($336 \mu\text{molNH}_3 \text{ g}^{-1}\text{h}^{-1}$). At 700 °C within 1 hour a much lower decay in conductivity was observed ($170 \mu\text{molNH}_3 \text{ g}^{-1}\text{h}^{-1}$). The probable explanation for the profile from 500 °C onwards is related the fact that the reaction is progressively becoming more thermodynamically limited as temperature is increased. Consequently, 500 °C has been found to be an optimal reaction temperature when applying $\text{Co}_3\text{Mo}_3\text{C}$ to ammonia synthesis. An understanding of the structure before and after activation may help elucidate the active material. In relation to this, as shown in Figure 4.2-22, when a 2 hour pre-treatment at 700 °C under 75 vol. % H_2 in N_2 is undertaken after which the $\text{Co}_3\text{Mo}_3\text{C}$ material can be anticipated to be nitrided, activity at 400 °C ($69 \mu\text{molNH}_3 \text{ g}^{-1}\text{h}^{-1}$) is apparent and the rate of reaction can be seen to be increased by further increase in reaction temperature to 500 °C ($449 \mu\text{molNH}_3 \text{ g}^{-1}\text{h}^{-1}$).

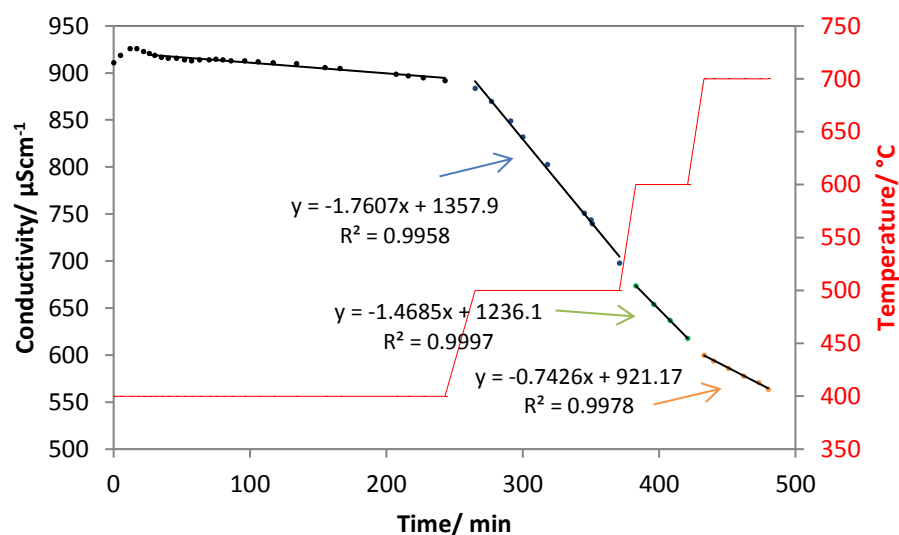


Figure 4.2-21: Reaction profile for $\text{Co}_3\text{Mo}_3\text{C}$ with 75 vol. % H_2 in N_2 under different temperatures and time on stream (400 °C, 4h), (500 °C, 2h), (600 °C, 1h), (700 °C, 1h).

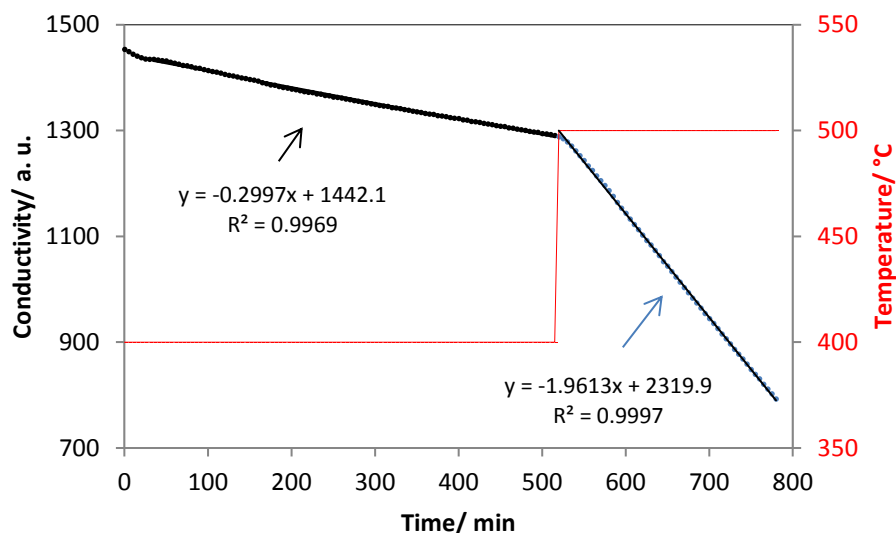


Figure 4.2-22: Extended reaction profile for $\text{Co}_3\text{Mo}_3\text{C}$ with 75 vol. % H_2 in N_2 under different temperatures and time on stream (400 °C, 8h), (500 °C, 4h) after pre-treatment for 2 hours at 700 °C.

4.2.6.5 Investigation of the induction period of the $\text{Co}_3\text{Mo}_3\text{C}$ material

An induction time, during which the activity “switched-on” was observed in the cases of CoMoO_4 and $\text{Co}_3\text{Mo}_3\text{C}$ for ammonia synthesis. This implies that the materials might undergo structural/surface changes that lead to the formation of active phases. Consequently, this aspect was further investigated for $\text{Co}_3\text{Mo}_3\text{C}$ using PND, PXRD and CHN analysis.

a) PND analysis

As explained in Chapter 3, Figure 3.2-80 (on page 104) presents selected *in-situ* neutron diffraction patterns collected at different temperatures and at 500 °C at different reaction times for the $\text{Co}_3\text{Mo}_3\text{C}$ material. All the patterns were analysed by the Rietveld method using the η -6 $\text{Co}_3\text{Mo}_3\text{C}$ structure as the starting model. The evolution of the lattice parameter during the different stages of reaction is presented in Figure 3.2-82 which can be found on page 106.

When increasing the temperature to 500 °C, a linear change of lattice parameter as a function of temperature was generally observed. This can be attributed to thermal expansion of the lattice. However, a change in the slope was detected at temperatures

ranging between 400 and 500 °C, which could relate to structural transformation. At 500 °C no variation of the lattice parameters was observed within the first 10 minutes of reaction. Thereafter, a gradual contraction of the lattice with reaction time was detected. In addition to lattice parameter determination, the evolution of the C/N occupancy at the 16c Wyckoff lattice site as a function of reaction time at 500 °C is presented Figure 3.2-83 which can be found on page 106. Gradual substitution of carbon with nitrogen under reaction conditions is evident.

Following 2 h of reaction at 500 °C, the sample temperature was decreased to room temperature under the same reaction atmosphere and a long neutron diffraction run was then performed. Initially, an attempt was made to refine the structure to the $\text{Co}_3\text{Mo}_3\text{C}$ model for this sample; however, the atomic displacement parameters were unrealistic. Instead a very good agreement was obtained when the structure was refined against the $\text{Co}_3\text{Mo}_3\text{N}$ reference (Figure 3.2-84 and Table 3.2-25, page 107). The lattice constants derived from Rietveld refinement of the neutron diffraction data was found to be $a = 11.0370(3) \text{ \AA}$, falling between the lattice parameter observed for $\text{Co}_3\text{Mo}_3\text{C}$ ($a = 11.0591(4)$) and $\text{Co}_3\text{Mo}_3\text{N}$ ($a = 11.0260(9)$) as presented in Table 3.2-13 and 3.2-3 respectively. An estimated chemical composition of $\text{Co}_3\text{Mo}_3\text{C}_{0.38}\text{N}_{0.62}$ was calculated applying Vegard's law. This was further confirmed by elemental analysis. Furthermore, refining the C/N mixing in the 16c Wyckoff lattice leads to a ratio of 0.33(5)/0.66(4), again similar to the composition estimated using Vegard's Law, revealing a significant carbon substitution by nitrogen during ammonia synthesis (Table 3.2-25, page 107).

b) PXRD analysis

Ex-situ experiments were performed at 500 °C and different times on stream to investigate the induction period and possible intermediate phases formed when the ternary carbide material undergoes transformation to the equivalent nitride material during the ammonia synthesis reaction. The pre- and post-reaction XRD patterns of $\text{Co}_3\text{Mo}_3\text{C}$ samples after reaction with 75 vol. % H_2 in N_2 at 500 °C stopped at 0, 1, 2, 3 and 4 hours on stream are presented in Figure 4.2-27 A $\text{Co}_3\text{Mo}_3\text{C}$ as prepared material, B (500, 0), C (500, 1h), D (500, 2h), E (500, 3h), F (500, 4h) respectively. All the diffraction patterns showed features attributable to the $\text{Co}_3\text{Mo}_3\text{C}$ structure without any extra-phases being present with a gradual shift to higher 2θ . The selected post-reaction PXRD analysis conducted after 3h of

reaction (Figure 3.2-77E, page 89), this shift from 42.4 to 42.5° confirms the conversion of $\text{Co}_3\text{Mo}_3\text{C}$ to a material of composition close to $\text{Co}_3\text{Mo}_3\text{C}_{0.56}\text{N}_{0.47}$ (42.5°). Moreover, to ascertain the evolution of the chemical composition of the $\text{Co}_3\text{Mo}_3\text{C}$ during ammonia synthesis reaction at 500 °C, elemental analysis of post-reaction material was conducted after different times on stream (Figure 4.2-23). The gradual substitution of carbon with nitrogen was observed and close to complete carbon substitution occurred after 48h of reaction (0.3 wt. % C and 2.5 wt. % N) as prior mentioned in section 4.2.7.2. This result confirmed that the material was converted to a carbonitride as intermediate single phase $\text{Co}_3\text{Mo}_3\text{C}_x\text{N}_{1-x}$.

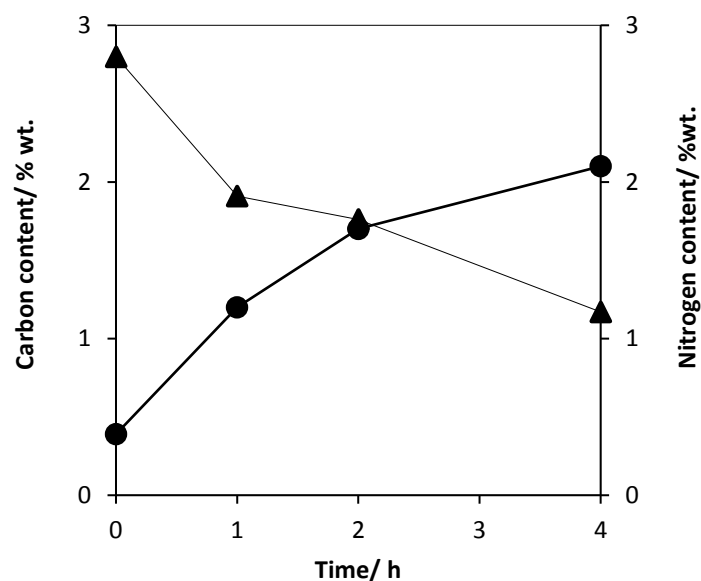


Figure 4.2-23: Evolution of the $\text{Co}_3\text{Mo}_3\text{C}$ chemical composition after different reaction time with 60 ml min^{-1} of 75 vol. % H_2 in N_2 (BOC, 99.98%) at 500 °C. (\blacktriangle) fractional carbon content and (\bullet) fractional nitrogen content as determined by elemental analysis. The first data point corresponds to a material which was immediately cooled under the reaction flow upon attaining 500 °C.

c) SEM analyses

SEM images of pre- and post-reaction $\text{Co}_3\text{Mo}_3\text{C}$ reacted with 75 vol. % H_2 in N_2 under 500 °C stopped at 0, 1, 2, 3 and 4 h on stream are presented (labelled as A, B, C, D, E and F respectively). Post-reaction SEM analysis demonstrated that the morphology was unaffected by reaction (Figure 4.2-24). All samples are pseudomorphic with the precursor. It can be seen that the morphologies of all samples appears to consist of aggregates and it still retains its precursor shape and size of the crystallites.

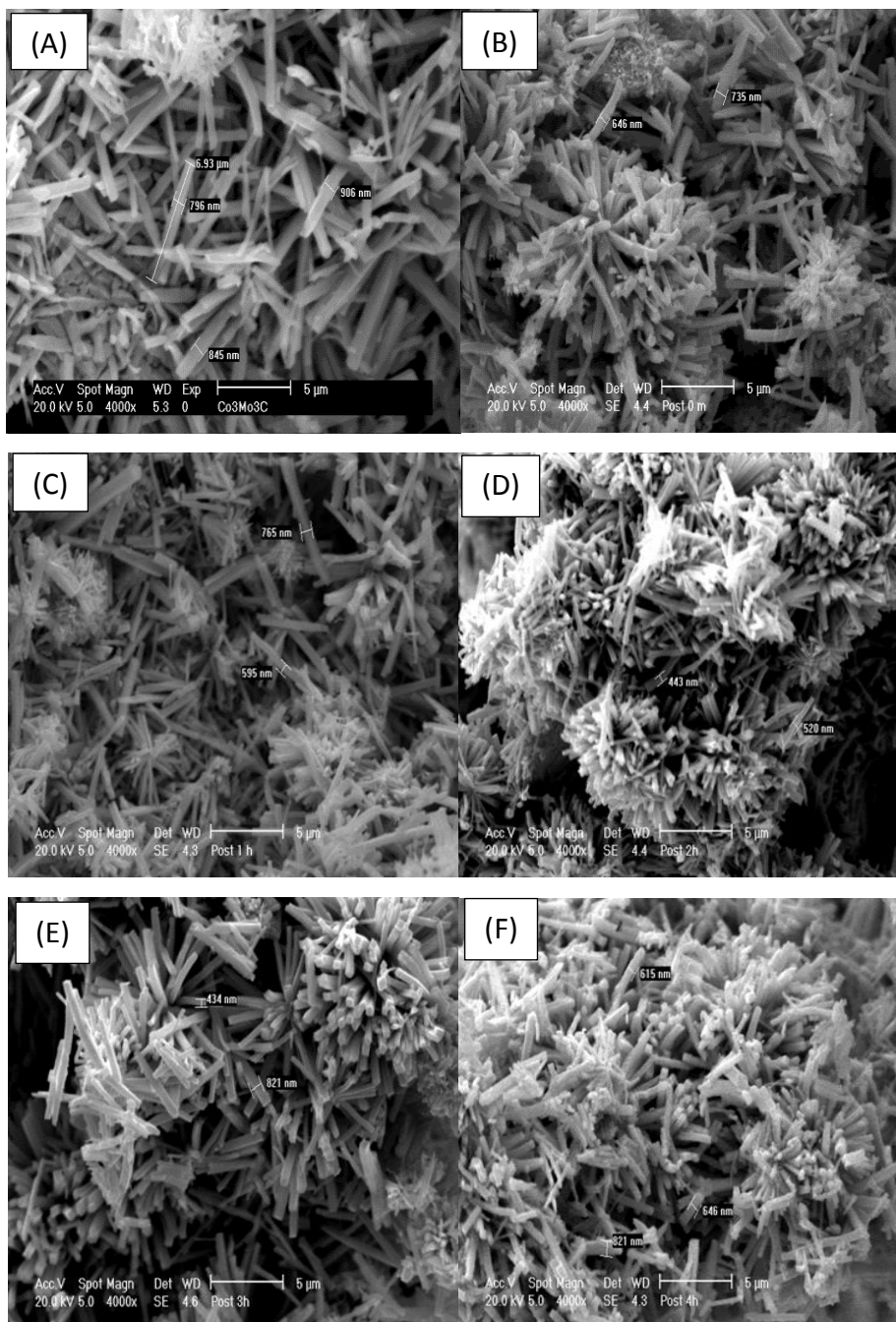


Figure 4.2-24: SEM images of pre- and post-reaction $\text{Co}_3\text{Mo}_3\text{C}$ reacted with 75 vol. % H_2 in N_2 under 500 °C stopped at 0, 1, 2, 3 and 4 h on stream (labelled as A, B, C, D, E and F respectively).

4.2.7 Cobalt molybdenum carbide (η -12 $\text{Co}_6\text{Mo}_6\text{C}$)

$\text{Co}_6\text{Mo}_6\text{C}$ was investigated for ammonia synthesis at 500 °C under 75 vol. % H_2 in N_2 for 48 hours and the post-reaction material was characterized using PXRD, SEM and CHN analysis as discussed in more detail below. The material was inactive at 400 °C.

4.2.7.1 Conductivity

The conductivity versus time on stream plots for the reaction of $\text{Co}_6\text{Mo}_6\text{C}$ under 75 vol. % H_2 in N_2 at 500 °C and ambient pressure for 48 hours is shown in Figure 4.2-25. It is evident that 500 °C gives an inactive material for ammonia synthesis since the overall change in conductivity is minimal and can be explained by thermal fluctuations in the laboratory.

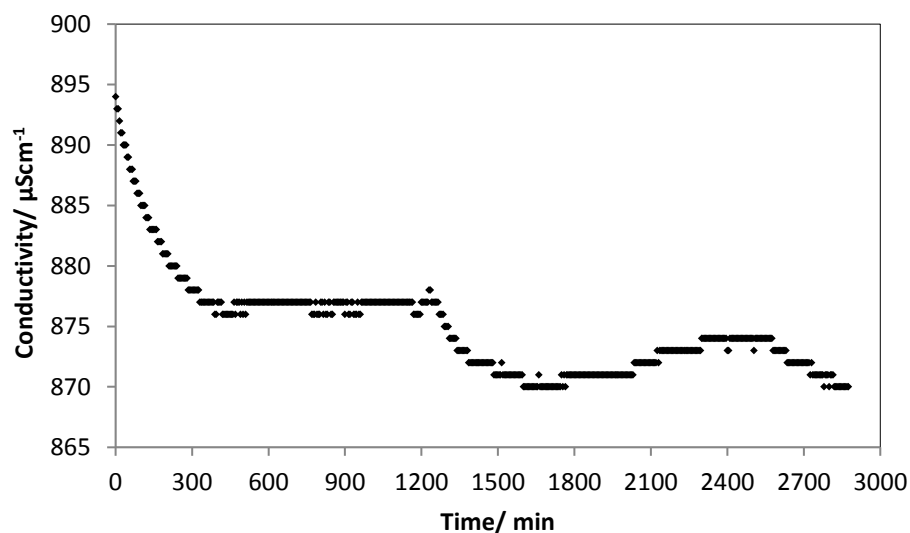


Figure 4.2-25: Reaction conductivity profile for $\text{Co}_6\text{Mo}_6\text{C}$ under 75 vol. % H_2 in N_2 at 500 °C for 48 h.

4.2.7.2 PXRD analysis

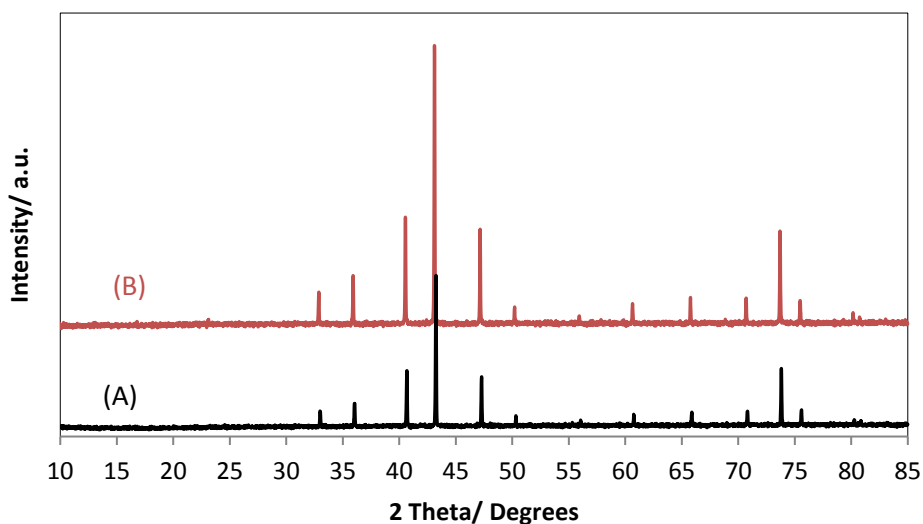


Figure 4.2-26: PXRD patterns for the pre and post-reaction $\text{Co}_6\text{Mo}_6\text{C}$ for A and B respectively.

The pre- and post-reaction X-ray diffraction patterns of the $\text{Co}_6\text{Mo}_6\text{C}$ samples are presented in Figure 4.2-26 A and B respectively. All diffraction patterns of the pre-reaction $\text{Co}_6\text{Mo}_6\text{C}$ sample in Figure A show the same characteristic reflections in B. Furthermore, the post-reaction microanalysis shows there is no change in the carbon content upon the reaction time being 1.3 wt. %.

In contrast to the $\text{Co}_3\text{Mo}_3\text{C}$, elemental analysis did not reveal any nitrogen insertion in the structure of $\text{Co}_6\text{Mo}_6\text{C}$ after the ammonia synthesis reaction test. To probe the possibility that the low surface area of $\text{Co}_6\text{Mo}_6\text{C}$ (ca. $3 \text{ m}^2 \text{ g}^{-1}$) was responsible for the limited incorporation of lattice N, the material was kept under reaction conditions for 48h. However, the material continued to be inactive with no nitrogen incorporation was observed and the resultant phase observed by PXRD corresponded to that expected for $\text{Co}_6\text{Mo}_6\text{C}$. The stability of the $\text{Co}_6\text{Mo}_6\text{C}$ phase during ammonia synthesis reaction might explain the inactivity of this material for ammonia generation, and the development of activity might be associated with the formation of an active nitride or carbonitride phase.

4.2.7.3 SEM analyses

Figure 4.2-27 shows representative SEM micrographs for the post-reaction $\text{Co}_6\text{Mo}_6\text{C}$ material. The SEM images for post-reaction $\text{Co}_6\text{Mo}_6\text{C}$ sample show a broadly similar morphology to that of the pre-reaction $\text{Co}_6\text{Mo}_6\text{C}$. It can be seen that the morphology of the post-reaction $\text{Co}_6\text{Mo}_6\text{C}$ appears to consist of aggregates of needles and it still retains its precursor morphology.

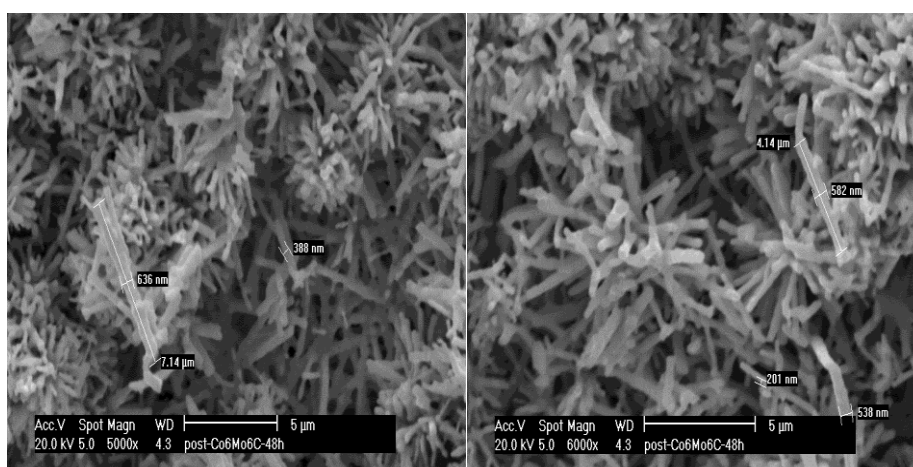


Figure 4.2-27: Typical SEM images of the post-reaction of $\text{Co}_6\text{Mo}_6\text{C}$ reacted with 75 vol. % H_2 in N_2 under 500 °C and 48 h on stream.

Comparison between $\text{Co}_3\text{Mo}_3\text{N}$, $\text{Co}_3\text{Mo}_3\text{C}$, $\text{Co}_6\text{Mo}_6\text{C}$, CoMoO_4 for ammonia synthesis

The role of the lattice nitrogen in the catalytic activity was studied by comparing the results of dehydrated CoMoO_4 , $\text{Co}_3\text{Mo}_3\text{C}$ and $\text{Co}_6\text{Mo}_6\text{C}$ for ammonia synthesis to the well-established activity of the $\text{Co}_3\text{Mo}_3\text{N}$ system. Figure 4.2-28 shows the evolution of ammonia at 500 °C as a function of time under an atmosphere of 75 vol. % H_2 in N_2 (BOC, 99.98 %) at a total gas feed of 60 ml min^{-1} . As expected, the $\text{Co}_3\text{Mo}_3\text{N}$ system was found to be highly active for ammonia synthesis at ambient pressure exhibiting a rate of $489 \pm 17 \mu\text{molNH}_3\text{g}^{-1}\text{h}^{-1}$ which can be compared to ca. $690 \mu\text{molNH}_3\text{g}^{-1}\text{h}^{-1}$ which would correspond to the thermodynamically limited yield of 0.129 %. Under the same reaction conditions, the $\text{Co}_3\text{Mo}_3\text{C}$ system displayed a comparable activity to $\text{Co}_3\text{Mo}_3\text{N}$ ($461 \pm 17 \mu\text{molNH}_3\text{g}^{-1}\text{h}^{-1}$). However, this was only exhibited after an induction time of ca. 40 minutes, during which the material demonstrated very poor activity, and beyond which the material exhibited steady state performance during 48 h of reaction with no sign of deactivation. It's noteworthy that $\text{Co}_3\text{Mo}_3\text{C}$ was found to be inactive at 400 °C, a temperature at which $\text{Co}_3\text{Mo}_3\text{N}$ is known to be highly active.¹⁰⁸ Similar general behaviour for $\text{Co}_3\text{Mo}_3\text{C}$ was found in dehydrated CoMoO_4 although with a longer induction period time and lower ammonia synthesis rate. In the case of $\text{Co}_6\text{Mo}_6\text{C}$, the material was found to be inactive at 500 °C even upon extended times on stream.

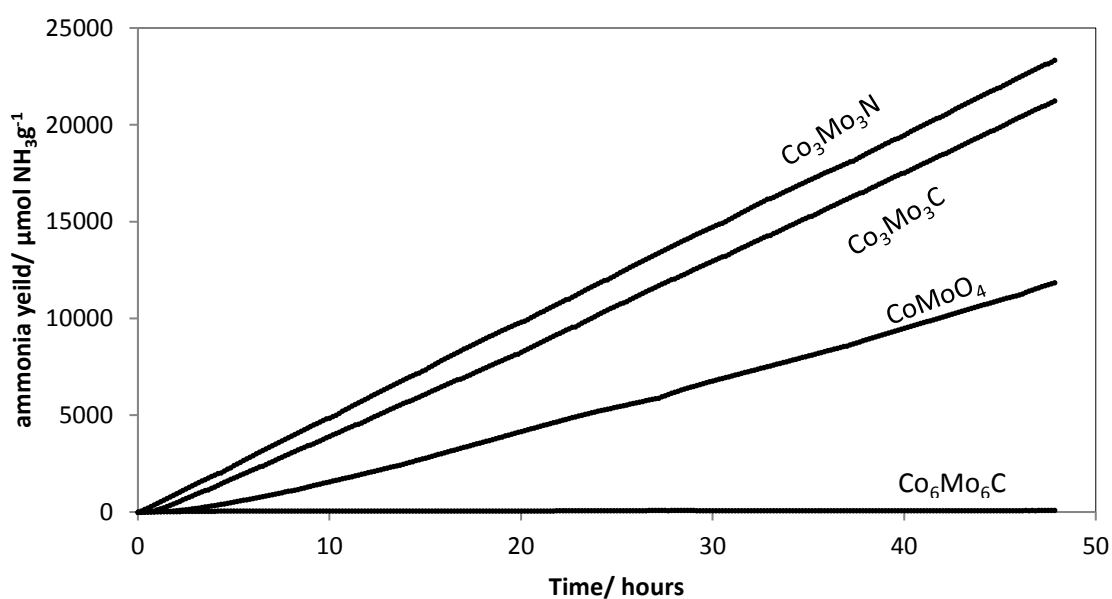


Figure 4.2-28: The rates of ammonia synthesis of CoMoO_4 , $\text{Co}_3\text{Mo}_3\text{N}$, $\text{Co}_3\text{Mo}_3\text{C}$, $\text{Co}_6\text{Mo}_6\text{C}$ at 500 °C for 48 h.

When considered in the context of their related structures, it is interesting to make direct comparisons between performance of the nitride and the two carbide materials. According to literature, the efficacy of $\text{Co}_3\text{Mo}_3\text{N}$ for ammonia synthesis has been attributed to the combination of the Co and Mo components having a close to optimal binding energy for N_2 .¹⁰⁴ In this model, it has been proposed that the active crystallographic face of the material is the (111) termination plane which expresses both Co and Mo. It was also proposed that the interstitial nitrogen is not active in itself but instead maintains the required crystallographic ordering. Alternatively, it has been proposed by others $\text{Co}_3\text{Mo}_3\text{N}$ might operate via Mars-van Krevelen mechanism in which the catalytic lattice nitrogen is hydrogenated to yield NH_3 and a lattice vacancy. This vacancy is subsequently replenished from N_2 with further hydrogenation of the resultant lattice N species continuing the catalytic cycle. There have been both experimental and modelling based studies which support this viewpoint.^{4, 37, 58-59, 70, 105-107} In the current study it is noted that, unlike $\text{Co}_3\text{Mo}_3\text{N}$, both carbides are inactive at 400 °C. In fact, $\text{Co}_6\text{Mo}_6\text{C}$ does not demonstrate any detectable activity under any of the conditions tested. Structure-sensitivity, which arises from the suggestion of the (111) surface plane being predicted to be the active termination plane, has yet to be experimentally demonstrated in the $\text{Co}_3\text{Mo}_3\text{N}$ system; in the current investigation the SEM studies indicate the gross morphology to be similar for all the materials tested. On this basis, there is strong evidence that the influence of difference in morphology can be discounted as the origin of the observed difference in performance and that rather it is the difference in composition between $\text{Co}_3\text{Mo}_3\text{N}$ and $\text{Co}_3\text{Mo}_3\text{C}$ that might be determining. Indeed, it is the case that the lag period associated with the development of activity in the case of the carbide corresponds to the further replacement of lattice C with N. This would be consistent with the operation of a Mars-van Krevelen mechanism in which the presence of lattice nitrogen has to be present for ammonia synthesis to occur once a critical population of lattice N was established. However, a degree of caution is necessary in drawing this tentative conclusion since it has yet to be established whether there is a complicating role of *in-situ* removal of the passivation layer⁷⁶ during reaction which could conceivably occur to different extents for the two materials, and also it has yet to be definitively established whether the nitridation of the carbide lattice precedes ammonia synthesis or indeed results from it. It is, however, noteworthy that upon attaining 500 °C under the reaction mixture, the lattice partially nitrides (the nitrogen content for a sample cooled under the mixture immediately upon attaining 500 °C was ~0.4 wt. %) which suggests that a critical degree of N incorporation into the material may be required for the

development of activity, since at this stage the material does not apparently produce detectable quantities of ammonia. It is also noteworthy that beyond the induction period, given the steady state nature of the reaction, the performance of the material does not further change with increasing lattice nitrogen content thereby demonstrating that $\text{Co}_3\text{Mo}_3\text{N}$ (as evident after 48 h on stream) and the intermediate carbonitride materials exhibit equivalent performance. In the case of $\text{Co}_3\text{Mo}_3\text{C}$ which develops activity as a function of time and $\text{Co}_6\text{Mo}_6\text{C}$ which does not produce ammonia or nitride even on prolonged reaction, the effect of the passivation layer would be expected to be less of a consideration due to the close chemical similarity of the materials. On this basis, it seems that the subtle difference in crystallography with the former material containing twice the carbon content of the latter and in a different crystallographic site (i.e. the 16c Wyckoff site as opposed to the 8a site) is determining. In this respect, it is interesting to note the comparative enhanced stability of carbides with respect to nitrides, with the latter being in general much more reactive to, for example, water as well as oxygen. Previous work involving the reaction of $\text{Co}_6\text{Mo}_6\text{N}$ with nitrogen containing feeds has shown the replenishment and relocation of lattice nitrogen resulting in the formation of $\text{Co}_3\text{Mo}_3\text{N}$. It appears that even with a potentially reactive N_2/H_2 source under conditions known to rapidly replenish the $\text{Co}_6\text{Mo}_6\text{N}$ system, the corresponding carbide is much less reactive and no analogous phase transformation occurs.

The observations reported in this chapter demonstrate that ammonia synthesis is associated with the presence of N in the 16c Wyckoff crystallographic site. Whether the origin of the activity is associated directly with the presence of this specific species or whether its presence is the result of secondary nitridation originating from the formation of ammonia has yet to be definitively established. It is also of interest that intermediate carbonitride phases do not exhibit substantially different performance from the $\text{Co}_3\text{Mo}_3\text{N}$ phases which is ultimately produced. This might be indicative of the fact that it is only a minority of the 16c lattice N, possibly in the near surface region, which participates in reaction. In the case of $\text{Co}_6\text{Mo}_6\text{C}$, the C in the 8a site seems much less reactive compared to the 16c site. This observation is to a degree consistent with the fact that upon reduction $\text{Co}_3\text{Mo}_3\text{N}$ stops at $\text{Co}_6\text{Mo}_6\text{N}$. However, unlike $\text{Co}_6\text{Mo}_6\text{N}$,⁸¹ $\text{Co}_6\text{Mo}_6\text{C}$ does not readily transform to $\text{Co}_3\text{Mo}_3\text{N}$ under the reaction conditions employed in this study.

4.3 Conclusion

This chapter is the first investigation of ammonia synthesis over γ -Mo₂N, β -Mo₂C and α -Mo₂C using 75 vol. % H₂ in N₂ at 500 °C. The order of ammonia synthesis activity was α -Mo₂C ($299 \pm 8 \mu\text{molNH}_3 \text{ g}^{-1}\text{h}^{-1}$) > γ -Mo₂N ($195 \pm 7 \mu\text{molNH}_3 \text{ g}^{-1}\text{h}^{-1}$) > β -Mo₂C ($123 \pm 8 \mu\text{molNH}_3 \text{ g}^{-1}\text{h}^{-1}$). This activity was only showed after an induction time of ca. 40 minutes for α -Mo₂C and 30 minutes for β -Mo₂C, however beyond the induction time, the materials demonstrated a steady state performance during 4 h of reaction with no sign of deactivation. γ -Mo₂N and β -Mo₂C were stable under reaction conditions whereas α -Mo₂C was transformed to carbonitride phase.

Also in this chapter, the effect of composition upon the reactivity of dehydrated CoMoO₄, Co₃Mo₃N, Co₃Mo₃C and Co₆Mo₆C for ammonia synthesis has been investigated. Despite the isostructural nature of Co₃Mo₃N and Co₃Mo₃C in particular, a significant difference in performance was evident. Co₆Mo₆C, which has a closely related structure to the Co₃Mo₃N and Co₃Mo₃C materials, was found to be inactive for ammonia synthesis under the conditions tested while an induction period time of 100 minutes for dehydrated CoMoO₄ and 40 minutes for Co₃Mo₃C were observed prior to the materials developing any activity. In the case of Co₃Mo₃C, *in-situ* PND and post-reaction analysis revealed the substitution of carbon by nitrogen is initiated during the induction time and continues during the reaction until complete conversion of the carbide to nitride. These results are consistent with the proposal of the origin of the high activity of the Co₃Mo₃N materials being the reactivity of its lattice nitrogen via a Mars-van Krevelen mechanism.

Chapter 5. Cracking of methane

5.1 Introduction

Environmental challenges rising from the current patterns of energy production and consumption have spurred the development of clean energy sources. The actual mode of energy production relies heavily on fossil fuels by the burning of natural gas (NG), oil and coal for heating, transportation and electricity production, resulting in a significant release of greenhouse-gas.¹¹² In this context, hydrogen has been studied extensively as a suitable clean energy carrier which can be produced from any primary energy source and used efficiently in fuel cells without any harmful emissions. Furthermore, hydrogen can also be used for the production of various high value chemicals such as methanol, ethanol and other products of industrial interest.¹¹³ However, hydrogen is presently produced by steam reforming and partial oxidation of methane resulting in the co-formation of CO and CO₂. However, for PEM fuel cell applications, even very low amounts of carbon monoxide can lead to rapid degradation of performance. As a potential alternative to these processes, catalytic decomposition of methane ($\text{CH}_4 \rightarrow \text{C} + 2\text{H}_2$) is a direct method of CO_x-free hydrogen production and valuable carbon structures such as nanofibers (CNFs) or nanotubes (CNTs) are produced as co-products.¹¹⁴ Consequently, there has recently been much effort to develop alternative catalysts for CO_x-free hydrogen production.

5.1.1 Hydrogen production

Hydrogen can be produced by different industrial processes such as steam reforming, partial oxidation or dry reforming of natural gas and biomass, and coal gasification. It can also be produced by electrolysis of water. Currently, hydrogen is predominantly produced from fossil fuels (96%) by conventional processes with 48% of H₂ being produced by steam reforming of methane, 18% by coal gasification and 30% by partial oxidation in oil refineries resulting in substantial greenhouse gas emissions.¹¹⁵ Therefore, the direct non-oxidative methane conversion method is an elegant route for CO-free H₂ generation that can meet the requirement of strict greenhouse gas emission legislation. In this approach, H₂ production is accompanied with carbon deposition that can be subsequently valorised for higher hydrocarbon production for example.¹¹⁵⁻¹¹⁶ In this chapter, the use of non-oxidic based catalysts such as cobalt molybdenum nitrides and carbides are investigated as alternative catalysts for direct non-oxidative thermo-catalytic methane cracking.

Information regarding the textural and structural as well as the catalytic properties of these materials is presented.

5.1.1.1 Hydrogen formation from methane

Methane is the simplest and most stable hydrocarbon molecule. It has the highest H/C ratio. Its conversion into higher value chemicals has been extensively studied both in gas-phase homogeneous routes and routes involving heterogeneous catalysis.¹¹⁷

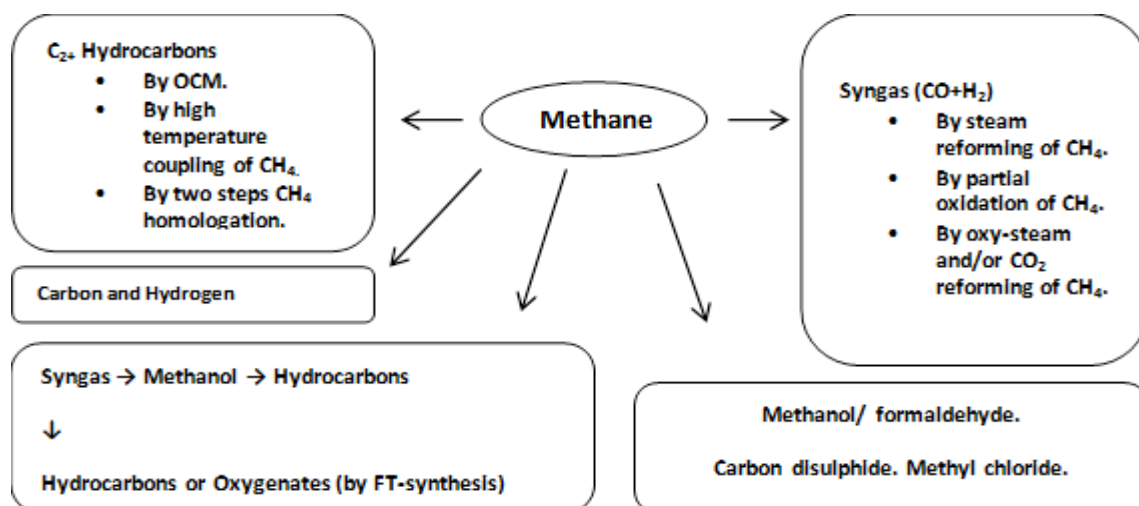
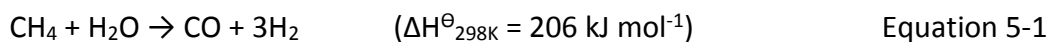


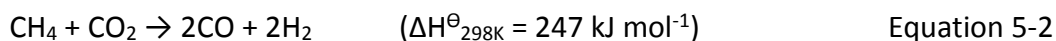
Figure 5.1-1: Schematic representation of various methods of activating methane.¹¹⁸

Over the past several decades, a significant research effort has been directed towards methane activation. The conversion of methane into hydrocarbons can be accomplished through either direct or indirect routes as depicted in Figure 5.1-1. The indirect methane conversion method involves the generation of hydrocarbons via intermediates formed from methane reacting with carbon dioxide, steam and oxygen, whilst the direct methane conversion method involves the generation of hydrocarbons from the coupling of methane under either oxidative or non-oxidative conditions (including high-temperature coupling and low-temperature two-step homologation) or partial oxidation to yield methanol and/or formaldehyde.¹¹⁸⁻¹¹⁹

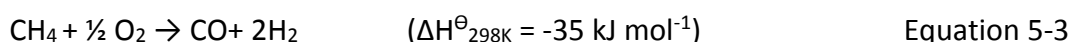
The most common process for methane activation for hydrogen generation is steam reforming (SMR). In this process, methane reacts with steam in the presence of a catalyst to produce hydrogen and carbon monoxide (Eq. 1).¹¹⁹



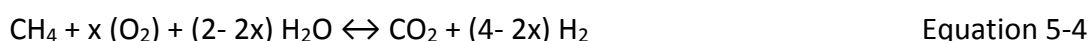
Dry reforming (DRM) of methane to produce syngas using carbon dioxide is also an important reaction. This reaction (Eq. 2) is extremely endothermic; and hence it requires high temperature to achieve suitable equilibrium transformations to syngas.¹²⁰⁻¹²¹



If only hydrogen is required, CO production from these processes is undesirable and has to be converted into CO₂ by the water gas shift reaction in subsequent processing causing additional costs in purification and separation systems and contributing to the overall cost of production, although this does provide a means of producing additional H₂ from H₂O indirectly. Furthermore, these processes require a large energy input. By contrast, partial oxidation (POM)(Eq. 3) which is exothermic is perhaps a more preferable route for hydrogen generation.¹²² With this approach, synthesis gas produced can be converted into hydrocarbons using a low-temperature exothermal process.



Autothermal reforming (ATR) is an alternative route for hydrogen generation based on the combination of both steam reforming and partial oxidation (Eq. 4).¹²³ It has a major advantage over classical reforming routes in terms of energy requirements due to the combination of endothermic steam reforming and exothermic methane oxidation. This reaction occurs in two simultaneous stages by feeding the fuel together with an air or oxygen feed and steam over the catalyst bed to produce syngas. However, autothermal reforming is an environmentally unattractive option for hydrogen production because it's accompanied with feed contamination such as CO₂ which is potentially harmful to the environment.¹²⁴



In this context, the non-oxidative, low-temperature homologation of methane has been proposed as an alternative to the oxidative coupling of methane (OCM).⁴² The process has been reported by van Santen's⁴³ and Amariglio's⁴⁴ research groups independently as a two-

step reaction designed to avoid deep oxidation of methane to CO and CO₂ (further details are presented in section 3.1.5).

In the approach investigated within the present chapter, the methane is decomposed into carbon and hydrogen in the presence of a catalyst and in the absence of oxygen as shown in Eq. 5.



Non-catalytic methane cracking at high temperature is not economical for commercial production of hydrogen. Thus, the use of a catalyst is essential to decrease the high temperature required for methane thermal cracking as illustrated in Figure 5.1-2. The catalytic methane cracking process^{115-116, 125-126} is a moderately endothermic process; the thermal energy demand per mole of hydrogen formed is only 37.8 kJ per mole of H₂ compared to 63 kJ per mole of H₂ for steam methane reforming.¹²⁷ This process does not produce CO or CO₂ in large amounts and as a consequence the overall process is simplified, as there is no requirement for any further purification as it is the case in the conventional hydrogen production methods (e.g., SMR, coal gasification and POM).

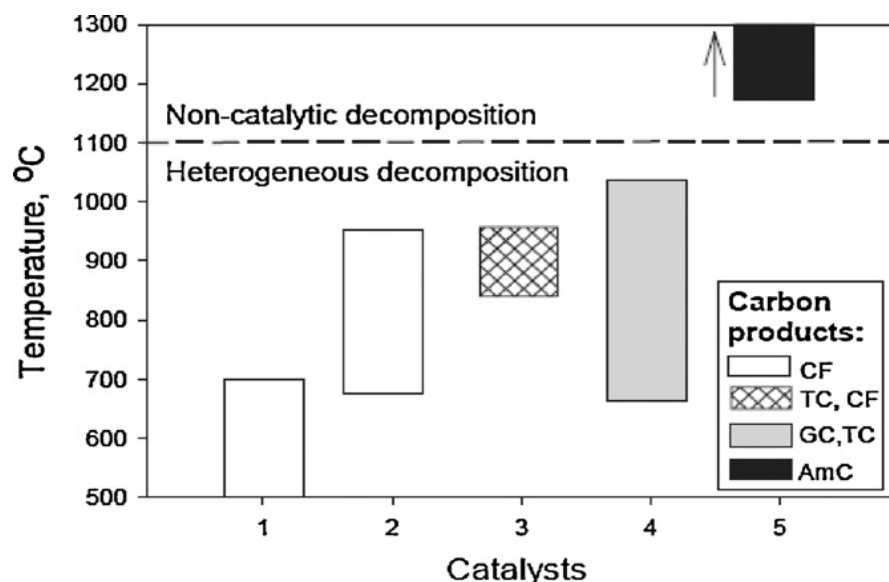


Figure 5.1-2: Graphical representation of the bulk of literature data on catalysts, preferred temperature range and carbon products related to catalytic methane decomposition reaction. Catalysts: 1—Ni-based, 2—Fe-based, 3—carbon-based, 4—summary of data related to Co, Ni, Fe, Pd, Pt, Cr, Ru, Mo, W catalysts, 5—non-catalytic decomposition. Carbon products: CF—carbon filaments, TC—turbostratic carbon, GC—graphitic carbon, AmC—amorphous carbon.¹²⁷

Furthermore, it is possible to decrease the cost of hydrogen production in such a route by valorising the carbon co-produced during the process. Depending upon the reaction conditions and the catalyst used, carbon nanotubes (CNTs) and carbon nanofibers (CNFs) with suitable chemical and physical properties such as high mechanical strength, high surface area, and high electrical conductivity can be formed and can be of potential interest in a number of technological applications such as adsorbents, catalysts and catalyst supports.¹²⁷ Several factors affecting the efficiency of the process such as the activity of catalysts, support type, promoters, synthesis methods, carbon products, reaction conditions (temperature, flow rate of methane), deactivation and regeneration of catalysts have been discussed in the literature.

Catalysts for catalytic methane cracking

Different transition metals such as cobalt, iron and nickel have been reported to be active for the catalytic cracking of methane. It has been demonstrated that the methane decomposition activity for transition metals follows the order: Co, Ru, Ni, Rh > Pt, Re, Ir > Pd, Cu, W, Fe, Mo.¹¹² Amongst the studied systems, Ni is the most intensively investigated catalyst due to his high activity and carbon yield. Co-based catalysts have been reported to exhibit lower catalytic activity compared to nickel based catalysts¹²⁸ and present higher price and higher toxicity.¹²⁹ Several supports have been used to enhance the activity of nickel including TiO₂, SiO₂, MgO, ZrO₂ and Al₂O₃. SiO₂ gives the best carbon yield.¹³⁰ Koerts *et al.* reported that Ni and Fe presented higher activity when supported on Al₂O₃.⁴³ In recent work by Hargreaves *et al.*, the activity of two waste iron-containing materials was reported, which were found to generate H₂, CO_x and carbon (both filaments and encapsulating graphite) during reaction at 800 °C using a 3:1 CH₄:N₂ feed.¹³¹ Methane decomposition into H₂ and C was investigated over Fe₂O₃/Al₂O₃ and Fe₂O₃/SiO₂ at 800 °C by Takenaka and co-workers.¹³²

The design of novel highly efficient materials for catalytic reactions has been a focus of research in recent years. Although most of the materials studied in heterogeneous catalysis are metal and metal oxide based, attention has been directed recently towards the development of entirely novel catalyst families that could display higher catalytic activities and selectivities and better thermal stabilities (e.g. carbides, nitrides etc.).^{58, 76, 133} Amongst these materials, carbides have attracted much attention due to their behaviour being

related to that of precious metals. The presence of interstitial carbon species has been argued to modify the catalytic properties of the parent metal, hence resulting in the modified electronic properties of carbides.¹³⁴

The exceptional catalytic properties of carbides has motivated high interest for these materials as replacements for precious metal catalysts in a variety of reactions. Carbides have been proved to be viable catalysts for applications including the Fischer-Tropsch process,¹³⁵⁻¹³⁷ hydrogenation reactions,^{14, 138-139} dehydroaromatisation,¹⁴⁰ oxygen/hydrogen evolution reactions¹⁴¹ and ammonia decomposition.^{12, 142} For instance, the catalytic activity of cobalt molybdenum carbide has been studied for ammonia synthesis at ambient pressure as outlined in Chapter 4. Although, $\text{Co}_3\text{Mo}_3\text{C}$ was found to be active for ammonia synthesis, the material was only active at higher temperature (500 °C) compared to its nitride counterpart which was active at 400 °C. Ammonia synthesis studies coupled with *in-situ* neutron diffraction studies indicated an important role of the chemical composition in the carbide's activity for ammonia synthesis.¹⁴³ The activity of vanadium nitride supported on silicon nitride for methane cracking was recently reported by Alshibane *et al.*¹⁴⁴ Izhar *et al.* investigated the methane decomposition over cobalt molybdenum catalysts (CoMo_{100-x} ; $x = 0, 25, 50, \text{ and } 75$) carburized at temperatures of 700- 973 K; they reported that the $\text{Co}_{50}\text{Mo}_{50}\text{C}$ -800 catalyst results in a higher conversion of methane and hydrogen production rate compared to the Mo_{100}C , $\text{Co}_{25}\text{Mo}_{75}\text{C}$, $\text{Co}_{75}\text{Mo}_{25}\text{C}$ and $\beta\text{-Mo}_2\text{C}$.¹⁴⁵

Deactivation in catalytic methane cracking

Catalyst deactivation involves a loss of catalyst activity over time and is a continuing concern for industrial catalytic processes due to the costs associated with catalyst replacement and process shutdown. The causes of catalyst deactivation are (i) chemical (poisoning, vapour compound formation by transport, vapour-solid and/or solid-solid reaction), (ii) mechanical (fouling) and (iii) thermal (sintering and/or evaporation of active phase).¹⁴⁶ Catalytic deactivation during methane cracking has been a subject of investigation over the years and the results of these studies have been summarised in a number of publications and reviews.¹⁴⁷⁻¹⁵² During catalytic methane cracking, coking and sintering are the predominant deactivation mechanisms reported.

Coking is defined as the physical deposition of carbonaceous species from the reacting species on the surface of the catalyst, resulting in loss of catalytic activity as an outcome of blocking of pores and/ or catalytic sites. In the case of large amounts of carbon deposit, coking may cause the disintegration of catalyst particles and reactor plugging. The formation of coke during hydrocarbon processing is dependent upon the nature of the reaction, the catalyst and the reaction conditions.¹¹⁶ The deactivation process resulting from carbon deposition can occur via different mechanisms as depicted in Figure 5.1-3. The carbon can adsorb strongly on the active phase surrounding and blocking access to the active phase surface; encapsulate the active metal particle; plug micro- and mesopores, thereby denying access to the active phase inside the pores; accumulate as strong carbon filaments leading to catalyst pellet disintegration and finally in extreme cases, physically blocking the reactor.^{146, 153}

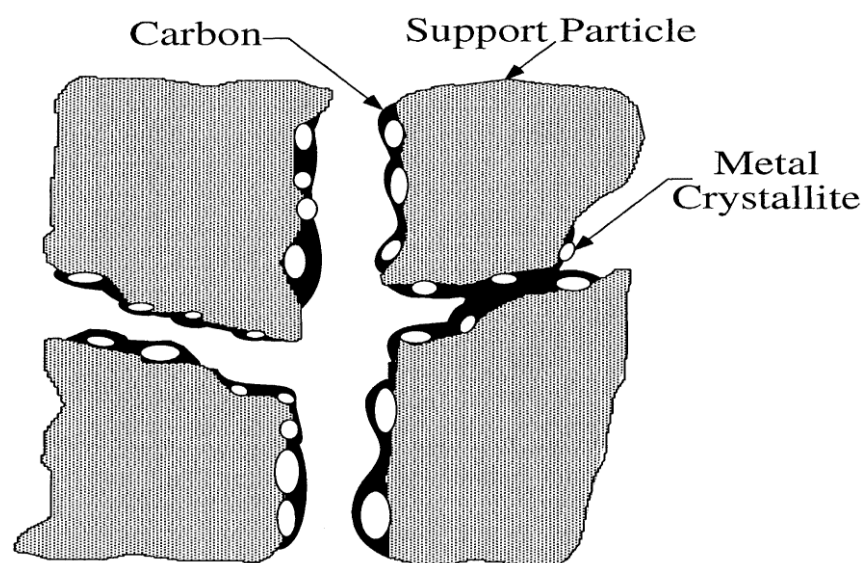


Figure 5.1-3: Theoretical model of fouling, crystallite encapsulation and pore plugging of a supported metal catalyst due to carbon deposition.¹⁵⁴

Sintering processes usually occur at high reaction temperatures (>500 °C). Sintering results in the loss of catalytic surface area caused by crystallite growth of the catalytic phase or loss of support area caused by pore collapse. Two basic mechanisms of metal crystallite growth have been observed: (A) crystallite migration and (B) atomic migration. The

processes of crystallite and atomic migration are presented in Figure 5.1-4. Crystallite migration includes the migration of whole crystallites over the support surface followed by collision and coalescence while atomic migration occurs via the detachment of metal atoms from crystallites and migration of these atoms over the support surface and eventually, capture by larger crystallites.

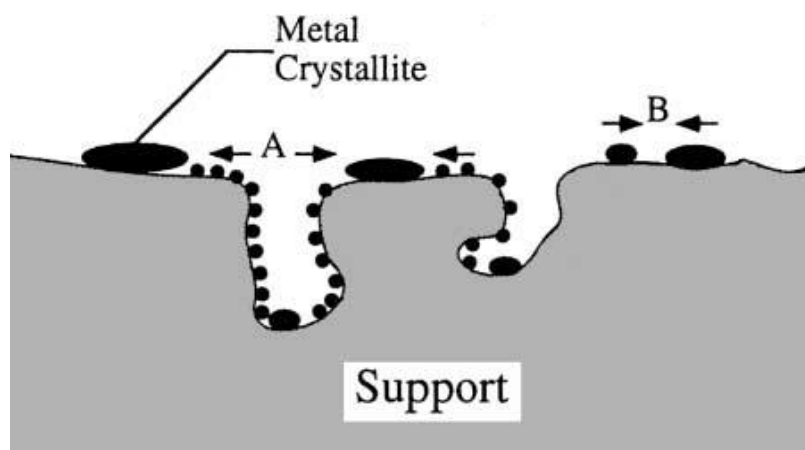


Figure 5.1-4: Two theoretical models for crystallite growth due to sintering by (A) atomic migration or (B) crystallite migration.¹⁵⁴

Catalyst regeneration

Due to the nature of the catalytic methane decomposition reaction, the deactivation of the catalyst over time is inevitable. Thus, a main challenge for researchers is the regeneration of the deactivated catalyst. In the literature, two different approaches are frequently suggested: air and steam regeneration. In the steam regeneration method, the deposited carbon reacts with the steam generating H_2 , CO_2 and CO , whereas in air regeneration, the deposited carbon is burnt in oxygen generating carbon oxides depending the amount of excess air used.^{112, 155} The choice of the regeneration method depends on three significant factors; the effect on catalyst performance, the energy needs for the process and the catalyst regeneration time.¹¹⁶

5.1.2 Carbon production

Carbon products via catalytic decomposition of methane should be considered as high value products due to their chemical and physical properties. Their unique properties can be of economic value for further applications resulting in more positive outcomes for CO_x-free hydrogen production via methane cracking. However, in many cases the carbon products are burned off for energy generation.¹⁵⁶

There are three types of carbon product generated via decomposition of methane: amorphous, filamentous, and graphitic carbon. Amorphous carbon is produced during thermal decomposition of hydrocarbons at very high temperature. Amorphous carbon is a highly disordered network of carbon atoms, mostly in the form of rings as shown in Figure 5.1-5A, while graphite has a layered hexagonal planar form stacked in an orderly fashion with weak van der Waals interlayer bonds as shown in Figure 5.1-5B; and filamentous carbon consists of carbon nanotubes and carbon nanofibers which will be discussed in more detail below.

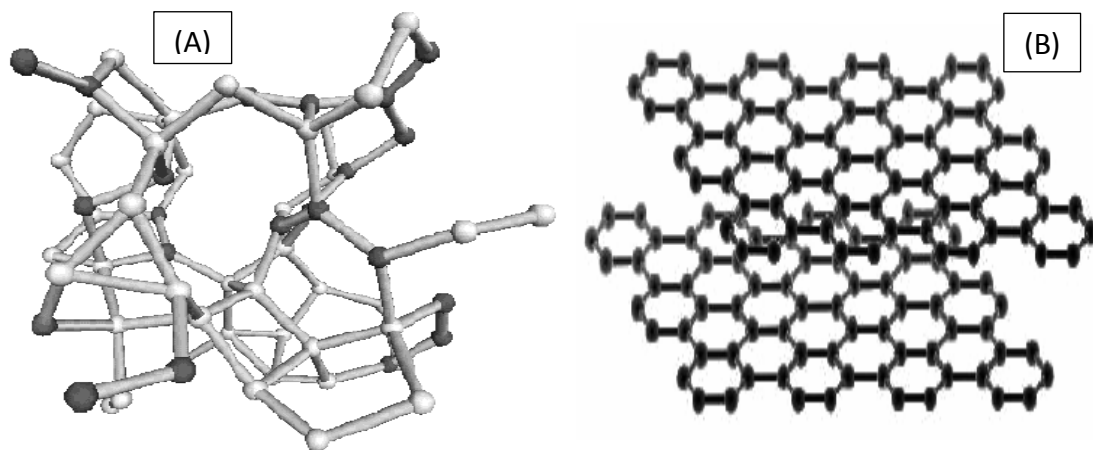


Figure 5.1-5: Schematic representation of an amorphous carbon (A)¹⁵⁷ and a graphitic carbon (B)¹⁵⁸ structures.

5.1.2.1 Carbon nanotubes (CNTs)

In 1991, carbon nanotubes (CNTs) were reported by Iijima.¹⁵⁹ Particularly since that time, they have been studied extensively in various fields such as physics, chemistry, electrical engineering and materials science. They have unique physical and mechanical properties which make them important for several applications such as fillers in polymers, in electronics and in catalysis.¹⁶⁰ Carbon nanotubes are hexagonal networks of carbon atoms rolled up into cylindrical forms. Structurally, CNTs are similar to graphite. There are two kinds of carbon nanotubes: single-walled carbon nanotubes (SWCNTs) comprising individual graphene cylinders and multi-walled carbon nanotubes (MWCNTs) which consist of several graphene cylinders bound together by weak van der Waals forces (Figure 5.1-6).¹⁶¹⁻¹⁶⁶

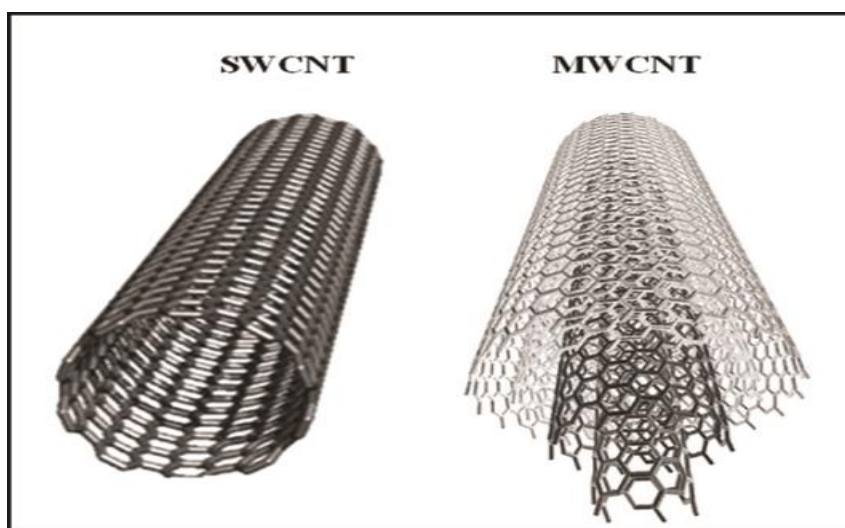


Figure 5.1-6: Schematic representation of the single-wall and multi-wall carbon nano-tubes.¹⁶¹

Historically, methane catalytic decomposition has been proposed as a viable route for the preparation of carbon nanotubes. For instance, Li *et al.* reported the formation of carbon nanotubes over the Fe/MgO catalysts.¹⁶² Both high quality single-wall and multi-wall carbon nanotubes were successfully synthesised as illustrated in Figure 5.1-7.

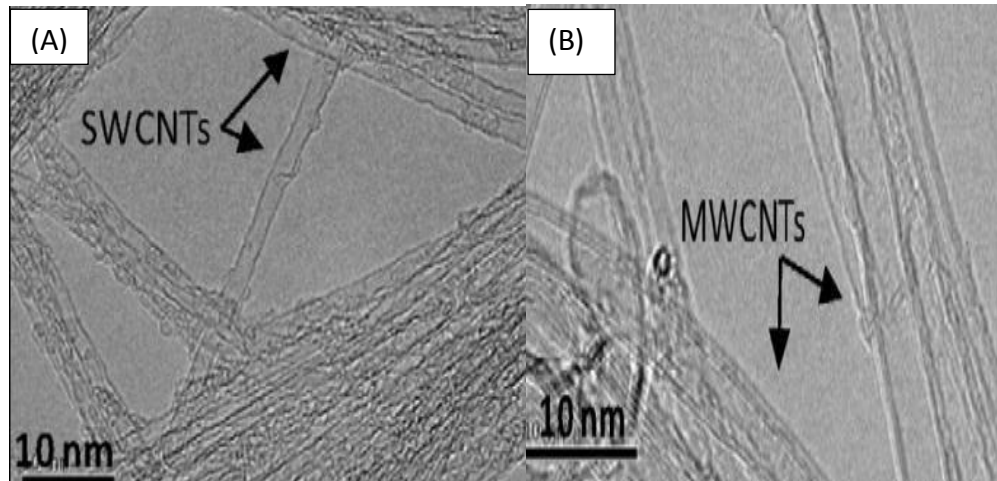


Figure 5.1-7: HRTEM images of the deposited carbon on the Fe/MgO catalysts.¹⁶²

Various methods are utilized for CNT synthesis such as arc discharge routes,¹⁵⁹ laser vaporization,¹⁶⁷ pyrolysis,¹⁶⁸ plasma-enhanced methods¹⁶⁹ or thermal chemical vapour deposition (CVD).¹⁷⁰⁻¹⁷¹ The catalytic chemical vapour deposition (CCVD) method is considered as a viable method to produce carbon nanotubes on a large scale and at low cost compared with other methods which require high energy input. The use of methane gas in this process is reported to be the most suitable and the most inexpensive carbon source. Two growth models are reported for the growth of CNTs¹¹⁴; the tip growth and base growth models. In the tip growth route, the catalytic particles typically remain at the tip of CNTs as shown in Figure 5.1-8B, whereas in the base growth mechanism, the catalytic particles are located at the base of CNTs as shown in Figure 5.1-8A.

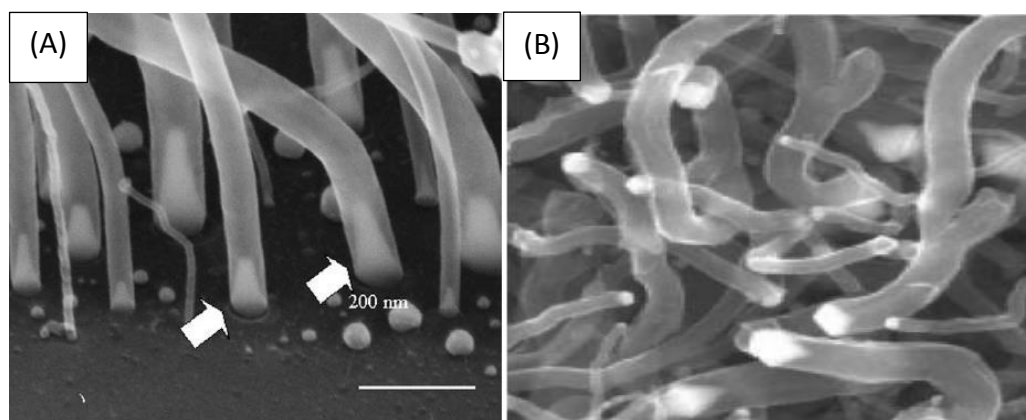


Figure 5.1-8: HRTEM images of the both tip and base growth types of CNTs.¹⁷²⁻¹⁷³

During tip growth, the methane decomposition reaction occurs on the catalyst metal surface. The carbon atoms deposited on the metal surface will dissolve in the metal and

diffuse through the metallic particle. Since the concentration of carbon dissolved in metal at the gas side of the metallic particle can exceed the solubility at the support side of the metallic particle, a concentration gradient over the metallic particle becomes possible, and thus, a driving force for the carbon diffusion through the metal particle is established.¹⁷⁴⁻¹⁷⁵ The diffused carbon precipitates as a graphitic layer at the interface between the metallic particle and the support. The formation of graphitic layers detaches the metallic particle from the support. Continuous formation of carbon atoms at the support side continues the growth of carbon nanotubes with the metal lifted at the tip of the carbon nanotubes. If the carbon deposited is not removed from the surface of metallic particles, the carbon will encapsulate the metal surface and deactivate the catalyst. Figure 5.1-9A shows the schematic image of carbon nanotubes where the metallic particles are found at the tips.

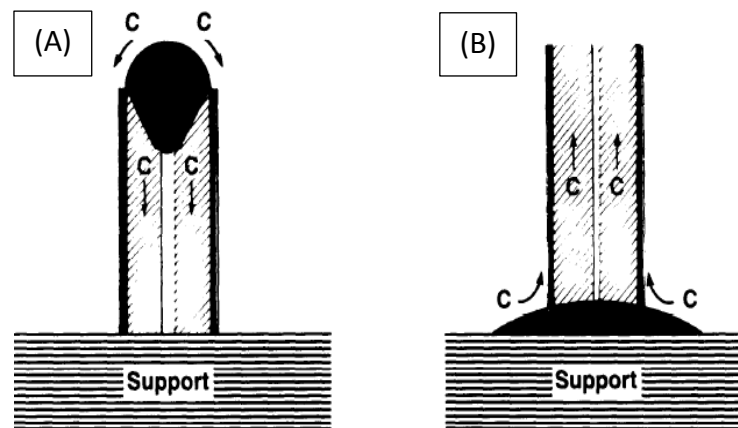


Figure 5.1-9: Schematic representation of the tip and base growth mechanisms of CNTs.¹⁷⁶

The base growth model¹⁷⁷ is similar to the tip growth model except that the metallic particle is located on the support (Figure 5.1-9B) and the growth of carbon nanotubes occurs upwards from the metallic particle attached on the support. This model assumes a strong interaction of the metallic particle with the catalyst support that cannot be easily separated by the graphitic layer formed at the metal-support interface.

5.1.2.2 Carbon nanofibers (CNFs)

Carbon nanofibers (CNFs) were initially synthesized from the interaction of carbon containing gases with hot metal surfaces in 1890 by Robertson.¹⁷⁸ CNFs have generated considerable interest as polymer additives, gas storage materials, biological protection materials, catalyst supports for many catalytic reactions, nanoprobe, sensors, in microelectronics and for energy storage particularly after the work of Iijima in 1991.¹⁵⁹ The catalytic chemical vapour deposition (CCVD) process is the most widely used route for the preparation of CNFs from decomposition of carbonaceous gas (e.g. methane, ethylene, carbon monoxide, ethane and propane). Usually, Fe, Co, Ni, Pt and Cu or their alloys at temperatures between 500 and 1200 °C are used as catalysts. Three types of CNFs are reported in the literature,¹⁷⁹ platelet (perpendicular), ribbon (parallel) and herringbone structures as shown in Figure 5.1-10. The distinction between CNFs and CNTs is related to the occurrence of hollow core and graphite sheet arrangements with a difference in the width range of 5 nm to hundreds nanometres, lengths from 5 to 10 microns for CNFs which are larger than the 5 to 30 nm widths for CNTs.

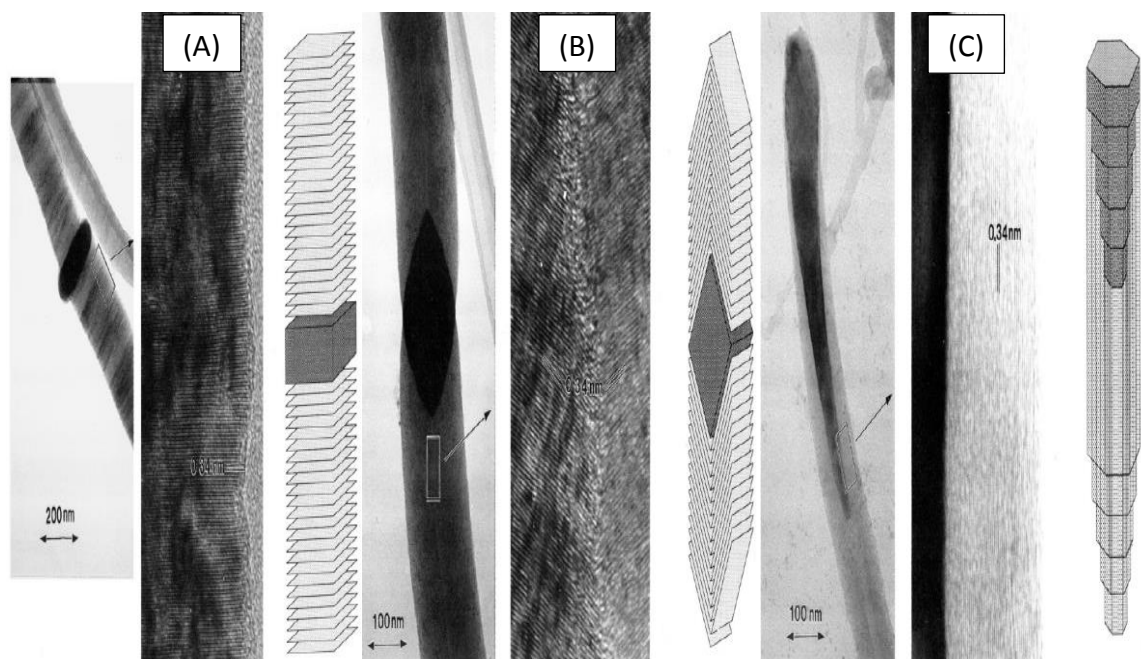


Figure 5.1-10: TEM and schematic representations of the (A) platelet, (B) herringbone, and (C) ribbon structure of CNFs.¹⁷⁹

Different parameters affect CNF growth, such as catalyst composition, reducibility of the catalyst, nature of the metal/support interaction, carbon source, particle size of the active metal, synthesis temperature, and composition of the reaction gas mixture. The mechanism of the catalytic growth of CNFs has been investigated and reported in the literature.¹¹⁶ It is now generally accepted that the growth of a carbon filament proceeds through three stages. The first stage is the decomposition of carbon-containing gases on the metal surface at the gas-particle interface. The second stage includes carbon dissolution in the particles, and carbon diffusion through the surface and bulk of the metal particles. Finally, precipitation of carbon atoms occurs on the crystal facets forming the CNFs at low temperature or CNTs at high temperature as shown in Figure 5.1-11A and B respectively.

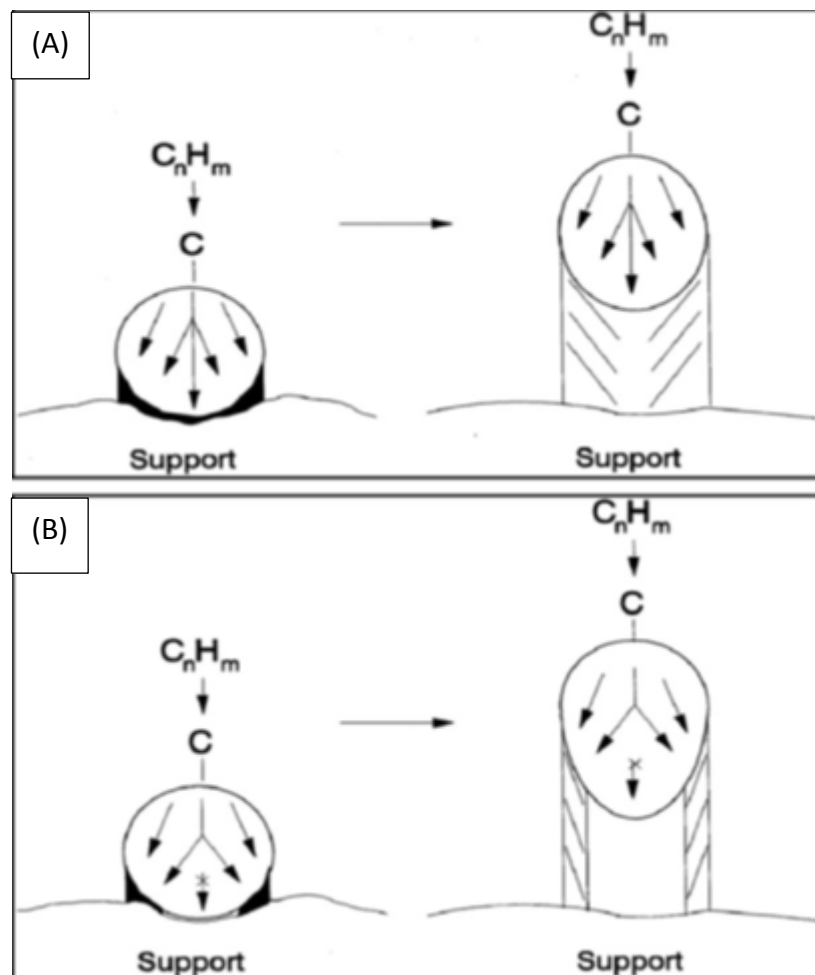


Figure 5.1-11: Schematic representation of the growth mechanisms of CNFs (A) and CNTs (B).¹¹⁶

5.1.2.3 Carbon nano-onions (CNOs)

Carbon onions are nano-spherical carbon particles comprising graphitic shells in the form of carbon layers or encapsulated metals. Due to their peculiar properties, CNOs have been studied for a range of applications including electromagnetic shielding, solid lubrication, gas and energy storage and heterogeneous catalysis.¹⁸⁰ After the onion-like structures were observed by Iijima in 1980¹⁸¹ using vacuum deposited amorphous carbon films, various physical methods to synthesise carbon nano-onions have been developed such as arc-discharge, high-energy electron irradiation or thermal treatment of carbonaceous materials and plasma enhanced chemical vapour deposition. Chemical vapour deposition is a widely applied method. Zhao *et al.*¹⁸² used this method in the presence of a Ni/Al catalyst containing 80 wt.% nickel at 600 °C to demonstrate two types of nano-onion carbon, the metal particle-filled core or the hollow core as shown in Figure 5.1-12A and B respectively.

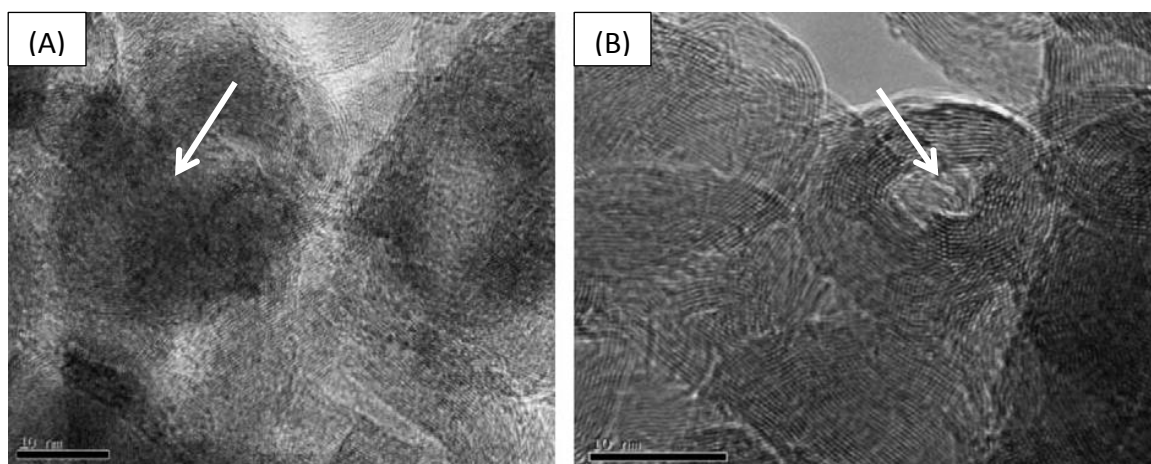


Figure 5.1-12: HRTEM images of the carbon nano-onion formed from methane cracking over Ni/Al catalyst, (A) metal particle-filled core and (B) hollow core.¹⁸²

The mechanism of growth of carbon nano-onions was investigated by Zhao *et al.*¹⁸³ using HRTEM and applying the CVD method as presented in Figure 5.1-13. First of all, after the catalytic decomposition of methane, the process of the dissolution of the decomposed carbon into the catalytic particles occurred (Figure 5.1-13B). Then, the catalytic particles became saturated by carbon due to the carbon solubility limit (Figure 5.1-13D) and carbon segregation began (Figure 5.1-13E), which resulted in the formation of carbon atom clusters on the catalytic particle surfaces (Figure 5.1-13F). When carbon cluster encapsulation was complete, the graphitization of the carbon clusters occurred. The

formation of graphitic layers on the catalytic particle surfaces led to the stress on the catalytic particle, which would give a pull stress to the catalytic particle to make it escape from encapsulation (Figure 5.1-13G). If the graphitic layer encapsulation was defective and the pull stress was enough, the catalyst particle can escape and the graphite layers close upon themselves to form hollow carbon onions (Figure 5.1-13I).

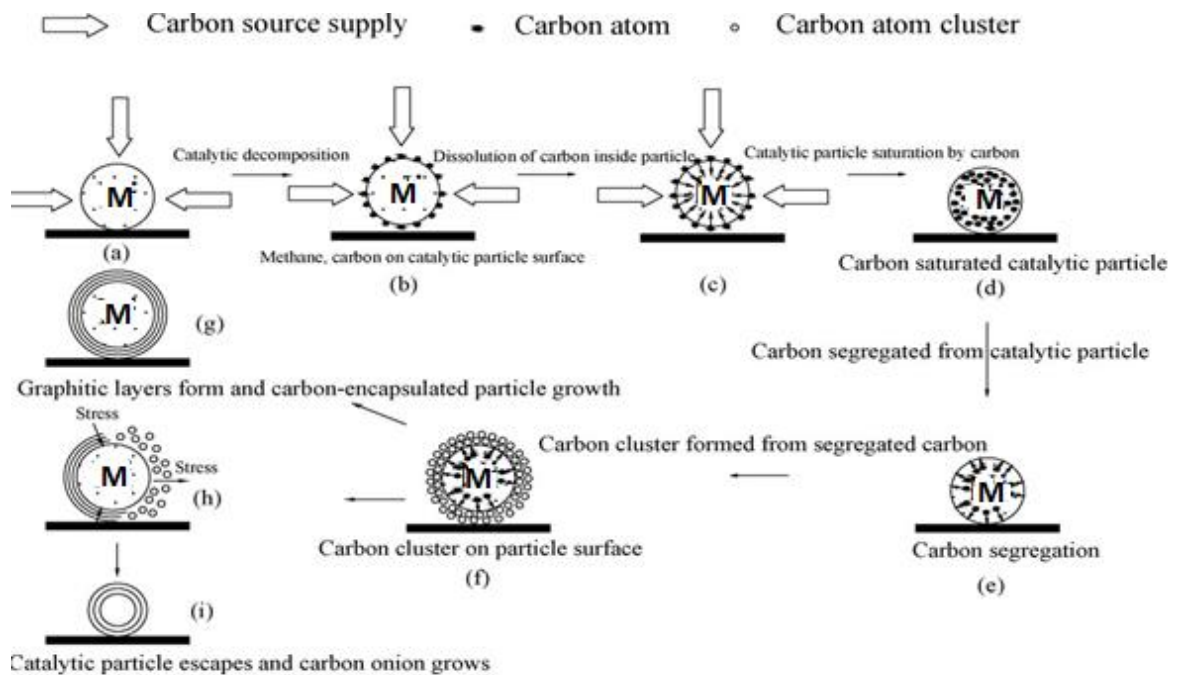


Figure 5.1-13: Schematic illustration of the growth processes of the carbon-encapsulated catalytic particles and hollow carbon onions by CVD.¹⁸³

In this work, the catalytic performance of $\text{Co}_3\text{Mo}_3\text{C}$ and $\text{Co}_6\text{Mo}_6\text{C}$ for methane cracking is studied. The process is reported as an environmentally friendly approach for carbon-free hydrogen production with no additional purification required ($\text{CH}_4 \rightarrow 2\text{H}_2 + \text{C}$). The role of the interstitial elements (carbon) upon the catalytic behaviour of $\text{Co}_3\text{Mo}_3\text{C}$ and $\text{Co}_6\text{Mo}_6\text{C}$ has been studied and compared against their nitride counterparts ($\text{Co}_3\text{Mo}_3\text{N}$ and $\text{Co}_6\text{Mo}_6\text{N}$). The interest in studying cobalt molybdenum nitride arises from the isostructural nature of these materials to their carbide counterparts. Further information of the effect of lattice species on the catalytic properties of cobalt molybdenum compounds can thus be obtained.

5.2 Results and discussion

In this chapter, the results of the characterisation and catalytic activity of the cobalt molybdenum related materials and silicon nitride supported vanadium nitride materials are presented for hydrogen production by methane cracking.

5.2.1 Molybdenum trioxide (MoO₃)

Methane cracking over MoO₃ was conducted at 800 °C using a 3:1 CH₄:N₂ gas mixture with a flow rate of 12 ml min⁻¹ for 8 hours.

5.2.1.1 Catalytic activity

Figure 5.2-1 displays the hydrogen formation rate as a function of time-on-stream for the molybdenum trioxide pre-catalyst. The reaction run was repeated to confirm reproducibility. From the data shown, it is apparent that the maximum H₂ production rate was observed after the 30 minutes on stream.

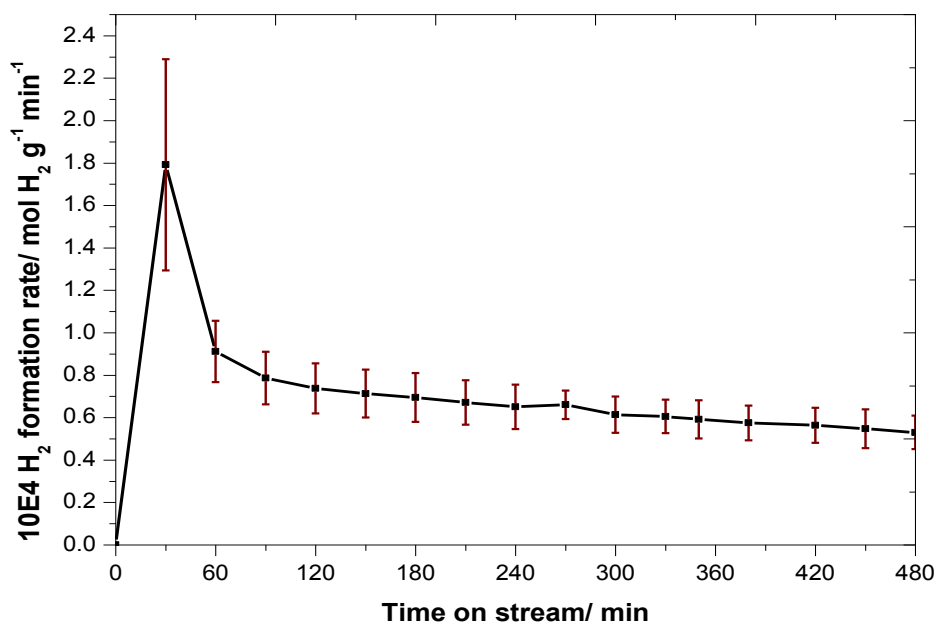


Figure 5.2-1: Hydrogen formation rate as a function of time on stream for CH₄ cracking over the MoO₃ catalyst at 800 °C. The solid line is a guide for the eye.

However due to the frequency of sampling it was not possible to pinpoint exactly where the true maximum may exist. Significant reduction in H₂ formation rate is observed

between 30 and 60 minutes, followed by a fairly steady state H_2 production for the duration of the experiment (at around $0.7 \times 10^{-4} \text{ molH}_2 \text{ g}^{-1} \text{ min}^{-1}$), although there is a slight decline with time on stream.

5.2.1.2 FTIR

The CO_x co-products were identified by FTIR analysis of aliquots of the vent reactor stream which were sampled by passage through an in-line gas-phase FTIR cell which could be periodically by-passed. FTIR analysis was undertaken using a Jasco 4100 FTIR spectrometer operating in the range of 400 to 4400 cm^{-1} acquiring 64 scans for each spectrum at a resolution of 4 cm^{-1} following background subtraction. In the case of MoO_3 , off-line FTIR spectra, recorded periodically during reaction, showed that the production of CO and CO_2 during methane cracking reaction was clearly observed as shown in Figure 5.2-2.

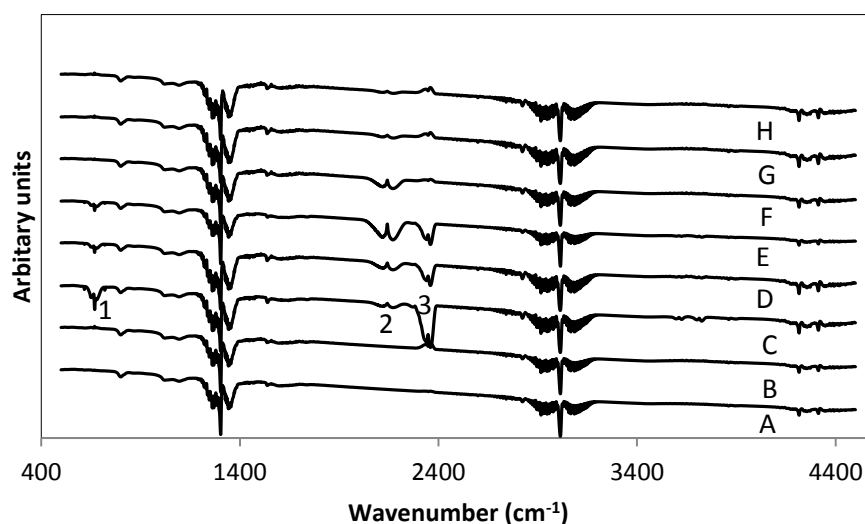


Figure 5.2-2: FTIR analysis of gas phase products from MoO_3 with CH_4/N_2 (A) background of the gas; (B) 800 °C; (C) 800 °C, 12 min; (D) 800 °C, 25 min; (E) 800 °C, 36 min; (F) 800 °C, 50 min; (G) 800 °C, 70 min; (H) 800 °C, 90 min.

FTIR analysis of gas phase products from reacting MoO_3 showed, after 12 minutes of reaction, bands at 660 and 2349 cm^{-1} (Bands 1,3- Figure 5.2-2C) which can be related to CO_2 ¹⁸⁴⁻¹⁸⁵ and at ca. 2143 cm^{-1} which can be related to CO (Band 2- Figure 5.2-2C). The production of CO and CO_2 as by-products in presence of oxides is documented in the literature.¹⁸⁶⁻¹⁸⁷ The production of CO and CO_2 ceased after 70 minutes of reaction as shown in Figure 5.2-2G which presumably corresponds to the point at which MoO_3 is converted to $\beta\text{-Mo}_2\text{C}$ (see later). It is worth mentioning that the production of CO, even in

small concentration, can be particularly harmful in the case of hydrogen production for PEMFC applications and can lead to rapid degradation of their performance and also that CO_2 could generate CO in the system by reaction with H_2 via the reverse water-gas shift reaction.

5.2.1.3 PXRD analysis

Figure 5.2-3 shows the indexed PXRD patterns of post-reaction MoO_3 which had been reacted with 3:1 $\text{CH}_4:\text{N}_2$ at 800 °C for 8 h. The PXRD data were collected with a scan step size of 0.0167° (2θ) over the range $5 \leq 2\theta/^\circ \leq 85$ for 52 minutes. It is clear from the PXRD pattern that $\beta\text{-Mo}_2\text{C}$ is formed from this reaction, with characteristic reflections occurring at $2\theta = 34.4, 37.9, 39.4, 52.1, 61.5, 69.5, 72.5, 74.6$ and 75.6° which can be assigned to this phase. This pattern was matched using the database of the Joint Committee on Powder Diffraction Standards (JCPDS) with the match being $\beta\text{-Mo}_2\text{C}$ with file number 001-1188. The reflections in the pattern have been indexed. It is noteworthy that the characteristic graphite reflection which would occur at 26° 2θ is absent from the pattern. The carbon content in this sample is 9.6 wt. % C which is close to double the calculated stoichiometric value of 5.8 wt. % for Mo_2C , and which suggests that the material contains excess carbon content.

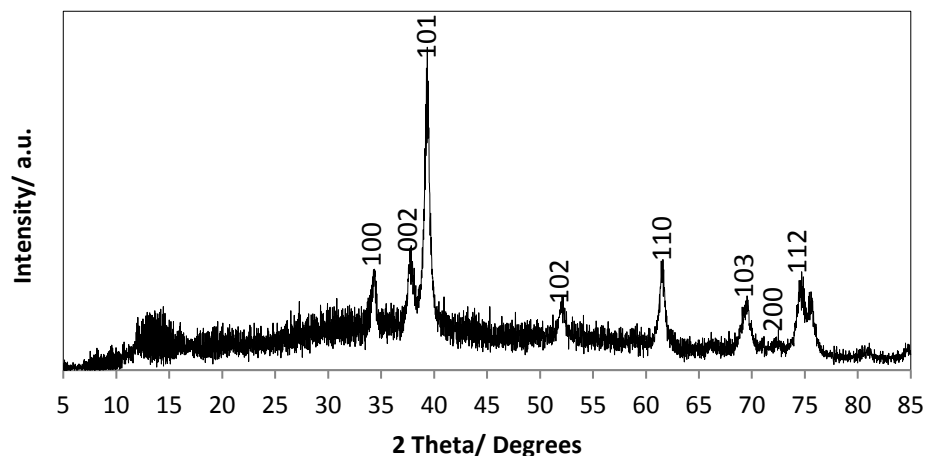


Figure 5.2-3: Indexed PXRD pattern of post-reaction MoO_3 material.

5.2.1.4 TGA analysis

To further characterise the nature of the carbon deposit after reaction, thermogravimetric analysis of the post-reaction MoO_3 was carried out in air in the temperature range between 100 – 1000 °C to estimate the amount of carbon deposited on it and to determine its reactivity profile. Figure 5.2-4 presents the TGA trace and derivative weight change profiles. Prior to the mass loss expected from the oxidation of post-reaction carbon deposited, an increase in the weight of the material was observed in the temperature window of 400 to 700 °C which may be related to the re-oxidation process of the post-reaction catalyst. Above 700 °C, a significant mass loss was observed and it can be related to carbon oxidation under these conditions. The weight loss of material was around 100 wt. %. This indicates that not only is the carbon lost, but also that the entire molybdenum component is lost. This is consistent with the known sublimation properties of MoO_3 .

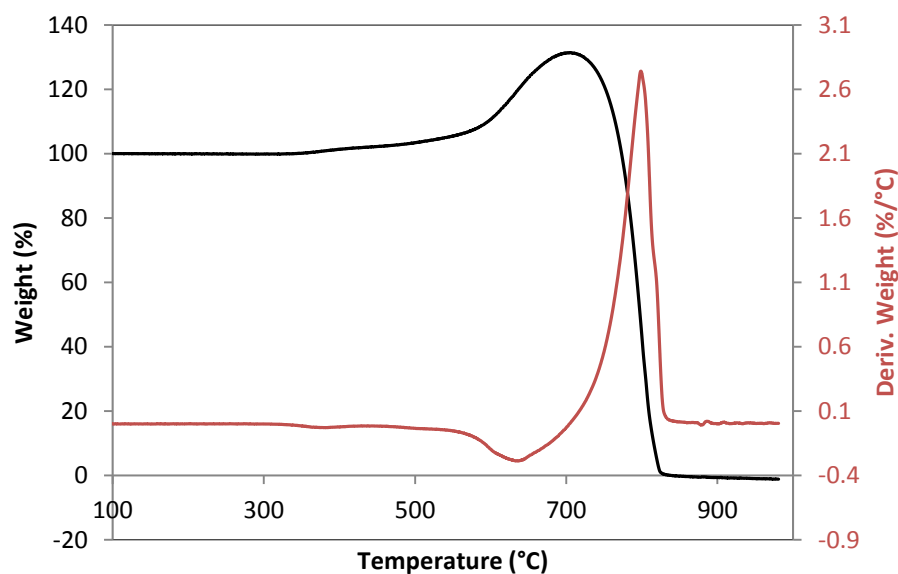


Figure 5.2-4: TGA trace and derivative weight of post-reaction MoO_3 under air up to 1000 °C.

5.2.1.5 EDX and SEM analyses

EDX and SEM analyses of the pre- and post- reaction samples have been undertaken. The EDX spectra taken from the sample from different areas, evidenced the presence of Mo and carbon in atomic ratio Mo : C of 32 : 68 (Figure 5.2-5) thus exceeding the percentage of stoichiometric carbon present in the β -Mo₂C phase but the limitations of EDX for light elements analysis and the fact that carbon stubs are used to mount the samples should be born in mind.

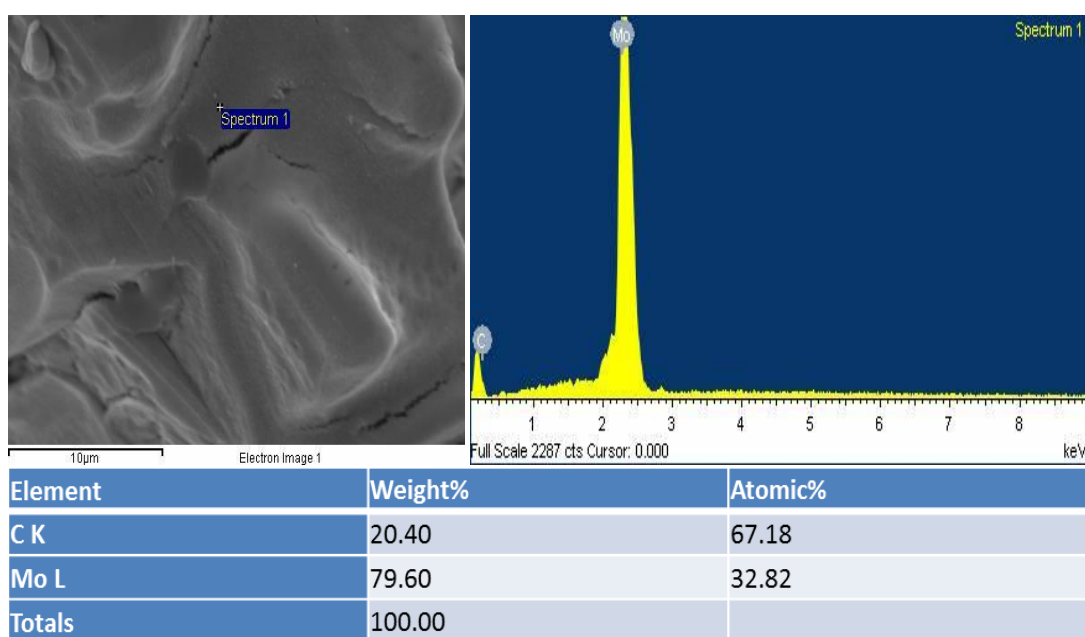


Figure 5.2-5: EDX analysis of post-reaction MoO₃ catalyst.

SEM images of pre- and post-reaction molybdenum trioxide are presented in Figure 5.2-6. It is evident from the images C, D that there are differences in the morphology of the post-reaction compared to A, B of the pre-reaction for MoO₃ material. At high magnification, it can be seen that the morphology from E, F, G and H images is comprised of numerous cubic structures or rods with different diameters and no carbon structures such as filamentous carbon can be observed.

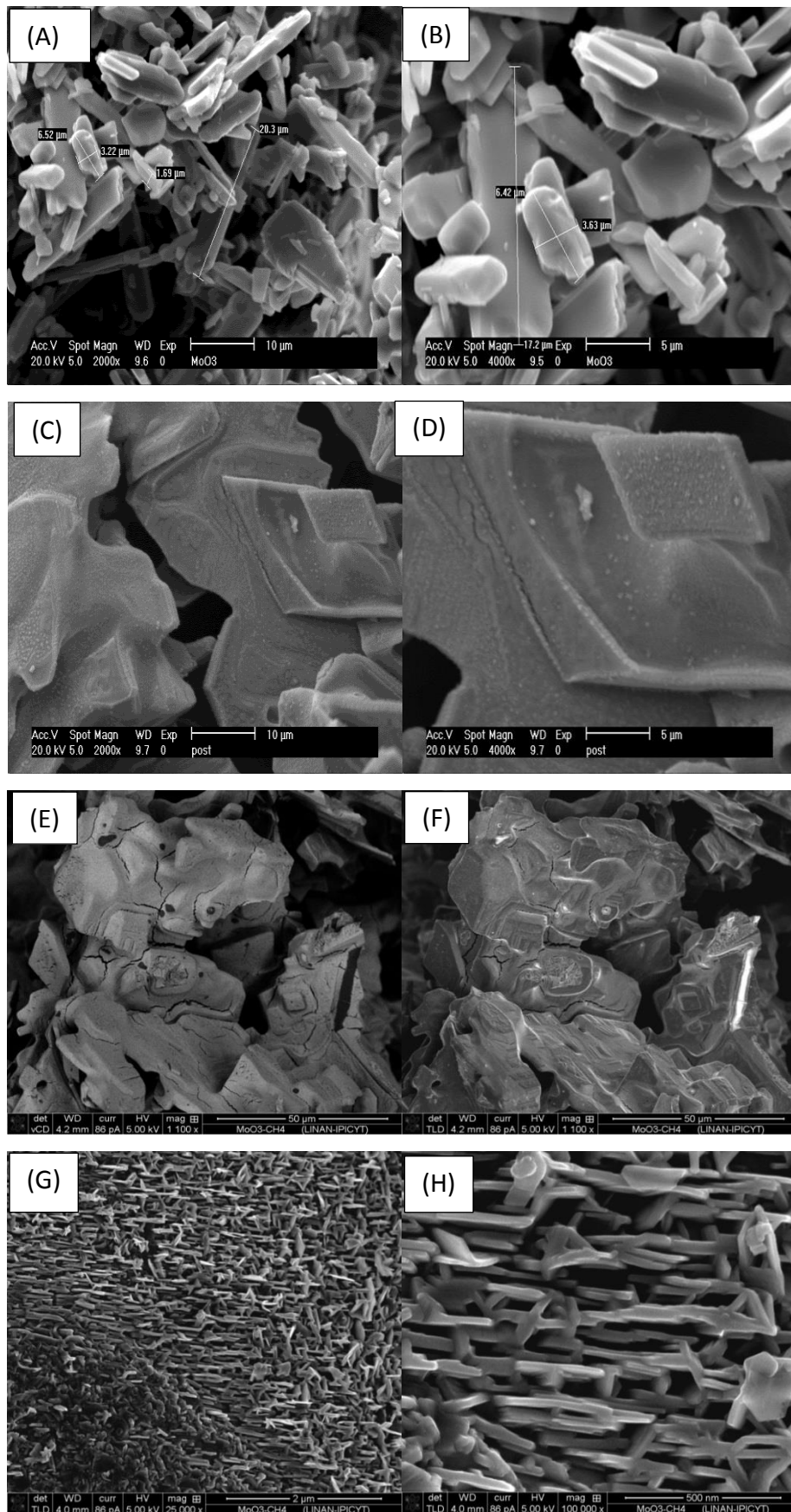


Figure 5.2-6: SEM images of pre and post-reaction MoO₃. (A, B pre-reaction at 2000, 4000 magnification), (C, D, E, F, G and H post-reaction at 2000, 4000, 10000, 10000, 25000 and 100000 magnification respectively).

5.2.1.6 Raman spectroscopy

Raman spectroscopy was conducted at room temperature and in air on the post-reaction MoO_3 sample. A Kimmon Ik Series He-Cd 532.17 nm laser was employed as the excitation source. The spectral range scanned was in the range of up to 3000 cm^{-1} since peaks beyond 3000 cm^{-1} were not expected. Raman bands associated with carbon were observed as shown in Figure 5.2-7, namely the D band, located at 1341 cm^{-1} and the G band, located at 1572 cm^{-1} respectively. The D band is attributed to the presence of structural imperfections in the graphitic layers. The G band is attributed to the in-plane carbon-carbon stretching vibration of the sp^2 atoms present in the graphite layers.¹⁸⁸ Additional to the G and D Raman bands, some of MoO_3 related bands were detected at 137, 168, 224 and 644 cm^{-1} . This result is in agreement with the result obtained for $\beta\text{-Mo}_2\text{C}$ reported in section 3.2.3.2.

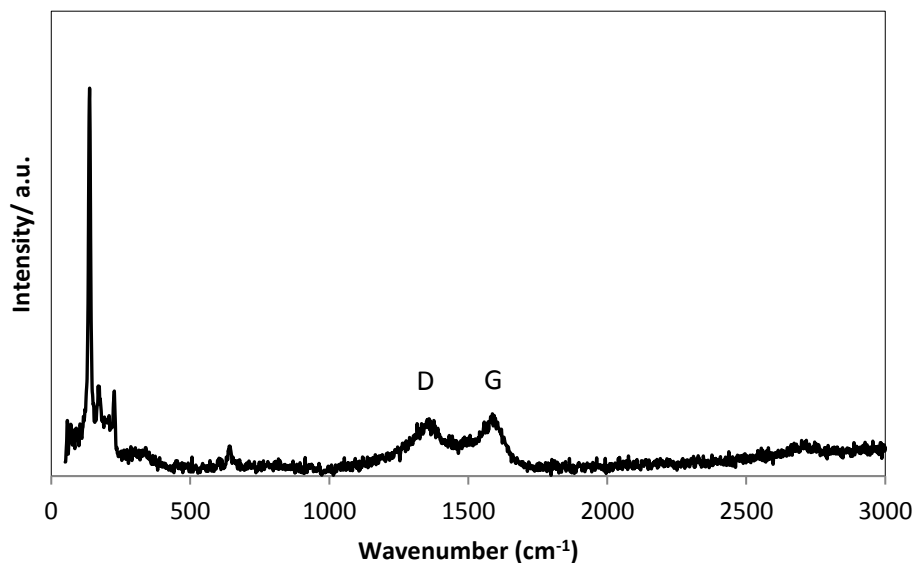


Figure 5.2-7: Raman spectrum of post-reaction MoO_3 material.

5.2.2 Cobalt molybdenum oxide (CoMoO₄)

Methane cracking over CoMoO₄ was conducted at 800 °C.

5.2.2.1 GC analysis

Figure 5.2-8 shows the hydrogen formation rate from methane decomposition over dehydrated cobalt molybdenum oxide at 800 °C for 8 hours. This reaction was repeated to confirm the reproducibility of this result. The results obtained indicated that the hydrogen formation rate reached an initial maximum around 30 minutes on stream, and then decreased slightly. A subsequent slow increase was then observed until the reaction reached a rate of around 8×10^{-4} molH₂ g⁻¹ min⁻¹. Deactivation of this material was not observed during the reaction time.

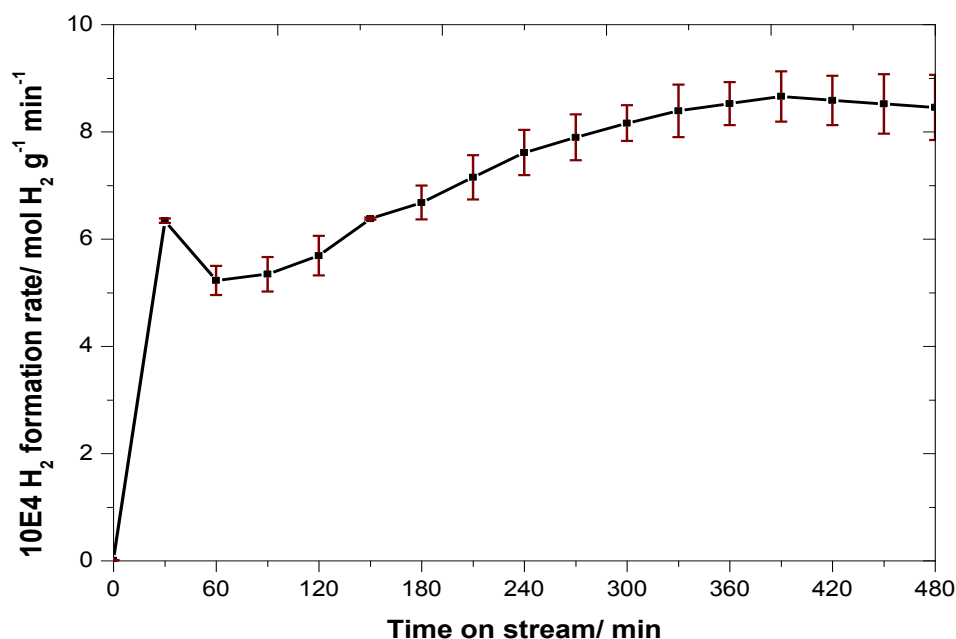


Figure 5.2-8: Hydrogen formation rate as a function of time on stream for CH₄ cracking over CoMoO₄ at 800 °C. The solid line is a guide for the eye.

5.2.2.2 FTIR

The production of CO and CO₂ during methane cracking was investigated by off-line FTIR spectroscopy as presented in Figure 5.2-9. In general all the recorded FTIR spectra displayed all bands corresponding to CH₄ which are comparable to the FTIR recorded in the absence of reaction (background). However, FTIR spectra recorded after 20 min of reaction,

extra bands at 665 and 2349 cm^{-1} (labelled as 1,3) at 2177 cm^{-1} (labelled as 2) was observed which can be related to CO_2 ¹⁸⁴⁻¹⁸⁵ and CO ¹⁸⁹ respectively. The production of CO and CO_2 in presence of oxides is documented in the literature.¹⁸⁶⁻¹⁸⁷ However, the production of CO and CO_2 stopped after 60 minutes of reaction as evident in Figure 5.2-9E. As mentioned previously, the presence of CO and CO_2 in H_2 feed streams can be detrimental for PEM fuel cell applications.

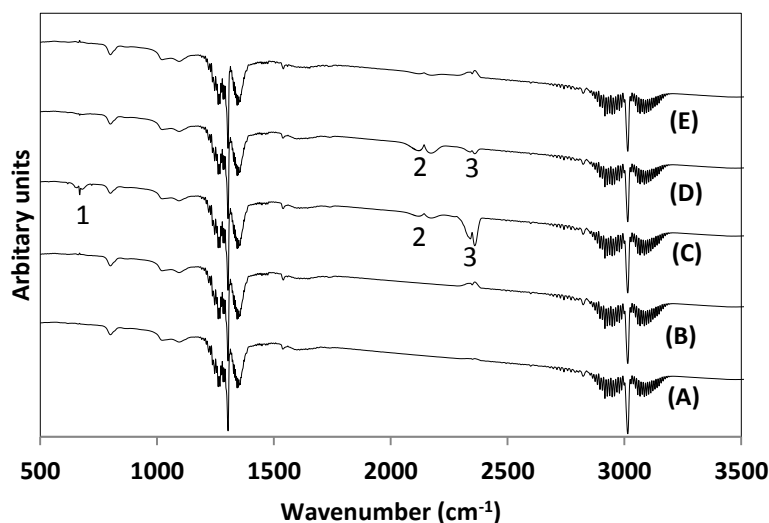


Figure 5.2-9: FTIR analysis of gas phase products from the reacted CoMoO_4 with CH_4/N_2 (A) background of the gas, (B) 800 °C, (C) 800 °C, 20 min; (D) 800 °C, 50 min; and (E) 800 °C, 60 min.

5.2.2.3 PXRD analysis

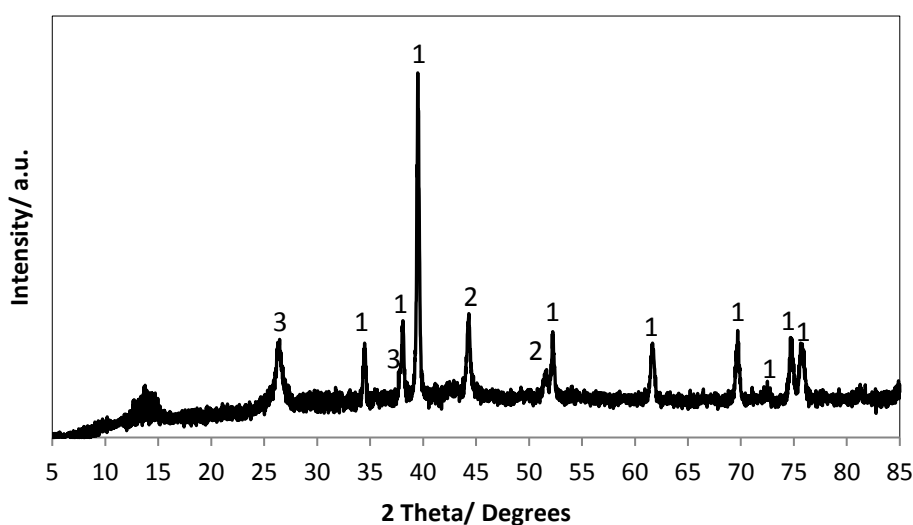


Figure 5.2-10: PXRD pattern of the post-reaction CoMoO_4 material (1, 2, 3 represent $\beta\text{-Mo}_2\text{C}$, $\alpha\text{-Co}$ and graphite respectively).

The PXRD data were collected applying the conditions described previously for the post-reaction CoMoO_4 sample. The resultant pattern is presented in Figure 5.2-10. Phase analysis showed the presence of graphite (PDF number 003-0401) at $2\theta = 26.2^\circ$, $\beta\text{-Mo}_2\text{C}$ (PDF number 001-1188 which was found to be the predominant phase), and $\alpha\text{-Co}$ (PDF number 01-089-7093) and graphite. The carbon content determined by elemental analysis in this sample was 71 ± 1 wt. % C which is in accordance with significant deposition of carbon.

5.2.2.4 TGA analysis

Thermogravimetric analysis of the post-reaction CoMoO_4 was carried out in air in the temperature range between 100 – 1000 °C. The TGA oxidation profile under air and the corresponding first derivative profile of the post-reaction CoMoO_4 are presented in Figure 5.2-11.

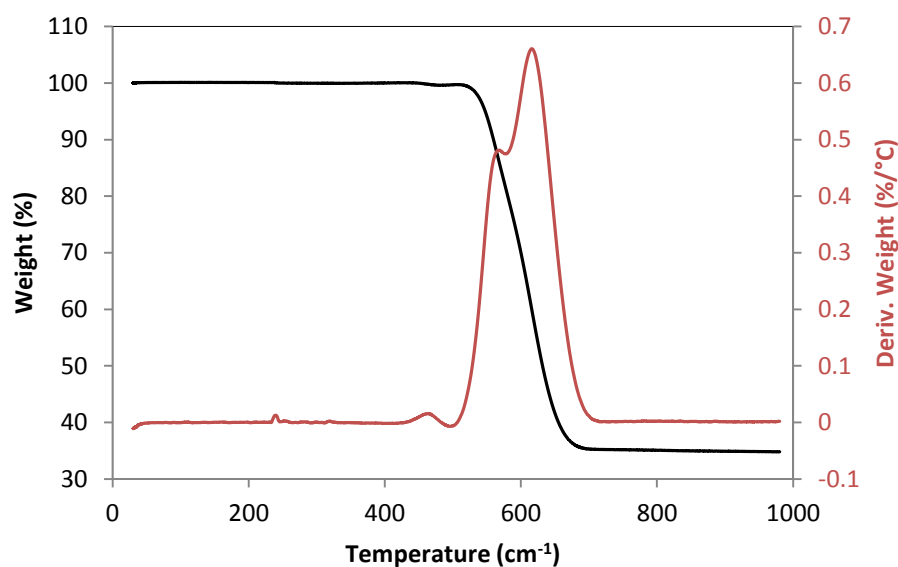


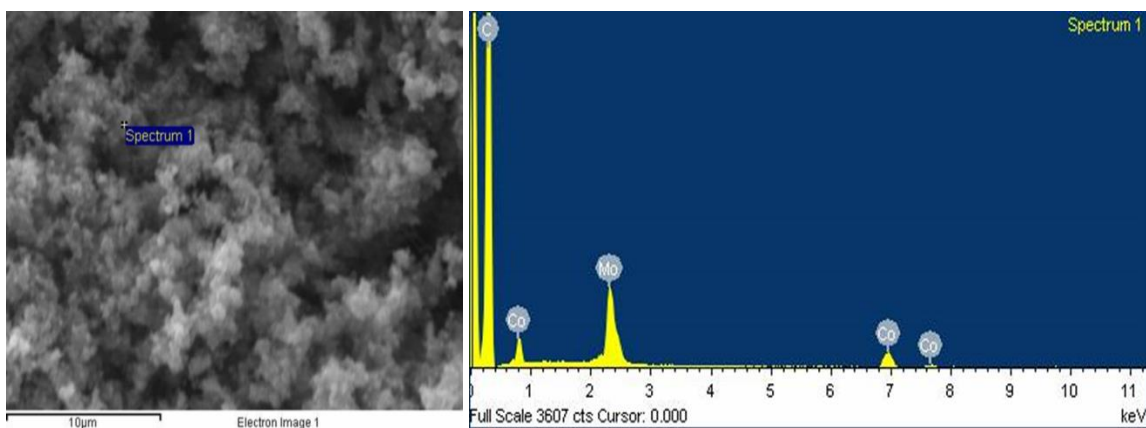
Figure 5.2-11: TGA trace and derivative weight profile of the post-reaction CoMoO_4 under air in the range from room temperature to 1000 °C.

The total mass loss from the TGA result was around 65 wt. % C which is in line with the results obtained with elemental analysis (71 ± 1 wt. % C). It is evident from the first derivative profile that there are two regions of the weight loss centred at 580 °C and at 700 °C suggesting the presence of two forms of carbon. This is suggestive of different carbonaceous residues of differing reactivity. In this case, unlike that for post-reaction

MoO₃, the Mo component does not appear to be completely lost during the measurement, nor does there seem to be a significant mass gain associated with sample oxidation.

5.2.2.5 EDX and SEM analyses

The morphology of the dehydrated cobalt molybdenum oxide as prepared present in rod-like particles as presented in Figure 5.2-13 (A and B). By contrast, reaction with 3:1 CH₄:N₂ at 800 °C for 8 hours results in the formation of rounded particles. Illustrative scanning electron microscopy images are presented in Figure 5.2-13 (C and D) where it can be seen that post-reaction CoMoO₄ material is comprised of circular crystallites which may reflect the morphology of the deposited carbon on the material. At higher magnification as shown in Figure 5.2-13 (E, F, G and H), it is evident that these circular crystallites are serpentine circles with tubular features sometimes evident. However, it's complicated to identify which type of carbon formed on this material using only SEM. EDX analysis (Figure 5.2-12) revealed the presence of carbon and there was no detectable nitrogen and hydrogen. The CoMoO₄ post-reaction sample was found to contain 71 ±1 wt. % C and there was not any hydrogen or nitrogen detected which is in agreement with the EDX analysis. The BET surface area recorded for CoMoO₄ as prepared is 7 m²g⁻¹ and that for the post-reaction material was 31 m²g⁻¹ which can be related to carbon deposition.



Element	Weight%	Atomic%
C K	89.42	98.25
Co K	3.36	0.75
Mo L	7.22	0.99
Totals	100.00	

Figure 5.2-12: EDX analysis of post-reaction CoMoO₄.

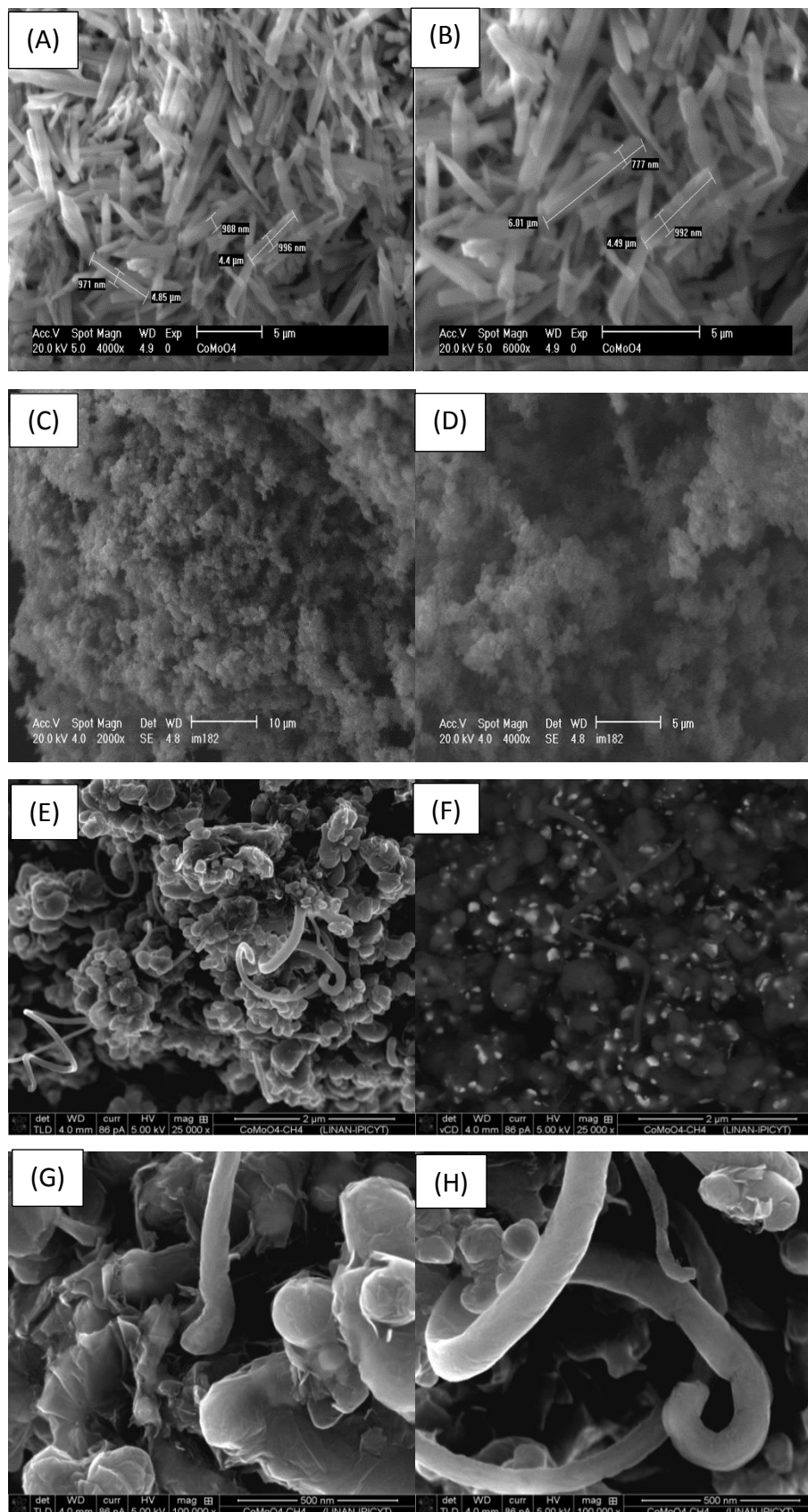


Figure 5.2-13: SEM images of pre- and post-reaction CoMoO₄. (A, B pre-reaction at 2000, 4000 magnification), (C, D, E, F, G and H post-reaction at 2000, 4000, 25000, 25000, 100000 and 100000 magnification).

5.2.2.6 Raman spectroscopy

The post-reaction Raman spectrum, displayed in Figure 5.2-14, provided strong evidence of the presence of disordered and graphitic carbon with Raman bands observed at 1348 and 1570 cm^{-1} labelled (D) and (G) respectively. A 2D peak is also observed at 2687 cm^{-1} associated with the two photon elastic scattering process, which can be used as an indicator of the purity and quantity of carbon. A small shoulder D' peak at 1600 cm^{-1} associated with some randomly distributed impurities or surface charges in the graphene was also observed.^{188, 190-191} Additional Raman bands related to the presence of the oxide phase were detected in the post-reaction CoMoO_4 sample and they are located below 1000 cm^{-1} .

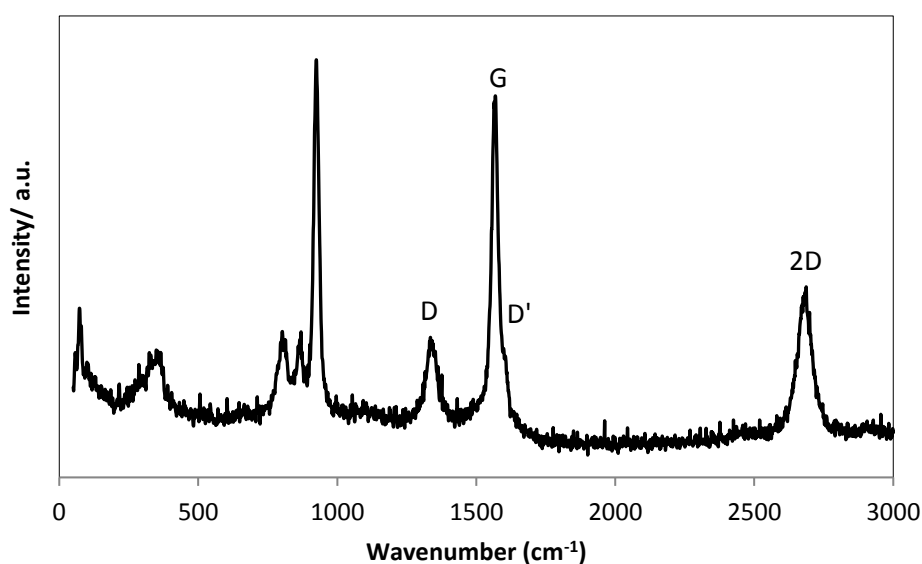


Figure 5.2-14: Raman spectrum of post-reaction CoMoO_4 .

5.2.3 Cobalt molybdenum nitride (η -6 structured $\text{Co}_3\text{Mo}_3\text{N}$)

Methane cracking over the η -6 carbide structured $\text{Co}_3\text{Mo}_3\text{N}$ was conducted at 800 °C.

5.2.3.1 GC analysis

The results of the catalytic activity of $\text{Co}_3\text{Mo}_3\text{N}$ for methane cracking are shown in Figure 5.2-12. It can be seen that the hydrogen formation rate increases slowly until it reaches steady state after ca. 120 minutes on stream. The activity of the material is found to stabilize around $12 \times 10^{-4} \text{ molH}_2 \text{ g}^{-1} \text{ min}^{-1}$ which is higher than the value achieved for CoMoO_4 . The origin of the difference of the catalytic activity between the oxide and the nitride may originate from the structural and textural evolution of these materials during methane cracking. Thus, it was of interest to characterise the post-reaction material using multiple characterisation techniques to assess the evolution of the material during methane cracking. Based on FTIR spectra, it is noteworthy that the only methane bands were observed during the whole reaction time on stream for methane cracking over this material and no CO_x bands were observed unlike for the case of the oxide materials.

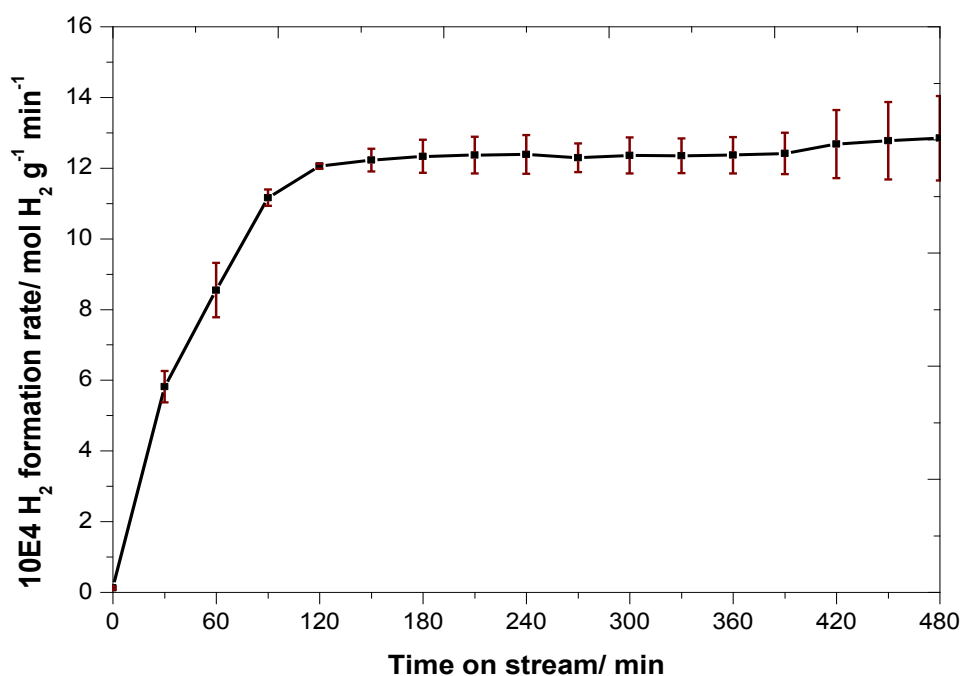


Figure 5.2-15: Hydrogen formation rate as a function of time on stream for CH_4 cracking over the $\text{Co}_3\text{Mo}_3\text{N}$ material at 800 °C. The solid line is a guide for the eye.

5.2.3.2 PXRD analysis

Figure 5.2-16 shows the PXRD pattern of $\text{Co}_3\text{Mo}_3\text{N}$ collected after reaction with CH_4/N_2 at 800 °C. The presence of graphite in the post reaction sample is clearly indicated by the strong reflection at $2\theta \sim 26^\circ$. The post-reaction PXRD revealed also carburisation of $\text{Co}_3\text{Mo}_3\text{N}$ to the $\text{Co}_3\text{Mo}_3\text{C}$ phase (PDF 03-065-7128; peaks marked as No. 1). Alongside the $\text{Co}_3\text{Mo}_3\text{C}$ phase, the presence of $\beta\text{-Mo}_2\text{C}$ and Co phases were also detected in the post-reaction sample. The peaks at $2\theta = 34.4, 39.4, 52.1, 61.5, 74.5$ and 75.5° are assigned to the $\beta\text{-Mo}_2\text{C}$ phase (PDF 001-1188, marked as No. 2) and the peaks at $2\theta = 44$ and 51.5° can be assigned to cobalt (PDF 01-089-7093, marked No. 4). The presence of the carbon deposit was further confirmed by elemental analysis of the post-reaction sample. The carbon content was found to be 85 ± 3 wt. % C. The large amount of carbon deposited during the reaction is due to the inevitable carbon deposition accompanying methane cracking.

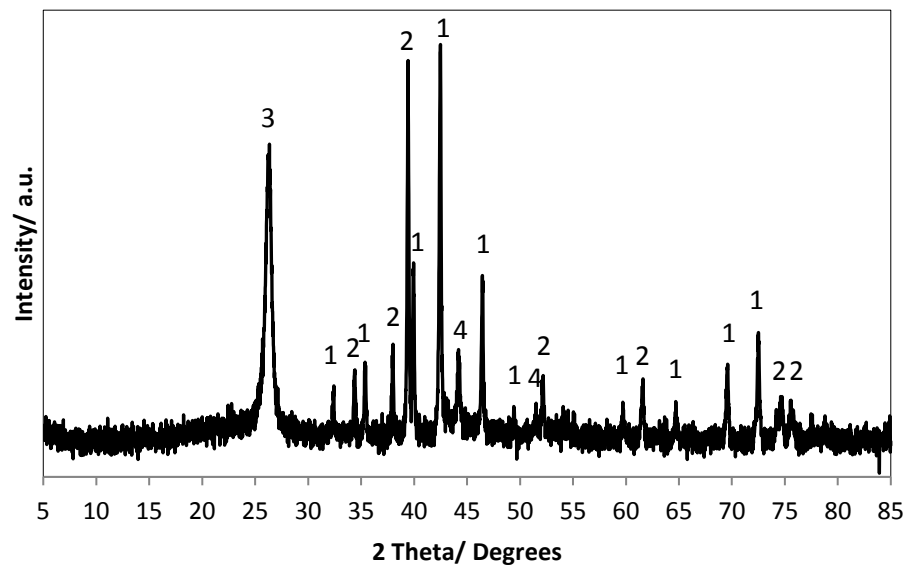


Figure 5.2-16: PXRD pattern of the post-reaction $\text{Co}_3\text{Mo}_3\text{N}$ material [1 $\text{Co}_3\text{Mo}_3\text{C}$ (03-065-7128), 2 $\beta\text{-Mo}_2\text{C}$ (001-1188), 3 Graphite (003-0401), 4 $\alpha\text{-Co}$ (01-089-7093)].

5.2.3.3 TGA analysis

Thermogravimetric analysis of the post-reaction $\text{Co}_3\text{Mo}_3\text{N}$ was carried out in air in the temperature range between 100 – 1000 °C. Figure 5.2-17 depicts the TGA oxidation profile and the first-derivative weight profile under air for the post-reaction sample. It is evident that the post-reaction $\text{Co}_3\text{Mo}_3\text{N}$ sample showed a weight loss in the region beyond 500 °C resulting from the burning off carbon formed on the samples (approximately 80 wt. % C) which is in good agreement with the results of elemental analysis (85 ± 3 wt. % C). It became therefore apparent, that the carbon deposition in the $\text{Co}_3\text{Mo}_3\text{N}$ system is higher than in the oxide systems. From the first-derivative weight change profile, it can be observed that the weight loss profile is characterised by two features, a small shoulder feature at range ca. 500 to 600 °C and a large peak at 600 to 700 °C that might both be related to carbon oxidation. These differences in the oxidation temperature could indicate the presence of different types of carbonaceous species (G and D) deposited on the material. These observations were further confirmed by Raman spectroscopy (Figure 5.2-20). These results are not surprising considering that the hydrogen formation rate was the highest, and that the results of the XRD patterns showed strong evidence of the presence of a significant graphite reflection at $2\theta \approx 26^\circ$.

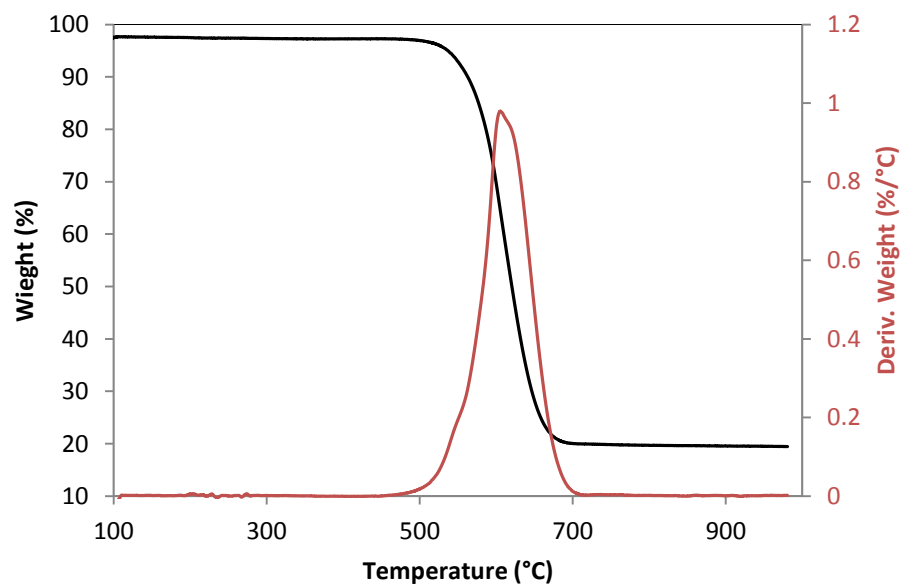


Figure 5.2-17: TGA trace and derivative weight of post-reaction $\text{Co}_3\text{Mo}_3\text{N}$ under air from RT to 1000 °C.

5.2.3.4 EDX and SEM analyses

The presence of a large amount of carbon was clearly detected by EDX analysis (Figure 5.2-18). Furthermore, no nitrogen, associated with $\text{Co}_3\text{Mo}_3\text{N}$, was detected. The results of elemental analysis are in line with EDX measurement as the post-reaction sample was found to be composed mostly of carbon 85 ± 3 wt. % C and no nitrogen was detected. It's also interesting to note that the post-reaction material displayed higher surface area, $62 \text{ m}^2 \text{ g}^{-1}$, than the pre-reaction material ($18 \text{ m}^2 \text{ g}^{-1}$) probably mainly due to the presence of the carbon. The morphology of the pre-reaction and post-reaction materials has been investigated by SEM (Figure 5.2-19). The pre-reaction material was present as rod like particles (Figure 5.2-19A, B) that possess similar morphology to the dehydrated cobalt molybdenum oxide, used as a precursor for the nitride preparation, confirming the pseudomorphic nature of the nitridation reaction. However, after the catalytic reaction, the material displayed a different morphology as can be seen in Figure 5.2-19C, D. The post-reaction material was composed of rounded particles that differ from the initial rod-like morphology observed for the pre-reaction material. At higher magnification as shown (Figure 5.2-19 E, F, G and H), it is evident that these crystallites are serpentine circular. The difference in the observed morphology may be due to the presence of the carbon deposit.

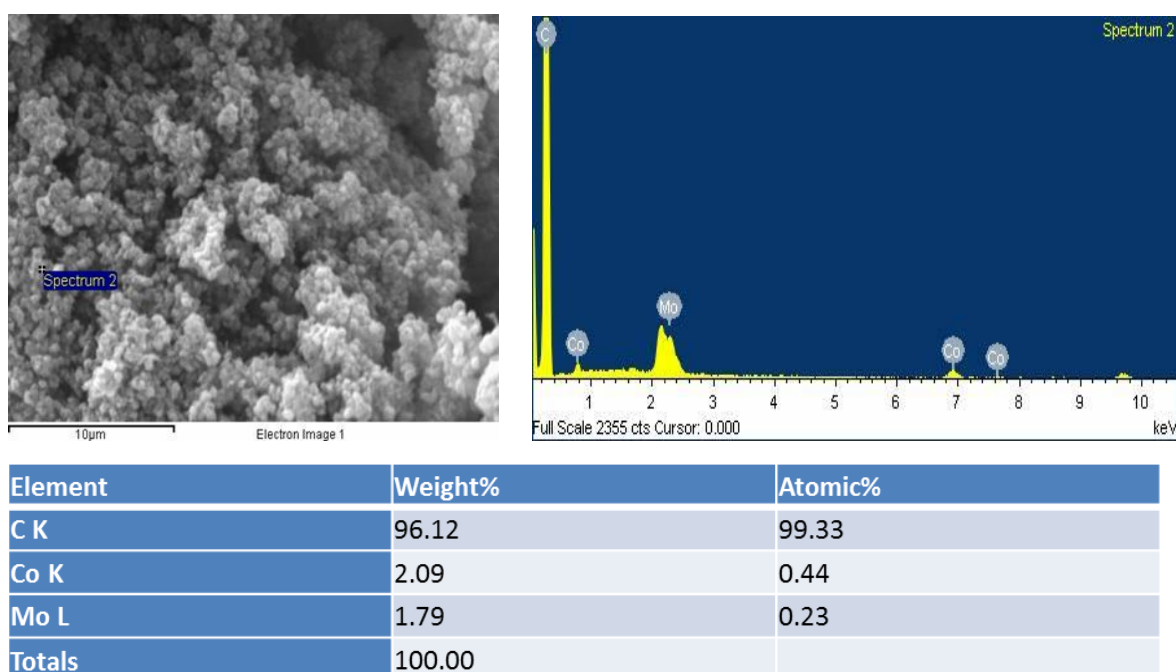


Figure 5.2-18: EDX analysis of post-reaction $\text{Co}_3\text{Mo}_3\text{N}$.

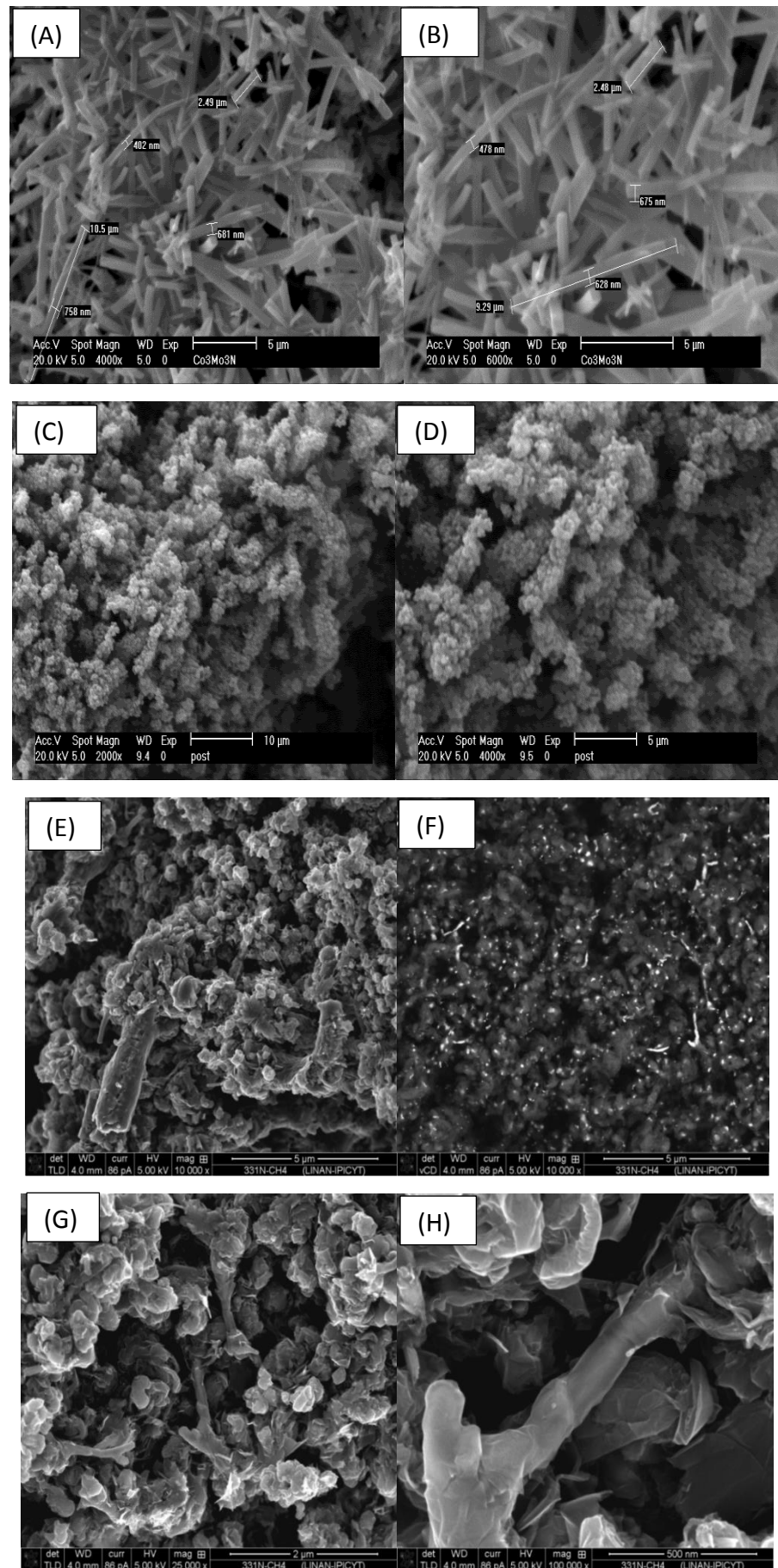


Figure 5.2-19: SEM images of pre (A, B) and post (C, D at low magnification and E, F, G, H at high magnification)-reaction $\text{Co}_3\text{Mo}_3\text{N}$.

5.2.3.5 Raman spectroscopy

Raman spectroscopy was conducted at room temperature and in air on the post-reaction $\text{Co}_3\text{Mo}_3\text{N}$ sample. The post-reaction Raman spectrum, presented in Figure 5.2-20, as for the post-reaction CoMoO_4 discussed previously, provided strong evidence of the presence of disordered and graphitic carbon with Raman bands observed at 1330 and 1565 cm^{-1} labelled (D) and (G) respectively. Furthermore, a 2D peak is also observed at 2672 cm^{-1} associated with the two photon elastic scattering process, and can be used as an indicator of the purity and quantity of carbon. A small shoulder D' peak at 1610 cm^{-1} associated with some randomly distributed impurities in the graphene was also detected. Additional Raman bands related to the oxide phase were detected in the post-reaction $\text{Co}_3\text{Mo}_3\text{N}$ located below than 1000 cm^{-1} .

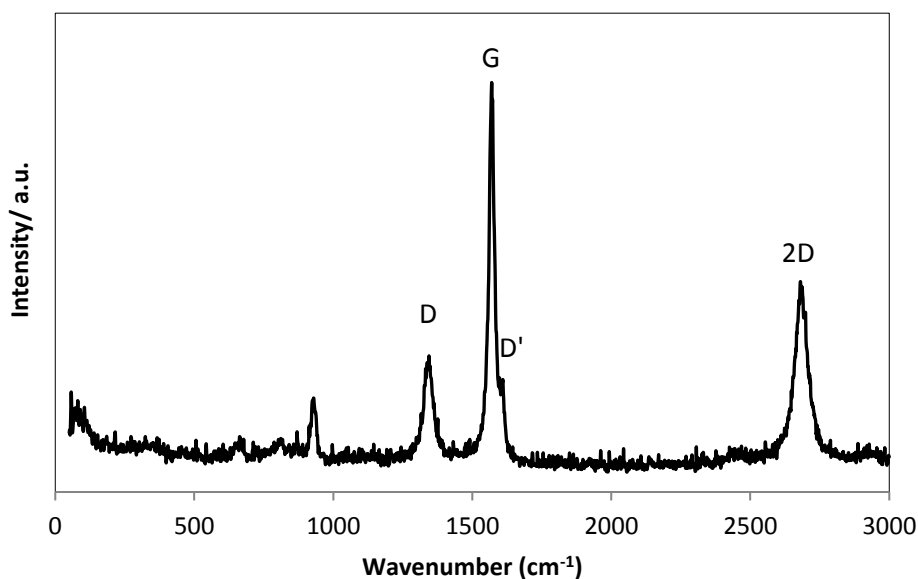


Figure 5.2-20: Raman spectrum of post-reaction $\text{Co}_3\text{Mo}_3\text{N}$.

5.2.4 Cobalt molybdenum nitride (η -12 structured $\text{Co}_6\text{Mo}_6\text{N}$)

Methane cracking over η -12 carbide structured $\text{Co}_6\text{Mo}_6\text{N}$ was conducted at 800 °C.

5.2.4.1 GC analysis

The hydrogen formation profile at temperature 800 °C of η -12 carbide structured $\text{Co}_6\text{Mo}_6\text{N}$ phase reacted with 3:1 $\text{CH}_4:\text{N}_2$ for 8 hours was determined. This experiment was repeated to confirm the reproducibility. Figure 5.2-21 presents the hydrogen formation rate against time-on-stream at 800 °C as a result of cracking of methane over the $\text{Co}_6\text{Mo}_6\text{N}$ material. It can be observed that the hydrogen formation rate increases with time on stream until reaching the maximum value at $17 \times 10^{-4} \text{ mol H}_2 \text{ g}^{-1} \text{ min}^{-1}$. The enhancement of the hydrogen formation rate in this material compared to $\text{Co}_3\text{Mo}_3\text{N}$ could be related to their structures. 661N was prepared using pre-treatment with N_2/H_2 gas for 2 hours to convert it from an amorphous phase to a more crystalline phase. In addition, deactivation of this material was not observed during the reaction time for 8 hours, and indeed it potentially further activated with time on stream. From FTIR analyses, it is notable that only methane bands were observed during the whole reaction time on stream for methane cracking over this material and no CO_x bands as co-products were observed.

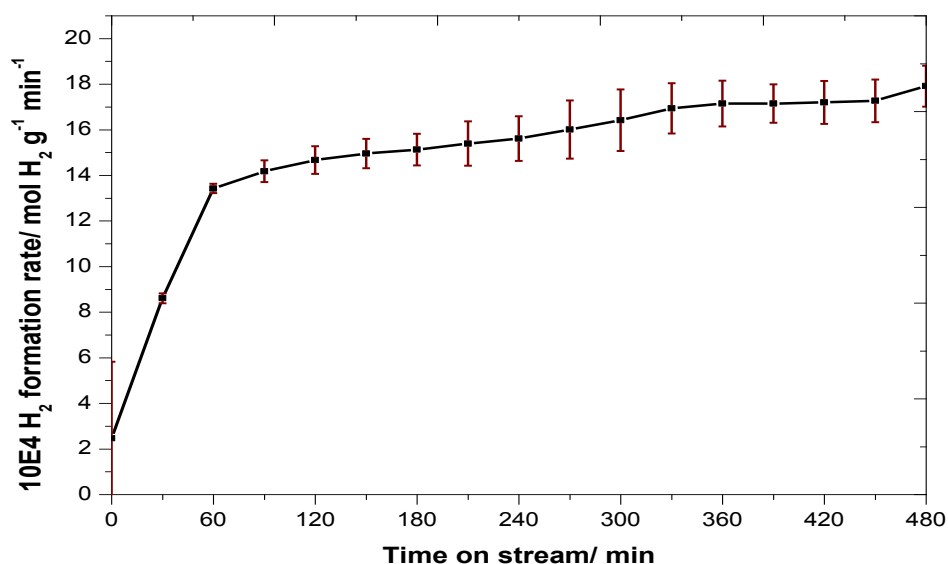


Figure 5.2-21: Hydrogen formation rate as a function of time on stream for CH_4 cracking over $\text{Co}_6\text{Mo}_6\text{N}$.

5.2.4.2 PXRD analysis

The change of the structural properties of the $\text{Co}_6\text{Mo}_6\text{N}$ following reaction was characterised by PXRD as presented in Figure 5.2-22. The post-reaction sample showed a phase composition similar to the post-reaction $\text{Co}_3\text{Mo}_3\text{N}$ material. The presence of graphite in the post-reaction sample was confirmed by a strong diffraction reflection at $2\theta \sim 26^\circ$. Carburisation of the $\text{Co}_6\text{Mo}_6\text{N}$ to $\text{Co}_3\text{Mo}_3\text{C}$ was also observed. Additionally, Co and $\beta\text{-Mo}_2\text{C}$ were observed as minor phases. In summary, the phase composition of the post-reaction $\text{Co}_6\text{Mo}_6\text{N}$ was very similar to the post-reaction $\text{Co}_3\text{Mo}_3\text{N}$. Based on CHN elemental analysis results, the carbon content of the post-reaction sample was found to be 84 ± 1 wt. % C.

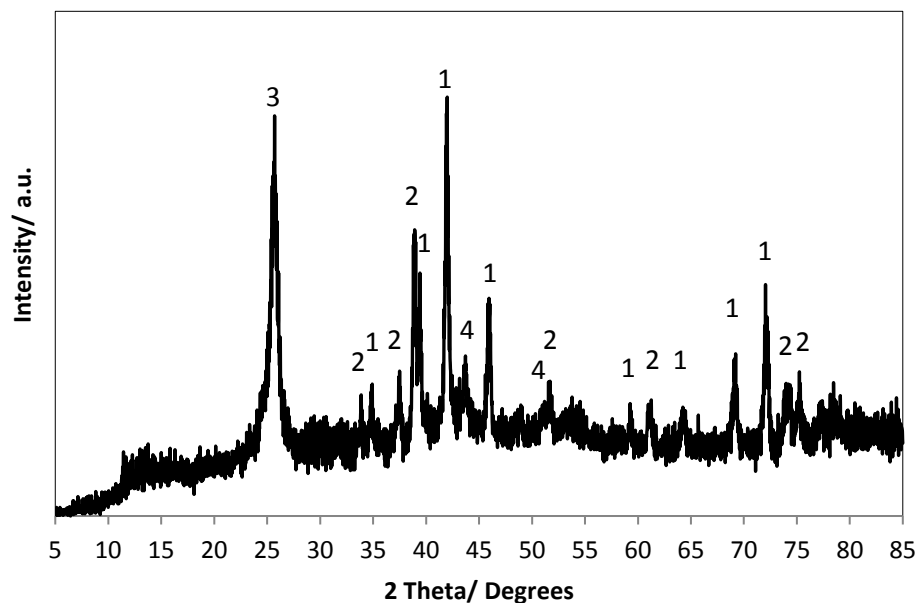


Figure 5.2-22: PXRD pattern of the post-reaction $\text{Co}_6\text{Mo}_6\text{N}$ material [1 $\text{Co}_3\text{Mo}_3\text{C}$ (03-065-7128), 2 $\beta\text{-Mo}_2\text{C}$ (001-1188), 3 Graphite (003-0401), 4 $\alpha\text{-Co}$ (01-089-7093)].

5.2.4.3 TGA analysis

The carbon deposition during the catalytic reaction was studied by thermogravimetric analysis under air. Figure 5.2-23 shows the mass loss profiles. The oxidation of carbon initiated at 500 °C and was complete at 700 °C. The percentage of weight loss, 78 wt. %, possibly associated with the removal of carbon is found to be consistent with the CHN elemental analyses of post-reaction material indicating the presence of 84 ± 1 wt. % C. The first derivative profile shows two mass loss features centred at around 552 and 602 °C suggesting the possible presence of two forms of carbon.

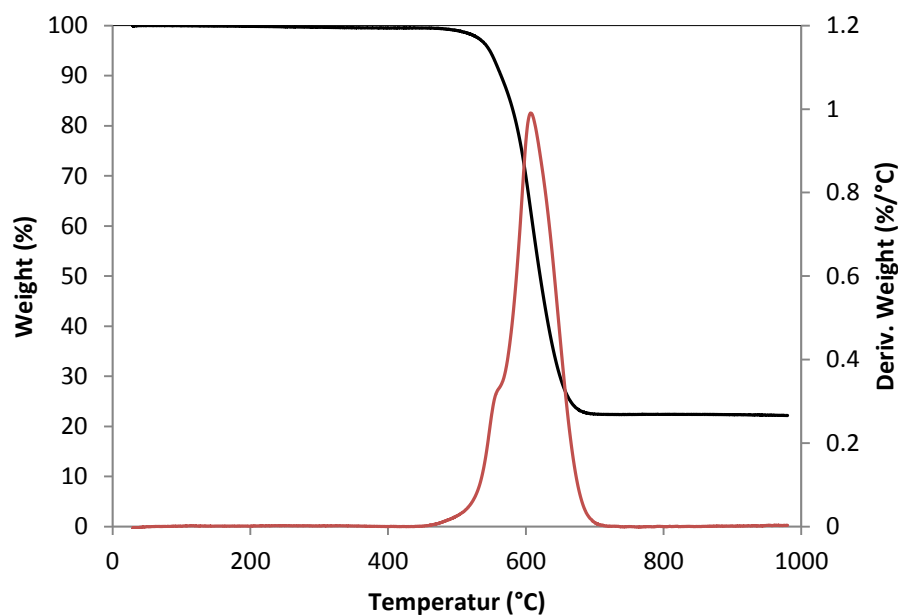
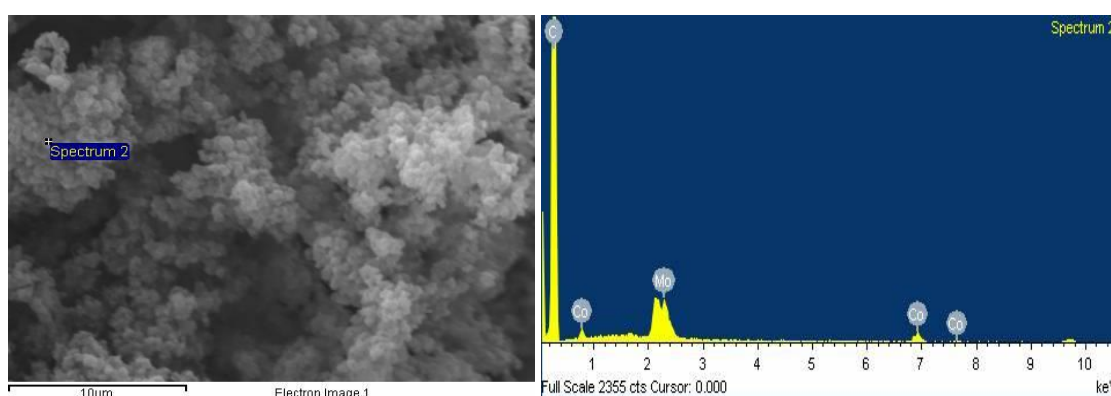


Figure 5.2-23: TGA trace and derivative weight of post-reaction $\text{Co}_6\text{Mo}_6\text{N}$ under air up to 1000 °C.

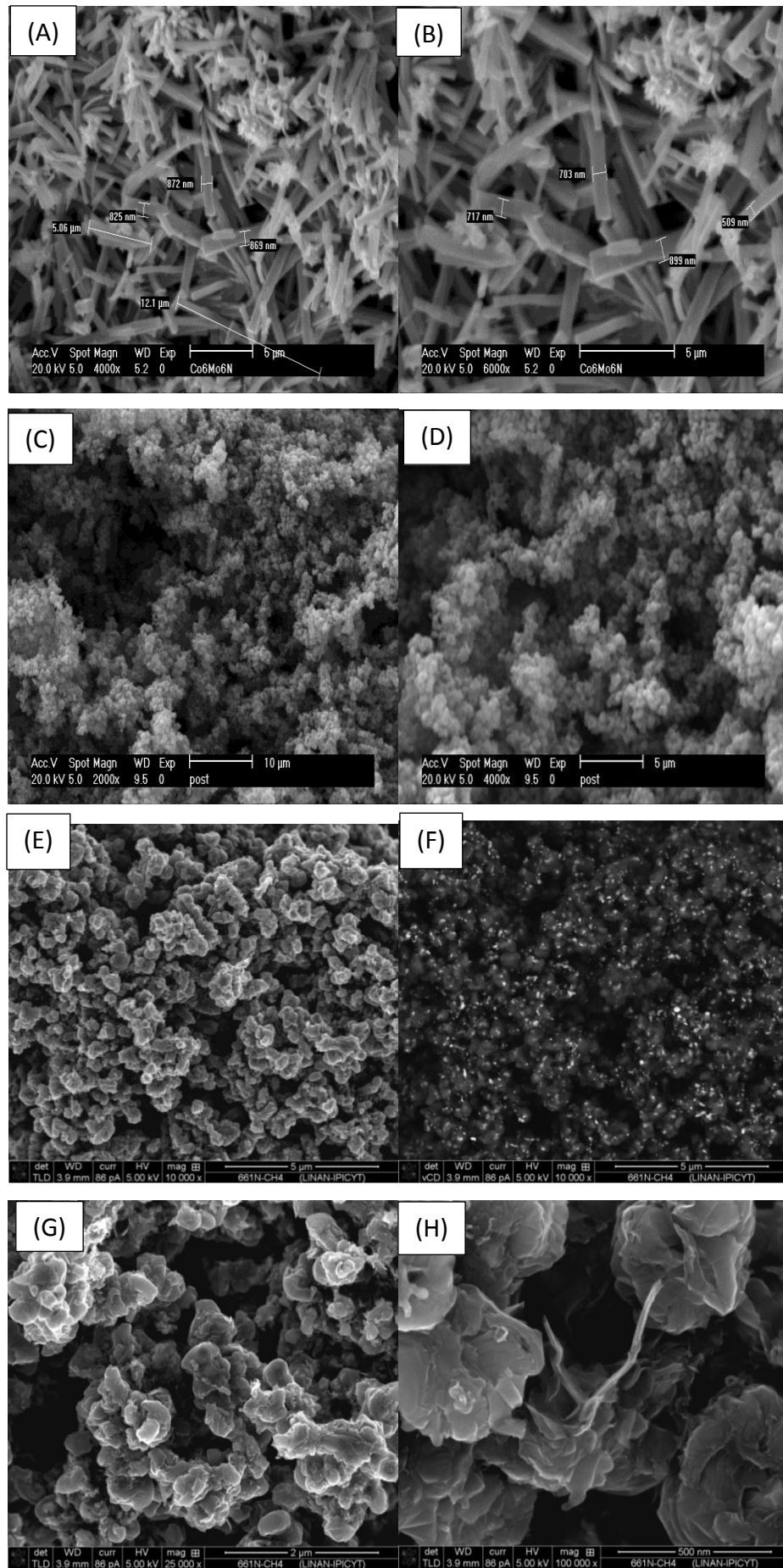
5.2.4.4 EDX and SEM analyses

The carbon deposition was clearly evidenced by the EDX analysis (Figure 5.2-24) which further confirms the results of the TGA and elemental analyses. The evolution of the textural and structural properties of the $\text{Co}_6\text{Mo}_6\text{N}$ was also accompanied by an increase in the surface area from 4 to $59 \text{ m}^2\text{g}^{-1}$ which is most probably mainly related to carbon laydown during the catalytic reaction. The morphology of the $\text{Co}_6\text{Mo}_6\text{N}$ is very similar to that observed of the $\text{Co}_3\text{Mo}_3\text{N}$ being in the form of nano-rods confirming that the reduction of $\text{Co}_3\text{Mo}_3\text{N}$ to $\text{Co}_6\text{Mo}_6\text{N}$ is a pseudomorphic reaction resulting in the material maintaining its initial morphology (Figure 5.2-25A, B). However, the post-reaction $\text{Co}_6\text{Mo}_6\text{N}$ was found to be present in the form of rounded particles. Representative scanning electron microscopy images are presented in Figure 5.2-25 (C and D) where it can be seen that post-reaction $\text{Co}_6\text{Mo}_6\text{N}$ is comprised of circular crystallites.



Element	Weight%	Atomic%
C K	94.57	99.04
Co K	2.95	0.63
Mo L	2.48	0.33
Totals	100.00	

Figure 5.2-24: EDX analysis of post-reaction $\text{Co}_6\text{Mo}_6\text{N}$.

Figure 5.2-25: SEM image of pre- and post-reaction $\text{Co}_6\text{Mo}_6\text{N}$.

5.2.4.5 Raman spectroscopy

Raman spectroscopy was conducted at room temperature and in air on the post-reaction $\text{Co}_6\text{Mo}_6\text{N}$ sample. Raman spectroscopy is an analytical technique that can be used to characterise carbon and also differentiated multi-layer graphene. Post-reaction Raman spectra, displayed in Figure 5.2-26 and as for the previous two samples (CoMoO_4 and $\text{Co}_3\text{Mo}_3\text{N}$), provided strong evidence of the presence of disordered and graphitic carbon with Raman bands observed at 1340 and 1565 cm^{-1} labelled (D) and (G) respectively. Furthermore, a 2D peak is also observed at 2672 cm^{-1} associated with the two photon elastic scattering process, and can be used as an indicator of the purity and quantity of carbon. A small shoulder D' peak at 1595 cm^{-1} associated with some randomly distributed impurities or surface charges in the graphene was observed. Additional Raman bands related to the oxide phase were detected in the post-reaction CoMoO_4 located below 1000 cm^{-1} .

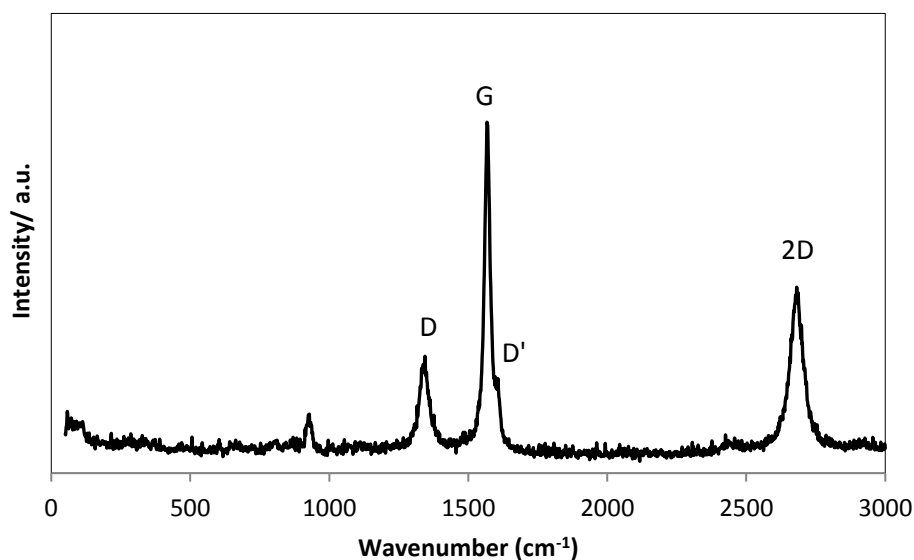


Figure 5.2-26: Raman spectrum of post-reaction $\text{Co}_6\text{Mo}_6\text{N}$.

5.2.5 Cobalt molybdenum carbide (η -6 structured $\text{Co}_3\text{Mo}_3\text{C}$)

Methane cracking over the η -6 carbide structured $\text{Co}_3\text{Mo}_3\text{C}$ was conducted at 800 °C.

5.2.5.1 GC analysis

Figure 5.2-27 presents the hydrogen formation rate against time on stream at 800 °C as a result of cracking of methane over the $\text{Co}_3\text{Mo}_3\text{C}$ material. In this case, the hydrogen formation rate was characterised by strong fluctuation of hydrogen production over time. Although, the catalytic behaviour of $\text{Co}_3\text{Mo}_3\text{C}$ seems peculiar, this kind of behaviour has been previously reported by Moliner *et al.* who stated that the methane decomposition reaction over a carbonaceous catalyst was controlled by two simultaneous processes, one a decrease in methane decomposition rate due to the blocking by carbon species deposited and the other an increase rate due to the formation of catalytically active carbon species produced from methane.¹⁹² It should be noted that the carbon deposition on both samples run in the present study led to pressure-drop effects during the reaction.

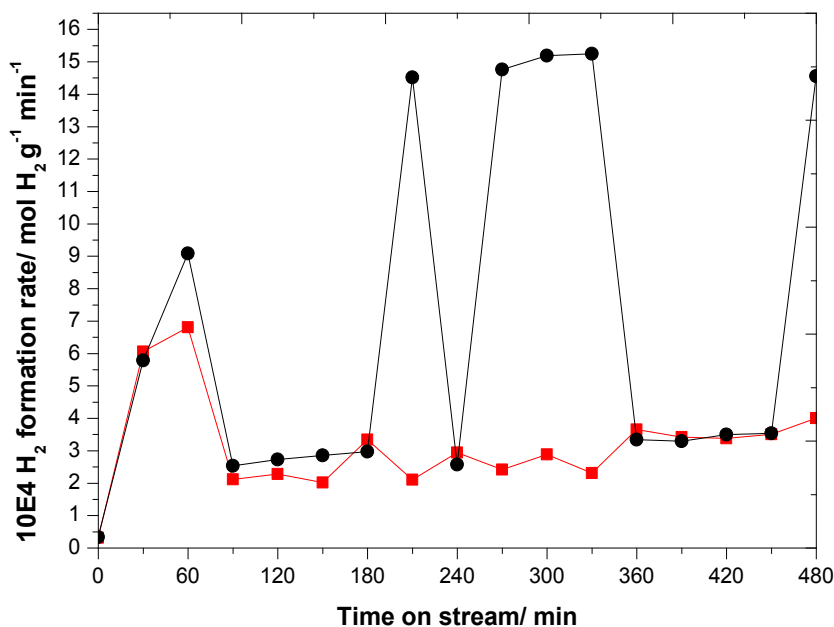


Figure 5.2-27: Hydrogen formation rate as a function of time on stream for CH_4 over $\text{Co}_3\text{Mo}_3\text{C}$ at 800 °C. (● First reaction run and ■ second reaction run) The solid line is a guide for the eye.

5.2.5.2 PXRD analysis

Figure 5.2-28 presents the powder X-ray diffraction pattern of $\text{Co}_3\text{Mo}_3\text{C}$ post-reaction materials. The PXRD of both post-reaction materials were very similar and no disparity between the two samples was observed. The phase analysis of both materials showed the presence of graphite at $2\theta = 26.2^\circ$ (PDF number 003-0401). Upon reaction, the materials were observed to undergo partial phase segregation with the formation of $\alpha\text{-Co}$ (PDF number 01-089-7093) and $\beta\text{-Mo}_2\text{C}$ (PDF number 001-1188). The carbon contents in these samples were 84 and 79 wt. % C for A and B respectively. No nitrogen or hydrogen were detected by CHN elemental analysis.

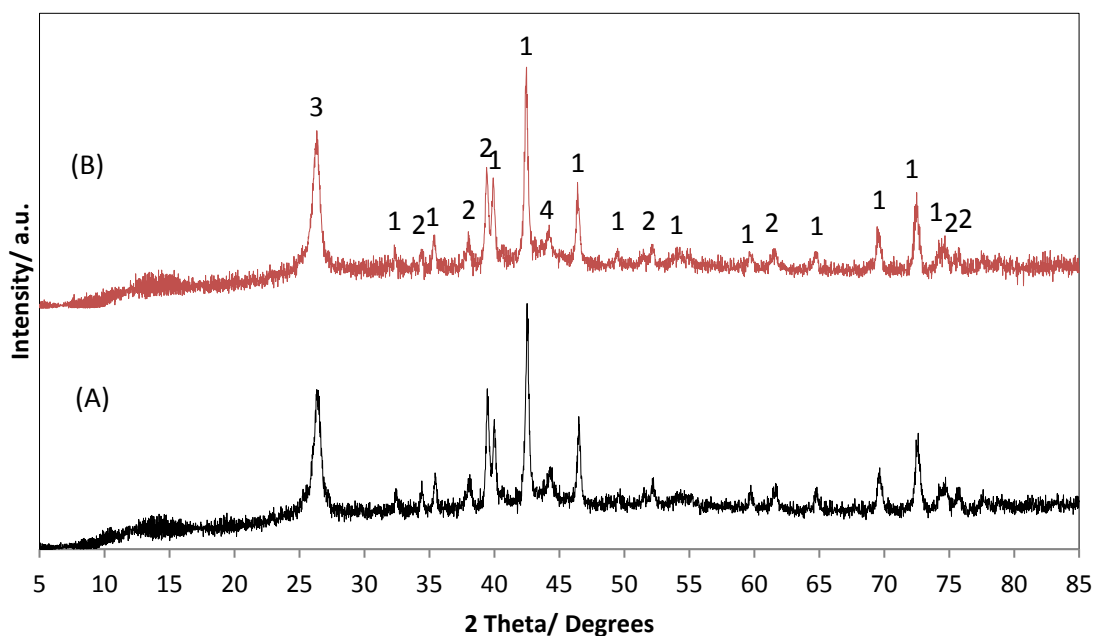


Figure 5.2-28: PXRD pattern of two attempts (A, B) of post-reaction $\text{Co}_3\text{Mo}_3\text{C}$ [1 for $\text{Co}_3\text{Mo}_3\text{C}$ (03-065-7128), 2 for $\beta\text{-Mo}_2\text{C}$ (001-1188), 3 for Graphite (003-0401), 4 for $\alpha\text{-Co}$ (01-089-7093)].

5.2.5.3 TGA analysis

To assess the reactivity of the carbon deposit, TGA analysis was performed under air. The change of the weight as function of temperature and the first derivative profile are presented in Figure 5.2-29. The removal of carbon started at a similar temperature, ~ 500 °C, to that observed for the cobalt molybdenum nitride systems and all the carbon was removed at ~ 700 °C as shown in Figure 5.2-29A. In both post-reaction materials, the total mass loss was around 76 wt. % C which is in line with the elemental analysis results (84 and 79 wt. % C).

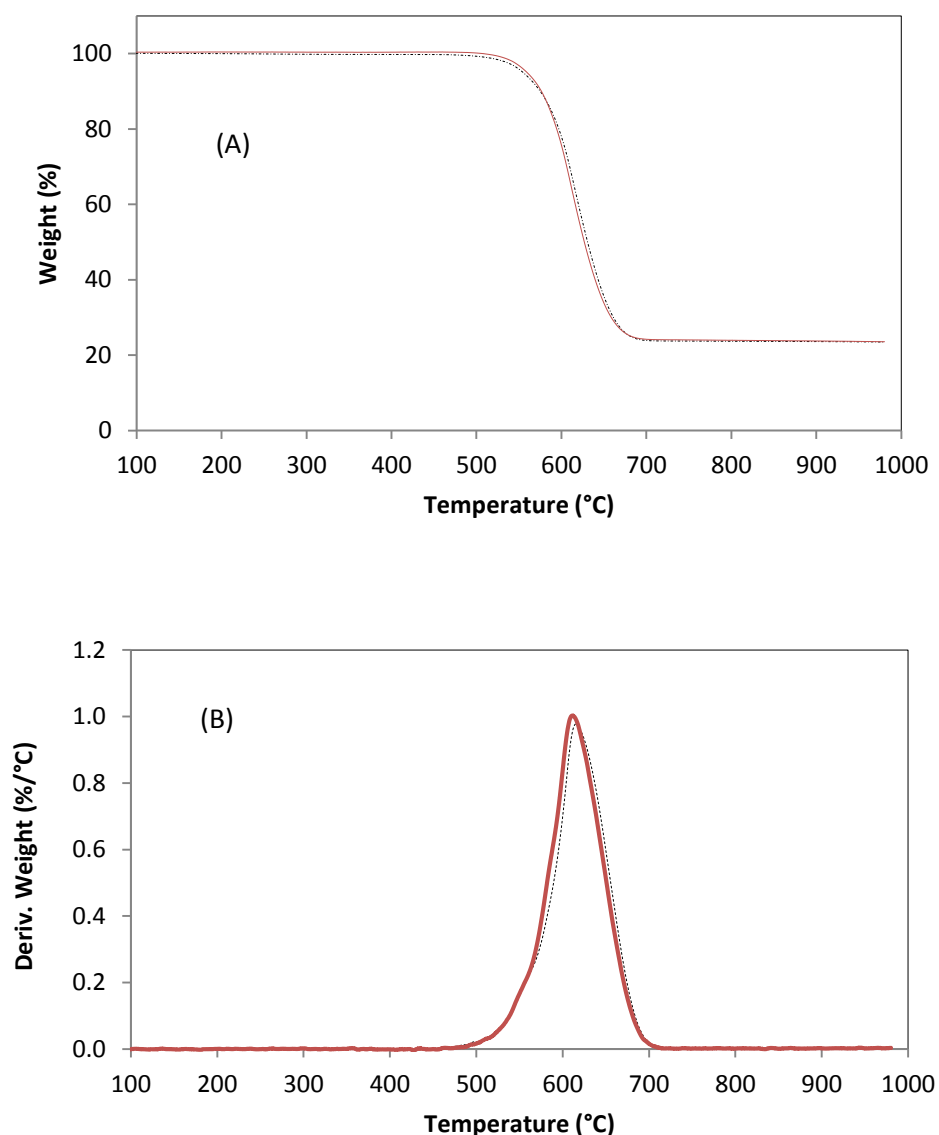


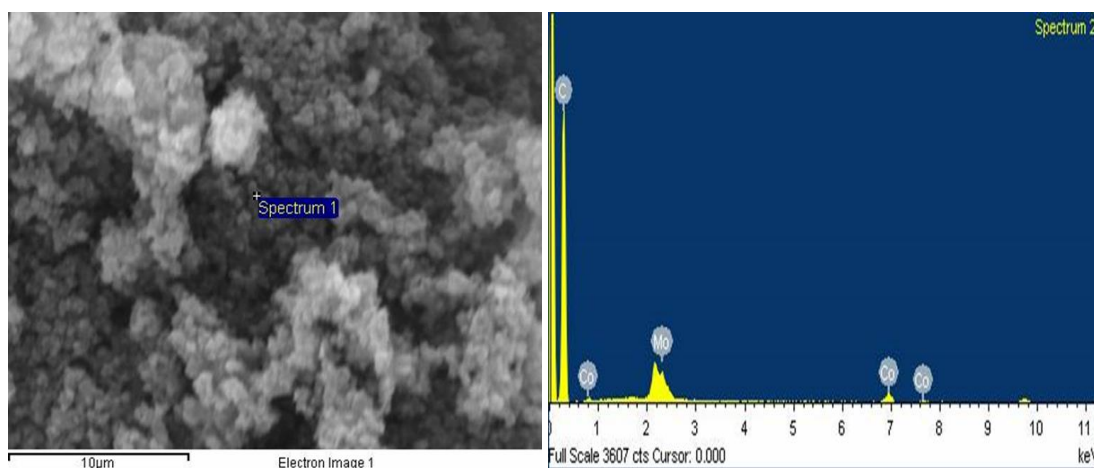
Figure 5.2-29: TGA trace (A) and derivative weight (B) of post-reaction $\text{Co}_3\text{Mo}_3\text{C}$ under air up to 1000 °C.

5.2.5.4 EDX and SEM analyses

SEM and EDX analyses of both samples have been undertaken. EDX analysis further confirmed the presence of carbon in a percentage that exceeds those expected for the pure carbide phase. For instance, in the post-reaction $\text{Co}_3\text{Mo}_3\text{C}$ the atomic ratio was found to be Co : Mo : C of 1.1 : 0.4 : 98.5 (Figure 5.2-30). This example shows also relative enrichment in Co, compared to Mo which is possible consistent with the phase segregation observed by XRD.

SEM images of pre- and post-reaction $\text{Co}_3\text{Mo}_3\text{C}$ samples are presented in Figure 5.2-31. Morphological differences were readily apparent between the pre-reaction and post-reaction samples. While, the pre-reaction $\text{Co}_3\text{Mo}_3\text{C}$ sample was present as nano-rod particles as shown in Figure 5.2-31 A, B, the post-reaction $\text{Co}_3\text{Mo}_3\text{C}$ material was present as an aggregated round particle morphology as apparent in Figure 5.2-31 C, D and Figure 5.2-31 E, F for the first and second reaction runs respectively.

The structural and textural evolution of the $\text{Co}_3\text{Mo}_3\text{C}$ during reaction altered additionally the accessible surface area. While the surface area of the post-reaction material was $13 \text{ m}^2\text{g}^{-1}$, the post-reaction material displayed an increase in the surface area to $\sim 50 \text{ m}^2\text{g}^{-1}$.



Element	Weight%	Atomic%
C K	92.37	98.54
Co K	5.26	1.14
Mo L	2.37	0.32
Totals	100.00	

Figure 5.2-30: EDX analysis of post-reaction $\text{Co}_3\text{Mo}_3\text{C}$ for first reaction run.

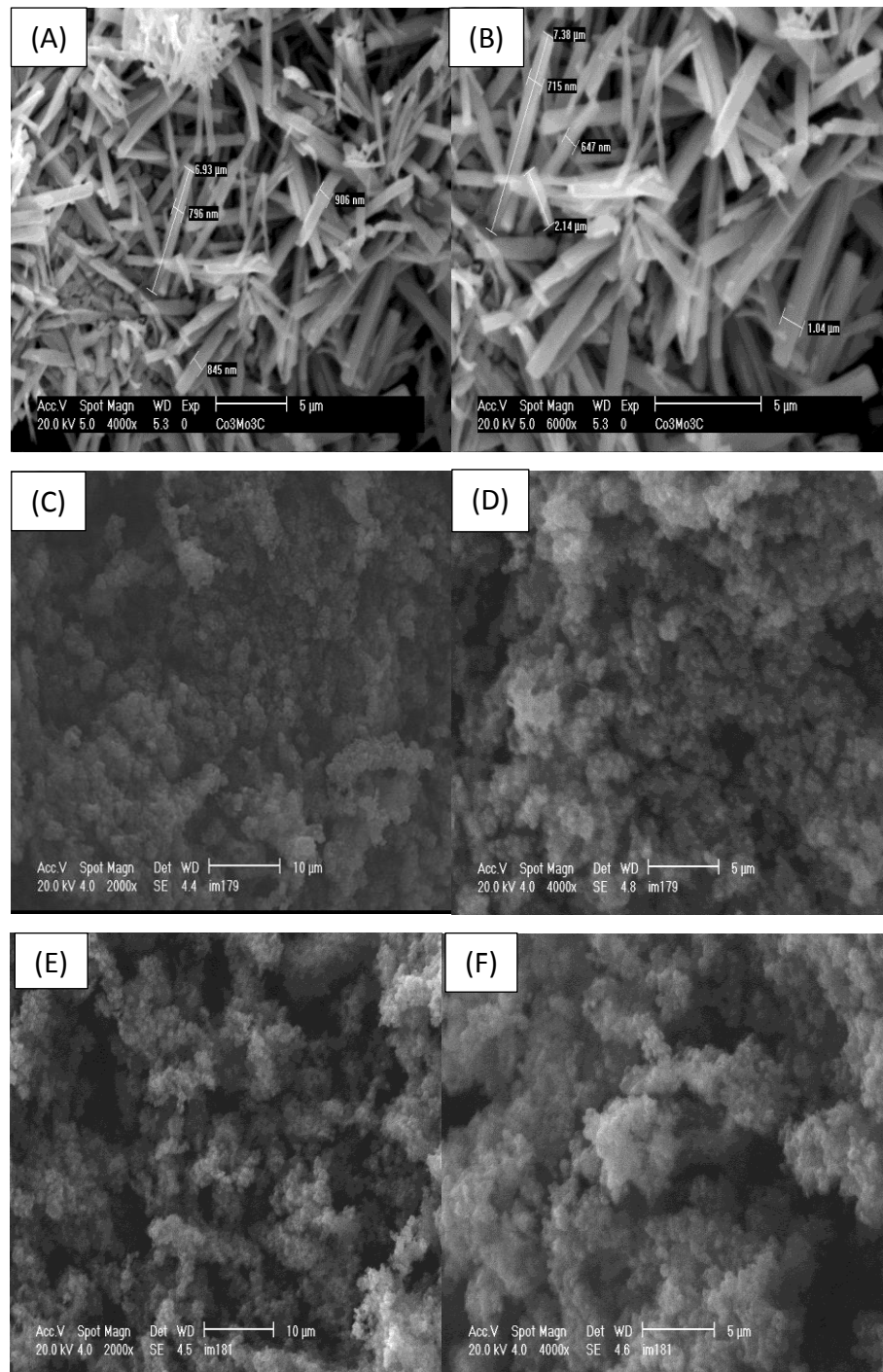


Figure 5.2-31: SEM images of pre- and post-reaction $\text{Co}_3\text{Mo}_3\text{C}$.

5.2.5.5 Raman spectroscopy

Post-reaction Raman spectra are shown in Figure 5-2-32. It can be seen that there are three main bands at 1280 cm^{-1} (D band), 1520 cm^{-1} (G band), and at 2640 cm^{-1} (2D band) which reveals the presence of graphitic and disordered structural carbon for both samples. A small shoulder D' peak at 1551 cm^{-1} associated with some randomly distributed impurities in the graphene was observed in both samples. Additional Raman bands related to the oxide phase located below 1000 cm^{-1} were detected in the both post-reaction $\text{Co}_3\text{Mo}_3\text{C}$ samples.

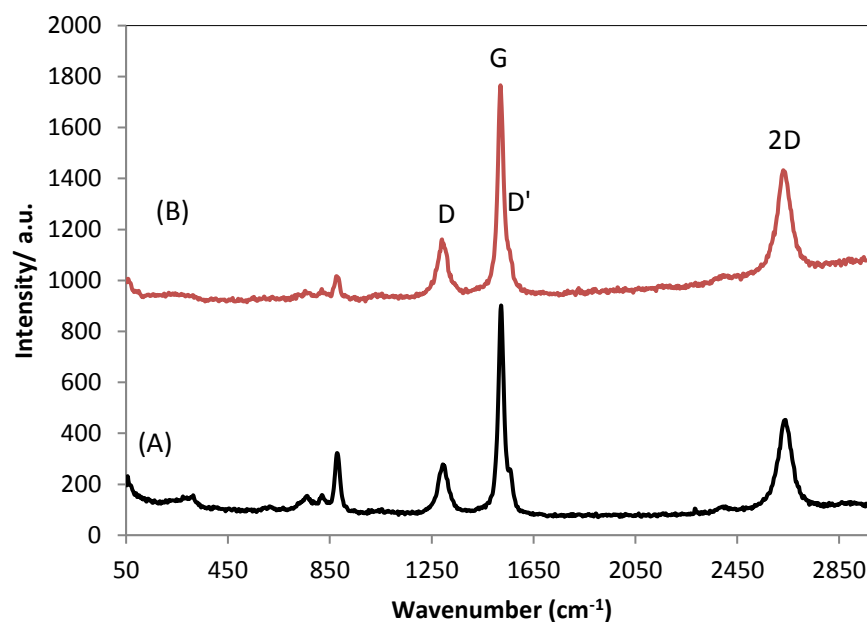


Figure 5.2-32: Raman spectrum of post-reaction $\text{Co}_3\text{Mo}_3\text{C}$: (A) first reaction run and (B) second reaction run.

5.2.6 Cobalt molybdenum carbide (η -12 structured $\text{Co}_6\text{Mo}_6\text{C}$)

Methane cracking over η -12 carbide structured $\text{Co}_6\text{Mo}_6\text{C}$ was conducted at 800 °C using a 3:1 $\text{CH}_4:\text{N}_2$ gas mixture flowing at 12 ml min^{-1} .

5.2.6.1 GC analysis

The reactivity of the $\text{Co}_6\text{Mo}_6\text{C}$ was studied for the methane cracking reaction. The hydrogen formation rate against time-on-stream at 800 °C is presented in Figure 5.2-33. As observed previously for the cobalt molybdenum carbide and nitrides, the hydrogen formation rate increased slowly, with the hydrogen formation rate being around $10 \times 10^{-4} \text{ mol H}_2 \text{ g}^{-1} \text{ min}^{-1}$ at the end of the reaction. The $\text{Co}_6\text{Mo}_6\text{C}$ presented slightly lower catalytic activity than the $\text{Co}_6\text{Mo}_6\text{N}$ ($17 \times 10^{-4} \text{ mol H}_2 \text{ g}^{-1} \text{ min}^{-1}$). In addition, no deactivation of this material was observed during the reaction time for 8 hours and, if anything, a gradual activation of the material was evident. From FTIR analyses methane bands were observed over the entire reaction time and no CO_x bands were observed.

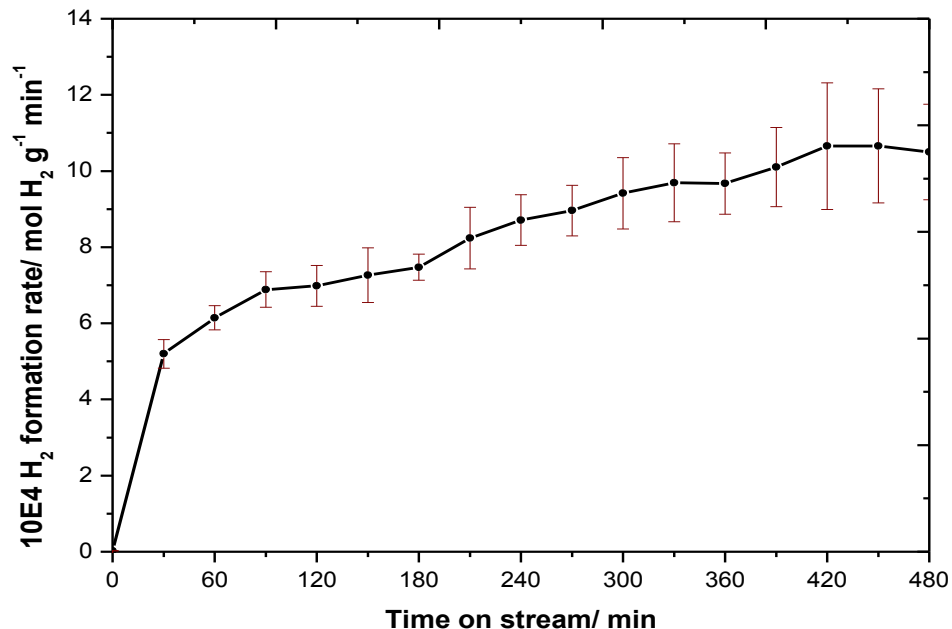


Figure 5.2-33: Hydrogen formation rate as a function of time on stream for methane cracking over $\text{Co}_6\text{Mo}_6\text{C}$ at 800 °C. The solid line is a guide for the eye.

5.2.6.2 PXRD analysis

The PXRD pattern of the post-reaction $\text{Co}_6\text{Mo}_6\text{C}$ is presented in Figure 5.2-34. The phases present were identified using the JCPDS database as η -6 $\text{Co}_3\text{Mo}_3\text{C}$ (PDF number: 03-065-7128), β - Mo_2C (PDF number: 001-1188), α -Co (PDF number 01-089-7093) and graphite (003-0401). η -6 $\text{Co}_3\text{Mo}_3\text{C}$ is depicted as 1, β - Mo_2C is depicted as 2 and α -Co is depicted as 3. Based on CHN elemental analysis results, the carbon content of the post-reaction sample was found to be 70 ± 1 wt. % C.

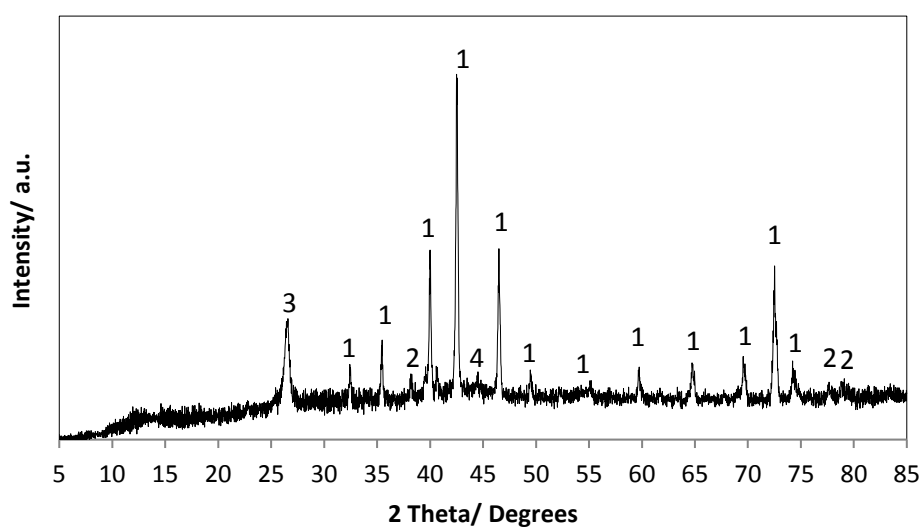


Figure 5.2-34: PXRD pattern of post-reaction $\text{Co}_6\text{Mo}_6\text{C}$ [1 $\text{Co}_3\text{Mo}_3\text{C}$ (03-065-7128), 2 β - Mo_2C (001-1188), 3 Graphite (003-0401) and 4 α -Co (01-089-7093)].

5.2.6.3 TGA analysis

The TGA profile of the post-reaction $\text{Co}_6\text{Mo}_6\text{C}$ conducted under static air is presented Figure 5.2-35. Similar to the previous results, the carbon removal characterised by weight loss during the experiment, which started at ~ 500 °C and which was complete by ~ 700 °C. The total mass loss was around 56 wt. % C which is slightly lower than the value expected from elemental analysis (70 ± 1 wt. % C). The first derivative profile (red colour) displays two mass loss components placed between 500 to 600 °C and 600 to 750 °C, which might be attributed to the loss of two different forms of carbon.

The similarity of the TGA profiles in all nitride and carbide related materials is consistent with analogous reactivity of the types of carbon species formed over all materials, although there are some differences in the peak-size and temperature profile.

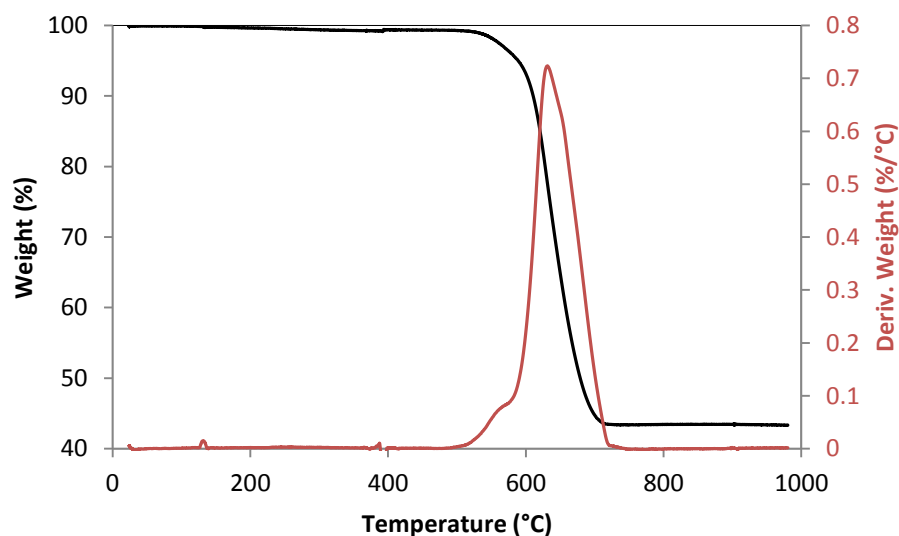
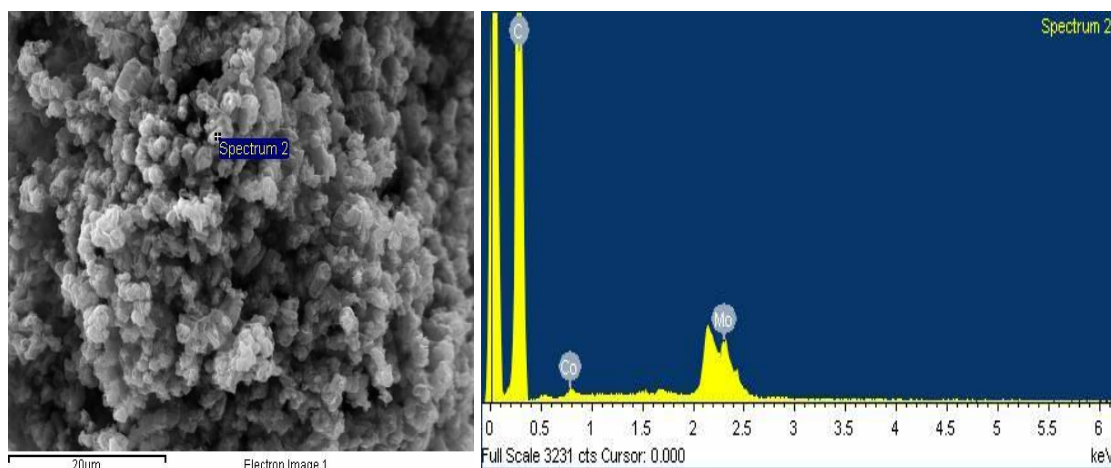


Figure 5.2-35: TGA trace and derivative weight of post-reaction $\text{Co}_6\text{Mo}_6\text{C}$ under air up to 1000 °C.

5.2.6.4 EDX and SEM analyses

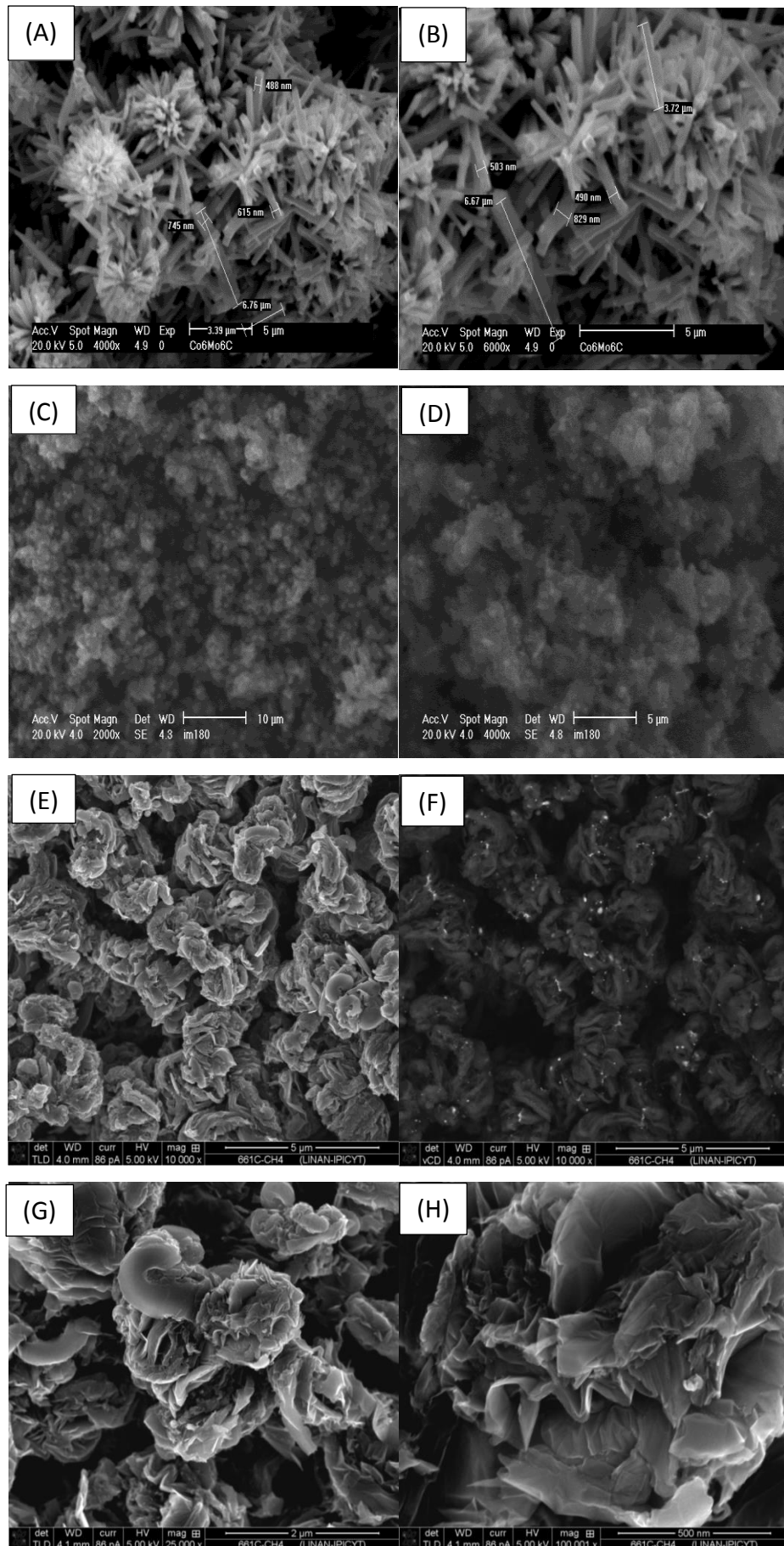
The significant carbon laydown during methane cracking was further confirmed by EDX analysis. EDX taken from different zones evidenced the presence of Co, Mo and carbon in an atomic ratio of C : Mo : C of 0.7 : 0.4 : 98.9 (Figure 5.2-36). Once more, the accessible surface area recorded for the post-reaction $\text{Co}_6\text{Mo}_6\text{C}$, $24 \text{ m}^2\text{g}^{-1}$, was higher than the surface area measured for the pre-reaction $\text{Co}_6\text{Mo}_6\text{C}$ which was around $3 \text{ m}^2\text{g}^{-1}$.

Figure 5.2-37 presents SEM images of the pre- and post-reaction $\text{Co}_6\text{Mo}_6\text{C}$ materials. The pre-reaction $\text{Co}_6\text{Mo}_6\text{C}$ displayed a needle morphology, while the post-reaction material presented similar morphology to the other post-reaction carbides and nitrides. The rounded circular shape of the post-reaction materials might originate from the growth of carbon deposits. It is interesting to mention that no filamentous carbon was observed in all the post- reaction samples presented within in this chapter.



Element	Weight%	Atomic%
C K	94.16	98.95
Co K	3.45	0.74
Mo L	2.39	0.31
Totals	100.00	

Figure 5.2-36: EDX analysis of post-reaction $\text{Co}_6\text{Mo}_6\text{C}$.

Figure 5.2-37: SEM images of pre- and post-reaction $\text{Co}_6\text{Mo}_6\text{C}$.

5.2.6.5 Raman spectroscopy

The Raman spectrum of the post-reaction $\text{Co}_6\text{Mo}_6\text{C}$ is shown in Figure 5.2-38. The presence of both G and D peaks at 1565 and 1365 cm^{-1} respectively can be observed. A 2D peak is also observed at 2679 cm^{-1} . Furthermore, it can be seen that the 2D peak is a roughly half the height of the G peak which indicated the presence of graphite in this material and not graphene because if there is graphene the 2D peak is expected to be four times more intense than the G peak. A small shoulder D' peak associated with some randomly distributed impurities in the graphene was not observed. The band D+D'' at 2450 cm^{-1} was first reported in graphite by Nemanich and Solin.¹⁹³ A small D+D' peak associated with the combination of phonons with different momenta was observed at 2910 cm^{-1} .¹⁹⁴ Furthermore, Raman bands positioned below than 1000 cm^{-1} corresponding to the trace oxide phase was observed.

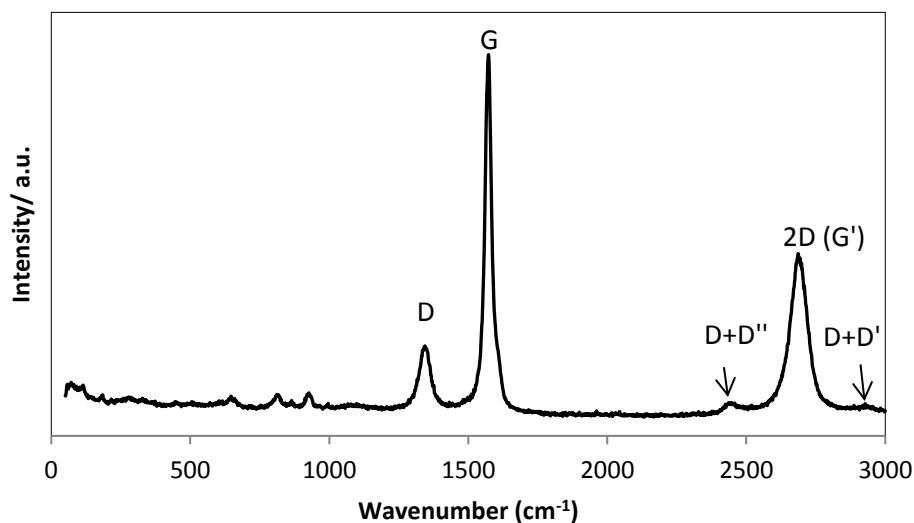


Figure 5.2-38: Raman spectrum of post-reaction $\text{Co}_6\text{Mo}_6\text{C}$.

Comparison of CoMo oxide, nitride and carbide for methane cracking

The isomorphism of the cobalt molybdenum carbide and nitride families offers, in principle, an elegant route to study the effect of interstitial carbon/nitrogen on the catalytic activity of cobalt molybdenum based materials. In this context, a range of materials with different chemical compositions namely $\text{Co}_3\text{Mo}_3\text{N}$, $\text{Co}_3\text{Mo}_3\text{C}$, $\text{Co}_6\text{Mo}_6\text{N}$ and $\text{Co}_6\text{Mo}_6\text{C}$, have been prepared and studied for the methane cracking reaction. All the prepared materials possess activity for hydrogen production upon methane cracking under the reaction conditions applied. Interestingly, the catalytic activity of these materials varied depending on initial composition, with $\text{Co}_6\text{Mo}_6\text{N}$ being the most active. The activity of the material was found to stabilise at around $1.8 \text{ mmol H}_2 \text{ g}^{-1} \text{ min}^{-1}$, which is very high when compared against the activity of some nitride systems (e.g. $180 \mu\text{mol H}_2 \text{ g}^{-1} \text{ min}^{-1}$ reported for a silicon-vanadium nitride nanocomposite under directly comparable conditions).¹⁴⁴ In fact, the activity of the $\text{Co}_6\text{Mo}_6\text{N}$ is directly comparable to the activity of iron oxide systems ($1 \text{ mmol H}_2 \text{ g}^{-1} \text{ min}^{-1}$ reported for iron oxide under the same reaction conditions).¹³¹ In general, the activity of carbides and nitrides presented a normalised hydrogen production rate ranging from 1.1 to $1.8 \text{ mmol H}_2 \text{ g}^{-1} \text{ min}^{-1}$ while a slightly lower activity ($0.8 \text{ mmol H}_2 \text{ g}^{-1} \text{ min}^{-1}$) was measured for the CoMoO_4 system. In addition to the enhanced activity of cobalt molybdenum carbide and nitride systems when compared to the oxide counterpart, the absence of the production of CO_x during methane cracking reaction is of potential interest in relation to CO_x free H_2 production.

As expected, the production of H_2 was accompanied by carbon deposition. Due to the nature of the reaction, the amount of carbon deposited in carbide and nitride systems can be correlated directly to the activity of methane cracking. Elemental analysis showed significant carbon deposition of $\sim 85 \text{ wt. \%}$ on $\text{Co}_3\text{Mo}_3\text{N}$, $\text{Co}_3\text{Mo}_3\text{C}$ and $\text{Co}_6\text{Mo}_6\text{N}$ confirming the high activity of these materials, in spite of the oscillatory hydrogen production behaviour of the $\text{Co}_3\text{Mo}_3\text{C}$ observed particularly in one case. Thermogravimetric analyses conducted under air confirmed that the weight loss associated with carbon oxidation to be consistent with the elemental analyses of post-reaction materials. The nature of the carbon present upon reaction has been investigated by Raman spectroscopy. The Raman features were dominated by the presence of two forms of carbon: disordered and graphitic carbon. The existence of several forms of carbon was also evident from the derivative weight curves for post- reaction samples.

While it is tempting to discuss the activity of the catalysts against their initial composition, post-reaction analysis revealed changes in the structural properties upon reaction. As expected, post-reaction PXRD showed the carburisation of all the catalysts studied upon reaction with methane. However, the products of carburisation slightly differ depending on the initial composition. In the post-reaction CoMoO_4 , only $\beta\text{-Mo}_2\text{C}$, $\alpha\text{-Co}$ and graphite are observed as results of the carburisation of CoMoO_4 . However, a mixture of $\text{Co}_3\text{Mo}_3\text{C}$, $\alpha\text{-Co}$ and $\beta\text{-Mo}_2\text{C}$ is detected upon reaction of $\text{Co}_3\text{Mo}_3\text{N}$, $\text{Co}_3\text{Mo}_3\text{C}$ and $\text{Co}_6\text{Mo}_6\text{N}$ with methane. In the case of $\text{Co}_6\text{Mo}_6\text{C}$ relocation of the carbon located in the 0 0 0 (8a) site to $1/8\ 1/8\ 1/8$ (16c) sites resulting in the formation of $\text{Co}_3\text{Mo}_3\text{C}$ occurs which is formed with traces of $\beta\text{-Mo}_2\text{C}$ and $\alpha\text{-Co}$ phases as observed for the other materials. The apparent similarity in H_2 production profile is a striking feature of both $\eta\text{-12}$ structured materials.

In summary, for the three most active catalysts, the phases detected after reaction were comprised of a mixture of $\text{Co}_3\text{Mo}_3\text{C}$, $\alpha\text{-Co}$ and $\beta\text{-Mo}_2\text{C}$. While, for the least active material CoMoO_4 , only the $\beta\text{-Mo}_2\text{C}$ and $\alpha\text{-Co}$ were detected. Another major aspect, where differences are evident, is the accessible surface area of the active phases. The surface area measured in post-reaction $\text{Co}_3\text{Mo}_3\text{N}$, $\text{Co}_3\text{Mo}_3\text{C}$ and $\text{Co}_6\text{Mo}_6\text{N}$ samples ranged between 50-63 $\text{m}^2\ \text{g}^{-1}$ while in the case of CoMoO_4 and $\text{Co}_6\text{Mo}_6\text{C}$ the surface area was limited to $\sim 30\ \text{m}^2\ \text{g}^{-1}$. Despite the fact that no simple link can be established between the catalytic activity to phase composition and accessible surface area, it can be argued that the presence of both $\text{Co}_3\text{Mo}_3\text{C}$ and $\beta\text{-Mo}_2\text{C}$ and high surface area leads to an enhanced activity for methane cracking when compared to phases where only $\text{Co}_3\text{Mo}_3\text{C}$ or $\beta\text{-Mo}_2\text{C}$ are present. In addition, the initial composition seems to play an important role in the final activity of the catalysts. These differences may indicate differences in the active surface composition resulting from the carburisation process of different cobalt molybdenum precursors.

5.2.7 Si₃N₄ and VN/Si₃N₄ materials

Si₃N₄ and VN/Si₃N₄ materials were prepared by Andrew Hector's group in Southampton University as described in a recent publication¹⁴⁴ and their methane cracking was investigated in Glasgow.

Introduction for Si₃N₄ and VN/Si₃N₄ materials

Gel-derived silicon imidonitrides have been investigated for catalytic reactions by a number of groups as base catalysts. For instance, the catalyst has been examined for alkene isomerization reactions¹⁹⁵ and for Knoevenagel condensation reactions¹⁹⁶. Silicon nitride possesses great thermal conductivity corresponding to the more widely utilised silicas, and therefore is employed as a catalyst support for in elevated temperature applications. Silicon nitride support in the form of α -Si₃N₄ has an oxidation resistance at typical catalytic process temperatures.¹⁹⁷ The gel-based ways to silicon nitrides and imidonitrides employ solution-phase reactions of precursor molecules. These precursors are usually amides with cross-linking groups for example isocyanate¹⁹⁸ or ammonia¹⁹⁹. The polymeric species were obtained in solution, and when the polymeric material immobilises, the liquid phase can be removed to deliver high surface area materials that often comprise basic surface groups.²⁰⁰ These reactions deliver widely applicable sol-gel chemistry that has been employed to yield films,²⁰¹ powders,²⁰² membranes²⁰³ and monolithic aerogels.²⁰⁴

The Mo₂N catalyst is a highly active Group 6 nitride catalyst and has been investigated extensively. Meanwhile, a number of metal nitrides have been previously investigated to have useful catalytic activities.²⁰⁵ Most of these investigations placed emphasis on the similarity of the activities of some metal nitrides to those of the platinum metals, with surface areas typically being maximised by careful temperature control in reactions between ammonia and high surface area metal oxides.²⁰⁶ However, the Group 5 nitrides can exhibit various selectivities, which can also differ between phases.²⁰⁷ VN has been reported to be a suitable catalyst in amination of ethanol²⁰⁸, dehydrogenation of propane²⁰⁹ and ammonia decomposition.²¹⁰ Recent studies have attempted to modify the properties of gel-derived silicon nitride materials by incorporating aluminium,²¹¹ titanium,²¹² boron²¹³ or terbium²¹⁴ into the silicon imidonitride framework, or by using it to support palladium nanoparticles,²¹⁵ but there is only a scant investigation in this area. In

this work, the catalytic activity of VN/ Si_3N_4 and Si_3N_4 composite materials in methane cracking was investigated.

Results and discussion

Methane cracking over Si_3N_4 and VN/ Si_3N_4 was conducted at 800 °C using at 75 vol. % CH_4 in N_2 gas mixture at a flow rate 12 ml min^{-1} with a temperature ramp rate 50 °C min^{-1} .

5.2.7.1 GC analysis

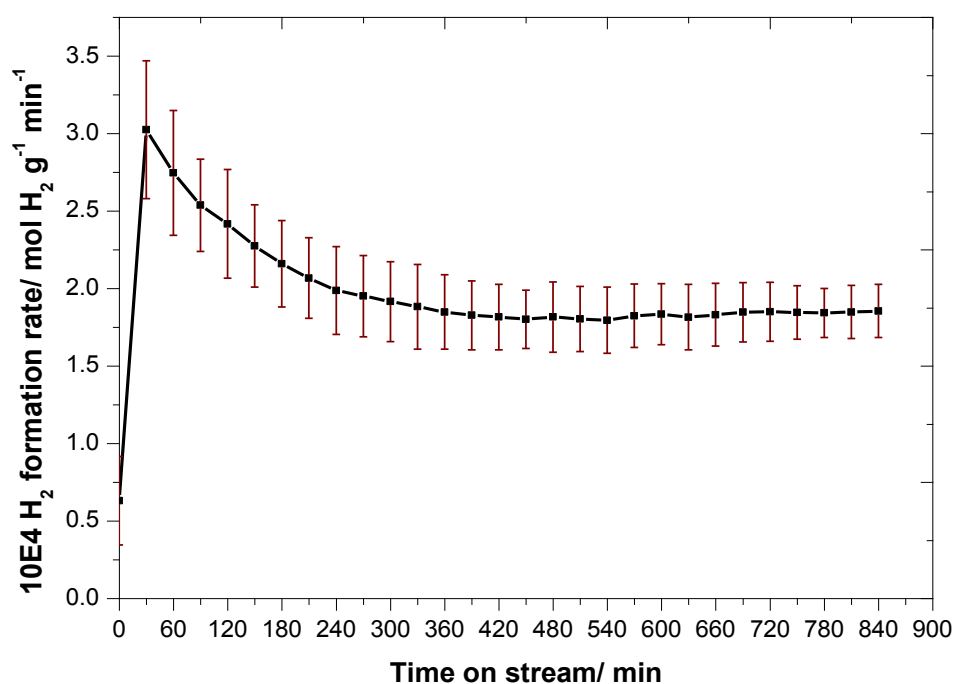


Figure 5.2-39: Hydrogen formation rate as a function of time on stream of VN/ Si_3N_4 at 800 °C. Similar values were obtained in a repeat run with the same mass of material; the solid line is a guide for the eye.

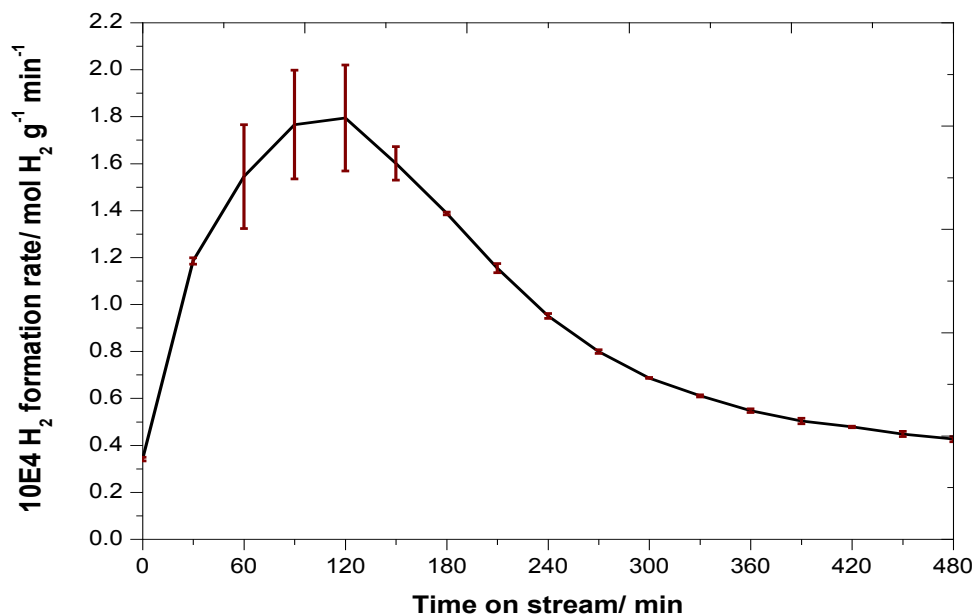


Figure 5.2-40: Hydrogen formation rate as a function of time on stream of Si_3N_4 at $800\text{ }^\circ\text{C}$. Similar values were obtained in a repeat run with the same mass of material; the solid line is a guide for the eye.

The reaction profile illustrating the mass normalised hydrogen formation rate over a period of 14 hours for VN/ Si_3N_4 is presented in Figure 5.2-39. Following an initial period of decay over the first 3-4 hours on stream, the activity of the material was found to stabilise to a value of around $180\text{ }\mu\text{mol H}_2\text{ g}^{-1}\text{ min}^{-1}$. Whilst this mass normalised rate does not compare favourably with, for example, iron oxide systems in the literature (for example, a peak rate of $1\text{ mmol H}_2\text{ produced g}^{-1}\text{ min}^{-1}$ under directly comparable reaction conditions has been reported for biogenic iron oxide) one potential advantage is that the absence of oxide phase in the system results in the absence of CO production which is particularly deleterious for H_2 streams applied to PEM fuel cells. Off line FTIR analysis taken at regular intervals throughout the catalyst runs showed the CO and CO_2 levels to be below the limit of detection. CO_2 formation, which can also occur in the presence of oxides, could also be problematic under these conditions since CO formation could occur via the reverse water gas-shift reaction which is particularly thermodynamically favourable at such high reaction temperature. In order to determine the background activity of the silicon nitride material, directly comparable catalytic reaction runs were undertaken (Figure 5.2-40). This material was also reasonably active for methane cracking, again without producing CO_x . However,

there is evidence of an induction period followed by deactivation leading to a rate of ca. $40 \mu\text{mol g}^{-1} \text{min}^{-1}$, which is much lower than that of its vanadium containing counterpart. This is indicative of the promotional effect of vanadium upon reaction. A particularly noteworthy aspect of the vanadium containing composite is the relative stability of H_2 production at extended periods upon stream.

5.2.7.2 PXRD analysis

X-ray diffraction (PXRD) of these materials mainly showed broad amorphous features as expected for silicon nitride at this temperature as shown in Figure 5.2-41A,¹⁹⁹ but with further broad peaks corresponding to the most intense expected reflection (the 200) for rocksalt-type VN at 600°C as shown in Figure 5.2-42A. The peaks at $2\theta = 10.7$ and 22.9° disappeared and become more amorphous in post-reaction VN/ Si_3N_4 as shown in Figure 5.2-42B.

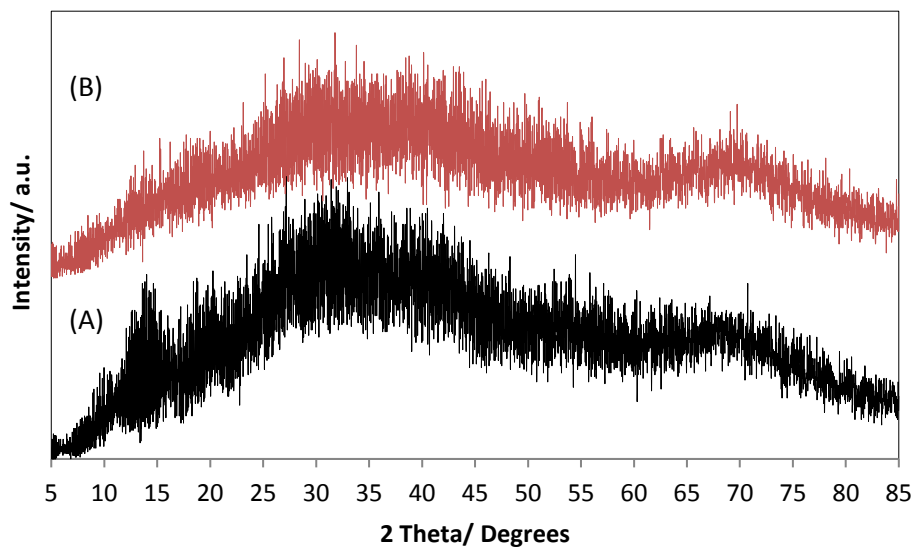


Figure 5.2-41: PXRD pattern of (A) pre- and (B) post- reaction Si_3N_4 .

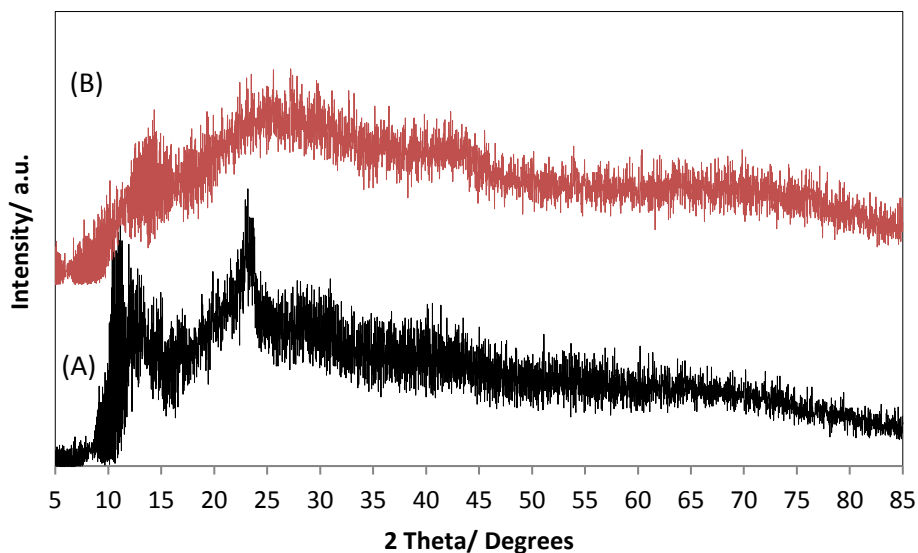


Figure 5.2-42: XRD pattern of (A) pre- and (B) post- reaction VN/Si₃N₄.

5.2.7.3 TGA analysis

To further characterise the nature of the carbon deposit after reaction, thermogravimetric analysis of the post-reaction Si₃N₄ and VN/ Si₃N₄ were carried out in air in the temperature range between 100 – 1000 °C to estimate the amount of carbon deposited and to determine its reactivity profile with respect to air.

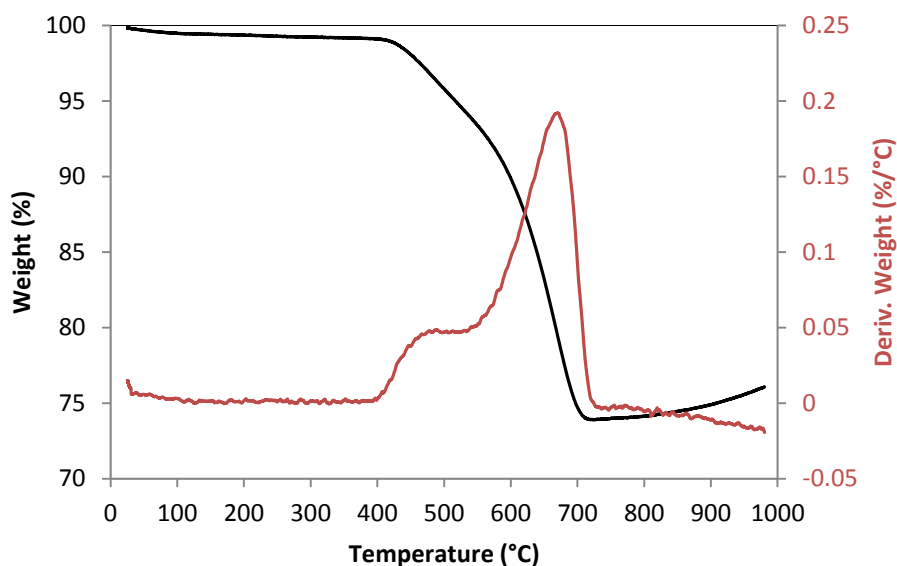


Figure 5.2-43: TGA trace and derivative weight of post-reaction VN/Si₃N₄ under air up to 1000 °C.

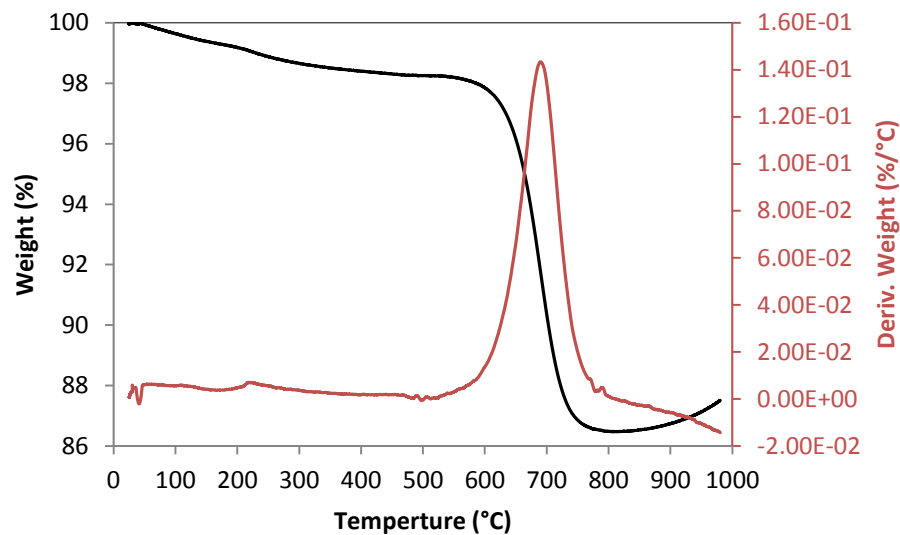


Figure 5.2-44: TGA trace and derivative weight of post-reaction Si_3N_4 under air up to 1000 °C.

TGA conducted under air for the both post-reaction materials (Figure 5.2-43 and Figure 5.2-44) shows the weight loss associated with the removal of carbon to be consistent with the CHN analyses of post-reaction materials. The first derivative profiles clear show two mass loss features centred at around 450 and 680 °C in the case of the vanadium based system, suggesting two forms of carbon as shown in Figure 5.2-43. This is in contrast with the single mass loss feature centred around 700 °C observed in the case of post-reaction silicon nitride as shown in Figure 5.2-44. However caution must be exercised in this respect, as it could be possible that the presence of vanadium catalyses the oxidation of a proportion of the carbon deposited causing its loss at lower temperature. As anticipated, the production of H_2 was associated with the deposition of carbon upon the materials. The vanadium-containing sample post catalysis was found to contain 23 wt. % C by combustion analysis in comparison to ca. 9 wt. % C deposited on the silicon nitride.

5.2.7.4 Raman spectroscopy

Raman spectroscopy was conducted at room temperature and in air on the post-reaction Si_3N_4 and VN/ Si_3N_4 samples. 532 nm laser was employed as the excitation source for laser. The spectral range scanned was in the range of up to 3000 cm^{-1} because peaks beyond 3000 cm^{-1} are not expected.

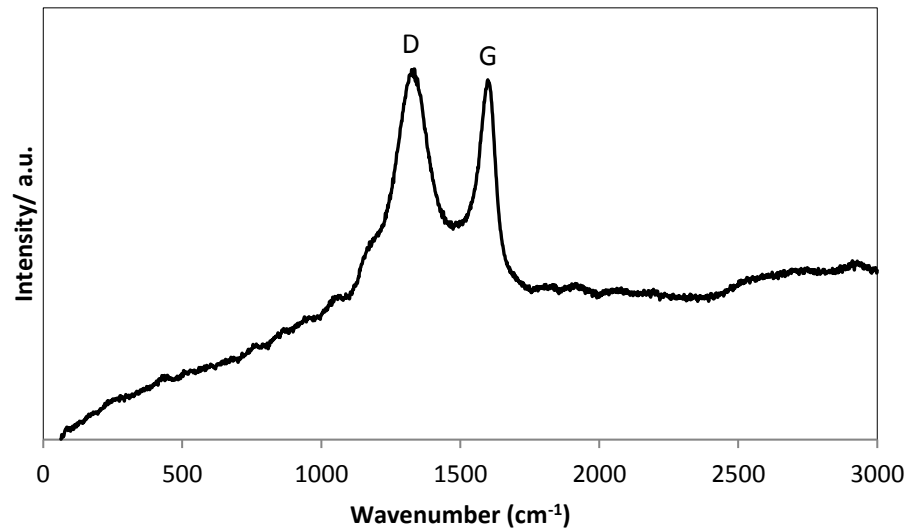


Figure 5.2-45: Raman spectrum of post-reaction Si_3N_4 .

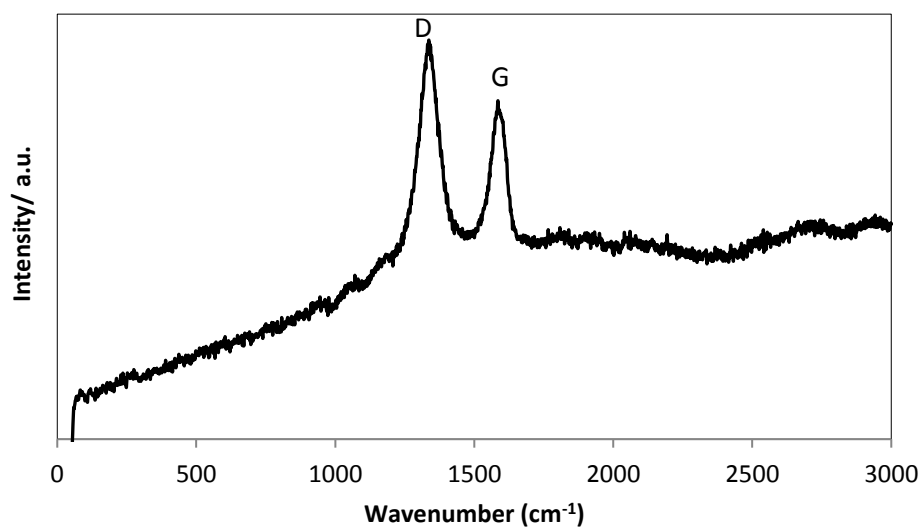


Figure 5.2-46: Raman spectrum of post-reaction VN/ Si_3N_4 .

Raman spectroscopic analyses of both post-reaction samples (Figure 5.2-45 and Figure 5.2-46) evidence disordered (D) and graphitic (G) bands; although the relative intensity implies that the carbon is less well ordered in the vanadium containing material.

5.2.7.5 EDX and SEM analyses

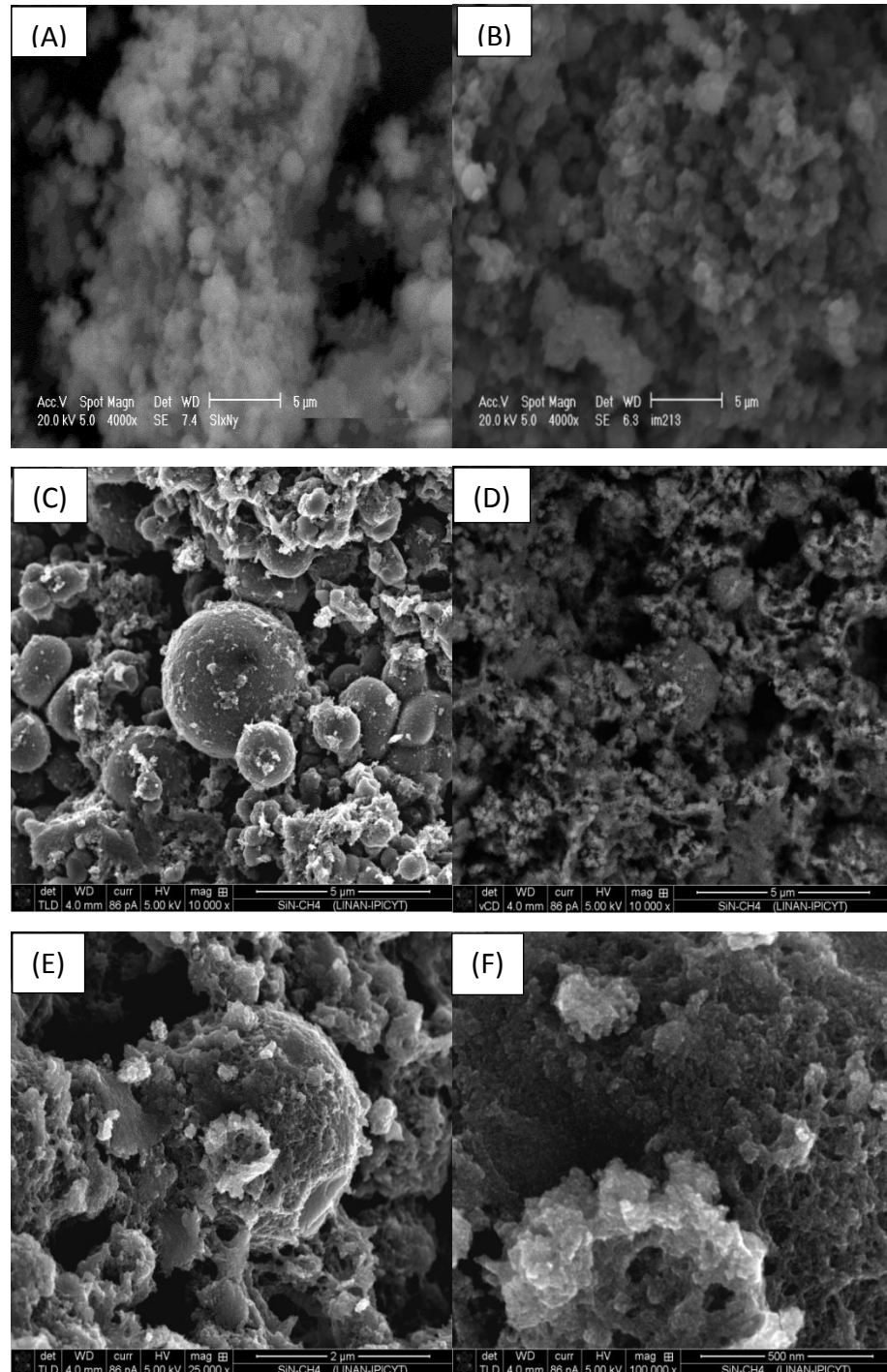
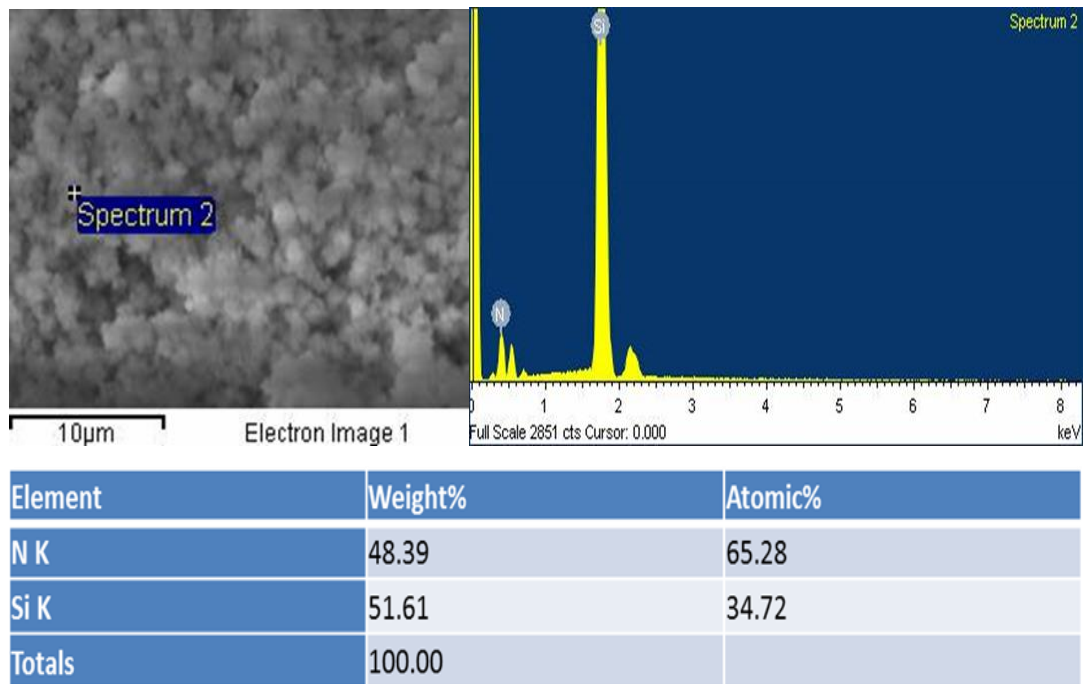
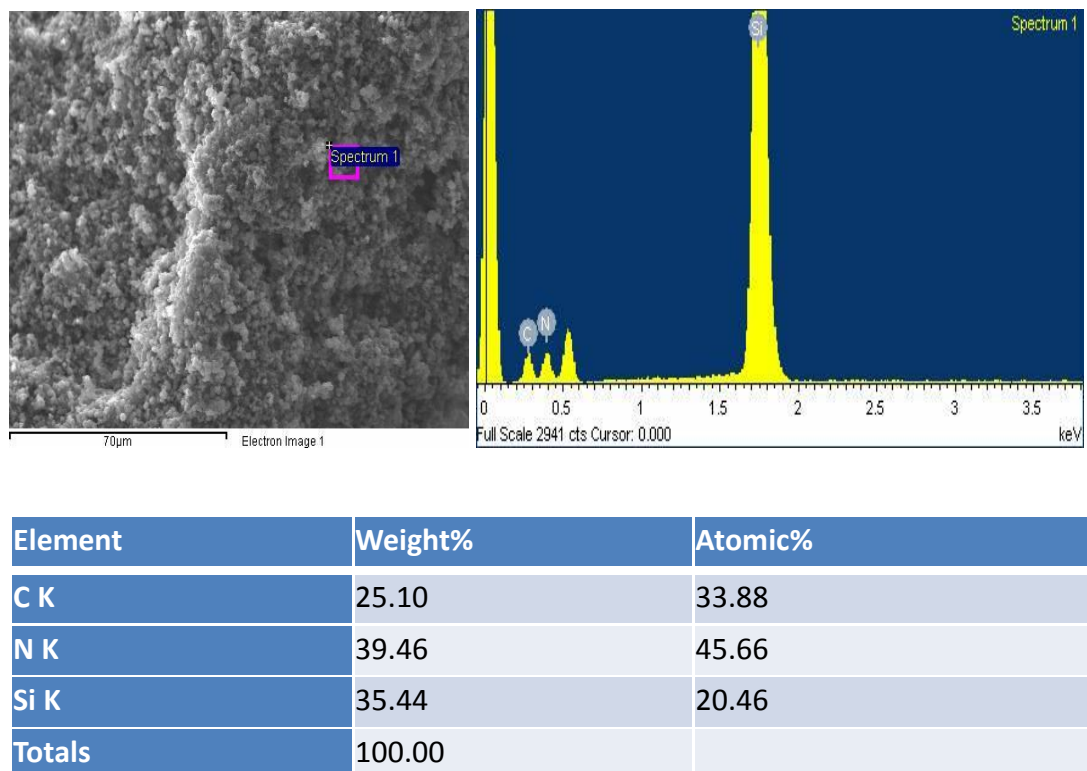


Figure 5.2-47: SEM images of (A) pre- and (B, C, D, E, F) post-reaction Si_3N_4 .

Figure 5.2-48: EDX analysis of pre-reaction Si_3N_4 .Figure 5.2-49: EDX analysis of post-reaction Si_3N_4 .

Figures 5.2-47A and 5.2-51A present the morphology of pre-reaction of Si_3N_4 and $\text{VN}/\text{Si}_3\text{N}_4$ samples respectively. It can be seen that both pre-reaction Si_3N_4 and $\text{VN}/\text{Si}_3\text{N}_4$ are comprised of spherical aggregate particles of various sizes. Energy dispersive X-ray (EDX) analyses yielded Si:N atomic ratio of 35:65 (as shown in Figure 5.2-48) for Si_3N_4 and Si:N:V atomic ratio of 30:69:1 (as shown in Figure 5.2-52) for $\text{VN}/\text{Si}_3\text{N}_4$ which suggest that the gel was well cross-linked with very low levels of volatile species and hence negligible loss of V or Si occurred upon pyrolysis. Both materials were found to contain 10 wt. % N by combustion analysis. The surface area was $162\text{ m}^2\text{g}^{-1}$ for Si_3N_4 and $126\text{ m}^2\text{g}^{-1}$ for $\text{VN}/\text{Si}_3\text{N}_4$ as prepared.

In contrast, the use of Si_3N_4 or $\text{VN}/\text{Si}_3\text{N}_4$ reacted with 3:1 $\text{CH}_4:\text{N}_2$ at $800\text{ }^\circ\text{C}$ for 14 hours results in the formation of rounded particles. Illustrative scanning electron microscopy images are presented in Figures 5.2-47B and 5.2-51B where it can be seen that both post-reaction samples of these materials are comprised of circular morphology feature. This possibly reflects the morphology of the deposited carbon. EDX analyses revealed the presence of carbon and nitrogen in these materials as shown in Figure 5.2-49 for Si_3N_4 and in Figure 5.2-53 for $\text{VN}/\text{Si}_3\text{N}_4$. The vanadium-containing sample post catalysis was found to contain 7 wt. % N and 23 wt. % C by combustion analysis in comparison to 3 wt. % N and ca. 9 wt. % C deposited for the silicon nitride. The BET surface area recorded for both post-reaction materials had fallen to $19\text{ m}^2\text{g}^{-1}$ for Si_3N_4 and $18\text{ m}^2\text{g}^{-1}$ for $\text{VN}/\text{Si}_3\text{N}_4$.

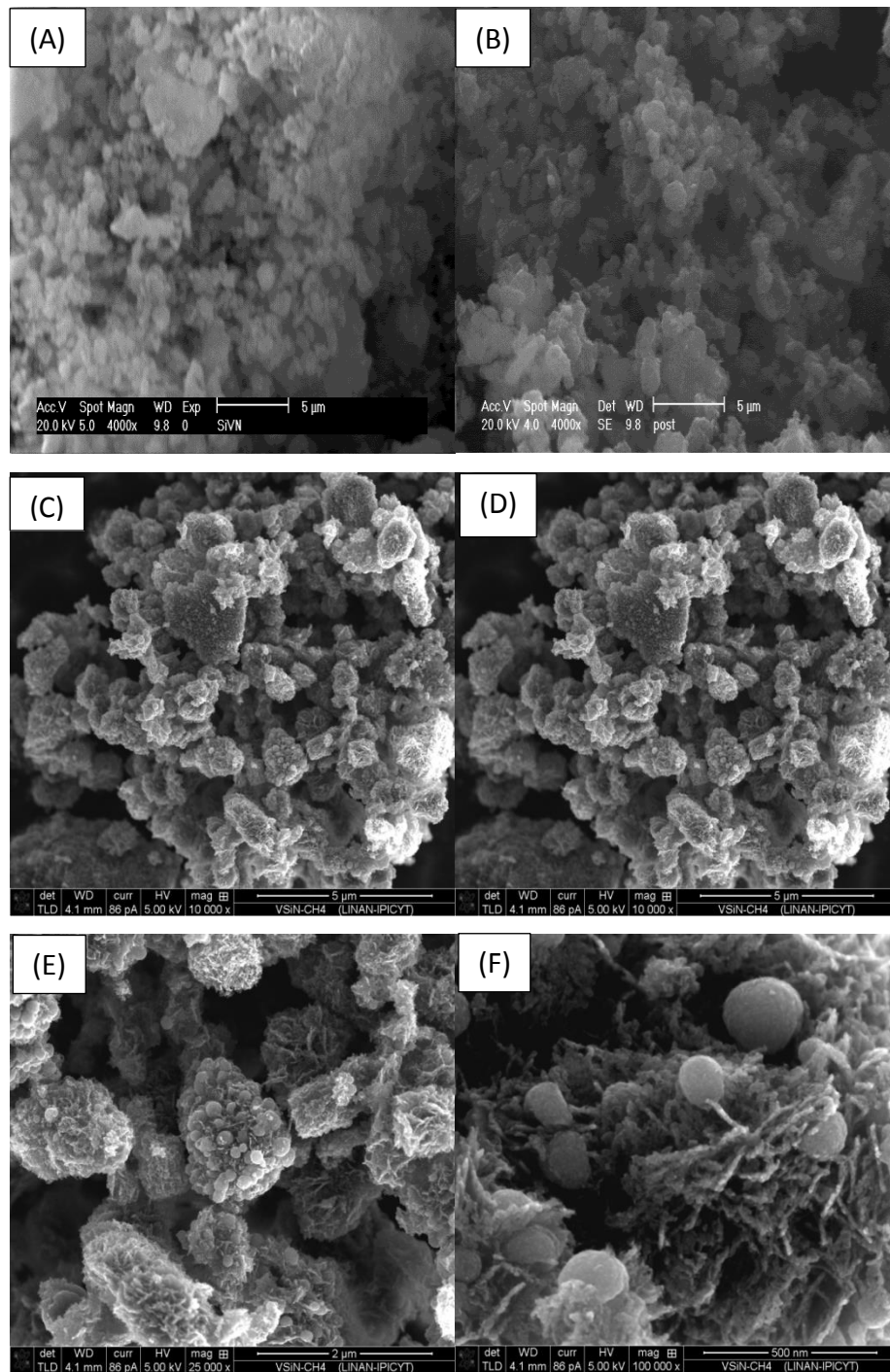
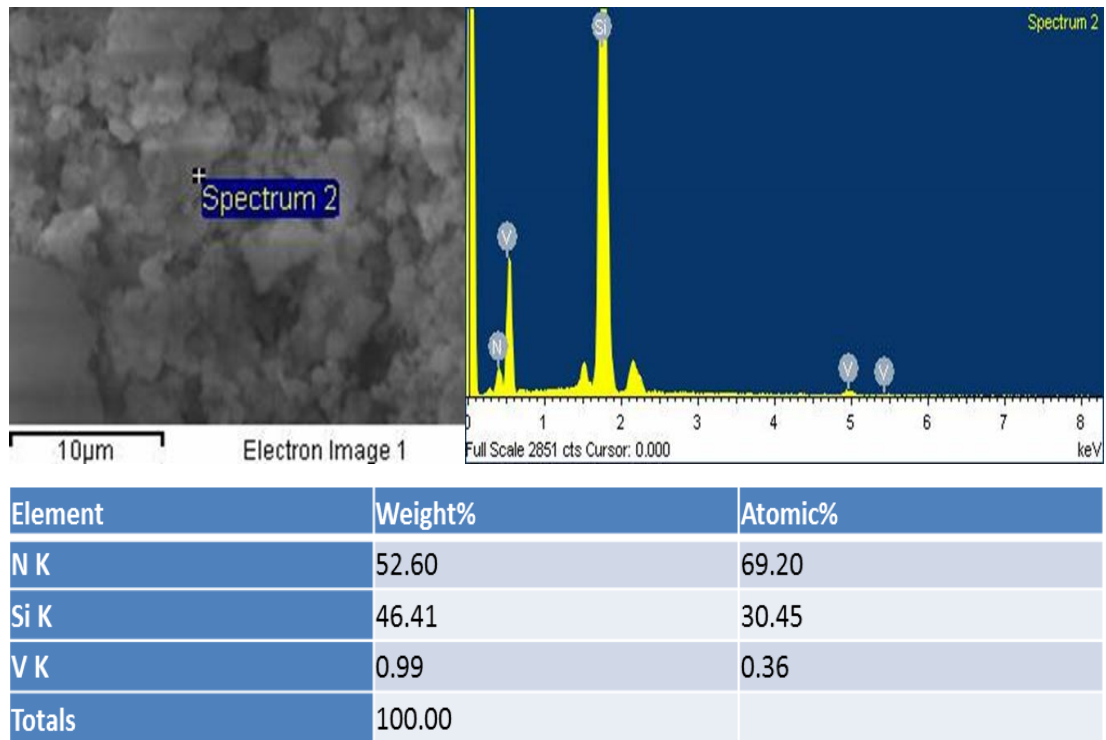
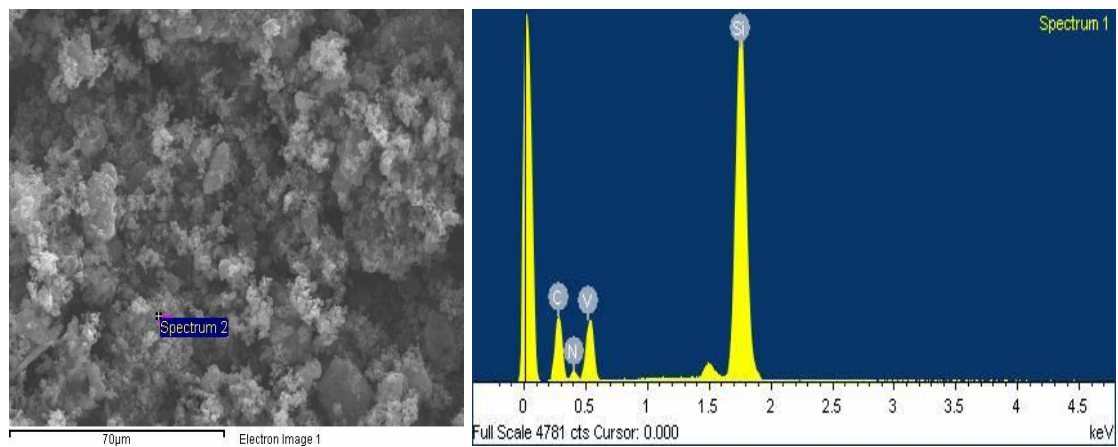


Figure 5.2-50: SEM image of (A) pre- and (B, C, D, E and F for 4000, 10000, 10000, 25000 and 10000 magnification respectively) post-reaction VN/ Si₃N₄.

Figure 5.2-51: EDX analysis of pre-reaction VN/ Si₃N₄.Figure 5.2-52: EDX analysis of post-reaction VN/ Si₃N₄.

5.3 Conclusion

In this study, catalytic methane cracking to produce hydrogen and carbon was investigated over MoO_3 , CoMoO_4 , $\text{Co}_3\text{Mo}_3\text{N}$, $\text{Co}_6\text{Mo}_6\text{N}$, $\text{Co}_3\text{Mo}_3\text{C}$, $\text{Co}_6\text{Mo}_6\text{C}$, Si_3N_4 and $\text{VN}/\text{Si}_3\text{N}_4$ materials. For comparison purposes, all the materials were tested for activity under the same conditions of temperature (800 °C), at atmospheric pressure and using a reactant composition of 75 vol. % CH_4 in N_2 (BOC, 99.98%) at a total gas feed of 12 ml min^{-1} . Hydrogen production was measured by online gas chromatography (GC) using a TCD. For most samples the gas exhaust was analysed in a periodical manner for the determination of CO_x by off-line FTIR analyses employing a gas-phase FTIR cell. The characterisation of post-reaction samples by Raman spectroscopy, X-ray diffraction (XRD), thermal analysis (TGA) and by scanning electron microscopy (SEM), N_2 -physisorption (BET), energy dispersive X-ray spectroscopy (EDX) and CHN elemental analysis was undertaken.

In general, $\text{Co}_6\text{Mo}_6\text{N}$, $\text{Co}_3\text{Mo}_3\text{N}$, $\text{Co}_6\text{Mo}_6\text{C}$ and CoMoO_4 materials showed better activity and stability during catalytic methane cracking over time with hydrogen formation rates in order respectively (1700, 1200, 1000 and 800 $\mu\text{mol H}_2 \text{ g}^{-1}\text{min}^{-1}$) while MoO_3 deactivated after 60 minutes to stay around 70 $\mu\text{mol H}_2 \text{ g}^{-1}\text{min}^{-1}$. In all cases, hydrogen production reached a plateau after 120 minutes on stream. However, significantly unstable performance was observed in the case of the $\text{Co}_3\text{Mo}_3\text{C}$ sample, which was possibly related to significant carbon deposition during the reaction resulting in the reactor blockage problems. Similar observations were observed upon repeating the reaction and the structural and textural properties of both the post-reaction samples were all similar.

For the $\text{Co}_6\text{Mo}_6\text{N}$, $\text{Co}_3\text{Mo}_3\text{N}$, $\text{Co}_3\text{Mo}_3\text{C}$ and $\text{Co}_6\text{Mo}_6\text{C}$ materials, the phases detected after reaction comprised of a mixture of $\text{Co}_3\text{Mo}_3\text{C}$, $\alpha\text{-Co}$, $\beta\text{-Mo}_2\text{C}$ and graphite. For the least active material CoMoO_4 , $\beta\text{-Mo}_2\text{C}$, $\alpha\text{-Co}$ and graphite were detected. For MoO_3 , only $\beta\text{-Mo}_2\text{C}$ was detected. Another major aspect, where differences are evident, is the accessible surface area of the active phases. The surface area measured in post-reaction $\text{Co}_3\text{Mo}_3\text{N}$, $\text{Co}_3\text{Mo}_3\text{C}$ and $\text{Co}_6\text{Mo}_6\text{N}$ samples ranged between 50-63 $\text{m}^2 \text{ g}^{-1}$ while in the case of CoMoO_4 and $\text{Co}_6\text{Mo}_6\text{C}$ the surface area was limited being $\sim 30 \text{ m}^2 \text{ g}^{-1}$. Despite the fact that no simple link can be established between the catalytic activity and the phase composition and accessible surface area, it can be argued that the presence of both $\text{Co}_3\text{Mo}_3\text{C}$ and $\beta\text{-Mo}_2\text{C}$

and high surface area lead to an enhanced activity for methane cracking when compared to phases where only β -Mo₂C is present.

In the case of cobalt molybdenum nitrides and carbides, off-line FTIR spectra, measured periodically during reaction, showed that the production of CO and CO₂ during methane cracking was below the detection limit. However, CO and CO₂ were clearly observed when MoO₃ and CoMoO₄ were used. It is worth considering that the production of CO, even in small concentrations, can be particularly harmful in the case of hydrogen production for PEMFC and can lead to rapid degradation of their performance. The use of nitride or carbide as catalysts for methane cracking affords the production of CO_x-free hydrogen.

Graphitic carbon was present at all materials except MoO₃ where only carbide observed and it was significantly higher for the cobalt molybdenum nitrides followed by the carbides and then the oxide. Carbon deposition studies by TGA and Raman spectroscopy showed that most of the carbon was present as two types of carbon graphitic and disordered forms.

Vanadium incorporation into silicon nitride is also worthy of further attention as a catalyst for the production of hydrogen from methane since, although the activity is lower than that of other systems, the absence of oxygen containing phases again results in effluent streams which are free from the presence of CO, a notable downstream poison for some applications.

Chapter 6. Conclusions and further work

6.1 Conclusion

The underlying objective of this work was to investigate the role of chemical composition and crystal structure on the reactivity of molybdenum related materials. To this end, a large number of molybdenum related materials presenting different characteristics and chemical compositions were prepared including binary molybdenum (γ -Mo₂N, β -Mo₂C, α -Mo₂C) and ternary cobalt molybdenum η -6 Co₃Mo₃N, η -12 Co₆Mo₆N, η -6 Co₃Mo₃C, η -12 Co₆Mo₆C systems. Although, the majority of studied phases were reported in the literature, the preparation of these phases required a careful control of the synthesis parameters. The nature of the starting precursors, reaction temperature, temperature rate and the reaction atmosphere were found to be of critical importance for the generation of monophasic materials especially in the case of the carbide systems. In Chapter 3, the ability of Co₃Mo₃N and Co₃Mo₃C to uptake and release carbon or nitrogen was studied.

The synthesis reaction paths for the preparation of carbide and nitride materials were studied extensively. *In-situ* neutron diffraction studies revealed that in both cases, nitridation of the Co₃Mo₃C or carburisation of Co₃Mo₃N in presence of hydrogen proceeded via the formation of an intermediate carbonitride phase (Co₃Mo₃C_xN_{1-x}) with carbon and nitrogen both occupying the 16c Wyckoff site. However, the results of carburisation of Co₆Mo₆N and the nitridation of Co₆Mo₆C followed a different reaction path.

The following bullet points highlight some of the major findings:

- **Preparation of η -6 Co₃Mo₃C:** η -6 Co₃Mo₃N was converted to η -6 Co₃Mo₃C using 20 vol. % CH₄ in H₂ via the formation of a range of intermediate Co₃Mo₃C_xN_{1-x} phases in the temperature range between 600 to 700 °C. The results showed that nitrogen and carbon atoms simultaneously occupy 16c sites within the intermediate carbonitride structures.
- **Synthesis of η -6 Co₃Mo₃C:** η -12 Co₆Mo₆N was converted to η -6 Co₃Mo₃C when reacted with methane. The reaction proceeded via the formation of Co₃Mo₃C phase

and destruction of the $\text{Co}_6\text{Mo}_6\text{N}$. However, the presence of the two segregated phases was observable at a narrow temperature window around 678 °C.

- **Synthesis of η -6 $\text{Co}_3\text{Mo}_3\text{N}$:** η -6 $\text{Co}_3\text{Mo}_3\text{C}$ was converted to η -6 $\text{Co}_3\text{Mo}_3\text{N}$ upon reaction with 75 vol. % H_2 in N_2 . As also observed in the case of carburisation of the η -6 $\text{Co}_3\text{Mo}_3\text{N}$, the reaction proceeded through the formation of $\text{Co}_3\text{Mo}_3\text{C}_x\text{N}_{1-x}$ intermediate phases at 500 °C and no additional phases were observed.
- **Synthesis of η -6 $\text{Co}_3\text{Mo}_3\text{N}$:** When reacted with N_2 , η -6 $\text{Co}_3\text{Mo}_3\text{C}$ was converted to η -6 $\text{Co}_3\text{Mo}_3\text{N}$. However, two segregated ($\text{Co}_3\text{Mo}_3\text{C}$, $\text{Co}_6\text{Mo}_6\text{N}$) phases were observed at 600 °C.
- **Synthesis of η -12 $\text{Co}_6\text{Mo}_6\text{C}$ and $\text{Co}_6\text{Mo}_6\text{N}$:** η -6 $\text{Co}_3\text{Mo}_3\text{C}$ was converted to 12- η $\text{Co}_6\text{Mo}_6\text{C}$ through two segregated ($\text{Co}_3\text{Mo}_3\text{C}$, $\text{Co}_6\text{Mo}_6\text{C}$) phases at 800 °C using 75 vol. % H_2 in Ar, whereas, when reacting η -6 $\text{Co}_3\text{Mo}_3\text{N}$ with 75 vol. % H_2 in Ar, the material reduced to η -12 $\text{Co}_6\text{Mo}_6\text{N}$ via two segregated ($\text{Co}_3\text{Mo}_3\text{N}_x$, $\text{Co}_6\text{Mo}_6\text{N}_x$) phases at 820 °C.
- **Synthesis of η -6 $\text{Co}_3\text{Mo}_3\text{N}$:** η -12 $\text{Co}_6\text{Mo}_6\text{C}$ was converted to η -6 $\text{Co}_3\text{Mo}_3\text{N}$ through two segregated ($\text{Co}_6\text{Mo}_6\text{C}_x$, $\text{Co}_3\text{Mo}_3\text{N}_x$) phases at 700 °C when using only N_2 .

In Chapter 4, the effect of composition of cobalt molybdenum related materials (CoMoO_4 , $\text{Co}_3\text{Mo}_3\text{N}$, $\text{Co}_3\text{Mo}_3\text{C}$ and $\text{Co}_6\text{Mo}_6\text{C}$) upon the catalytic activity for ammonia synthesis reaction was explored. Despite the isostructural nature of $\text{Co}_3\text{Mo}_3\text{N}$ and $\text{Co}_3\text{Mo}_3\text{C}$ disparate performance was evident. $\text{Co}_6\text{Mo}_6\text{C}$ was found to be inactive for ammonia synthesis under the conditions tested. An induction period time of 100 minutes for dehydrated CoMoO_4 and 40 minutes for $\text{Co}_3\text{Mo}_3\text{C}$ were observed prior to the materials developing any activity. In the case of $\text{Co}_3\text{Mo}_3\text{C}$, *in-situ* PND and post-reaction analysis revealed the substitution of carbon by nitrogen is initiated during the induction time and continues during the reaction until complete conversion of the carbide to nitride. These results are consistent with the proposal of the origin of the high activity of the $\text{Co}_3\text{Mo}_3\text{N}$ materials being the reactivity of its lattice nitrogen via a Mars-van Krevelen mechanism. Furthermore, the incorporation of a cobalt in ternary materials has resulted in greater activity for ammonia synthesis relative to the binary materials.

In Chapter 5, catalytic methane cracking to produce hydrogen and carbon was investigated on MoO_3 , CoMoO_4 , $\text{Co}_3\text{Mo}_3\text{N}$, $\text{Co}_6\text{Mo}_6\text{N}$, $\text{Co}_3\text{Mo}_3\text{C}$, $\text{Co}_6\text{Mo}_6\text{C}$, Si_3N_4 and $\text{VN/Si}_3\text{N}_4$. For comparison purposes, all the materials were tested for activity under the same conditions of temperature (800 °C), atmospheric pressure and reactant composition of 75 vol. % CH_4 in N_2 (BOC, 99.98%) at a total gas feed of 12 ml min^{-1} . In general, $\text{Co}_6\text{Mo}_6\text{N}$, $\text{Co}_3\text{Mo}_3\text{N}$, $\text{Co}_6\text{Mo}_6\text{C}$ and CoMoO_4 showed better activity and stability during catalytic methane cracking over time with hydrogen formation rates in order respectively (1700, 1200, 1000 and 800 $\mu\text{mol H}_2 \text{ g}^{-1} \text{ min}^{-1}$) while MoO_3 deactivated after 60 minutes to around 70 $\mu\text{mol H}_2 \text{ g}^{-1} \text{ min}^{-1}$. In all cases, hydrogen production reached a plateau after 120 min on stream. However, unstable performance was observed in the case of the $\text{Co}_3\text{Mo}_3\text{C}$ sample, which was possibly related to significant carbon deposition during the reaction resulting in reactor blockage problems. Similar observations were observed upon repeating the reaction and the structural and textural properties of both the post-reaction samples were all similar. For the $\text{Co}_6\text{Mo}_6\text{N}$, $\text{Co}_3\text{Mo}_3\text{N}$, $\text{Co}_3\text{Mo}_3\text{C}$ and $\text{Co}_6\text{Mo}_6\text{C}$, the phases detected after reaction comprised a mixture of $\text{Co}_3\text{Mo}_3\text{C}$, $\alpha\text{-Co}$, $\beta\text{-Mo}_2\text{C}$ and graphite. For the least active material CoMoO_4 , $\beta\text{-Mo}_2\text{C}$, $\alpha\text{-Co}$ and graphite were detected. For MoO_3 , only $\beta\text{-Mo}_2\text{C}$ was detected. Another major aspect, where differences are evident, is the accessible surface area of the active phases. The surface area measured in post-reaction $\text{Co}_3\text{Mo}_3\text{N}$, $\text{Co}_3\text{Mo}_3\text{C}$ and $\text{Co}_6\text{Mo}_6\text{N}$ samples ranged between 50-63 $\text{m}^2 \text{ g}^{-1}$ while in the case of CoMoO_4 and $\text{Co}_6\text{Mo}_6\text{C}$ the surface area was limited $\sim 30 \text{ m}^2 \text{ g}^{-1}$. Despite the fact that no simple link could be established between the catalytic activity and the phase composition and accessible surface area, it can be argued that the presence of both $\text{Co}_3\text{Mo}_3\text{C}$ and $\beta\text{-Mo}_2\text{C}$ and high surface area led to an enhanced activity for methane cracking when compared to instances where only $\text{Co}_3\text{Mo}_3\text{C}$ or $\beta\text{-Mo}_2\text{C}$ were present.

In the case of cobalt molybdenum nitride and carbide, off-line FTIR spectra, recorded periodically during reaction, showed that the production of CO and CO_2 during methane cracking reaction was below the detection limit. However, CO and CO_2 were clearly observed when MoO_3 and CoMoO_4 were used. It is worth considering that the production of CO, even in small concentration, can be particularly harmful in the case of hydrogen production for PEMFC and can lead to rapid degradation of their performance. The use of nitrides or carbides as catalyst for methane cracking potentially affords the production of CO_x -free hydrogen. Graphitic carbon was present at all materials except MoO_3 where only carbide observed and it was significantly higher for the cobalt molybdenum nitrides

followed by the carbides and then the oxide. Carbon deposition studies by TGA and Raman spectroscopy showed that most of the carbon was present as two types of carbon graphitic and disordered forms. Vanadium incorporation into silicon nitride is also worthy of further attention as catalysts for the production of hydrogen from methane since, although the activity is lower than that of other systems, the absence of oxygen containing phases results in effluent streams which are free from the presence of CO, a notable downstream poison for some applications.

In conclusion, we have demonstrated an important effect of the chemical composition of the cobalt molybdenum related materials in the catalytic activity of these materials.

6.2 Further work

It would be beneficial and complimentary to this project if the $\text{Fe}_3\text{Mo}_3\text{C}$ and $\text{Ni}_2\text{Mo}_3\text{C}$ systems were also studied in a similar manner, which would allow a more complete understanding of catalytic behaviour of these types of material in ammonia synthesis. In addition, it would be good to further expand this study to cover the quaternary systems such as Fe-Co-Mo-C. Doping $\text{Co}_3\text{Mo}_3\text{C}$ with promoters such as Cs, K^+ , Ba^{2+} , or by supporting $\text{Co}_3\text{Mo}_3\text{C}$ might also enhance catalytic performance relative to ammonia synthesis or methane cracking. Application of complementary techniques such as X-ray absorbance spectroscopy, HRTEM and computational studies could provide a method to understand the complex relationship between structure, composition and activity for these materials in terms of nitrogen and carbon mobility, and thereby lead on to new discoveries and applications.

7 References

1. Volpe, L.; Boudart, M., Compounds of molybdenum and tungsten with high specific surface area: I. Nitrides. *Journal of Solid State Chemistry* **1985**, *59* (3), 332-347.
2. Volpe, L.; Boudart, M., Compounds of molybdenum and tungsten with high specific surface area: II. Carbides. *Journal of Solid State Chemistry* **1985**, *59* (3), 348-356.
3. Lee, J. S.; Volpe, L.; Ribeiro, F. H.; Boudart, M., Molybdenum carbide catalysts: II. Topotactic synthesis of unsupported powders. *Journal of Catalysis* **1988**, *112* (1), 44-53.
4. Hunter, S. M.; McKay, D.; Smith, R. I.; Hargreaves, J. S. J.; Gregory, D. H., Topotactic nitrogen transfer: structural transformation in cobalt molybdenum nitrides. *Chemistry of Materials* **2010**, *22* (9), 2898-2907.
5. Toby, B.; EXPGUI, A graphical user interface for GSAS. *Journal of Applied Crystallography* **2001**, *34* (2), 210-213.
6. Larson, A. C.; von Dreele, R. B., General Structure Analysis System (GSAS). *Los Alamos National Laboratory Report LAUR* **2004**, 86-748.
7. Oyama, S. T., Introduction to the chemistry of transition metal carbides and nitrides. In *The Chemistry of transition metal carbides and nitrides*, Oyama, S. T., Ed. Springer Netherlands: Dordrecht, **1996**; pp 1-27.
8. Pierson, H. O., *Handbook of refractory carbides and nitrides*. Technology & Engineering: The USA, **1996**.
9. Chen, J. G., Carbide and nitride overlayers on early transition metal surfaces: preparation, characterization, and reactivities. *Chemical Reviews* **1996**, *96* (4), 1477-1498.
10. Zhong, Y.; Xia, X.; Shi, F.; Zhan, J.; Tu, J.; Fan, H. J., Transition metal carbides and nitrides in energy storage and conversion. *Advanced Science* **2016**, *3* (5), 1500286.
11. Levy, R.; Boudart, M., Platinum-like behavior of tungsten carbide in surface catalysis. *science* **1973**, *181* (4099), 547-549.
12. Pansare, S. S.; Torres, W.; Goodwin, J. G., Ammonia decomposition on tungsten carbide. *Catalysis Communications* **2007**, *8* (4), 649-654.
13. Ribeiro, F. H.; Boudart, M.; Dalla Betta, R. A.; Iglesia, E., Catalytic reactions of n-Alkanes on β -W₂C and WC: The effect of surface oxygen on reaction pathways. *Journal of Catalysis* **1991**, *130* (2), 498-513.
14. Ranhotra, G. S.; Bell, A. T.; Reimer, J. A., Catalysis over molybdenum carbides and nitrides: II. Studies of CO hydrogenation and C₂H₆ hydrogenolysis. *Journal of Catalysis* **1987**, *108* (1), 40-49.
15. Oyama, S. T., Preparation and catalytic properties of transition metal carbides and nitrides. *Catalysis Today* **1992**, *15* (2), 179-200.
16. P. E. York, A.; B. Claridge, J.; J. Brungs, A.; Chi Tsang, S.; L. H. Green, M., Molybdenum and tungsten carbides as catalysts for the conversion of methane to synthesis gas using stoichiometric feedstocks. *Chemical Communications* **1997**, (1), 39-40.
17. Claridge, J. B.; York, A. P. E.; Brungs, A. J.; Marquez-Alvarez, C.; Sloan, J.; Tsang, S. C.; Green, M. L. H., New catalysts for the conversion of methane to synthesis gas: molybdenum and tungsten carbide. *Journal of Catalysis* **1998**, *180* (1), 85-100.
18. Brungs, A. J.; York, A. P. E.; Green, M. L. H., Comparison of the group V and VI transition metal carbides for methane dry reforming and thermodynamic prediction of their relative stabilities. *Catalyst Letters* **1999**, *57* (1), 65-69.
19. Lee, J. S., Metal carbides. In *Encyclopedia of catalysis*, John Wiley & Sons, Inc.: **2002**.
20. Hyeon, T.; Fang, M.; Suslick, K. S., Nanostructured molybdenum carbide: sonochemical synthesis and catalytic properties. *Journal of the American Chemical Society* **1996**, *118* (23), 5492-5493.

21. Preiss, H.; Meyer, B.; Olschewski, C., Preparation of molybdenum and tungsten carbides from solution derived precursors. *Journal of Materials Science* **1998**, *33* (3), 713-722.
22. Lee, J. S.; Oyama, S. T.; Boudart, M., Molybdenum carbide catalysts: I. Synthesis of unsupported powders. *Journal of Catalysis* **1987**, *106* (1), 125-133.
23. Oyama, S. T., *Chemistry of Transition Metal Carbides and Nitrides*. Springer: **1996**.
24. Montéverdi, S.; Bettahar, M. M.; Bégin, D.; Maréché, F., Characteristics and hydrogenating properties of active carbon supported β -Mo₂C. *Fuel Processing Technology* **2002**, *77-78* (Supplement C), 119-124.
25. Wang, H.-M.; Wang, X.-H.; Zhang, M.-H.; Du, X.-Y.; Li, W.; Tao, K.-Y., Synthesis of Bulk and Supported Molybdenum Carbide by a Single-Step Thermal Carburization Method. *Chemistry of Materials* **2007**, *19* (7), 1801-1807.
26. Ribeiro, F. H.; Dalla Betta, R. A.; Guskey, G. J.; Boudart, M., Preparation and surface composition of tungsten carbide powders with high specific surface area. *Chemistry of Materials* **1991**, *3* (5), 805-812.
27. Claridge, J. B.; York, A. P. E.; Brungs, A. J.; Green, M. L. H., Study of the temperature-programmed reaction synthesis of early transition metal carbide and nitride catalyst materials from oxide precursors. *Chemistry of Materials* **2000**, *12* (1), 132-142.
28. Oshikawa, K.; Nagai, M.; Omi, S., Characterization of molybdenum carbides for methane reforming by TPR, XRD, and XPS. *The Journal of Physical Chemistry B* **2001**, *105* (38), 9124-9131.
29. Xiao, T.; Wang, H.; Da, J.; Coleman, K. S.; Green, M. L. H., Study of the preparation and catalytic performance of molybdenum carbide catalysts prepared with C₂H₂/H₂ carburizing mixture. *Journal of Catalysis* **2002**, *211* (1), 183-191.
30. Xiao, T.-C.; York, A. P. E.; Al-Megren, H.; Williams, C. V.; Wang, H.-T.; Green, M. L. H., Preparation and characterisation of bimetallic cobalt and molybdenum carbides. *Journal of Catalysis* **2001**, *202* (1), 100-109.
31. Wang, X.-H.; Hao, H.-L.; Zhang, M.-H.; Li, W.; Tao, K.-Y., Synthesis and characterization of molybdenum carbides using propane as carbon source. *Journal of Solid State Chemistry* **2006**, *179* (2), 538-543.
32. Xiang, M.; Li, D.; Li, W.; Zhong, B.; Sun, Y., Synthesis of higher alcohols from syngas over K/Co/ β -Mo₂C catalysts. *Catalysis Communications* **2007**, *8* (3), 503-507.
33. Bouchy, C.; Schmidt, I.; Anderson, J. R.; Jacobsen, C. J. H.; Derouane, E. G.; Derouane-Abd Hamid, S. B., Metastable fcc α -MoC_{1-x} supported on HZSM5: preparation and catalytic performance for the non-oxidative conversion of methane to aromatic compounds. *Journal of Molecular Catalysis A: Chemical* **2000**, *163* (1), 283-296.
34. Zhu, Q.; Chen, Q.; Yang, X.; Ke, D., A new method for the synthesis of molybdenum carbide. *Materials Letters* **2007**, *61* (29), 5173-5174.
35. Bouchy, C.; Derouane-Abd Hamid, S. B.; Derouane, E. G., A new route to the metastable fcc molybdenum carbide α -MoC. *Chemical Communications* **2000**, (2), 125-126.
36. Kojima, R.; Aika, K.-i., Cobalt molybdenum bimetallic nitride catalysts for ammonia synthesis. *Chemistry Letters* **2000**, *29* (5), 514-515.
37. McKay, D.; Gregory, D. H.; Hargreaves, J. S. J.; Hunter, S. M.; Sun, X., Towards nitrogen transfer catalysis: reactive lattice nitrogen in cobalt molybdenum nitride. *Chemical Communications* **2007**, (29), 3051-3053.
38. Newsam, J. M.; Jacobson, A. J.; McCandlish, L. E.; Polizzotti, R. S., The structures of the η -carbides Ni₆Mo₆C, Co₆Mo₆C, and Co₆Mo₆C₂. *Journal of Solid State Chemistry* **1988**, *75* (2), 296-304.

39. Korlann, S.; Diaz, B.; Bussell, M. E., Synthesis of bulk and alumina-supported bimetallic carbide and nitride catalysts. *Chemistry of Materials* **2002**, *14* (10), 4049-4058.
40. Alconchel, S.; Sapina, F.; Martinez, E., From nitrides to carbides: topotactic synthesis of the η -carbides $\text{Fe}_3\text{Mo}_3\text{C}$ and $\text{Co}_3\text{Mo}_3\text{C}$. *Dalton Transactions* **2004**, (16), 2463-2468.
41. Wang, X.-H.; Zhang, M.-H.; Li, W.; Tao, K.-Y., Synthesis and characterization of cobalt–molybdenum bimetallic carbides catalysts. *Catalysis Today* **2008**, *131* (1), 111-117.
42. Xu, Y.; Bao, X.; Lin, L., Direct conversion of methane under nonoxidative conditions. *Journal of Catalysis* **2003**, *216* (1), 386-395.
43. Koerts, T.; Deelen, M. J. A. G.; van Santen, R. A., Hydrocarbon formation from methane by a low-temperature two-step reaction sequence. *Journal of Catalysis* **1992**, *138* (1), 101-114.
44. Amariglio, H.; Saint-Just, J.; Amariglio, A., Homologation of methane under non-oxidative conditions. *Fuel Processing Technology* **1995**, *42* (2), 291-323.
45. Amariglio, H.; Pareja, P.; Amariglio, A., Periodic operation of a catalyst as a means of overcoming a thermodynamic constraint. The case of methane homologation on metals. *Catalysis Today* **1995**, *25* (2), 113-125.
46. Amariglio, H., Belgued, M., Pareja, P., Amariglio, A., Oxygen-free conversion of methane to higher hydrocarbons through a dual-temperature two-step reaction sequence on platinum and ruthenium - 2. Removal of products at a fixed temperature. *Journal of Catalysis* **1998**, *177* (1), 121-128.
47. Guzzi, L.; Sarma, K. V.; Borko, L., Non-oxidative methane coupling over Co-Pt/NaY bimetallic catalysts. *Catalysis Letters* **1996**, *39* (1-2), 43-47.
48. Koranne, M. M.; Goodman, D. W., Two-step, oxygen-free route to higher hydrocarbons from methane over ruthenium catalysts. In *Methane and alkane conversion chemistry*, Bhasin, M. M.; Slocum, D. W., Eds. Springer US: Boston, MA, **1995**; pp 49-58.
49. Solymosi, F.; Cserenyi, J., Enhanced formation of ethane in the conversion of methane over Cu-Rh/SiO₂. *Catalysis Letters* **1995**, *34* (3-4), 343-350.
50. Wang, L., Tao, Longxiang, Xie, Maosong, Xu, Guifen, Huang, Jiasheng, Xu, Yide, Dehydrogenation and aromatization of methane under non-oxidizing conditions. *Catalysis Letters* **1993**, *21* (1-2), 35-41.
51. Chithambararaj, A.; Rajeswari Yogamalar, N.; Bose, A. C., Hydrothermally synthesized h-MoO₃ and α -MoO₃ nanocrystals: new findings on crystal-structure-dependent charge transport. *Crystal Growth & Design* **2016**, *16* (4), 1984-1995.
52. Kihlberg, L., Least squares refinement of the crystal structure of molybdenum trioxide,. *Ark. Kemi* **1963**, *21* (34), 357-364.
53. Siciliano, T.; Tepore, A.; Filippo, E.; Micocci, G.; Tepore, M., Characteristics of molybdenum trioxide nanobelts prepared by thermal evaporation technique. *Materials Chemistry and Physics* **2009**, *114* (2), 687-691.
54. MS Shekhawat MC Rao; K Ravindranadh; Kasturi, A., Structural stoichiometry and phase transitions of MoO₃ thin films for solid state microbatteries. 2: *Research Journal of Recent Sciences*, **2013**; pp 67-73.
55. Klinbumrung, A.; Thongtem, T.; Thongtem, S., Characterization of orthorhombic α -MoO₃ microplates produced by a microwave plasma process. *J. Nanomaterials* **2012**, *2012*, 10-10.
56. Bull, C. L.; Kawashima, T.; McMillan, P. F.; Machon, D.; Shebanova, O.; Daisenberger, D.; Soignard, E.; Takayama-Muromachi, E.; Chapon, L. C., Crystal structure and high-pressure properties of γ -Mo₂N determined by neutron powder diffraction and X-ray diffraction. *Journal of Solid State Chemistry* **2006**, *179* (6), 1762-1767.

57. Suszko, T.; Gulbiński, W.; Jagielski, J., The role of surface oxidation in friction processes on molybdenum nitride thin films. *Surface and Coatings Technology* **2005**, *194* (2), 319-324.
58. Hargreaves, J. S. J., Nitrides as ammonia synthesis catalysts and as potential nitrogen transfer reagents. *Applied Petrochemical Research* **2014**, *4* (1), 3-10.
59. McKay, D.; Hargreaves, J. S. J.; Rico, J. L.; Rivera, J. L.; Sun, X. L., The influence of phase and morphology of molybdenum nitrides on ammonia synthesis activity and reduction characteristics. *Journal of Solid State Chemistry* **2008**, *181* (2), 325-333.
60. Leclercq, L.; Imura, K.; Yoshida, S.; Barbee, T.; Boudart, M., Synthesis of new catalytic materials: metal carbides of the Group VI B elements. In *Studies in surface science and catalysis*, Delmon, B.; Grange, P.; Jacobs, P.; Poncelet, G., Eds. Elsevier: **1979**; Vol. 3, pp 627-639.
61. Lander, J.; Germer, L., *Transactions of the American Institute of Mining and Metallurgical Engineers* **1947**, *14*.
62. Roohi, P.; Alizadeh, R.; Fatehifar, E., Thermodynamic study and methanothermal temperature-programmed reaction synthesis of molybdenum carbide. *International Journal of Minerals, Metallurgy, and Materials* **2016**, *23* (3), 339-347.
63. Fries, R. J.; Kempter, C. P., 195. Dimolybdenum carbide. *Analytical Chemistry* **1960**, *32* (13), 1898-1898.
64. Lee, J. S.; Locatelli, S.; Oyama, S. T.; Boudart, M., Molybdenum carbide catalysts 3. Turnover rates for the hydrogenolysis of n-butane. *Journal of Catalysis* **1990**, *125* (1), 157-170.
65. Sathish, C. I.; Guo, Y.; Wang, X.; Tsujimoto, Y.; Li, J.; Zhang, S.; Matsushita, Y.; Shi, Y.; Tian, H.; Yang, H.; Li, J.; Yamaura, K., Superconducting and structural properties of .DELTA.-MoCo.681 cubic molybdenum carbide phase. *Journal of Solid State Chemistry* **2012**, *196*, 579-585.
66. Smith, G. W.; Ibers, J. A., The Crystal structure of cobalt molybdate, CoMoO₄. *Acta Cryst* **1965**, *269* (19).
67. Sleight, A. W.; Chamberland, B. L., Transition metal molybdates of the type AMoO₄. *Inorganic Chemistry* **1968**, *7* (8), 1672-1675.
68. Livage, C.; Hynaux, A.; Marrot, J.; Nogues, M.; Ferey, G., Solution process for the synthesis of the "high-pressure" phase CoMoO₄ and X-ray single crystal resolution. *Journal of Materials Chemistry* **2002**, *12* (5), 1423-1425.
69. Eda, K.; Uno, Y.; Nagai, N.; Sotani, N.; Stanley Whittingham, M., Crystal structure of cobalt molybdate hydrate CoMoO₄·nH₂O. *Journal of Solid State Chemistry* **2005**, *178* (9), 2791-2797.
70. Hargreaves, J. S. J.; McKay, D., A comparison of the reactivity of lattice nitrogen in Co₃Mo₃N and Ni₂Mo₃N catalysts. *Journal of Molecular Catalysis A: Chemical* **2009**, *305* (1), 125-129.
71. Rico, J. L.; Ávalos-Borja, M.; Barrera, A.; Hargreaves, J. S. J., Template-free synthesis of CoMoO₄ rods and their characterization. *Materials Research Bulletin* **2013**, *48* (11), 4614-4617.
72. Karlsruhe, F. <http://icsd.cds.rsc.org/viscalc/jsp/listView.action>.
73. Rodriguez, J. A.; Chaturvedi, S.; Hanson, J. C.; Albornoz, A.; Brito, J. L., Electronic properties and phase transformations in CoMoO₄ and NiMoO₄: XANES and time-resolved synchrotron XRD studies. *The Journal of Physical Chemistry B* **1998**, *102* (8), 1347-1355.
74. Herrera, J. E.; Resasco, D. E., Role of Co-W interaction in the selective growth of single-walled carbon nanotubes from CO disproportionation. *The Journal of Physical Chemistry B* **2003**, *107* (16), 3738-3746.

75. Ding, Y.; Wan, Y.; Min, Y.-L.; Zhang, W.; Yu, S.-H., General Synthesis and Phase Control of Metal Molybdate Hydrates $M\text{MoO}_4 \cdot n\text{H}_2\text{O}$ ($M = \text{Co}, \text{Ni}, \text{Mn}, n = 0, 3/4, 1$) Nano/Microcrystals by a Hydrothermal Approach: Magnetic, Photocatalytic, and Electrochemical Properties. *Inorganic Chemistry* **2008**, *47* (17), 7813-7823.
76. Alexander, A.-M.; Hargreaves, J. S. J., Alternative catalytic materials: carbides, nitrides, phosphides and amorphous boron alloys. *Chemical Society Reviews* **2010**, *39* (11), 4388-4401.
77. Alconchel, S.; Sapina, F.; Beltran, D.; Beltran, A., Chemistry of interstitial molybdenum ternary nitrides MnMo_3N ($M=\text{Fe}, \text{Co}, n=3; M=\text{Ni}, n=2$). *Journal of Materials Chemistry* **1998**, *8* (8), 1901-1909.
78. Perret, N.; Alexander, A.-M.; Hunter, S. M.; Chung, P.; Hargreaves, J. S. J.; Howe, R. F.; Keane, M. A., Synthesis, characterisation and hydrogenation performance of ternary nitride catalysts. *Applied Catalysis A: General* **2014**, *488* (Supplement C), 128-137.
79. Kojima, R.; Aika, K.-i., Cobalt molybdenum bimetallic nitride catalysts for ammonia synthesis: Part 3. Reactant gas treatment. *Applied Catalysis A: General* **2001**, *219* (1), 157-170.
80. Jackson, S. K.; Layland, R. C.; zur Loye, H.-C., The simultaneous powder X-ray and neutron diffraction refinement of two η -carbide type nitrides, $\text{Fe}_3\text{Mo}_3\text{N}$ and $\text{Co}_3\text{Mo}_3\text{N}$, prepared by ammonolysis and by plasma nitridation of oxide precursors. *Journal of Alloys and Compounds* **1999**, *291* (1), 94-101.
81. Gregory, D. H.; Hargreaves, J. S. J.; Hunter, S. M., On the regeneration of $\text{Co}_3\text{Mo}_3\text{N}$ from $\text{Co}_6\text{Mo}_6\text{N}$ with N_2 . *Catalyst Letters* **2011**, *141* (1), 22-26.
82. Erisman, J. W.; Sutton, M. A.; Galloway, J.; Klimont, Z.; Winiwarter, W., How a century of ammonia synthesis changed the world. *Nature Geoscience* **2008**, *1*, 636.
83. Nørskov, J.; Chen, J.; Miranda, R.; Fitzsimmons, T.; Stack, R. *Sustainable Ammonia Synthesis – Exploring the scientific challenges associated with discovering alternative, sustainable processes for ammonia production*; ; US DOE Office of Science: **2016**; p Medium: ED; Size: 33 p.
84. Smith, B. E., Nitrogenase reveals its inner secrets. *Science* **2002**, *297* (5587), 1654-1655.
85. Hardy, R. W. F., *Biological nitrogen fixation*. National Academy Press: Washington, D.C., **1994**.
86. Arvin Mosier; J. Keith Syers; Freney, J. R., *Agriculture and the nitrogen cycle: assessing the impacts of fertilizer use on food production and the environment*. Science: Island Press, **2013**.
87. Smil, V., Global Population and the Nitrogen Cycle. *Scientific American* **1997**, *277* (1), 76-81.
88. Mathew, M.; Thaker, A., *A Review of ammonia fuel cells*. **2015**.
89. Gert-Jan Monteny; Hartung, E., *Ammonia emissions in agriculture*. Science: Wageningen Academic Publishers, the Netherlands, **2007**; p 403.
90. Kandemir, T.; Schuster, M. E.; Senyshyn, A.; Behrens, M.; Schlögl, R., The Haber-Bosch Process Revisited: On the Real Structure and Stability of "Ammonia Iron" under Working Conditions. *Angewandte Chemie International Edition* **2013**, *52* (48), 12723-12726.
91. Haber, F.; Rossignol, R. L., Über die technische Darstellung von Ammoniak aus den Elementen. *Zeitschrift für Elektrochemie und angewandte physikalische Chemie* **1913**, *19* (2), 53-72.
92. Rayment, T.; Schlögl, R.; Thomas, J. M.; Ertl, G., Structure of the ammonia synthesis catalyst. *Nature* **1985**, *315*, 311.

93. Leigh, G. J., *The world's greatest Fix: A history of nitrogen and agriculture*. Science: Oxford University Press, USA, **2004**; p 242.
94. Mittasch, A. *Catalytic agents and process of making them*. **1916**.
95. Walas, S. M., *Reaction kinetics for chemical engineers: butterworths series in chemical engineering*. Butterworth-Heinemann: the USA, **2013**.
96. Aika, K.; Ozaki, A., Kinetics and isotope effect of ammonia synthesis over ruthenium. *Journal of Catalysis* **1970**, *16* (1), 97-101.
97. Ozaki, A., Development of alkali-promoted ruthenium as a novel catalyst for ammonia synthesis. *Accounts of Chemical Research* **1981**, *14* (1), 16-21.
98. Liu, H., *Ammonia synthesis catalysts: innovation and practice*. World Scientific: **2013**.
99. Rhodes, A. K., New ammonia process, catalyst proven in Canadian plant. *Oil and Gas Journal* **1996**, Medium: X; Size: pp. 37-41.
100. McAulay, K.; Hargreaves, J. S. J.; McFarlane, A. R.; Price, D. J.; Spencer, N. A.; Bion, N.; Can, F.; Richard, M.; Greer, H. F.; Zhou, W. Z., The influence of pre-treatment gas mixture upon the ammonia synthesis activity of Co–Re catalysts. *Catalysis Communications* **2015**, *68*, 53-57.
101. King, D. A.; Sebba, F., The catalytic synthesis of ammonia over vanadium nitride containing oxygen: I. The reaction mechanism. *Journal of Catalysis* **1965**, *4* (2), 253-259.
102. Segal, N.; Sebba, F., Ammonia synthesis catalyzed by uranium nitride: II. The transient behavior. *Journal of Catalysis* **1967**, *8* (2), 113-119.
103. Kojima, R.; Aika, K.-i., Molybdenum nitride and carbide catalysts for ammonia synthesis. *Applied Catalysis A: General* **2001**, *219* (1), 141-147.
104. Jacobsen, C. J. H.; Dahl, S.; Clausen, B. S.; Bahn, S.; Logadottir, A.; Nørskov, J. K., Catalyst design by interpolation in the periodic table: bimetallic ammonia synthesis catalysts. *Journal of the American Chemical Society* **2001**, *123* (34), 8404-8405.
105. Hunter, S. M.; Gregory, D. H.; Hargreaves, J. S. J.; Richard, M.; Duprez, D.; Bion, N., A study of ¹⁵N/¹⁴N isotopic exchange over cobalt molybdenum nitrides. *ACS Catalysis* **2013**, *3* (8), 1719-1725.
106. Zeinalipour-Yazdi, C. D.; Hargreaves, J. S. J.; Catlow, C. R. A., Nitrogen activation in a Mars–van Krevelen mechanism for ammonia synthesis on Co₃Mo₃N. *The Journal of Physical Chemistry C* **2015**, *119* (51), 28368-28376.
107. Zeinalipour-Yazdi, C. D.; Hargreaves, J. S. J.; Catlow, C. R. A., DFT-D3 study of molecular N₂ and H₂ activation on Co₃Mo₃N surfaces. *The Journal of Physical Chemistry C* **2016**, *120* (38), 21390-21398.
108. Kojima, R.; Aika, K., Cobalt molybdenum bimetallic nitride catalysts for ammonia synthesis: Part 2. Kinetic study. *Applied Catalysis A: General* **2001**, *218* (1), 121-128.
109. Kojima, R.; Aika, K., Rhenium containing binary catalysts for ammonia synthesis. *Applied Catalysis A: General* **2001**, *209* (1), 317-325.
110. Wang, X. H.; Zhang, M. H.; Li, W.; Tao, K. Y., A simple synthesis route and characterisation of Co₃Mo₃C. *Dalton Transactions* **2007**, (44), 5165-5170.
111. Fu, X.; Su, H.; Yin, W.; Huang, Y.; Gu, X., Bimetallic molybdenum nitride Co₃Mo₃N: a new promising catalyst for CO₂ reforming of methane. *Catalysis Science & Technology* **2017**, *7* (8), 1671-1678.
112. Abbas, H. F.; Wan Daud, W. M. A., Hydrogen production by methane decomposition: A review. *International Journal of Hydrogen Energy* **2010**, *35* (3), 1160-1190.
113. Holladay, J. D.; Hu, J.; King, D. L.; Wang, Y., An overview of hydrogen production technologies. *Catalysis Today* **2009**, *139* (4), 244-260.

114. Li, Y.; Li, D.; Wang, G., Methane decomposition to CO_x-free hydrogen and nano-carbon material on group 8–10 base metal catalysts: A review. *Catalysis Today* **2011**, *162* (1), 1-48.
115. Abánades, A.; Rubbia, C.; Salmieri, D., Thermal cracking of methane into Hydrogen for a CO₂-free utilization of natural gas. *International Journal of Hydrogen Energy* **2013**, *38* (20), 8491-8496.
116. Amin, A. M.; Croiset, E.; Epling, W., Review of methane catalytic cracking for hydrogen production. *International Journal of Hydrogen Energy* **2011**, *36* (4), 2904-2935.
117. Solymosi, F.; Erdöhelyi, A.; Cserényi, J., A comparative study on the activation and reactions of CH₄ on supported metals. *Catalyst Letters* **1992**, *16* (4), 399-405.
118. Choudhary, T. V.; Aksoylu, E.; Goodman, D. W., Nonoxidative activation of methane. *Catalysis Reviews-Science and Engineering* **2003**, *45* (1), 151-203.
119. Lunsford, J. H., Catalytic conversion of methane to more useful chemicals and fuels: a challenge for the 21st century. *Catalysis Today* **2000**, *63* (2), 165-174.
120. Brungs, A. J.; York, A. P. E.; Claridge, J. B.; Márquez-Alvarez, C.; Green, M. L. H., Dry reforming of methane to synthesis gas over supported molybdenum carbide catalysts. *Catalyst Letters* **2000**, *70* (3), 117-122.
121. Wang, S.; Lu, G. Q.; Millar, G. J., Carbon dioxide reforming of methane to produce synthesis gas over metal-supported catalysts: state of the art. *Energy & Fuels* **1996**, *10* (4), 896-904.
122. Freni, S.; Calogero, G.; Cavallaro, S., Hydrogen production from methane through catalytic partial oxidation reactions. *Journal of Power Sources* **2000**, *87* (1), 28-38.
123. Halabi, M. H.; de Croon, M. H. J. M.; van der Schaaf, J.; Cobden, P. D.; Schouten, J. C., Modeling and analysis of autothermal reforming of methane to hydrogen in a fixed bed reformer. *Chemical Engineering Journal* **2008**, *137* (3), 568-578.
124. Dias, J. A. C.; Assaf, J. M., Autothermal reforming of methane over Ni/γ-Al₂O₃ catalysts: the enhancement effect of small quantities of noble metals. *Journal of Power Sources* **2004**, *130* (1), 106-110.
125. Konieczny, A.; Mondal, K.; Wiltowski, T.; Dydo, P., Catalyst development for thermocatalytic decomposition of methane to hydrogen. *International Journal of Hydrogen Energy* **2008**, *33* (1), 264-272.
126. Ahmed, S.; Aitani, A.; Rahman, F.; Al-Dawood, A.; Al-Muhaish, F., Decomposition of hydrocarbons to hydrogen and carbon. *Applied Catalysis A: General* **2009**, *359* (1–2), 1-24.
127. Muradov, N. Z.; Veziroğlu, T. N., From hydrocarbon to hydrogen–carbon to hydrogen economy. *International Journal of Hydrogen Energy* **2005**, *30* (3), 225-237.
128. Ermakova, M. A.; Ermakov, D. Y.; Kuvshinov, G. G., Effective catalysts for direct cracking of methane to produce hydrogen and filamentous carbon: Part I. Nickel catalysts. *Applied Catalysis A: General* **2000**, *201* (1), 61-70.
129. Avdeeva, L. B.; Kochubey, D. I.; Shaikhutdinov, S. K., Cobalt catalysts of methane decomposition: accumulation of the filamentous carbon. *Applied Catalysis A: General* **1999**, *177* (1), 43-51.
130. Ermakova, M. A.; Ermakov, D. Y.; Kuvshinov, G. G.; Plyasova, L. M., New nickel catalysts for the formation of filamentous carbon in the reaction of methane decomposition. *Journal of Catalysis* **1999**, *187* (1), 77-84.
131. Alharthi, A.; Blackley, R. A.; Flowers, T. H.; Hargreaves, J. S. J.; Pulford, I. D.; Wigzell, J.; Zhou, W., Iron ochre – a pre-catalyst for the cracking of methane. *Journal of Chemical Technology and Biotechnology* **2014**, *89* (9), 1317-1323.
132. Takenaka, S.; Serizawa, M.; Otsuka, K., Formation of filamentous carbons over supported Fe catalysts through methane decomposition. *Journal of Catalysis* **2004**, *222* (2), 520-531.

133. Chaturbedy, P.; Ahamed, M.; Eswaramoorthy, M., Oxidative dehydrogenation of propane over a high surface area boron nitride catalyst: exceptional selectivity for olefins at high conversion. *ACS Omega* **2018**, *3* (1), 369-374.
134. Vojvodic, A.; Hellman, A.; Ruberto, C.; Lundqvist, B. I., From electronic structure to catalytic activity: a single descriptor for adsorption and reactivity on transition-metal carbides. *Physical Review Letters* **2009**, *103* (14), 146103.
135. Weller, S.; Hofer, L. J. E.; Anderson, R. B., The role of bulk cobalt carbide in the Fischer–Tropsch synthesis. *Journal of the American Chemical Society* **1948**, *70* (2), 799-801.
136. Ordonsky, V. V.; Legras, B.; Cheng, K.; Paul, S.; Khodakov, A. Y., The role of carbon atoms of supported iron carbides in Fischer-Tropsch synthesis. *Catalysis Science & Technology* **2015**, *5* (3), 1433-1437.
137. Vo, D.-V. N.; Adesina, A. A., Evaluation of promoted Mo carbide catalysts for Fischer-Tropsch synthesis: synthesis, characterisation, and time-on-stream behaviour. In *Synthetic Liquids Production and Refining*, American Chemical Society: **2011**; Vol. 1084, pp 155-184.
138. Kojima, I.; Miyazaki, E.; Inoue, Y.; Yasumori, I., Catalysis by transition metal carbides: IV. Mechanism of ethylene hydrogenation and the nature of active sites on tantalum monocarbide. *Journal of Catalysis* **1982**, *73* (1), 128-135.
139. Lee, J. S.; Yeom, M. H.; Park, K. Y.; Nam, I.-S.; Chung, J. S.; Kim, Y. G.; Moon, S. H., Preparation and benzene hydrogenation activity of supported molybdenum carbide catalysts. *Journal of Catalysis* **1991**, *128* (1), 126-136.
140. Perret, N.; Wang, X.; Delannoy, L.; Potvin, C.; Louis, C.; Keane, M. A., Enhanced selective nitroarene hydrogenation over Au supported on β -Mo₂C and β -Mo₂C/Al₂O₃. *Journal of Catalysis* **2012**, *286*, 172-183.
141. Jiang, J.; Liu, Q.; Zeng, C.; Ai, L., Cobalt/molybdenum carbide@N-doped carbon as a bifunctional electrocatalyst for hydrogen and oxygen evolution reactions. *Journal of Materials Chemistry A* **2017**, *5* (32), 16929-16935.
142. Choi, J.-G., Ammonia decomposition over vanadium carbide catalysts. *Journal of Catalysis* **1999**, *182* (1), 104-116.
143. AlShibane, I.; Daisley, A.; Hargreaves, J. S. J.; Hector, A. L.; Laassiri, S.; Rico, J. L.; Smith, R. I., The role of composition for cobalt molybdenum carbide in ammonia synthesis. *ACS Sustainable Chemistry & Engineering* **2017**, *5* (10), 9214-9222.
144. AlShibane, I.; Hargreaves, J. S. J.; Hector, A. L.; Levason, W.; McFarlane, A., Synthesis and methane cracking activity of a silicon nitride supported vanadium nitride nanoparticle composite. *Dalton Transactions* **2017**, *46* (27), 8782-8787.
145. Izhar, S.; Kanetsugi, H.; Tominaga, H.; Nagai, M., Cobalt molybdenum carbides: Surface properties and reactivity for methane decomposition. *Applied Catalysis A: General* **2007**, *317* (1), 82-90.
146. Argyle, M.; Bartholomew, C., Heterogeneous catalyst deactivation and regeneration: a review. *Catalysts* **2015**, *5* (1), 145.
147. Figueiredo, J. L. In *Carbon formation and gasification on nickel*, Dordrecht, Springer Netherlands: Dordrecht, **1982**; pp 45-63.
148. Denny, P. J.; Twigg, M. V., Factors determining the life of industrial heterogeneous catalysts. In *Studies in surface science and catalysis*, Delmon, B.; Froment, G. F., Eds. Elsevier: **1980**; Vol. 6, pp 577-599.
149. Bartholomew, C. H., Catalyst deactivation. *Chemistry and Engineering* **1984**, *91*, 96-112.
150. Hughes, R., *Deactivation of catalysts*. London, UK, **1984**.
151. Oudar, J.; Wise, H., *Deactivation and poisoning of catalysts*. Marcel Dekker: New York, NY, **1985**.

152. Butt, J. B.; Petersen, E. E., *Activation, deactivation, and poisoning of catalysts*. Academic Press: San Diego, CA, USA, **1988**.
153. Zhang, Y.; Smith, K. J., Carbon formation thresholds and catalyst deactivation during CH₄ decomposition on supported Co and Ni catalysts. *Catalyst Letters* **2004**, *95* (1), 7-12.
154. Bartholomew, C. H., Mechanisms of catalyst deactivation. *Applied Catalysis A: General* **2001**, *212* (1), 17-60.
155. Abbas, H. F.; Daud, W. M. A. W., Thermocatalytic decomposition of methane for hydrogen production using activated carbon catalyst: Regeneration and characterization studies. *International Journal of Hydrogen Energy* **2009**, *34* (19), 8034-8045.
156. Shekhawat, D.; Spivey, J. J.; Berry, D. A.; Gardner, T. H., "Catalytic reforming of liquid hydrocarbon fuel cell applications" *Catalysis*. Royal Society of Chemistry: USA, **2006**; Vol. 19, p 186-257 pages.
157. Marks, N. A.; McKenzie, D. R.; Pailthorpe, B. A.; Bernasconi, M.; Parrinello, M., Microscopic structure of tetrahedral amorphous carbon. *Physical Review Letters* **1996**, *76* (5), 768-771.
158. Lau, A. K.-T.; Hui, D., The revolutionary creation of new advanced materials—carbon nanotube composites. *Composites Part B: Engineering* **2002**, *33* (4), 263-277.
159. Iijima, S., Helical microtubules of graphitic carbon. *Nature* **1991**, *354*, 56.
160. Rafique, M. M. A.; Iqbal, J., Production of carbon nanotubes by different routes-a review. *Journal of Encapsulation and Adsorption Sciences* **2011**, *Vol.01No.02*, 6.
161. Yellampalli, S., Carbon nanotubes-polymer nanocomposites. *InTech* **2011**, *978-953* (307), 498-6.
162. Jin, Y.; Wang, G.; Li, Y., Catalytic growth of high quality single-walled carbon nanotubes over a Fe/MgO catalyst derived from a precursor containing Feitknecht compound. *Applied Catalysis A: General* **2012**, *445-446*, 121-127.
163. Donaldson, K.; Aitken, R.; Tran, L.; Stone, V.; Duffin, R.; Forrest, G.; Alexander, A., Carbon nanotubes: a review of their properties in relation to pulmonary toxicology and workplace safety. *Toxicological Sciences* **2006**, *92* (1), 5-22.
164. Saifuddin, N.; Raziah, A. Z.; Junizah, A. R., Carbon nanotubes: a review on structure and their interaction with proteins. *Journal of Chemistry* **2013**, *2013*, 18.
165. Ying, L. S.; bin Mohd Salleh, M. A.; b. Mohamed Yusoff, H.; Abdul Rashid, S. B.; b. Abd. Razak, J., Continuous production of carbon nanotubes – A review. *Journal of Industrial and Engineering Chemistry* **2011**, *17* (3), 367-376.
166. Tessonier, J.-P.; Su, D. S., Recent progress on the growth mechanism of carbon nanotubes: a review. *ChemSusChem* **2011**, *4* (7), 824-847.
167. Thess, A.; Lee, R.; Nikolaev, P.; Dai, H.; Petit, P.; Robert, J.; Xu, C.; Lee, Y. H.; Kim, S. G.; Rinzler, A. G.; Colbert, D. T.; Scuseria, G. E.; Tománek, D.; Fischer, J. E.; Smalley, R. E., Crystalline ropes of metallic carbon nanotubes. *Science* **1996**, *273* (5274), 483-487.
168. Terrones, M.; Terrones, H.; Grobert, N.; Hsu, W. K.; Zhu, Y. Q.; Hare, J. P.; Kroto, H. W.; Walton, D. R. M.; Kohler-Redlich, P.; Rühle, M.; Zhang, J. P.; Cheetham, A. K., Efficient route to large arrays of CN_x nanofibers by pyrolysis of ferrocene/melamine mixtures. *Applied Physics Letters* **1999**, *75* (25), 3932-3934.
169. Ren, Z. F.; Huang, Z. P.; Xu, J. W.; Wang, J. H.; Bush, P.; Siegal, M. P.; Provencio, P. N., Synthesis of large arrays of well-aligned carbon nanotubes on glass. *Science* **1998**, *282* (5391), 1105-1107.
170. Li, W. Z.; Xie, S. S.; Qian, L. X.; Chang, B. H.; Zou, B. S.; Zhou, W. Y.; Zhao, R. A.; Wang, G., Large-scale synthesis of aligned carbon nanotubes. *Science* **1996**, *274* (5293), 1701-1703.

171. Fan, S.; Chapline, M. G.; Franklin, N. R.; Tomblor, T. W.; Cassell, A. M.; Dai, H., Self-oriented regular arrays of carbon nanotubes and their field emission properties. *Science* **1999**, *283* (5401), 512-514.
172. Takenaka, S.; Kobayashi, S.; Ogihara, H.; Otsuka, K., Ni/SiO₂ catalyst effective for methane decomposition into hydrogen and carbon nanofiber. *Journal of Catalysis* **2003**, *217* (1), 79-87.
173. Chen, X.; Wang, R.; Xu, J.; Yu, D., TEM investigation on the growth mechanism of carbon nanotubes synthesized by hot-filament chemical vapor deposition. *Micron* **2004**, *35* (6), 455-460.
174. Moshkalev, S. A.; Verissimo, C., Nucleation and growth of carbon nanotubes in catalytic chemical vapor deposition. *Journal of Applied Physics* **2007**, *102* (4), 044303.
175. Kumar, M.; Ando, Y., Chemical vapor deposition of carbon nanotubes: a review on growth mechanism and mass production. *Journal of Nanoscience and Nanotechnology* **2010**, *10* (6), 3739-3758.
176. Baker, R. T. K., Catalytic growth of carbon filaments. *Carbon* **1989**, *27* (3), 315-323.
177. Kumar, M., Carbon nanotube synthesis and growth mechanism. In *Carbon nanotubes - synthesis, characterization, applications*, Yellampalli, S., Ed. InTech: Rijeka, **2011**; p Ch. 08.
178. Rodriguez, N. M., A review of catalytically grown carbon nanofibers. *Journal of Materials Research* **2011**, *8* (12), 3233-3250.
179. Rodriguez, N. M.; Chambers, A.; Baker, R. T. K., Catalytic engineering of carbon nanostructures. *Langmuir* **1995**, *11* (10), 3862-3866.
180. Han, F.-D.; Yao, B.; Bai, Y.-J., Preparation of carbon nano-onions and their application as anode materials for rechargeable lithium-ion batteries. *The Journal of Physical Chemistry C* **2011**, *115* (18), 8923-8927.
181. Iijima, S., Direct observation of the tetrahedral bonding in graphitized carbon black by high resolution electron microscopy. *Journal of Crystal Growth* **1980**, *50* (3), 675-683.
182. He, C.; Zhao, N.; Shi, C.; Du, X.; Li, J., Carbon nanotubes and onions from methane decomposition using Ni/Al catalysts. *Materials Chemistry and Physics* **2006**, *97* (1), 109-115.
183. He, C. N.; Shi, C. S.; Du, X. W.; Li, J. J.; Zhao, N. Q., TEM investigation on the initial stage growth of carbon onions synthesized by CVD. *Journal of Alloys and Compounds* **2008**, *452* (2), 258-262.
184. Sandford, S. A.; Salama, F.; Allamandola, L. J.; Trafton, L. M.; Lester, D. F.; Ramseyer, T. F., Laboratory studies of the newly discovered infrared band at 4705.2 cm⁻¹ (2.1253 μm) in the spectrum of Io: The tentative identification of CO₂. *Icarus* **1991**, *91* (1), 125-144.
185. Asscher, M.; Kao, C. T.; Somorjai, G. A., High-resolution electron energy loss spectroscopic study of carbon dioxide adsorbed on rhenium(0001). *The Journal of Physical Chemistry* **1988**, *92* (10), 2711-2714.
186. Witko, M., Oxidation of hydrocarbons on transition metal oxide catalysts — quantum chemical studies. *Journal of Molecular Catalysis* **1991**, *70* (3), 277-333.
187. Ruiz Puigdollers, A.; Schlexer, P.; Tosoni, S.; Pacchioni, G., Increasing oxide reducibility: the role of metal/oxide interfaces in the formation of oxygen vacancies. *ACS Catalysis* **2017**, *7* (10), 6493-6513.
188. Livneh, T.; Haslett, T. L.; Moskovits, M., Distinguishing disorder-induced bands from allowed Raman bands in graphite. *Physical Review B* **2002**, *66* (19), 195110.
189. Li, C.; Sakata, Y.; Arai, T.; Domen, K.; Maruya, K.-i.; Onishi, T., Carbon monoxide and carbon dioxide adsorption on cerium oxide studied by Fourier-transform infrared spectroscopy. Part 1.-Formation of carbonate species on dehydroxylated CeO₂, at room temperature. *Journal of the Chemical Society, Faraday Transactions 1: Physical Chemistry in Condensed Phases* **1989**, *85* (4), 929-943.

190. Dresselhaus, M. S.; Dresselhaus, G.; Saito, R.; Jorio, A., Raman spectroscopy of carbon nanotubes. *Physics Reports* **2005**, *409* (2), 47-99.
191. Ferrari, A. C.; Meyer, J.; Scardaci, V.; Casiraghi, C.; Lazzeri, M.; Mauri, F.; Piscanec, S.; Jiang, D.; Novoselov, K.; Roth, S., Raman spectrum of graphene and graphene layers. *Physical review letters* **2006**, *97* (18), 187401.
192. Pinilla, J. L.; Suelves, I.; Lázaro, M. J.; Moliner, R., Kinetic study of the thermal decomposition of methane using carbonaceous catalysts. *Chemical Engineering Journal* **2008**, *138* (1), 301-306.
193. Nemanich, R. J.; Solin, S. A., First- and second-order Raman scattering from finite-size crystals of graphite. *Physical Review B* **1979**, *20* (2), 392-401.
194. Antunes, E. F.; Lobo, A. O.; Corat, E. J.; Trava-Airoldi, V. J.; Martin, A. A.; Veríssimo, C., Comparative study of first- and second-order Raman spectra of MWCNT at visible and infrared laser excitation. *Carbon* **2006**, *44* (11), 2202-2211.
195. Farrusseng, D.; Schlichte, K.; Spliethoff, B.; Wingen, A.; Kaskel, S.; Bradley, J. S.; Schüth, F., Pore-size engineering of silicon imido nitride for catalytic applications. *Angewandte Chemie International Edition* **2001**, *40* (22), 4204-4207.
196. Bradley, J. S.; Vollmer, O.; Rovai, R.; Specht, U.; Lefebvre, F., High surface area silicon imidonitrides: a new class of microporous solid base. *Advanced Materials* **1998**, *10* (12), 938-942.
197. Kurzina, I.; Cadete Santos Aires, F. J.; Bergeret, G.; Bertolini, J. C., Total oxidation of methane over Pd catalysts supported on silicon nitride: Influence of support nature. *Chemical Engineering Journal* **2005**, *107* (1), 45-53.
198. Balan, C.; Völger, K. W.; Kroke, E.; Riedel, R., Viscoelastic properties of novel silicon carbodiimide gels. *Macromolecules* **2000**, *33* (9), 3404-3408.
199. Sardar, K.; Bounds, R.; Carravetta, M.; Cutts, G.; Hargreaves, J. S. J.; Hector, A. L.; Hriljac, J. A.; Levason, W.; Wilson, F., Sol-gel preparation of low oxygen content, high surface area silicon nitride and imidonitride materials. *Dalton Transactions* **2016**, *45* (13), 5765-5774.
200. Hector, A. L., Materials synthesis using oxide free sol-gel systems. *Chemical Society Reviews* **2007**, *36* (11), 1745-1753.
201. Hassan, S.; Hector, A. L.; Kalaji, A., Sol-gel processing of silicon nitride films from Si(NHMe)₄ and ammonia. *Journal of Materials Chemistry* **2011**, *21* (17), 6370-6374.
202. Rovai, R.; Lehmann, C. W.; Bradley, J. S., Non-oxide sol-gel chemistry: preparation from tris(dialkylamino)silazanes of a carbon-free, porous, silicon diimide gel. *Angewandte Chemie International Edition* **1999**, *38* (13-14), 2036-2038.
203. Cheng, F.; Kelly, S. M.; Clark, S.; Bradley, J. S.; Baumbach, M.; Schütze, A., Preparation and characterization of a supported Si₃N₄ membrane via a non-aqueous sol-gel process. *Journal of Membrane Science* **2006**, *280* (1), 530-535.
204. Hassan, S.; Hector, A. L.; Hyde, J. R.; Kalaji, A.; Smith, D. C., A non-oxide sol-gel route to synthesise silicon imidonitride monolithic gels and high surface area aerogels. *Chemical Communications* **2008**, (42), 5304-5306.
205. Hargreaves, J. S. J., Heterogeneous catalysis with metal nitrides. *Coordination Chemistry Reviews* **2013**, *257* (13), 2015-2031.
206. Spivey, J. J.; Dooley, K. M., *Catalysts*. Technology & Engineering: **2007**.
207. Neylon, M.; Choi, S.; Kwon, H.; Curry, K.; Thompson, L., Catalytic properties of early transition metal nitrides and carbides: n-butane hydrogenolysis, dehydrogenation and isomerization. *Applied Catalysis A: General* **1999**, *183* (2), 253-263.
208. Neylon, M. K.; Bej, S. K.; Bennett, C. A.; Thompson, L. T., Ethanol amination catalysis over early transition metal nitrides. *Applied Catalysis A: General* **2002**, *232* (1), 13-21.

209. Krawiec, P.; De Cola, P. L.; Gläser, R.; Weitkamp, J.; Weidenthaler, C.; Kaskel, S., Oxide foams for the synthesis of high-surface-area vanadium nitride catalysts. *Advanced Materials* **2006**, *18* (4), 505-508.
210. Oyama, S. T., Kinetics of ammonia decomposition on vanadium nitride. *Journal of Catalysis* **1992**, *133* (2), 358-369.
211. Cheng, F.; Kelly, S. M.; Lefebvre, F.; Clark, S.; Supplit, R.; Bradley, J. S., Preparation of a mesoporous silicon aluminium nitride via a non-aqueous sol-gel route. *Journal of Materials Chemistry* **2005**, *15* (7), 772-777.
212. Cheng, F.; Kelly, S. M.; Clark, S.; Young, N. A.; Archibald, S. J.; Bradley, J. S.; Lefebvre, F., ammonothermal synthesis of a mesoporous Si-Ti-N composite material from a single-source precursor. *Chemistry of Materials* **2005**, *17* (22), 5594-5602.
213. Cheng, F.; Archibald, S. J.; Clark, S.; Toury, B.; Kelly, S. M.; Bradley, J. S.; Lefebvre, F., Preparation of mesoporous silicon boron imide gels from single-source precursors via a nonaqueous sol-gel route. *Chemistry of Materials* **2003**, *15* (24), 4651-4657.
214. Hassan, S.; Carravetta, M.; Hector, A. L.; Stebbings, L. A., Nonoxide sol-gel synthesis of terbium-doped silicon nitride phosphors. *Journal of the American Ceramic Society* **2010**, *93* (4), 1069-1073.
215. Cheng, F.; Kelly, S. M.; Young, N. A.; Clark, S.; Francesconi, M. G.; Lefebvre, F.; Bradley, J. S., General method of preparation of mesoporous M/Si₃N₄ nano-composites via a non-aqueous sol-gel route. *Chemical Communications* **2005**, (45), 5662-5664.

8 Appendix

Appendix 1

The Rietveld refinement equations were used in GSAS and EXPGUI software

$$t = 505.56 L \sin \theta d \quad \text{or} \quad d = \frac{1.977 \times 10^{-3}}{L \sin \theta} t$$

where t is the total time of flight (μs); L is the total flight path from moderator to sample to detector (m); d is the interplanar spacing (\AA); and θ is half the Bragg scattering angle (2θ).

$$y_i^c = s \sum_i L_k F_k^2 \varphi (2\theta_i - 2\theta_k) P_k A + y_i^b$$

where y_i^c is calculated intensity at point i ; s is phase scale factor; k is miller indices (hkl); L_k contains Lorentz, polarisation and multiplicity factors; φ is profile function; P_k is preferred orientation; A is absorption factor; F_k is structure factor for the K^{th} Bragg peak; y_i^b is background intensity at point i .

$$M = \sum_i W_i (y_i^o - \frac{1}{c} y_i^c)$$

where M is the residual difference between a calculated profile and the observed data; W_i is the statistical weight; c is overall scale factor.

$$R_p = \frac{\sum_i (y_i^o - y_i^c)}{\sum_i y_i^o}$$

where R_p is profile factor, y^o is observed intensity, y^c is calculated intensity

$$R_{\text{exp}} = \sqrt{\frac{(N-C+P)}{\sum_i W_i (y_i^o)^2}}$$

where N is number of observations; P is number of refinable parameters; c is number of constraints and $W_i = \frac{1}{y_i^o}$.

$$R_{\text{wp}} = \sqrt{\frac{\sum_i W_i (y_i^o - y_i^c)^2}{\sum_i W_i (y_i^o)^2}}$$

$$\chi^2 = \left(\frac{R_{\text{wp}}}{R_{\text{exp}}} \right)^2 = \left(\frac{\sum_i W_i (y_i^o - y_i^c)}{N-C-P} \right)^2$$

For a goodness fit χ^2 is equal to 1, however commonly a value less than 5 can be considered as a good fit.

Appendix 2

Table 8.2-1: Evolution of the C/N occupancy of the 16c Wyckoff lattice site in $\text{Co}_3\text{Mo}_3\text{N}$ as a function of reaction at different temperature with 60 ml min^{-1} of 20 vol. % CH_4 in H_2 . Fractional nitrogen and carbon content as determined from the Rietveld refinement against *in-situ* powder neutron diffraction data.

T/ °C	Phase	N % (16c)	C % (16c)	a (Å)	% 331N	% 331C
RT	331N	1.019		11.027	100	0
17-23	331N	1.035		11.029	100	0
24-43	331N	1.008		11.028	100	0
44-67	331N	1.033		11.031	100	0
67-90	331N	1.036		11.033	100	0
92-121	331N	1.042		11.037	100	0
122-157	331N	1.011		11.038	100	0
159-205	331N	0.998		11.042	100	0
207-263	331N	1.007		11.050	100	0
266-331	331N	1.043		11.058	100	0
334-413	331N>+331C	0.975	0.025	11.070	97.50	2.50
418-519	331N>+331C	0.883	0.117	11.077	88.27	11.73
522-580	331N>+331C	0.794	0.206	11.091	79.41	20.59
582-632	331N<+331C	0.152	0.848	11.131	15.24	84.76
634-679	331N<+331C	0.032	0.968	11.142	3.20	96.80
680-684	331C		1.096	11.145	0	100
685-685	331C		0.983	11.145	0	100
685-695	331C		0.981	11.145	0	100
700 °C	331C		0.949	11.145	0	100

Table 8.2-2: analysis of phase fractions of $\text{Co}_6\text{Mo}_6\text{N}$ and $\text{Co}_3\text{Mo}_3\text{C}$ present during the reaction.

T/ °C	Phase	661N % (8a)	331C % (16c)	661a (Å)	331a (Å)	Phase fraction % 661N	Phase fraction % 331C
RT	661N	1.024		10.881		100	0
17-23	661N	1.079		10.883		100	0
24-41	661N	0.964		10.885		100	0
42-68	661N	1.013		10.886		100	0
69-98	661N	0.919		10.891		100	0
100-132	661N	1.009		10.892		100	0
134-171	661N	1.016		10.895		100	0
173-219	661N	1.128		10.899		100	0
221-278	661N	1.074		10.908		100	0
280-347	661N	1.007		10.912		100	0
350-428	661N	1.150		10.924		100	0
433-513	661N	0.950		10.931		100	0
516-572	661N	0.986		10.940		100	0
574-626	661N	0.974		10.950		100	0
628-678	331C>661N	0.967	1.033	10.952	11.119	20.91	79.09
680-728	331C		0.994		11.134	0	100

Table 8.2-3: analysis of phase fractions of Co₃Mo₃N and Co₆Mo₆N present during the reaction.

T/ °C	Time /min	Phase	331N % (16c)	661N % (8a)	331a (Å)	661a (Å)	Phase Fraction% 331N	Phase Fraction% 661N
37-41		331N	0.853		11.039		100.00	0
42-67		331N	0.861		11.040		100.00	0
68-95		331N	0.845		11.041		100.00	0
96-119		331N	0.863		11.043		100.00	0
121-151		331N	0.855		11.048		100.00	0
152-188		331N	0.858		11.051		100.00	0
190-239		331N	0.886		11.056		100.00	0
242-301		331N	0.859		11.064		100.00	0
304-373		331N	0.850		11.072		100.00	0
376-439		331N	0.856		11.081		100.00	0
441-496		331N	0.842		11.089		100.00	0
498-549		331N	0.808		11.095		100.00	0
551-600		331N	0.811		11.104		100.00	0
602-650		331N	0.791		11.115		100.00	0
701-748		331N	0.767		11.133		100.00	0
750-812		331N	0.746		11.143		100.00	0
814-839	10 m	331N	0.746		11.143		100.00	0
839-825	20	331N>661N	0.764	1.236	11.152	10.994	96.33	3.67
824-822	30	331N>661N	0.754	1.246	11.151	10.986	90.59	9.41
822-822	40	331N>661N	0.801	1.199	11.152	10.989	86.66	13.34
822-822	50	331N>661N	0.761	1.239	11.154	10.987	81.29	18.71
822-822	60	331N>661N	0.807	1.193	11.154	10.989	79.02	20.98
822-822	70	331N>661N	0.751	1.249	11.154	10.989	75.61	24.39
822-822	80	331N>661N	1.008	0.908	11.153	10.985	68.72	31.28
822-821	90	331N>661N	0.780	1.220	11.156	10.985	67.50	32.50
821-821	100	331N>661N	1.097	0.903	11.155	10.986	66.67	33.33
821-821	110	331N>661N	0.769	1.231	11.159	10.986	64.75	35.25
821-821	120	331N>661N	0.746	1.254	11.156	10.988	64.75	35.25
821-820	130	661N>331N	0.746	1.254	11.159	10.987	63.38	36.62
820-820	140	661N>331N	0.741	1.259	11.158	10.987	60.39	39.61
820-819	150	661N>331N	0.792	1.208	11.160	10.987	58.27	41.73
819-819	160	661N>331N	0.734	1.266	11.159	10.988	59.71	40.29
819-819	170	661N>331N	0.797	1.203	11.160	10.987	58.62	41.38
819-818	180	661N>331N	0.838	1.162	11.161	10.986	55.24	44.76
818-818	190	661N>331N	0.811	1.189	11.162	10.987	53.58	46.42
817-817	200	661N>331N	0.789	1.211	11.162	10.988	53.74	46.26
817-816	210	661N>331N	0.861	1.239	11.160	10.988	53.32	46.68
816-815	220	661N>331N	0.913	1.087	11.162	10.987	51.37	48.63
433-394		661N>331N	0.895	1.105	11.118	10.943	46.81	53.19

Table 8.2-4: analysis of phase fractions of $\text{Co}_6\text{Mo}_6\text{C}$ and $\text{Co}_3\text{Mo}_3\text{N}$ present during the reaction.

T/ °C	Phase	661C % (8a)	331N % (16c)	661a (Å)	331a (Å)	Fraction % 661C	Phase Fraction % 331N
RT	661C	1.038		10.909		100	0
17-22	661C	1.087		10.911		100	0
23-36	661C	1.025		10.913		100	0
37-59	661C	1.116		10.913		100	0
60-83	661C	1.053		10.915		100	0
84-115	661C	1.056		10.919		100	0
117-157	661C	1.073		10.922		100	0
160-215	661C	1.064		10.928		100	0
218-283	661C	1.044		10.936		100	0
286-359	661C	1.037		10.944		100	0
362-443	661C	1.104		10.953		100	0
447-516	661C	1.155		10.962		100	0
518-573	661C	1.081		10.969		100	0
575-626	661C	1.049		10.975		100	0
628-674	661C	1.104		10.979		100	0
675-681	661C	1.082		10.982		100	0
681-695	661C>331N	1.025	0.975	10.987	11.121	58.16	41.84
695-697	331N>661C	1.170	0.829	10.990	11.121	26.18	73.82
700°C /10 m	331N		0.839		11.123	0	100
30°C	331N		0.908		11.051	0	100

Appendix 3

During the ammonia synthesis reaction, the formation of ammonia was monitored through a drop in the conductivity of a 200 mL of 0.0018 mol l⁻¹ solution of H₂SO₄. This drop relates to the consumption of H⁺ ions by NH₃ and forming NH₄⁺ ions.

To calculate the calibration value which was used for ammonia synthesis rate, the conductivity of six different 0.0018 mol l⁻¹ solutions of H₂SO₄ and (NH₄)₂SO₄ was investigated and listed in the table below:

Conductivity H ₂ SO ₄ / μScm ⁻¹	Conductivity (NH ₄) ₂ SO ₄ / μScm ⁻¹
886	311
881	324
898	329
876	315
894	318
885	327
Mean ca. 887	Mean ca. 321

Number of moles of H₂SO₄ = Concentration (H₂SO₄) x Volume (H₂SO₄)

$$= 0.0018 \text{ mol l}^{-1} \times 0.2 \text{ l} = 3.6 \times 10^{-4} \text{ moles}$$

Due to stoichiometric concerns 2 x 3.6 x 10⁻⁴ moles of ammonia are required to entirely react with H₂SO₄.

The change in conductivity = the mean Conductivity H₂SO₄ – the mean Conductivity (NH₄)₂SO₄ = 887 μScm⁻¹ – 321 μScm⁻¹ = 566 μScm⁻¹

The calibration value = the number of moles of ammonia required/ the change in conductivity

$$= 7.2 \times 10^{-4} \text{ moles} / 566 \text{ μScm}^{-1} = 1.27 \times 10^{-7} \text{ mol} / \text{ μScm}^{-1}$$

Appendix 4

Standard error calculation

To calculate the standard error during this work following points were used:

- Calculate the mean. (M)
- Calculate each measurement's deviation from the mean. (M-i)
- Square each deviation from mean. (M-i)²
- Sum the squared deviations. $\sum(M-i)^2$
- Divide that sum by one less than the data point (n-1). $\frac{\sum(M-i)^2}{(n-1)}$
- Take the square root of the number. That gives you the standard deviation (SD).

$$SD = \sqrt{\frac{\sum(M-i)^2}{(n-1)}}$$
- Divide the standard deviation by the square root of the data points (n). That gives you the standard error (SE). $SE = \frac{SD}{\sqrt{n}}$
- To gives: mean experimental rate $M \pm 1 SE$

Hydrogen formation rate:

Nitrogen was used as an internal standard; calculation of the hydrogen formation rate was performed taking into account the change in volume on reaction, and then data was calculated as follows:

$$\text{Hydrogen formation rate (molH}_2\text{g}^{-1}\text{min}^{-1}) = \frac{\left[\left[\%H_2 * \frac{\left(\frac{N_2 \text{ in}}{N_2 \text{ out}} \right)}{100} \right] * \left[\frac{\text{flow rate ml min}^{-1}}{22400 \text{ ml}} \right] \right]}{\text{Mass of material}}$$

